

Sheffield Hallam University

The effect of nitrogen and inclusions on fracture and fatigue of steel.

CORRIGAN, Martin Robert.

Available from the Sheffield Hallam University Research Archive (SHURA) at:

<http://shura.shu.ac.uk/19502/>

A Sheffield Hallam University thesis

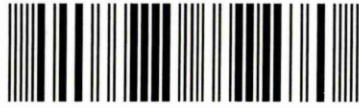
This thesis is protected by copyright which belongs to the author.

The content must not be changed in any way or sold commercially in any format or medium without the formal permission of the author.

When referring to this work, full bibliographic details including the author, title, awarding institution and date of the thesis must be given.

Please visit <http://shura.shu.ac.uk/19502/> and <http://shura.shu.ac.uk/information.html> for further details about copyright and re-use permissions.

101 905 920 6



Sheffield Hallam University
Learning and IT Services
Adsett's Centre City Campus
Sheffield S1 1WB

REFERENCE

ProQuest Number: 10694383

All rights reserved

INFORMATION TO ALL USERS

The quality of this reproduction is dependent upon the quality of the copy submitted.

In the unlikely event that the author did not send a complete manuscript and there are missing pages, these will be noted. Also, if material had to be removed, a note will indicate the deletion.



ProQuest 10694383

Published by ProQuest LLC (2017). Copyright of the Dissertation is held by the Author.

All rights reserved.

This work is protected against unauthorized copying under Title 17, United States Code
Microform Edition © ProQuest LLC.

ProQuest LLC.
789 East Eisenhower Parkway
P.O. Box 1346
Ann Arbor, MI 48106 – 1346

**The Effect of Nitrogen and Inclusions on
Fracture and Fatigue of Steel.**

Martin Robert Corrigan.

A thesis submitted in partial fulfilment of the requirements of
Sheffield Hallam University for the degree of Doctor of Philosophy.

August 2007.



Abstract.

The dynamic strain ageing behaviour of seven heats of C-Mn steel and an interstitial free steel has been examined from 20°C to 350°C, using slow strain rate tests (SSRT's) at strain rates of $2 \times 10^{-6} \text{ s}^{-1}$ and $2.67 \times 10^{-6} \text{ s}^{-1}$. The steels were chemically analysed for the key elements, and additional specialised testing was carried out using internal friction to determine the free nitrogen and carbon content. The effects of temperature on the mechanical properties were investigated in detail. In agreement with previous studies, work hardening peaks, minima in ductility, and negative strain rate dependences of the flow stress were observed between 100°C and 350°C. The positions of which depended on the free nitrogen content and strain rate. It was found that the DSA strengthening due to interstitials was found to be proportional to the log of the free carbon plus free nitrogen.

An investigation has been undertaken to examine the ductility and J_{1C} , dJ/da response of a range of experimental steels containing a range of carbon, nitrogen and sulphur values on 25 mm CT specimens. The tests were carried out at 20°C and 200°C, in the so called blue - brittle range. It was found that the crack initiation resistance J_{1C} and the crack growth resistance dJ/da in the dynamic strain ageing region were 30% - 40% lower than at room temperature. Increasing the sulphur content resulted in a 5% - 10% reduction of these values. With a further reduction of 8% of these values in a 8 ppm DOW environment at 200°C. Environmental testing was done in a chamber specifically designed for the purpose. It was also found that a linear relationship approximates the relationship between the integral of the J vs δa curve and the Charpy upper shelf energy.

From Charpy tests carried out it was found that the Impact Transition Temperature is proportional to the square root of the free nitrogen content, and that a reciprocal type relationship exists between the Charpy upper shelf energy and volume fraction of inclusions. In agreement with previous studies.

Fatigue testing was done at 150°C in air on 11.85 mm thickness specimens. Post test examination of fracture surfaces was carried out using scanning electron microscopy. It is shown that increased levels of free nitrogen and carbon reduced fatigue crack growth rates. This is also confirmed by reduced striation spacing. The effect of interstitials on da/dN is shown to be related to increased yield strength.

A modified Ashby model is presented which enables engineering evaluations of the effect of volume fraction of MnS inclusions (V_f), and free interstitial content (N_f) on the strain to fracture from 20°C to 300°C. When the model was compared to two sets of published data it was found that, within an error bar tolerance of $\pm 20\%$, that 66% and 75% of the data points fell within them.

Statement of Postgraduate Study.

This dissertation is submitted for the degree of Doctor of Philosophy at Sheffield Hallam University. The research work undertaken in this thesis was conducted under the supervision of Professor J.D. Atkinson in the Materials Engineering Research Institute, Sheffield Hallam University.

The work is original to the best of my knowledge, except where acknowledgements and references are made to previous work. Neither this nor any similar dissertation has been or is being submitted for any other degree or any other qualification at any other university.

Part of this work has been presented and published in the public domain.

1. Atkinson, J.D., Corrigan, M.R., Loo-Morrey, M., ***“Recent advances in understanding corrosion fatigue crack propagation in low alloy steels exposed to high temperature water”***, Engineering Integrity Society Meeting, Corrosion Fatigue II, British Aerospace, Bristol, 27th June 2000.
2. Corrigan, M.R., ***“The Environmentally Assisted Crack Growth of Low Alloy Steels, and the Effect of Water on the Ductile Fracture of Steel”***, Poster Presentation, Materials Engineering Research Institute, Open Day, Sheffield Hallam University, January 2001.
3. Atkinson, J.D., Corrigan, M.R., Higgins, A.D., ***“Comparison of Free Nitrogen measurement methods and their relevance to low temperature creep mechanisms”***, I.C.G.E.A.C, Meeting Antwerp, 10th to 15th April 2005.
4. Atkinson, J.D., Corrigan, M.R., Higgins, A.D., ***“The Interaction of Environmentally Assisted Cracking and Dynamic Strain Ageing in C-Mn Piping Steels, 13th International Conference on Environmental Degradation of Materials in Nuclear Power systems”***, Canadian Nuclear Society, 19th to 23rd August 2007, Whistler, British Columbia, Canada.

Acknowledgements.

I acknowledge the support which I have received from Sheffield Hallam University whilst doing this work, particularly from the Graduate Studies Team and the Research Degrees Sub-Committee. Deserving particular mention is my Director of Studies Professor J.D. Atkinson who guided me, and gave me inspiration when it was most needed especially in directing the work. He truly did teach me "*from the ground up*" so to speak guiding me over the difficult times with his inspiration.

I would also like to thank Professor J. Byrne, from the University of Portsmouth, and Dr. S. Hasan from Sheffield Hallam University in offering constructive criticism concerning the manuscript.

An acknowledgement goes to Mr Clive Brashaw for without his expertise some of the testing done in this work would not have been possible. Unfortunately Clive passed away in 2005.

Other people I would like to acknowledge are all the staff in the Aces and the MERI sections of the university. Deserving particular mention are the technicians, Mr. T. O'Hara, Mr. K. Wright, Mr. J. Bradshaw, Mr. T. Earnshaw, and all the staff in the engineering workshops.

Contents.

Abstract.....	i
Statement of Postgraduate study.....	ii
Acknowledgements.....	iii
Chapter 1.	1
1. Introduction.....	1
1.1. Objectives of this study.....	16
Chapter 2.	18
2. Literature Review.....	18
2.1. Elastic Plastic Fracture Mechanics.....	18
2.1.1. The J Integral its Significance and Use.....	20
2.1.2. J Terminology	20
2.1.3. LEFM and EPFM Fracture Mechanics and SCC Testing.....	23
2.1.4. The J Integral and Environmentally Assisted Crack Growth.	29
2.1.5. The Effect of an Elevated Temperature Environment on J_{IC} in Air and Aqueous Environments.	34
2.2. Nitrogen in Steel.	38
2.2.1. Forms of Nitrogen in Steel.	40
2.2.2. Interstitial nitrogen (free nitrogen).	40
2.2.3. Combined nitrogen.	41
2.2.4. Occluded nitrogen	41
2.2.5. The Metallurgical Significance and the Effect of Nitrogen in Steel.	42
2.2.6. Methods available to measure the Nitrogen content of Steel.	49
2.2.7. The Chemical method	49
2.2.8. The Thermal Method.....	50
2.2.9. The Internal Friction method.....	52
2.3. Historical Review of Dynamic Strain Ageing Phenomena in Ferritic Steel.	55
2.3.1. Static Strain Ageing and Dynamic Strain Ageing.....	62
2.3.2. Dynamic Strain Ageing in Iron and Ferritic Steels.	66
2.3.3. Composition effects.....	70
2.3.4. Strain Rate effects.	72
2.3.5. Strain Rate Sensitivity.	74
2.3.5.1. Strain Rate Sensitivity Parameters.	77
2.3.5.2. Transients following a strain rate jump	79
2.3.5.3. Problems encountered in the measurement of Strain Rate Sensitivity Using the Step-ramp Method.	88
2.4. Fatigue Crack Propagation in Metals.....	89
2.4.1. Fatigue Striations.	92
2.4.2. Fatigue crack growth at high ΔK Levels.	98

2.4.3.	Fatigue crack growth at low ΔK levels.....	100
2.4.4.	Crack Closure.....	102
2.4.5.	The Effect of specimen thickness on fatigue crack propagation.....	105
2.5.	Corrosion Fatigue.....	107
2.5.1.	Mechanisms of Corrosion Fatigue.....	107
2.5.2.	Stress - Ratio.....	112
2.5.3.	The Role of Inclusions.....	112
2.5.4.	Crack tip strain rate.....	113
2.5.5.	Estimation of Crack Tip Strain Rate Using the Dugdale Crack Model.....	114
2.5.6.	Summary of section.....	116
2.6.	Ductile to Brittle Transition Temperature.....	119
2.6.1.	Impact Transition Temperature.....	120
2.6.2.	Correlation between Charpy Impact Energy and Fracture Toughness.....	123
2.6.3.	Toughness.....	124
2.6.4.	Effects of Microstructural and Compositional Variables on the Impact Transition Temperature.....	125
Chapter 3.....		126
3. Materials and Experimental Techniques Used.....		126
3.1.	Materials.....	126
3.1.1.	Chemical composition.....	126
3.1.2.	Mechanical Properties.....	126
3.1.3.	Specimen Orientation.....	126
3.2.	Fatigue Testing.....	130
3.2.1.	Specimen preparation.....	130
3.2.2.	Test Equipment.....	131
3.2.3.	Testing Parameters.....	133
3.3.	Fracture Toughness Testing.....	133
3.3.1.	Specimen preparation.....	133
3.3.2.	Test Equipment.....	134
3.3.3.	For testing in water at 200°C.....	134
3.3.4.	Test Parameters.....	136
3.3.5.	Air Testing Rig.....	139
3.3.6.	The Clevises.....	141
3.3.7.	Clip Gauges.....	142
3.3.8.	Loading rates.....	142
3.3.9.	Test Parameters.....	142
3.4.	Constant Extension Rate Testing In Air.....	144
3.4.1.	Specimen preparation.....	144

3.4.2.	Test Equipment.....	144
3.5.	Internal Friction Measurement.	146
3.5.1.	Specimen Preparation.....	146
3.6.	Impact behaviour.....	148
3.7.	Calculation of the Volume Fraction of Inclusions for the VS Steel Heats.....	149
3.7.1.	Microstructure.....	151
3.8.	Determination of the Strain Rate Sensitivity (m).	155
	Chapter 4.....	156
4.	Results... ..	156
4.1.	Internal Friction Results.	157
4.2.	Charpy Testing Results.....	158
4.3.	Fatigue Testing Results (for steel heats F8104 and F8105).	158
4.4.	Strain Rate Sensitivity (m) Results for the F81 series of steel heats.....	158
4.5.	Air Tensile Testing Results.	159
4.5.1.	For steel heats VS3764A and VS3764B.	159
4.5.2.	For steel heats VS3783A and VS3783B.	160
4.5.3.	For steel heats F8104, F8105, and F8106.....	161
4.5.4.	For steel heat Interstitial Free Steel.....	161
4.6.	Fracture Toughness Testing Results. (J_{IC} test results).....	197
	Chapter 5.....	212
5.	Discussion of results.....	212
5.1.	Parameters used to characterise the effect of dynamic strain ageing.	212
5.2.	Discussion of the tensile testing results for VS3764A, VS3764B, VS3783A and VS3783B.....	215
5.2.1.	Discussion of the Ductilities and Flow Stresses for VS3764A, VS3764B, VS3783A and VS3783B.	220
5.2.2.	Discussion of the Effect of Free Nitrogen Content for VS3764A, VS3764B, VS3783A and VS3783B.	222
5.2.3.	Discussion of the Effect of Sulphur Content for VS3764A, VS3764B, VS3783A and VS3783B.	227
5.3.	Discussion of the tensile testing results for F8104, F8105, and F8106.....	230
5.3.1.	Discussion of the effect of free Nitrogen on the Ductilities and Flow Stresses for F8104, F8105, and F8106.....	230
5.3.2.	Discussion of the Effect of Free Nitrogen on the Stress vs Strain curve for F8104, F8105, and F8106.....	233
5.3.3.	Discussion of the Interstitial-Free Tensile Results.	234
5.3.4.	Determination of the Law of $\Delta\sigma_p$ vs Free Nitrogen and Free Carbon.....	242
5.4.	Charpy testing discussion of results.	244

5.4.1.	Discussion of results for VS3764A, VS3764B, VS3783A and VS3783B the effect of sulphur content.....	244
5.4.2.	Discussion of results for VS3764A, VS3764B, VS3783A and VS3783B the effect of free nitrogen content on the Impact Transition Temperature.....	249
5.4.3.	Discussion of results for F8104, F8105 , and F8106.....	252
5.4.4.	Discussion of the results for Interstitial free steel.	268
5.5.	Fracture Toughness Testing (J_{1C}) discussion of results.....	271
5.5.1.	Comparison of Charpy and J Integral Tests.	283
5.6.	Strain rate sensivity (m) discussion of results for the F81 series of steel heats.....	294
5.7.	Fatigue testing- discussion of the results for F8104 and F8105.	298
5.8.	Calculation of the crack tip strain rate for fatigue testing.	299
5.8.1.	Comparison of F8104 and F8105 fatigue crack growth rates with the literature..	303
5.8.2.	Relationship between da/dN and striation spacing for F8104 and F8105.....	307
5.9.	Residual Life Model.....	312
5.9.1.	Fatigue life calculations.....	312
5.9.2.	Residual Life Model part 2.....	319
5.9.3.	The relationship between C_M and m for the F81 series of steel heats.	331
5.9.4.	Model Predictions Compared to Published work.....	336
5.9.4.1.	Model Predictions Compared to Miglen's work [65].....	336
5.9.4.2.	Model Predictions Compared to Wagner's work [48].....	340
Chapter 6.....	344	
6.	Conclusions.	344
Chapter 7.....	348	
7.	Suggestions and further work.....	348
8.	References.	350

Appendices.

Appendix 1.	The J Integral as a fracture parameter.....	372
Appendix 2.	Monitoring of crack growth during mechanical tests.....	374
Appendix 3.	Loading rates and specimen type for references in Figure 14.....	378
Appendix 4.	Apparent negative crack growth.....	379
Appendix 5.	Fatigue data for F8104 and F8105.....	387
Appendix 6.	Micro – mechanisms and Models of Ductile Fracture.....	388
Appendix 7.	The autoclave for environmental J testing.....	398
Appendix 8.	Finite Element Analysis of the strain at the crack tip of a J specimen.....	400
Appendix 9.	Comparison of Wagner's [272] internal friction plot for A48 with this work...	402

List of Illustrations.

Figure 1. A schematic representation of the ductile fracture process in metals [3].	4
Figure 2. The formation of the ductile fracture surface, by internal microscopic necking [3].	5
Figure 3. The effect of sulphur content on Charpy shelf energy [8].	7
Figure 4. The effect of volume fraction (V_f) of inclusions or voids in copper on the true tensile strain at fracture (e_f) [12].	8
Figure 5. The relationship of the strain to fracture (based on reduction of area in a tensile test) as a function of the volume of cementite particles in a spheroidised carbon steel [14].	8
Figure 6. Evolution of Sulphur and Phosphorus content, and associated histograms to steelmaking practice. (A508 and 18 MND5 – 1260 used for French nuclear components) [21].	11
Figure 7. Variation of fracture toughness J_{1C} with temperature for Armco iron [22].	13
Figure 8. Temperature dependence of fracture toughness J_{1C} for A533B class 1 steel [22].	13
Figure 9. Ranges of applicability of LEFM and EPFM for describing fracture behaviour [23].	19
Figure 10. Definition of the J integral in terms of the potential energy difference for cracks of slightly different length [23].	21
Figure 11. Diagram of the relation between δ and knife edge displacement V_q in a bend test [32].	26
Figure 12. Schematic representation of crack tip profile: (a) static crack, (b) growing crack in rigid/plastic material, (c) growing crack in elastic/plastic material.	27
Figure 13. Illustration of the crack tip displacements which accompany small discrete crack extensions.	28
Figure 14. Graph of J_{1C} vs Temperature in Air and Water Environments.	37
Figure 15. The Distribution of Nitrogen in Steel [72].	39
Figure 16. The Influence of Free Nitrogen on Charpy Impact Transition Temperature	45
Figure 17. Influence of Free Nitrogen on Strain Ageing Response [83].	46
Figure 18. The Influence of Nitrogen and Cooling Rate on the Strength and Toughness of Vanadium Steels [83].	47
Figure 19. Effect of passed time after sample preparation and milling size of sample on free nitrogen extraction [89].	51
Figure 20. Effect of extraction temperature on free nitrogen extraction [89].	52
Figure 21. Octahedral interstice in the α iron [91].	53
Figure 22. Elastic after effect in the α iron [90].	53
Figure 23. Effect of grain size on measurement of the solubility of nitrogen in iron.	54
Figure 24. Changes in Mechanical Properties of Low Carbon Steel during strain ageing illustrating four stages of ageing response (Ageing at 60°C) [110].	57

Figure 25. Schematic diagram of the various manifestations of DSA [139].....	63
Figure 26. Flow stress versus deformation temperature curve for a pure metal: the thermal flow stress σ^* and athermal σ_μ , are indicated [140].....	64
Figure 27. Flow stress versus deformation temperature curve for an alloy [93].....	64
Figure 28. Curves illustrating the various serration types [93].....	65
Figure 29. Stress - Strain curves of low carbon rimmed steel of grain size: (a) 0.02 mm, and (b) 0.20mm (strain rate 10^{-4} sec^{-1}) [82].....	68
Figure 30. Variation of LYS and Luders strain with temperature in mild steel [92].	69
Figure 31. Average dislocation density (N) versus plastic shear strain (γ) for a 0.035% C steel deformed in tension at three temperatures. $\dot{\gamma} = 6 \times 10^{-4} \text{ sec}^{-1}$ [102]	69
Figure 32. Effect of nitrogen level on LYS and true stress for 10% and 20 % elongation of iron strained at 225°C [142].....	70
Figure 33. Effect of total nitrogen level on elongation to fracture of iron strained at 225°C [142].	71
Figure 34. Temperature Dependence of the UTS at various strain rates [84].....	72
Figure 35. Temperature and strain rate range over which serrations are observed [84].	73
Figure 36. Both a localized strain gradient (A) and a localized neck (B) are characterized by a higher rate of straining at location 1 and a lower rate of straining at location 2 [276].	75
Figure 37. Strain-rate sensitivity as measured by rapid strain-rate changes during a standard tensile test [276].....	76
Figure 38. The width neck occurring at the maximum load during a tensile test [276].....	77
Figure 39. A Schematic diagram showing how the strain rate sensitivity of the flow stress m was obtained from the load P, versus extension e curve in the differential strain rate test. The load extrapolation method is also indicated [155].	80
Figure 40. Schematic of the two different strain rate sensitivities [156].....	81
Figure 41. Transients following strain rate jumps. [154].....	83
Figure 42. The transient component of the SRS parameter, m_t , as a function of strain. [154]..	84
Figure 43. Negative strain rate sensitivity map in the inverse temperature-strain rate plane [154].....	85
Figure 44. The temperature dependence of the strain rate sensitivity of flow stress m in Zircaloy 2 from room temperature upwards at selected strain rates [155].	86
Figure 45. The strain rate dependence of the strain rate sensitivity of flow stress m [155].....	86
Figure 46. True stress strain curve obtained for a strain rate jump at room temperature [153].	87
Figure 47. Strain rate sensitivity parameter obtained from strain rate jumps [154].....	87
Figure 48. The growth of a fatigue crack as a function of the number of fatigue cycles N [167].	90
Figure 49. Constant load fatigue test (ΔK increasing) [168].....	91

Figure 50. Summary diagram showing the primary fracture mechanisms associated with the sigmoidal variation of fatigue crack propagation rate da/dN with alternating stress intensity ΔK . ΔK_{th} is the threshold stress intensity for crack growth and K_{max} the stress intensity at final failure [169].	92
Figure 51. Diagrammatic representation of striation formation by a plastic blunting process Laird [173].	94
Figure 52. Diagrammatic representation of the formation of striations of saw tooth profile Pelloux [175].	94
Figure 53. Scheme for producing an intrusion [270].	95
Figure 54. Crack extension by alternating shear in a single grooved tensile specimen.[175].	96
Figure 55. The relationship between the rate of crack propagation da/dN and cyclic stress intensity ΔK , for several ferrous alloys [168].	97
Figure 56. Fatigue crack propagation rates of ASTM A533 B-1 steel data from Ramsamooj [183] citing Paris et al.	100
Figure 57. Dark bands of oxide debris formed on fracture surfaces of 2½ Cr -1 Mo steel in region associated with ΔK_{th} [184].	102
Figure 58. Definition of terms in a fatigue cycle affected by crack closure [193].	105
Figure 59. Summarised Data showing the Effect of Temperature on da/dN of RPV Steels [52]	111
Figure 60. Influence of free nitrogen content on impact transition temperature of low-silicon (~0.03%), and silicon-killed (~0.3%), 0.6% Mn steels. [219].	122
Figure 61. Orientation of the specimens for determining mechanical properties.	129
Figure 62. Inclusion orientation in relation to specimen	129
Figure 63. Dimensions of 11.85 mm compact tension specimen (prior to fatigueing):	130
Figure 64. Schematic Diagram of the DCPD Crack Monitoring system.	131
Figure 65. Dimensions of the compact tension specimen used for J testing.	135
Figure 66. Schematic showing control of environmental test rig for J testing.	136
Figure 67. Schematic representation of the circulating loop for J testing.	137
Figure 68. Photograph of environmental J test rig	138
Figure 69. Schematic of the air testing rig.	139
Figure 70. Photograph of rig used for J testing in air from room temperature to 200°C.	140
Figure 71. Photograph of clevises, specimen and clip gauge. Also shown is the thermocouple located on top of specimen.	140
Figure 72. The Clevises and Pins used and a 25 mm Compact Tension Specimen.	143
Figure 73. Dimensions of tensile specimen used for determining the dynamic strain ageing peak ($\Delta\sigma_p$) in air and for SCC work; and "m" the strain rate sensitivity from room temperature to 350°C.	144

Figure 74. The air testing rig for testing tensile specimens used for determining the dynamic strain ageing peak ($\Delta\sigma_p$); and "m" the strain rate sensitivity from room temperature to 350°C.....	145
Figure 75. Specimen for free nitrogen measurement.	146
Figure 76. Apparatus for measuring free nitrogen content by internal friction. The Vibran System.	147
Figure 77. The Equipment used for Charpy Testing.....	148
Figure 78. Positioning of the specimen on the anvil relative to striker.....	149
Figure 79. VS3764A 3D view.....	152
Figure 80. VS3764B 3D view.....	152
Figure 81. Graph of Inclusion Distribution on the three orthogonal planes for VS3764A and VS3764B (L, ST, and T).....	154
Figure 82. Internal friction analysis for VS3764B.....	157
Figure 83. Internal friction analysis for VS3783B.....	157
Figure 84. Graph of Impact Energy absorbed vs Temperature for all the steel heats.	162
Figure 85. Graph of Impact Energy absorbed vs Sulphur content for all VS series of steel heats.	162
Figure 86. Fractograph of Charpy specimen VS3783B temperature -176°C.....	163
Figure 87. Fractograph of Charpy specimen VS3783B temperature 135°C.....	163
Figure 88. Graph of da/dN vs ΔK for steel heats F8104 and F8105	164
Figure 89. Measured striation growth vs Macroscopic (P.D.) da/dN for steel heats F8104 and F8105.....	164
Figure 90. Plan view of F8104 and F8105 after the test.	165
Figure 91. Photograph of specimen F8105 after test. (before being broken open).....	165
Figure 92. SEM photograph of specimen F8104 at 22 mm $\Delta K = 20 \text{ MPa}\sqrt{\text{m}}$	166
Figure 93. SEM photograph of specimen F8105 at 22 mm $\Delta K = 20 \text{ MPa}\sqrt{\text{m}}$	166
Figure 94. SEM photograph of specimen F8104 at 25 mm $\Delta K = 29.48 \text{ MPa}\sqrt{\text{m}}$	167
Figure 95. SEM photograph of specimen F8105 at 25 mm $\Delta K = 29.48 \text{ MPa}\sqrt{\text{m}}$	167
Figure 96. SEM photograph of specimen F8104 at 27 mm $\Delta K = 36.45 \text{ MPa}\sqrt{\text{m}}$	168
Figure 97. SEM photograph of specimen F8105 at 27 mm $\Delta K = 35.63 \text{ MPa}\sqrt{\text{m}}$	168
Figure 98. SEM photograph of specimen F 8104 at 33 mm $\Delta K = 57.39 \text{ MPa}\sqrt{\text{m}}$	169
Figure 99. Graph of m vs strain for F8104 and F8105 for different temperatures.....	170
Figure 100. Strain rate jump test result for F8105 150°C (used for calculation).....	172
Figure 101. Strain rate jump test result for F8105 100°C (used for calculation).....	172
Figure 102. Stress vs Strain results for VS3764A and VS3764B.	174
Figure 103. Charted Load vs Extension curves for VS3764A and VS3764B for the specimens which showed serrated flow.	175
Figure 104. Increase in UTS vs Temperature for VS3764A and VS3764B Steel Heats	176

Figure 105. Reduction in Area (Z) vs Temperature for VS3764 and VS3764B.....	176
Figure 106. Photographs of VS3764A tensile specimens after slow strain rate tests at temperatures of 20°C to 350°C.....	177
Figure 107. Transverse and Longitudinal Results for VS3764A at 200°C.....	178
Figure 108. Comparison of SEM Photographs of VS3764A & VS3764B 20°C.....	179
Figure 109. Comparison of SEM Photographs of VS3764A & VS3764B 200°C	180
Figure 110. Figure 108 D x 2000. (Clearly visible type 1 MnS inclusion).....	181
Figure 111. Figure 109 H x 2000.....	181
Figure 112. Figure 108 D1 x 2000.....	182
Figure 113. Figure 109 H1 x 2000.....	182
Figure 114. Graph of Stress vs Strain for VS3783A.....	186
Figure 115. Graph of Increase in UTS vs Temperature for the VS series of steel heats.....	187
Figure 116. Graph of Reduction in Area (Z) vs Temperature for the VS series of steel heats.	187
Figure 117. Elongation to Fracture vs Free Nitrogen for VS3764A and VS3783A.	188
Figure 118. True Strain to Fracture vs Free Nitrogen for VS3764A and VS3783A.....	188
Figure 119. True strain to Fracture vs Sulphur content for the VS series of steel heats. ...	189
Figure 120. True strain to Fracture vs Volume Fraction for the VS series of steel heats.	189
Figure 121. True Strain to Fracture vs $\sqrt{\text{Volume Fraction}}$ for the VS series of steel heats.....	190
Figure 122. Elongation to Fracture vs Temperature for the VS series of steel heats.....	190
Figure 123. Graph showing the specimens which had maximum Luders deformation and serrations for steel heats F8104, F8105 and F8106.....	192
Figure 124. Elongation to Fracture for steel heats F8104, F8105 and F8106 vs Free Nitrogen.	193
Figure 125. True strain to Fracture vs Free Nitrogen for F8104, F8105, and F8106.....	193
Figure 126. Elongation to UTS and to Fracture vs Temperature for steel heats F8104, F8105 and F8106.....	194
Figure 127. Graph showing Mechanical Properties of Interstitial Free Steel from tensile testing done in air.....	195
Figure 128. Graph showing True strain to fracture vs Temperature for VS3764A, VS3764B VS3783A, VS3783B, F8104, F8105 F8106 and Interstitial Free steel done in air.	195
Figure 129. Increase in UTS vs Temperature for VS3764A, VS3764B, VS3783A, VS3783B, F8104, F8105, F8106, and Interstitial Free steel. (results courtesy of Professor J.D.Atkinson).....	196
Figure 130. Reduction in area vs Temperature for VS3764A, VS3764B, VS3783A, VS3783B, F8104, F8105, F8106 and Interstitial Free steel.....	196

Figure 131. Unloading Compliance Curve for all the VS specimens.....	200
Figure 132. J vs Δa curves for steel heats VS3764A and VS3764B.	200
Figure 133. J vs Δa curves for VS3764A in Air and Water at 200°C.	201
Figure 134. Half sections of specimen J1A (VS3764A 20°C Air).....	202
Figure 135. Half sections of specimen J7B (VS3764B 20°C Air).	202
Figure 136. Half sections of specimen J2A (VS3764A 200°C Air).....	203
Figure 137. Half sections of specimen J11B (VS3764B 200°C Air).	203
Figure 138. Half sections of specimen J3A (VS3764A 200°C Water).	204
Figure 139. Photograph of J3A prior to breaking open (oblique view).....	205
Figure 140. Photograph of J3A prior to breaking open (side view).	205
Figure 141. Photograph of J2A prior to breaking open (oblique view).....	206
Figure 142. Photograph of J2A prior to breaking open (side view).	206
Figure 143. Photograph of J7B prior to breaking open (oblique view).....	207
Figure 144. Photograph of J7B prior to breaking open (side view).	207
Figure 145. Photograph of J1A prior to breaking open (oblique view).....	208
Figure 146. Photograph of J1A prior to breaking open (side view).	208
Figure 147. J1A 20°C Mag x 17 total $V_{LL} = 6.6$ mm $\Delta a = 2.12$ mm.....	209
Figure 148. J7B 20°C Mag x 17 total $V_{LL} = 6.6$ mm $\Delta a = 8.55$ mm.....	209
Figure 149. J7B 20°C Mag x 17 total $V_{LL} = 6.6$ mm $\Delta a = 8.55$ mm.....	210
Figure 150. J2A 200°C Mag x 17 total $V_{LL} = 5$ mm $\Delta a = 5.01$ mm.....	211
Figure 151. J3A 200°C 8ppm DOW Mag x 17 total $V_{LL} = 3.19$ mm $\Delta a = 2.1$ mm.....	211
Figure 152. Log/log plot of true stress-strain curve.	214
Figure 153. Load vs Elongation curves of a 0.035 C steel strained in tension at a crosshead speed of $0.0025 \text{ in min}^{-1}$ (cross sectional area 0.014 in^2 , gauge length 1") [102].	216
Figure 154. Stress vs strain curves (for specimens tensile tested at various temperatures and a strain rate of: (a) $\dot{\epsilon} = 10^{-5} \text{ s}^{-1}$ (b) $\dot{\epsilon} = 10^{-4} \text{ s}^{-1}$ [84].	216
Figure 155. Work hardening exponents vs Temperature for VS3764A, VS3764B, VS3783A and VS3783B compared to Wagner's work [85].	217
Figure 156. Elongation to Fracture vs Temperature for the VS series of steel heats compared to Kim et al [68] and Wagner et al's [85] work.	221
Figure 157. The effect of Nitrogen content on the elongation of iron wire strained in tension [246].	223
Figure 158. Elongation to Fracture of Fe and Fe – 1% Mn base alloys with varying nitrogen contents at (a) 20°C (b) 225°C and (c) 450°C [142].	225
Figure 159. Illustration of the concept of the frontal radius of curvature for voids formed at second phase particles during plastic straining [78].	229
Figure 160. The influence of nitrogen on the hot ductility of a C – Mn – Al – Nb HSLA steel [251].	231

Figure 161. Comparison of increase in UTS for VS3764A, VS3764B, VS3783A, VS3783B, F8104, F8105, F8106 and Interstitial Free steel with refs [68,85].....	232
Figure 162. Work hardening exponents vs Temperature for F8104, F8105, and F8106.....	233
Figure 163. Plots of pct change in ultimate tensile strength vs temperature at strain rates of (a) $6 \times 10^{-6} \text{ s}^{-1}$ (b) $8 \times 10^{-4} \text{ s}^{-1}$ (c) 10^{-2} s^{-1} [94].....	236
Figure 164. Plots of pct change in uniform elongation v testing temperature at strain rates of (a) $6 \times 10^{-6} \text{ s}^{-1}$ (b) $8 \times 10^{-4} \text{ s}^{-1}$ (c) 10^{-2} s^{-1} [94].....	237
Figure 165. Comparison of strain to fracture vs temperature with Sachdev's work.	238
Figure 166. Graph of Reduction in Area vs Elongation to Fracture for all the steels tested. .	239
Figure 167. $\Delta\sigma_p$ vs Free Nitrogen Content for all the steels tested.....	242
Figure 168. $\Delta\sigma_p$ vs Free Nitrogen plus Free Carbon Content for all the steels tested....	243
Figure 169. Results of this work compared with Franklin [249] and Hertzberg [250]	248
Figure 170. Variation in 80 J Charpy transition temperature with weld metal nitrogen content [252].....	250
Figure 171. Effect of Nitrogen on the Brittleness of rimmed steels. [246].	250
Figure 172. Graph of Impact Energy absorbed vs Temperature for F8104 and F8105 steel heats.	253
Figure 173. Graph of Impact Transition Temperature vs $\sqrt{\text{Free nitrogen}}$ based on 27J standard.	257
Figure 174. Graph of Impact Transition Temperature vs $\sqrt{\text{Free nitrogen}}$ based on 50% FATT.	257
Figure 175. Comparison of Impact Temperature vs $\sqrt{\text{free nitrogen}}$ with Mintz's work [219] and Gladman's [256].....	258
Figure 176. Graph of Impact transition temperature vs $\sqrt{\text{free nitrogen plus free carbon}}$	259
Figure 177. Charpy impact energy vs temperature behaviour for several engineering alloys [184].....	259
Figure 178. Strength toughness relationships for bainitic steels [256].....	260
Figure 179. Modes of ductile fracture separation [224].	262
Figure 180. Schematic representation of theoretical models for (a) critical stress controlled model for cleavage fracture and (b) stress modified critical strain controlled model for microvoid coalescence. [260].....	263
Figure 181. The effect of second phase particles on the ductility of steel [78].....	265
Figure 182. The effect of pearlite on toughness measured by Charpy impact transition temperature [239].....	266
Figure 183. Temperature dependence of the Charpy impact energy for an A283 steel [263]	267
Figure 184. True strain to fracture vs the logarithm of the shelf energy for all the steels tested.	268

Figure 185. Portions of unloading compliance traces [65].	271
Figure 186. Load Displacement Curve (temperature 100°C) [48].	272
Figure 187. Load Displacement Curve (temperature 200°C) [48].	272
Figure 188. Compliance curve for specimen J2A.	273
Figure 189. Degradation in J_{IC} and tearing modulus [41].	275
Figure 190. J vs Δa curves and Charpy upper shelf energy for ref [264].	276
Figure 191. dJ/da vs Temperature for VS3764A and VS3764B.	277
Figure 192. J – R curves from Miglen et al [65].	278
Figure 193. Variation in the Tearing modulus and J_{IC} with temperature [68].	279
Figure 194. J vs Δa for F2 forging [265].	280
Figure 195. Charpy upper shelf energy vs area under J vs Δa curve at 8mm (20°C and 200°C).	286
Figure 196. Charpy upper shelf energy vs area under J vs Δa curve at 8mm (50°C and 200°C).	286
Figure 197. Charpy upper shelf energy vs J_{IC} (based on temperatures of 20°C and 200°C and 50°C and 200°C).	287
Figure 198. Slip line fields for a blunted crack tip in plain strain [253].	290
Figure 199. The effect of strength coefficient and work hardening exponent in wire drawing [8].	292
Figure 200. Diagram showing relative fatigue crack propagation behaviour of several materials [184].	300
Figure 201. Monotonic and reversed plastic zone development at tip of advancing fatigue crack [184].	301
Figure 202. Graph of F8104 & F8105 da/dN v ΔK compared with Tseng et al data [245].	304
Figure 203. Graph of F8104 & F8105 da/dN v ΔK compared with Ramsamooj et al work [183] citing Paris et al.	305
Figure 204. Comparison of Huang's work [267] with this work.	306
Figure 205. Correlation between striation spacing, crack growth rate and crack tip opening displacement for C – Mn steel tested in air $R = 0$ [171].	309
Figure 206. Stress Intensity K factor for single edge notched plate [23].	315
Figure 207. C_M vs Temperature and UTS vs Temperature for VS3764A and VS3783A.	322
Figure 208. C_M vs Temperature and UTS vs Temperature for VS3764B and VS3783B.	322
Figure 209. Graph of UTS vs free nitrogen and m vs free nitrogen for the steel heats.	323
Figure 210. C_M vs Free Nitrogen for VS3764A & VS3783A and VS3764B & VS3783B at 20°C and 100°C.	327
Figure 211. Sulphur vs Volume fraction for VS3764A and VS3764B and VS3783A and VS3783B.	329
Figure 212. C_M vs m for F8105 and F8106 at 100°C and 145°C.	331

Figure 213. C_M vs m for F8104, F8105, & F8106 at 100°, 145°, 200°, and 250°C.....	333
Figure 214. Percent reduction of area vs Temperature for the two heats of SA Grade 70 steel Heat 645 and Heat 649. The stars denote serrated flow [65].....	336
Figure 215. Actual True strain to fracture vs Temperature from Miglen et al data [65] compared to True strains to fracture vs Temperature predicted from model.....	339
Figure 216. Variation of Strain to failure vs Temperature for different specimen geometries [48].....	341
Figure 217. Actual True strain to fracture vs Temperature from Wagner et al data [48] compared to True strains to fracture vs Temperature predicted from model.....	343

List of Tables.

Table 1.	Approximate Nitrogen Contents of Commercial Steels [71].	38
Table 2	Familiar Nitrides found in Steel [72].	40
Table 3.	Summary of formulae for Charpy impact transition temperatures (°C) 50% fibre fracture appearance transition, unless otherwise stated [219].	121
Table 4.	Table of Formulae Correlating Charpy Impact Energy with Fracture Toughness [223].	124
Table 5.	Chemical composition of VS series of steel heats and Interstitial free steel and free nitrogen content.	127
Table 6.	Chemical composition of F8104, F8105 and F8106 steel heats.	128
Table 7.	Calculated Volume Fraction for the VS steel heats.	150
Table 8.	Grain size, and Volume fraction of Ferrite and Pearlite for the VS and F81 series of steel heats.	153
Table 9.	Matrix table of steels tested and testing variables.	156
Table 10.	Tabulated results of the strain rate sensitivity for F8104, F8105, and F8106.	171
Table 11.	Tensile testing results for steel heats VS3764A and VS3764B.	173
Table 12.	Tensile testing results for steel heats VS3783A and VS3783B.	183
Table 13.	Comparison of the main mechanical parameters for VS series of steel heats.	184
Table 14.	Tensile testing results for steel heats F8104, F8105, and F8106.	191
Table 15.	Tabulated Fracture Toughness Results.	199
Table 16.	Effect of solutes on flow stress and work hardening rate at a true strain $\epsilon = 0.2$ [78].	213
Table 17.	Composition of the base alloys used in Baird and Jamieson's work [142].	224
Table 18.	Manganese, carbon, and nitrogen contents used in Baird and Jamieson's work [142].	224
Table 19.	Chemical Composition of the Steels studied by Sachdev [94].	235
Table 20.	Mechanical Properties of the steel tested at a strain rate of $2 \times 10^{-4} \text{ sec}^{-1}$ at room temperature [94].	235
Table 21.	Ranked data for elongation to fracture vs reduction in area graph for all the steels tested.	240
Table 22.	Chemical analysis of the five low alloy steels used by Franklin [249].	245
Table 23.	Input values used in the Pickering equation.	251
Table 24.	Observed temperatures vs calculated temperatures using the Pickering equation.	251
Table 25.	Degradation in J_{IC} of the steel heats tested.	274
Table 26.	Chemical composition of SA 106 Gr C steel used by Kim et al [68].	280
Table 27.	Chemical Analysis of Materials studied by Ingham et al [265].	281
Table 28.	Results of testing Programme studied by Ingham et al [265].	281

Table 29. Toughness values for W1 forging [265].	281
Table 30. Comparison of Charpy fracture energy and J-integral data [43].	284
Table 31. Increase in work hardening exponents for VS3764A and VS3764B at 20° and 200°C.	291
Table 32. Tabulated values of the Paris exponent for steel heats F8104 and F8105 in air at R = 0.2.	298
Table 33. Y the compliance function [26].	314
Table 34. Stress Intensity K factors for various loading geometries [26].	315
Table 35. Results from integrated Paris equation for F8104 and F8105.	317
Table 36. Values used to calculate the C_M value in the modified Ashby equation for the VS series of steel heats	321
Table 37. F81 data series values used to plot data in Figure 209.	324
Table 38. Values used to determine C_M for the F81 series of steel heats.	332
Table 39. Chemical composition of SA 515 Grade 70 steel Heats 645 and 649 [65].	336
Table 40. Reduction of area converted to True strain to fracture and compared with model predictions.	337
Table 41. Chemical composition of A48 and MMAW MF48 [48].	340
Table 42. Tabulated results of strains to fracture predicted from model compared to Wagner et al data [48].	343

Nomenclature.

AC	Air-Cooled.
ASME BPV	ASME Boiler and Pressure Vessel Code.
ASTM	American Society of Testing and Materials.
ASTM E 1737	Test Method for Plane Strain Fracture Toughness of Metallic Materials.
BWR	Boiling Water Reactor.
CT	Compact Tension Specimen.
CERT	Constant Extension Rate Test.
CF	Corrosion Fatigue.
CGR	Crack Growth Rate.
COD _{LL}	Crack Opening Displacement at Load Line.
DCPD	Direct Current Potential Drop Method.
DO	Dissolved Oxygen.
DSA	Dynamic Strain Ageing.
EAC	Environmentally-Assisted Cracking.
EPFM	Elastic Plastic Fracture Mechanics.
HCF	High cycle fatigue.
HRC	Rockwell Hardness.
IF	Internal Friction.
LAS	Low Alloy Steel.
LCF	Low Cycle Fatigue.
LEFM	Linear Elastic Fracture Mechanics.
LFCF	Low Frequency Corrosion Fatigue.
LWR	Light Water Reactor.
NDT	Non-Destructive Testing.
PWR	Pressurized Water Reactor.
RPV	Reactor Pressure Vessel.
SCC	Stress Corrosion Cracking.
SEM	Scanning Electron Microscopy.
SRLT	Slow Rising Load Test.
SSRT	Slow Strain Rate Test.
SSY	Small Scale Yielding.
UTS	Ultimate Tensile Strength.
YS	Yield Strength.

Designations.

Symbol	Unit	Designation
Δa	mm	Crack advance.
a	mm	Crack length.
a_o	mm	Initial crack length.
a_f	mm	Final crack length.
da/dN	$\mu\text{m}/\text{cycle}$	Crack advance per fatigue cycle.
da/dt	m/s	Time-based crack growth rate: time-derivate of $a(t)$.
δ	mm	Crack opening displacement.
δ_{tip}	mm	Crack opening displacement at the crack tip.
ε	%	Engineering strain.
ε_f	$\text{Ln}(A_o/A_f)$	True fracture stress.
ε_T	$\text{Ln}(1 + \varepsilon)$	True strain.
E	GPa	Young's Modulus.
ΔK	$\text{MPam}^{1/2}$	Total stress intensity factor range $\Delta K = K_{\text{max}} - K_{\text{min}}$
ΔK_{th}	$\text{MPam}^{1/2}$	ΔK threshold for fatigue.
K	$\text{MPam}^{1/2}$	Stress intensity factor.
K_{max}	$\text{MPam}^{1/2}$	The maximum value of K .
K_{min}	$\text{MPam}^{1/2}$	The minimum value of K .
K_{1C}	$\text{MPam}^{1/2}$	Plane strain fracture toughness [27].
K_c	$\text{MPam}^{1/2}$	Plane strain fracture toughness using Forman et al [181] and Heald et al [182] notation.
K_{cl}	$\text{MPam}^{1/2}$	The stress intensity value due to crack closure using Austen's notation [193].
K_{op}	$\text{MPam}^{1/2}$	The stress intensity value due to crack closure using Hertzberg's [184] and Elber's [185] notation.
K_{eff}	$\text{MPam}^{1/2}$	$K_{\text{eff}} = K_{\text{max}} - K_{cl}$
P	Kn	Load.
R	-	Load ratio $R = K_{\text{min}}/K_{\text{max}}$
σ	MPa	Applied stress.
σ_p	MPa	Peak strengthening stress, the difference of the peak tensile strength and the tensile strength on the base line at the corresponding temperature. The baseline can be deemed to be the tensile strength without the influence of DSA for a given strain rate.

Designations.

Symbol	Unit	Designation
σ_{uts}	MPa	Ultimate tensile stress.
σ_y	MPa	Yield stress.
m	-	Strain rate sensitivity.
n	-	Strain hardening exponent.
ν	-	Poissons ratio.
T	° C	Temperature.
Z	%	Reduction of area.

Chapter 1.

1. Introduction.

One of the most important and key concepts in the entire field of Materials Science and Engineering is fracture. In its simplest form, fracture can be described as a single body being separated into pieces by an imposed stress. For engineering materials there can only be two possible modes of fracture, ductile and brittle. In general, the main difference between brittle and ductile fracture can be attributed to the amount of plastic deformation that the material undergoes before fracture occurs. Ductile materials demonstrate large amounts of plastic deformation while brittle materials show little or no plastic deformation before fracture. Crack initiation and propagation are essential to fracture. The manner through which the crack propagates through the material gives insight into the mode of fracture. In ductile materials the crack moves slowly and is accompanied by a large amount of plastic deformation. The crack will usually not extend unless an increased stress is applied. On the other hand in brittle fracture, cracks spread at the speed of sound with little or no plastic deformation.

Cracks that propagate in a brittle manner will continue to grow and increase in magnitude once they are initiated. Another important feature of crack propagation is the way in which advancing cracks travel through the material. In an aqueous environment, depending on the specific conditions, material is corroded away, thereby aiding the fracture mechanism. This is due to such things as the temperature, dynamic strain ageing, oxygen, nitrogen, and hydrogen content, strain rate and the aggressiveness of the species present in the aqueous environment.

On both the microscopic and macroscopic levels, ductile fracture surfaces have distinct features. Macroscopically ductile fracture surfaces have larger necking regions and an overall rougher appearance than a brittle fracture surface. On the microscopic level, ductile fracture surfaces also appear rough and regular.

In body centred cubic (BCC) and face centred cubic (FCC) polycrystalline

metals of very high purity, the absence of inclusions and second phase particles leads virtually to a complete absence of microvoids in any sustained process of plastic flow. Under these conditions a uniaxial tension specimen will usually fail by virtually 100% reduction in area of the external neck that develops when the specimen becomes plastically unstable [1]. However, all engineering metals and alloys contain inclusions and second-phase particles, to a greater or lesser extent, and this leads to microvoid nucleation and growth, which is terminated at a very much earlier stage in a tension test by a localised internal necking of the intervold matrix across a sheet of microvoids [2,3]. Under these conditions ductile fracture occurs in tension specimens at approximately 70% reduction in area of the external neck, by the classical 'cup and cone' fracture mechanism. The general effect of an increasing volume fraction V_f of inclusions or second-phase particles is to reduce both the true fracture strain $\epsilon_F = \ln(A_0/A_f)$ and the % reduction in area $RA = 100(A_0 - A_f)/A_0$ where A_0 and A_f , are the original and final cross-sectional areas of the specimen-neck region.

Much attention has been devoted recently to brittle fractures in metals. In these, the macroscopic plastic deformation preceding fracture is extremely small, although failure may be due to small amounts of highly localised plastic deformation [4]. In other materials large amounts of macroscopic plastic deformation can precede fracture, as in the tensile straining of ductile metals, and although these failures may not be so dangerous from an engineering standpoint, they are of considerable fundamental and practical interest.

To explain the fact that common ductile metals normally show less than 100% reduction in area at fracture and begin to crack internally, much attention has been focused on the importance of second-phase particles, particularly hard non-metallic inclusions [5,6]. Such particles can act as barriers against which dislocations can pile up, and this leads to a concentrated local stress which is difficult to relieve owing to the hard nature of the obstacle. The stress can build up until the theoretical strength of the interface between inclusion and matrix is exceeded, so that a crack forms and then grows by plastic deformation. Many such cracks link together to produce macroscopic failure by internal necking.

The ductile fracture of metals generally occurs by the formation and subsequent growth and coalescence of voids or cavities. If cavity nucleation could be delayed or suppressed altogether, large increases in ductility could be achieved.

The mechanism of ductile fracture consists of three principal stages [2].

1. The nucleation of microvoids, at the sites of second phase particles or inclusions, when the plastic deformation of the matrix has elevated the particle matrix interface stress to the level where they crack or debond from the matrix.
2. The extensional and dilational growth of the microvoids under the applied plastic stress and strain field, to the point where the intervoid matrix reaches its plastic limit load.
3. Plastic limit load failure of the intervoid matrix, across a sheet of microvoids, when a catastrophic process of internal microscopic necking causes localised plastic failure and separation of the intervoid matrix. (see Figures 1 and 2).

Other factors affecting the nucleation, growth, and coalescence process, are the geometry of the specimen, the mode of loading, the load history, the orientation of the specimen, its toughness and strength and the temperature at which the tests are carried out.

It is now well established that inclusions play an important part in the ductile rupture of metals. These inclusions are the sources of the cavities which grow by plastic deformation and link together to produce dimpled rupture. Most of the models proposed for cavity nucleation use the same postulation, that cavity formation takes place at a critical stress σ_C (see Appendix 6).

According to Thomason [3], the models of nucleation suggest that in general increased temperatures and reduced strain rates, which are likely to promote local recovery at particle sites, will reduce the maximum interface stress σ_T , thus making it more difficult to achieve the condition $\sigma_T = \sigma_C$ for decohesion at the particle matrix interface. This is in broad agreement with experimental results which show that microvoid nucleation is generally reduced by elevated temperatures and lower strain rates, and can virtually be eliminated at high homologous temperatures to give tensile failure by complete rupture (or

the 100% reduction in area of an external neck). It follows from the inverse effects of temperature and strain rate on the magnitude of the material flow stress, that increased strain rates and reductions in the test temperature should promote microvoid nucleation and this also is in broad agreement with experiment [3].

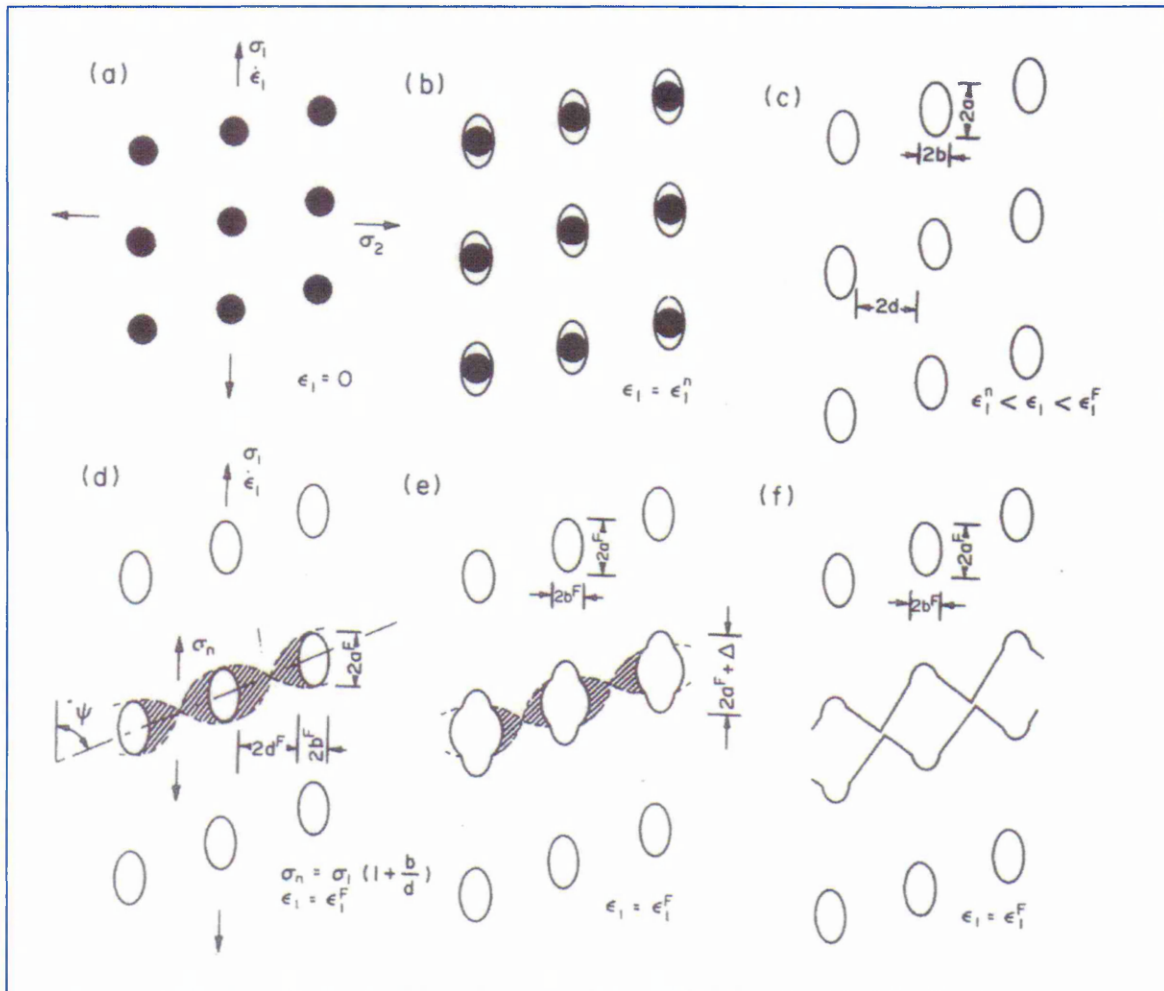


Figure 1. A schematic representation of the ductile fracture process in metals from the undeformed state (a), through microvoid initiation (b), and growth (c), to the three principal stages of fracture surface formation (d), incipient microvoid coalescence (e), internal microscopic necking and (f), knife edge separation [3].

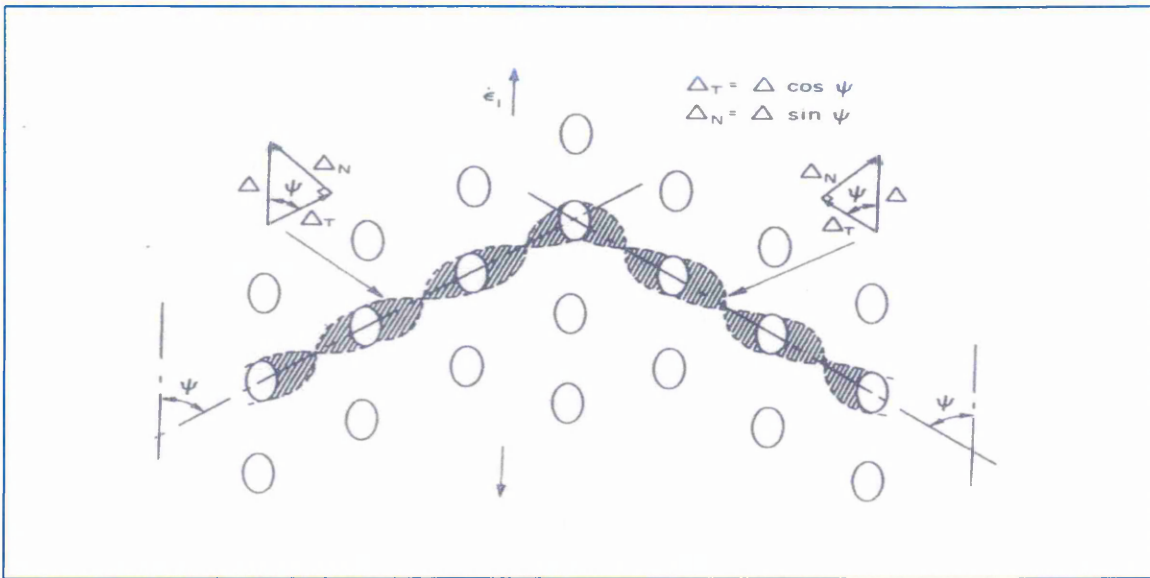


Figure 2. The formation of the ductile fracture surface, by internal microscopic necking along the characteristic Σ orientations Ψ showing the jump or discontinuity Δ in the velocity gradients across the incipient fracture surface and the compatible normal Δ_N and tangential Δ_T components [3].

Once microvoids have been nucleated at the sites of particles and inclusions the subsequent growth of the voids is likely to be influenced by temperature and strain rate primarily through their effect on the material yield stress and work hardening rate. Restricting attention to the temperature range 0.1 to 0.7 T_m and strain range 10^{-4} and 10^3 sec^{-1} , where inertia and stress wave effects are negligible, it can be broadly assumed that increased temperature and reduced strain rates will tend to reduce both the material yield stress and work hardening rate. This suggests that increased temperatures and reduced strain rates will promote the growth of microvoids, whilst the reverse effect will tend to reduce microvoid growth rate [2,3].

A departure from the normal inverse relationship between the effects of increasing strain rate on a materials flow stress is found in the temperature range 200°C to 400°C for low carbon steels. This is the so called **blue brittle** range where dynamic strain ageing effects have a strong influence on the material flow stress, (this is discussed in section 2.3).

Strain ageing occurs in both iron and steel owing to elastic interactions between interstitials and dislocations resulting in strong dislocation pinning. Two types of strain aging can be characterised.

- (i). Static strain aging – where the aging process takes place after pre-straining.
- (ii). Dynamic strain aging – where aging is sufficiently rapid to occur during straining. Dynamic strain aging occurs when the rate of straining is such that the interstitials can diffuse and pin the mobile dislocations, and serrations appear because of a rapid generation of new dislocations, which are needed to sustain plastic flow.

The microvoid nucleation problem is greatly complicated by a range of particle types that can exist in a commercially produced alloy system and this can result in a variety of microvoid nucleation mechanisms operating simultaneously; for example in alloy steel systems, there can exist a wide range of carbide, oxide, sulphide and nitride particles and in the hot working production process the hard oxide inclusions (such as aluminium oxide) retain their spheroidal shape, while the softer sulphide inclusions become slightly elongated in the direction of working. In addition in carbon steels, a substantial proportion of the carbides are insoluble in the austenite matrix at the hot working temperatures and these primary carbides are subjected to severe damage and fragmentation in the course of the hot working process. Consequently the larger oxides, sulphides and *primary* carbides in primary steel systems are likely to be in a partially damaged state at the end of the steel production process, and this might consist of partial debonding of the particle matrix interface or partial internal cracking of the hard particles. Hence in the case of steels, only the *secondary* spheroidal carbides, precipitated from the austenitic phase by quenching and tempering treatments, can be regarded with any confidence as undamaged and strongly bonded to the matrix [2,3].

The detrimental effects of non metallic inclusions on the ductility and toughness of both cast and wrought steels are now well established. The important features of the inclusion dispersion which can affect toughness are the shape, size and distribution of the inclusions and their total volume fraction.

When distributed within any steel matrix, they can influence the

mechanical properties in three basic ways [7].

- (1). They provide an easy fracture path through which the crack can extend.
- (2). They provide initiation sites for fracture.
- (3). They reduce the cross sectional area of load supporting material.

Such effects of non-metallic inclusions can be greatly amplified when segregation effects are considered because such effects can greatly increase the non-metallic inclusion density.

It has been found that a reciprocal type of relationship between toughness and inclusion volume fraction has been found for many inclusion systems [9,10] (see Figure 3). Likewise a similar behaviour has been observed for the effect of volume fraction on tensile ductility [11-17] (see Figure 4) and plane strain fracture toughness [18].

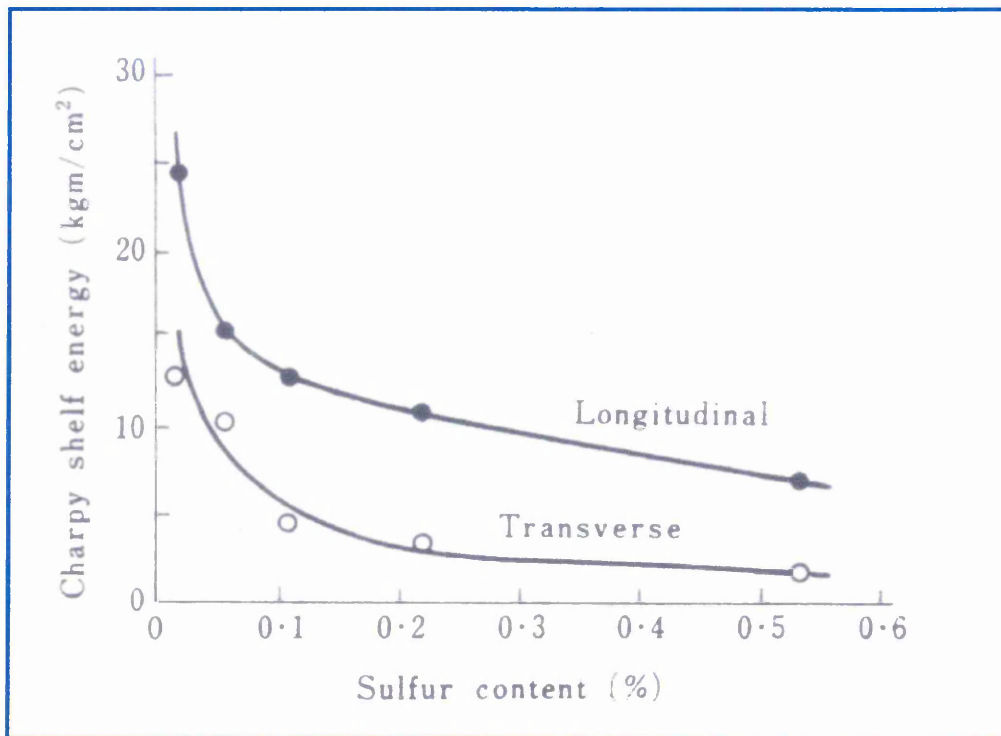


Figure 3. The effect of sulphur content on charpy shelf energy [8].

Where inclusions dominate the fracture behaviour the mechanism of fracture is almost invariably microvoid formation, due to the decohesion of the inclusion matrix interface, followed by void coalescence. Consequently it might be expected that the strength of the particle matrix bond would have a prominent effect on the fracture behaviour. In the case of carbide particles in

steel which are strongly bonded to the matrix [11]. The collated work of references 11, 12, 14, and 17 are shown in Figure 5 which is taken from reference 14.

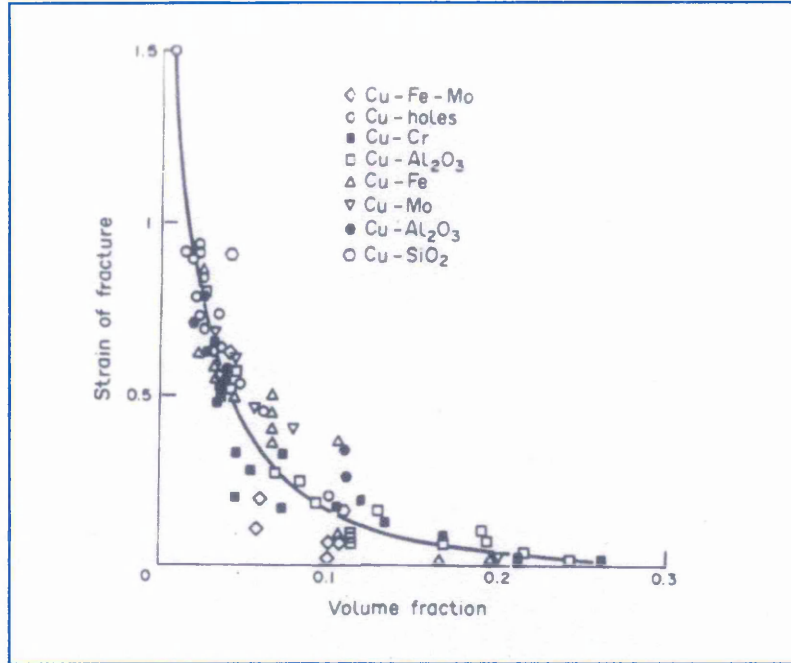


Figure 4. The effect of volume fraction (V_f) of inclusions or voids in copper on the true tensile strain at fracture (ϵ_f) [12].

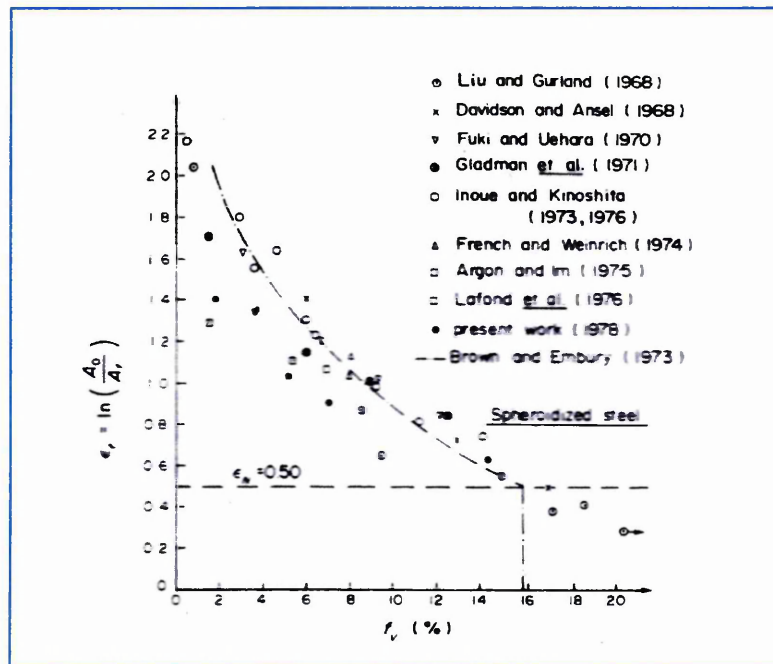


Figure 5. The relationship of the strain to fracture (based on reduction of area in a tensile test) as a function of the volume of cementite particles in a spheroidized carbon steel [14].

From the point of view of void initiation Ashby's model [14,15] predicts an inverse relationship between inclusion size and the stress required for void initiation, and this tends to be confirmed by Palmer's [16] observations of voids associated with very small SiO₂ particles in copper. This was quantified by Atkinson [17, 269] and Thomason [3].

The steels used for the construction of pressure vessels, boilers and steam water piping viz.; Mn - Ni - Mo, C - Mn, Cr - Mo grades are noted for their combination of strength ($\sigma_y \sim 400$ MPa, $\sigma_{UTS} \sim 600$ MPa) and fracture toughness (around 120 - 200 MPam^{0.5}). Above 50°C the failure mode is ductile, involving nucleation of voids around non metallic inclusions.

The main inclusions to be found in reactor pressure vessel steels are manganese sulphide inclusions, and these are usually the sites where cavity nucleation takes place. The toughness of steel is dependent on the inclusion volume fraction, from Figures 3, 4 and 5 it can be seen that as the volume fraction is decreased the toughness increases.

Major occurrences in the nuclear power industry have contributed to improved steel cleanliness in the manufacture of it from a metallurgical point of view. An extensive inspection program was conducted after the catastrophic rupture of a turbine disc in the Hinkley point 'A' nuclear power plant, and cracks were found in 124 discs and another 50 British rotors [19,20]. Cracking in turbine discs of power plants in many countries was reported later [20]. It was generally agreed that the mechanism responsible for the cracking was stress corrosion cracking (SCC) [19,20].

To ensure adequate tolerance to postulated defects under normal reactor operation and faulted conditions, these materials must exhibit a high resistance to ductile crack growth. Traditionally, this resistance has been assessed using notched impact testing (Charpy tests), and much of our understanding of the microstructural control of ductile fracture in steels has come from this type of test. In particular, the inverse relationship between inclusion content (sulphides + oxides) and upper-shelf (that is totally ductile) fracture energy has long been

recognised.

Over the past 25 years there have been advances in both material fabrication and toughness assessment techniques. Secondary steelmaking and vacuum deoxidation now provide steels with low inclusion content and bulk sulphur levels less than 0.002 percent by weight [21]. The example chosen is taken from the French Nuclear Power Industry (Creusot – Loire Industrie). Figure 6 shows the reductions in sulphur and phosphorus content in the steel used in their Nuclear Power plants from 1972 to 1990. The graphs in Figure 6 show the evolution of sulphur and phosphorus content for steel A508 Cl3, and 18MND -1260. The associated histograms and the text APC graph denotes the use of a secondary refining facility, which allows them to perform vacuum treatment and stirring of the steel by argon blowing. The modifications made to their steel making processes have led to much lower sulphur and phosphorus contents as can be seen from Figure 6. It also resulted in a significant decrease in the gas content of the steel for nitrogen, hydrogen and oxygen. This trend in the steelmaking process has been followed on a global scale, to improve the safety of the power plants, and to reduce the construction and operating costs, for a given safety level.

Many investigations have been devoted to the study of ductile tearing, which takes place in the upper shelf region in low and medium strength steels. In those materials the methodology derived from linear elastic fracture mechanics cannot be employed.

Fracture mechanics has evolved to embrace quantitative defect assessment, where fracture is preceded by large-scale plasticity. The J integral test is the most developed of the post-yield fracture tests and is capable of quantifying changes in material resistance during the initial stages of crack extension.

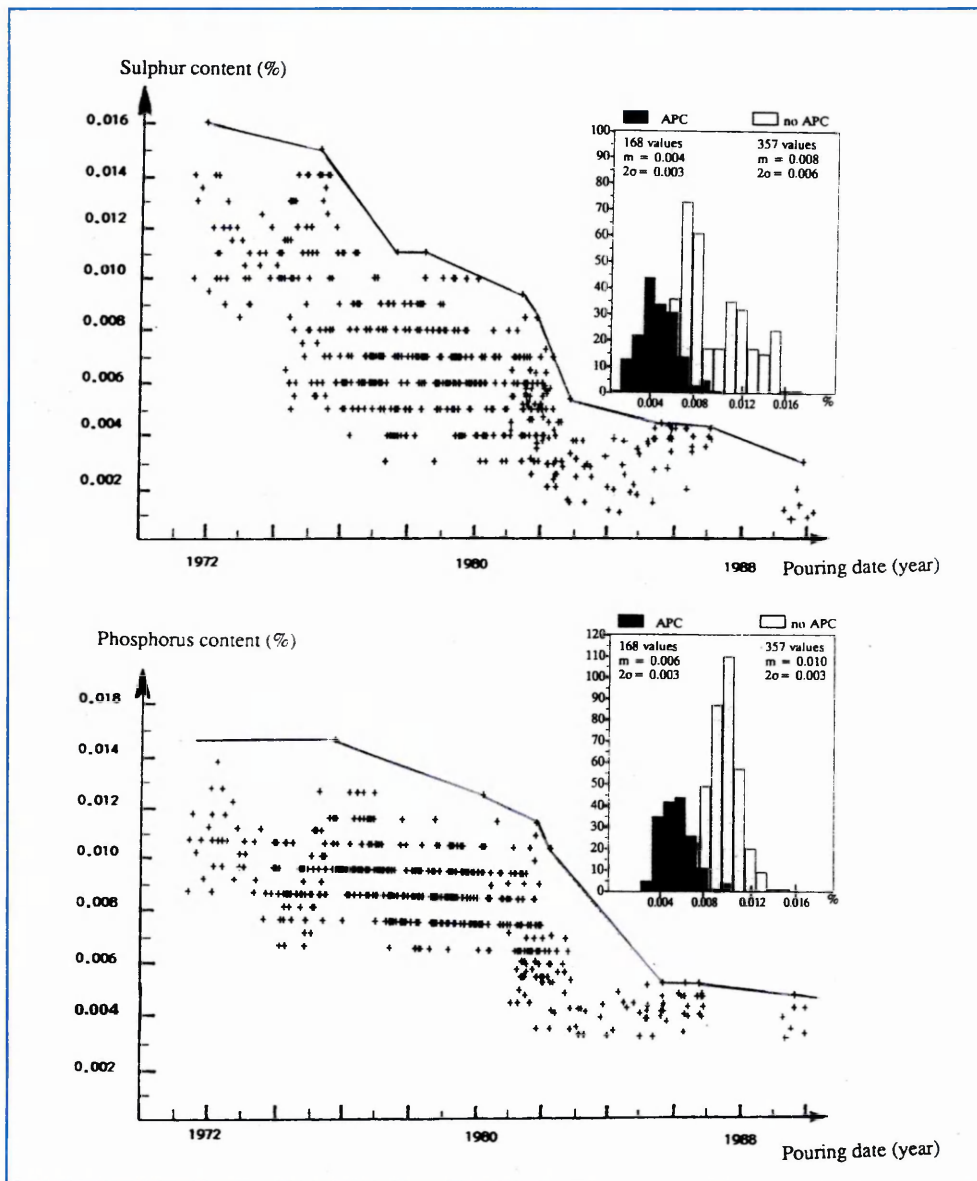


Figure 6. Evolution of Sulphur and Phosphorus content, and associated histograms to steelmaking practice. (A508 and 18 MND5 – 1260 used for French nuclear components) [21].

Metallic materials and alloys in general show a decrease in strength with an increase in temperature. At the same time ductility increases and rate effects become pronounced. Exceptions to this behaviour are usually limited to certain temperature regions. Examples are regions of strength increase with temperature increase, serrated flow and negative or zero rate sensitivity. Collectively these phenomena are called dynamic strain aging.

The flow stress decreases with an increase in loading rate when negative

rate sensitivity is present whereas normally the flow stress increases. The expression 'flow stress' refers to the stress in the region of a stress-strain diagram where inelastic flow is fully established and where the tangent modulus is much smaller than the elastic modulus.

The term 'Portevin Le Chatelier' effect is usually, but not always, reserved for the observation of serrated flow, which in turn seems to imply the strain-aging phenomenon. Dynamic strain aging is found in certain temperature regions for solid solution alloys, in carbon steels, in ferritic steels and in virtually every alloy designed for high temperature service. It is generally attributed to the attachment and breaking loose of interstitial or solute atoms such as nitrogen, from crystals and their interaction with dislocations. As the stress increases, the dislocations break loose, travel and become re-attached. This process gives rise to the observed jerky motions.

Pipes plates and associated welds in carbon manganese steels, are commonly used for the secondary systems (feedwater line and steam line) of pressurised water reactors. These steels are well known to be sensitive to dynamic strain aging (DSA) when insufficiently killed. This phenomenon, which is observed in metals dislocations, induces an increase in flow stress, ultimate tensile strength (UTS) and work hardening rate, as well as a decrease in ductility (elongation, reduction of area, strain rate sensitivity coefficient and fracture toughness).

In C - Mn steels, it is well established that the diffusing solute species are interstitial carbon and nitrogen atoms. Moreover, due to its greater solubility limit nitrogen content seems to exert a more pronounced influence on strain aging than carbon content. Depending on the diffusion coefficients, the chemical composition of the steels and the strain rate, DSA occurs in the temperature range 200° - 350°C.

From the literature review in chapter 2 it can be seen that in commercial C - Mn steels sensitive to DSA (base metals and deposited metals) and at normal strain rate tests, the fracture toughness (crack initiation resistance J_{1C}

and tearing modulus dJ/da) decreases from room temperature to about 200°C, and then increases for higher temperatures. This behaviour is also observed in low alloy steels sensitive to DSA.

This detrimental effect of DSA on ductile tearing resistance does not occur in all iron base materials. Srinivas et al [22] show the opposite behaviour in pure armco iron, i.e. the fracture toughness (crack initiation resistance and tearing modulus) increases from room temperature to 200°C and then decreases see Figures 7 and 8. However, this material shows the same DSA effect as other materials on tensile properties (i.e. a maximum in UTS and work hardening rate, a minimum in elongation and reduction of area). This different behaviour is attributed to the absence of inclusions in pure iron which modifies the ductile damage mechanism as discussed earlier.

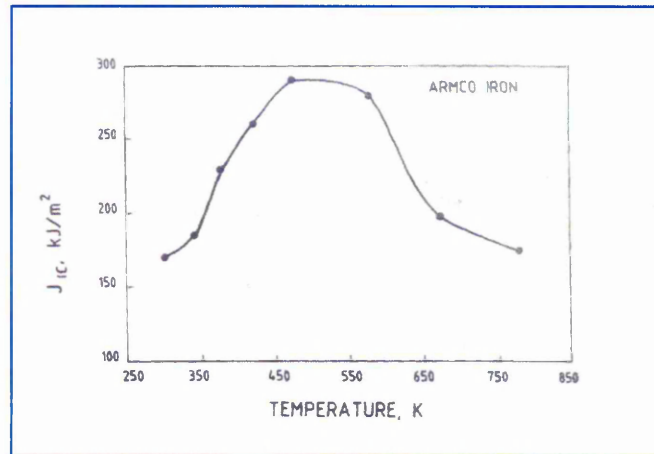


Figure 7. Variation of fracture toughness J_{1C} with temperature for Armco iron [22].

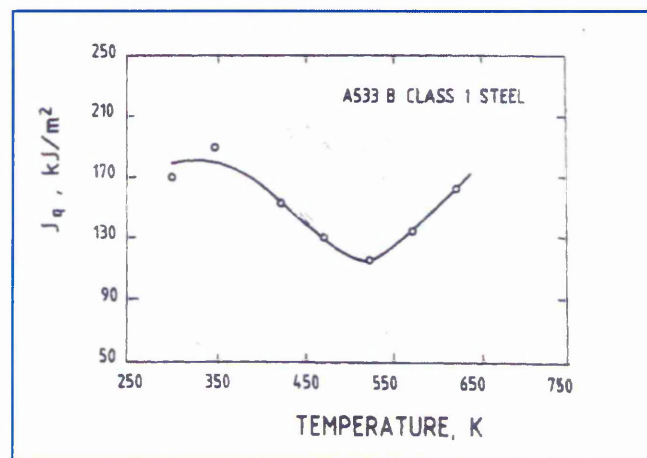


Figure 8. Temperature dependence of fracture toughness J_{1C} for A533B class 1 steel [22].

When a material fails during tensile deformation it is either the result of unstable plastic flow or a consequence of the growth and interlinkage of internally nucleated voids. In the former process, inhomogeneities in the cross sectional area of a test piece lead to a localised increase in the strain rate and the difference in the cross sectional area increases. The rate at which the discontinuity in the cross sectional area increases depends on both the rate of strain hardening and the strain rate sensitivity. In superplastic materials, where true strain hardening is minimal, any neck which is present will always grow, although the rate of growth decreases with increasing strain hardening. Unstable plastic flow normally results in the material pulling out to a fine point prior to failure. Where failure occurs as the result of the nucleation, growth and interlinkage of internal voids, the fracture surface is much more abrupt. The value of the strain rate sensitivity is important in determining the rate at which the voids grow and thus to some extent controls the elongation to failure [2,3].

In engineering components subject to cyclic loading fatigue crack initiation and propagation are important precursors to fracture. For pre-existing defects, for example in welded regions stable crack growth is observed to occur at cyclic stresses as low as 10% of the level required to cause fracture, and fatigue crack growth normally precedes fracture.

In the mid ΔK or Paris region, in some cases, it has been observed that there may be a one to one correlation between da/dN and the regular spaced markings on the fracture surface perpendicular to the growth direction. In the threshold region striations may not be visible, and at high ΔK values non striation modes of crack advance such as void coalescence and cleavage are often present.

Models of striation formation and stage 2 fatigue crack growth have been proposed by numerous authors, and they indicate that small scale plasticity at the crack tip at K_{max} is converted to small increments of crack growth at K_{min} . This is the plastic blunting model of fatigue crack growth. In its simplest form this model predicts a relationship between da/dN and the crack tip opening displacement (CTOD) [183].

$$\frac{dc}{dN} = \frac{0.041}{EY} (\Delta K_1 - \Delta K_{th})^2 \frac{1}{1 - \left(\frac{K_{1max}}{K_{1c}} \right)^2} \quad (1)$$

where; E = Young's Modulus, Y = yield strength.

Hence crack growth rates should be inversely proportional to alloy strength.

The carbon steels, low alloy steels and stainless steels, that are used in nuclear reactors, all experience a reduction in the fatigue life as the loading strain rate is decreased. While it is agreed that most of this reduction is due to the influence of the aqueous environments that exist in these reactors, there may be other factors that also contribute to this. This study examines the influence of dynamic strain aging on this fatigue behavior in air.

In the dynamic strain ageing regime the flow stress and work hardening behavior are strain rate and temperature dependent [52,53]. This is due to the high mobility of C and N atoms that interact with dislocations, impeding their motion. This causes the flow stress to increase as the strain rate decreases.

Lowering the strain rate of a fatigue test produces several important responses. The stress required to produce the control strain can increase or decrease. The fatigue life can also be altered [184]. The question here is whether or not the influence of strain rate on the stress is also important in controlling the fatigue life.

The steels used for the construction of pressure vessels, boilers and steam water piping viz.; Mn - Ni - Mo, C - Mn, Cr - Mo grades are noted for their combination of strength ($\sigma_y \sim 400$ MPa, $\sigma_{UTS} \sim 600$ MPa) and fracture toughness (around 120 - 200 MPam^{0.5}). Above 50°C the failure mode is ductile, involving nucleation of voids around non metallic inclusions. This necessitates the use of the J contour integral for the assessment of fracture rather than the LEFM term, the stress intensity factor, K. The two are related:

$$J = \frac{K_1^2}{E} (1 - \nu^2) \quad (2)$$

where ν = Poisson's ratio.

this is for plane strain conditions. Paris et al [34,40] showed how the tearing

modulus (T) could be measured during a fracture resistance test in which J vs Δa_T curves are constructed (where Δa_T is the length of the ductile tear which has grown from an initially blunted crack in a ductile alloy).

$$T = (dJ/da)(E/\sigma_y^2) \quad (3)$$

A number of studies of the fracture of Mn - Ni - Mo and C - Mn steels have reported a considerable reduction (up to 40%) in J_{IC} and dJ/da around 200° - 250°C. This is often attributed to the blue brittleness phenomenon, which is also apparent in tensile tests.

Two studies have revealed changes in J_{IC} and dJ/da in high temperature water at 243°C and 288°C, both accompanied by a change in fracture mode to "quasi - cleavage" like. Detailed examination of the crack tips were not made and the test conditions used (100 ppb DO_2) were not necessarily producing the maximum effect.

1.1. Objectives of this study.

The objectives of this thesis was to assess the role of free nitrogen in dynamic strain ageing and ductile fracture processes. This was achieved by doing tensile, J, Charpy V notch and fatigue testing with specially prepared experimental steels using variable aluminium additions to control the free nitrogen. Which was measured by internal friction methods. The J specimens were made as 25 mm CT specimens.

Limited fatigue tests on controlled nitrogen alloys were also carried out on 11.85 mm CT specimens to link the research programme to the fatigue crack growth area.

The key objectives of the research programme were to:

1. To investigate the role of MnS inclusions and free nitrogen on the tensile mechanical properties of a range of C – Mn experimental steels.

2. To evaluate and compare the tearing modulus $(dJ/da)(E/\sigma_y^2)$ at 20°C and 200°C, in air and water environments using purpose built equipment.
3. To determine the mode of fracture and crack tip opening angle (CTOA) by post test fractography and metallographic techniques.
4. To investigate the effect of free nitrogen content on fatigue crack growth rates at 150°C, and investigate a possible effect on fracture mode.
5. To extend published models of ductile fracture of steel to the blue brittle range of temperature and strain rates.

Chapter 2.

2. Literature Review.

2.1. Elastic Plastic Fracture Mechanics.

Linear Elastic Fracture Mechanics (LEFM) was originally developed to describe crack growth under essentially elastic conditions, as the name implies. However such conditions are met only for plane strain fracture of high strength metallic material and for fracture of intrinsically brittle materials like glass, ceramics, rocks and ice.

Later it was shown that LEFM concepts could be slightly altered to cope with the plasticity in the crack tip region. In this category falls the treatment of fracture mechanics problems in Plane Stress, for example the R curve concept. Nevertheless there are many important classes of materials that are too ductile to permit description of their behaviour by LEFM, where the crack tip plastic zone is simply too large and for these cases other methods must be found.

Elastic Plastic Fracture Mechanics (EPFM) can be used for these materials. The methods used in EPFM significantly extend the description of fracture mechanics beyond the elastic regime, but they too are limited. EPFM cannot treat the occurrence of general yielding leading to so called plastic collapse (see Figure 9).

Note that these ranges of applicability of LEFM and EPFM overlap. It is now generally accepted that a proper description of elastic plastic behaviour which usually involves stable crack growth, is not possible by means of a straightforward, single parameter concept.

So far the only notable success of EPFM for practical applications is the ability to predict crack initiation using one or two parameters. Of the two concepts developed for this purpose two have found a fairly general acceptance. The J Integral, and the COD approaches (crack opening displacement) approaches. The method used in this thesis will be the J integral.

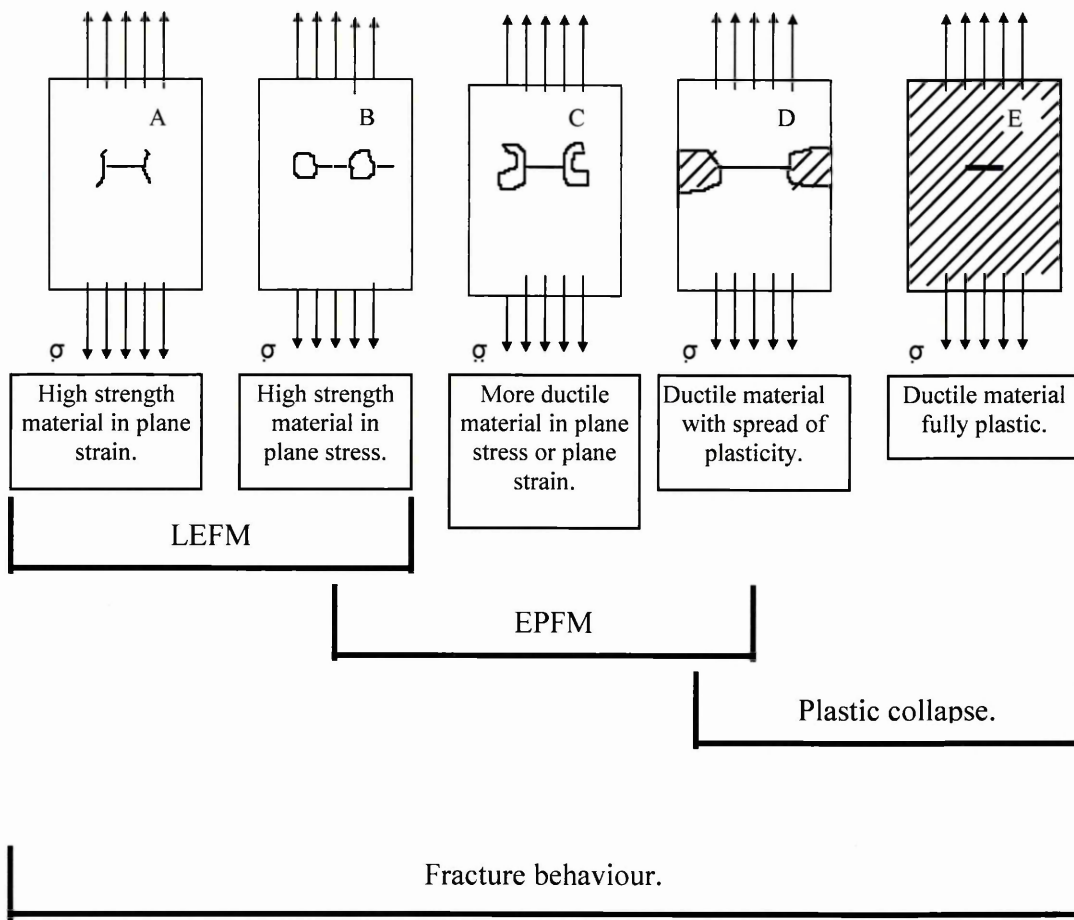


Figure 9. Ranges of applicability of LEFM and EPFM for describing fracture behaviour [23].

2.1.1. The J Integral its Significance and Use.

The J Integral values can be used as indices of material toughness for alloy design, materials processing, materials selection and specification, and quality assurance. The J Integral value for most structural metals is independent of testing in the quasi - static regime. The value becomes a function of testing speed in the dynamic regime. Cyclic loads or environmental attack under sustained stress, or both, can cause additional contributions to crack extension. Therefore the application of J Integral values in design of service components should be made with full recognisance of service conditions.

J Integral values can be used to evaluate materials in terms that can be significant to design, and for the evaluation of materials with flaws. This thesis is basing the J test method on ASTM E1737 96 [24] which superseded ASTM E813 in 1996.

The ASTM E1737 test method is applicable for a wide range of ductile engineering materials. However there are a high ductility, high toughness materials for which this test method is not applicable, because of extremely high tearing resistance. Here crack growth due to the physical tearing of the material may be virtually indistinguishable from extensive crack tip blunting.

J_{IC} as determined by ASTM E1737 characterises the toughness of materials near the onset of stable crack extension from a pre - existing fatigue crack.

2.1.2. J Terminology [24].

J_{IC} A value of J (the crack extension resistance under conditions of crack tip plane strain) near the onset of stable crack extension (see Appendix 1).

J_C A value of J (the crack extension resistance under conditions of crack tip plane strain) at fracture instability prior to the onset of significant stable crack extension.

J Integral A mathematical expression, a line or surface integral over a path that encloses the crack front from one crack surface to the other, used to characterise the local stress strain field around the crack front.

This advanced approach is capable of handling even large amounts of yielding. The J integral can be thought of as the generalisation of the strain energy release rate, G, to cases of non linear elastic stress - strain curves. This is shown in Figure 10. However for most cases of engineering interest, the non linear stress strain (and hence P - v) behaviour is due to elasto - plastic behaviour in metals. For elasto - plastic behaviour J loses the physical interpretation related to potential energy. But it retains its significance as a measure of the intensity of the elasto - plastic stress and strain fields around the crack.

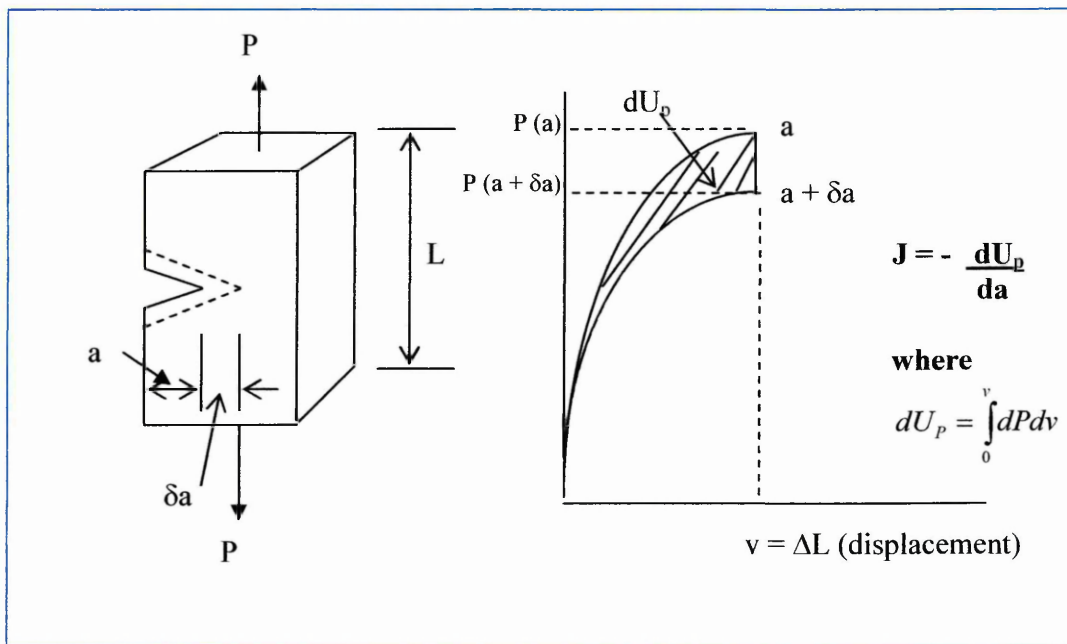


Figure 10. Definition of the J integral in terms of the potential energy difference for cracks of slightly different length (for constant displacement) [23].

Values can be determined experimentally or analytically using P - v curves as in Figure 10. However the two different P - v curves for crack lengths a and (a + delta a) need to be determined by independent tests or analysis on two different members, rather than by extending the crack delta a after a single member is loaded. Since the plasticity limitations of LEFM can now be exceeded the

need for large test specimens is removed.

One complexity encountered in J_{IC} testing is that non linearity in the $P - v$ behaviour is now due to a combination of crack growth and plastic deformation.

Hence the beginning of cracking cannot be determined in a straight forward manner from the $P - v$ curve, and special means are needed to more directly measure crack growth. This is discussed in Appendix 2.

2.1.3. LEFM and EPFM Fracture Mechanics and SCC Testing.

The J integral based fracture toughness tests are the most widely accepted for the characterisation of the elastic plastic behaviour of metallic materials, showing elastic plastic mechanisms at fracture [25,26,27]. The ease of performing these tests, together with their reliability have extended their use to fields such as stress corrosion cracking. Where subcritical cracking exists in the elastic plastic regime [28,29].

Over the last 20 or 30 years it has become common to study crack growth in engineering materials using the concepts of fracture mechanics. More specifically linear elastic fracture mechanics has been extensively applied in studies of crack growth under monotonic loading, fatigue crack growth, and stress corrosion cracking. Studies of stress corrosion cracking have been directed at identifying the stress intensity associated with the onset of environmentally assisted cracking (K_{ISCC}). Two of the early tests for determining this were the precracked cantilever beam test and the modified wedge opening load test (WOL). The precracked cantilever beam test involved the application of a deadweight load and therefore an increasing K field for crack growth. The WOL test is conducted at constant deflection and therefore involves crack extension to arrest in a decreasing K field.

One of the earliest studies which departed from these techniques was done by Clark and Landes [29], by evaluating compact tension specimens under increasing load and displacement to determine the stress corrosion cracking susceptibility of high strength steels, but this study was performed using the traditional stress intensity. Abramson et al [28] evaluated the application of the J integral to cases of environmentally assisted cracking of a magnesium alloy in NaCl solution and concluded that with suitable modifications to allow for steady state crack growth, J integral techniques should apply to SCC. One of their more interesting results is the occurrence of the drastically reduced J - R curves obtained from air tests conducted on specimens which were previously tested for K_{ISCC} at a constant deflection. They suggested that stable mechanical cracking proceeding from a SCC crack is easier than that occurring

from a fatigue pre - crack.

If the plastic zone at the crack tip remains small throughout a fracture test then Linear Elastic Fracture Mechanics can be used to quantify and characterise fracture [27]. It would also follow that the force displacement would always be linear so that the non linearity appearing in the force displacement record would always be due to crack extension. This is a simple system and analysis of crack growth would be straight forward. Difficulties arise when the plastic deformation is large enough to appear in the force displacement diagram. This would present problems such as:

(i). The results of plastic deformation and crack extension would have to be separated in order to analyse the results.

(ii). The use of the stress intensity factor as a controlling parameter of fracture breaks down, when plasticity is widespread.

(iii). Plane strain conditions cannot be maintained when the plastic zone size is large relative to the specimen thickness [30].

The size restriction for plane stress is given by [24,27] :

$$B = 2.5 \left[\frac{K_{IC}}{\sigma_y} \right]^2 \quad (4)$$

To account for plasticity use is made use of a correction factor [26]. In this the plastic zone radius preceding fast fracture was considered to be an additional contribution to the crack length. For a plastic zone of $2r_y$ where r_y is given by.

$$r_y = \frac{a}{2} \left(\frac{\sigma_F}{\sigma_Y} \right)^2 \quad (5)$$

It was argued that the distribution of stress was equivalent to that for an elastic crack of length $(a + r_y)$ and that plastic deformation increased the effective crack length.

$$K = \sigma(\pi(a + r_y))^{1/2} \quad (6)$$

where K is the applied stress intensity factor, σ the applied stress, a is the original crack length, r_y the plastic zone radius.

The discrepancy between the elastic calculation and the corrected result becomes greater as the ratio of the applied stress to the yield stress increases. That is the plastic zone becomes larger.

Both crack opening displacement (COD) and the J integral offer a reasonable description of the condition at the crack tip of an elastic plastic crack. The COD offers a microscopic approach related to the region immediately ahead of the crack tip. J is a macroscopic term related to the rate of change of energy associated with crack growth and can be regarded as the energy flow to the crack tip. For elastic plastic materials J and COD are related so in principle describing the same phenomenon. It should be noted that the aims of the J integral testing and COD are essentially the same when applied to metallic materials. Both methods seek to characterise the phenomenon of fracture in terms of displacement at the tip of the crack. As stated earlier in the J integral test the start of fracture is specified by J_{IC} which is freely convertible to δ_{IC} . In the COD test the result is reported in terms of δ_{IC} , but as in the J integral test, measurement of δ_{IC} is partly indirect. In other words in both kinds of test the aim is to know about the microscopic parameter δ_{TIP} , from measurement of the macroscopic parameters of load and surface displacement.

Given that fracture starts at a point specified by J_{IC} or δ_{IC} , what happens subsequently is also of importance, that is, is fracture stable or unstable. This is recognised in the standard COD test [31] and procedures for evaluating stability as δ_m or δ_C are specified. In the J integral testing the equivalent procedure is the determination of the J vs Δa curve [24].

The COD approach is attractive because it is more easily understood than the more abstract J integral, and at first sight seems the more direct method. However it is the case that measurement of COD in reality is just as indirect as it is for the J - Integral.

Barr et al [32], proposed an equation for crack tip displacement, based on the system shown in Figure 11, as:

$$\delta = \frac{0.33(W - a)V_g}{0.33W + 0.67a + Z} \quad (7)$$

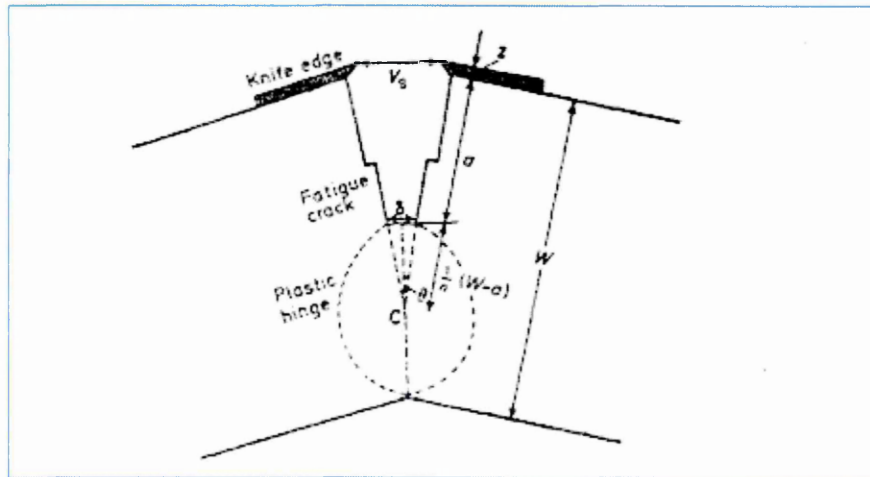


Figure 11. Diagram of the relation between δ and knife edge displacement V_q in a bend test [32].

It was assumed that deformation occurred around a centre of rotation depth $0.33(W-a)$ producing results compatible with experimental observations.

Often the profile of the load displacement plot tends to indicate there is no one single unique value of δ identifiable with fracture. Where, as mentioned earlier, values of δ_c in the ductile brittle transition region show large amounts of scatter. This is attributed to the presence of slow stable crack growth between initiation and complete failure, rapid fracture. These are taken to be δ_i and δ_m respectively δ_m denoting COD at the maximum load which may or may not coincide with the onset of fast fracture. Results [33] tend to indicate that δ_i is

more independent of geometry (thickness) giving a conservative value of fracture toughness. The regime of stable cracking remains a problem and will be considered in more detail below. For the moment the relationship between the front face clip gauge displacement and δ has been developed to the point of a standard test procedure [31], with the relationship:

$$\delta_i, \delta_m, \text{ or } \delta_c = \frac{K^2(1-\nu^2)}{2\sigma_y E} + \frac{0.4(W-a)V_g}{0.4+0.6a+Z} \quad (8)$$

This is a two term expression. The first term is elastic and based on a finite element calculation of δ and K in plane strain. The second is a plastic term dependent on the specimen geometry and a centre of rotation (see Figure 11) at a distance $0.45(W-a)$ below the crack tip.

The measurement of COD is relatively simple when a crack is stationary and where δ_{tip} occurs as a discrete opening at the tip as shown in Figure 12(a).

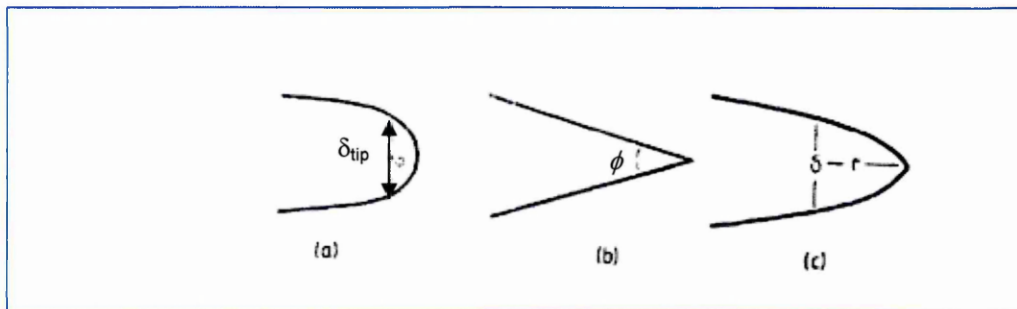


Figure 12. Schematic representation of crack tip profile: (a) static crack, (b) growing crack in rigid/plastic material, (c) growing crack in elastic/plastic material.

A more difficult situation arises when plastic displacement occurs during crack growth. Consider first the ideal case where the material is rigid plastic, (case 12b), and that only plastic strain occurs, i.e. no elastic deformation.

Since J and δ_{tip} are linearly related an increment ΔJ produces an increment δ_{tip} . However, if the crack extends by Δa after each increment ΔJ the crack faces will contain steps of height $\Delta \delta_{tip}$ at intervals Δa behind the tip. Thus,

the crack faces will be inclined at an average angle $\Delta\delta/\Delta a$ and in the limiting case of infinitesimally small steps, the crack opening angle $d\delta/da$ as illustrated in Figure 13.

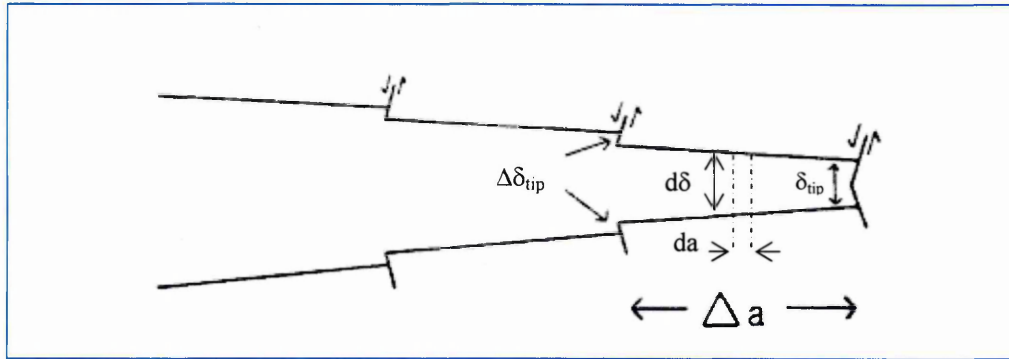


Figure 13. Illustration of the crack tip displacements which accompany small discrete crack extensions.

Expressing this in terms of J and crack opening angle ϕ .

$$\frac{\delta}{r} = \frac{d\delta}{da} = \left(\frac{\alpha}{\sigma_0} \right) \frac{dJ}{da} = 2 \tan\left(\frac{\phi}{2}\right) \quad (9)$$

Where r is a small characteristic distance behind the crack tip (see Figure 12c), and α is a material dependent non-dimensional number [36,37,216]. This is the basis for the tearing modulus as used by Paris et al [34,40] in the dimensionless form.

$$T = \frac{E}{\sigma_y^2} \frac{dJ}{da} \quad (10)$$

Where either dJ/da or T can be used to measure the resistance to tearing the larger T the larger the crack opening angle (see Appendix 1).

This definition of toughness can be applied to very ductile materials when their behaviour approximates to purely plastic. More realistically the effect of elastic displacement should be considered see Figure 12(c).

Because of this effect another term must be added in equation 9 as described by Rice [35] and Rice and Sorensen [36] to give.

$$\delta = \frac{\alpha}{\sigma_y} \frac{dJ}{da} r + \beta \frac{\sigma_y}{E} r \ln\left(\frac{eR}{r}\right) \quad (11)$$

where R is a dimension of the order of the magnitude of the plastic zone size and $\beta \approx 3.9$, e is the natural logarithm base = 2.718, (the constant β in equation 11 was later redetermined as $\beta = 5.08$ [37]).

The criterion for stable crack growth is now taken to be the development of a critical displacement δ , at a small characteristic distance, r, behind the crack tip. The crack growth criterion therefore comprises two independent terms. The first, involving dJ/da , can be regarded as an externally driven component, i.e. energy is provided from outside the specimen and flows to the crack tip to increase δ . The second can be regarded as contributing self generated strain accompanying crack growth in the absence of an outside increasing driving force, i.e. at constant J.

Equation 11 can also be treated as a differential equation describing stable crack growth. On the basis of an assumed constant profile criterion Rice and Sorensen [36] estimated the condition under which stable crack growth would occur and derived the J vs Δa curve by integrating equation 10. This was taken further by Herman and Rice [37] who applied their results satisfactorily to experiments on quenched and tempered steel.

2.1.4. The J Integral and Environmentally Assisted Crack Growth.

In considering the application to stress corrosion cracking, it seems unlikely that an early move towards establishing test standards will be made, considering the multi - parameter problem of SCC involving electrochemical conditions. Nevertheless parameters such as the stress intensity K_{ISCC} have been used in LEFM to establish SCC data. The same limitations apply to these data in developing standards.

The primary objectives of studies of environmentally assisted cracking have been so far to understand the basic mechanisms, and also to find suitable

test methods for screening materials according to their degree of susceptibility, in order to avoid failures due to Environmentally assisted cracking in various applications and environments. However it has not been easy to understand the underlying mechanism or develop test methods, because of the complexity of the interplay among the various mechanical, metallurgical and environmental factors. As a consequence, several different mechanisms have been proposed to explain metal - environment interaction failures, and the subject is still open for criticism and discussion.

Parkins [38] in his work describes it succinctly by supporting “**a continuous spectrum of mechanisms**” responsible for SCC, with the assumption that no single mechanism is responsible.

In the case of test methods [39], there also have been developments from earlier classical test methods, in which constant load or constant strain used to be applied to slow strain rate tests. However, some of these methods, involve a long duration of the tests, and the results obtained from such tests are not always suitable to analyse cases where cracks or defects are already present, or are produced during the service life of a structural component. In order to overcome such situations fracture mechanics concepts have been applied in the last few decades to study EAC using precracked specimens.

In non linear elastic conditions there is no alternative to using either COD or J Integral methods if fully quantified results are to be reported. Furthermore as in the case of mechanical fracture, one must think in terms of strain controlled fracture processes occurring at the crack tip, and the J integral approach is well adapted to dealing with this. Experimental values of dJ/da could be taken as a measure of the contribution of the external applied forces to the strain at the tip of a growing crack, and in some situations dJ/da specifies the crack opening angle which in turn could be taken to be a measure of the material's ductility. Thus dJ/da or J/a could be a significant parameter in measuring SCC. Compare this to the slow strain rate test testing procedure done on tensile specimens, where a plot of say reduction in area versus strain rate is used to detect the influence of SCC. In the J integral test a plot of T (the

tearing modulus as derived by Paris [40]) versus displacement would be of more fundamental significance with the advantage of gaining additional information on J_{ISCC} .

On examination of the literature it seems that the advanced level of understanding and investigations described for the J integral in air has not been achieved to the same degree in aqueous environments. Although numerous studies have been conducted by James and Porr [41], Gibson [42] Druce [43], Gabetta [44], Alvarez [45], Kawakubo and Hishida [46], Dietzel [47] Wagner [48], and earlier workers like Hackett, Moran and Gudas [49] to name but a few. The method employed i.e. the single specimen unloading compliance or multispecimen test technique. A description of the unloading compliance is given in Appendix 2. The testing environments and loading rates used by these authors can be found in the table Appendix 3, if not stated in the following paragraphs.

Kim et al [50] was one of the few researchers who came across negative crack growth (where crack growth Δa goes negative, see Appendix 4) in the early stages of their testing and had to make the necessary modifications to their equipment, as had to be done in this study. A detailed account of the causes, occurrence and prevention are given in Appendix 4.

Schellenberger and Diemel [51], did a study on 20 MnMoNi 5 5 to determine the J - R curves of the steels with two different sulphur contents (0.003 and 0.011 wt%). The tests were done at 240°C in 8ppm DOW high temperature water and air. The single specimen unloading compliance technique was used at load line displacement rates from $1 \times 10^{-4} \text{ mm sec}^{-1}$ down to $1 \times 10^{-6} \text{ mm s}^{-1}$ on 20% side-grooved 2T CT specimens in an autoclave testing facility. A pressure of 7MPa was used under quasi-stagnant flow conditions.

In the case of testing in high temperature water, remarkably lower J_R curves than in air at the same load line displacement rate ($1 \times 10^{-4} \text{ mm s}^{-1}$ were obtained). A decrease in the load line displacement rate as well as an increase

in the sulphur content of the steel caused a reduction of the J_R curves. At the fastest load line displacement rate a stretch zone could be detected fractographically on the specimens tested in air and in high temperature water and consequently J_{1C} could be determined. When testing in high temperature water, the J value of the higher sulphur material decreased from 45 N mm^{-1} in air to 3 Nmm^{-1} much more than that of the optimised material type from 51 Nmm^{-1} in air to 20 Nmm^{-1} at $1 \times 10^{-4} \text{ mms}^{-1}$.

Kawakubo and Ishida [46] did constant extension rate tests on 2mm thin CT specimens made from a sensitized austenitic stainless steel A304 at extension rates from $1.7 \times 10^{-4} \text{ mm sec}^{-1}$ down to $5 \times 10^{-6} \text{ mm sec}^{-1}$. This was done in quasi stagnant high temperature water at a temperature of 250°C . It was the primary aim of this investigation to correlate the crack growth rate da/dt with the time differential of the J integral in order to estimate the crack tip deformation rate $\dot{\epsilon}_{ct}$. The analytical results showed that the crack growth rate has a best correlation with a time differential of the J integral, which is an estimate of crack tip deformation rate.

Dietzel [47] performed stress corrosion cracking studies of shielded metal arc weld joints of a carbon manganese steel, on fatigue precracked compact tension specimens ($W = 40\text{mm}$, $B = 15\text{mm}$) using slow rising displacement rates ($1\mu\text{m/h}$). The tests were conducted at room temperature. The aim of the work was to assess the feasibility of a rising displacement type test from SCC testing of weldments. Also to compare the influences of the nitrogen content (83 ppm and 213 ppm respectively) on the fracture behaviour of the welds in air and under environmental assisted cracking conditions in substitute ocean water at a cathodic potential of -900mv versus Ag/AgCl electrode promoting hydrogen charging of the material.

The conclusions that were drawn by Dietzel from the SCC tests show that the differences in the fracture behaviour observed in an inert environment (laboratory air) could be attributed to the effect of nitrogen, and that this was completely overridden by the influence of the corrosive environment. He attributed the embrittlement, thereby a decrease in fracture toughness of the

welds to hydrogen uptake from the environment. He also concluded from the results that rising displacement tests may be used to determine SCC. This is in line with other researchers [28].

The rising load displacement tests came about because Deitzel doubted the applicability of LEFM methodologies, and so applied elastic plastic fracture mechanics for data evaluation. As stated in earlier sections in EPFM the results of rising displacement tests are expressed either in the form of the J integral or crack tip opening displacement curves (R curves). Other workers have demonstrated the applicability of SCC and EPFM in various aqueous media [28,51].

To summarise this section the following points can be made.

(i). In the majority of materials where LEFM does not give a valid result within the limits of laboratory testing one is forced into using either crack opening displacement or J_C integral testing. This applies to mechanical fracture as well as SCC.

(ii). The fracture processes are often strain controlled in the crack growth of metallic materials, and the parameters of LEFM do not deal effectively with this aspect unless small scale yielding conditions apply. In SCC, fracture may additionally be stress or strain rate controlled and the J integral method is well adapted for dealing with this aspect. If there is to be any advance in understanding the interactions involved in SCC, the J integral approach or something equivalent to it will have to be employed.

(iii). The J integral test gives a number of potentially useful results. One of those involving dJ/da is analogous to the results from the empirical slow strain rate test in which ductility is plotted against strain rate. Although it is undoubtedly a more expensive test in this context, the J integral test is attractive because it can incorporate geometry and plasticity effects into structural integrity assessments.

2.1.5. The Effect of an Elevated Temperature Environment on J_{1C} in Air and Aqueous Environments.

The Reactor Pressure Vessel steels (RPV) in world wide use today are the C – Mn, Cr – Mo, Mn, N, Mo type low alloy steels. The requirements for these steels up to the normal steam – water operating temperatures are good strength and ductility. The A533B, A508 (Mn, N, Mo) steels have been used for over 20 years as a pressure boundary material in nuclear plant in temperatures between 200° – 350°C, and there is now an extensive data base of the mechanical properties and the influence of water environments on crack initiation by both stress corrosion (SCC) and corrosion fatigue (CF) [52,53]

Steels used for low to medium temperature non - corrosive applications, are often based on carbon manganese steels. Care is usually taken that they are operating in the upper shelf region of the Charpy curve. Many studies have consistently shown that the micro-mechanism in this regime is void nucleation and coalescence [2,14,17]. Numerous studies have shown that important trace elements nitrogen [54,55,56,57,58,59] and carbon [60,61] can have a large impact on the ductile fracture mechanism.

Many investigations have been devoted to the study of ductile tearing, which takes place in the upper shelf region in low and medium strength steels in air [62,63,64,65,66] and aqueous environments [41]. It is generally found that there is a decrease in J_{1C} (the crack extension resistance under conditions of crack tip plain strain) and the tearing modulus (the crack growth resistance dJ/da) in the dynamic strain ageing regime. Kim and Kang [62,67,68] found that the tearing modulus was 30% - 40% smaller than that at room temperature in the dynamic strain aging region at elevated temperature. Druce [42] and James [41] conducted similar tests in aqueous environments and found the same observations. (see Figure 14 for the collated work of the above mentioned authors).

After reviewing the literature there is strong evidence to suggest that

dynamic strain aging influences ductile fracture in the temperature range 200°C – 250°C this is a manifestation of the *blue brittleness* phenomena. Two authors in their work Atkinson [52,53] and Chu [69] noticed that there was increased susceptibility to stress corrosion cracking, at the dynamic strain ageing peak temperature (i.e maximum UTS, minimum ductility).

The purpose of this review is to consider the mechanisms of ductile fracture for the steels investigated particularly in the blue brittle temperature range 150°C - 350°C and how this is influenced by the aqueous environment and what effect this has on J_{IC} in the upper shelf region. This temperature range is critical as the average reactor operating temperature is around 290°C to 300°C.

Many investigations have been devoted to the study of ductile tearing, which takes place in the upper shelf region in low and medium strength steels. In those materials the methodology derived from linear elastic fracture mechanics cannot be employed. Other approaches using either a global parameter based on non-linear fracture mechanics such as J_{IC} , or local criteria based on the mechanisms of ductile rupture must be developed. The tearing modulus T represents the increase in energy that would be necessary to apply to continue stable crack extension for a given crack increment Δa .

$$T = (dJ/da) \cdot (E/\sigma_y^2) \quad (3)$$

Paris et al [40] noted that there appear to be two distinct possibilities for instability. First is the so called *cleavage* instability which is normally attributed to a local material instability on a microscopic scale (such as inclusion spacing). The second type of instability is associated with the global conditions in a test specimen or component and loading arrangement providing the driving force to cause continuous crack extension by a so called *tearing mechanism*. Cleavage is associated with very flat fracture on crystalline planes whereas tearing is normally associated with dimpled rupture mechanisms on a microscopic level. Cleavage is associated with a sudden instability where the crack jumps ahead,

severing the test piece almost instantaneously. At low temperatures this occurs prior to the beginning of tearing. At higher temperatures just above transition steady tearing commences first, followed by some amount of stable tearing by the sudden cleavage instability. At yet higher temperatures much more extensive stable tearing occurs prior to cleavage, if the sudden cleavage occurs at all.

James and Porr [41] conducted tests on ASTM A508 Class 2 steel in both air and water environments at 243°C using the monotonic rising load tests, and specimen loading rates of 0.0254mm/min and 0.1524mm/min respectively. The multi-specimen method was used to eliminate corrosion fatigue interactions that could occur in the unloading compliance method. They verified that subsequent tearing appears to require less energy in the water environment, than it does in air, and also observed that post J_{IC} tearing in the water environment was characterised by *pop - in* events and that these were more numerous in the water environment and were of greater magnitude than those in air. They postulated that this phenomenon was due to strain aging in the steel. A *pop - in* is a discontinuity in the load against displacement record. This discontinuity is characterised by a sudden increase in displacement and generally a decrease in the load. Pop in's that occur in pressure vessel steels on the upper shelf region under J controlled tearing are not necessarily followed by subsequent increase in load, displacement may increase but loads often will not. According to Sculley [70] these pop - in events are ideal points for crack initiation he quotes "Any combination of mechanical parameters which can expose, a large area of metal rapidly to a corrodant will create suitable conditions for initiation and propagation of a stress corrosion crack in a susceptible alloy. The most striking combination arises in thick specimens of high strength alloys where sub-critical crack propagation under plane strain conditions, particularly rapid pop in crack extension, provides an ideal initiating reaction". James [41] postulated that the main cause of these could be attributed to MnS inclusions.

Because of the metallurgical significance of nitrogen in steel, it is the subject of the next section, giving an insight into the beneficial as well as the detrimental effects of its presence.

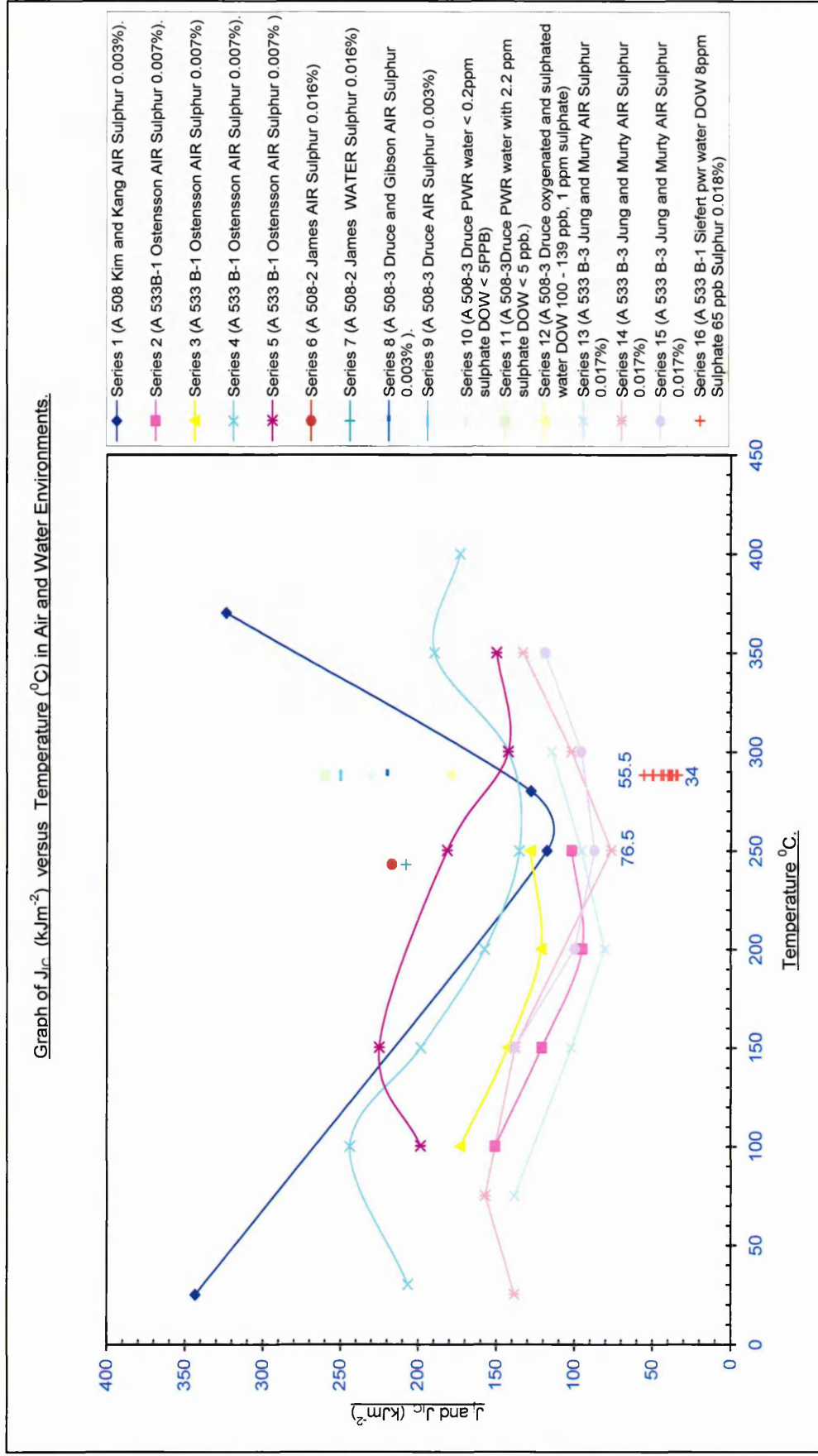


Figure 14. Graph of J_{1c} vs Temperature in Air and Water Environments.

2.2. Nitrogen in Steel.

Nitrogen is present in all steels, usually within the range 0.001 to 0.005% (10ppm and 50ppm respectively), although some special steels such as austenitic or duplex may contain up to 0.5%. The amount present depends on the type of steel produced, the method of production and whether nitrogen is a trace element or a deliberate alloying addition. The approximate nitrogen contents of the most common commercial steels are listed in Table 1 [71], although this should only be treated as a rough indication of the nitrogen concentration range expected. Nitrogen concentrations can vary widely from the expected range. Steels melted or cast in a vacuum can be expected to contain less nitrogen than air melted or air cast steels.

Type of Steel.	Nitrogen (ppm)
Plain - Carbon Steel : basic - oxygen process, Open hearth or electric furnace	30 - 100
Alloy : basic - oxygen process, Open hearth or electric furnace	30 - 200
Stainless.	100 - 500
High Alloy Vacuum Melted.	<10 - 100
Austenitic Mn - Cr - N (N added).	2000 - 4000
Plain Carbon	150 -250

Table 1. Approximate Nitrogen Contents of Commercial Steels [71].

Nitrogen enters the steel whilst in the molten state, the solubility being governed by several factors, the most important being the temperature of the bath and the composition of the steel.

Nitrogen is found in steels as both mobile nitrogen and combined nitrogen, and occluded nitrogen [72,73]. The mobile nitrogen is less strongly bonded in steel and is present as nitrogen atoms interstitially bound in the lattice, in association with alloy clusters, dislocations and on grain boundaries [72]. Also the relatively unstable nitrides of iron and manganese are always

included in the mobile nitrogen figure (see Figure 15). The combined nitrogen is present as stable nitrides of elements such as Al, Si, Ti, V, and as certain complex nitrides, for example TiCN.

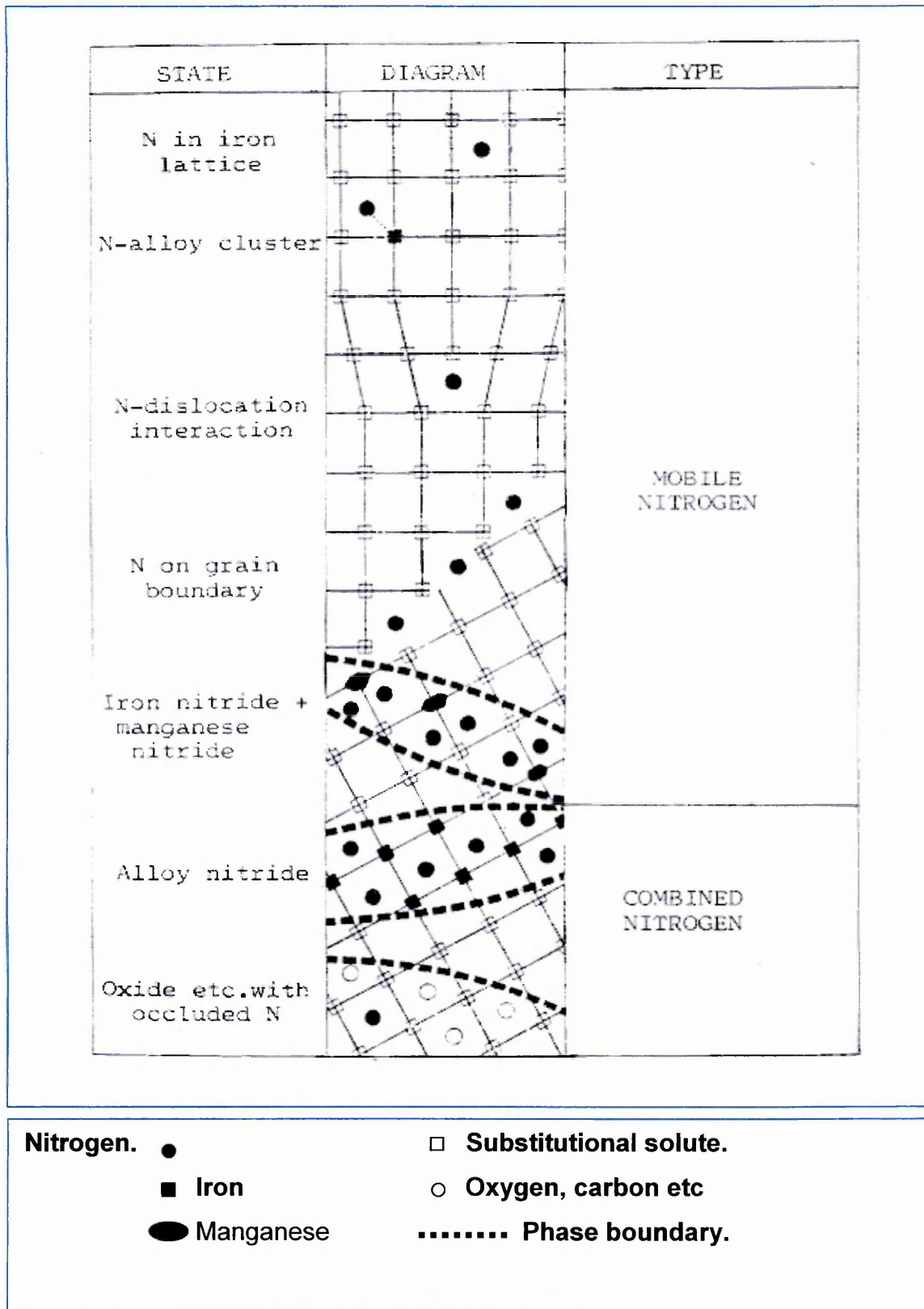


Figure 15. The Distribution of Nitrogen in Steel [72].

Most of the alloying elements found in steels can form nitrides under suitable conditions some of the more familiar nitrides are shown in Table 2.

Nitride		Complex Nitrides
Mn_3N_2		
Fe_2N		
Fe_4N		
AlN	αSi_3N_4	TiC_xN_y
BN	βSi_3N_4	NbC_xN_y
TiN	SiN	VC_xN_y
VN	ZrN	$NbO_{0.1} N_{0.9}$
Cr_2N	cubic Nb N	$Nb_2Cr_2N_2$
CrN	hexagonal Nb	
ZrN	Nb_2N	Mn, SiN
	TaN	

Table 2. Familiar Nitrides found in Steel [72].

Many complex nitrides can form in steels although knowledge of these is very limited. These complex compounds may consist of two metals with nitrogen or one metal with nitrogen and carbon or oxygen. Even the simple nitrides are not always definite stoichiometric compounds in steel. Vanadium nitride for example can be formed in non stoichiometric ratios.

2.2.1. Forms of Nitrogen in Steel.

It is known that nitrogen can be present in steels in three forms [73]:

2.2.2. Interstitial nitrogen (free nitrogen).

(a). Dispersed interstitial nitrogen is formed by the atoms (or ions) occupying interstitial sites in the crystal lattice of the metal and obeying the law of volume diffusion (Fick's Law).

(b). Interstitial nitrogen collected around defects is formed by atoms (or ions)

occupying favoured interstitial sites near crystalline defects (which must be considered in the widest sense of the term).

2.2.3. Combined nitrogen.

Present as nitrides which may consist of either simple or complex precipitated phases. This is the nitrogen entering into the composition of a phase other than the ferritic, austenitic, or martensitic matrix.

(a). Nitrogen in nitrides is that combined with an element to form a crystalline or amorphous phase with a constant atomic ratio (allowing for possible vacancies). The element combined with the nitrogen may be partially replaced by other elements (substitution).

(b). Nitrogen in complex phases can be:

(i). Inserted or substituted nitrogen in a phase other than those listed above. Thus, in a carbide, the nitrogen may either substitute for certain carbon atoms or occupy certain vacancies in the carbide lattice.

(ii). In a crystalline nitride containing a substituted or inserted element. For example, carbon can substitute for certain nitrogen atoms (substituted carbon) or occupy certain vacancies in the nitride lattice (inserted carbon).

(iii). In a crystalline nitride in a lattice with dimensions very close to those of a phase containing the same element as that which is combined with the nitrogen in the nitride. The two bodies form one crystalline network.

2.2.4. Occluded nitrogen .

Present in the molecular gaseous state and contained in pores within the metal (or ions) occupying favoured interstitial sites near crystalline defects (which must be considered in the widest sense of the term). This exists in gaseous form in the pores, either microscopic or macroscopic, and in flaws in

the metal. The term porosity indicates an absence of metal and not the lattice vacancies which can occur on an atomic scale.

2.2.5. The Metallurgical Significance and the Effect of Nitrogen in Steel.

The mechanical properties of steel are greatly affected by the content of nitrogen. Its presence can be beneficial, improving the strength and creep properties of steel or very harmful, causing intergranular fracture, depending on the form in which nitrogen is found in a steel, i.e as mobile nitrogen or as a nitride precipitate.

A serious effect of nitrogen is the precipitation of AlN at grain boundaries which can result in intergranular fracture [78]. Formation of Cr₂N at grain boundaries causes a phenomenon known as intergranular corrosion. This effect can be prevented by the addition of Ti, a much stronger nitride former than Cr, which forms titanium nitride preferentially.

Additions of boron are sometimes used to increase the hardenability of steel. If boron nitride is formed however, the hardenability effect is no longer achieved and to overcome this problem Ti or Zr is added to the steel before the boron addition to combine with any nitrogen.

Interstitial nitrogen is responsible for strain ageing, which means that after a steel has been stored for some time it cannot be drawn into car body parts, for example, because it tears and does not draw uniformly [80]. Segregation of nitrogen to dislocations and precipitation of Fe₄N at the grain boundaries is thought to be one of the causes of strain ageing. Strain ageing is also accompanied by an increase in yield strength and a loss of ductility and notch toughness.

Chromium - manganese austenitic steels contain nitrogen as a deliberate alloying element in concentrations up to 0.5% to give high yield strength. Nitride precipitates are rarely encountered in these steels. However the

reduced ductility of these steels in both hot and cold working can give rise to fabrication problems.

Silicon nitride in transformer grade silicon steel affects the grain orientation and the magnetic permeability of the steel. Titanium is added to mild steels in the correct stoichiometric ratio with respect to the nitrogen content. The preferential formation of titanium nitride, resulting in a low mobile nitrogen content, increases the ductility and reduces the impact transition temperature. This is the temperature at which the fracture of the steel changes to ductile mode from a cleavage or brittle fracture.

In low carbon steels carbon and nitrogen are primarily responsible for ageing manifestations [75,81,82]. With nitrogen these occur when a saturated solid solution in α iron releases nitrogen to form iron nitride, Fe_4N ; this is accompanied by a reduction of impact strength and an increase in hardness. In non-killed and semi-killed steels the nitrogen will be present principally as iron nitride. However, in steels deoxidised with aluminium, titanium, or zirconium the nitrogen occurs as nitrides of these elements which have different solubility patterns from iron nitride, resulting in drastically changed ageing characteristics.

Internal friction measurements put the solid solubility of nitrogen in ferrite at 20°C at less than 0.001 % by weight, and Dijkstra [74] has shown that nitrogen is precipitated in two different phases: one is the iron nitride Fe_4N_2 , the other not being identified. Iron nitride predominates above 230°C and it is suggested that two precipitation processes occur independently of each other and at rates having a different temperature dependence.

There are two types of ageing:

(a). Quench ageing is caused by the precipitation of an element, or a compound such as a nitride or carbide, from a supersaturated solution in α iron; it is likely to have an embrittling effect. Quench ageing is temperature dependent, therefore controlled thermal treatment offers a means of controlling ageing phenomena.

(b). Strain ageing is a consequence of cold work and is more important than quench ageing. The embrittlement which follows cold work is further promoted by subsequent heating to temperatures in the range 250°C to 425°C and is perhaps more correctly called strain-induced precipitation hardening. The effect is more likely to be encountered in high strength alloy steels than in mild steels, but in any event it is dependent upon the actual nitrogen content.

Strain ageing can be considered to be primarily due to migration of carbon and nitrogen atoms to dislocations causing locking. It is characterised by an increase in yield stress and lower yield elongation and a decrease in impact transition temperature [75].

A direct relationship is evident between nitrogen content and increase in tensile strength. An investigation by Waber and McDonald [76] and more recently [53,77] indicated that stress corrosion cracking is a phenomenon associated with the presence of nitrogen in steel and that there is an interrelationship between this type of cracking and the strain ageing of steel.

Because strong deoxidisers such as aluminium and titanium form stable nitrides, deoxidation with these elements is an essential part of the control of ageing. When the nitrogen is present as aluminium nitride ageing tendencies are inhibited. Deoxidation with aluminium can be sufficient to suppress strain age embrittlement and should be supplemented by a stabilising heat treatment where age hardening is important.

An extensive critical review of the strain ageing of steel was made by Baird [75] and is an important source of information on this subject.

Small amounts of nitrogen uniformly distributed throughout the ferrite have no ill effects on ferritic grades of metal, and often even improve the strength without reducing the toughness or ductility, provided the composition of the alloying elements is correct and the structure is fine grained.

Traditionally nitrogen has been regarded as a detrimental 'residual

element' which must be minimised. One of the driving forces behind this is for the production of strip steels with high formability, and it is now possible to routinely produce interstitial free steels with nitrogen of 20ppm [80]. For heavy plates and sections, the minimum nitrogen requirements are much higher, but there is still a trend within national standards for lower nitrogen contents in steels for more demanding applications. However, it is now recognised that for certain applications and certain conditions, control of nitrogen is more important than a simple drive to minimise nitrogen, and that nitrogen can also have some beneficial effects on steel properties.

Free nitrogen is associated with a wide range of mechanical and physical effects, such as increased strength, and reduced toughness, impact transition temperature (ITT, Figure 16) and reduced ductility and formability. Nitride or carbo - nitride precipitates can also influence mechanical properties, either directly, or indirectly by controlling grain size or recrystallisation behaviour.

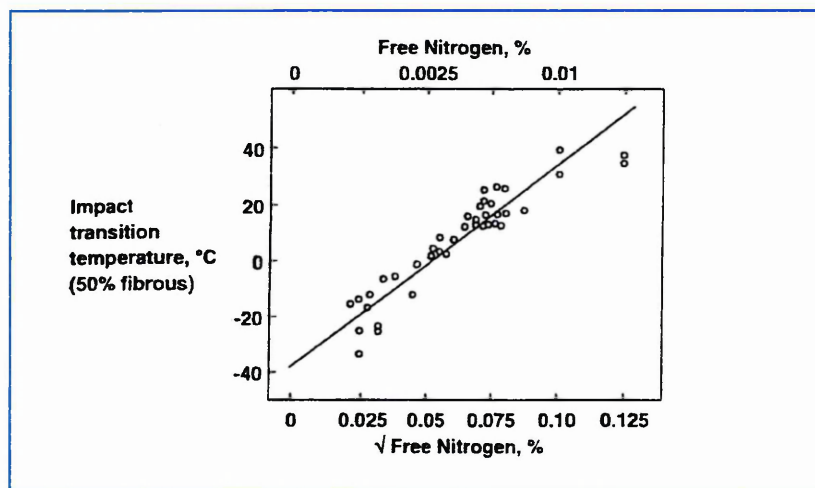


Figure 16. The Influence of Free Nitrogen on Charpy Impact Transition Temperature [83].

At ageing temperatures less than 100°C, in slow cooled steels, the phenomenon of strain ageing is mostly due to free nitrogen, due to the higher solubility and higher diffusion coefficient of nitrogen in comparison to carbon at these temperatures. Only very small amounts of nitrogen in solution are required: approximately 0.0001% produces detectable ageing, whilst 0.001% to

0.002% gives severe ageing [55] (see Figure 17).

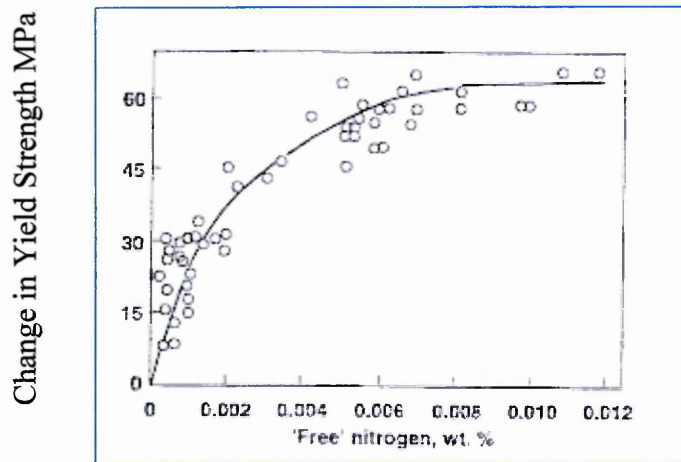


Figure 17. Influence of Free Nitrogen on Strain Ageing Response [83].

Strain ageing has several commercially important effects. These include the return of the yield point in temper rolled strip, leading to stretcher-strain marks during forming operations, a loss of toughness after cold forming operations or due to the imposition of in-service strains, reduced ductility during wire drawing operations, and reduced toughness after welding [85,86].

Quench ageing has some of the same characteristics as strain ageing, but does not require the imposition of strain, and is characterised by precipitation phenomenon. Nitrogen can exacerbate quench ageing behaviour, and lead to reduced drawability of wire rods [84].

Precipitates may indirectly influence phenomenon such as strain ageing by removing nitrogen from solution. Precipitates may also influence mechanical properties more directly by controlling recrystallisation and grain growth, or by giving precipitation strengthening. Nitrogen has an important effect on the volume fraction, temperature of formation and composition of these precipitates. In vanadium containing steels, nitrogen additions are known to give a powerful increase in strength (see Figure 18), and this has been attributed to the formation of finer V(C,N) precipitates. However, there is also some loss in toughness accompanying the increase in strength, but this is partially offset by a reduction in grain size [83].

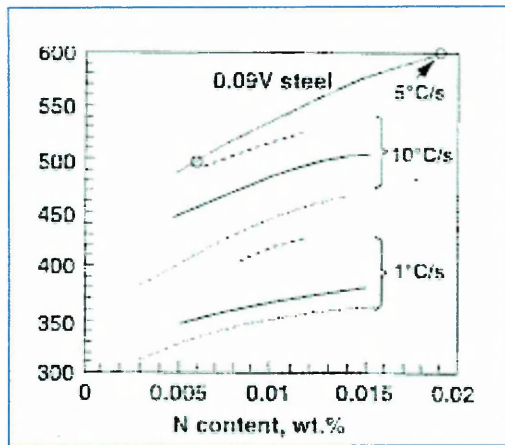
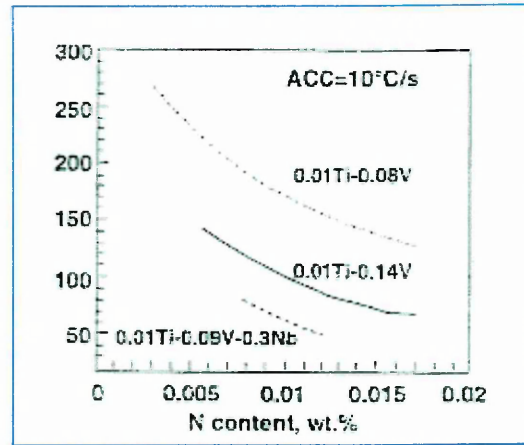
Yield Stress MPa**Impact Energy (J) at - 40°C.**

Figure 18. The Influence of Nitrogen and Cooling Rate on the Strength and Toughness of Vanadium Steels [83].

It is well known that precipitates can restrict grain growth, and that effectiveness of precipitates in restricting grain growth depends on the size and volume fraction of precipitates. As precipitates are in turn influenced by nitrogen content, it is expected that nitrogen will have an effect on grain coarsening behaviour. AlN has an important effect in producing fine grained normalised steels. The normalising heat treatment leads to the rapid formation of AlN , which restricts austenite grain, and hence produces a fine austenite grain size on cooling. If very low nitrogen contents are used in normalised steels, there can be a loss of grain size control, and hence a loss of strength and toughness.

Because TiN is the least soluble of the common microalloy nitrides, it is stable at high temperatures. Unlike AlN , TiN can precipitate easily during cooling, giving the possibility of grain size control during soaking prior to rolling, during the rolling process itself, and during welding. The Ti:N ratio, as well as the total nitrogen content, is also important. However, the influence of nitrogen on the grain coarsening behaviour of Ti containing steels is complicated, and dependent on factors such as the cooling rate during solidification [83].

There is substantial evidence to suggest that increasing nitrogen content in the weld metal can lead to a significant deterioration in toughness. It is believed that this is partly due to increases in free nitrogen, and partly due to

microstructural changes. The situation in the weld heat affected zone (HAZ) is complicated. Even for steels in which all nitrogen is combined in precipitates, it is possible that for the high temperatures and rapid thermal cycle experienced in the HAZ, microalloy nitrides and carbo-nitrides may be dissolved, giving the possibility of the presence of free nitrogen. There are reports that increasing free nitrogen in simulated weld HAZs decreased toughness. However, in multipass welds in vanadium containing steels, nitrogen has been shown to have little effect on HAZ toughness. Very low nitrogen steels may have a coarser HAZ grain size, which reduces toughness. The presence of other microalloying elements is also important, and for example in titanium steels, the Ti:N ratio, as well as the nitrogen content are important. Heat input can also have an effect, with increasing nitrogen in V-Ti steels improving HAZ toughness at low heat inputs, but decreasing toughness at high heat inputs. The complicated effects of nitrogen in the HAZ are explained by changes in microstructure, as well as free nitrogen effects [83].

In conclusion, nitrogen can have both detrimental and positive effects on steel properties. In some cases, these detrimental effects of nitrogen can be limited by the addition of strong nitride forming elements. The beneficial effects include improved grain size control, and enhanced precipitation strengthening. Therefore it is important to control nitrogen for specific property requirements, rather than simply minimising nitrogen.

A few of the effects of nitrogen have been illustrated, although there are many more effects that nitrogen can impart on a steel. Heat treatments are also very important as mobile nitrogen can be freed at elevated temperatures, the nitrogen being available to form a nitride precipitate with an element present in the steel, thereby changing the properties of the steel.

Due to the metallurgical significance of nitrogen in steel it is important to know the amount of both interstitial and combined nitrogen contained within a steel. The methods available to do this are described in the next section.

2.2.6. Methods available to measure the Nitrogen content of Steel.

It is well known that the mechanical properties of steel are generally influenced by the control of nitrogen, its presence can be harmful or beneficial as described in the previous section. So analytical methods are required to quantify the modes of occurrence of nitrogen in steel.

Three methods used to determine the free nitrogen are:

2.2.7. The chemical method.

This uses the difference between the total nitrogen and combined nitrogen in sample to obtain the free nitrogen content.

The chemical method relies upon the complete solution of the sample in hydrochloric acid followed by conversion of the nitrogen to ammonia [71,87,88]. After getting the nitrogen into solution as ammonia it is recovered by distillation over sodium hydroxide and the determinations are completed volumetrically by titration with hydrochloric acid this will give the N_{TOTAL} . A sample of 3.5g is specified. Determination of the combined nitrogen using the same procedure after the separation of the stable nitrides and other compounds followed by dissolution of the metal by using a methyl acetate — bromine mixture this method known as the ester/halogen method. The difference between the total and combined nitrogen is the free nitrogen. Complete recovery of nitrogen is not obtained using the chemical method if silicon nitride is present in steel. Nitrides present in carbon steels are readily dissolved in dilute hydrochloric acid, but nitrides of vanadium, titanium, aluminium, are not so soluble. These nitrides are separated by centrifuging and taken into solution by fuming with sulphuric acid [71,87,88]. Using a 1 gramme sample it is possible by using the high sensitivity of the ammonia - indophenol blue reaction, using a 1 gramme sample enables the use of different techniques such as the semi-micro Kjeldhal distillation unite. The chemical method is suitable for all types of steel, with the reservation that complete recovery of nitrogen cannot be obtained from those containing silicon nitride.

2.2.8. The Thermal Method.

This uses the hydrogen reaction with free nitrogen outgassing from the steel millings, which are heated at about 500°C, to obtain the free nitrogen content. This method is known as the hydrogen hot extraction method in which the hydrogen is passed over steel millings at 450° to 500°C. The mobile nitrogen is then converted into ammonia, which is absorbed in a suitable solution and determined spectrophotometrically as indophenol blue. Being done spectrophotometrically has the disadvantage in that one cannot be certain that all of the mobile nitrogen in the sample has been converted to ammonia. An improvement to this method, to overcome the disadvantage of a spectrophotometric determination is the use of an ammonium ion selective electrode in a triethanolamine - triethanolammonium ion buffer solution. The potential difference between this electrode and mercury is passed to a digital voltmeter and continuously recorded.

The collection time for the ammonia depends on the flow rate of the hydrogen and on the dimensions of the steel millings. Millings that have at least one dimension less than 0.5 mm with sample of 1 gramme weight are normally used for this method [71,87]. The success of the analysis using the thermal method depends mainly on two factors:

1. There must be no reaction at the heating temperature (450° to 500°C) between the mobile nitrogen and a metal in the steel; which will result in the precipitation of more stable nitride. Such a reaction will lead to a low result of mobile nitrogen. Such a reaction will not occur with most commercial steels since it has been established that aluminium, silicon or titanium does not react with mobile nitrogen at these temperatures. The interfering reaction will occur only with certain special steels, which contain appreciable concentration of vanadium and niobium.

2. No stable nitrides should dissociate at these temperatures, as this would give rise to a high result of mobile nitrogen. This interfering effect normally appears for steels that contain appreciable concentration of chromium nitride.

Carbon and low alloy steels does not have this type.

Thus the thermal method is suitable for the determination of mobile nitrogen in most commercial carbon and low alloy steels. The factors which determine the success and accuracy of the thermal method, which should be considered are sample preparation and during the experimental analysis, are, the milling size and extraction temperature.

Concerning milling size it has been reported that the smaller the milling size is desirable for a more accurate result as shown in Figure 19 [89] which shows also that extraction should be as soon as sample prepared and the waiting time after sample preparation will lead to a low nitrogen result.

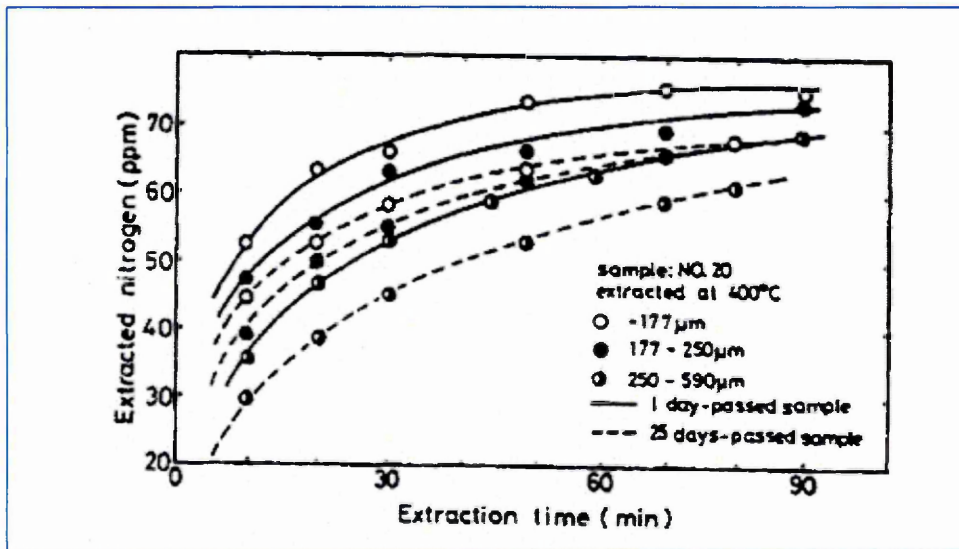


Figure 19. Effect of passed time after sample preparation and milling size of sample on free nitrogen extraction [89].

Concerning the extraction temperature some studies shown that 400°C is enough for complete extraction of nitrogen as shown in Figure 20 [89].

The best results are obtained by analysis of small samples as soon as possible after preparation, together with the condition of not using heating for cleaning or drying the sample, will give the more accurate result.

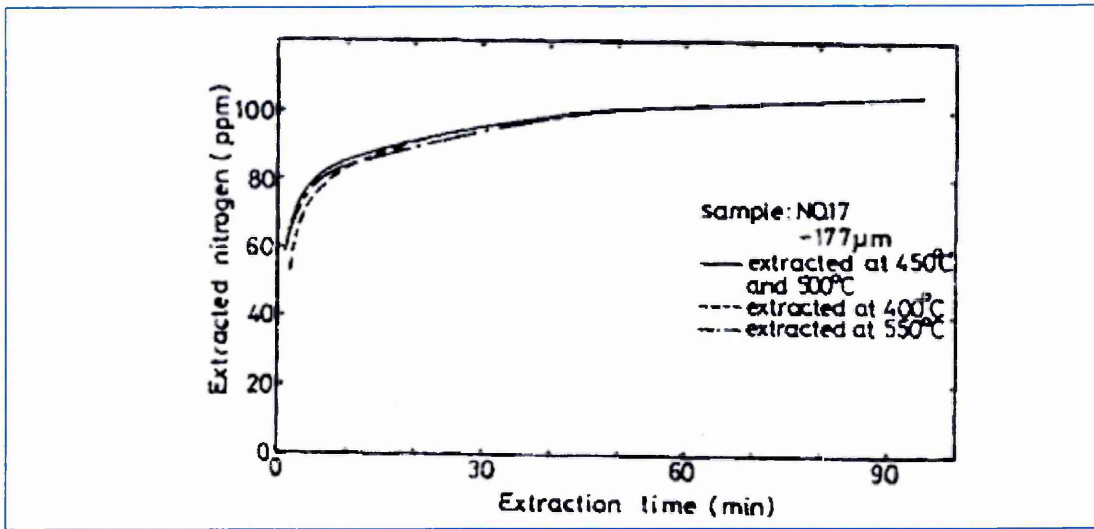


Figure 20. Effect of extraction temperature on free nitrogen extraction [89].

2.2.9. The Internal Friction method.

This method uses the elastic after effect of nitrogen in α iron and the internal friction produced as a damping system to get the free nitrogen.

This method uses a damping mechanism as it is well known that there is a tendency for nitrogen atoms to move from randomly placed sites to the favourable sites in α iron as shown in Figure 21. There is a considerable distortion in the tetrad direction, with small contraction along the diad axes. The movement of nitrogen occurs at a rate dependent upon the diffusion coefficient D for the solute atoms [90,91].

As more atoms move into favourably placed sites, further extension occurs under the action of applied stress. This extension increases with time even though the material is still well within the elastic range. The extension becomes greater the more solute atoms there are available to take part in the process. When the stress is removed there will be an instantaneous elastic contraction as the process is reversible as shown in Figure 22.

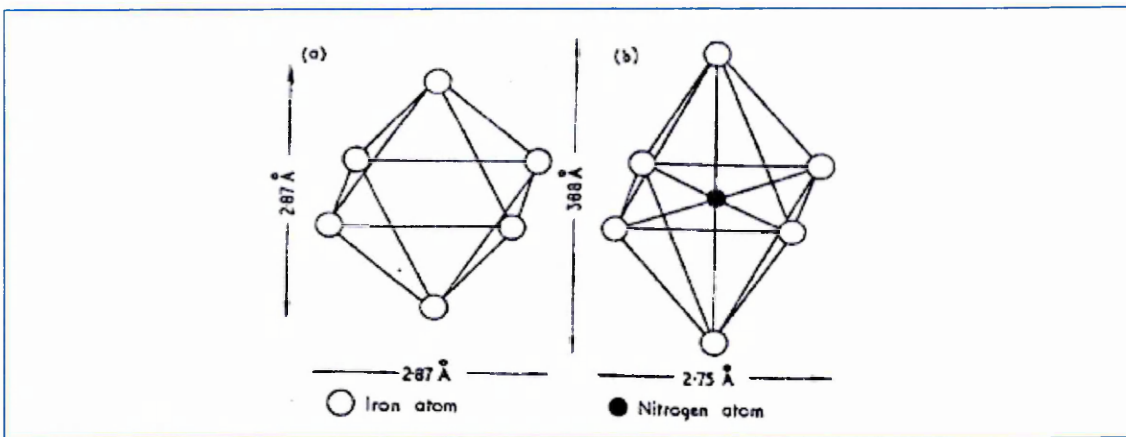


Figure 21. Octahedral interstice in the α iron [91].

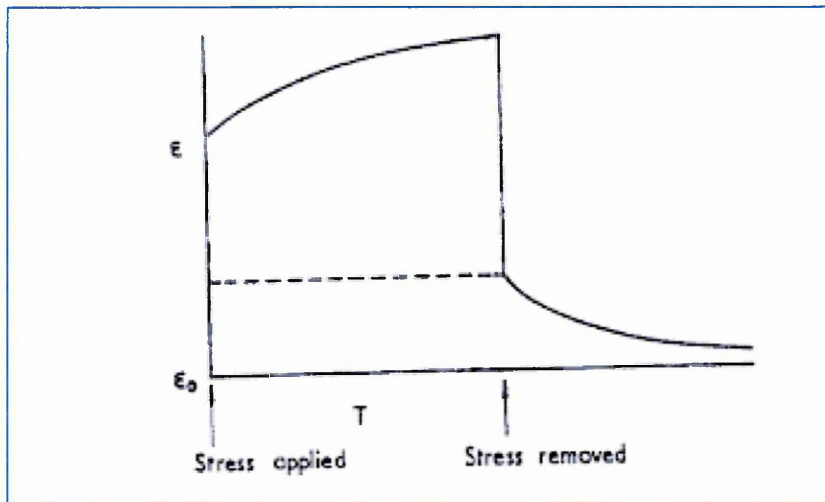


Figure 22. Elastic after effect in the α iron [90].

The nitrogen atoms will reoccupy the original randomly oriented sites. As they do so there is an associated redistribution of their individual tetragonal distortions and consequently a further contraction of the specimen. Under an oscillating stress a free vibration in the specimen exhibiting internal friction will gradually be damped. The logarithmic decrement of a free vibration is a measure of the internal friction. When plotting internal friction against temperature for a constant frequency, the weight per cent of nitrogen in interstitial solution will be directly proportional to the height of the Snoek peak above the background, so that, if the proportionality constant K has been determined the amount of lattice nitrogen can be calculated.

The internal friction method has many interfering side effects such as:

1. Carbon and manganese if present has to be determined with the nitrogen as they cause interference. So the content of them has to be known.
2. Grain size of the specimen can affect the result obtained as solute atoms can be absorbed in a relatively loose structure of the grain boundaries as shown in Figure 23.
3. Proportionality constant K will vary with the type and degree of texture present in the specimen since it depends upon the elastic distortions introduced by the solute atoms, which are anisotropic.

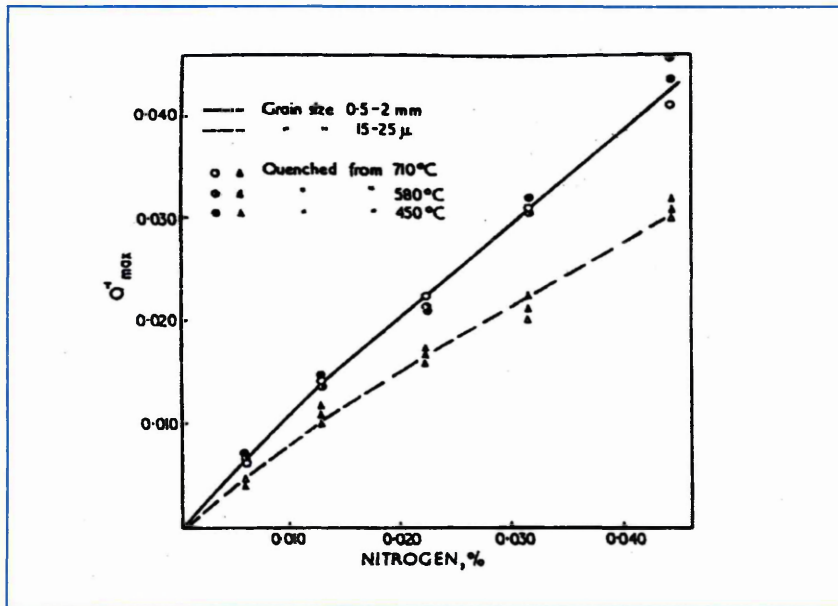


Figure 23. Effect of grain size on measurement of the solubility of nitrogen in iron [90].

This means that the interstitial nitrogen determination by the internal friction method will depend upon the accurate determination of the value of K and upon the resolution of the internal friction spectrum. The technique may be suitable for metallurgical research rather than as an analysis method.

2.3. Historical Review of Dynamic Strain Ageing Phenomena in Ferritic Steel.

Dynamic strain ageing (DSA) in low alloy steels occurs most readily between 150°C and 300°C, and is observed as serrated flow on the stress strain curve (Portevin le Chatelier effect). DSA requires either the presence of interstitial nitrogen or carbon in the alloy in order to occur. It is generally assumed that applied strain causes interstitial nitrogen atoms to flow to the crack tip interact with the dislocations there, locking them. This is followed by the rapid generation of new dislocations so that flow can start again. DSA causes embrittlement of the material (dislocation locking) followed by premature failure with a higher ultimate tensile stress (UTS).

Other manifestations of dynamic strain ageing are, a high work hardening rate, a negative temperature and strain dependence of the flow stress and a reduction of ductility in a limited range of strain, strain rate and temperature.

Strain ageing manifests itself chiefly by an increase in yield stress or flow stress on ageing after or during straining. Ageing after straining being classed as '**static**' and ageing during straining as dynamic strain ageing. Other properties may also change during strain ageing [55].

- (i). A return of a sharp yield point.
- (ii). A rise in the ductile brittle transition temperature and tensile strength.
- (iii). A reduction in ductility.
- (iv). A decrease in the Snoek peak internal friction peaks.

Most of the observed effects can be explained qualitatively as arising from the segregation of solute (*the metal which is present in the larger proportions is often referred to the parent metal or solvent, whilst the metal or non metal*

present in the smaller proportion is known as the solute) atoms to dislocations producing pinning of the dislocations by solute atmospheres. Two of the first people who postulated the above theory were Cottrell and Bilby [108]

The temperature and strain rate dependence for the onset and disappearance of serrations can be represented by Arrhenius type plot of different activation energies. The stress strain curves of a material often begin smoothly but develop serrations as inelastic deformation progresses. This phenomena is termed the Portevin-le Chatelier (PLC) effect.

Dynamic strain ageing denotes a series of ageing phenomena, which take place during the plastic deformation of metal or alloy. Even before the turn of the century, it was noted that when mild steel is heated to a blue colour (in the region 250°C), it became brittle if worked. This work was reported by C.E.Stromeyer in the Minutes of the Proceedings of Civil Engineers, vol 80, as early as 1885. Blue brittleness is thus a manifestation of dynamic strain ageing. In 1909, Le Chatelier studied the tensile properties of mild steel, an increase in tensile strength was observed within the blue brittle region, and noted that this increase was a function of deformation rate. Within certain combination of temperature and strain rate, serrated stress strain curves were observed [109].

The important role of dislocation theory is the prediction of the macro-mechanical properties and their understanding in terms of physical material properties [93]. The main achievement of dislocation theory is concerned with the interaction of mobile dislocations with localised defects which are considered to distributed either randomly or periodically.

The changes in mechanical properties in steel associated with dynamic strain ageing were first related to static ageing phenomena by Fettweiss in 1919, until the development of dislocation theory, when an atomic model of dynamic strain ageing was proposed. Nabarro first suggested that serrated yielding in steel would be observed where carbon or nitrogen atoms can diffuse fast enough to allow strain ageing to take place during deformation [58].

In their classic 1949 work [108] Cottrell and Bilby proposed that strain ageing effects were due to the segregation of interstitial solutes to form atmospheres around dislocations, which then require an increased force to break away from these atmospheres and become mobile. This model became the basis for much of the study of strain ageing, which has been most widely studied in alpha - Iron.

Four general stages in the strain ageing of alpha iron were identified by Wilson and Russell [110], stages which follow each other as ageing time is increased, the time required for the onset of each stage decreasing as the ageing temperature is increased. The stages are illustrated in Figure 24. Stage 1 is characterised by an increase in the lower yield stress and yield point elongation (Luders strain), and a return of the sharp yield point. In stage 2 the flow stress beyond the Luders strain also begins to increase. In stage 3 the strain hardening rate increases, causing an increase in the tensile strength and a decrease in the fracture strain. Stage 4 consists of 'overageing', where the yield stress decreases, although the Luders strain is maintained.

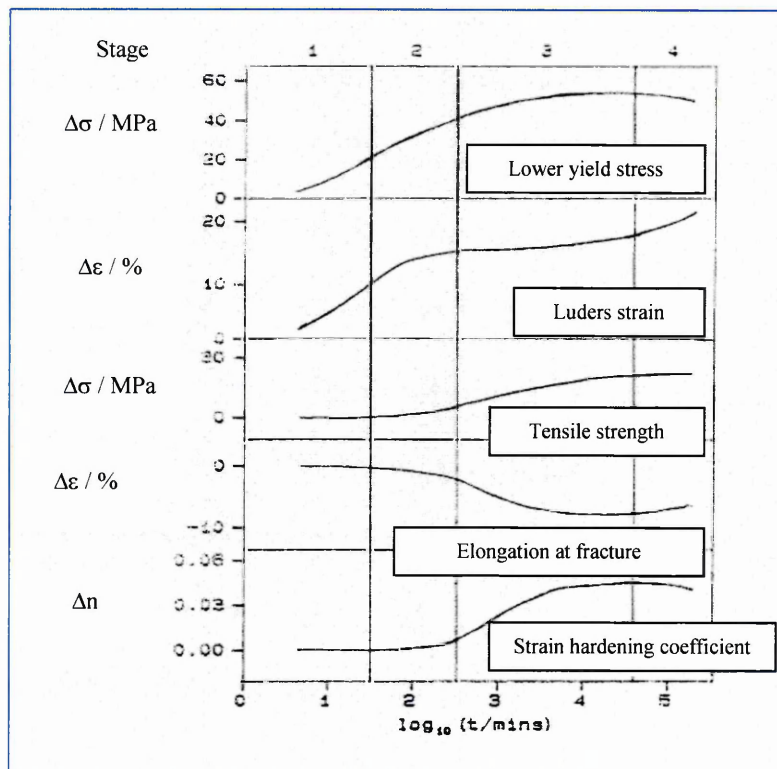


Figure 24. Changes in Mechanical Properties of Low Carbon Steel during strain ageing illustrating four stages of ageing response (Ageing at 60°C) [110].

Wilson and Russell attributed stage 1 of strain ageing to the Cottrell-Bilby mechanism, the formation of atmospheres of interstitial atoms at dislocations, and proposed that stage 2 was due to pinning of dislocations by precipitates of carbides or nitrides, which increase the unpinning stress (yield stress) and also the flow stress after unpinning (beyond the Luders strain) by an Orowan mechanism [111]. Keh and Leslie [112] proposed that in the later stages of strain ageing dislocations were pinned by precipitates, and that stage 3 of ageing corresponds to a regime where the stress required to generate new dislocations is less than the unpinning stress, so that the increase in the strain hardening rate in this stage was due to the activation of new dislocation sources, and the consequent increase in dislocation density. Wilson [113] proposed that in stage 4 of ageing, re-resolution of precipitates on dislocations, and the segregation of solute to dislocation sources, causes an increase in the stress required to activate new sources, while reducing the lower yield stress. Although the principal investigators into strain ageing in iron discussed hardening in terms of precipitation, there is little direct evidence for precipitation of carbides or nitrides on dislocations in strain ageing. Keh and Leslie [112] and Phillips [114] failed to observe precipitates on dislocations following straining and ageing. Rudee and Huggins [115] found some precipitation of carbides at grain boundaries on low-temperature ageing, but again could find no evidence for precipitation of carbides or nitrides on dislocations.

In his 1971 review of strain ageing, Baird [55] stressed the differences between carbon and nitrogen in strain ageing. In particular, the very low equilibrium solubility of carbon in alpha-Iron at low temperatures compared to that of nitrogen [116] should result in negligible strain-ageing by carbon below about 100°C. However, at higher temperatures, some fine carbides in the steel may redissolve, releasing carbon which can contribute to strain ageing. Differences in the availability of carbon and nitrogen at different temperatures, and their respective contributions, are thought to produce different strain ageing mechanisms in differing temperature regimes, with nitrogen being the solute primarily responsible for ageing effects at lower temperatures [55]. According to the diffusional model of Cottrell and Bilby, the fraction of the available solute which has migrated to dislocations, q , should be given by:

$$q = A(Dt/kT)^{2/3} \quad (12)$$

where t represents time, T temperature, D the diffusivity of the diffusing solute, and A is a constant, incorporating dislocation density and other terms. This expression was found to describe the kinetics of strain ageing in alpha-iron for values of q up to approximately 0.3. The model was extended by Harper [117] who considered 'competition' for solute among precipitates growing on dislocations. Harper derived an expression for q under these conditions,

$$q=1-\exp(-A(Dt/kT)^{2/3}) \quad (13)$$

He found the expression to give reasonable agreement with experimental data on strain ageing in interstitial solutions in iron, up to values of q of 0.7, and found apparent activation energies for strain ageing equal to the activation energies for diffusion of carbon and nitrogen in iron. The value of the rate constant, A , depends upon the energy of interaction between interstitials and dislocations, and various attempts have been made to determine this experimentally, and from theoretical considerations, using elasticity theory [118,119,120]. Wilson and Russell [110] found that the $t^{2/3}$ law holds to beyond 60% completion of strain ageing, and Stephenson and Conard [121] found the law to apply up to 70% completion. However, other experimental results, for example those of Thomas and Leak [122] appear to show deviations much earlier. These deviations have been explained in terms of the non-diffusional mechanism of Snoek ordering, which is the localised ordering of interstitials in the stress fields around dislocations [123]. In a perfect crystal, interstitial solutes would be distributed randomly among the available sites; the application of a uniaxial stress will tend to cause interstitials to become ordered into those sites lying in lattice planes parallel to the applied stress, reducing the elastic strain energy of the solvent lattice.

Ordering of interstitials around dislocations will therefore cause a pinning effect, and alter the dislocation stress field. Rose and Glover [124] studied this process of Snoek ordering of carbon in austenite, and found an apparent activation energy for the reaction of $84\text{kJ}\cdot\text{mol}^{-1}$, consistent with theoretical estimates. Rosinger et al [125] and Rosinger [126] found a $t^{2/3}$ relation for the Snoek ordering reaction in alpha-iron, with an activation energy of between $58.8\text{kJ}\cdot\text{mol}^{-1}$ and $62.2\text{kJ}\cdot\text{mol}^{-1}$, but a relationship with a time exponent of

between 0.33 and 0.50 for the stage attributed to interstitial solute diffusion, with an activation energy of between $84\text{kJ}\cdot\text{mol}^{-1}$ and $100\text{kJ}\cdot\text{mol}^{-1}$, similar to that for diffusion of carbon or nitrogen in iron. Humphreys et al [127] found similar results, with a time exponent of $2/3$ for Snoek ordering, and of $1/2$ for the later stage. Humphreys et al [127] proposed that the later stages of strain ageing were due to long range diffusion, but that the time exponent differs from that predicted by the Cottrell and Bilby model because of the modification of the dislocation stress field due to the prior Snoek ordering, so that the principal reason for the failure of the $t^{2/3}$ law is that there is a continuous variation in the interaction energy between interstitial solutes and dislocations.

Also, at high levels of dissolved interstitials, quench-ageing effects can be superimposed on strain - ageing [128,129,130], causing deviations from the kinetics expected from the work of Cottrell and Bilby and of Harper. The drift-capture mechanism and the $t^{2/3}$ law proposed by Cottrell and Bilby [108] appears to be applicable only in the earliest stages of strain ageing in alpha-iron, with Harper's expression for the kinetics giving reasonable agreement at later times. Most authors agree that the principal mechanism of strain ageing below about 150°C is diffusion of nitrogen to dislocations to form atmospheres, which raise the stress required for these dislocations to become mobile. Later, it becomes energetically favourable for new dislocation sources to become active, causing an increase in dislocation density. At higher temperatures carbon solubility may increase sufficiently for pinning by carbon to become significant [55]. The effects can be enhanced by supersaturation of interstitial solutes by rapid cooling from austenite, so that quench ageing phenomena are superimposed on strain ageing [130]. Ageing is generally slower than is predicted by the Cottrell and Bilby [108] and Harper [117] models, for two main reasons: a) drift-capture is preceded by rapid Snoek ordering [123] which partly relieves the stress fields near dislocations [127], and b) solute becomes depleted near dislocations, and long range diffusion takes over from short range drift as the rate limiting mechanism. Precipitation is generally thought to occur in the later stages of strain ageing (independently of that due to quench-ageing), but there seems to be little convincing experimental evidence for this, although it is a well known feature of quench ageing [114,131].

Cottrell [132] in 1953 proposed a model based on interaction of diffusing solute atoms with mobile dislocations, since the diffusion rate of solute atoms at temperature where serrated flow occurs are too small to cause the effect. Cottrell proposed that the vacancies and other atomic defects increases by plastic deformation may speed up the diffusion of solute atoms, and then the diffusion rate increased enough can cause strain ageing during plastic deformation. Cottrell also concluded that the temperature and strain rate for the start of serrated yielding in iron showed an Arrhenius relation producing the same activation energy as that for the diffusion of nitrogen in alpha-iron. The diffusion rate is affected by temperature, deformation rate and solute concentration.

On reviewing the literature, it seems that three different approaches have been used in modeling. In Cottrell's solute dragging model [133], an impurity atmosphere is formed during dislocation movement. McCormick [134] and Van Beukel [135] developed an arrested model based on an original paper by Sleswyk [136], in which the solute atoms are considered to segregate to the dislocations during their arrest at obstacles, taking account of the jerky nature of the thermally activated motion of dislocations. Rose and Glover [124] introduced the pair reorientation model which is based on Snoek [137] theory. Here the dislocation movement is postulated to be obstructed by the interaction between the dislocations elastic field and that of vacancy solute pairs. In the Rose and Glover model long range solute diffusion is not required. The above models can all be related to the drop in flow stress of the Portevin Le Chatelier effect on the basis either of dislocations breaking away from the pinning atoms or of new dislocations being formed.

The main reason that new theories have been conceived since Cottrell's original proposition is the discrepancy observed between the time dependence of jerky flow and the diffusion rate of the solute, this difference being at times several orders of magnitude, especially at low temperatures. Early attempts by Cottrell [132] and Mulford and Kochs [138] were that Cottrell considered vacancy assisted solute solute diffusion and Kochs proposed a dislocation dislocation interaction. The basis of which was that arrested dislocations may become locked through a redistribution of solute within the dislocation core

(solute core diffusion) at temperatures too low for bulk diffusion. It was also suggested that the glide resistance of a dislocation due to solute accumulation rather than by locking along its length.

2.3.1. Static strain aging and Dynamic strain ageing.

Dynamic strain ageing refers to the attractive interaction between diffusing solute species in the alloy and mobile dislocations during deformation. Originally, it was considered that the solute clouds interact with dislocations during a quasi-viscous type of motion. Ageing has been proposed to occur, not during the free flight motion of dislocations, but rather during the period when the dislocation are temporarily held up at local obstacles in the glide plane, known as the waiting time t_w . The phenomenological approach has associated the PLC effect with negative strain rate sensitivity of the flow stress. One of the major changes of dislocation motion induced by temperature is the effect of thermal activation. This lowers the effective height of all barrier potentials along the dislocation line and then induces the decreased waiting time of the dislocation at obstacles.

The main method to get insight into the process of thermal activation of dislocations as discrete obstacles is to measure strain rate sensitivity at various temperatures since an Arrhenius equation can explain the effect of thermal activation at single obstacle while the real situation is more complex.

While serrated flow curves are the most commonly observed macroscopic manifestations of dynamic strain ageing process, there are various other phenomena. A peak or plateau is observed in the variation with temperature of the flow stress, the work hardening rate ($\theta = \Delta\sigma/\Delta\varepsilon$), and the Hall-Petch slope K_ε . In addition, minima occur in the variation of ductility and strain rate sensitivity ($\gamma = \Delta\sigma/\Delta\ln\dot{\varepsilon}$) with temperature [93]. All are illustrated schematically in Figure 25.

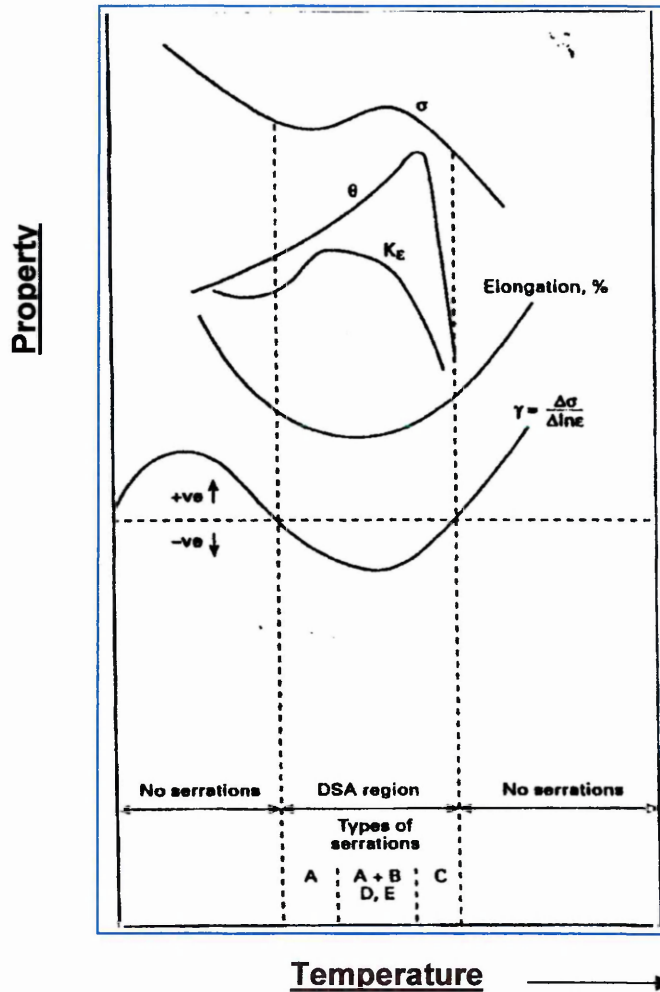


Figure 25. Schematic diagram of the various manifestations of DSA [139].

Bands of localised deformation are frequently observed to appear on the surface of a deforming specimen, which is producing a serrated flow curve at apparently random locations on the specimen.

The most potent indicator of underlying dynamic strain ageing process are considered to be the peak in flow stress variation with temperature and the negative macroscopic strain rate sensitivity of the flow stress [52,55,93]. The generalised flow stress deformation temperature curve for a pure metal is illustrated in Figure 26 and the corresponding curve for an alloy where DSA occurs is shown in Figure 27.

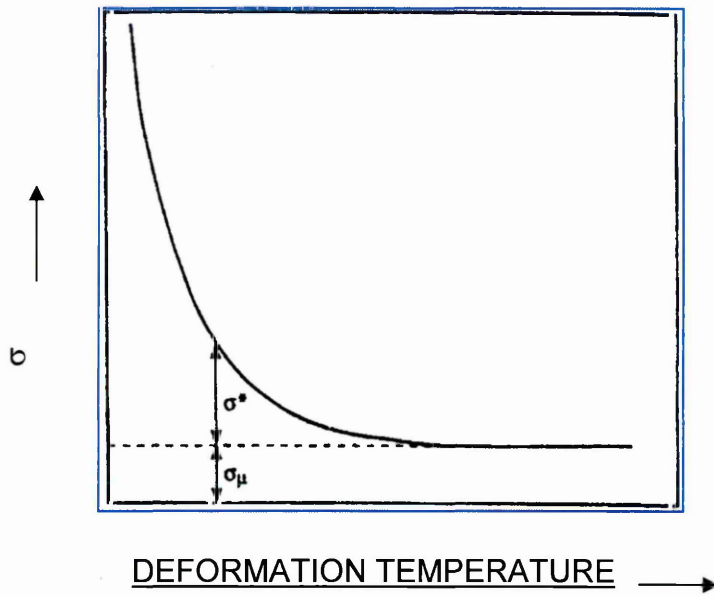


Figure 26. Flow stress versus deformation temperature curve for a pure metal: the thermal flow stress σ^* and athermal σ_{μ} , are indicated [140].

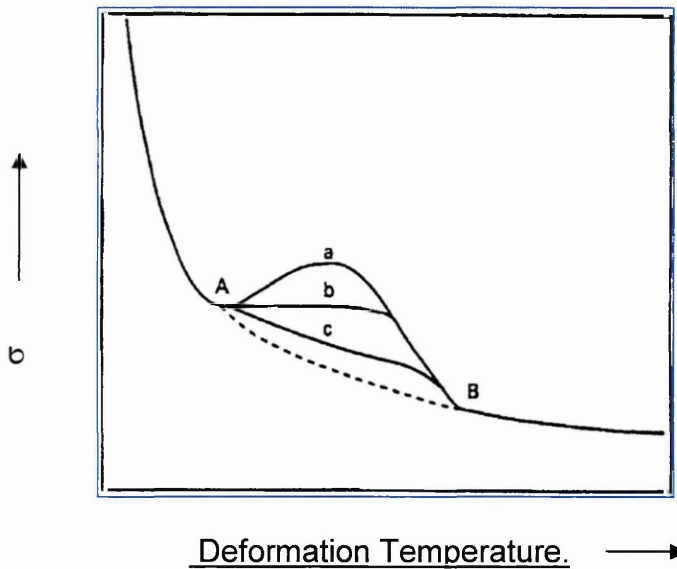


Figure 27. Flow stress versus deformation temperature curve for an alloy in a the effects of DSA are dominant, whereas in c dynamic recovery and softening remain the dominant processes [93],

There are various typical characteristics of serration depending on solute concentration and deformation conditions such as strain, strain rate and temperature. They were recognised and their characteristics were discussed by Worthington and Brindley [141], Rodriguez [139] and summarised by Robinson and Shaw [93]. Type "A" was associated with the repeated initiation and

continuous propagation of dislocation bands along the entire specimen length. This showed periodic peaks, which rose above the average stress level. Type "B" was not periodic but oscillating with respect to the average stress level. Here PLC bands was strongly localised and only propagated short distances in a discontinuous manner. Type "C" showed extremely large stress drops with plastic bands appearing randomly, which was generally observed at high temperatures or low strain rates as shown in Figure 28.

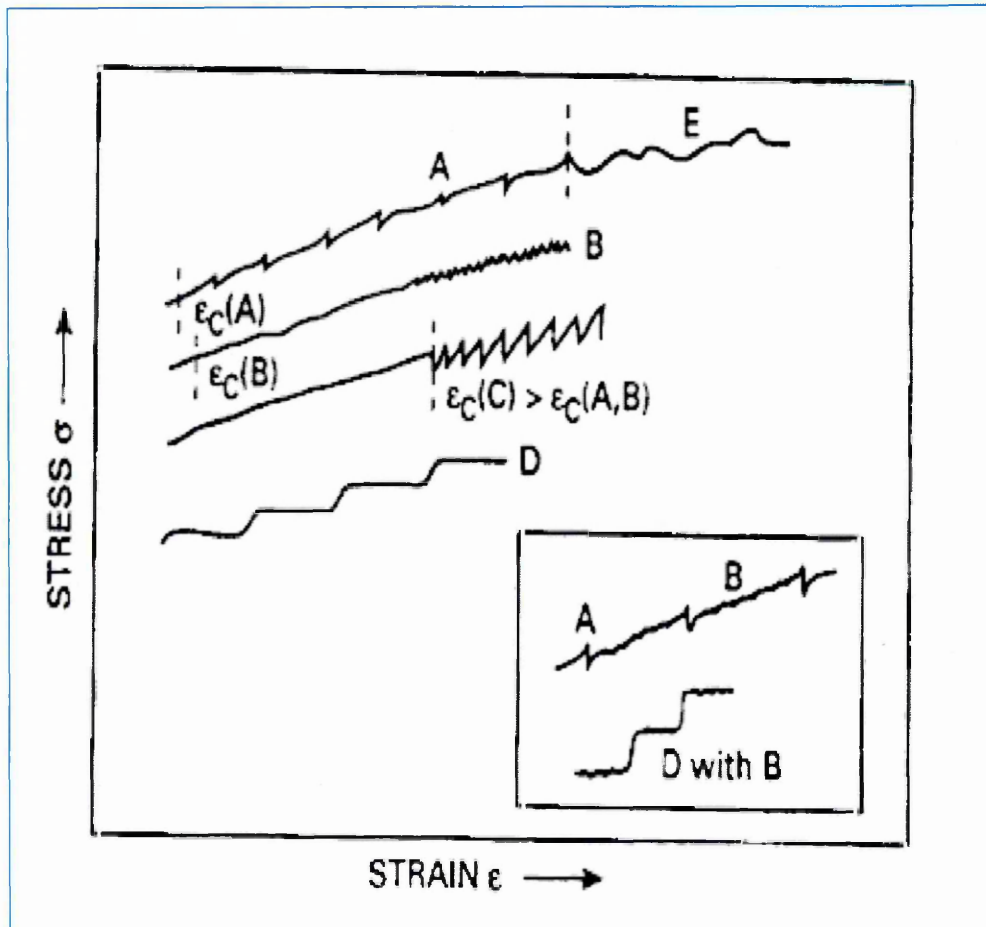


Figure 28. Curves illustrating the various serration types [93].

2.3.2. Dynamic Strain Ageing in Iron and Ferritic Steels.

Dynamic strain ageing can occur at around room temperature in slow tensile deformation (10^{-6}s^{-1}). At normal tensile deformation rates (10^{-4}s^{-1}) dynamic strain ageing occurs in the range 100° - 300°C . Although at very high interstitial solute levels its effects may extend down to room temperature. At high strain rates (10 - 300s^{-1}), the effect appears at 400° - 670°C . As carbon and nitrogen still segregate strongly to dislocations up to at least 670°C . As reported in the Baird review [55].

As shown in the stress vs strain curves in Figure 29, with increasing temperature of deformation the strain hardening rate first increases and serrated flow occurs at 100°C . In the fine grained specimen as the temperature increases to 200°C the frequency of serrations on the flow curve decreases, although the strain hardening rate increases slightly: at the same time yielding develops and the serrations increase in the amplitude. In the same temperature range the coarse-grained specimen shows very little yield point elongation and no serrated yielding. Above 200°C the strain hardening rate decreases in both fine and coarse-grained specimens.

In most steels the elongation to fracture drops in the blue brittleness range, this is not an essential consequence of dynamic strain ageing. Serrated yielding shows that dynamic strain ageing is affecting the yielding behaviour and a slight rise in yield stress is usually obtained in the dynamic strain ageing range and Luders strain follows a similar pattern to the yielding as shown in Figure 30. Generally the strain hardening rate, the flow stress and the UTS are the properties most affected by dynamic strain ageing, there is an associated rise in the increase of dislocation density with strain over the same temperature range as shown in Figure 31.

Metallic materials and alloys in general show a decrease in strength with an increase in temperature. At the same time ductility increases and rate effects become pronounced. Exceptions to this behavior are usually limited to certain temperature regions. Examples are regions of strength increase with temperature increase, serrated flow and negative or zero rate sensitivity.

Collectively these phenomena are called dynamic strain aging. The flow stress decreases with an increase in loading rate when negative rate sensitivity is present whereas normally the flow stress increases. The expression 'flow stress' refers to the stress in the region of a stress-strain diagram where inelastic flow is fully established and where the tangent modulus is much smaller than the elastic modulus.

The term 'Portevin Le Chatelier' effect is usually, but not always, reserved for the observation of serrated flow, which in turn seems to imply the strain-aging phenomenon. Dynamic strain ageing is found in certain temperature regions for solid solution alloys, in carbon steels, in ferritic steels and in virtually every alloy designed for high temperature service. It is generally attributed to the attachment and breaking loose of interstitial or solute atoms from crystals and their interaction with dislocations. As the stress increases, the dislocations break loose, travel and become re-attached. This process gives rise to the observed jerky motions. Serrated yielding, rate-independence or negative strain rate sensitivity and an increase of strength with temperature are also observed in age hardening Aluminum alloys. Although the phenomena associated with age-hardening alloys are similar, the mechanisms of age hardening involve precipitation reactions and appear to be different from those that cause dynamic strain ageing.

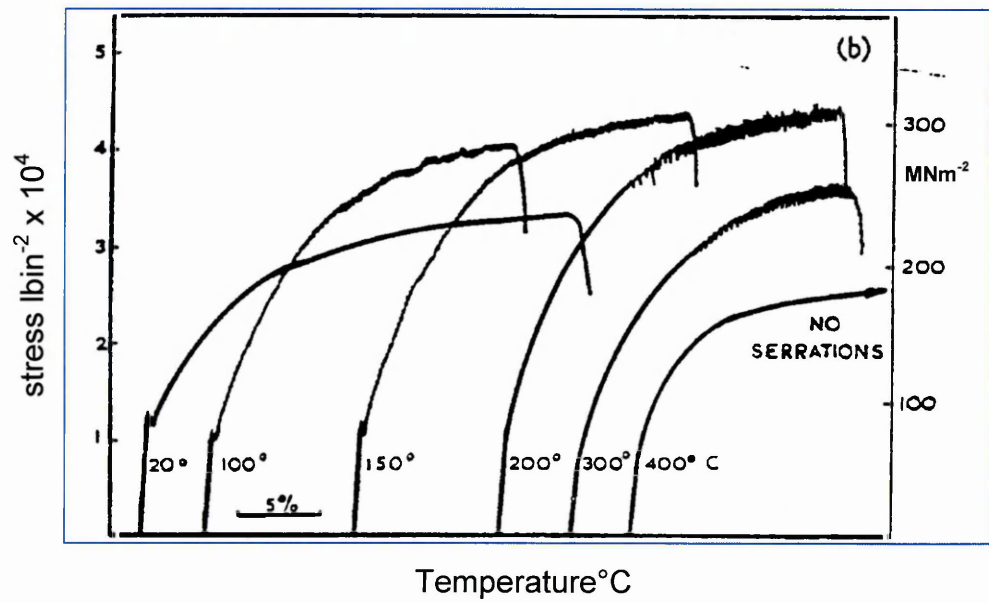
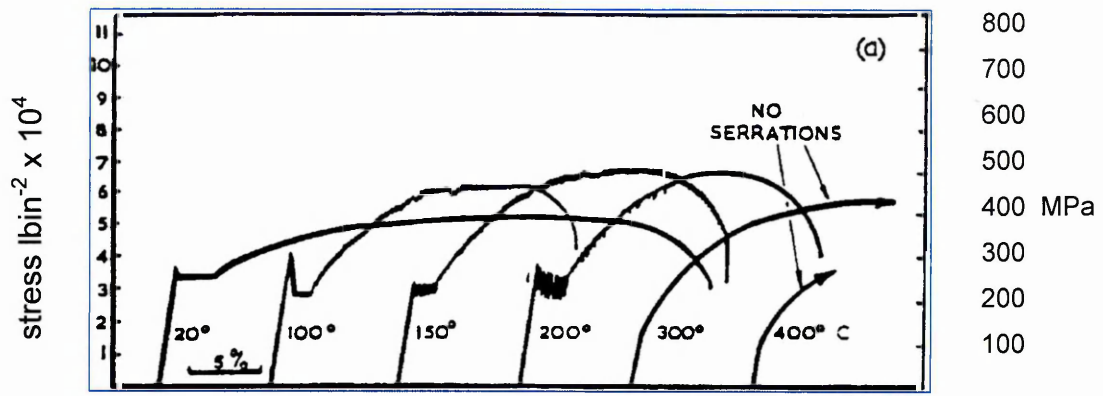


Figure 29. Stress - Strain curves of low carbon rimmed steel of grain size: (a) 0.02 mm, and (b) 0.20mm. Strain rate 10^{-4} sec^{-1} [82].

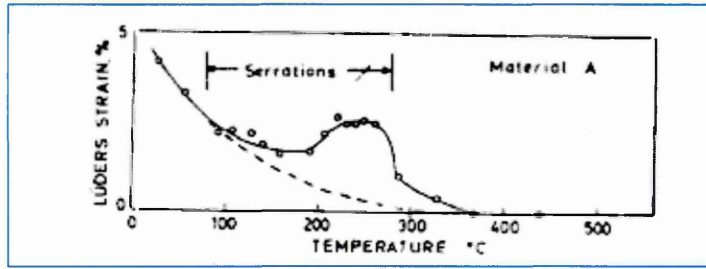
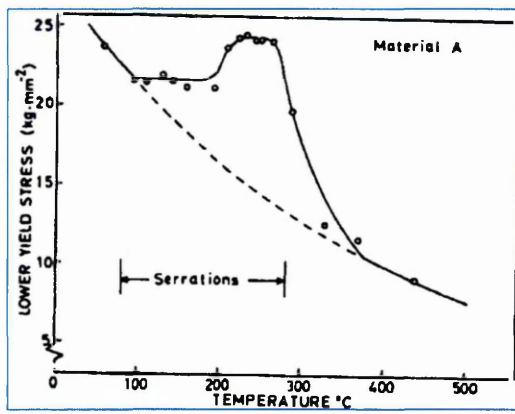


Figure 30. Variation of LYS and Luders strain with temperature in mild steel [92].

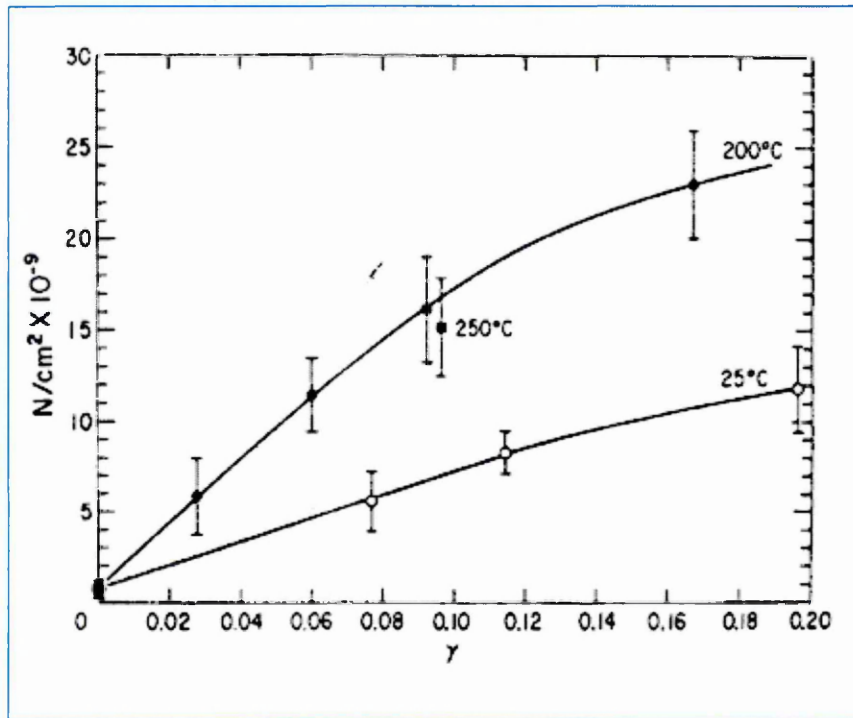


Figure 31. Average dislocation density (N) versus plastic shear strain (γ) for a 0.035% C steel deformed in tension at three temperatures. $\dot{\gamma} = 6 \times 10^{-4} \text{ sec}^{-1}$ [102].

2.3.3. Composition effects.

It is generally accepted that carbon and nitrogen are the main elements responsible for dynamic strain ageing in steel. If nitrogen is removed from mild or carbon-manganese steel by hydrogenation the magnitude of the strain hardening rate peak is greatly diminished, although there is no shortage of carbon available in the form of cementite.

The blue brittleness strengthening effect increases as the nitrogen level increases, as shown in Figure 32, increasing nitrogen levels raise the strain hardening rate up to 10% strain. The range of rapid strain hardening induced by dynamic strain ageing is extended, by increasing strain at which the supply of nitrogen to pin freshly generated dislocations becomes exhausted.

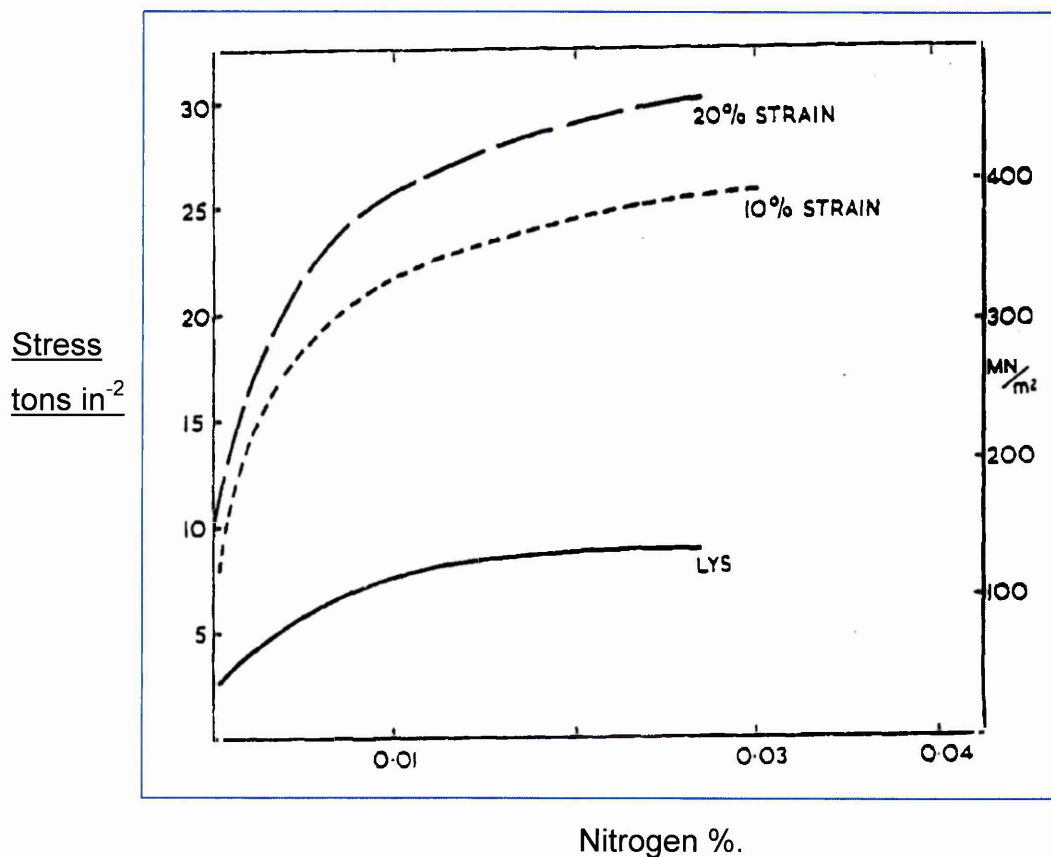


Figure 32. Effect of nitrogen level on LYS and true stress for 10% and 20 % elongation of iron strained at 225°C [142].

Localised exhaustion of nitrogen is often manifested by coarse serrations, these serrations correspond to the formation of very localised bands of high deformation in which nitrogen is exhausted. If the material in these bands can not work harden sufficiently to compensate the reduction in area of the test piece in the band, the specimen breaks within the band with low elongation. Increasing the nitrogen level raises the strain at which this occurs and thus increases the elongation to fracture as shown in Figure 33 [142].

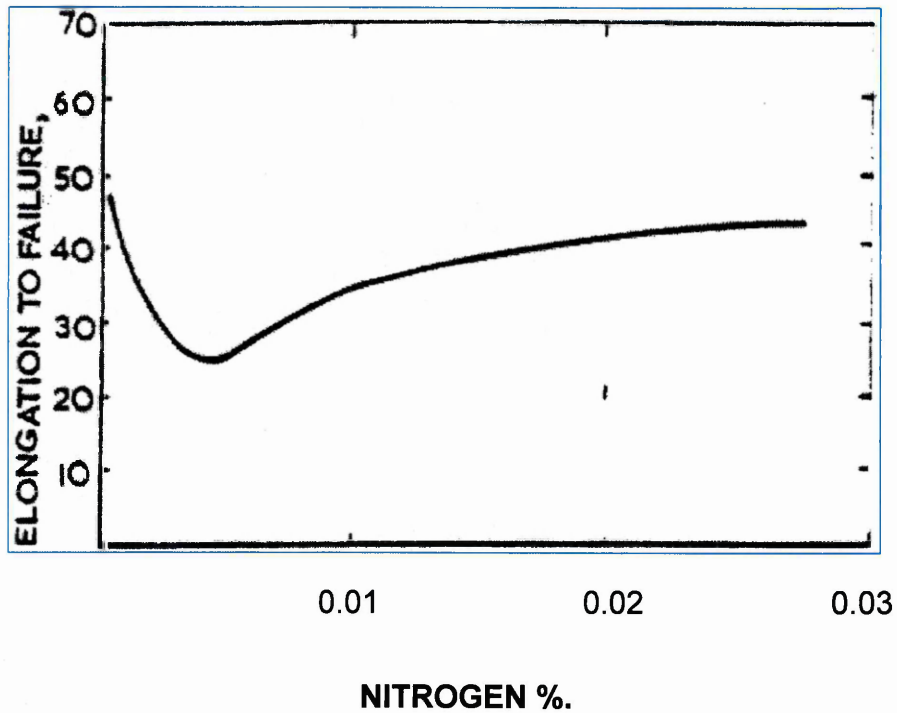


Figure 33. Effect of total nitrogen level on elongation to fracture of iron strained at 225°C [142].

2.3.4. Strain Rate effects.

The temperature for the occurrence of dynamic strain ageing increases with increasing strain rate while the peak strengthening stress due to dynamic strain ageing decreases linearly with increase of strain rate. As shown in Figure 34 for low carbon steel the data taken from the work of A. K.Taheri et al [84]. There is a temperature at which the ultimate tensile stress displays a maximum at each strain rate. Other authors have observed the same phenomena [52,53].

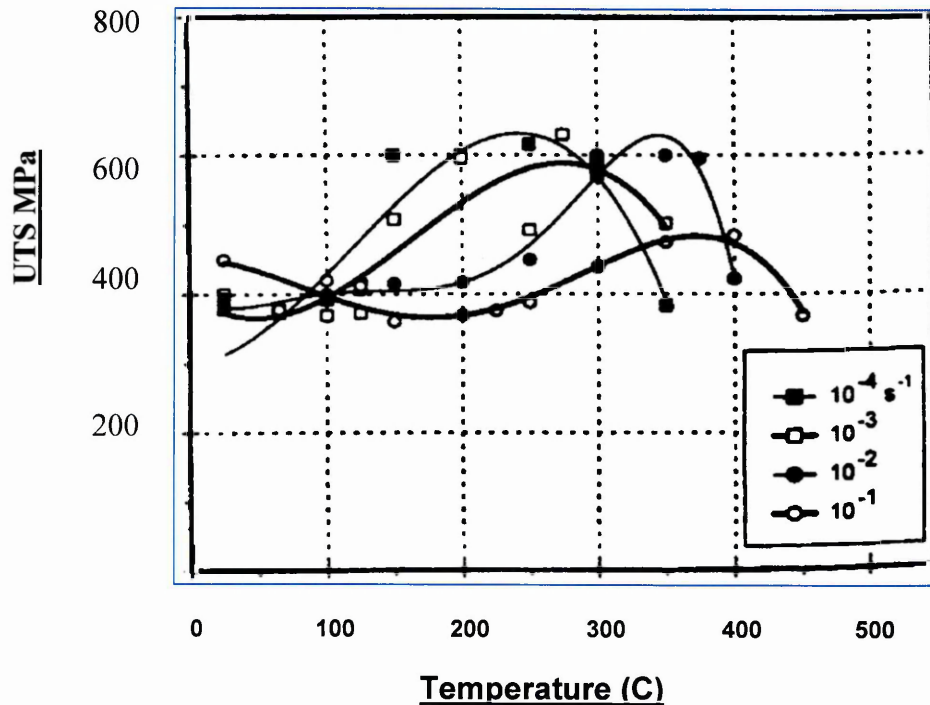


Figure 34. Temperature Dependence of the UTS at various strain rates (for low carbon steel) [84].

Strain ageing in steel, is generally analysed by measuring the minimum and maximum temperature associated with the occurrence of serrations and then expressing their dependence on strain rate by means of an Arrhenius equation:

$$\dot{\epsilon} = A \exp(-Q/RT) \quad (14)$$

Where $\dot{\epsilon}$ is the strain rate, R the gas constant, A a frequency factor, Q the activation energy, and T the absolute temperature. Figure 35 shows the condition associated with the serrations by an Arrhenius plot.

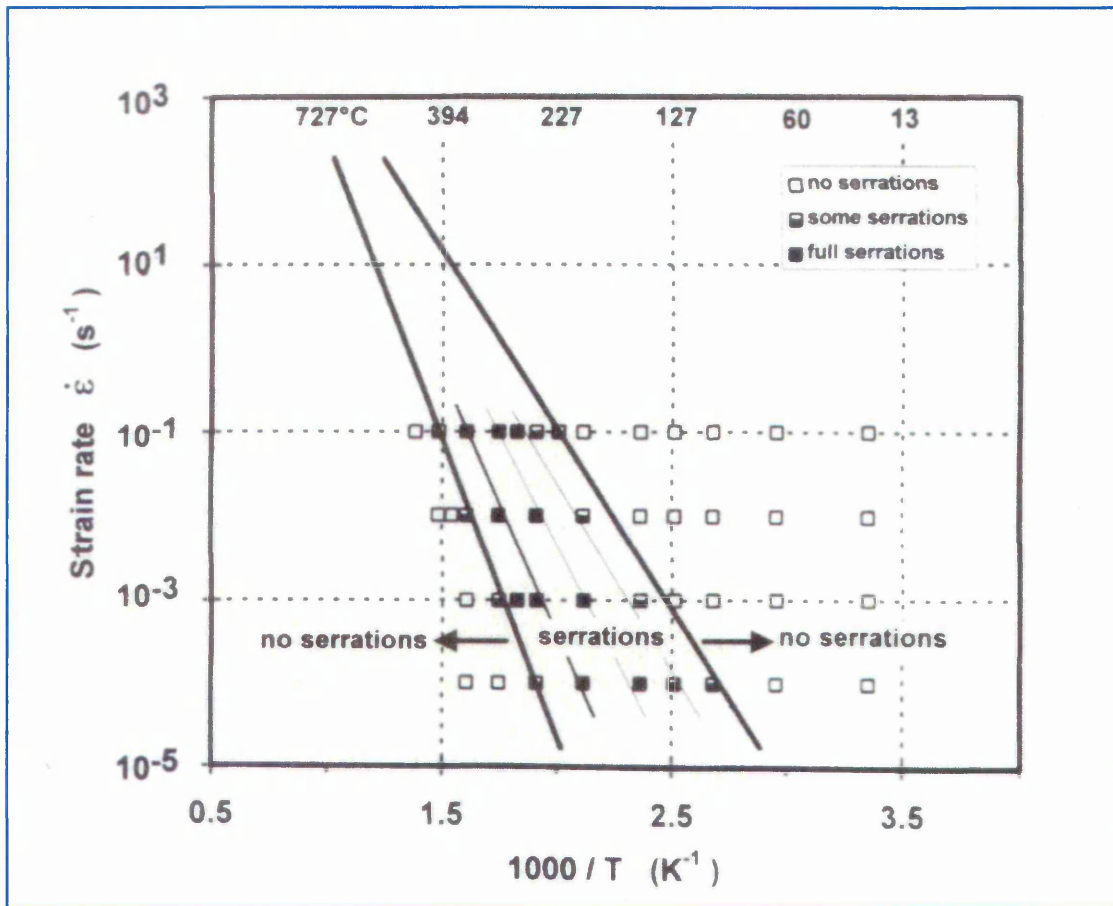


Figure 35. Temperature and strain rate range over which serrations are observed [84].

In modern commercial steels to minimise the effect of dynamic strain ageing, free nitrogen is controlled by the addition of strong nitride forming elements like aluminium, vanadium, titanium as mentioned in the nitrogen in steel section. Hence the importance of free nitrogen measurements and its control is essential for the control of the steel product quality.

2.3.5. Strain Rate Sensitivity.

The flow stress of many commercial alloys depends on the applied strain rate. This dependence, usually called strain rate sensitivity (SRS), has been identified as a major property affecting the formability of metals and alloys. Sheet metal forming processes are among the most important metal-working operations. These processes account for a sizable proportion of the manufactured goods made in industrialised countries each year. Furthermore, to reduce the cost and increase the performance of the manufactured products, in addition to the environmental concern, more and more light weight and high strength materials have been used as a substitute to the conventional steel. These materials usually have limited formability, thus a thorough understanding of the deformation processes and the factors limiting the forming of sound parts is important, not only from a scientific or engineering viewpoint, but also from an economic viewpoint [276].

In sheet metal forming operations, the amount of useful deformation is limited by the occurrence of unstable deformation which mainly takes the form of localised necking or wrinkling. Failure by wrinkling occurs when the dominant stresses are compressive, tending to cause thickening of the material. Localised necking occurs when the stress state leads to an increase in the surface area of the sheet at the cost of a reduction in the thickness. There are two kinds of neck i.e, the diffuse neck (so called because its extension is much greater than the sheet thickness), and the localised necking (through thickness thinning), which is terminated by final separation or fracture. After the localised neck initiates, further deformation of the material concentrates in this localised region, and the deformation in the homogeneous region vanishes completely. So the localised neck is a very important phenomenon in determining the amount of useful deformation that can be imposed on a work piece. The mechanism for the initiation of the localised band is very complicated, roughly speaking, this phenomenon can be attributed to the softening effect, for example, the geometric softening (i.e. the decrease with strain of the cross-section area which bears the forming load, the generation of voids), or material softening (flow stress decreases with the increase of the effective strain) [276].

To answer the question, sheet metal forming must be divided into two different effects global and local. Global effects directly relate to the press speed (more accurately the punch speed), while local effects are differences in forming speed between adjacent areas of the stamping. The relative rate of deformation of adjacent elements in sheet metal forming is the local effect. These rates of deformation are more accurately called strain rates. This local effect of strain rate is extremely important in sheet metal forming.

Two important examples of local effects in sheet metal forming are controlling local strain gradients (Figure 36, 1A) and delaying the onset of thickness necks characterised by the forming limit diagram (Figure 36. 1B). Examining either example in Figure 36, one quickly realises that the material in the gradient or neck (zones 1) has deformed more than the material outside the gradient or neck (zones 2). Therefore, the strain rate of the material in zone 1 exceeds the strain rate of zone 2.

Depending on the particular type of sheet metal being used, the yield strength may increase or decrease as the strain rate increases. This strain-rate sensitivity is the strain-rate exponent m often described in a power law equation similar to the work-hardening exponent n : $\sigma = K \dot{\epsilon}^m$ where $\dot{\epsilon}$ is the strain rate.

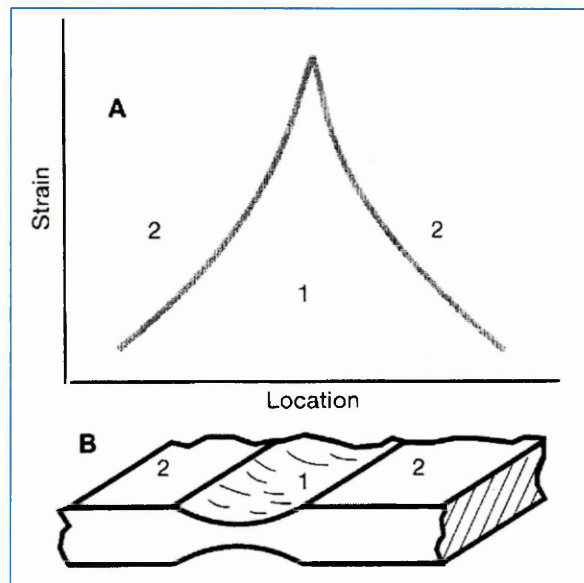


Figure 36. Both a localized strain gradient (A) and a localized neck (B) are characterized by a higher rate of straining at location 1 and a lower rate of straining at location 2 [276].

The m value can be measured during a tensile test. Unlike the constant test speed used to measure traditional mechanical properties and the n value, the test for m value has its speed rapidly changed during the test. Figure 37 shows several such test-speed changes. Unlike only positive values of n , the m values can be positive, zero or negative. The values of m are small relative to the n values. For example, AKDQ steel may have an n value of +0.21 and an m value of +0.012. Because of the small magnitude of the m values, their importance was unappreciated by the metal forming community for many decades.

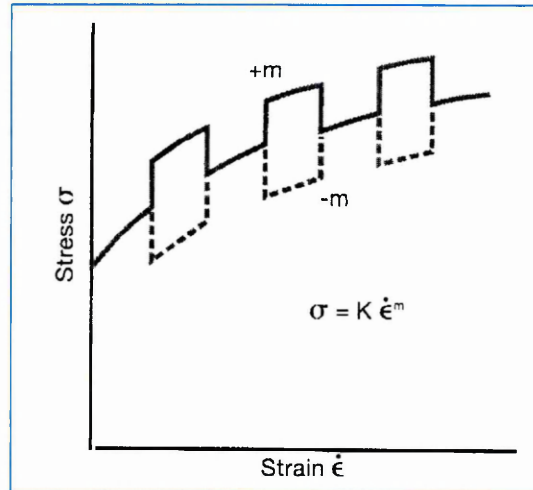


Figure 37. Strain-rate sensitivity as measured by rapid strain-rate changes during a standard tensile test. The m value is the magnitude of the stress change for a given change in strain rate and may be positive, zero or negative [276].

A positive m value means the material in an impending gradient (area 1 in Figure 36, 1A and B) that is straining faster will become stronger than its neighbour elements (area 2). This retards the development of the gradient and tends to spread the deformation more uniformly throughout the stamping.

In contrast, a material with a negative m value in the impending gradient will become weaker than its neighbour elements and will create a more localized gradient with a higher peak strain. A schematic of tensile test data (Figure 38) illustrates the concept of global and local strain rates. At the load maximum a neck attempts to form. All deformation along the length of the

tensile - test sample stops except for material inside the incipient neck that must increase in strain rate to maintain cross head extension. If the m value is negative, the material in the incipient neck becomes weaker (lower flow stress) and the strain localises more and more as the neck becomes more highly developed. Fracture in the neck soon follows.

However, if the m value is positive, the increased strain rate in the incipient neck strengthens the material relative to its neighbouring elements and the development of the neck is retarded. The strain rate inside and outside the neck is a local effect. It operates independently of the global effect, which is the actual test speed the machine applies to the entire test specimen.

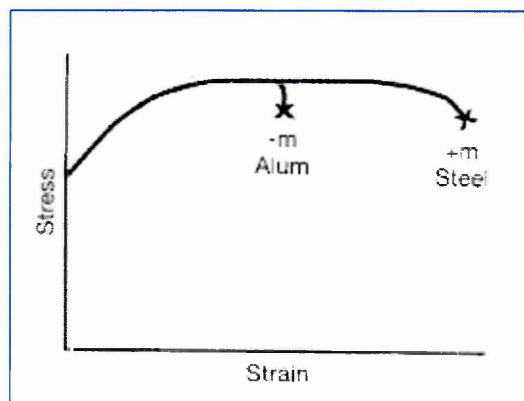


Figure 38. The width neck occurring at the maximum load during a tensile test is similar to the thickness neck in Fig. 36B. If the m value is negative, the strain rapidly concentrates in the neck and leads to early fracture. If the m value is positive, the formation of the neck is delayed [276].

2.3.5.1. Strain Rate Sensitivity Parameters.

There are various descriptions of SRS based on different constitutive laws, but the logarithmic SRS index, defined by:

$$m = [d(\ln\sigma)/d(\ln\epsilon^0)]_{T\epsilon} \quad (15)$$

is most frequently used.

Experimental observations indicate that m depends upon a number of

factors, strain, strain rate, temperature, microstructure evolution, deformation mode, and kind of loading [143,144,145]. Some investigations have shown that m is independent of strain [143,146]. However it is also reported that m may vary with strain [147]. In general, the strain-rate exponent increases with m . It is low (<0.02) for most of the pure metals and alloys except for some alloys in which solute drag dominates the deformation kinetics [148].

There are two common rate sensitivity parameters, measured in two different ways. The “instantaneous’ SRS index, m_i is measured over a rapidly changing strain rate (jump test) at an essentially constant strain and presumably corresponds to a constant structure. The “total” SRS index, m_t , is obtained by comparing two work hardening curves generated at different but constant strain rates and is associated with the formation history of the microstructure. Klepacko et al [148] have reviewed the phenomenon of SRS in fcc metals, emphasizing the differences between m_i and m_t values. They showed experimentally that while m_i is practically independent of strain, the m_t values show a sharp increase with strain. This indicates the dominant role of the rate sensitivity of strain hardening as a contribution to the total rate sensitivity, m_t . On the basis of these observations it has been concluded that two different types of micro mechanisms are responsible for SRS of metals. One is the currently operating micro mechanism of thermally activated motion of dislocations over stationary strong obstacles which controls m_i , and the other is the dynamic recovery process associated with collision and annihilation of moving dislocations which is responsible for m_t values. The dependence of SRS on strain for different aluminium alloys shows a complicated pattern. In the case of pure aluminum SRS has been reported to be almost independent of strain at room temperature [149], while for Al-Cu alloys measurements of m values showed a decrease with increasing strain [150]. The observed difference in the SRS of various aluminum alloys is believed [151] to be due to micro structural features such as solute atoms and fine precipitates which influence the development of dislocation structure and subsequently the dynamic recovery in these materials.

It is usual to distinguish between the instantaneous SRS, m_i , corresponding to the immediate response of the flow stress to a jump in strain

rate, and the steady-state SRS, m_t which is measured after a transient. Hence, $m = m_i + m_t$. The instantaneous measure is always positive, while the transient is negative in the DSA regime. When the total SRS parameter, m , becomes negative, conditions exist for the macroscopic observation of the PLC effect [152].

2.3.5.2. Transients following a strain rate jump [153].

The strain rate sensitivity is measured in most instances in strain rate jump tests in order to avoid issues related to the loading history of the respective specimen. The response of the material consists in an instantaneous variation characterized by positive strain rate sensitivity and a transient. The length of the transient measured along the strain axis of the stress-strain plot depends on the current loading rate (after the jump). Jumps up in strain rate lead to longer transients than the equivalent jump performed in the reverse direction and at the same strain.

The transient component of the SRS parameter, m_t , must be evaluated from strain rate jump tests. The quantity is computed from eq. 16 [154].

$$m_t = \log(\sigma_1/\sigma_2) / \log(\dot{\epsilon}_1 / \dot{\epsilon}_2) \quad (16)$$

In order to find the two stress levels, σ_1 and σ_2 , the procedure requires that the stress-strain curve from far after the jump is extended to the moment of the jump. This is illustrated by Lee [155] in Figure 39 and McCormick [156] in Figure 40 although Lee used the load vs extension curve to determine the strain rate sensitivity of the flow stress, instead of the conventional stress vs strain curve.

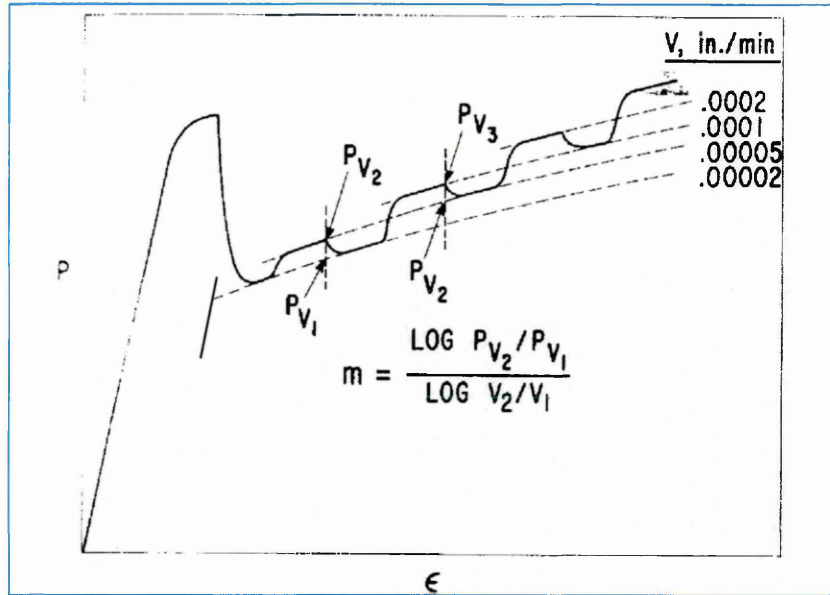


Figure 39. A Schematic diagram showing how the strain rate sensitivity of the flow stress m was obtained from the load P , versus extension ϵ curve in the differential strain rate test. The load extrapolation method is also indicated [155].

The formula Lee used to determine m was [155]:

$$m = \frac{\text{LOG}(P_{V_2}/P_{V_1})}{\text{LOG}(V_2/V_1)} \quad (17)$$

The load extension graph lines are extrapolated and a vertical line dropped at the intersection to give the corresponding rise in load. The load extrapolation method was used as the material always strain hardened.

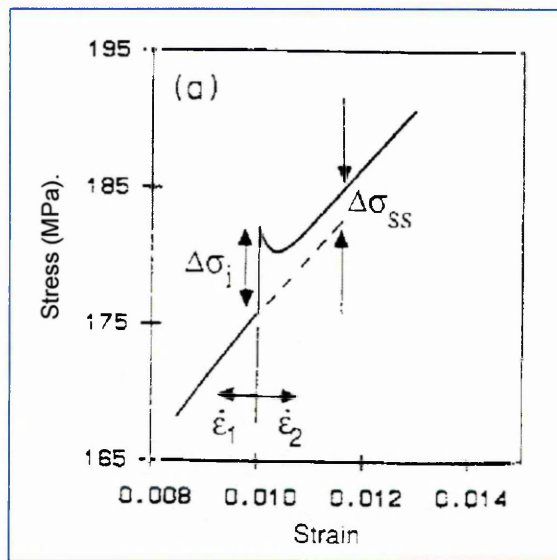


Figure 40. Schematic of the two different strain rate sensitivities [156].

Van den Beukel [157] first showed that a negative strain rate dependence of the flow stress can result from the diffusion of solute atoms to dislocations temporarily arrested at obstacles in the slip path. At temperatures and strain rates where solute diffusion to dislocations occurs [158] the local solute composition at arrested dislocations, C_s is a function of the waiting time at obstacles, in the slip path. A decrease in flow stress may then accompany an increase in strain rate due to the decrease in C_s resulting from the decrease in t_w however, the solute composition at dislocations cannot instantaneously respond to a change in strain rate. As a consequence a transient period may be expected too follow the change in strain rate C_s adjusts to its new quasi-steady state value C_s as shown in Figure 40. In the transient region the time dependent variation of the flow stress is determined by the rate of change of the flow stress associated with the time dependent change in C_s and the rate of strain hardening.

Although the actual process by which the new quasi-steady state value of C_s is reached may differ for increases and decreases respectively in strain rate the time constant of the transient period should be of the order of t_w of the new strain rate. For example if the strain rate is abruptly decreased the mobile dislocations must on the average wait for a period of time $t \sim t_w$ before acquiring the higher quasi-steady state composition characteristic of the new strain rate by solute diffusion. For an increase in strain rate it appears that the dislocations

on the average must move at least once before quasi-steady conditions are restored.

As shown in Figure 40 two different strain rate sensitivities may be defined. The instantaneous strain rate sensitivity $m_i = \Delta\sigma/\Delta\dot{\epsilon}$ corresponds to conditions of constant ϵ and C_s . The quasi-steady state strain rate sensitivity, $m_{ss} = \Delta\sigma/\Delta\dot{\epsilon}$ includes the effect of the steady state strain rate dependence of C_s on the change in flow stress. Numerous experimental measurements have shown that m_i remains positive at all strains. While m_t decreases with increasing strain, becoming negative at a strain ϵ_0 . The extent of the transient region is observed to increase with increasing strain [158,159,160].

Soare and Picu [154,277], found in their work by model prediction, that the transients always asymptoted to the constant strain rate stress-strain curve corresponding to the strain rate after the jump (Figure 41). Hence, m_t measured from numerical strain rate jump tests is identical to the parameter evaluated from constant strain rate tests [154]. Figure 42 [154] shows m_t as a function of strain at various temperatures. The parameter is evaluated based on their model predictions and eqn. 16 and using a strain rate differential of 1:100.

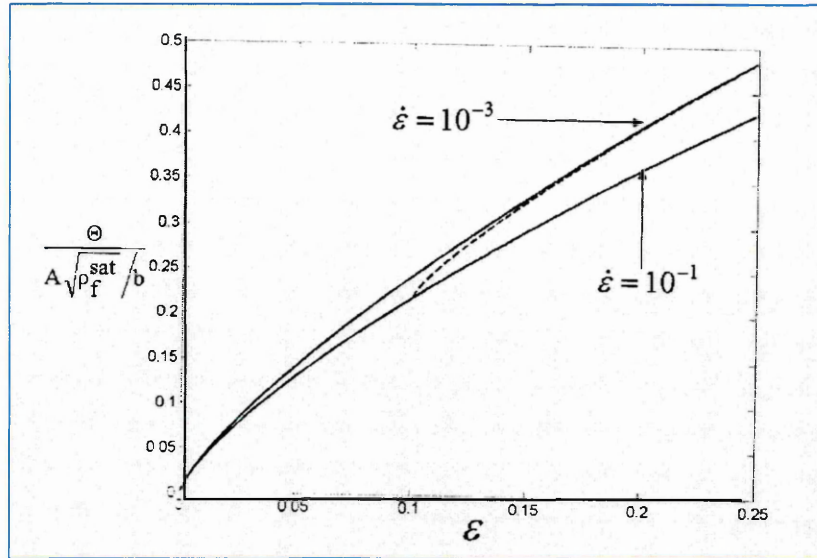


Figure 41. Transients following strain rate jumps. The continuous lines represent predictions of their model and equation 16. At constant strain rates of 10^{-3}s^{-1} and 10^{-1}s^{-1} . The transient shown corresponds to a strain rate jump from the fast to the slow rate at a strain of $\epsilon = 10\%$. The model does not capture the instantaneous response and hence, only the transient is visible. The transients eventually converge to the curve corresponding to the respective current strain rate [153,154].

They included experimental data at room temperature, 50°C and 100°C for reference. The parameter decreases sharply at small strains and returns toward positive values at larger strains. As the temperature increases toward the upper limit of the range in which negative SRS is observed in experiments, m_t takes very small negative values. Hence, increasing temperature leads to positive values for the total m (since m_i is always positive). A similar behavior is observed in the low temperature range.

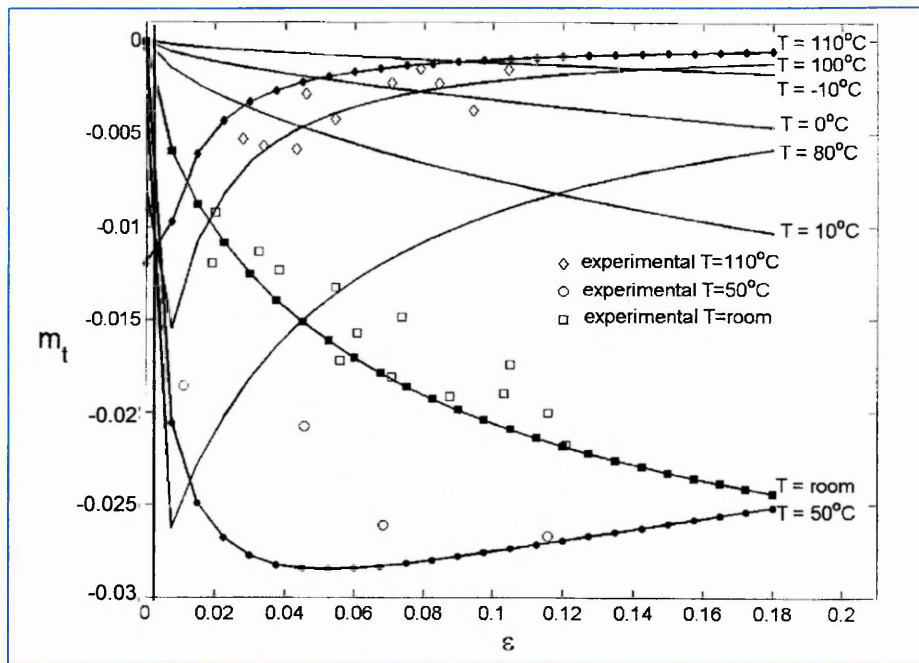


Figure 42. The transient component of the SRS parameter, m_t , as a function of strain. The data points are experimental values [153] while the lines are model predictions, m_t initially decreases with strain and then reaches a plateau at larger strain values. The effect is more pronounced in the temperature range 0° to 80°C , in agreement with experimental observations [154].

They used the model to predict a map of the negative SRS in the inverse-temperature, strain rate plane. To this end, the transient SRS is evaluated with eqn. 16 and the model, and used an experimental value of m_i obtained from earlier work [153]. The map is plotted in Figure 43 for the plastic strain $\epsilon = 5\%$ for which the measured instantaneous SRS in the Al-5%Mg alloy is $m_i = 0.0075$. The shaded area in the figure represents conditions in which negative SRS and PLC are experimentally observed in this material at the given strain. The domain is bounded at high rates ($m > 0$ for $\dot{\epsilon} > 10^{-1}\text{s}^{-1}$) and expands towards lower rates and lower temperatures. The curves represent the model predictions. The predictions overlap with the high temperature range of the experimental data.

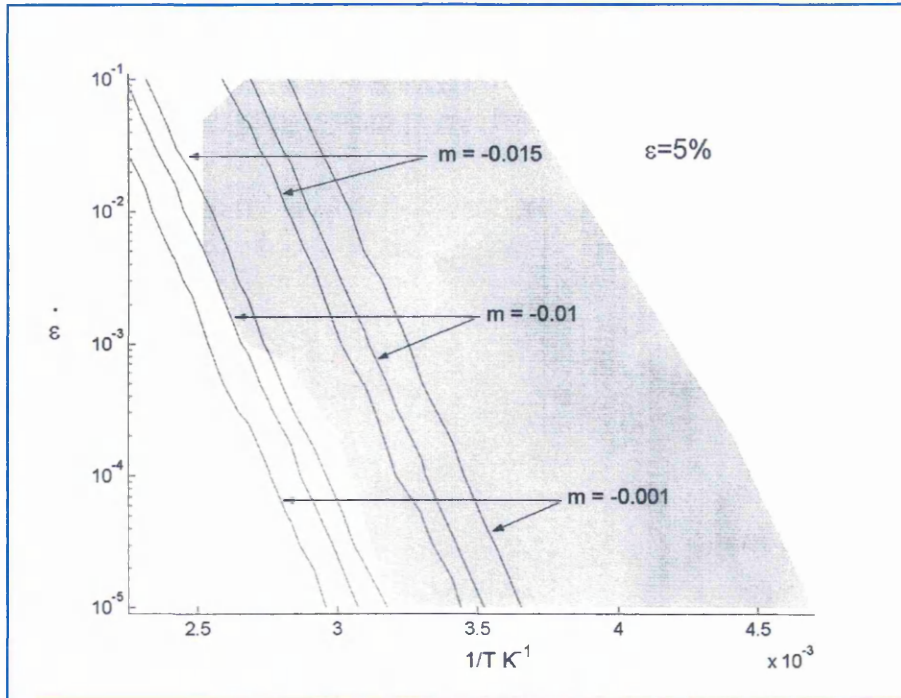


Figure 43. Negative strain rate sensitivity map in the inverse temperature-strain rate plane. The curves represent the total SRS parameter, m , predicted by the model (with the measured value of m_i 0.0075). The shaded area represents the domain in which the PLC effect and negative SRS are observed experimentally in the Al-5% Mg alloy. This field is defined based on data from [153]. The plot corresponds to $\dot{\epsilon} = 5\%$ in experiments, the material does not exhibit negative SRS at strain rates larger than 10%, while test data at strain rates lower than 10^{-6} s^{-1} are not available for this material [154].

The transient nature and dependence on temperature and strain rate on the strain rate sensitivity parameter are shown quite clearly in the work done by Lee [155] on zirconium in Figure 44 and Figure 45.

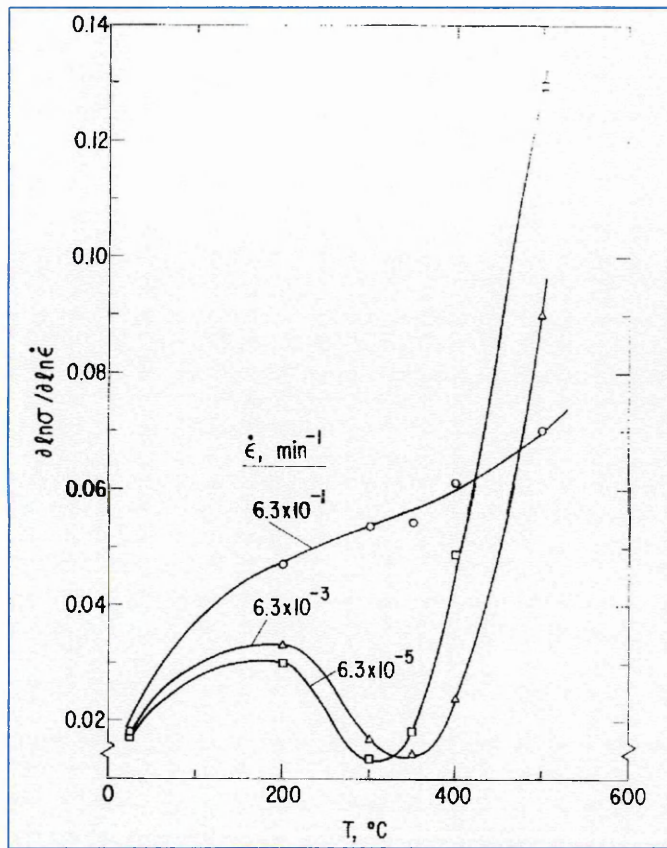


Figure 44. The temperature dependence of the strain rate sensitivity of flow stress m in Zircaloy 2 from room temperature upwards at selected strain rates [155].

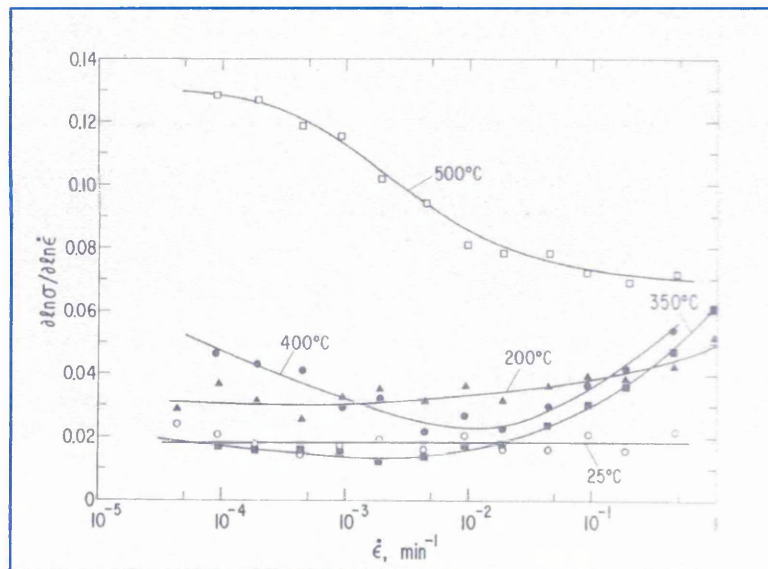


Figure 45. The strain rate dependence of the strain rate sensitivity of flow stress m ($\dot{\epsilon}$) = $\frac{\partial \ln \sigma}{\partial \ln \dot{\epsilon}}$, for zircaloy 2 at selected temperatures [155].

Examples of the inverse relationship of m in the dynamic strain ageing regime and the strain dependencies are taken from Picu et al [153,154] in Figures 46 and 47.

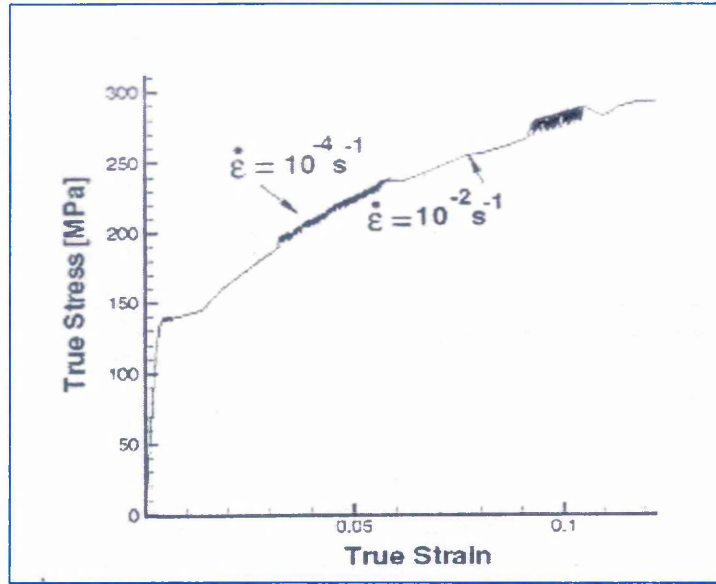


Figure 46. True stress strain curve obtained for a strain rate jump at room temperature [153].

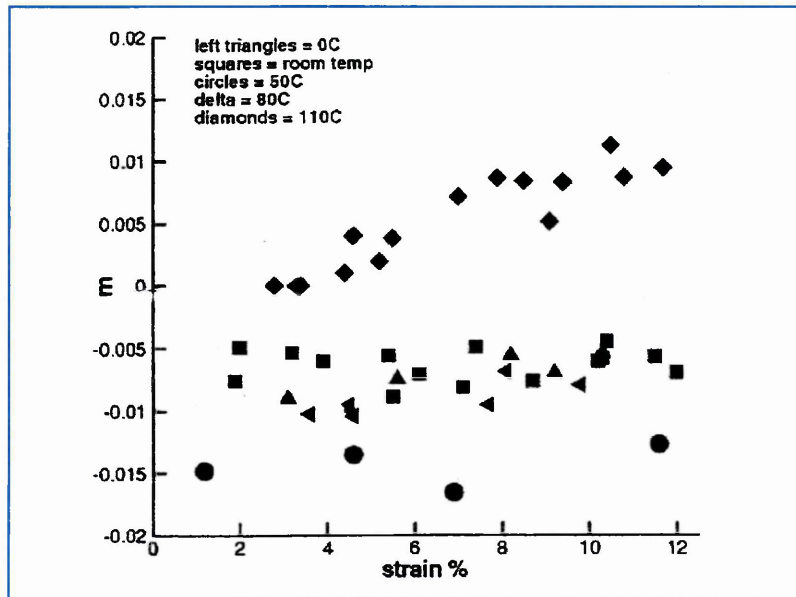


Figure 47. Strain rate sensitivity parameter obtained from strain rate jumps [153,154].

2.3.5.3. Problems encountered in the measurement of Strain Rate Sensitivity Using the Step-ramp Method.

Current interest in modelling metal processing using constitutive relations is reliant on precision determination of materials testing parameters. One parameter, the strain rate sensitivity, is extensively quoted, but means to measure it precisely are generally unavailable. The best method to measure this parameter is by intermittent strain rate change tests whereby, in theory, the internal structure is kept constant during the rate change. Conventionally, it is difficult to achieve this constant structure requirement, since the load frame's elastic interaction with the specimen, as well as the specimen's elastic compliance, causes inelastic transients.

Jackson [161] and Welke et al [162], described at length the problems associated in the determination of m , noting that even strain rate change experiments, as compared to temperature change experiments, are fraught with difficulties. The major difficulty is that of keeping the defect position, array and distribution constant (the structure), except for a small stress change near the local obstacles. The imposition of this state is not possible by conventional materials testing practice, since the machine (including the test frame, linkage, grips and the specimen outside the gauge length) elastically interacts with the deforming elastic plastic specimen.

2.4. Fatigue Crack Propagation in Metals.

In engineering components subject to cyclic loading fatigue crack initiation and propagation are important precursors to fracture. For pre – existing defects, for example in welded regions, stable crack growth is observed to occur at cyclic stresses as low as 10% of the level required to cause fracture, and fatigue crack growth often precedes fracture. Frost [163], and Liu [164] showed for aluminum sheet that the crack growth rate, could be expressed:

$$da/dN = \Delta S^m \cdot a^n \quad (18)$$

where ΔS is the gross sectional stress range [164], and a is the crack length.

Liu [164] theorised m and n to be 2 and 1 respectively, while Frost [163] found that m was 3 and n was 1. Paris and Erdogan in 1963 [165] using fracture mechanics on pre-cracked specimens originally proposed that the rate of fatigue crack propagation da/dN , is related to the stress intensity range ΔK , by the equation:

$$da/dN = C \Delta K^m \quad (19)$$

C and m are constants. For a given material the equation has been shown to provide a reasonable fit to the data. The exponent m is typically found to lie in the range 2 to 3 but values as high as 10 have been observed [166]. Values less than 2 are generally found when testing in aqueous environments [248]. The Paris equation does not describe fully the relationship between da/dN and ΔK , being valid only for the intermediate range of growth rates (typically 10^{-3} $\mu\text{m}/\text{cycle}$). The variation of da/dN with ΔK is actually sigmoidal in form, being bounded at extremes by the values of K_{1C} (characterising the materials fracture toughness) and ΔK_{th} (characterising a threshold for crack growth).

In fracture mechanics the region of greatest interest in the growth of a fatigue crack is that from a_d to a_c in Figure 48, where a_d represents the minimum crack length that can be detected using a non-destructive investigation (NDI) technique, and a_c represents the maximum crack length before catastrophic failure. Figure 48 is a schematic plot of fatigue crack length, a , versus the number of fatigue cycles, N , for a specimen fatigued using a stress cycle with a

constant stress amplitude.

As may be seen in Figure 48, the rate by which the crack grows becomes greater the larger the length of the crack. Because it is not physically possible to detect cracks smaller than a_d , with non-destructive investigations, it is necessary to assume for design purposes that inherent cracks may exist as large as a_d . Consequently, there is an incentive for increasing the resolution of the NDI techniques because this would increase the range of the useful fatigue lives of structures [167].

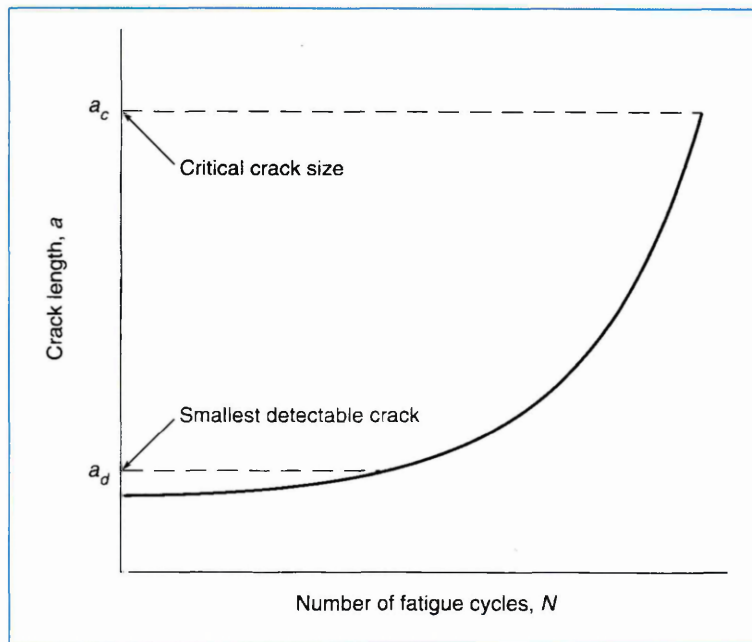


Figure 48. The growth of a fatigue crack as a function of the number of fatigue cycles N [167].

Although in a constant stress amplitude cycle, the maximum stress σ_{\max} and the stress range in a cycle (σ_{\max} to σ_{\min}) may remain constant during a fatigue test this is not true for the corresponding stress intensity factors since the stress intensity factors are a function of $a^{1/2}$ that is, $K_{\max} = \sigma_{\max} (\pi a)^{1/2}$ and $K_{\min} = \sigma_{\min} (\pi a)^{1/2}$ Figure 49 shows this. As might be expected, this has a significant effect on the crack growth rate da/dN which is the increase in fatigue crack length per fatigue cycle.

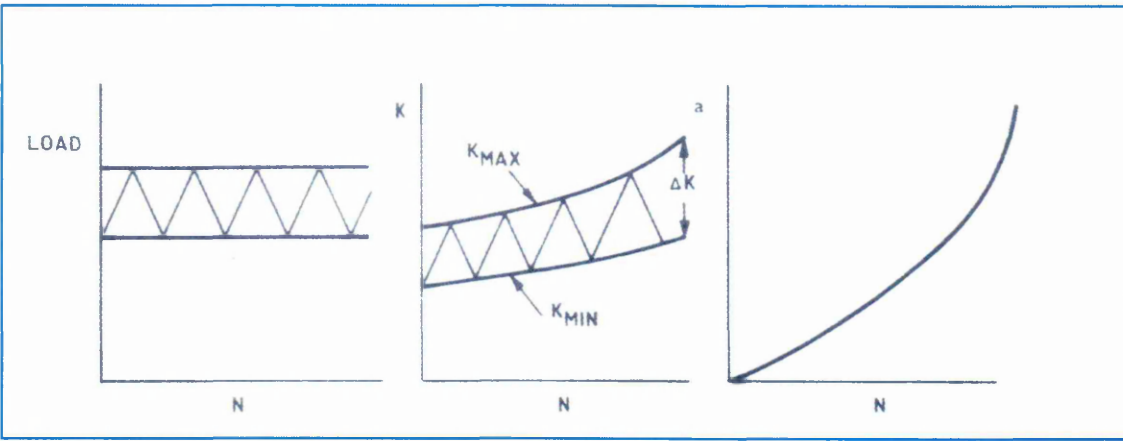


Figure 49. Constant load fatigue test (ΔK increasing) [168].

This dependence of the fatigue crack growth rate on the stress intensity is commonly demonstrated in plots of da/dN versus the stress intensity range $\Delta K = (K_{\max} - K_{\min}) = (\sigma_{\max} - \sigma_{\min}) [\pi a]^{1/2}$ using double logarithmic coordinates. A schematic plot of this kind is shown in Figure 50 a curve of this type can be divided into three distinct regions because of its sigmoidal form.

In the first region, the crack growth increases rapidly with ΔK . The fact that the crack growth rate begins its rise in this interval with an essentially vertical slope implies the existence of a threshold value, ΔK_{th} of the stress intensity factor range below which the fatigue crack cannot propagate. The rapid increase in the crack growth rate in Region I decreases as Region II is entered. Here, the data often tends to plot in a straight line over an extensive interval of ΔK values. Region II eventually gives way to Region III, in which the slope of the $\log(da/dN)$ against $\log(\Delta K)$ curve again rises. This rapid increase in da/dN with increasing ΔK is due, first, to the approach of K_{\max} to K_c , the critical stress intensity factor for fracture, and second, to the cross-section area carry the load becoming reduced to where it can no longer support the load. [167].

Region II is the most generally interesting since it corresponds largely to useful fatigue life of the specimen. Since $\log(da/dN)$ varies linearly with $\log(\Delta K)$ this interval, one may write a power law between da/dN and ΔK known as the Paris equation $da/dN = C(\Delta K)^m$ [165].

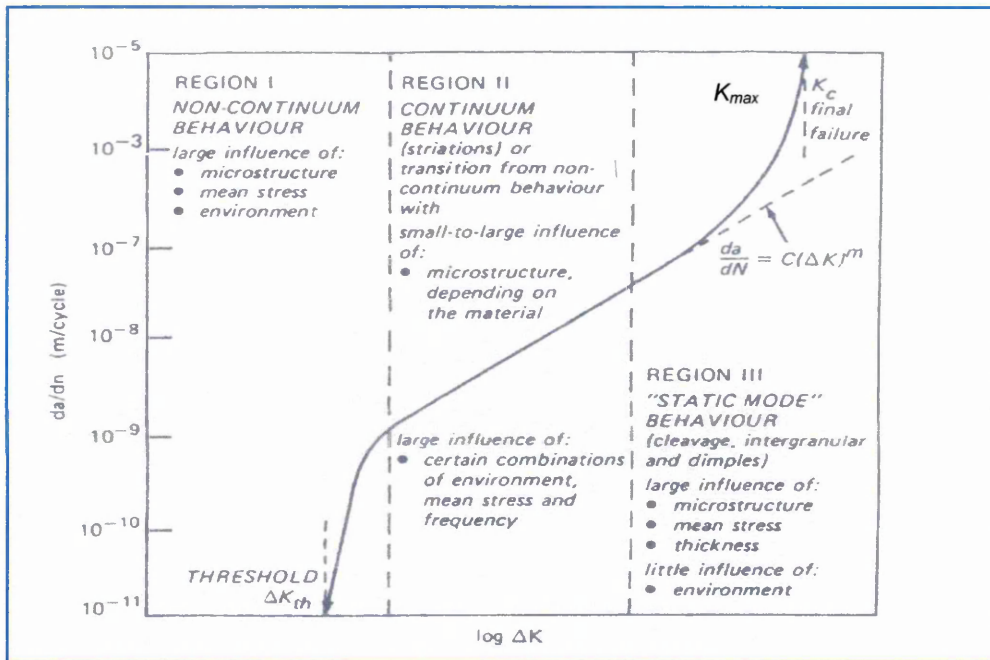


Figure 50. Summary diagram showing the primary fracture mechanisms associated with the sigmoidal variation of fatigue crack propagation rate da/dN with alternating stress intensity ΔK . ΔK_{th} is the threshold stress intensity for crack growth and K_{MAX} the critical stress intensity at final failure [169].

2.4.1. Fatigue Striations.

Zappfe and Worden [170] first observed a pattern of ripples or striations on a fatigue fracture surface, and subsequently this has been characterised by many authors as the accepted mechanism of fatigue failure. Programmed loading has shown that each striation is produced by one cycle of stress although every cycle does not necessarily produce a striation [171]. The morphology of the striations differs widely and depends on strength level, symmetry and number of available slip systems.

In the mid ΔK or Paris region it has been observed that there may be a one to one correlation between da/dN and the regular spaced markings on the fracture surface perpendicular to the growth direction [172]. In the threshold region striations may not be visible, and at high ΔK values non striation modes of crack advance such as void coalescence and cleavage are often present.

Models of striation formation and stage 2 fatigue crack growth have been proposed by Laird [173], Neumann [174], and Pelloux [175], they indicate that small scale plasticity at the crack tip at K_{\max} is converted to small increments of crack growth at K_{\min} . This is the plastic blunting model of fatigue crack growth of Pelloux [175]. In its simplest form this model predicts a relationship between da/dN and the crack tip opening displacement (CTOD) [183].

$$\frac{dc}{dN} = \frac{0.041}{EY} (\Delta K_1 - \Delta K_{th})^2 \frac{1}{1 - \left(\frac{K_{1\max}}{K_{1c}} \right)^2} \quad (1)$$

Where $Y = \sigma_y$ yield stress.

Hence crack growth rates should be inversely proportional to alloy strength.

Barsom has confirmed the relationship for structural steel [273,274].

The precise mechanism of striation formation has yet to be established, although it is generally accepted that it involves alternate blunting and resharping of the crack tip, a mechanism first popularised by Laird and Smith [176]. Two such models due to Laird [173] and Pelloux [175] are illustrated in Figures 51, 52, and 54 (Figure 53 due to Fischer [270]). In both cases [173,175] the area of the crack tip is increased during the loading part of the cycle and the crack tip is sharpened during the unloading portion. Under such conditions growth is controlled by the local crack tip alternating plastic strain, and thus when applied specifically to propagation under linear elastic conditions, we would expect the growth rate to be dependent upon ΔK , the alternating stress intensity.

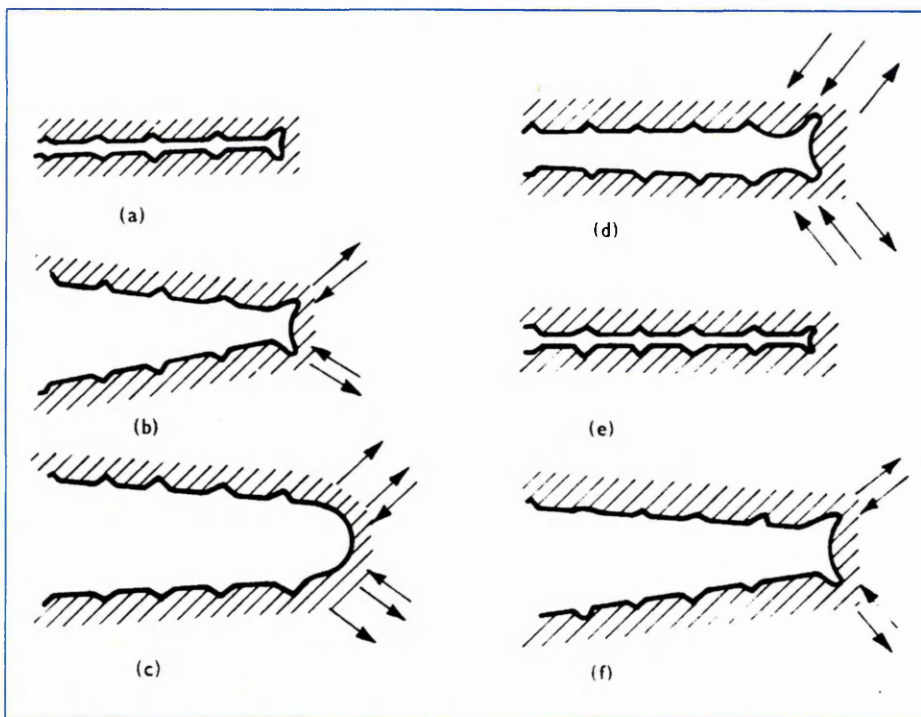


Figure 51. Diagrammatic representation of striation formation by a plastic blunting process Laird [173].

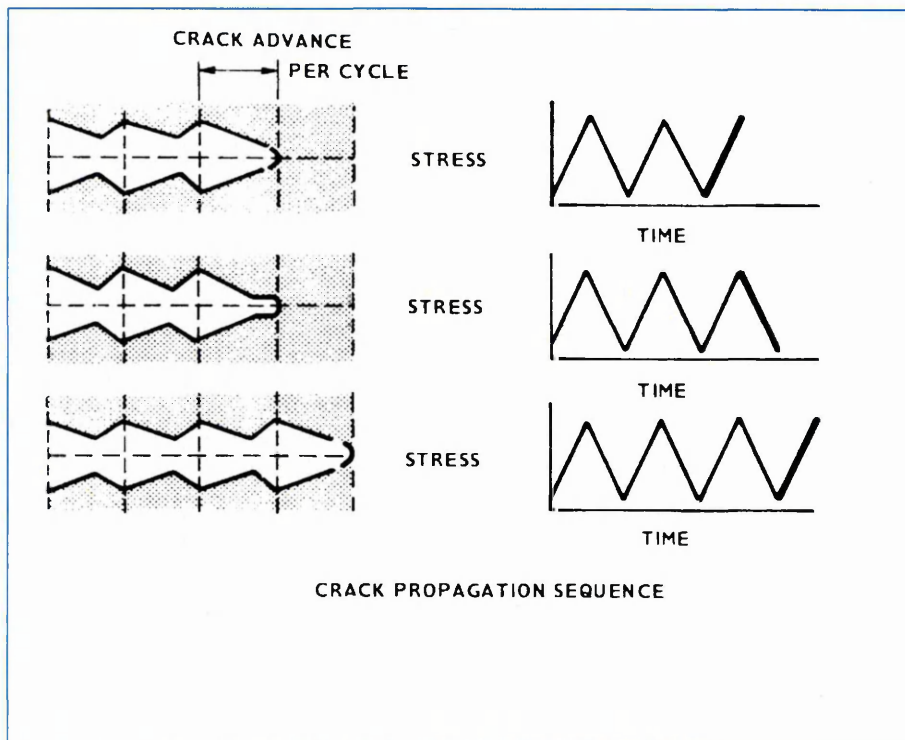


Figure 52. Diagrammatic representation of the formation of striations of saw tooth profile Pelloux [175].

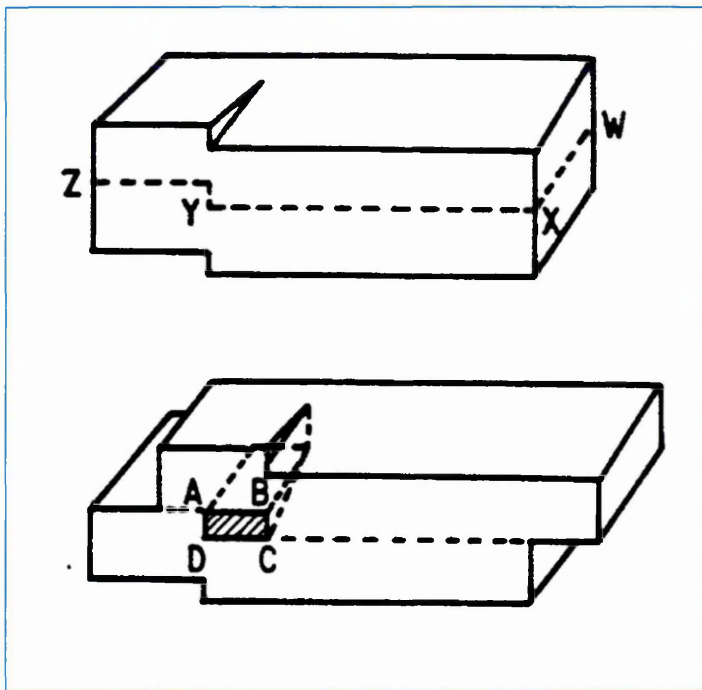


Figure 53. Scheme for producing an intrusion .

A mechanism suggested in connection with fracture under static stress was proposed by Fischer [270].

A screw dislocation traverses the slip plane WXZ and produces a step in it at Y. Slip on the plane in the direction ZX then produces a cavity opening

on the front face at ABCD. Such a cavity would close up on reversing the stress if the slip movements were exactly reversed. The basic fatigue mechanism illustrated in Figure 53 relates to a plain sample and not the situation at the crack tip. In real structures the presence of pre – existing defects must be assumed, therefore it is important to consider the effect of cyclic loading at the crack tip.

Pelloux [175] showed that crack tip extension by alternating shear is a mechanism of rupture which plays an important part in fracture, resulting from deformation by shear at the tip of a sharp crack. Crack extension by alternating shear was observed at the tip of cleavage and fatigue cracks. Pelloux concluded that fatigue crack propagation was in part the result of repeated cyclic crack extension by alternating shear. Figure 54 shows a sketch of a singly grooved tensile specimen with an infinitely sharp crack. For a perfectly rigid plastic material, deformation can take place only by shear on the two planes AB and AC. Deformation can proceed either alternately on one band and then on the other or simultaneously. Figures 54b and 54c show that if shear starts on plane AC and if there is some strain hardening on that plane it will be easier for the shear to proceed on a second plane A'B' which has not been deformed so that the shear would tend to be alternating. The process of deformation by alternating shear results in an extension of the notch length by a mechanism of rupture and not by fracture. In the case of alternating shear the

crack tip always remains sharp. This mechanism of crack extension also accounts for the striated appearance of the crack surface. If the material were totally non-hardening or if the hardening became saturated, simultaneous shear would be expected on planes AB and AC leading to the development of a blunted notch as shown in Figures 54d and 54e.

In the two cases of alternating and simultaneous shear, the deformation process should be entirely reversible, at least in theory. However, in practice the fact that the freshly exposed crack surface is immediately oxidised will limit the amount of reversibility of the deformation at the crack tip.

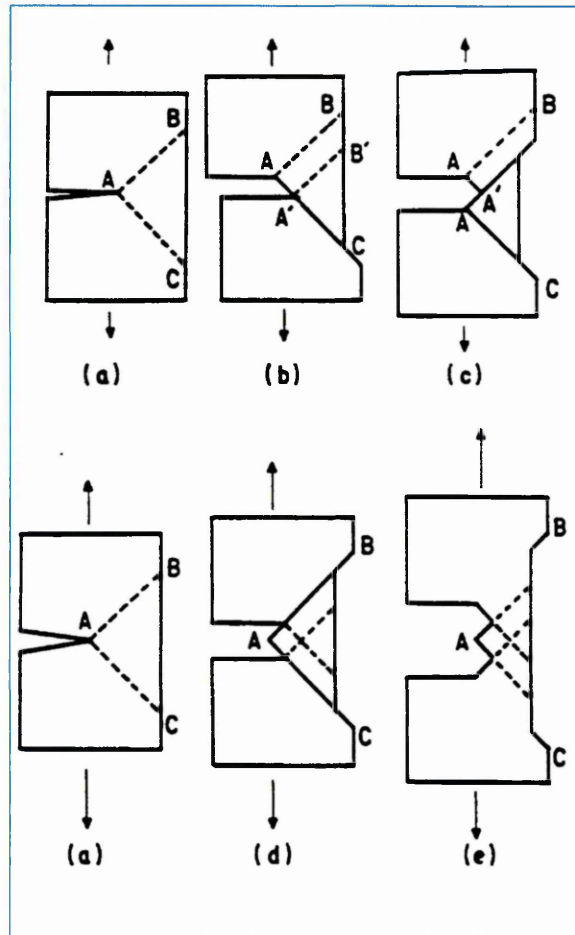


Figure 54. (a), (b) and (c) Crack extension by alternating shear in a single grooved tensile specimen. (a), (d) and (e) Crack blunting by simultaneous shear in a single grooved tensile specimen [175].

The model due to Pelloux [175] predicts that the growth increment per cycle is some proportion of the cyclic crack opening displacements δ such that

$$da/dN \propto \delta = \beta \Delta K/E\sigma_y \quad (20)$$

where β is the efficiency of blunting and can be taken as constant. The correlation of the growth rate with the elastic modulus, E , has been well established, but the inverse dependence on yield stress is rarely observed. Lindley and Richards [168] citing the work of Clark et al [166], in Figure 55 for example, shows the large variation of yield stress ($\times 7$) of the materials, yields only a variation of crack growth rate (by the striation mode) of around 2.

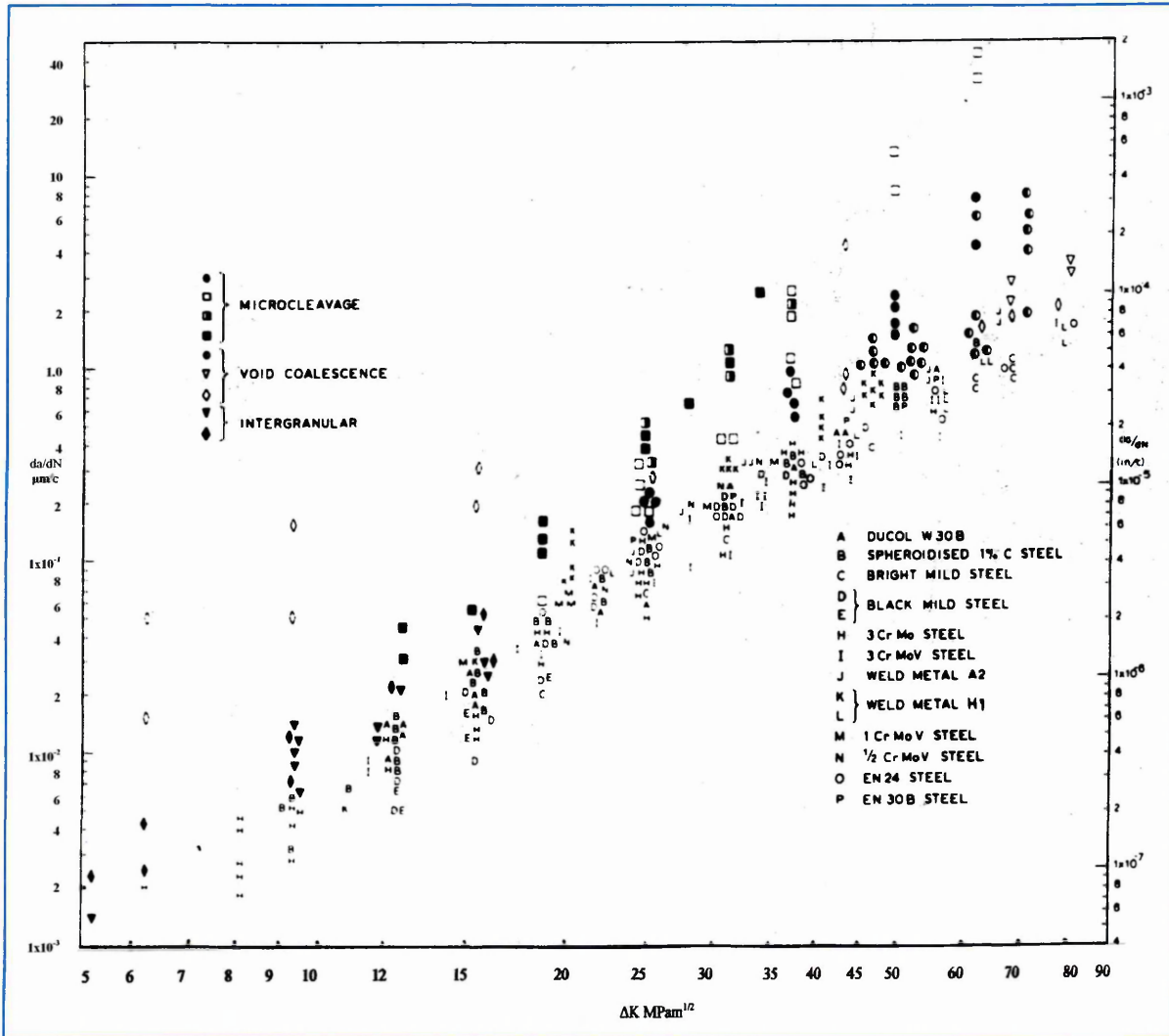


Figure 55. The relationship between the rate of crack propagation da/dN and cyclic stress intensity ΔK , for several ferrous alloys the letters indicate growth by the striation mechanism and the symbols, growth partly or wholly by other mechanisms [168].

However, since σ_y in equation 20 represents a flow stress characteristic of the cyclic plastic zone, it is possible at high strains that this approaches a common value. Further, the microstructural factors which affect σ_y may also alter the proportionality constant β , or the ΔK dependence in opposing fashion. With regard to the latter fact there is increasing evidence that, for striation

growth, although high strength steels generally show a ΔK dependence of 2 [177] the exponent for low strength steels, such as mild steel [178,179] and stainless steels [180] is closer to 3 or 4. Since this is not a result of a change in fatigue fracture mechanism, it is conceivable that the small variation in 'n' of between 2 and 4 for striation growth is related to the difference in work hardening characteristics of low and high strength steels [178].

2.4.2. Fatigue crack growth at high ΔK Levels.

Although the Paris equation does provide a simple relation by which crack growth rates may correlated with the stress intensity factor range, it does not account for crack growth with characteristics at both low and high levels of ΔK . If enough data are obtained for a given material say, four to five decades of crack growth rates the da/dN versus ΔK curve assumes a sigmoidal shape, as shown in Figure 50. That is, the ΔK dependence of crack growth rate increases markedly at both low and high ΔK values. At the high growth rate end of the spectrum, part of this deviation sometimes may be accounted for by means of a plasticity correction since the plastic zone becomes large at high ΔK levels. This has the effect of increasing ΔK_{eff} and thus tends to straighten out the curve. Another factor to be considered is that as K_{max} approaches K_c local crack instabilities occur with increasing frequency, as evidenced by increased amounts of microvoid coalescence and/or cleavage on the fracture surface. As might be expected, this effect is magnified with increasing mean stress. Characterising the mean stress level by R , the ratio of minimum to maximum loads. From the sigmoidal shape of the curve it can be seen that crack growth rates at high ΔK values increase with increasing mean stress, and little mean stress sensitivity is observed at lower ΔK levels. One relationship expressing crack growth rates in terms of ΔK , K_{Ic} and a measure of K_{mean} was proposed by Forman et al [181] in the form:

$$\frac{da}{dN} = \frac{C\Delta K^n}{(1-R)(K_c - \Delta K)} \quad (21)$$

where C , n = material constants, K_c = Fracture toughness [181].

R = load ratio (K_{min}/K_{max}).

From, it is seen that the simple Paris power law has been modified by the term $(1 - R)(K_c - \Delta K)$, which decreases with increasing load ratio R decreasing fracture toughness K_c , both of which lead to higher crack growth rates a given ΔK level. Although equation 21 correctly identifies material fatigue crack propagation response under combinations of high ΔK and K_{mean} conditions, the relation is difficult to apply because of difficulties associated with the determination of the K_c value, which, varies with width, orientation and thickness dimensions of the test sample.

Fatigue crack propagation involving cleavage and microcleavage of particles clearly results in enhanced rates of crack propagation when compared with a purely striation mechanism. The amount of increase in rate has been shown to be critically dependent on microstructure in ferrite/pearlite steels [179,182]. A comparison [182] between spheroidized, mixed spheroidized/pearlite and coarse pearlite structures in a 1% carbon steel showed that rates of crack propagation were least in the spheroidized condition where there was no microcleavage. As the proportion and coarseness of pearlite was increased by raising the reheat treatment temperature, the amount of microcleavage and rate of crack propagation increased.

Heald et al [182] proposed the following equation to describe the enhanced growth rates associated with a non striation mechanism in ferritic materials. The Heald equation predicts faster growth rates for low toughness materials, which may be associated with microcleavage, void coalescence or intergranular separation. It provides a useful prediction of the influence of strength, constraint and mean stress on the rate of fatigue crack propagation for conditions approaching failure.

Heald et al equation [182].

$$\frac{da}{dN} = A \left(\frac{\Delta K^4}{\sigma_1^2 (K_c^2 - K_{max}^2)} \right)^n \quad (22)$$

where A is a material constant, σ_1 a strength parameter, K_{max} the maximum stress intensity in the fatigue cycle, K_c the fracture toughness of the material [182].

2.4.3. Fatigue crack growth at low ΔK levels.

At the other end of the crack growth rate spectrum, the simple Paris power law relationship is violated again for low ΔK conditions, where the fatigue propagation rate diminishes rapidly to small levels as can be seen from the sigmoidal curve. From such data (Ramsamooj et al [183] citing Paris) shown in Figure 56 a limiting stress intensity factor range (the threshold level ΔK_{th}) is defined and represents a service operating limit below which fatigue crack propagation is highly unlikely.

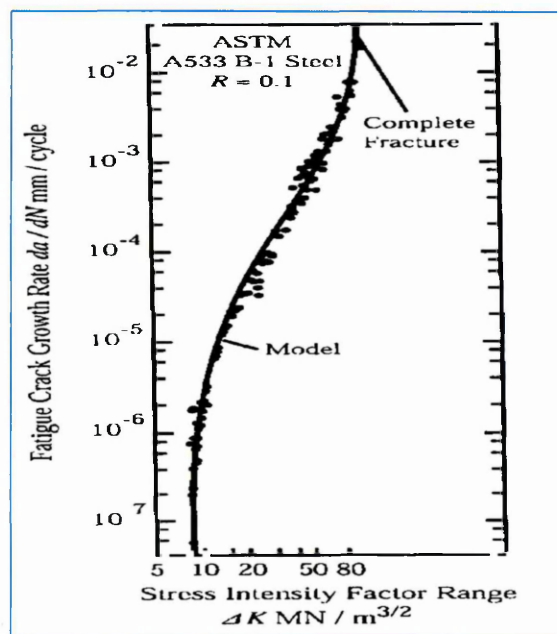


Figure 56. Fatigue crack propagation rates of ASTM A533 B - 1 steel data from Ramsamooj et al [183] citing Paris et al.

In this sense, ΔK_{th} is much like K_{IEAC} , the threshold level for environmental assisted cracking. Designing a component such that $\Delta K \leq \Delta K_{th}$ would be a highly desirable objective, but it is sometimes not very realistic in the sense that for engineering materials ΔK_{th} often represents only 5% to 10% of anticipated fracture toughness values. Therefore, to operate under $\Delta K \leq \Delta K_{th}$ conditions would require that virtually all defects be eliminated from a component and/or the design stress be extremely low. This is desirable in the design of nuclear power generation equipment where safety is of prime concern. Since many engineering structures do fulfill their intended service life without incident, it is apparent that some components do operate under $\Delta K \leq \Delta K_{th}$ conditions.

The effect of K_{mean} (i.e., R ratio) on propagation becomes important once again at very low ΔK levels and has been the focus of considerable attention. In this crack growth regime, different crack closure mechanisms other than residual plasticity have been identified that strongly influence K_{op} levels and associated ΔK_{eff} values [184] (see section 2.4.4). For example, crack-tip zone shielding, this occurs when an irregular crack path is generated, with the coarse facets or the mating fracture surfaces coming in contact during fatigue cycling. With increasing surface roughness, K_{op} levels increase, whereas ΔK_{eff} and the corresponding crack growth rates decrease. It follows that the sensitivity of ΔK to R ratio for a given material depends on the observed level of crack closure. At one extreme where measured closure levels are minimal, no appreciable change in ΔK_{eff} would occur with increasing R ratio.

An alternative crack closure mechanism has been proposed by Suresh et al [184] to account for differences in ΔK_{th} for 2½ Cr-1Mo steel when tested in different gaseous atmospheres. The threshold fatigue value in this material decreased when the atmosphere was changed from air to hydrogen. While it is tempting to rationalise difference in terms of a hydrogen embrittlement type argument, these authors pointed out that dry argon also accelerated near threshold fatigue crack growth rates relative to air, in fact dry argon behaved like dry hydrogen. To explain the enhanced fatigue resistance of this material when tested in air as compared to dry argon and hydrogen. Hertzberg [184] citing Suresh et al [184] noted that fatigue testing in air creates an oxide layer on the fracture surface that thickens in the threshold region as a result of closure induced fretting. Similar oxide layers have been reported by others. The thicker oxide layer would be expected to increase K_{op} and bring about a corresponding decrease in ΔK_{eff} thereby leading to lower crack growth (see Figure 57).

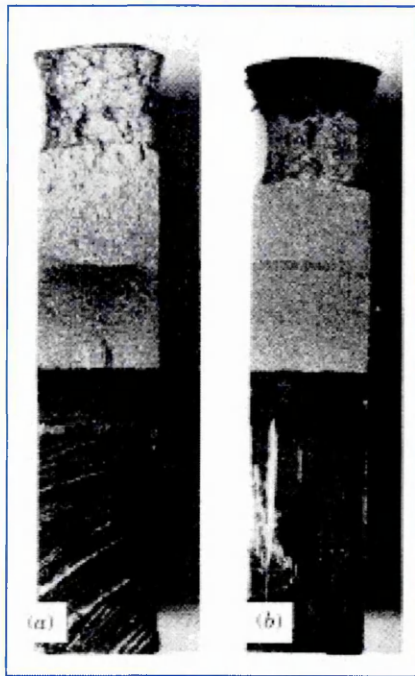


Figure 57. Dark bands of oxide debris formed on fracture surfaces of 2½ Cr - 1 Mo steel in region associated with ΔK_{th} .

(a) $\Delta K_{th} = 7.7 \text{ MPa m}$, $R = 0.05$

(b) $\Delta K_{th} = 3.1 \text{ MPa m}$, $R = 0.75$.

Note that the oxide band almost disappears at high R ratios Hertzberg [184] citing Suresh.

2.4.4. Crack Closure.

Some authors [66,236] view the unloading compliance test as a low cycle fatigue test, the relationship becomes apparent if compared with the unloading compliance technique (see Appendix 2). This section and section 2.5 are included to give an insight into how environmental conditions assist in material degradation processes. That is if the loading rates are low enough on the load cycle and unload cycle of the compliance curve, and if the unload cycle load percentage is high enough, sufficient to cause crack closure (see Appendix 2).

Crack closure is the name given to the phenomenon whereby the opposing faces of a fatigue crack bear some of the load during the unloading part of a fatigue cycle thus reducing the ΔK value seen by the crack tip and plastic zone, to an effective value ΔK_{eff} which is a portion of the nominal applied

ΔK (see Figure 58), therefore:

$$\Delta K_{\text{eff}} = K_{\text{max}} - K_{\text{cl}} \quad (23)$$

Where K_{cl} the closure stress intensity is the value of K obtained upon removing the load which is greater than K_{min} due to wedging of the crack by some material.

In the early 1970's Elber [185] proposed the phenomenon of crack closure. Briefly in an elastic plastic medium that undergoes limited plastic deformation at the crack tip during loading, it is possible for the crack faces to impinge before the tensile load is completely removed. For thin plates Elber suggested that this reduced the effective ΔK and from his results on aluminium derived the following relationship, for R ratios between - 0.1 to + 0.7.

$$\Delta K_{\text{eff}} = (0.5 + 0.4R)\Delta K \quad (24)$$

Plasticity induced crack closure occurs when plastically strained material in the wake of the advancing crack wedges the crack open. A comprehensive theoretical study of plasticity induced closure and oxide wedging is given by Heald et al [186], and Roselmeir et al [187].

In corrosion fatigue oxide induced closure caused by corrosion products within the crack is an important factor. The corrosion products if present in sufficient quantity, do not necessarily need to be near the crack tip to cause significant crack closure.

Oxides can also form in fatigue tests conducted in air in the near threshold region. This is due to abrasion caused by crystallographic facets sliding over one another, spalling existing protective oxides, raising the surface energy and thus leading to rapid creation of surface oxide.

Closure is also caused by calcareous deposits formed under cathodic protection. These deposits are not usually very thick so they need to be formed

near the crack tip with their thickness being of the order of the CTOD (crack tip opening displacement) to have an effect [186,187,188]. Whilst calcareous deposits may cause low crack growth rates in laboratory tests, it is very doubtful as to whether this effect can be relied upon to control crack growth in practise. Since the calcareous deposit needs to be of the order of the CTOD to be effective near the crack tip, da/dN must be slow enough for calcareous deposition to maintain a sufficient wedge in the crack tip region. If for any reason da/dN exceeds a critical value such that the rate of deposition cannot keep up then its large effect can quickly diminish with a resultant enhancement in the crack growth rate. DCPD (direct current potential drop) techniques have been used to investigate crack closure [189] but there is always an element of doubt since the contact between asperities which is capable of shorting a DPCD system may not necessarily bear much of the load.

There are a number of mechanisms which can cause crack closure, ie contact between opposite faces of the crack at low loads, during fatigue and corrosion fatigue crack growth [190,191,192]. Figure 58 [193] gives a definition of terms. If crack closure occurs at a stress intensity factor K_{cl} that is above K_{min} in the cycle, the effective range of stress intensity factor becomes:

$$\Delta K_{eff} = K_{max} - K_{cl} \text{ as stated in eq. 23.}$$

The crack growth rate, da/dN , decreases as the driving force that the crack experiences is reduced from ΔK_{appl} to ΔK_{eff} . In the final case, growth will cease as K_{cl} approaches K_{max} and $\Delta K_{eff} = \Delta K_{th}$.

Austen et al [193] outline the predominant mechanical mechanisms for closure as follows:

1. Plasticity-induced closure, which arises from crack tip compression caused by the residual tensile stress behind the crack wake from plastic deformation;
2. Roughness-induced closure, caused by mismatch and asperity of striation peaks;
3. Metallurgically induced closure, arising from deformation induced phase

changes at the crack tip leading to “volumetric dilation”.

4. Environmentally-induced closure, including oxide induced closure in air and humid or aqueous environments, corrosion product-induced closure in seawater environments (calcareous deposit) and wedging by incompressible viscous fluid, though the latter is rare [191]. It has been observed that threshold ΔK values, and by inference closure levels, can be higher in aqueous environments. This is attributed by some to corrosion product-induced closure and by others to the reduction in effective ΔK due to crack tip blunting.

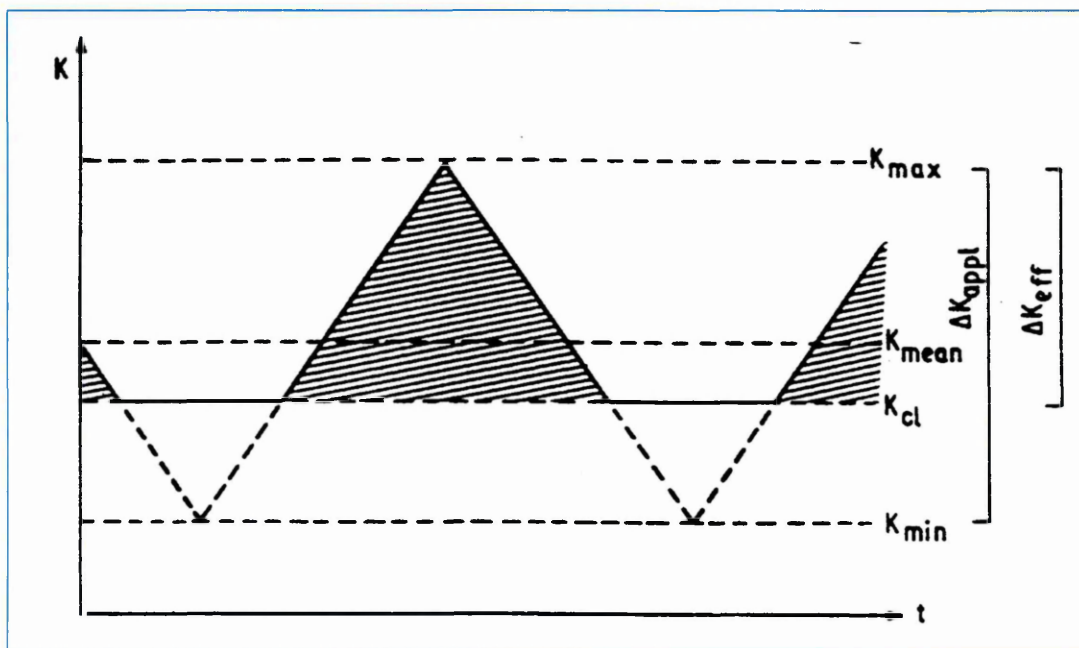


Figure 58. Definition of terms in a fatigue cycle affected by crack closure. [193]

2.4.5. The Effect of specimen thickness on fatigue crack propagation.

The influence of specimen thickness on fatigue crack propagation by the striation mechanism is small, and critically dependent on the specimen geometry and on how close the stresses are to general yield. The thickness effect has been reviewed by Griffiths et al [194] and Ritchie and Knott [195]. Small differences in crack growth rates between thin and thick specimens can arise from variations in test piece geometry and the accompanying

displacement restraints. In addition, through thickness constraint influences the load to cause yielding across the uncracked ligament (general yield) by an amount that depends on specimen geometry and this can lead to faster propagation rates in thin specimens [195]. In other instances slightly faster growth rates are to be expected in thick specimens where the plane strain conditions at the crack tip create a greater concentration of strain, and restrict the crack closure stresses which may limit the “effective” stress intensity experienced at the crack tip.

Ritchie [195] observed faster rates of crack propagation with increasing thickness in a coarse grained high nitrogen mild steel where the mechanism of growth involved cleavage. In a finer grained steel no such cracking was obtained, and the influence of specimen thickness was correspondingly far smaller. The void coalescence mechanism of fatigue crack growth is also sensitive to the degree of constraint [196].

2.5. Corrosion Fatigue.

Corrosion fatigue is a term which is commonly used to denote the damage and failure of a material under the combined action of cyclic stresses and any embrittling medium, although it's most widespread adaption is in the context of aqueous environments.

When a material is subjected to a varying load, changes in the material can occur which results in damage, even if the load is considerably lower than the ultimate strength of the material. Changes in load can in unfavourable conditions lead to crack formation and fracture this type of damage is called fatigue. The rate of attack can be considerably increased if corrosion takes place simultaneously. The rate of attack being environment specific. Failure at a given strength usually occurs within fewer cycles in a corrosive environment. The damage is usually greater than the sum of the damage by corrosion and fatigue acting separately.

2.5.1. Mechanisms of Corrosion Fatigue.

For ductile aqueous environments systems subjected to cyclic loads, interpretations of embrittlement involve the mechanism of electrochemical reaction at freshly formed slip steps or at the crack tip. The process involves two principal mechanisms of environmental damage, cathodic slip dissolution or hydrogen embrittlement. The advance of fracture by slip dissolution occurs by;

(i). The diffusion of the active species (such as water molecules or halide ions).

(ii). The rupture of the protective oxide film at a slip step or in the immediate wake of the crack tip by strain concentration, or fretting contact between the crack faces respectively.

(iii). The dissolution of water molecules or hydrogen ions between crack walls toward the crack tip.

(iv). The reduction of these species to create absorbed atoms to preferential surface locations.

(v). The surface diffusion of absorbed atoms to preferential surface locations.

(vi). The absorption of atoms to a critical location (for example a grain boundary) the region of high triaxiality ahead of a crack tip or void.

In situations involving the formation of a passivating oxide film on the freshly created surface, the reaction at the crack tip which influences dissolution hydrogen ion reduction, or crack growth is controlled (at a given electrochemical potential) by three factors;

(i). The oxide renewal rate.

(ii). The solution renewal rate.

(iii). The passivation rate.

Under cyclic loading conditions, fretting contact between the mating crack faces, and continual blunting will strongly influence the rate of anodic dissolution. Therefore both cyclic frequency and stress waveform are known strongly to influence crack growth. It is also known that deformation fields ahead of a fatigue crack are strongly affected by the presence of an aggressive environment. Atkinson and Lindley [203] performed tests on similar low alloy steels, over the temperature range 25° – 85°C, and found that in aqueous environments the crack propagation rates over the values measured in air increased by up to a factor of 7, and that the degree of enhancement was found to be frequency dependant. They also found that waveforms with a very fast rise time such as negative sawtooth or squarewave did not lead to environmental enhancement of fatigue crack propagation rates, and that growth rates increased with increasing water temperature over the range covered. The hold time had no significant effect on the fatigue condition studied.

It is also known from crack tip strain measurements that deformation fields ahead of a fatigue crack are affected by the presence of an aggressive environment. This theory has been postulated by Hanninen et al [205] as one of the reasons for hydrogen embrittlement.

Duquette [197] indicated that corrosion fatigue falls into four categories.

- (i). Stress corrosion at the base of hemispherical pits created by the corrosive medium.
- (ii). Electrochemical attack at plastically deformed areas of metal with the non deformed metal acting as a cathode.
- (iii). Electrochemical attack at ruptures in an otherwise protective surface film.
- (iv). A lowering of the surface energy of the metal due to environmental absorption and increased propagation of microcracks.

A number of unique characteristics serve to define and differentiate corrosion fatigue from other failure mechanisms. Unlike stress corrosion, no specific chemical corrodents are necessary to produce corrosion fatigue. Most corrosive environments accelerate cracking. Aeration of the environment decreases the fatigue life of carbon steel. Corrosion fatigue cracks are predominantly straight, transgranular, and unlike most stress corrosion cracks contain little or no branching. Many nucleate at corrosion pits and exhibit multiple origins. One of the most striking features of corrosion fatigue is the multiplicity of origins [198]. Often multiple cracks originate in pits, while outside no crack occurs. If oxidation is appreciable, most cracks contain considerable oxide or other corrosion products. Cracks may be needle or wedge shaped. Where a brittle oxide layer is present, the oxide layer will crack when the surface undergoes tensile deformation, opening microscopic cracks through the oxide to the metal surface forming a notch during repeated tensile cycles, the oxide preferentially re - fractures at the notch causing the crack to grow. Frequently the crack abruptly widens internally forming cavities.

Frequency, stress amplitude and super imposed stresses all materially influence corrosion fatigue. In aggressive environments, the fatigue strength is strongly dependent on the frequency. A positive correlation of fatigue life with frequency is often considered definitive in assigning corrosion fatigue as the primary failure mechanism. The frequency dependence is a natural outcome of

the associated corrosion process. The more aggressive the attack, the fewer cycles necessary to produce a given amount of crack growth, this has been extensively covered by Atkinson [199,200] and others [201,209]. Low cycle corrosion fatigue in an aggressive environment tends to produce fairly blunt V shaped fissures, while higher frequency and less aggressive environments produce tighter finer cracks. The greatest influence of the aggressive environment generally occurs at intermediate frequencies, at very high frequencies insufficient time is available for the effect of corrosion to manifest itself and at very low frequencies passivation of the crack tip can occur leading to a reduction of the corrosive effect [70,199,200,202,203].

Atkinson et al [52,200,202,203] studied the factors influencing the rate of fatigue crack growth in RPV steels in air [52] and in water [200,203] over the temperature ranges 20°C – 350°C. They reported that a threshold stress intensity amplitude needed to be exceeded to trigger sustained environmentally assisted fatigue crack growth rates. Important factors found to influence this threshold value were the frequency, water chemistry, flow rate, temperature and the size and distribution of manganese sulphide inclusions in the steel. A tendency was shown for the crack growth rate to increase with the decreasing frequency, and that maximum crack growth rate was at a particular frequency. They also found that the temperature dependence was split into two categories, at low temperatures 25°C – 100°C a low temperature dependence exists with only a small increase in crack growth rate with increasing temperature, but in the range 150°C – 290° C crack growth rates increased more markedly as the water temperature increased. Atkinson [52] found that the occurrence of environment assisted cracking of A533B steel in high temperature water is correlated to the dynamic strain ageing behaviour, by superimposing their results on Katada and Nagata [204] results there was a very good correlation between the two sets of results (see Figure 59).

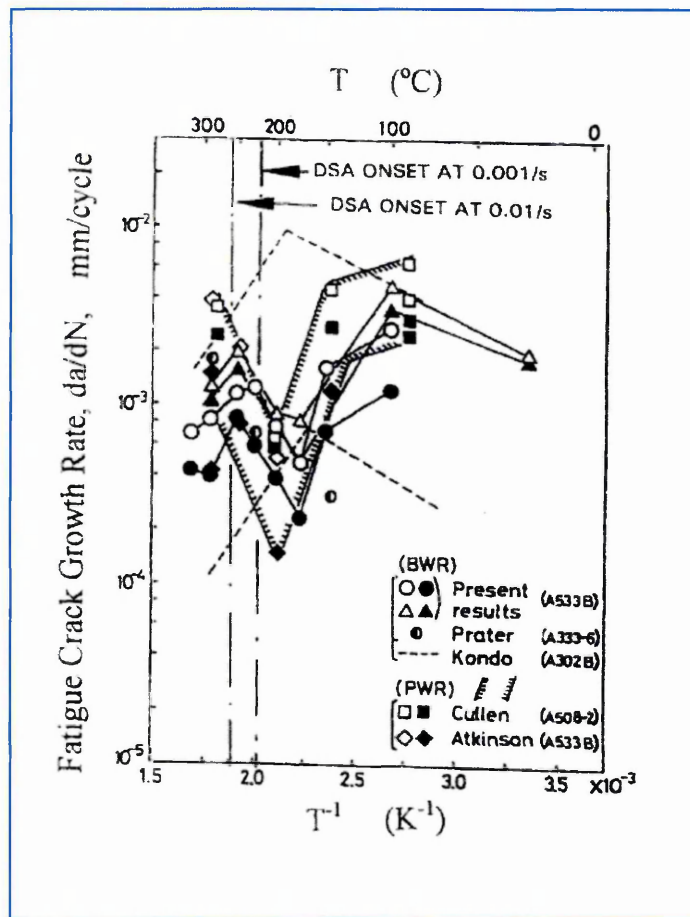


Figure 59. Summarised Data showing the Effect of Temperature on da/dN of RPV Steels (Katada et al [204]). The legend “Present” represents the results produced by Atkinson and Yu [52]. The onset of Dynamic Strain Ageing at possible strain rates at the crack tip are indicated. Frequency 0.0167 Hz, $R = 0.2$ to 0.7 .

Congleton and Craig [207] also found like Atkinson and other researchers that fatigue crack growth rates on a cyclic basis are observed to increase with decreasing frequency and that the results could usually be explained by the longer times available for environmental crack growth in each cycle as the frequency is reduced. They postulated that in the limit of testing carried out at very low frequency and with $K_{\text{mean}} > K_{1\text{SCC}}$ the situation tends to that of a slow strain rate monotonic loading stress corrosion test. Like Atkinson they also found that the effects of loading wave form in corrosion fatigue systems exhibiting above $K_{1\text{SCC}}$ behaviour can be singly related to the different times the stress intensity exceeds $K_{1\text{SCC}}$, and that the time dependent component of cracking will also increase with waveforms that have significant hold times at

stress intensities above K_{1SCC} .

2.5.2. Stress - Ratio.

The mean stress has a substantial effect on both the rate of corrosion fatigue crack growth and the threshold stress intensity of reactor pressure vessel steels in high temperature water at stress ratios ($R = K_{MIN}/K_{MAX}$) from 0.2 to 0.7. The effect of increasing R is to reduce the threshold stress intensity factor range for environmentally assisted cracking and increase the crack growth rate.

2.5.3. The Role of Inclusions.

It is now well established that inclusions play an important part in the ductile rupture of metals. These inclusions are the sources of the cavities which grow by plastic deformation and link together to produce dimpled rupture. Most of the models proposed for cavity nucleation use the same postulation, that cavity formation takes place at a critical stress σ_c .

The main inclusions to be found in reactor pressure vessel steels are manganese sulphide inclusions, and these are usually the sites where cavity nucleation takes place [208].

The effects of steel sulphur content are synergistic with environmental variables such as anionic contaminants, dissolved oxygen and the flow rate. This is believed to be due to the creation of a sulphur rich crack tip environment responsible for the environmentally induced cracking which arises from the dissolution of manganese sulphide inclusions intercepted by the crack.

The size, shape and orientation of these inclusions is important. Arai [210] citing Anzai, found that the sulphur in alloy is supposed to be the most effective material factors on SCC behavior, and that the susceptibility increased with the sulphur content, and that alloys with numerous small MnS inclusions, had a lower susceptibility than an alloy with a few large MnS inclusions. They also found that the effect of MnS inclusion distribution is smaller than that of content, and that the loading direction also affected SCC behavior. Higher

susceptibility was observed in the loading direction parallel to the short transverse direction in rolled steel.

Beremin [211] found that cavity formation in A 508 steel from elongated MnS inclusions takes place differently in the longitudinal and the short transverse direction. In the longitudinal direction most inclusions break, while in the short transverse direction inclusion damage corresponds to the decohesion of the interface between particles and the parent metal, his model is also based on a critical local stress σ_c (see Appendix 6).

Hanninen et al [205] proposed a mechanistic crack growth model based on hydrogen induced cracking, where anodic dissolution creates the conditions for hydrogen absorption at the crack tip. The hydrogen induced cracking starts from the manganese sulphide inclusions, which act as strong hydrogen traps. The model postulates that the crack growth exposes manganese sulphide inclusions, they dissolve, the crack tip becomes more aggressive and conducive to hydrogen absorption. Hanninen [205] also found like Bulloch [238] that a fairly dense distribution of elongated MnS inclusions are evident whenever the fracture mode exhibits brittle features and that the crack growth spread like a fan over the fracture path in A533 B steel. The ductile striated fracture surfaces contained fewer inclusions. Hanninen [205] postulates that the deformation around voids may be due to hydrogen gas evolution in these voids, and thus due to the build up of hydrostatic pressure, which is added to the applied stress, thereby assisting discontinuous fracture (a discontinuous fracture is one in which isolated voids open up ahead of the main crack).

2.5.4. Crack tip strain rate.

It can be inferred from the above that the crack tip strain rate is an important in determining the environmental contribution to corrosion fatigue. The increase in crack tip strain with time occurs either because of a monotonically increasing or cyclic stress, or because of creep processes under constant stress. Once the film is ruptured, crack tip advance is governed by oxidation on the bared surface. Under monotonically increasing load conditions, the crack propagation rate will be governed by both the oxidation kinetics and the frequency of oxide rupture at the strained crack tip. Under

cyclic loading conditions the crack is advancing not only by oxidation processes, but by irreversible cyclic plastic deformation. So the crack tip strain rate determines the periodicity of the film rupture at the crack tip. A number of estimates have been made of the crack tip strain rate under cyclic loading conditions. The one used in this work is the one proposed by Lidbury [206].

2.5.5. Estimation of Crack Tip Strain Rate Using the Dugdale Crack Model.

It is often assumed that the crack tip strain rate is proportional to the loading rate that is $\dot{\epsilon}_{ct}(t) \propto P \sin(\omega t)$ for sinusoidal loading but this has been shown to be an over simplistic assumption. Lidbury [206] obtained a different dependance on K by using the Dugdale model and applying Rice's principle of plastic superposition in Lidbury's paper the estimation of crack tip strain rate is reviewed with reference to:

(i). Cyclically loaded cracks under small scale yielding.

(ii). Monotonically loaded cracks under conditions of large scale yielding.

Lidbury shown that if the variation in shear strain occuring within the symmetrically inclined 45° flow bands contained by the crack tip work hardening zone is considered, then the strain rate may be expressed as a simple function of the loading period, T, and $\Delta K/K$. Lidbury's approach is outlined below.

Under monotonic tensile loading, the crack tip opening displacement is assumed to be given by:

$$\delta = \frac{\sigma K^2}{E \sigma_Y} \quad (25)$$

According to the principle of plastic superposition, the instantaneous value of δ upon unloading or subsequent loading is:

$$\delta(t) = \frac{\alpha K_{\max}^2}{E \sigma_y} - \frac{\alpha}{2E \sigma_y} (K_{\max} - K_{MIN})^2 + \frac{\alpha}{2E \sigma_y} (K(t) - K_{\min})^2 \quad (26)$$

$K(t)$ is given by the loading function depending upon the waveform. For

triangular or ramp loading.

$$K(t) = K_{\min} + \Delta K \left(\frac{t}{T} \right) \quad (27)$$

And for sinusoidal loading where:

$$K(t) = K_{\min} + \Delta K \text{Sin}^2 \left(\frac{\pi t}{2T} \right) \quad (28)$$

One of the means of obtaining $\dot{\varepsilon}(t)$ suggested by Lidbury was to normalise δ with respect to itself:

$$\dot{\varepsilon}(t) = \frac{1d\delta(t)}{\delta(t)dt} \quad (29)$$

Substituting equation 27 or 28 into equation 26 and using equation 29 Lidbury obtained for ramp loading:

$$\dot{\varepsilon}(t) = \frac{\left(\frac{1}{T} \right) (1-R)^2 \left(\frac{t}{T} \right)}{1 - \frac{1}{2} (1-R)^2 + \frac{1}{2} (1-R) \left(\frac{t}{T} \right)^2} \quad (30)$$

And for sinusoidal loading:

$$\dot{\varepsilon}(t) = \frac{\frac{\pi}{T} (1-R)^2 \text{Sin}^3 \left(\frac{\pi t}{2T} \right) \text{Cos} \left(\frac{\pi t}{2T} \right)}{1 - \frac{1}{2} (1-R)^2 + \frac{1}{2} (1-R)^2 \text{Sin}^4 \left(\frac{\pi t}{2T} \right)} \quad (31)$$

By integrating either of the above equations Lidbury found that they both gave the same average value of crack tip strain rate:

$$\dot{\varepsilon}_{av} = \frac{1}{T} \int_0^T \dot{\varepsilon}(t) dt = -\frac{1}{T} \ln \left(1 - \frac{1}{2} (1-R)^2 \right) \quad (32)$$

One very important consequence of Lidbury's derivation of the expression for crack tip strain rate is that the ΔK and σ_y terms in equation 26 cancel out when deriving equations 31 and 32. This indicates that crack tip strain rate is independent of ΔK and yield strength. It only appears to be a function of cycling frequency, waveform, and R ratio.

2.5.6. Summary of section.

From the literature survey it can be concluded that when low alloy steels are exposed to elevated temperatures (in aqueous environments) it causes a change in the fracture and fatigue properties.

In general the ductility and fracture toughness are lowered and the main variable to bring this about is environmental assisted cracking. It has been shown by Atkinson [200] and James [209] that when low alloy steels are immersed in aqueous environments subjected to various cyclic loading conditions, and held at different potentials may follow intergranular or transgranular paths depending upon the test conditions. Different potentials can accelerate transgranular cracking, promote intergranular cracking or delay crack initiation.

Because of the complexity of the interplay among the various mechanical, metallurgical and environmental effects, it seems that most of the models formulated, base this degradation in fracture toughness and ductility, mainly to the following variables.

Environmental variables include the water flow rate, water chemistry, particularly the concentration of dissolved oxygen, and of certain anionic impurities. Closely related to environmental variables are metallurgical and micro-structural variables, such as the steel sulphur content. Mechanical loading variables influencing the crack growth process include loading, frequency, mean stress, (R ratio) and the loading waveform.

The sulphur content in steel is of major importance, this is precipitated as a sulphide phase (mainly manganese sulphide). When these are exposed to an aqueous environment, the inclusions will dissolve leading to a locally aggressive environment. The concentration of the environment will depend on these inclusions. Generally the lower the sulphur content, the smaller is the environmental effect. Hanninen [205] reported lower crack growth in A533B steel containing spherical inclusions as opposed to elongated inclusions, and that when EAC was occurring this was assisted by these inclusions.

Film Rupture is a critical element in any mechanism of EAC and this is determined by the passivation - repassivation characteristics of the material and is environment specific. The strain rate is another important variable; this determines the rate at which the oxide film is locally broken.

The literature suggests that the aqueous environment assists the mechanisms of anodic dissolution and corrosion, and that this relieves the strain hardening at the crack tip surface, and so reduces the fracture stress thereby facilitating the nucleation of brittle cracks.

Dissolved oxygen has a major effect on fatigue crack propagation, very small concentrations generally ≥ 10 ppb cause large anodic shifts in low alloy steel corrosion potential, and it has been found that at the higher potentials, many of the cracks nucleate at shallow pits associated with inclusions and that initiation occurs more readily at sites of high anodic activity in the surface oxide film.

It has been shown that the general trend to increased susceptibility to stress corrosion cracking increases with increasing oxygen content, and that this is related to the electrochemical potential, and that there is a threshold potential at which SCC is possible. This is controlled by the oxygen and hydrogen levels. The electrochemical potential is important as it controls the rate of dissolution, and the rate of formation of protective oxide.

Of the models proposed for this degradation in J and T, and in the fracture toughness and ductility in aqueous environments, of the models proposed to account for this the most feasible models are those based on the West criterion [275].

Models such as those as West's provide a more comprehensive and feasible explanation of why this occurs. He postulates that because anodic action at the crack tip supplies an additional electrochemical energy component, to the elastic strain energy, by introducing cathodically generated hydrogen reducing the overall energy required for fracture.

To conclude from the literature review it can be seen that aqueous environments in general assist in the degradation of a materials properties. The main properties to be affected are a loss in ductility and fracture toughness, usually resulting in a degradation of J and T. In the aqueous environment this degradation is assisted by such agents as stress corrosion cracking and corrosion fatigue. The initiation of these mechanisms are dependant upon three factors. **Metallurgical factors** such as the sulphur content, void inclusion density and distribution. **The stress - strain factors**, strain rate it has been shown from the literature survey, that the occurrence of DSA is known to cause increases in the tensile strength and strain hardening exponent with an accompanying loss in ductility. It was also shown how the aqueous environment relieves the strain hardening, thus reducing the strain hardening exponent n. The strain hardening exponent n assumes significance in the ductile fracture process which involves formation of a plastic zone ahead of the crack tip, void nucleation, growth and linkage parameters which govern the fracture toughness. The applied stress, strain level, and the cyclic stress are other important stress strain factors. **Environmental factors**, probably the most important factors are dissolved oxygen concentration, the temperature, the flow rate, and the conductivity.

2.6. Ductile to Brittle Transition Temperature.

In modern industry a large number of engineering structures are used in the ductile to brittle transition temperature region. For many years the Charpy V notch impact test, crack opening displacement (COD) [212], and the J integral [213] have been developed to evaluate fracture toughness (K_{IC}). From fracture tests at various temperatures it has been found that a salient feature of toughness data measured at the ductile – brittle temperature region is its great variability and temperature dependence.

The characterisation of fracture behaviour of structural steels and its dependence on temperature are subjects of special importance when designing components made with such materials. Experimental data for example the Charpy test is a basic tool for characterising the fracture behaviour of ductile materials, as these materials present a ductile to brittle transition, and the precise location of this transition with respect to temperature is an essential requirement when using these components in structural applications

Further studies [214] on the scattering of toughness values of low carbon alloy steel showed that in the ductile to brittle transition temperature region, a fibrous crack was initially formed at the pre-crack tip or the notch root in the specimen, and the toughness value was mainly determined by the extension length that the fibrous crack could reach before a brittle fracture initiated. The scattering of the toughness values corresponds to the scattering of the fibrous crack length. Therefore in the transition region, it is essential to investigate the mechanism of the ductile to brittle fracture transition for explaining and controlling the scatter of toughness values.

The Ductile - Brittle Transition temperature (DBTT) T_{DB} has been most commonly used to characterise the fracture properties of materials. Extensive studies [212,216,217,218,224] have been made on the macroscopic and microscopic analysis of brittle and ductile fracture. The ductile to brittle fracture processes are briefly outlined.

In the lower shelf regime where brittle fracture dominates. The energy balance criterion [225] where brittle fracture dominates controls the critical condition of the brittle microcrack propagation. That is the elastic strain energy release rate must exceed the plastic work γ_p expended by dislocation emissions at the crack tip during crack growth and the ideal work of fracture γ both of which are mutually dependent [226,227]. Generally the brittle microcrack propagation induces spontaneous failure of specimens unless extremely high degrees of microstructural heterogeneities are present. The brittle fracture in the lower shelf region is considered to be an athermal propagation controlled process because the critical local tensile stress σ_c necessary for the brittle fracture propagation has been found to be independent of temperature.

The macroscopic analysis of linear elastic fracture mechanics represents the resistance to the brittle fracture propagation in terms of the plane strain fracture toughness K_{1C} . In the upper shelf region ductile fracture occurs by the formation of voids and localised shear deformation. The plasticity related ductile fracture is a thermally activated process. The macroscopic characterisation of ductile crack initiation and growth have been made in terms of the critical J Integral value J_{1C} and the ductile tearing modulus respectively.

2.6.1. Impact Transition Temperature.

It has been known for many years that uncombined or free nitrogen has an adverse effect on impact transition temperature, and various empirical equations have been derived to take this into account. Table 3 shows a comparison of some of the published equations relating impact transition temperature to structural and compositional variables [219].

Type of steel	Formula	Ref.
As-rolled 0.6 % Mn steels		
(a) < 0.1 % Si	$15 + 700\sqrt{\% N_f} + 2.2 \times \% P - 11.0l^{-\frac{1}{2}} + 70 \times \% Al$	[5]
(b) > 0.1 % Si	$15 + 2750 \times \% N_f + 2.2 \times \% P - 11.0l^{-\frac{1}{2}} + 70 \times \% Al + 50 \times \% Si$	[5]
As-rolled steels	$60 + 1500 \times \% N_f + 2 \times \% P - 9.1l^{-\frac{1}{2}} - 48 \times \% Mn$	[4]
Normalized and as-rolled steels	$-19 + 700\sqrt{\% N_f} + 2.2 \times \% P - 11.5l^{-\frac{1}{2}} + 75 \times \% Al + 44 \times \% Si$	[3,6]
Silicon-free	$43 + 1.5 \times \% P - 6.2l^{-\frac{1}{2}} - 37 \times \% Mn$ (15 % F.A.T.T., °C)	[2]

Table 3. Summary of formulae for Charpy impact transition temperatures (°C), 50% fibre fracture appearance transition, unless otherwise stated.

N_f = Free nitrogen content (%), l = grain size obtained by mean linear intercept method ($\text{mm}^{-1/2}$), P = pearlite volume fraction (%) [219].

It can be seen that Gladman [220] references 3 and 6 in the table, observed that the change in impact transition temperature is proportional to the square root of free nitrogen content, while Bucher et al [221] reference 4 in Table 3, found that it varied linearly with nitrogen content. The equations proposed also differ slightly in their effects of pearlite content, silicon level etc, but their general form is similar.

Mintz [219,222] determined the effect on the impact transition temperature by changing the free-nitrogen content (N_f) in steels of different silicon and manganese levels. The equations obtained for steels containing about 0.6% Mn and either 0.03 % or greater than 0.1% Si is shown in Table 3. It can be seen that for low silicon or balanced steels a square root relationship is obtained, while for higher silicon steels corresponding to silicon-killed steels there is a linear relationship with nitrogen content. The results are shown in Figure 60. Mintz found that when the results are corrected for differences in grain size and pearlite volume fraction and correction is made for the effect of silicon in solid solution on toughness, that at zero nitrogen the curves for silicon killed and balanced steels come together. He found that the effect of adding

nitrogen is considerably greater in the case of the low-silicon steel than in the silicon-killed steel.

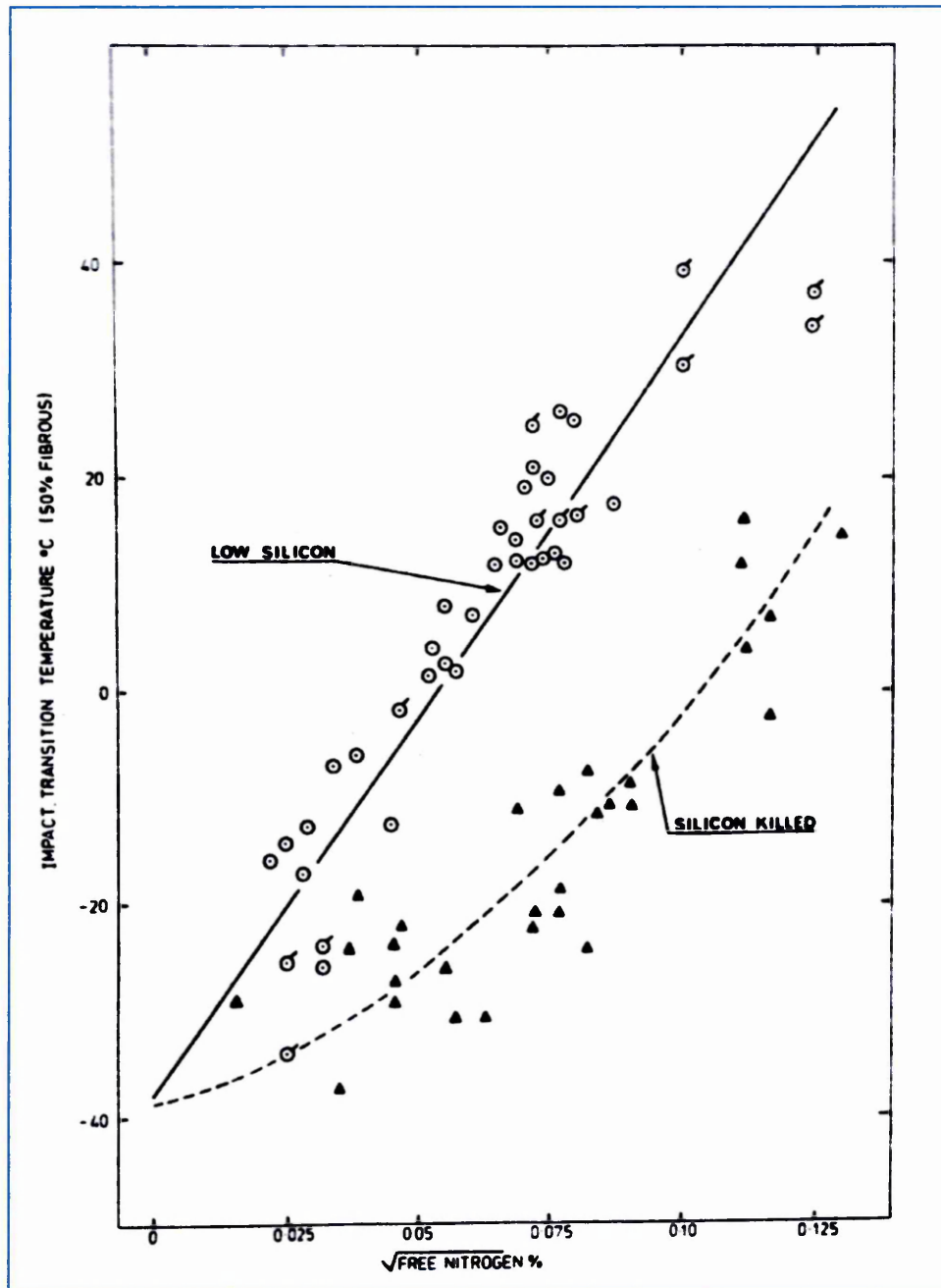


Figure 60. Influence of free nitrogen content on impact transition temperature of low-silicon ($\sim 0.03\%$), and silicon-killed ($\sim 0.3\%$), 0.6% Mn steels. Data standardized to grain size of $l^{-1/2} = 8 \text{ mm}^{-1/2}$ and to zero Al and Si levels using correction factors given in Table 3. Pearlite volume fraction $16 \pm 2\%$. [219,222].

2.6.2. Correlation between Charpy Impact Energy and Fracture Toughness.

J - R curve testing is both expensive and difficult. Either a multispecimen technique, requiring comparatively much material, or a single specimen technique, requiring very sophisticated test equipment, must be used. In both cases, and especially in the case of single specimen techniques, there is a comparatively large possibility of undetected performance related systematic errors. This has limited the use of J - R curve testing only to the most demanding applications such as nuclear installations. More conventional structures, which otherwise could benefit from a fracture mechanics based tearing resistance assessment, are not presently assessed due to the high costs and uncertainties of testing.

In order to simplify the determination of the ductile fracture resistance, several correlations between ductile fracture parameters and simplified tests have been developed. The most common correlator is the Charpy - V notch (CVN) impact test. The CVN test is a logical choice, since in the test a specimen is broken in half and the required energy is measured. As ductile fracture is also related to the energy of fracture, the CVN test measures the materials fracture resistance. The CVN test is however, so crude that a direct determination of the fracture toughness from it is not possible, as a result correlations between the charpy test and the fracture toughness have been made.

Wallin in his paper gave a list of the eight well known correlations between the upper shelf energy (CVN_{US}) and fracture toughness, and these are given in Table 4 [223].

$\left(\frac{K_{IC}}{\sigma_Y}\right)^2 = 0.646 \cdot \left(\frac{CVN_{US}}{\sigma_Y} - 0.01\right) \dots [\text{MPa}\sqrt{\text{m}}, \text{J}, \text{MPa}]$	(1)
$\left(\frac{K_{IC}}{\sigma_Y}\right)^2 = 0.18 \cdot \frac{CVN_{US}}{\sigma_Y} - 0.0011 \dots [\text{MPa}\sqrt{\text{m}}, \text{J}, \text{MPa}]$	(2)
$\left(\frac{K_{IC}}{\sigma_Y}\right)^2 = 0.52 \cdot \left(\frac{CVN_{US}}{\sigma_Y} - 0.02\right) \dots [\text{MPa}\sqrt{\text{m}}, \text{J}, \text{MPa}]$	(3)
$\left(\frac{K_{IC}}{\sigma_Y}\right)^2 = 0.893 \cdot \left(\frac{CVN_{US}}{\sigma_Y} - 0.0291\right) \dots [\text{MPa}\sqrt{\text{m}}, \text{J}, \text{MPa}]$	(4)
$\left(\frac{K_{IC}}{\sigma_Y}\right)^2 = 1.23 \cdot \left(\frac{CVN_{US}}{\sigma_Y} - 0.0061\right) \dots [\text{MPa}\sqrt{\text{m}}, \text{J}, \text{MPa}]$	(5)
$K_{IC} = (0.068 \cdot CVN_{US} + 9.9)^2 \dots [\text{MPa}\sqrt{\text{m}}, \text{J}]$	(6)
$K_{IC} = (18 \cdot \sqrt{CVN_{US}} + 16.6) \dots [\text{MPa}\sqrt{\text{m}}, \text{J}]$	(7)
$J_i = 43.37 + \left(\frac{CVN_{US}}{12.23}\right)^2 - \left(\frac{CVN_{US}}{47.655}\right)^3 \dots [\text{kJ}/\text{m}^2, \text{J}]$	(8)

Table 4. Table of Formulae Correlating Charpy Impact Energy with Fracture Toughness [223].

The K values obtained were transformed into the J integral though the correlation.

$$J = \frac{K^2(1-\nu^2)}{E} \quad (2)$$

The correlations in the above eight equations are limited to certain types of nuclear pressure vessel steels [223].

2.6.3. Toughness.

The presence of interstitial nitrogen is known to cause embrittlement of ferrite [228]. Whilst many factors are known to control the toughness of ferrite, there is still a direct and significant effect of nitrogen which may be expressed by an equation of the form. For Charpy Testing [229].

$$ITT = -19 + 44 (\%Si) + 700 (N_f)^{1/2} + 2.2 (\%Pearlite) - 11.5d^{-1/2} \quad (33)$$

where N_f is the 'free' nitrogen content expressed as wt %, and d is the mean linear intercept ferrite grain size (mm). There is no evidence whether the nitrogen which is particularly detrimental is the interstitial, grain boundary, or that associated with dislocation atmospheres. It is possible that all of these forms of 'free' nitrogen can contribute to embrittlement. The general magnitude of embrittlement can be evaluated from the above equation. A decrease in the free nitrogen content from 0.010 wt% to 0.002 wt%, can give a lowering of the impact transition temperature by about 40°C [228].

2.6.4. Effects of Microstructural and Compositional Variables on the Impact Transition Temperature.

The evaluation of microstructural variables on the impact transition temperature is complex, in that many solute additions will have effects on the microstructure in addition to causing solid solution strengthening. For example, manganese additions will affect the transformation characteristics during cooling from the austenite temperature range by depressing the transformation temperature. The depression of the transformation temperature will in general decrease the growth rate of the newly formed ferrite grains and will result in a significant refinement of the ferrite grain size of the transformed product. The depression of the transformation temperature also results in the formation of a larger volume fraction of pearlite, the pearlite formed under these conditions having a lower carbon content than is observed in lower manganese steels cooled at the same rate, or steels of similar manganese content cooled at a slower rate (giving a higher transformation temperature). In order to produce information on the solid solution effects of manganese, it is important that variations in grain size and pearlite content are produced by independent means. This applies to all variables used in regression work, and it is necessary to relate all variables to ensure that no statistically inter-related variables exist. Results obtained in this way have been published by Pickering and Gladman [229], giving a relationship for the Charpy V Notch impact transition temperature (based on the 50% fracture appearance transition temperature see eq. 33). References 3 and 6 in Table 3.

Chapter 3.

3. Materials and Experimental Techniques Used.

3.1. Materials.

3.1.1. Chemical composition.

The materials used in this study were six low carbon steels specifically made for their nitrogen, sulphur and aluminium content. A VS series of steel heats and an interstitial free steel were made by Corus at Swindon Laboratories, at Rotherham and Port Talbot, and an SA106 (F81) series of heats made in Canada. Tables 5 and 6 give their chemical composition.

The steel heats from Corus were received as ingots (vacuum induction melted) each 45 cm x 150 cm x 150 cm. They were forged at Corus Stocksbridge, to a section of 20 cm x 4 cm x 7.5 cm. The forging was done at temperatures from 1250°C to 900°C, and was followed by air cooling. Two of the above section sizes were obtained for each of the steel heats from the original ingots.

The F81 series of steel heats was received in the form of 1/2" (1.3 cm) plate x 30 cm lengths. The heat treatment is given in Table 6.

3.1.2. Mechanical Properties.

The mechanical properties for the VS series of steel heats are given in Tables 11, 12, and 13 in the results section as are F8104 and F8105 and F8106 (Table 14).

3.1.3. Specimen Orientation.

The orientation of all the specimens used in this project are given in Figure 61, Figure 62 shows the orientations of inclusions relative to the three principal planes, longitudinal, transverse, and short transverse.

Comparison of the test methods to determine the free nitrogen content of the steel heats also showing the chemical composition of the steel heats.

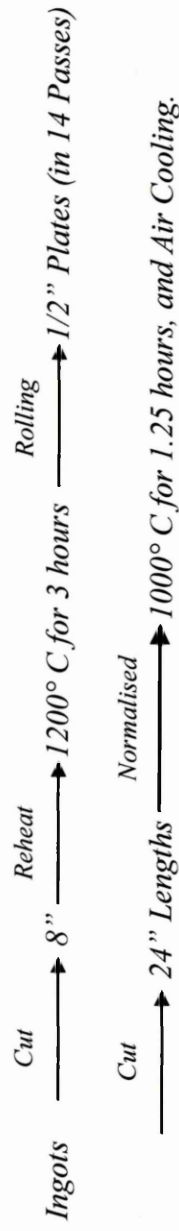
Steel	Chemical Analysis as specified by Corus (Swindon Laboratories).										N (Total). wt %	N (Free).ppm	N (Free).ppm	N (Free).ppm	Al to Total Nitrogen ratio
	C	Si	Mn	S	Cr	Mo	Al	Torsion Pendulum 23°C		Torsion Pendulum 23°C					
Heat VS3763A	0.21	0.2	0.7	0.002	0.2	0.005	0.005	0.005	0.008	34	25	14	0.63		
VS3763B	0.2	0.2	0.69	0.024	0.2	0.005	0.005	0.005	0.007	25	24	14	0.71		
VS3764A	0.22	0.2	0.7	0.002	0.2	0.005	0.005	0.034	0.005	22	12	7	6.80		
VS3764B	0.21	0.2	0.7	0.027	0.2	0.005	0.005	0.032	0.005	58	12	7	6.40		
VS3783A	0.21	0.19	0.72	0.002	0.2	0.005	0.005	0.005	0.008	38	38	24	0.63		
VS3783B	0.22	0.19	0.71	0.024	0.2	0.005	0.005	0.005	0.007	38	36	25	0.71		
Chemical Analysis for Interstitial free as specified by Port Talbot.															
Interstitial Free	0.0038	0.002	0.15	0.013	0.009	0.040			0.0024					0.06	

Table 5. Chemical Composition of VS series of steel heats and Interstitial free steel and free nitrogen content.

Chemical Compositions for the F81 series of steel heats in wt%.

	C (ladle)	Mn (ladle)	Si (ladle)	Al (ladle)	S (ladle)	P (ladle)	O			N		Al: N wt%:wt%	
							(melt)	(plate edge)	(plate centre)	(melt)	(plate edge)		(plate centre)
F8106	0.16	0.93	0.39	0.04	0.004	0.005	0.0085	0.0057	0.0062	0.006	0.0067	0.0067	6.19
F8104	0.17	0.83	0.33	0.03	0.005	0.008	0.010	0.0063	0.0066	0.013	0.013	0.013	2.31
F8105	0.16	0.84	0.33	< 0.004	0.005	0.010	0.014	0.0110	0.0110	0.012	0.014	0.013	< 0.31

Thermo – treatment History of the F81 series of Steels Heats, As Received Condition.

**Table 6. Chemical composition of F8104, F8105, and F8106 steel heats.**

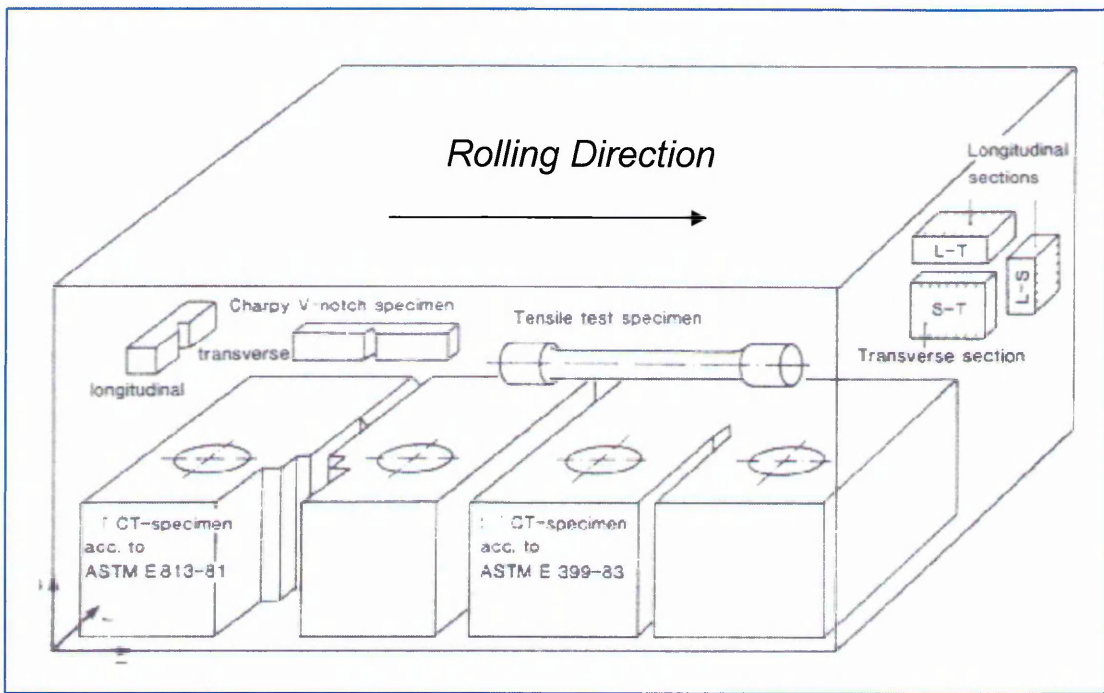


Figure 61. Orientation of the specimens for determining mechanical properties.

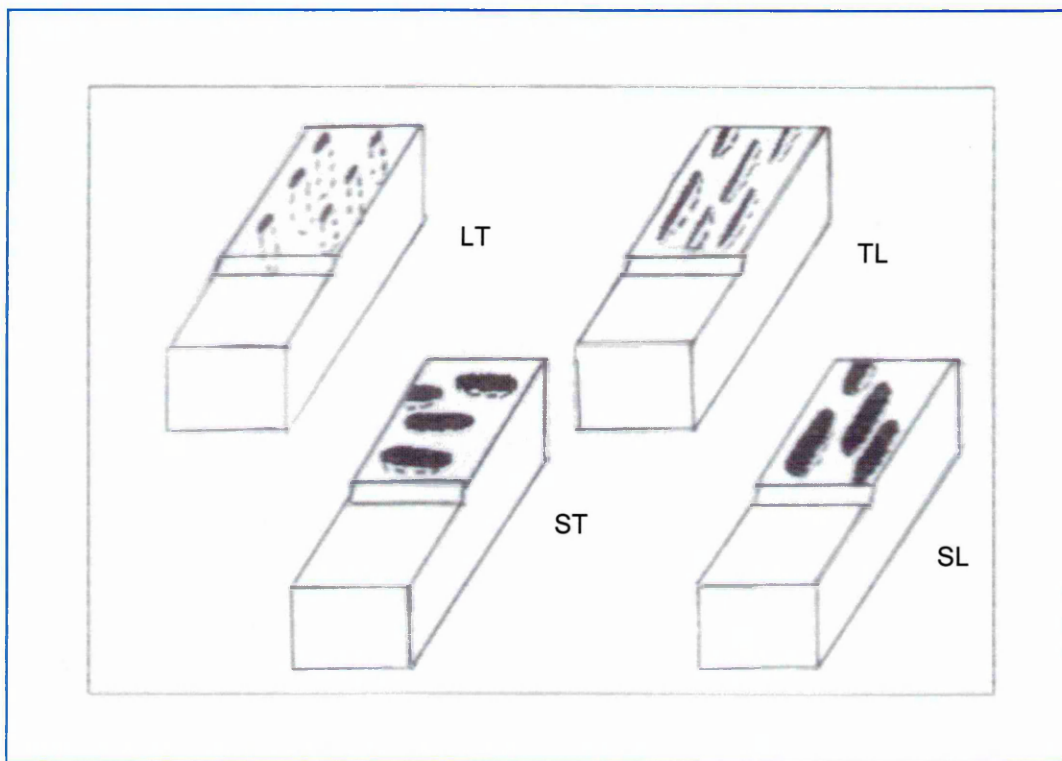


Figure 62. Inclusion orientation in relation to specimen.

3.2. Fatigue Testing.

3.2.1. Specimen preparation.

The fatigue tests were conducted on 11.85 mm thick compact tension specimens, the dimensions of which are given in Figure 63.

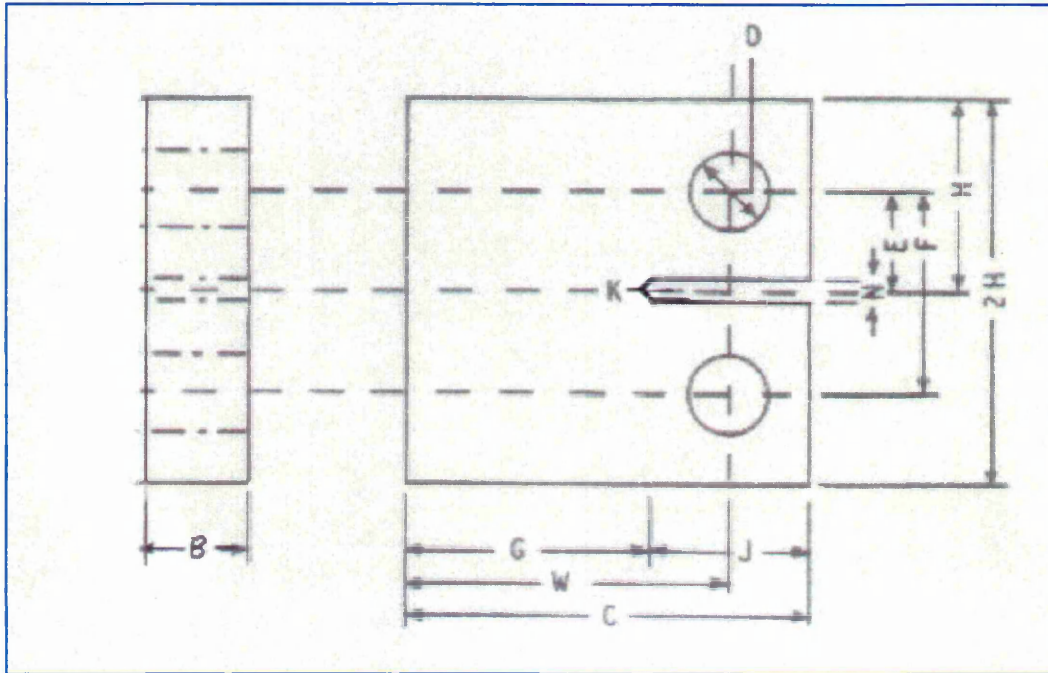


Figure 63. Dimensions of 11.85 mm compact tension specimen (prior to fatigueing): B = 11.85; W = 50; C = 62.5; N = 3; E = 13.75; F = 27.5; H = 30; D = 12.5; G = 35; 25; J = 27.5; K = 1 spark eroded notch (all dimensions in mm).

All specimens were machined in the longitudinal-transverse direction. Final machining of the notch was conducted by spark erosion to facilitate the subsequent initiation of fatigue cracking.

The compact tension specimens were pre-cracked in air using a 100 kN ESH servo-hydraulic testing machine at a frequency of 10 Hz an R ratio of 0.2 and a ΔK of $14 \text{ MPam}^{1/2}$. All specimens were pre-cracked to a ratio of crack length to specimen width (a/W) of 0.375. Prior to each test all specimens were ultrasonically cleaned in industrial methylated spirit and dried in hot air.

3.2.2. Test Equipment.

A 10 kN ESH servohydraulic machine was used for fatigue testing. A direct current potential drop method was used to monitor crack growth in which a constant current (dc) is applied to the specimen and the potential drop across the cracked region is monitored. As the crack grows the remaining ligament becomes smaller so the electrical resistance and hence potential drop increases. A schematic diagram is shown in Figure 64.

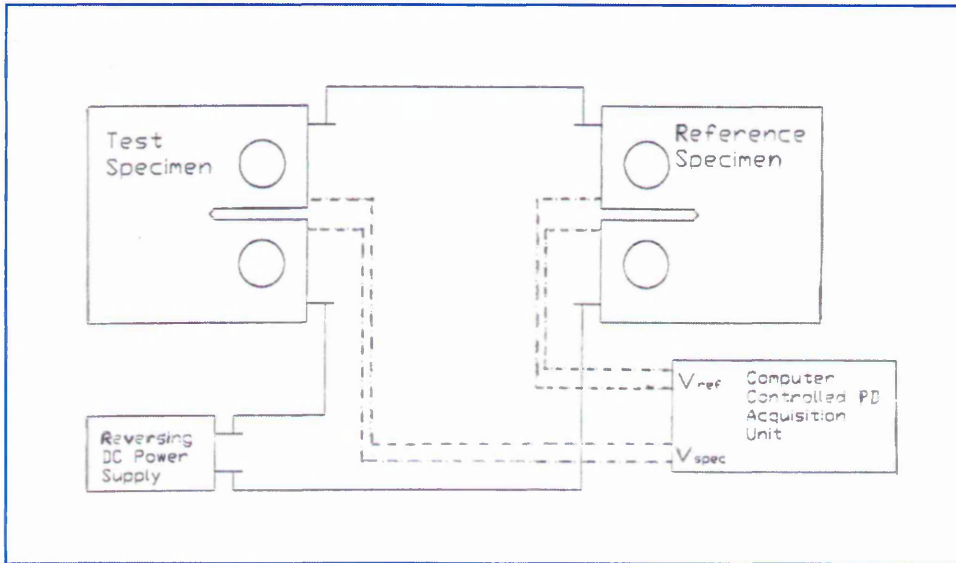


Figure 64. Schematic Diagram of the DCPD Crack Monitoring system.

A constant current was passed through the specimens in series as illustrated. A current of 10 amps was applied in each test. Potential readings across each specimen were measured every second and averaged every 20 minutes, using p.d. averages of 2 for 0.0167 Hz and 8 for 5Hz respectively. This data was then captured and stored by the acquisition system, specifically designed for the monitoring of fatigue crack growth [230].

The quotient of each set of potential readings taken across both the specimen and the reference specimen (V_S/ V_R) were converted into a crack length according to Johnson [231] (equation 34) and normalised to eliminate temperature and current fluctuations.

$$\frac{a}{W} = \frac{2}{\pi} \cos^{-1} \left[\cosh\left(\frac{\pi y}{2W}\right) / \cosh\left[\left(\frac{U}{U_0}\right) \cosh^{-1}\left[\frac{\cosh\left(\frac{\pi y}{2W}\right)}{\cos\left(\frac{\pi a_0}{2W}\right)}\right]\right] \right] \quad (34)$$

Where:

U = electrical potential signal

U₀ = initial electric potential signal

a = crack length

a₀ = the initial crack length

W = specimen width

2y = the spacing of the potential probes.

resulting in a fifth order polynomial of the form.

$$y = ax + bx^2 + cx^3 + cx^4 + cx^5 \quad (35)$$

to describe the curve generated for crack growth from which an array of crack length data against number of fatigue cycles was built. To confirm the accuracy of the test, the calculated crack length was compared with the measured crack length from the broken open specimen.

Every 20 minutes the values in this array were averaged. If the change in crack length δa exceeded a statistically significant increment (defined as 50 μm for this project) the change in crack length was logged as significant. Otherwise the array-building process continued.

Control of the ESH machine for applying the loads, frequency, determining the number of cycles etc, was done using the Rubicon computer system. The measurement of crack length was done on an independent computer system. The p.d. monitoring system was calibrated at the test temperature of 150°C, before commencement of testing.

Heating of the specimen was done by a circular half section hinged furnace mounted on the ESH columns. Temperature control was within $\pm 1^\circ\text{C}$.

3.2.3. Testing Parameters.

Testing was done at 150°C , step loading was carried out using alternating frequencies of 5 Hz and 0.0167 Hz both frequencies were sine wave. The steps were done in at least 1 mm increments. Steps were done at ΔK 's of 15, 25, 35, 50, 65, and 80.

At the end of each test the specimens were broken apart and the fracture surfaces photographed. The fracture surface of one half of each specimen was then stripped of its oxide by immersion in a solution of hydrochloric acid and hexamine in an ultrasonic bath to reveal the fracture surface which was then photographed.

Beach marks were occasionally created during testing. This was done by reducing the load to zero or by changing (lowering or raising) the frequency. This was usually done at the end of steps during load or if some event occurred such as a power loss. These beach marks were readily detectable on the fracture surfaces of the specimens. Where they were detectable, their distance from the starter notch was measured at the specimen edges and at an additional 7 points evenly spaced between them and where they differed from the DCPD readings were used to calculate correction factors for the DCPD readings.

3.3. Fracture Toughness Testing.

3.3.1. Specimen preparation.

The J - R tests were performed on 20% side grooved 25 mm compact tension specimens, the dimensions of which are given in Figure 65. All specimens were machined in the longitudinal transverse direction. Final machining of the notch was conducted by spark erosion to facilitate the subsequent initiation of fatigue cracking. The compact tension specimens were pre-cracked in air using a 100 kN ESH servo-hydraulic testing machine at a

frequency of 10 Hz an R ratio of 0.1 and a ΔK of 14 MPam^{1/2}. All specimens were pre-cracked to a ratio of crack length to specimen width (a/W) of 0.5. Prior to each test all specimens were ultrasonically cleaned in industrial methylated spirit and dried in hot air.

3.3.2. Test Equipment.

3.3.3. For testing in water at 200°C.

A 100 kN screw type machine was used for J - R testing which was conducted in a stainless steel autoclave system specifically designed for the purpose (see Appendix 7). A flowing autoclave system was employed, specifically designed for the purpose, Finite Element Analysis was used to ensure it could withstand the internal pressures (see Appendix 7).

The water is heated in the autoclave by means of a 200W external heating tape. The flow rate of the water is slow enough (200 ml hr⁻¹) to ensure that a constant temperature is maintained.

Control of the machine for applying the loads, and executing the J_{1C} unloading compliance programme was done using the Rubicon computer system. The control of the environmental conditions, oxygen content (dow), heating of the autoclave was done on an independent computer system Figure 66 is a schematic of the system. A schematic of the recirculating loop is shown in Figure 67. The actual test rig is shown in Figure 68, being opened after the end of the first test. Inset is the on screen computer display of the test.

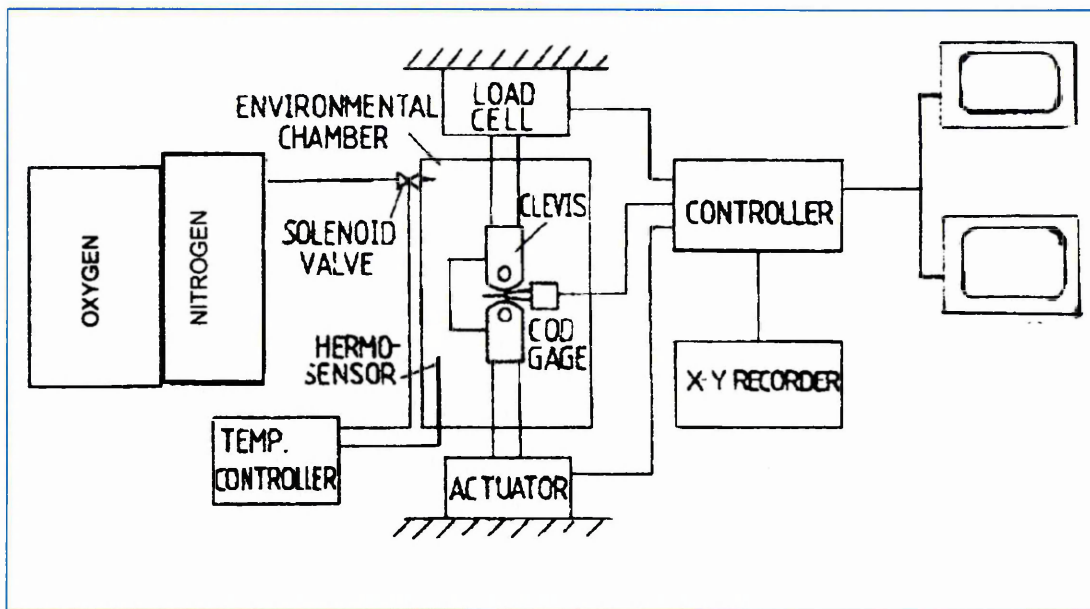


Figure 66. Schematic showing control of environmental test rig for J testing.

3.3.4. Test Parameters.

Tests were conducted at 200°C under high oxygen conditions (8 ppm), using distilled deionised water, pH typically 7 and conductivity < 0.2 μ S/cm.

The Rubicon Unloading Compliance programme, executed the programme with the following input parameters, bedding cycles 2, compliance cycles 3, unload every 0.1 mm and unload to 30% of the current load [232] This was done to preset fixed load line displacements to test completion. The data was then input into the J_{1C} Analysis programme to determine J_Q .

After testing the specimens were broken open in liquid nitrogen, then ultrasonically cleaned in hexamine and hydrochloric acid .

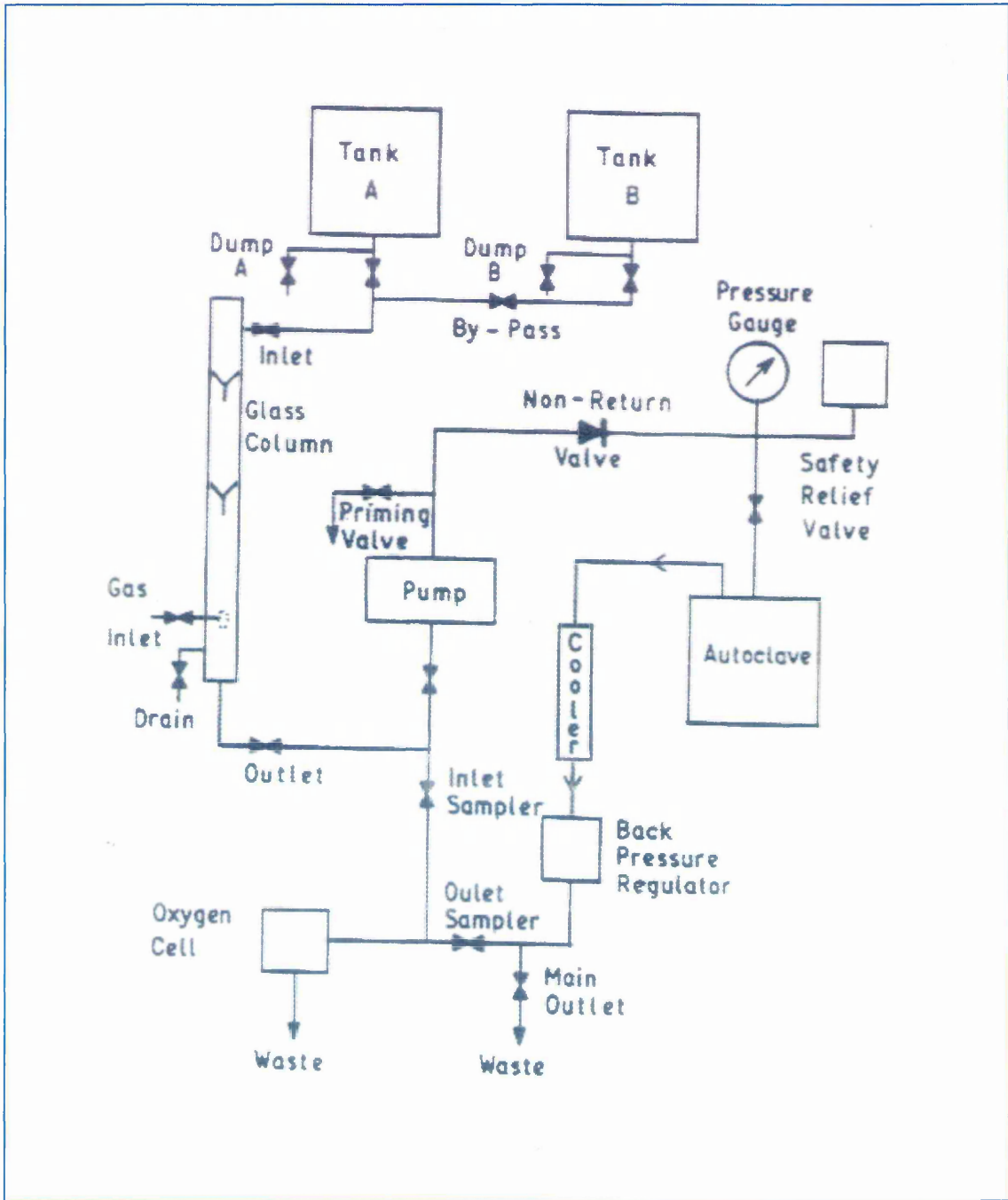


Figure 67. Schematic representation of the circulating loop for J testing.



**Figure 68. Photograph of environmental J test rig
Also showing test result at 200°C on computer screen display.**

3.3.5. Air Testing Rig.

The J tests that were performed in air at temperature were done on a 250 kN ESH servo hydraulic machine (manufactured by Babcock and Wilcox). Heating of the specimen was done using an Instron model 3111 fan assisted furnace capable of 250° centigrade. This was used to avoid damage to the clip gauges, which may have arisen by the use of a three zone furnace. A schematic of the control system is shown in Figure 69.

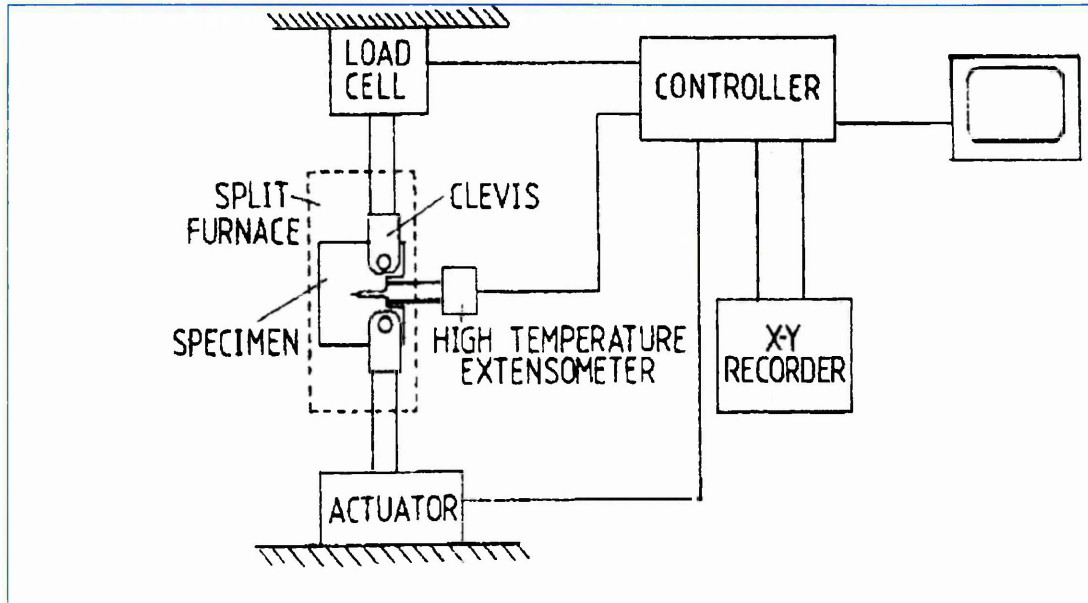


Figure 69. Schematic of the air testing rig.

The actual rig is shown in Figure 70. An enlarged view of the clevises and specimen after a test is shown in Figure 71.



Figure 70. Photograph of rig used for J testing in air from room temperature to 200°C.

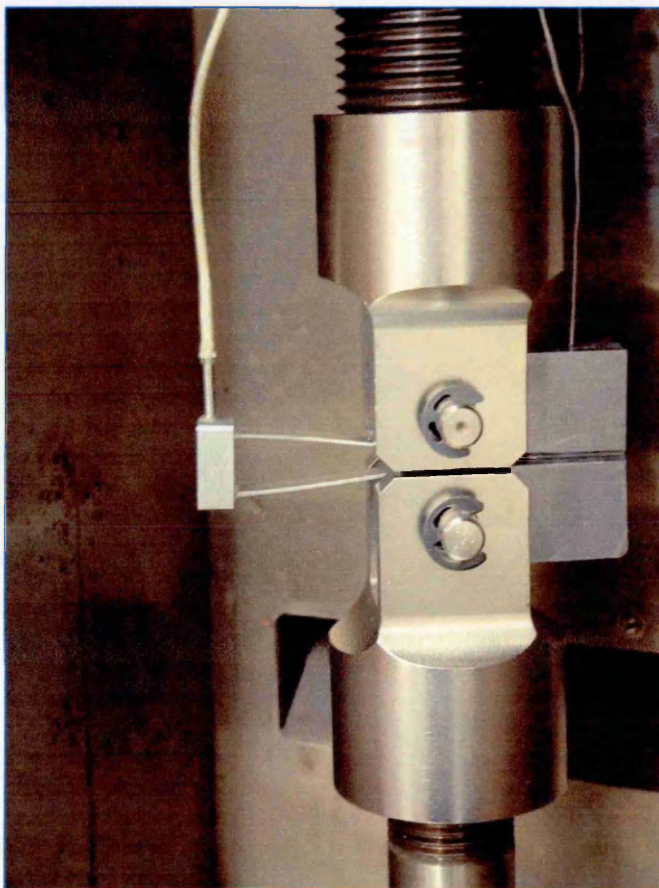


Figure 71. Photograph of clevises, specimen and clip gauge. Also shown is the thermocouple located on top of specimen. Photograph taken after test at 200°C.

3.3.6. The Clevises.

The materials used for the clevis holders and pins was a 250 grade maraging steel, supplied by Aviation Metals (based in Milton Keynes) as G110 in the form of solution treated round bar 12.5mm diameter (for the pins) and 70mm diameter for the clevises. From these the grips and pins were made, then heat treated (see Figure 72).

The heat treatment consisted of heating in a furnace to 485° centigrade for 6 hours and then air cooled. At this temperature [233] a very rapid age hardening occurs and greatly strengthen the material. Although the nature of the precipitates formed is still uncertain, the consensus of opinion is that aging for several hours at 485°C results in a Ni₃Mo phase while longer times produce an Fe₃Mo phase. There may also be a titanium precipitate η-Ni₃Ti or Ni₃(MoTi). Ageing at higher temperatures or longer times results in some reversion to austenite, which may be stable at room temperature (depending on time and temperature of aging) and a lower strength. This gave the grips and pins a hardness of between 45 - 47 HRC and a corresponding ultimate tensile strength of 1750 MPa to 1850 MPa. The pins and clevises were then given a 5 micron nickel coating. After the coating had been applied the, they were put into a furnace (baked) for 12 hours to remove any internal hydrogen that may have arisen because of the plating process.

The nickel coating was done to minimise hydrogen embrittlement, as the susceptibility of maraging steels to hydrogen embrittlement in aqueous environments is well known. In general susceptibility to stress corrosion cracking increases with increasing yield strength, for this reason a mid range maraging steel was chosen, in preference to a higher strength maraging steel, such as the 300M. The shape and hardness of the clevises conformed to ASTM 1737 96 although the load bar holding section was modified, to enable use of the clevises in air as well as water environments.

3.3.7. Clip Gauges.

The clip gauges for the experimental work were manufactured by Gauge Factors (based in Andover, Hampshire). They were made from titanium and stainless steel to minimise corrosion. They were of the full bridge type, and had a working range of 4mm to 16mm. The gauges had a theoretical operating temperature range up to 250° centigrade.

Prior to commencement of any testing in air or in the environmental tests, the gauges were calibrated at the relevant temperature.

3.3.8. Loading rates.

Loading rates of 0.1 mm per minute were used in both the air and environment tests as this is approaching the lower practical limit for use of the unloading compliance technique for J - R curve determination [234]. The standard test rate for J - R curve testing is 0.25 mm per minute [235,236]. So 0.1 mm per minute was chosen as the lowest loading rate feasible to generate any environmental effect. Figure 72 shows the clevises, pins, and specimen prior to testing.

3.3.9. Test Parameters.

Tests were conducted at 20°C and 200°C the Rubicon Unloading Compliance programme, executed the programme with the following input parameters, bedding cycles 2, compliance cycles 3, unload every 0.1 mm and unload to 30% of the current load. This was done to preset fixed load line displacements to test completion. The data was then input into the J_{1C} Analysis programme to determine J_Q.

After testing the specimens were heat tinted, and broken open in liquid nitrogen.

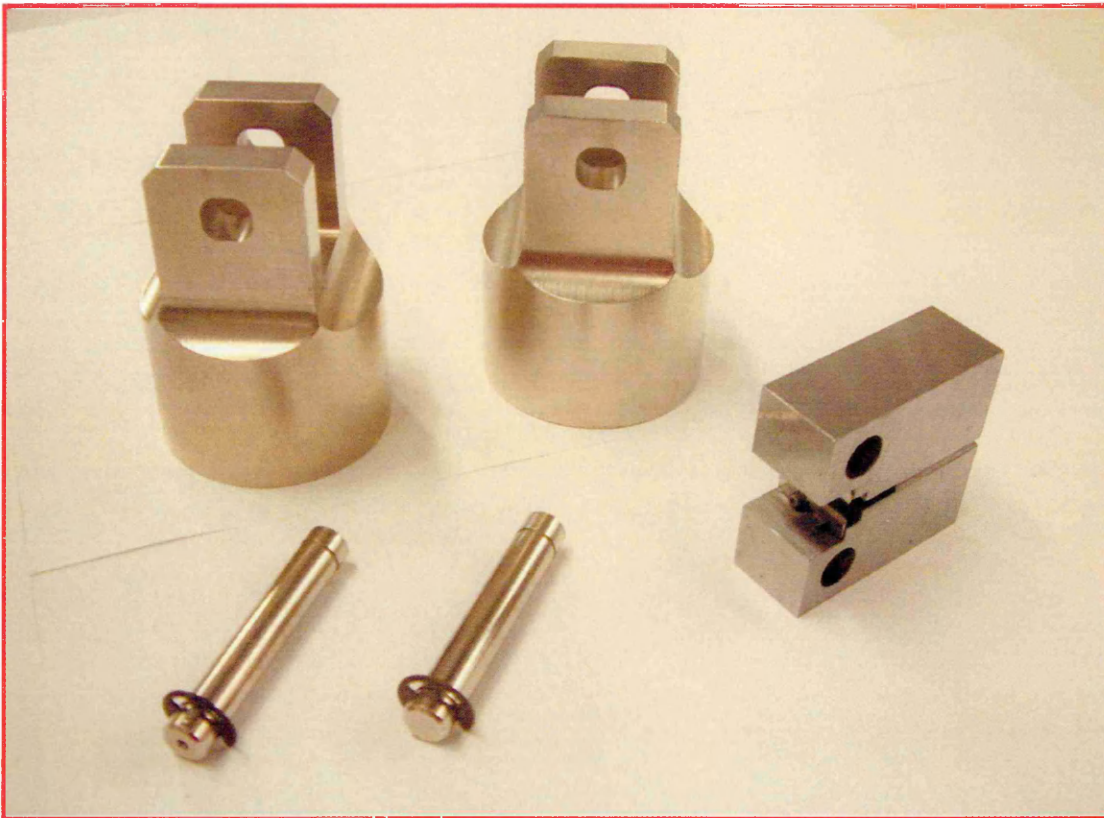


Figure 72. The Clevises and Pins used and a 25 mm Compact Tension Specimen.

The clevises and pins were made out of a 250 Grade maraging steel. The steel was heat treated at a temperature of 485°C for 6 hours, and this gave the steel an HRC hardness of 48 to 50. This hardness is required to resist indentation as, friction caused through the indentation, was found to cause negative crack growth. Also shown is a 25 mm CT based on the ASTM 1737, [24] and ASTM 1820 Standards [232] used in the programme.

3.4. Constant Extension Rate Testing In Air.

3.4.1. Specimen preparation.

The constant extension rate tests done in air were conducted on tensile specimens with the dimensions given in Figure 73.

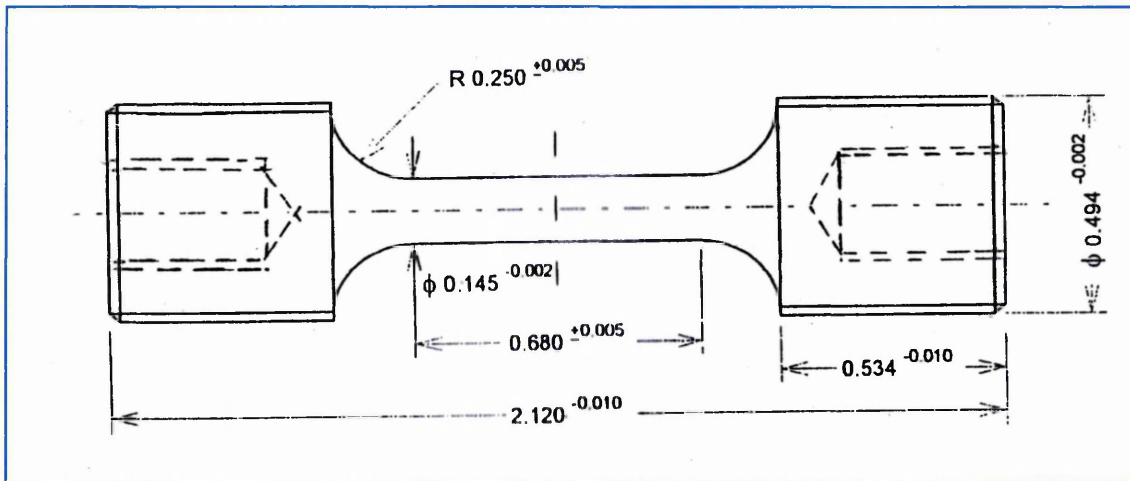


Figure 73. Dimensions of tensile specimen used for determining the dynamic strain ageing peak ($\Delta\sigma_p$) in air and " m " the strain rate sensitivity from room temperature to 350°C.

The specimens were ground to 0.8 micron finish. All specimens were machined with longitudinal orientation. Prior to each test all specimens were ultrasonically cleaned in industrial methylated spirit and dried in hot air.

3.4.2. Test Equipment.

A 100 kN screw type machine was used for tensile testing of specimens. Heating was done by a wrap round furnace. The machine was analogue, so it was adapted so that the output could be computerized for data analysis. Figure 74 is a photograph of the system.

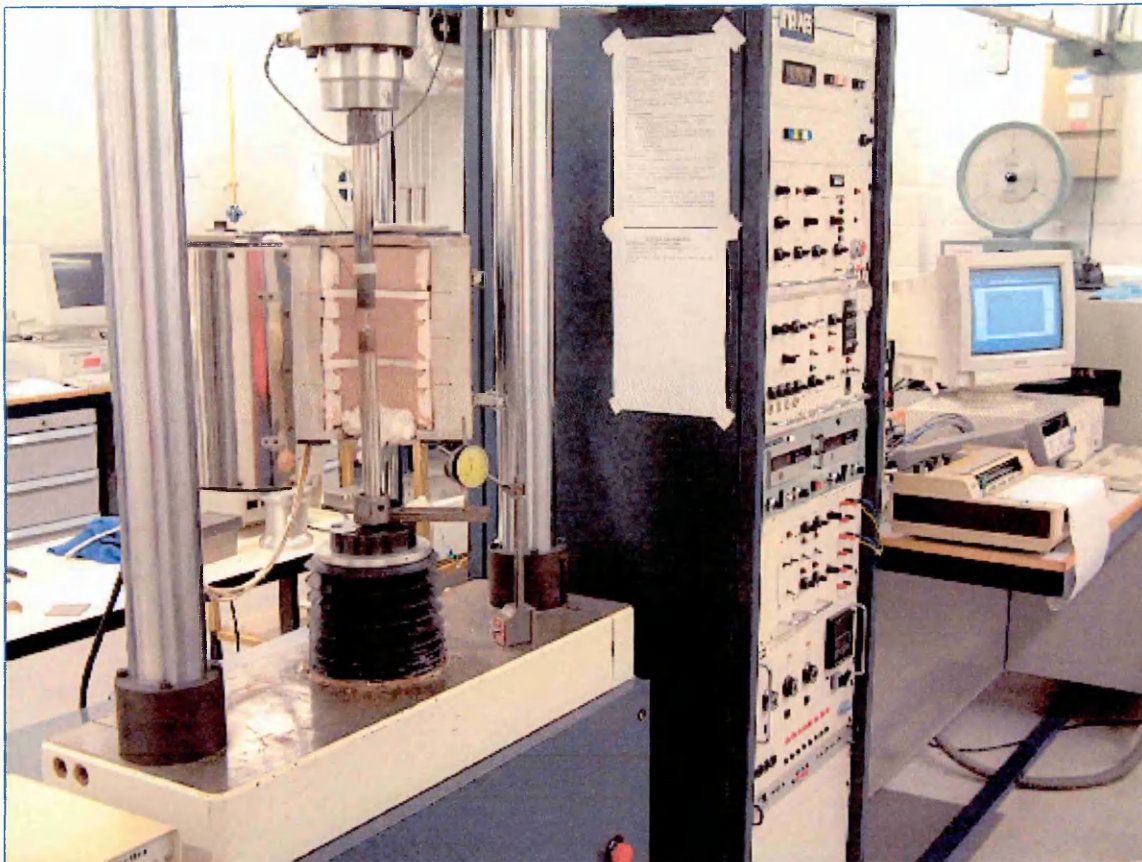


Figure 74. The air testing rig for testing tensile specimens used for determining the dynamic strain ageing peak ($\Delta\sigma_p$); and " m " the strain rate sensitivity from room temperature to 350°C.

A strain rate of $2 \times 10^{-6} \text{ sec}^{-1}$ was used. The temperature range was from room temperature up to 350°C. Increments of 50°C were used. This was done to determine $\Delta\sigma_p$ and the mechanical properties for the particular steel heat. The external threaded specimens were used.

3.5. Internal Friction Measurement.

3.5.1. Specimen Preparation.

The specimen dimensions are given in Figure 75.

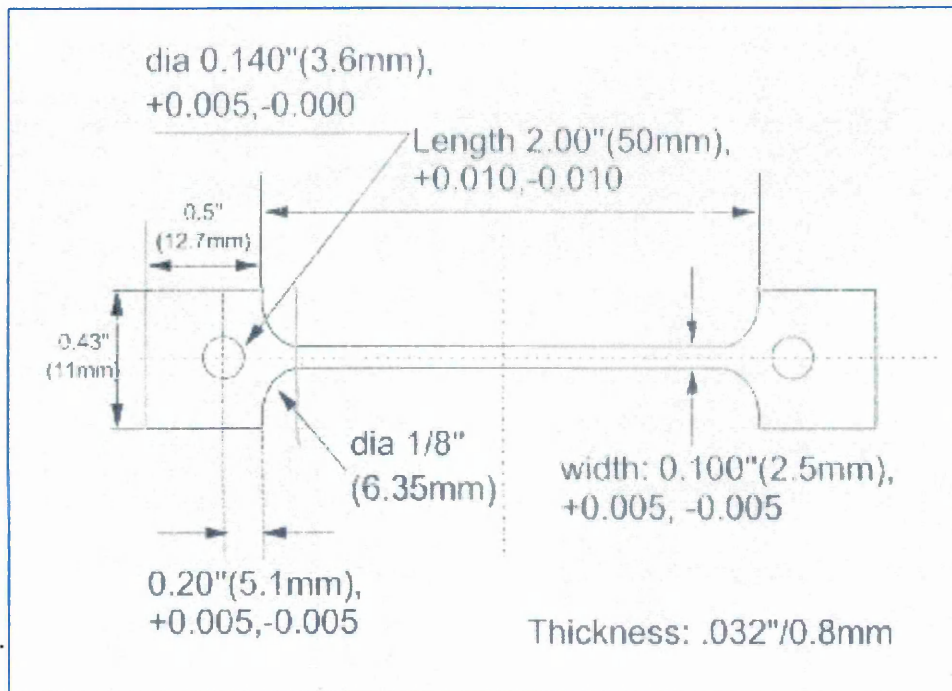


Figure 75. Specimen for free nitrogen measurement.

The specimens were ground to a 1 micron finish. All specimens were spark eroded in the longitudinal orientation. Prior to each test all specimens were ultrasonically cleaned in industrial methylated spirit and dried in hot air.

Mechanical Spectroscopy was used to determine the free nitrogen and carbon in the steel heats and was done by Mr A.D.Higgins [257], the results are given in the composition Table 5 also included for comparison are the same samples done by the Polaron method. Figure 76 is a photograph of the Torsion Pendulum system. The system used was Vibran.



Figure 76. Apparatus for measuring free nitrogen content by internal friction. The Vibran System.

For a description of the operating procedure see section 2.2 (Nitrogen in Steel).

3.6. *Impact behaviour.*

To complete the characterisation of the five carbon steels, Charpy impact tests were conducted over the temperature range -196 to $+200^{\circ}\text{C}$. The specimens conformed to BS EN 10 045 - 1:45. The specimen was 55mm long of square section with 10 mm sides. The V notch was machined with a 45° included angle with a 0.25 mm radius of curvature at the base of the notch and conformed to the tolerances of the above standard. The striking impact velocity was 5.24ms^{-1} . Temperature control during heating was $\pm 1^{\circ}\text{C}$, and during cooling $\pm 2^{\circ}\text{C}$ (as control of the temperature was hit and miss due to mixing of chemicals to achieve the required temperature).

Figures 77 and 78 show the apparatus set up, and the positioning of the specimen on the anvil before striking.



Figure 77. The Equipment used for Charpy Testing.

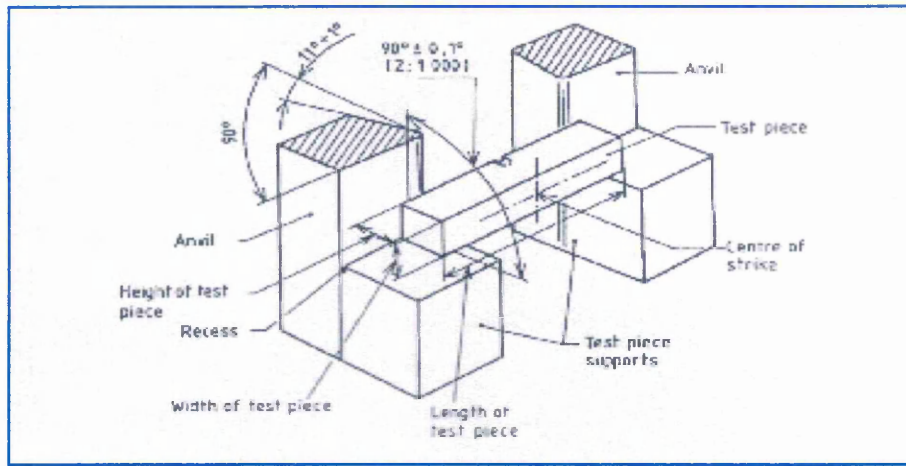


Figure 78. Positioning of the specimen on the anvil relative to striker.

3.7. Calculation of the Volume Fraction of Inclusions for the VS Steel Heats.

Three heats of C – Mn steel were manufactured at Corus the composition of which is given in the Table 5.

The volume fraction of inclusions was estimated from the chemical composition according to Franklin [237], and to Bulloch et al [238]. It was expected that there would be a certain amount of inhomogeneity within the material as the material was upset forged at 1280°C down to red heat 800°C. With air cooling afterwards. The calculated values are given in Table 7 for the VS series of steel heats.

$$f_v = 0.054 \left[\%S - \frac{0.001}{\%Mn} \right] + 0.05\%O \quad (36)$$

The oxygen content of the steel heats was not specified in the analysis but a typical value for a normal steel of this type is in the range 7 – 8 ppm. So the oxygen term in the Franklin formula was omitted for calculation purposes.

Quantitative metallography was used to measure the inhomogeneity in the distribution of inclusions using image analysis (Image Pro Plus version 4.0

for Windows). The distribution of inclusions was characterised on polished sections perpendicular to the three principal directions relative to the rolling direction (longitudinal - length), short transverse (S - thickness) and transverse (T - width). The area fraction was calculated for each of the three faces L, S, and T and graphed as was expected the higher sulphur content steel resulted in significantly higher area fractions on all three planes. Two populations were observed small spherical particles and clusters of large mixed inclusions. The metallographic analysis also provided the average distances between inclusion and inclusion clusters. This was done for steel heats VS3764A and VS3764B.

Steel Heat	Volume Fraction (F_v) Based on 0.053%S	Characteristic (weight per cent).				
		Low sulphur	High Sulphur	Low Nitrogen	High Nitrogen	Mn
VS3763A	1.06×10^{-2}	0.002			0.008	0.70
VS3763A	3.08×10^{-3}					
VS3763B	1.272×10^{-1}		0.024		0.007	0.69
VS3763B	1.21×10^{-1}					
VS3764A	1.06×10^{-2}	0.002		0.005		0.70
VS3764A	3.08×10^{-3}					
VS3764B	1.431×10^{-1}		0.027	0.005		0.70
VS3764B	1.38×10^{-1}					
VS3783A	1.06×10^{-2}	0.002			0.008	0.72
VS3783A	3.29×10^{-3}					
VS3783B	1.272×10^{-1}				0.007	0.71
VS3783B	1.21×10^{-1}		0.024			

Table 7. Calculated Volume Fraction for the VS steels heats.

The bold figures are volume fraction calculated using the Bulloch et al [238] formula. The area fractions using SEM for steel heat VS3764A were 0.146%,

0.40%, and 0.1316% and for heat VS3764B 1.097%, 0.5%, and 1.6% for the L, T, and S directions respectively. This is based on a frame size of 1600 x 1200 pixels at 1 μ m per pixel an objective lens of 8 x 1.25, and a threshold lighting intensity of 175 for data capture on the image pro system.

3.7.1. Microstructure.

Quantitative metallography was performed on several heats of steel. Grain size and pearlite volume fraction were computed using image analysis software. Grain size measurements were done using the line intercept method as prescribed by ASTM E112.

In addition, 3-dimensional images were formulated for the microstructure for the heats as shown for heats VS3764A and VS3764B in Figures 80 and 81, respectively. These constructions show the distribution of the ferrite and pearlite with respect to orientation. The distribution of pearlite in both steel heats in Figure 79 and Figure 80 appears to be relatively isotropic. But there seems to be regions of banding in VS3764B. This implies that the extent of banding can be location specific. It is thought that this is due to the material being upset forged.

Pearlitic banding is usually attributed to microsegregation of manganese in these steels, but may also be caused by precipitation of non-metallic inclusions or hot rolling at low finishing temperatures and cooling rates [241]. Pearlitic banding has been observed to be altered by heat treatment and changes to the thermomechanical process schedules of the steel. Banding has several effects on mechanical properties. The layered structure resembles a crack divider orientation, in the L-T as well as the T-L orientation. This has been found to increase toughness through a delamination induced toughening process [242].

Delamination of pearlite from ferrite decreases the effective thickness inducing plane stress conditions, and thereby increasing toughness. In general, banding may increase toughness variation between orientations. However, one study on banding in steels [241] determined that the effect of inclusion content had a larger impact than banding on the orientation dependence of upper-shelf fracture properties. In any case, the test range thickness variation is far within bounds of plane stress conditions, minimising the effects of delamination-induced toughening.

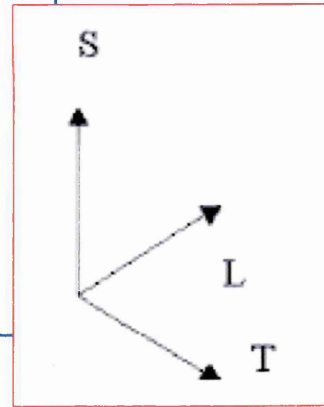
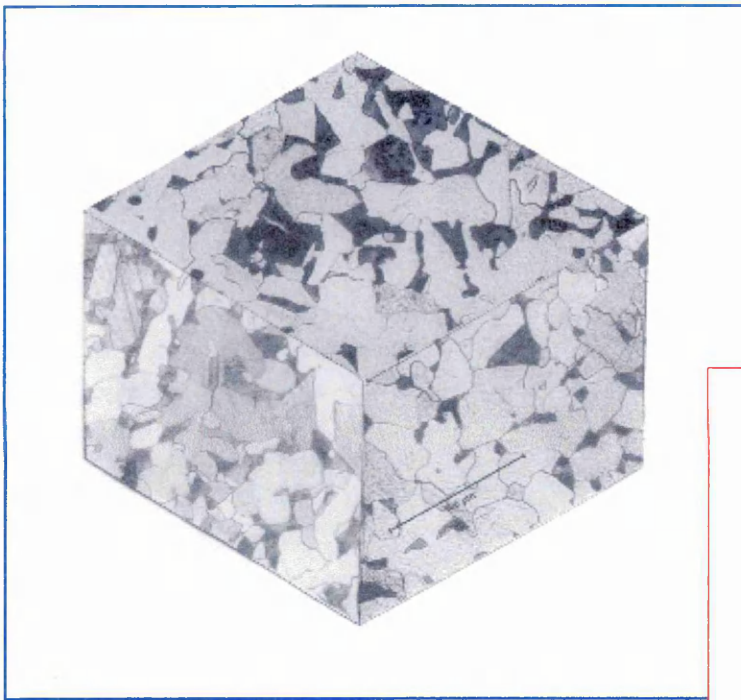


Figure 79. VS3764A 3D view.

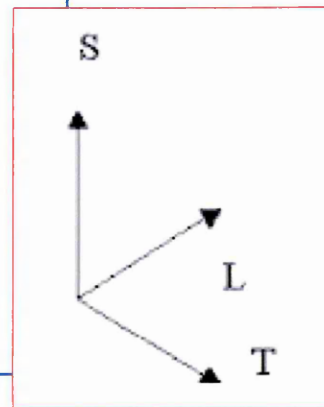
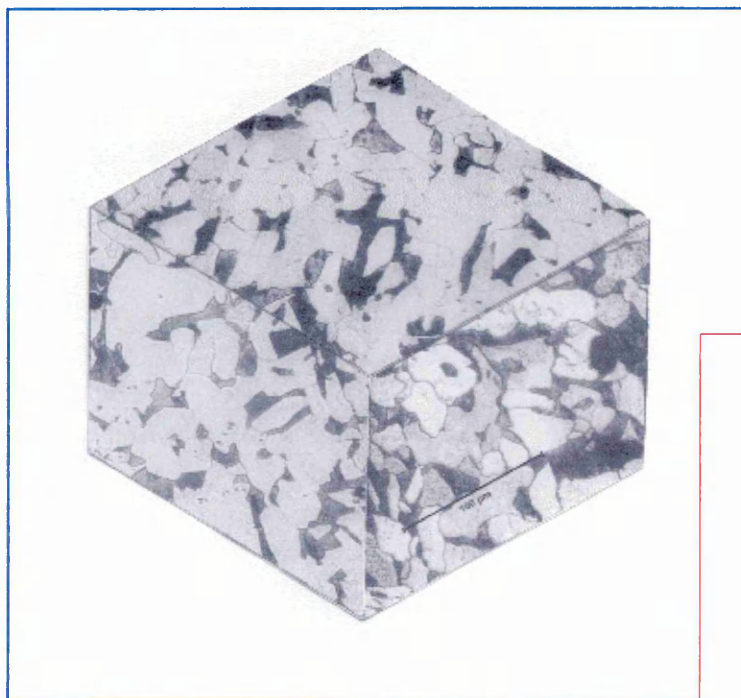


Figure 80. VS3764B 3D view.

Fracture surfaces on three mutually perpendicular planes, for steel heats VS3764A and VS3764B. L, T and S indicate the longitudinal (rolling), transverse (width) and short transverse (thickness directions) respectively.

The percentage of pearlite and ferrite was calculated using the image pro software, five readings were taken for each steel heat and the average taken. Grain size measurement was done using the linear intercept method conforming to ASTM E 112 [240], on the Image Pro software. Ten readings were taken and the average used. The results are given in Table 8. The inclusion distribution on each of the three mutually perpendicular faces for the steel heats VS3764A and VS3764B is shown in Figure 81.

Steel Heat	Grain Size μm	V_f Pearlite	V_f Ferrite
VS 3764 A	12 (ASTM 9.33)	29.30	70.70
VS 3764 B	14 (ASTM 9)	22.90	77.09
VS 3783 B	17.89	28.25	71.75
F 8104	7.5 [257]	26.32 [258]	73.68
F8105	13 [257]	41.13 [258]	58.87

Table 8. Grain size, and Volume fraction of Ferrite and Pearlite for the steel heats.

Graphs of Number of Clusters v No of Inclusions per unit area for Steel Heats VS3764A (0.002%S) and VS3764B (0.027%S) for the three orthogonal planes (Longitudinal, Transverse and Short Transverse directions).

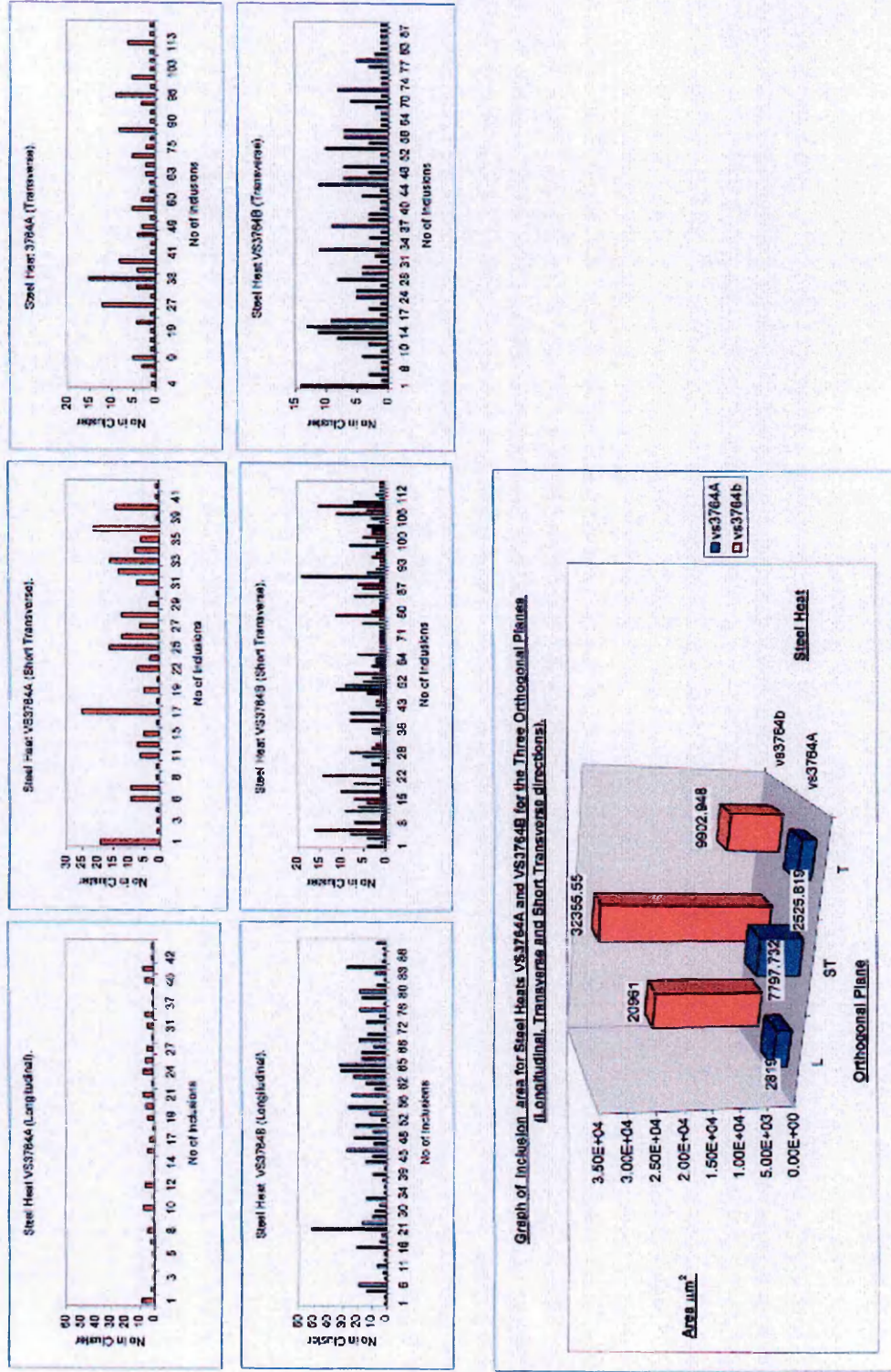


Figure 81. Graph of Inclusion Distribution on the three orthogonal planes for VS3764A and VS3764B (L, ST, and T).

3.8. Determination of the Strain Rate Sensitivity (m).

To determine the strain rate sensitivity of the steel heats, strain rate jump tests were carried out. The base strain rate to just past the yield point of the material was $2.7 \times 10^{-4} \text{ sec}^{-1}$ this was then changed to $2.7 \times 10^{-6} \text{ sec}^{-1}$ up to 2% strain and then changed back to the base strain rate ($2.7 \times 10^{-3} \text{ sec}^{-1}$) up to 3% strain and then back to $2.7 \times 10^{-6} \text{ sec}^{-1}$ up to 4%. This was carried out up a selected strain of 6%. This was done to ensure that the conditions for the determination of m were not violated. This was done at three temperatures 150° , 200° , and 250°C . One exception to this was the high nitrogen steel heat, where a temperature of 100°C was also included as it was thought that this would show the strain rate sensitivity effect quite clearly. Strain rate differentials of 10, 100, and 1000 were used, see Table 10 in results section.

The machine that was used for the determination of m was an analogue control machine, so the strain rate jumps had to be done manually. So in some of the tests there was a bit of overrun by the actuator (so this was one problem that had to be overcome as well as experimental problems encountered during strain rate change tests). Prior to testing spreadsheets were made out for each specimen to determine where the strain rate change had to be done, as the only facility available was a computer screen showing the load vs extension plot (this was set up as discussed in the experimental section). When the extension (on the load vs extension trace on the computer) reached the required value, the strain rate change was made. Speed was of the essence as a 10^{-3} sec^{-1} strain rate is fast.

In some of the tests other strain rates were used to see the effect, and some of the specimens were taken to strains in excess of 6% after the required data was obtained. This was done to see if there was any correlation with the strain rates used to determine the UTS of the tensile tests.

Chapter 4.

4. Results.

Initially the test programme was to be carried out as per the testing matrix in Table 9 but due to machine availability and time constraints only selected parts of the matrix could be done. The parts ticked are the tests completed or partially done for this work.

Steel Heat	wt% Sulphur	Free Nitrogen ppm.	Free Carbon ppm.	Tensile tests	Charpy tests	J Tests	Fatigue Crack Growth tests
VS 3763A	0.002	25	14	x	x	x	x
VS 3763B	0.024	24	14	x	x	x	x
VS 3764A	0.002	12	7	√	√	√	x
VS 3764B	0.027	12	7	√	√	√	x
VS 3783A	0.002	38	24	√	√	x	x
VS 3783B	0.024	36	25	√	√	x	x
F8104	0.005	8	3	√	√	x	√
F8105	0.005	54	28	√	√	x	√
F8106	0.004	1.45	1.25	x	x	x	x
I.Free	0.012	-	-	√	√	x	x

Table 9. Matrix table of steels tested and testing variables.

4.1. Internal Friction Results.

As stated earlier in the experimental section mechanical spectroscopy was used to determine the free nitrogen content of the steel heats. Figure 82 and Figure 83 show two of the graphs obtained for steel heats VS3764B and VS3783B [257].

Initially the output of the Vibran system graphs showed the combined peak of the free nitrogen and carbon present in the steel heat (the blue line in the graphs). This was then modelled (the purple dashed line) to see the correlation of the fit, and from this the free nitrogen N_f (the red dashed line in the graph), and free carbon were obtained (the green dashed line) for the steel heats.

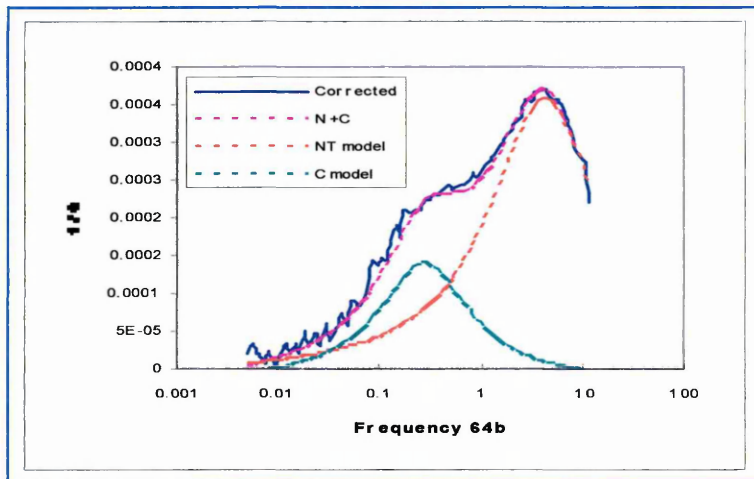


Figure 82. Internal friction analysis for VS3764B.

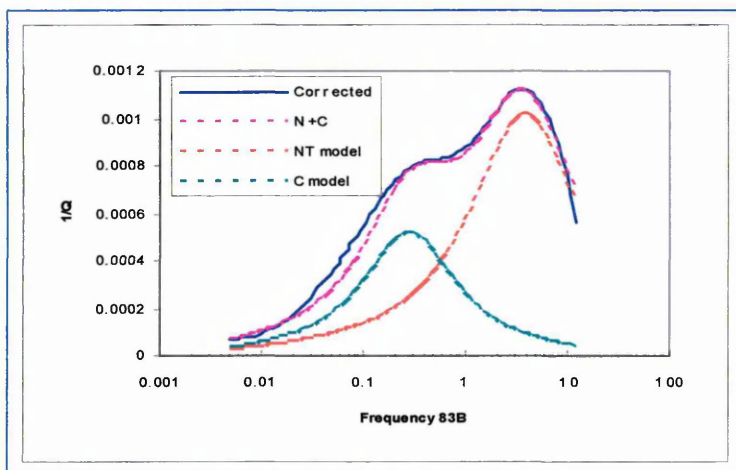


Figure 83. Internal friction analysis for VS3783B.

It can be seen from the graphs that the model in both cases, has a good correlation, and this was the same for all the steel heats. The free nitrogen

content for steel heat VS3764B was 12 ppm with 7 ppm free carbon and for VS3783B was 36 ppm N_f and 25 ppm C_f respectively. The full list of steels tested are given in Tables 5 and 6 (experimental section). The results were obtained between frequencies of 0.01 Hz and 1 Hz.

4.2. Charpy Testing Results.

The Charpy tests were carried out from -196°C to 200°C the results are shown graphically in Figure 84. Figure 85 shows the results of the impact energy absorbed, plotted against the sulphur content of the steel for all the steels tested. An ultra low interstitial free steel is shown for comparison (it is included because the free nitrogen level is zero). Figures 86 and 87 are fractographs of the fracture surfaces of VS3783B tested at -176°C and 135°C , respectively.

4.3. Fatigue Testing Results (steel heats F8104 and F8105).

The results of the fatigue tests carried out at 150°C are shown in Figure 88 as a da/dN v ΔK plot. Figure 89 is a da/dN v ΔK plot of the measured striation spacing on the SEM fracture surfaces. The data was obtained by measuring the striation width, and dividing by number of striations, to obtain an average growth rate in that region. The SEM photographs were taken in pairs so that the ΔK levels for each steel heat were the same for each steel heat, or as close as possible. Figure 90 is a photograph plan view of two half sections on test termination, the top section is F8105 and the bottom section is F8104. Figure 91 is an oblique view of specimen F8105 prior to breaking open. Figures 92 to 98 are SEM photographs of the fracture surfaces of both the steel heats. The white lines with arrowheads on them on Figures 92 to 98 show the regions where the data was obtained for Figure 89 and also indicate the direction of fatigue crack propagation.

4.4. Strain Rate Sensitivity (m) Results.

The results of the strain rate sensitivity tests are shown graphically in Figure 99. The tabulated results are given in Table 10. The corresponding colours indicate, blue the strain at which it was measured at, black, the strain rate sensitivity, and red, the strain rate differential at which m was determined.

Initially the strain rates to be used were $2.7 \times 10^{-3} \text{ sec}^{-1}$ and $2.7 \times 10^{-6} \text{ sec}^{-1}$, but $2.7 \times 10^{-3} \text{ sec}^{-1}$ was found to be too fast, to allow monitoring of the computer screen to determine the next strain rate change. So strain rate differentials of 10 and 100 were used, instead of 1000. It could not be ascertained as to what was actually happening at the faster strain rate, the machine response was instant not allowing for the transient in the determination of m .

In the first test done on specimen F5111B this was quickly realised after the second change after the first serrated region in Figure 101. So just after the $2.7 \times 10^{-3} \text{ sec}^{-1}$ rate change was made, the decision was made to change back to the lower rate of $2.7 \times 10^{-6} \text{ sec}^{-1}$ and $2.7 \times 10^{-4} \text{ sec}^{-1}$.

Figures 100 and 101 show the actual stress strain curve for F8105 at 150° and 100° C respectively, and were used for calculation purposes. The dotted lines indicate where the values were taken from.

4.5. Air Tensile Testing Results.

4.5.1. For steel heats VS3764A and VS3764B.

The results of the slow strain rate tests done in air from 20°C to 350°C are tabulated in Table 11. Figure 102 shows the stress vs strain curves for VS 3764A and VS 3764B. Figure 103 shows the charted load vs extension curves for both the steel heats for the specimens which showed serrated flow and Luders extension. Figure 104 shows the increase in UTS vs temperature for both the steel heats. Figure 105 shows the reduction in area vs temperature for the heats. Figure 106 a to e are photographs of tensile specimens from 20°C to 250°C . Figure 107 a to h shows photographs and optical fractographs of two tensile specimens tested in the transverse direction at 200°C VS3764A (photos a, c, e, g) and VS3764 B (photos b, d, f, h). Figure 108 shows a collage of SEM fractographs of VS3764 A (photos A, B, C, D) and VS3764B (photos A1, B1, C1, D1) at magnifications of 80, 500, 1000 and 2000 respectively tested at room temperature. Figure 109 shows a collage of SEM fractographs of VS3764A (photos E, F, G, H) and VS3764B (photos E1, F1, G1, E1) at magnifications of 80, 500, 1000, and 2000 respectively tested at 200°C . Figure 110 to 113 are enlarged views of both collages (x 2000).

Figure 108A shows a white rectangle, this indicates the position where all the SEM fractographs were taken, on each specimen or as close to that region as possible on the other specimens.

4.5.2. For steel heats VS3783A and VS3783B.

The results of the slow strain rate tests done in air are given in Table 12 for both the steel heats. Figure 114 and Figure 114A shows the stress vs strain curve for the heats. Figure 115 shows the increase in UTS vs temperature for all the VS series of steel heats (64A, 64B, 83A, and 83B). Figure 116 shows the reduction in area vs temperature for all the VS series. Figure 117 shows the engineering elongation to fracture vs free nitrogen content for all the VS series. Figure 118 shows the true strain to fracture vs free nitrogen content for VS3764A and VS3783A. Figure 119 shows the true strain to fracture vs sulphur content for all the VS series. Figure 120 shows the true strain to fracture vs volume fraction for all the VS series. Figure 121 shows the true strain to fracture vs square root of the volume fraction for all the VS series. Figure 122 Shows the elongation to fracture vs temperature for all the VS series.

VS3764A, VS3764B, VS3783A were tested at a strain rate of $2 \times 10^{-6} \text{ s}^{-1}$. VS3783B was tested at a strain rate of $2.67 \times 10^{-6} \text{ sec}^{-1}$. The test temperatures for all the steel heats were the same, except for VS3783B which was tested at 225°C, whereas the other three VS steel heats 64A, 64B, and 83A were tested at 200°C and 250°C. Initially VS3783B was to be tested at these temperatures but due to a specimen breaking prematurely during testing, at 200°C. A decision was made to take an average of both temperatures and test at 225°C. A comparison between the steel heats is 225°C for VS3783B and 200°C for VS3764A. Table 13 is a comparison of the main mechanical properties for all the VS series of steel heats taken from Tables 11 and 12. Text in red are the true mechanical properties as opposed to engineering mechanical properties. Text in purple means that the test may have been influenced by the Mayes machine.

4.5.3. For steel heats F8104, F8105, and F8106.

The results of the slow strain rate tests done in air are given in Table 14 for the steel heats F8104, F8105 and F8106. Figure 123 is a collage of the charted load vs extension curves for the heats showing the specimens which had maximum serration height and maximum Luders deformation. Figure 124 shows the engineering elongation to fracture vs free nitrogen for the heats. Figure 125 shows the true strain to fracture vs free nitrogen for the heats. Figure 126 shows the engineering elongation to UTS vs temperature, and to fracture for the heats.

4.5.4. For steel heat Interstitial Free Steel.

The results from the slow strain rate tests done in air are shown graphically in Figure 127 (done at a strain rate of $2 \times 10^{-6} \text{ sec}^{-1}$).

Figure 128 shows the true strain to fracture vs temperature for all the steels tested. Figure 129 shows the increase in UTS vs temperature for all the steels tested. Figure 130 shows the reduction in area vs temperature for all the steels tested.

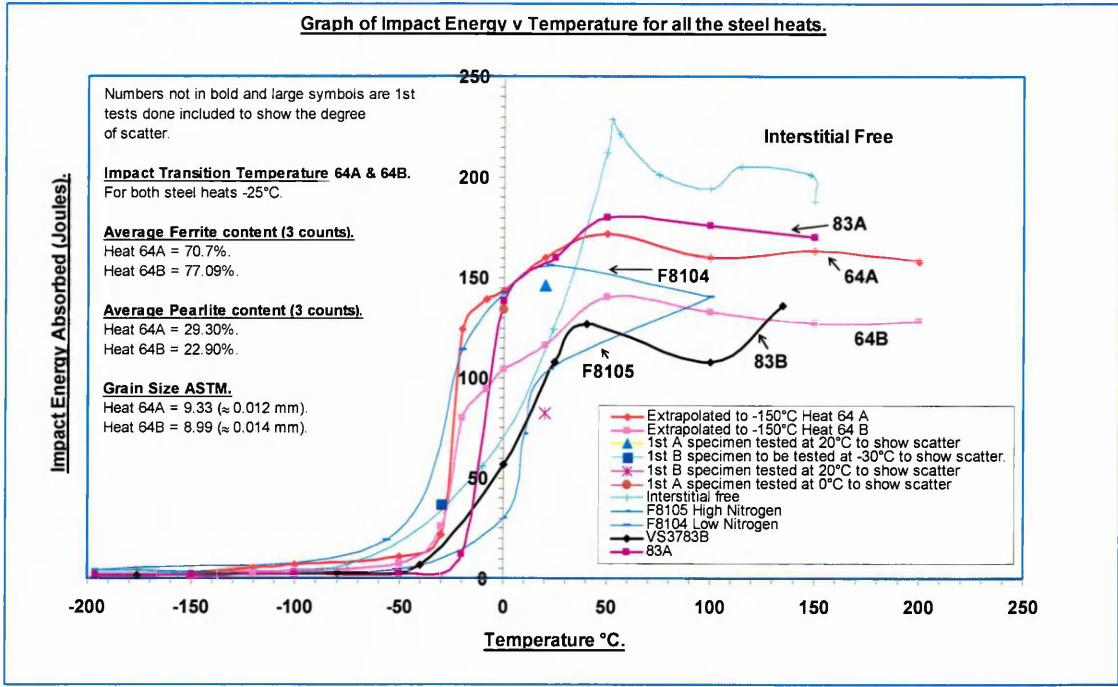


Figure 84. Graph of Impact Energy absorbed vs Temperature for all the steel heats.

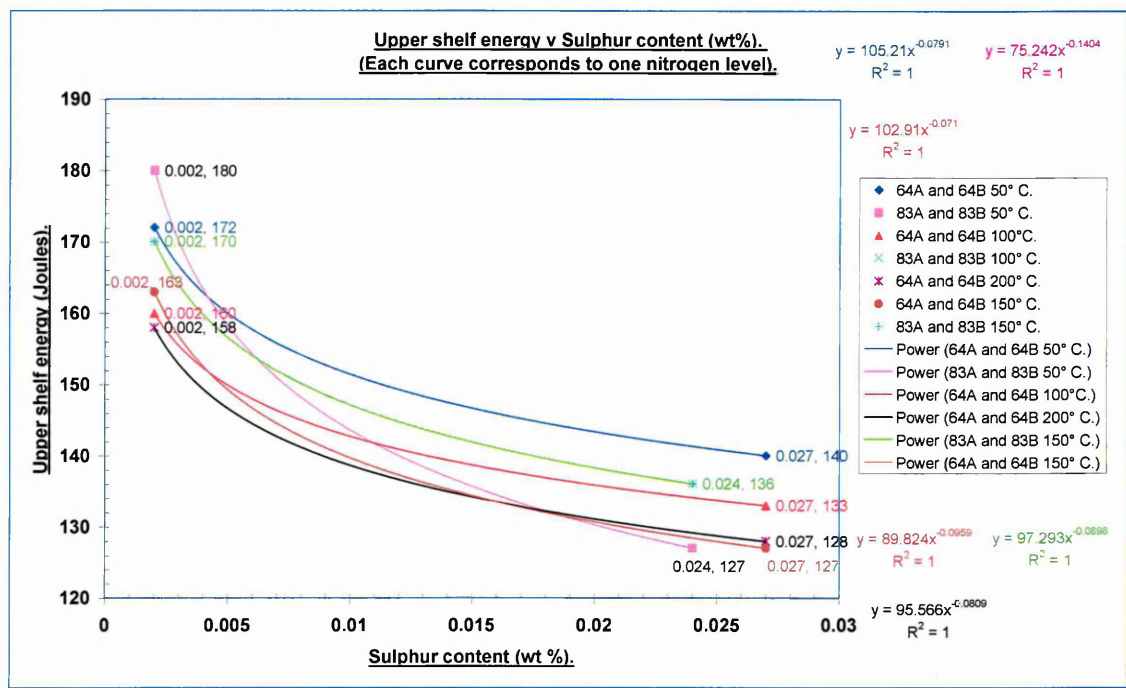


Figure 85. Graph of Impact Energy absorbed vs Sulphur content for all VS series of steel heats.

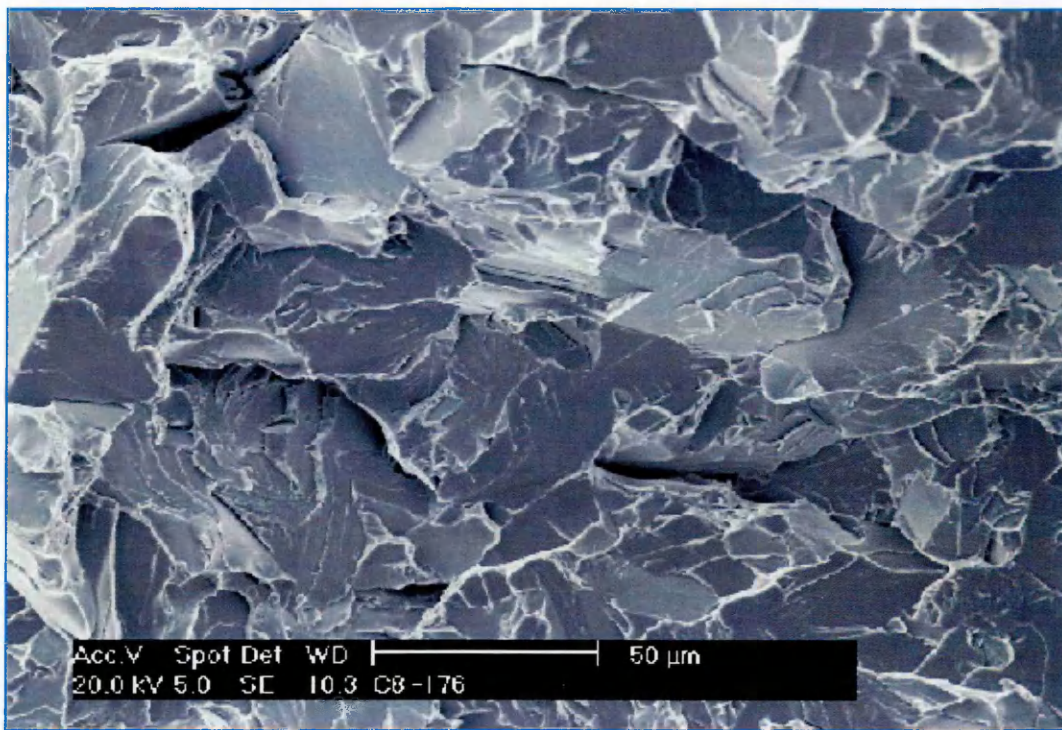


Figure 86. Fractograph of Charpy specimen VS3783B temperature -176°C. (cleavage facets clearly visible).

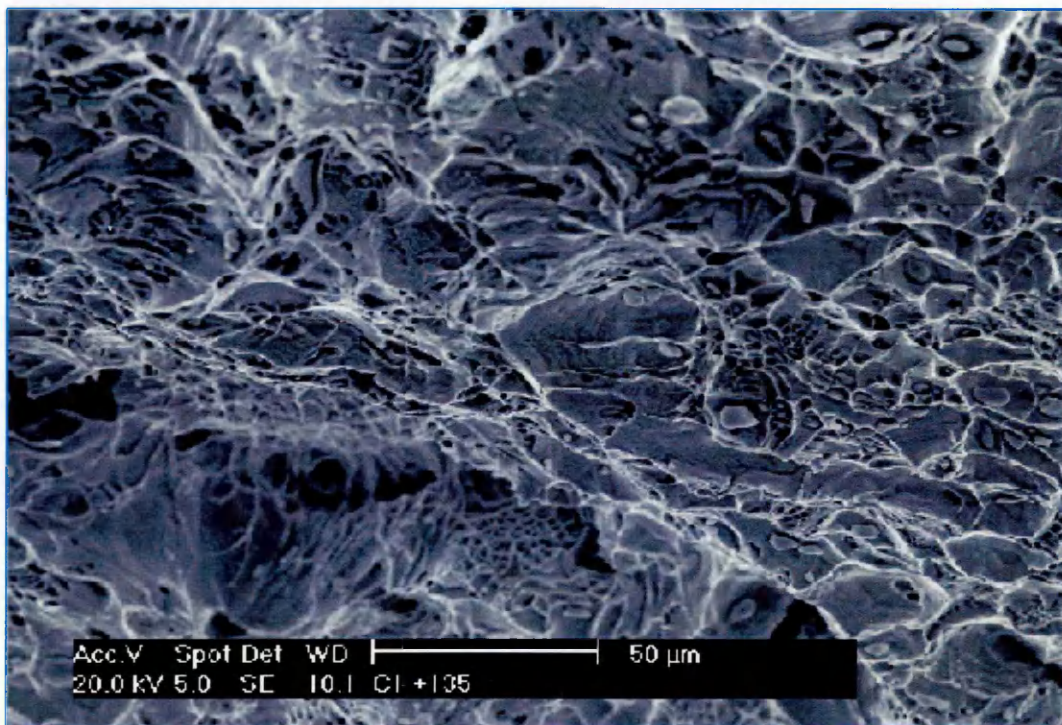


Figure 87. Fractograph of Charpy specimen VS3783B temperature 135°C. (showing microvoid coalescence).

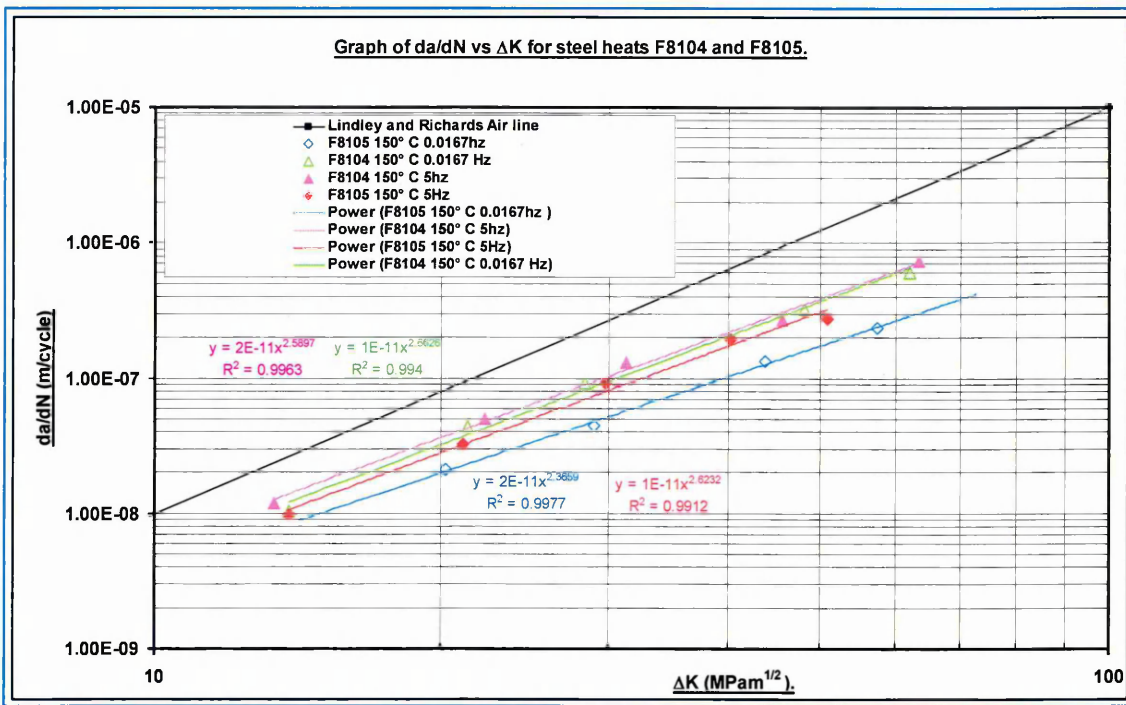


Figure 88. Graph of da/dN vs ΔK for steel heats F8104 and F8105 (see Appendix 5).

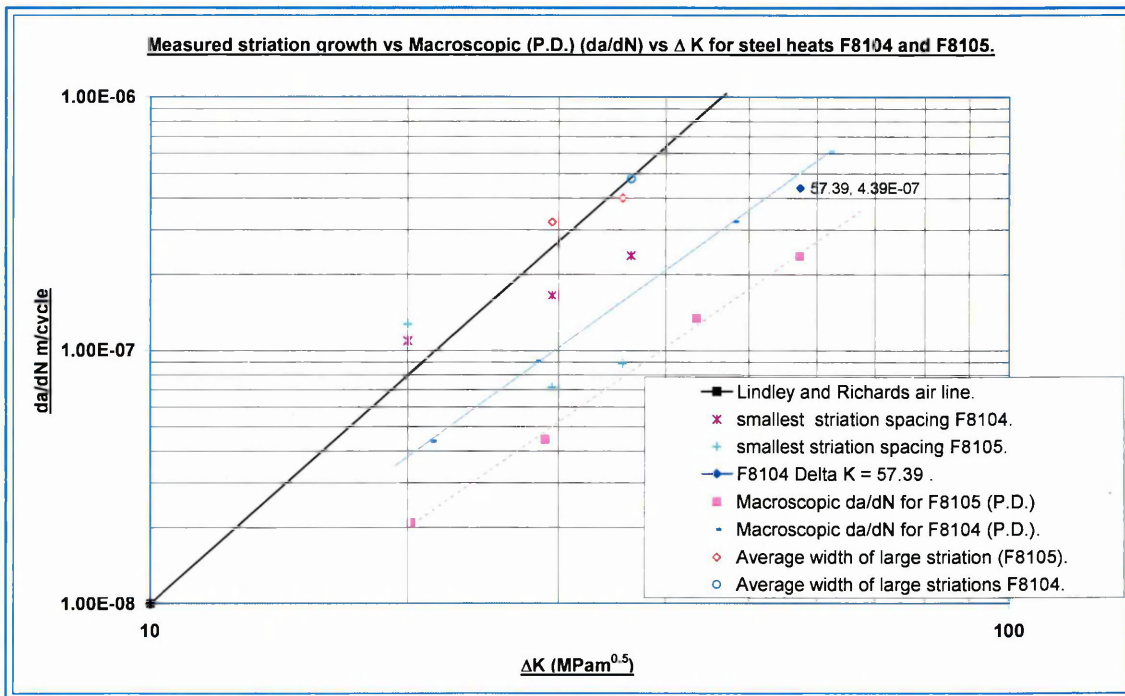


Figure 89. Measured striation growth vs Macroscopic (P.D.) da/dN for steel heats F8104 and F8105 at ΔK 's of 20, 29.48, 35.63, 36.45, and 57.39 MPa \sqrt{m} .

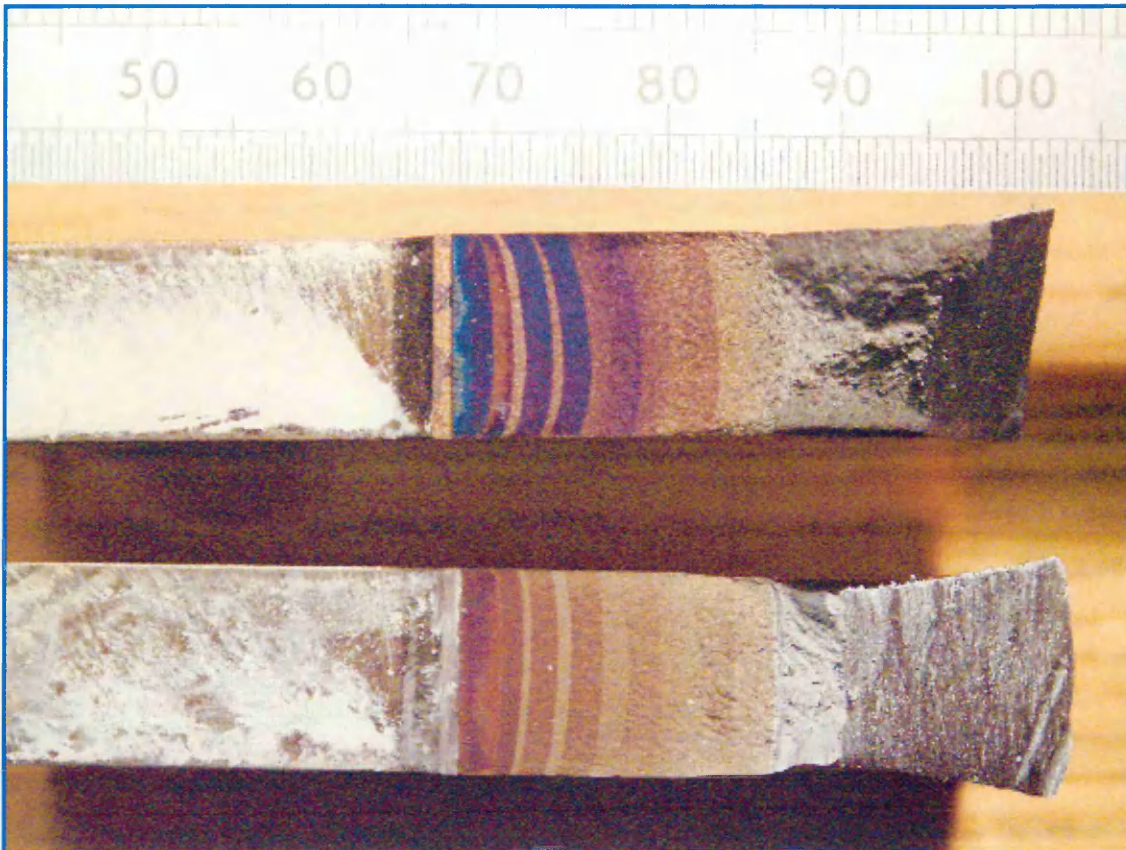


Figure 90. Plan view of F8104 and F8105 after the test.

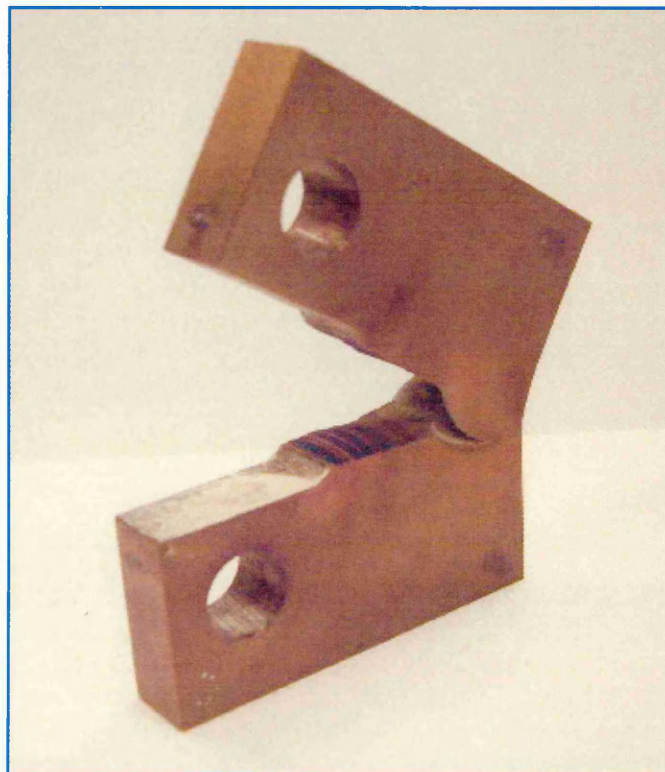


Figure 91. Photograph of specimen F8105 after test. (before being broken open).

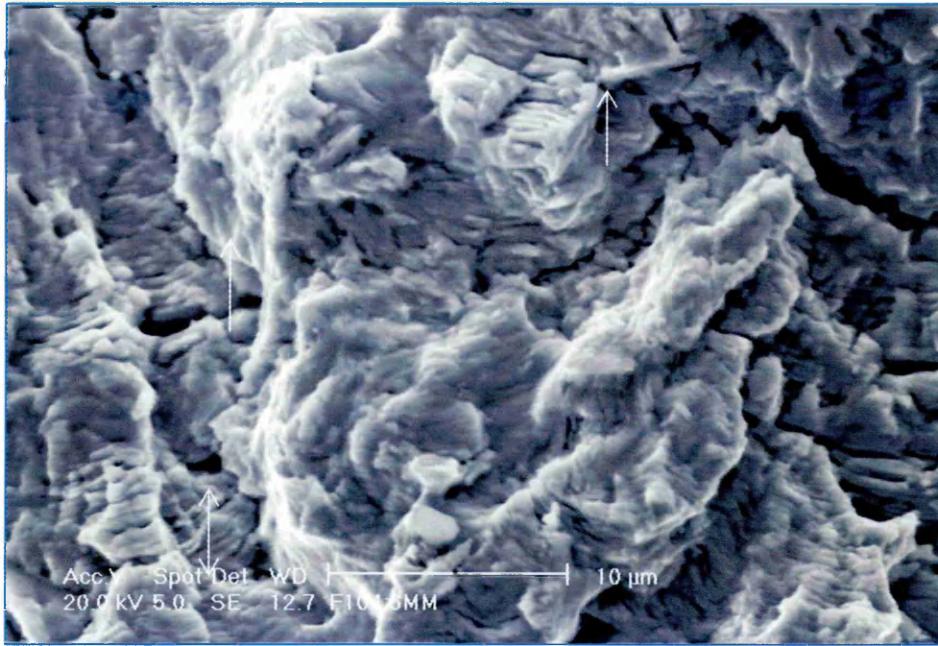


Figure 92. SEM photograph of specimen F8104 at 22 mm $\Delta K = 20 \text{ MPa}\sqrt{\text{m}}$.

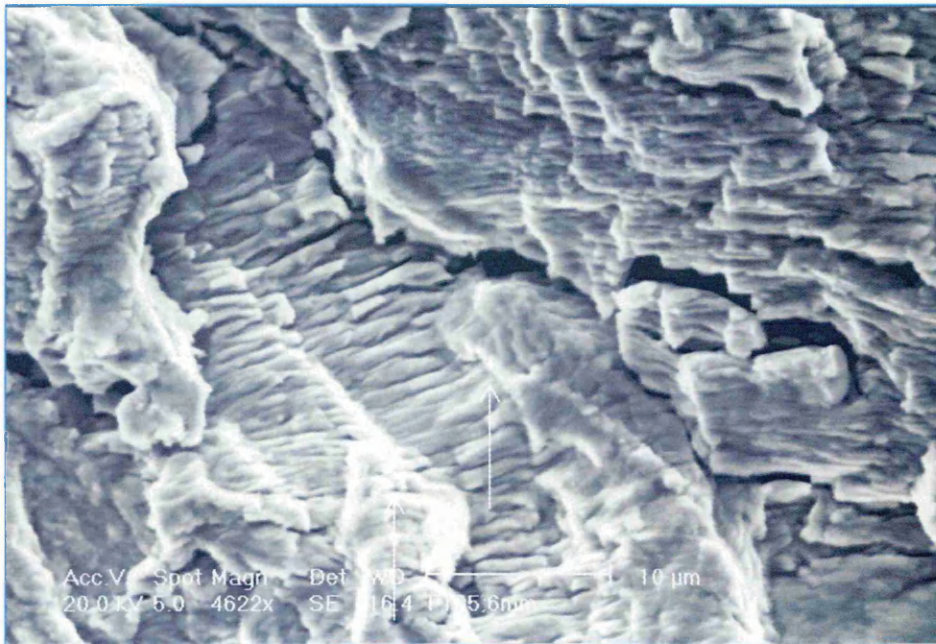


Figure 93. SEM photograph of specimen F8105 at 22 mm $\Delta K = 20 \text{ MPa}\sqrt{\text{m}}$.

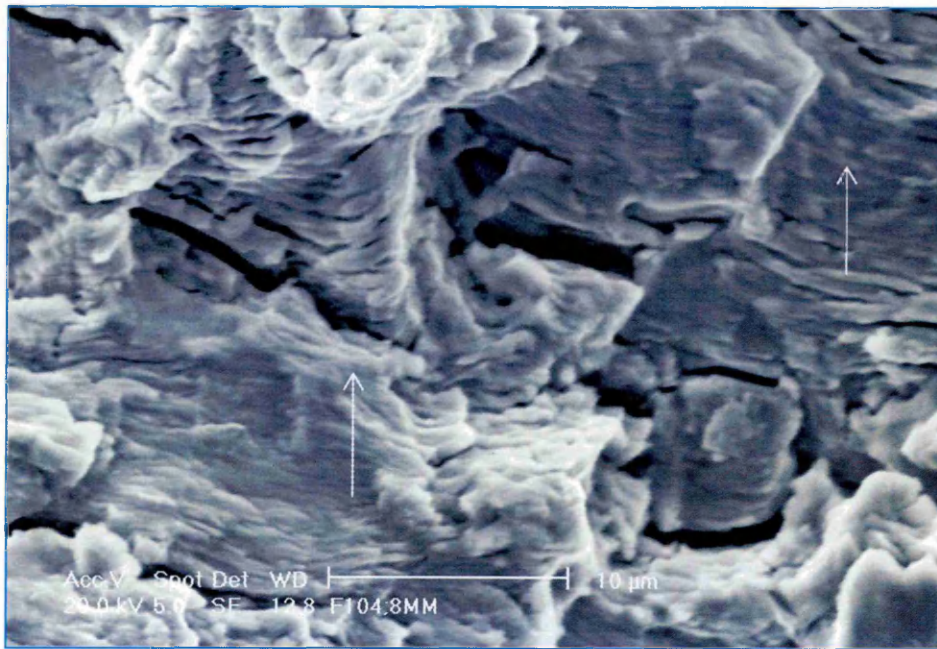


Figure 94. SEM photograph of specimen F8104 25 mm $\Delta K = 29.48 \text{ MPa}\sqrt{\text{m}}$.

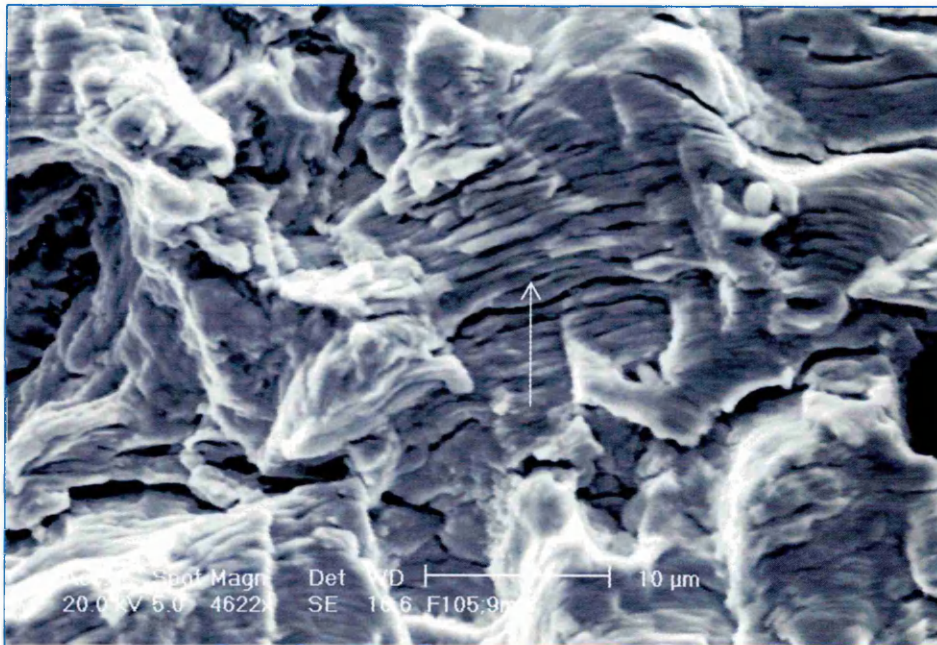


Figure 95. SEM photograph of specimen F8105 25 mm $\Delta K = 29.48 \text{ MPa}\sqrt{\text{m}}$.

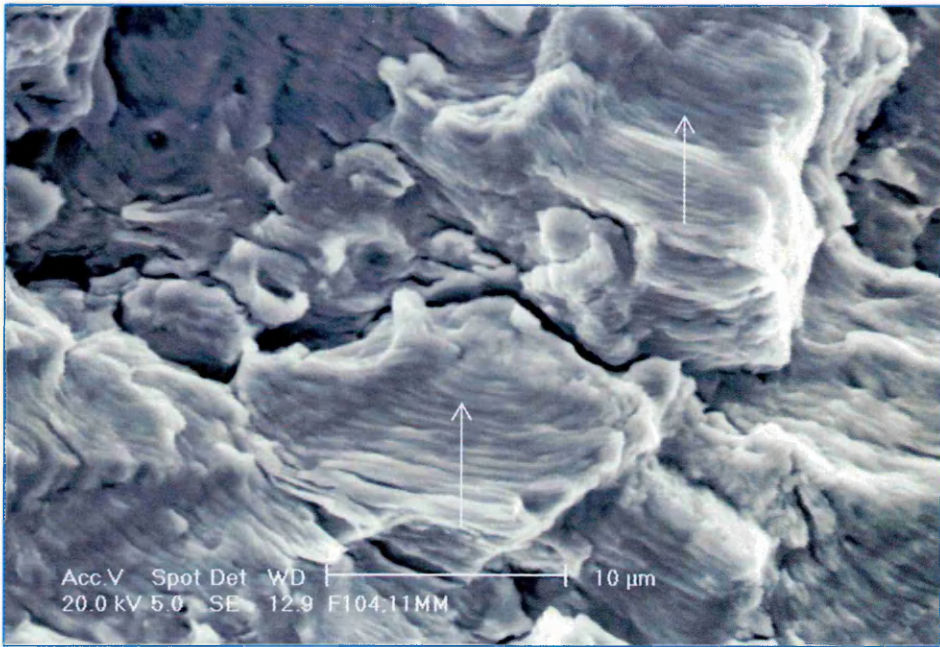


Figure 96. SEM photograph of specimen F8104 27 mm $\Delta K = 36.45 \text{ MPa}\sqrt{\text{m}}$.

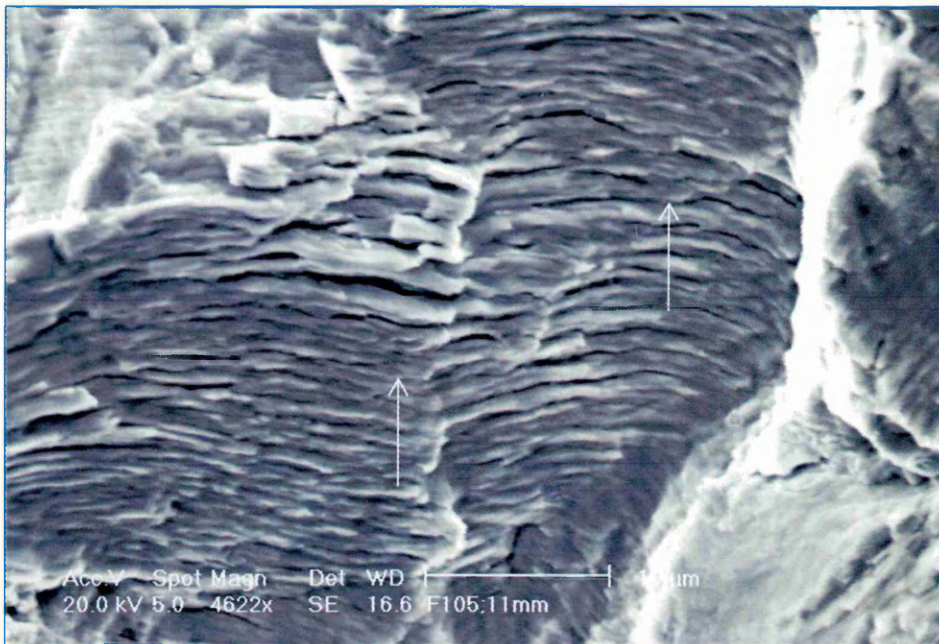


Figure 97. SEM photograph of specimen F8105 27 mm $\Delta K = 35.63 \text{ MPa}\sqrt{\text{m}}$.

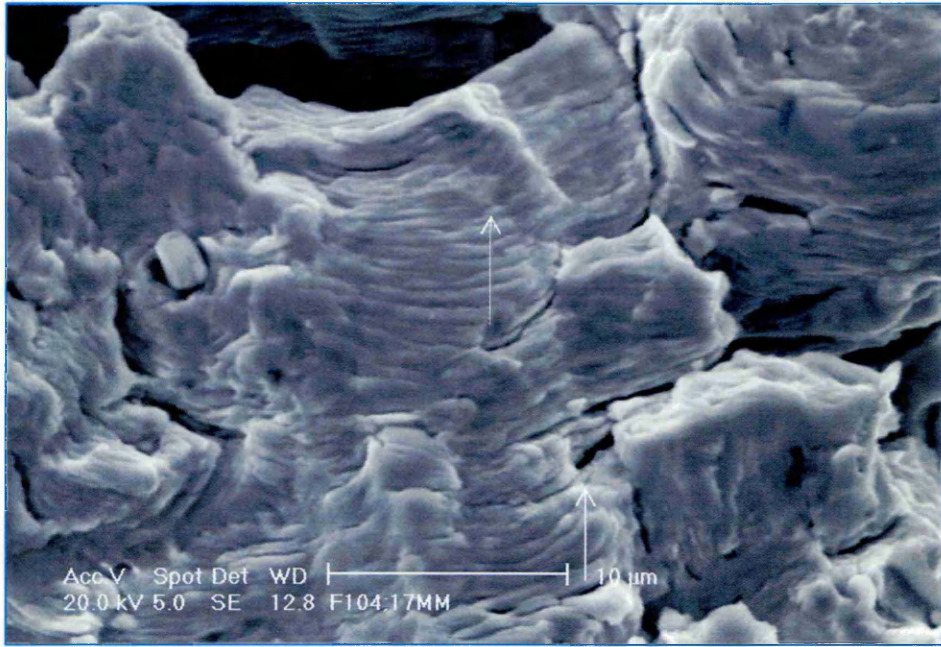


Figure 98. SEM photograph of specimen F 8104 33 mm $\Delta K = 57.39 \text{ MPa}\sqrt{\text{m}}$.

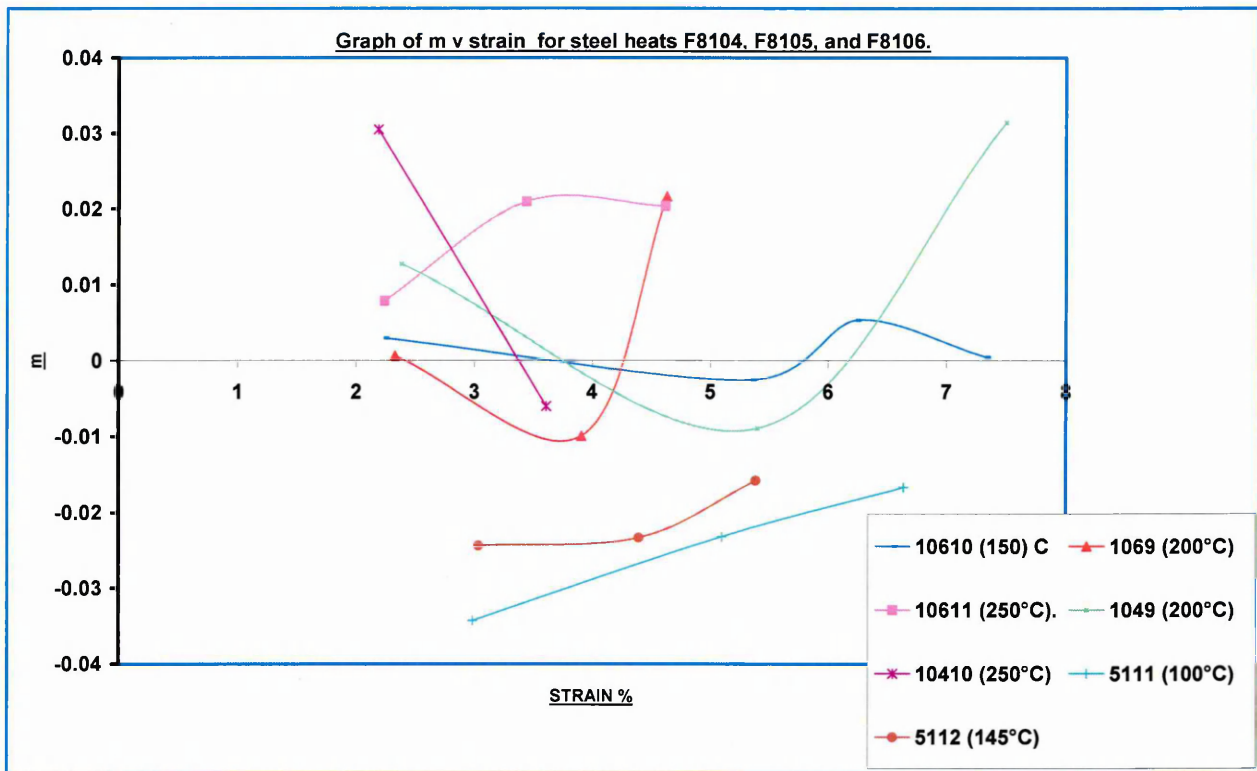


Figure 99. Graph of m vs strain for F8104 and F8105 for different temperatures.

Steel Heat.	Specimen Number.	Test Temperature °C.	m @ 2% ε or value used	m @ 4% ε or value used	m @ 6% ε or value used	m @ 8% ε or value used	Max UTS attained (MPa) what temperature and strain rate of tensile test. (°C & sec ⁻¹)	Free N ₂ (ppm)	Free C (ppm)	Total N ₂ (ppm).	Al:N ₂ ratio (wt%).
Figures in blue denote the strain at which m was measured below them in black the m value, figures in red the strain rate differential.											
F8104	104/9	200°	2.3	3.4	5.4	7.5	250°C & 2.7x 10 ⁻⁶	8	3	44	2.31
			1.1e-2	2.37e-2	-8.9E-3	3.1e-2					
			-5 to -6	-6 to -5	-3 to -5	-6 to -5					
F8104	104/10	250°	2.2	3.6	Power loss to machine.		2.7x 10 ⁻⁶	8	3	44	2.31
			3e-2	-5.9e-3	-4 to -6	Specimen broke					
F8104	104/11	150°	Power loss to machine								
F8105	5111B	100°	2.99%	5.1%	6.64%	-	150°C & 2.7x 10 ⁻⁶	54	28	130	<0.31
			-3.4e-2	-2.3e-2	-1.7e-2	-					
			-2 to -6	-6 to -2	-6 to -4	-					
F8105	5112B	145°	3.04%	4.39%	5.38%	-	2.7x 10 ⁻⁶	54	28	130	<0.31
			-2.4e-2	-2.3e-2	-1.6e-2	-					
F8105	5112A	100°	Power loss to machine								
F8106	106/9	200°	2.33%	3.77%	4.63%	-	300°C & 2.7x 10 ⁻⁶	1.45	1.25	16	6.19
			6.9e-4	-9.8e-4	2.17e-2	-					
			-5 to -6	-4 to -6	-5 to -6	-					
F8106	106/10	150°	2.48%	5.38%	6.24%	7.33%	2.7x 10 ⁻⁶	1.45	1.25	16	6.19
			3 e-3	-2.5e-3	5.38e-3	5.29e-4					
F8106	106/11	250°	2.24%	3.43%	4.617%	-	2.7x 10 ⁻⁶	1.45	1.25	16	6.19
			7.08e-2	1.98e-2	2.08e-2	-					

Table 10. Tabulated results of the strain rate sensitivity for F8104, F8105, and F8106.

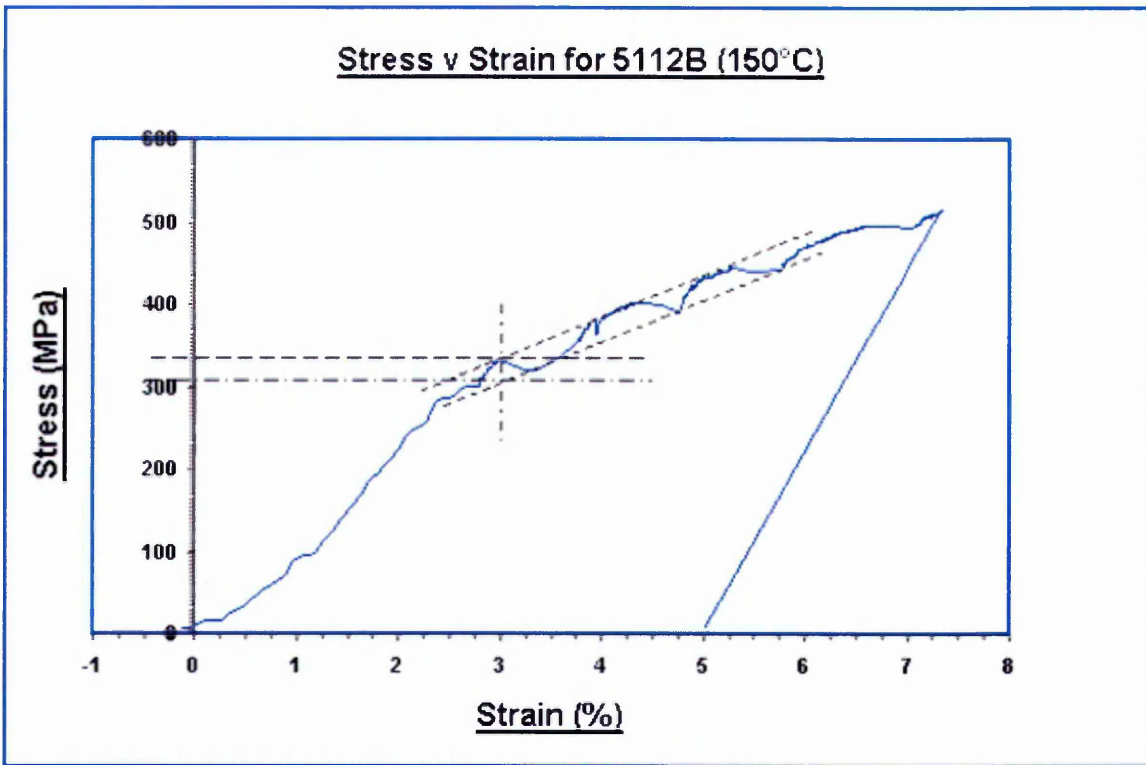


Figure 100. Strain rate jump test result for F8105 150°C (used for calculation).

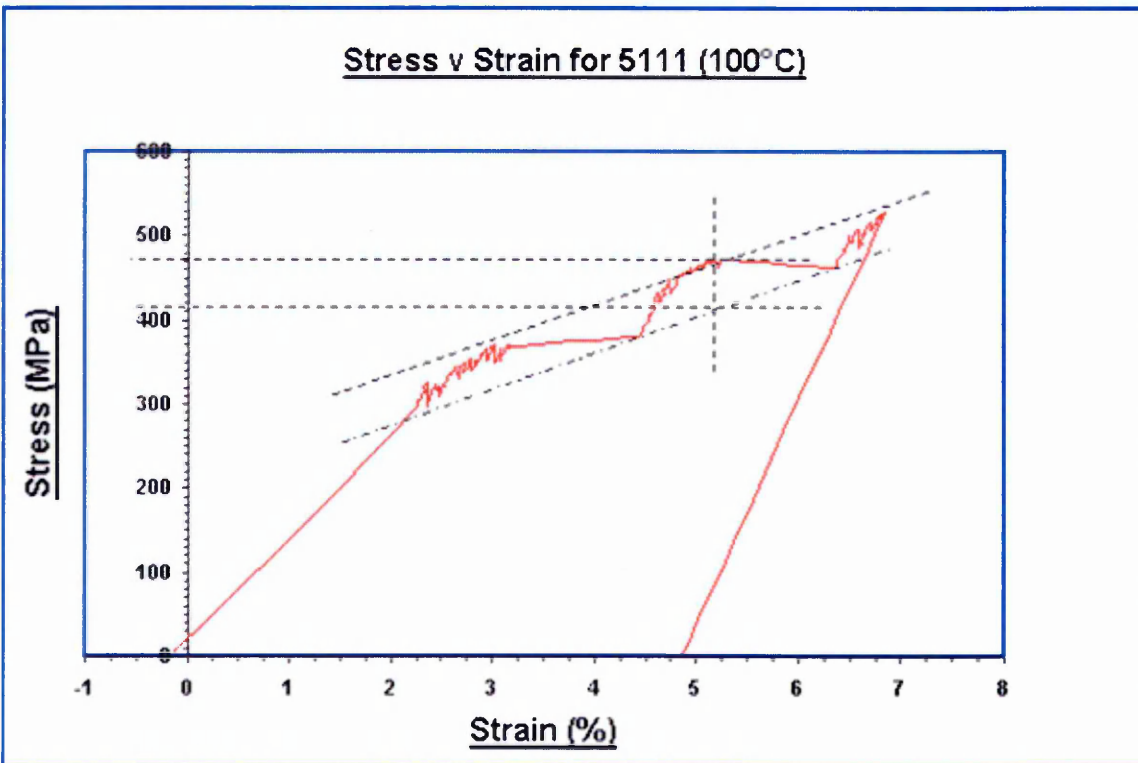


Figure 101. Strain rate jump test result for F8105 100°C (used for calculation).

Temperature (°C)	Strain Rate (sec ⁻¹)	Steel Heat	Orientation	Strength Coefficient (K), MPa	Work Hardening Exponent (n)	0.1% Proof Stress, MPa	Lower Yield Stress, MPa	Upper Yield Stress, MPa	UTS, MPa	ϵ_u % based on eng strain & True Strain based on $\ln(1+\epsilon)$, Z_u	ϵ_F % based on eng strain & True Strain based on Z_u	Reduction in Area (%) Z	Luders Strain Yes or No & %	Serration and Type	Specimen Number	True Fracture
20	2×10^{-5}	A	L	812	0.2212	N/A	-	303.6	459.7	18.4	31.2	70.10	No	None	64A1	94A
		A	T	749	0.179	-	-	-	444.9	15.5	28.3	68.39	No	None	64AT2	-
	5.7×10^{-5}	B	L	912	0.2854	298.0	-	-	452.2	15.7	26.6	66.18	No	None	64BT1	80A
		-	T	780	0.2189	-	-	-	442.1	14.4	24	1.084	62.61	No	A & B	64BT2A
50	2×10^{-5}	A	L	866	0.2419	274.5	282.0	-	466.3	15.6	24.6	65.22	No	D	64A2	92A
		B	L	-	-	-	-	-	-	-	-	-	-	-	-	-
100	2×10^{-5}	A	L	1113	0.2857	N/A	N/A	N/A	534.0	12.3	21.3	59.22	-	A & B	64A3	95A
		B	L	1049	0.244	253.8	272.6	251.9	507.7	11.8	20.4	54.94	Yes 1.7	A & B	64BT10	84A
150	2×10^{-5}	A	L	1310	0.3238	-	-	-	576.3	12.5	20.6	49.07	None	None	64A4	85A
		B	L	1049	0.2322	-	-	-	565.9	11.8	19.5	47.35	No	None	64BT5	80A
200	2×10^{-5}	A	L	1188	0.2777	-	-	-	582.9	15.4	24.7	44.97	No	None	64A5	75A
		A	T	1140	0.2522	-	-	-	583	13.7	20.8	33.54	No	None	64AT1	-
	2×10^{-5}	B	L	1268	0.2838	N/A	-	380	580.9	16.8	25.3	43.85	None	-	64BT3	77A
		B	T	1064	0.2250	-	-	-	578.0	15.5	23.2	44.15	-	-	64BT1A	-
250	2×10^{-5}	A	L	1205	0.3184	-	-	-	561.2	16.8	28.1	58.17	No	None	64A6	86A
		B	L	1177	0.3006	-	-	-	553.7	16.6	26.2	55.13	No	B	64BT2	83A
300	2×10^{-5}	A	L	1121	0.3009	N/A	-	-	542.7	16.0	27.7	62.42	No	None	64A7	87A
		B	L	1126	0.2957	-	-	-	538.7	13.8	26.5	60.22	No	-	64BT4	85A
350	2×10^{-5}	A	L	1091	0.3325	N/A	-	-	475.0	13.8	26.5	67.44	No	None	64A8	81A
		B	L	1013	0.2837	-	-	-	486.0	13.1	26.3	64.91	No	None	64BT7	75A

Table 11. Tensile testing results for steel heats VS3764A and VS3764B (the text in red is the true stress and true strains).

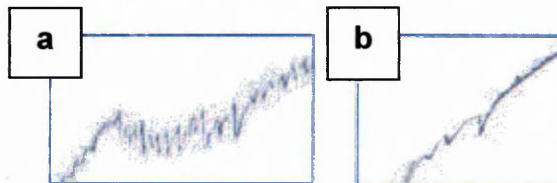
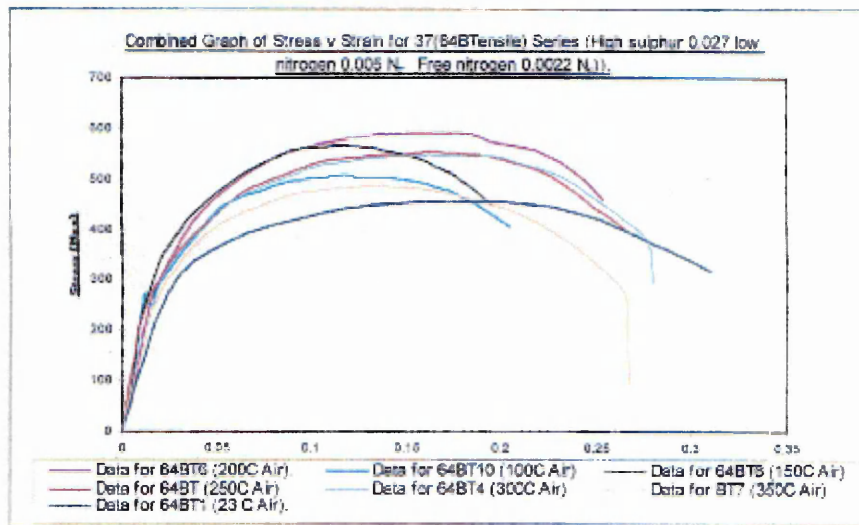
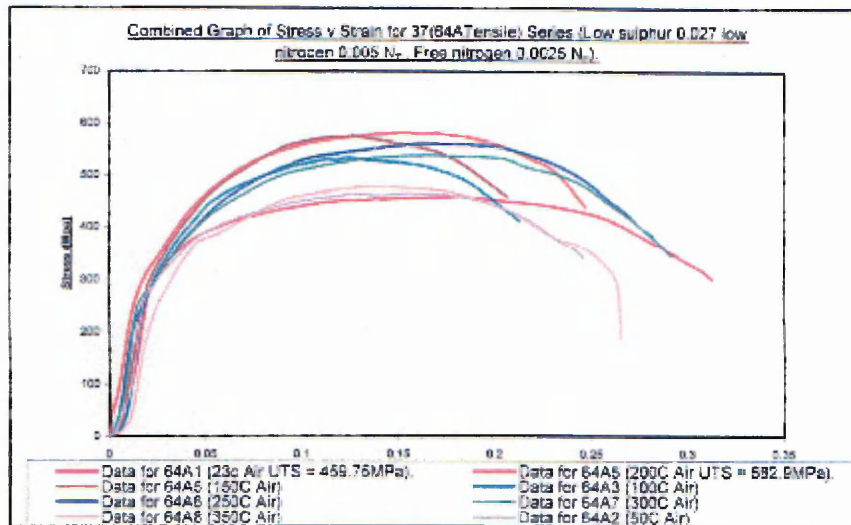


Figure 102. Stress vs Strain results for VS3764A and VS3764B.

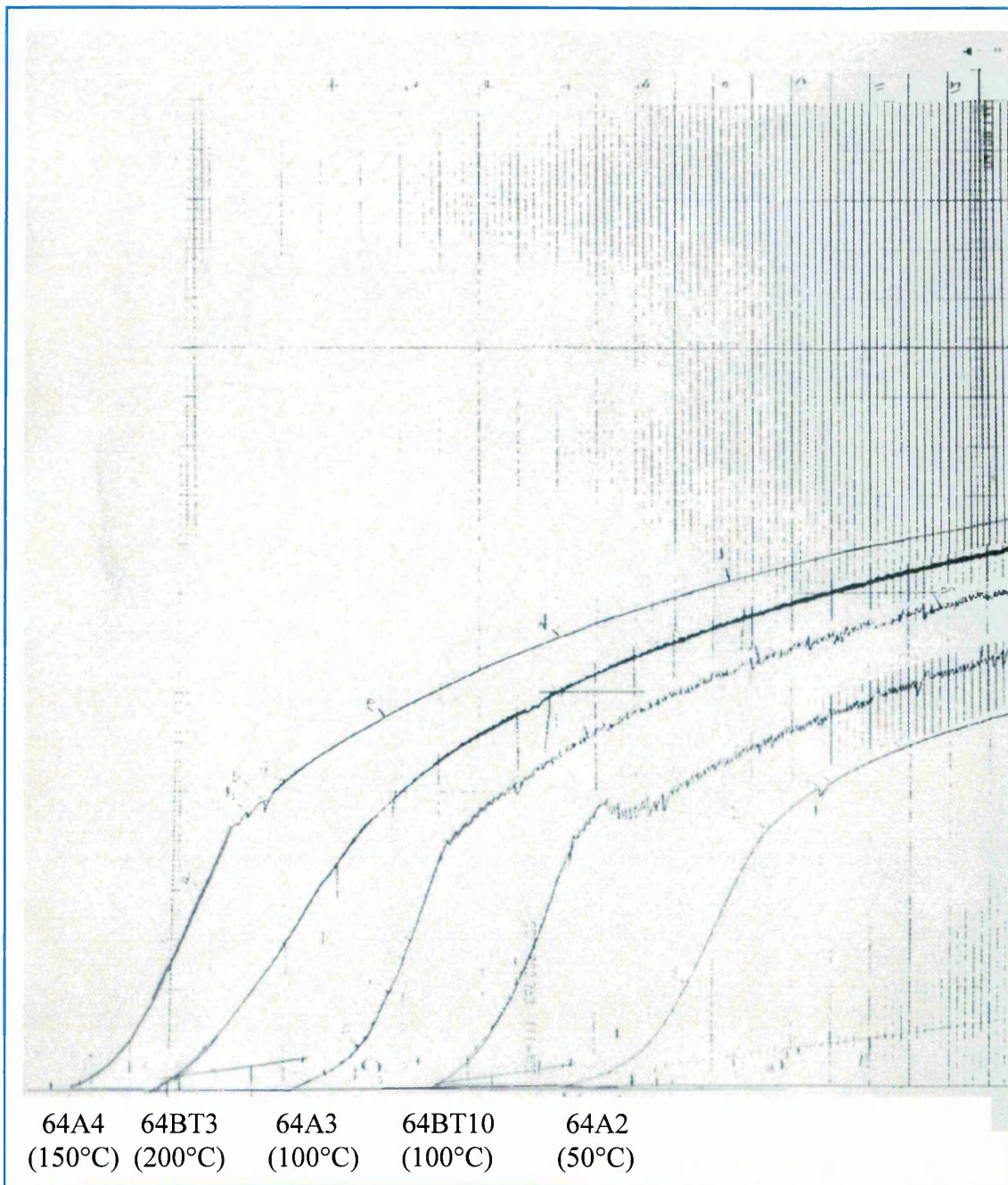


Figure 103. Charted Load vs Extension curves for VS3764A and VS3764B for the specimens which showed serrated flow.

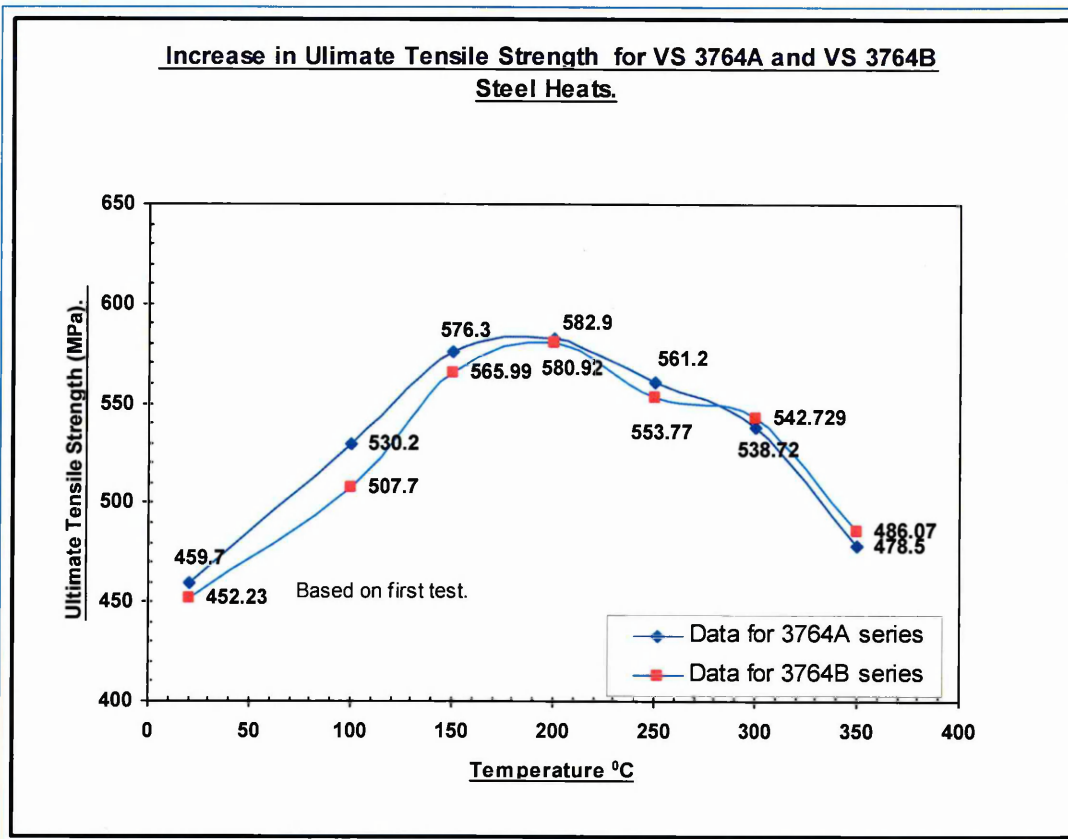


Figure 104. Increase in UTS vs Temperature for VS3764A and VS3764B.

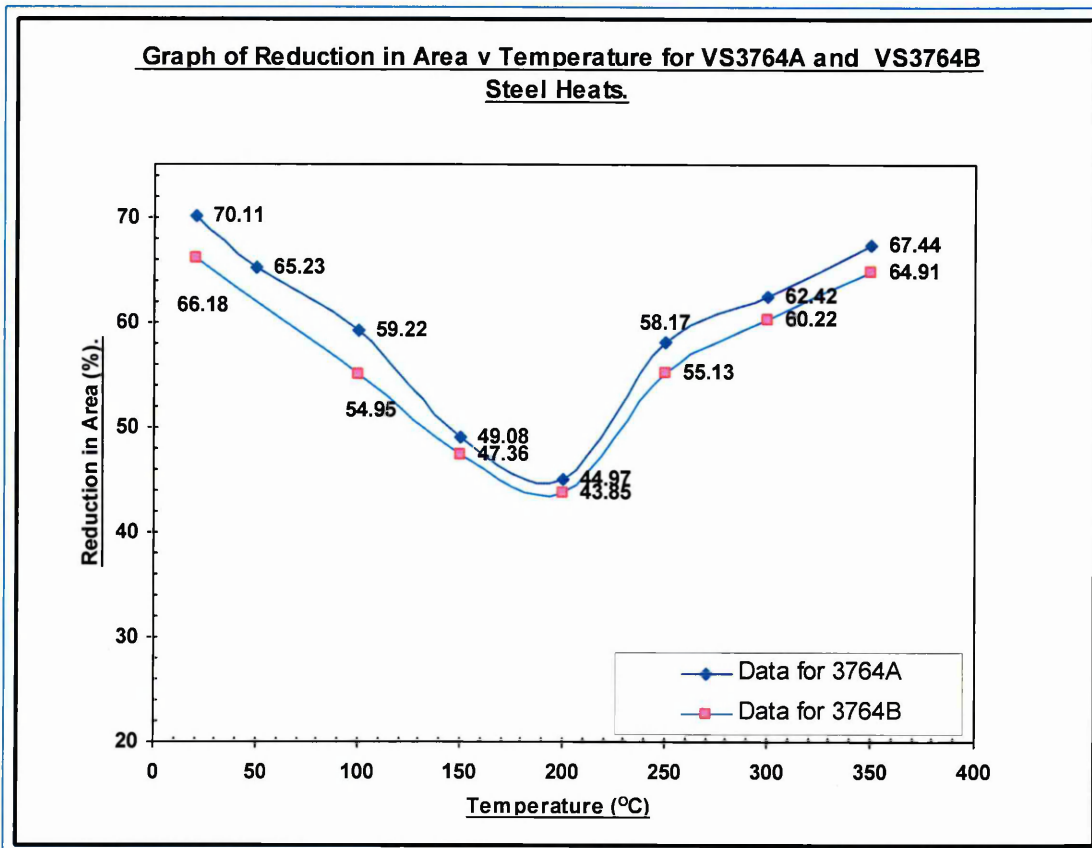
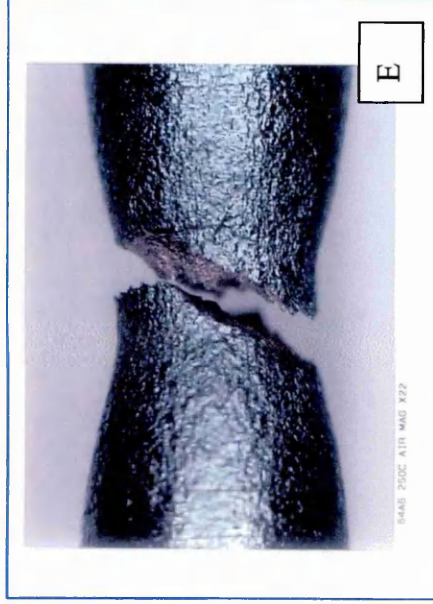
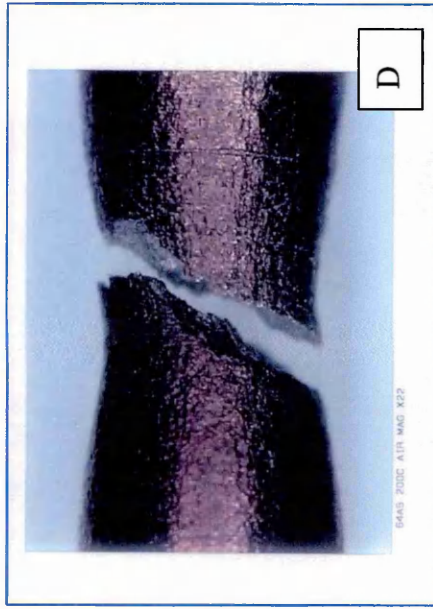
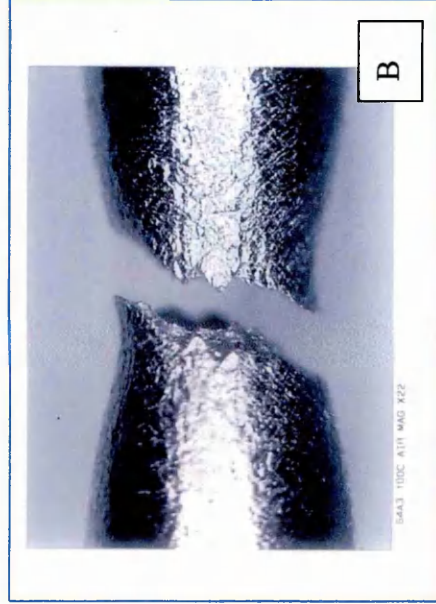
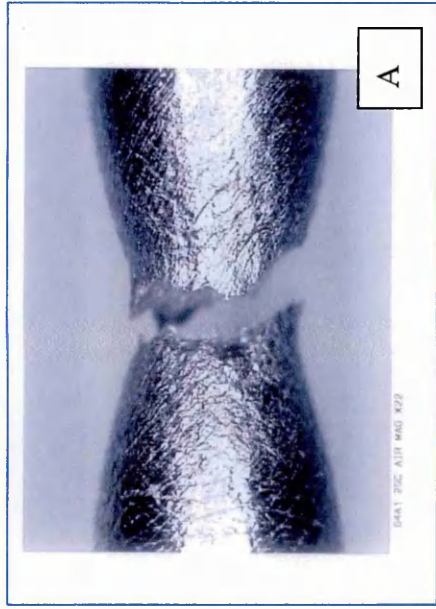


Figure 105. Reduction in Area (Z) vs Temperature for VS3764 and VS3764B.



A = 20° C
B = 100° C
C = 150° C
D = 200° C
E = 250° C

Figure 106. Figures show the results of five tensile tests over the range 20°C to 250°C at a strain rate of $2 \times 10^{-6} \text{ sec}^{-1}$. Here the fracture mode is more evident. i.e. from cup and cone fracture at 20°C to the characteristic shear fracture in the blue brittle range. Maximum in UTS attained at 200°C.

Figure 107. Transverse and Longitudinal Results for VS3764 A at 200° C.

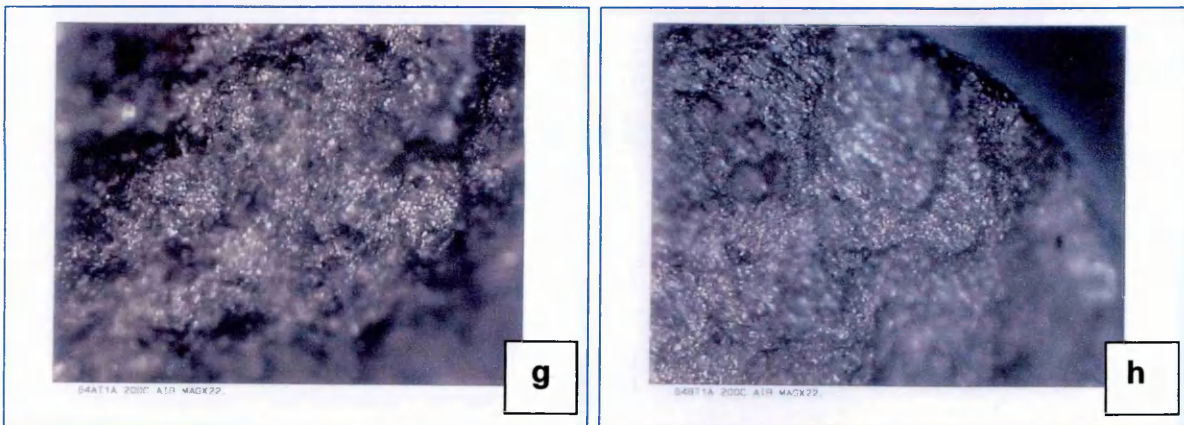
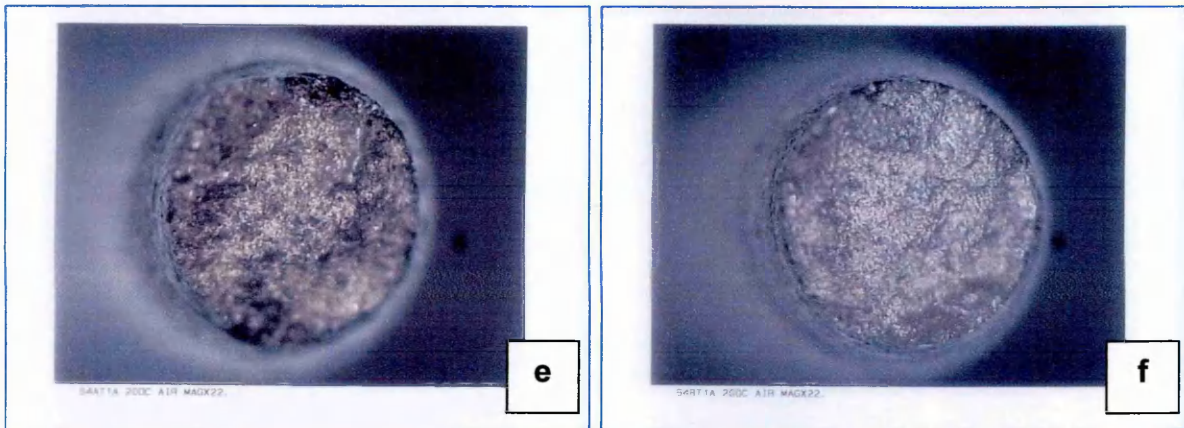
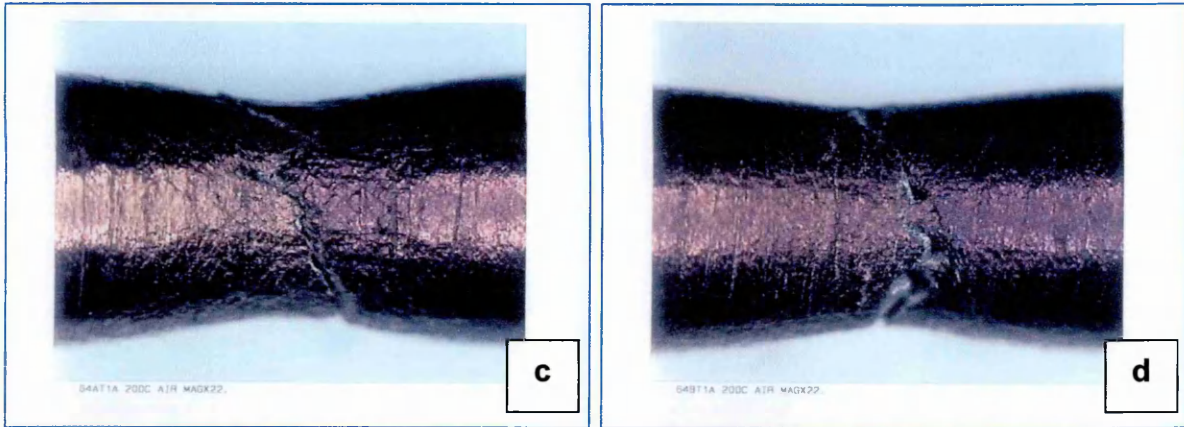
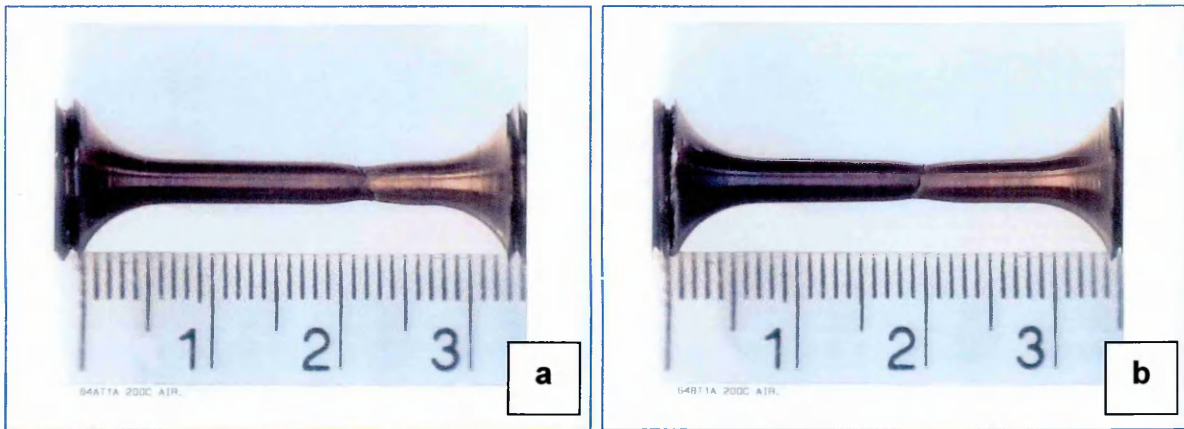
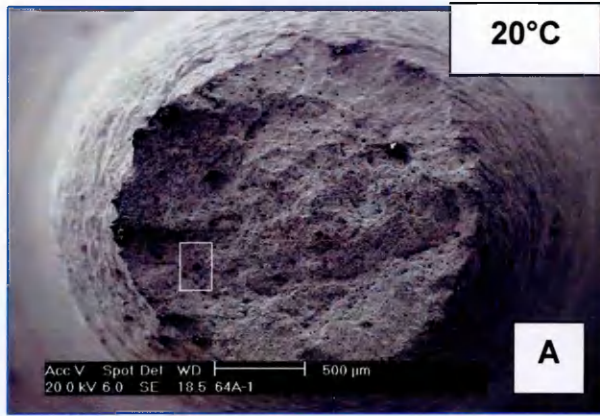
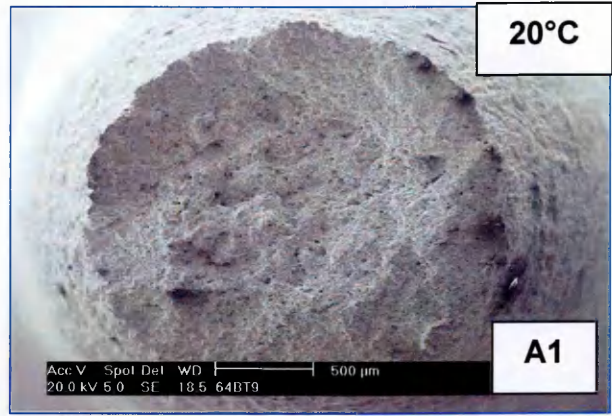


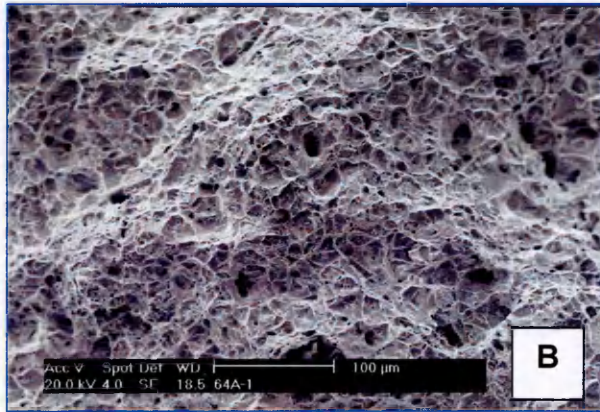
Figure 108. Comparison of SEM Photographs of VS3764A & VS3764B 20° C.



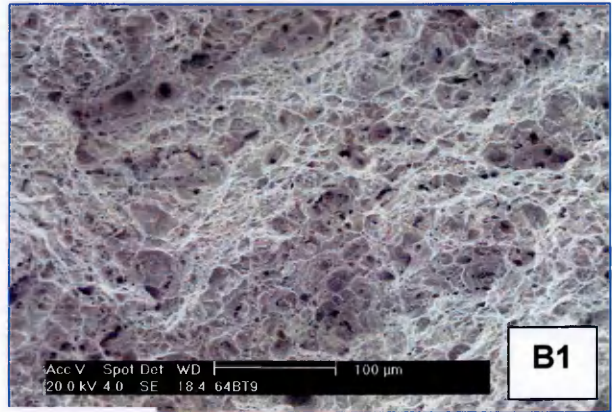
x 75



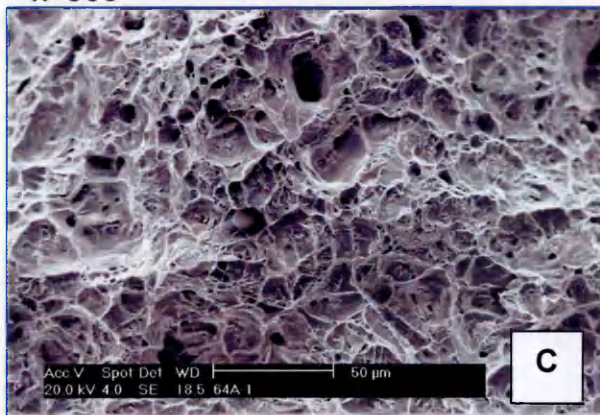
x 80



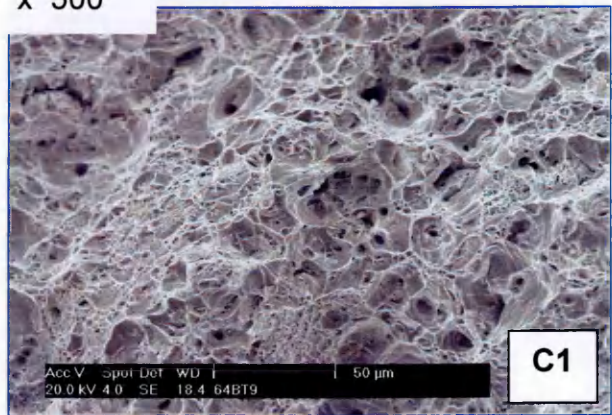
x 500



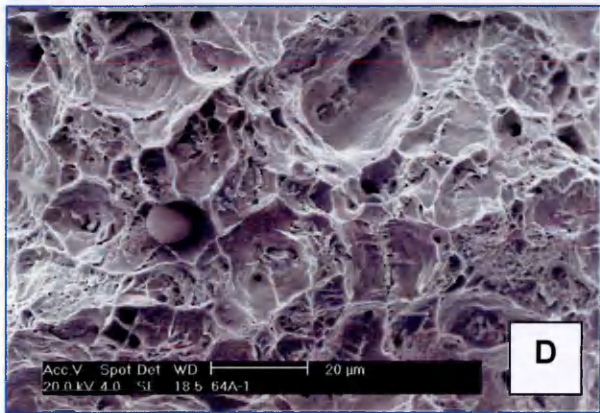
x 500



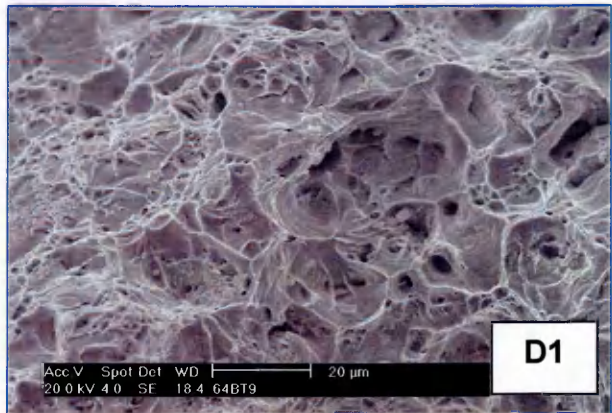
x 1000



x 1000

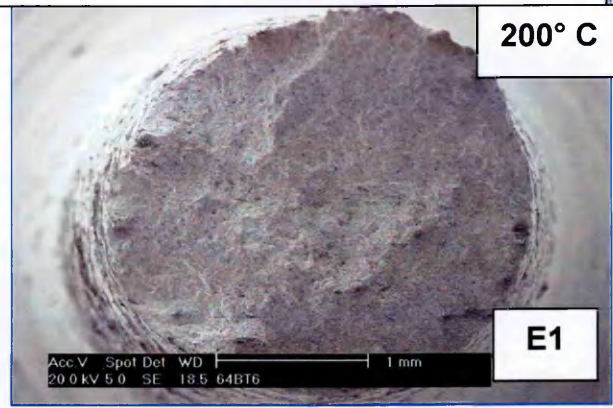


x 2000



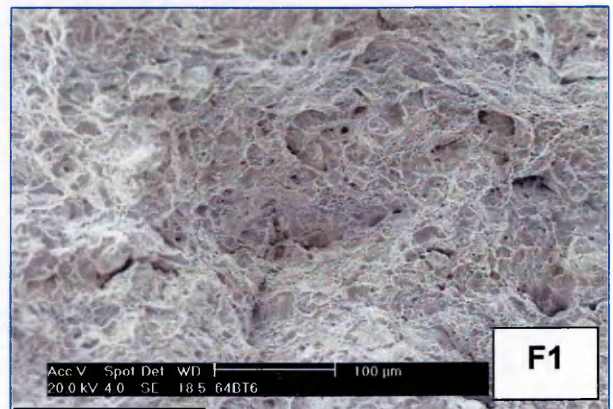
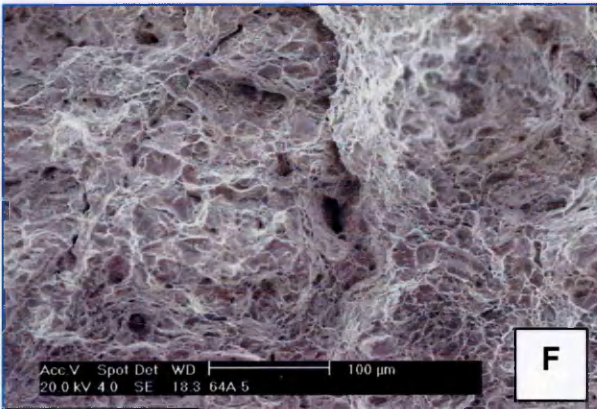
x 2000

Figure 109. Comparison of SEM Photographs of VS3764A & VS3764B at 200°C.



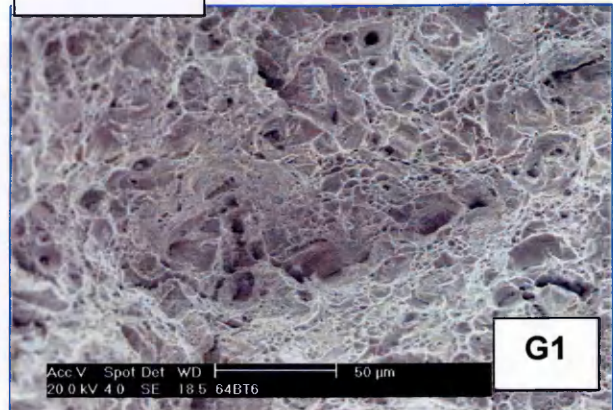
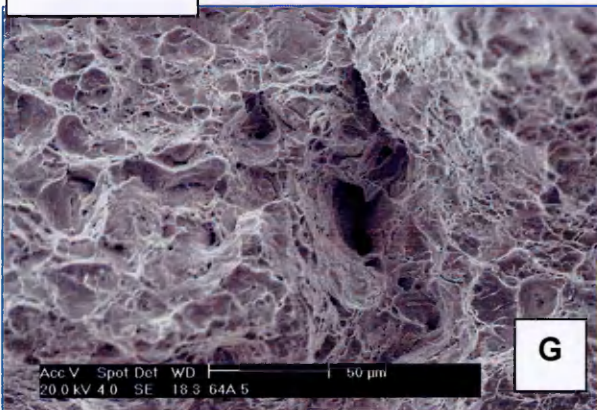
x 63

x 63



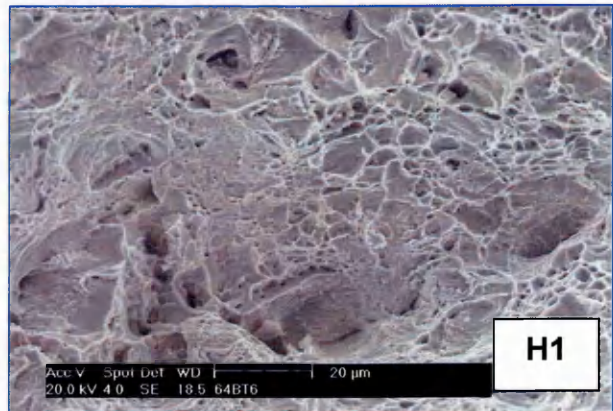
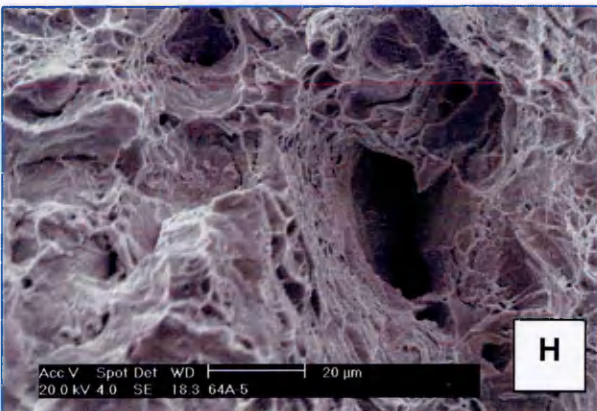
X 500

X 500



x 1000

x 1000



x 2000

x 2000

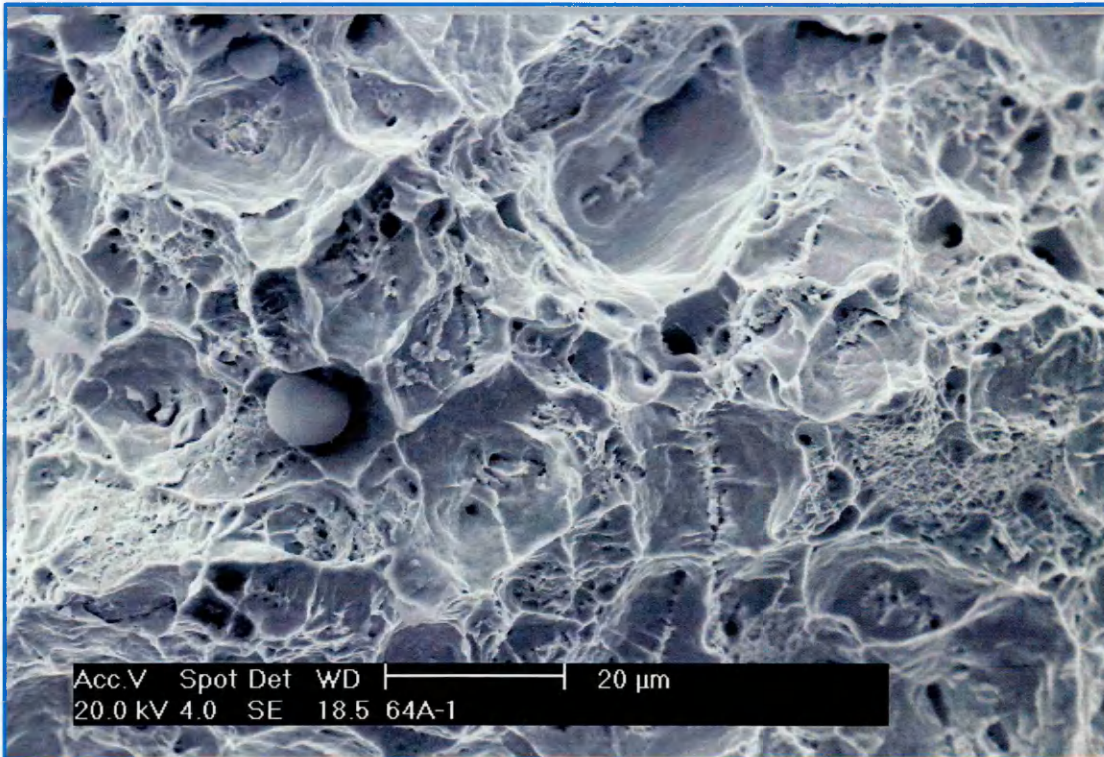


Figure 110. Figure 108 D x 2000. (Clearly visible type 1 MnS inclusion).

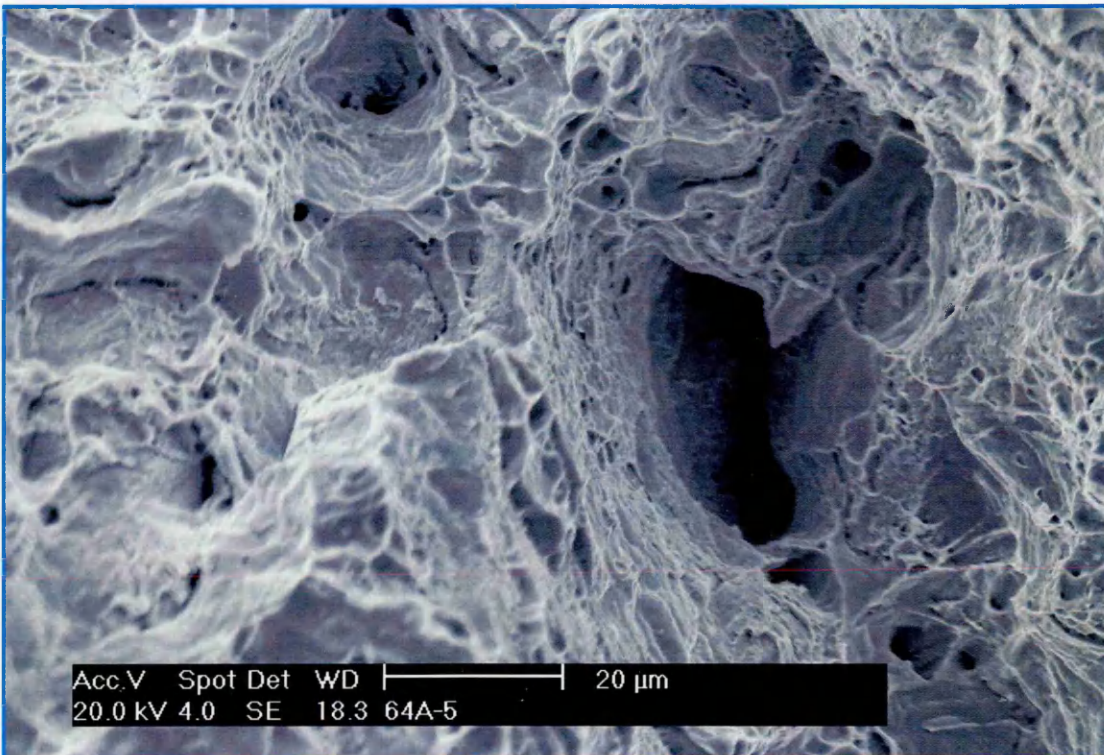


Figure 111. Figure 109 H x 2000.

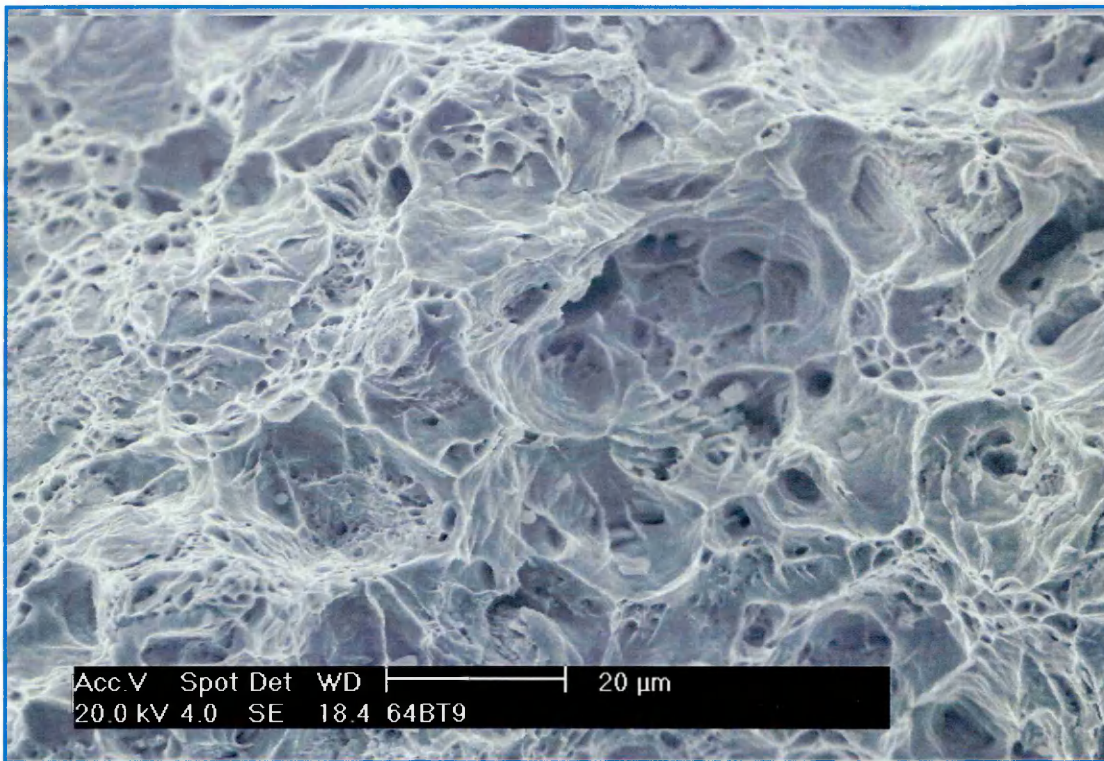


Figure 112. Figure 108 D1 x 2000.

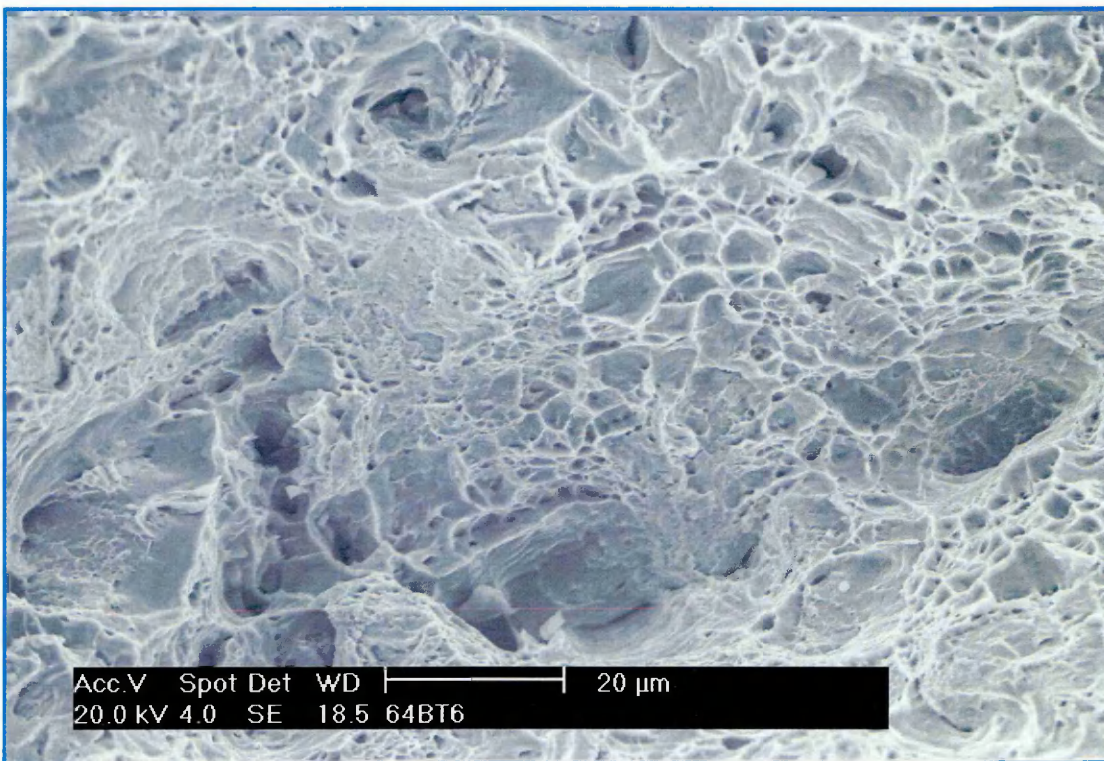


Figure 113. Figure 109 H1 x 2000.

Temperature (°C)	Strain Rate. (sec ⁻¹).	Steel Heat.	Orientation.	Strength Coefficient (K), MPa	Work Hardening (n).	0.1% Proof Stress. (MPa).	Lower Yield Stress (MPa).	Upper Yield Stress (MPa).	UTS. (MPa)	ϵ_u % based on eng strain and true strain based on $\ln(1+\epsilon)$.	ϵ_F % based on eng strain & true strain based on Z .	Reduction in Area Z (%)	Luders Strain Yes or No & %	Serration and type.	Specimen Number.	True fracture Stress (MPa).
25	2×10^{-6}	A	L	983.1	0.2651	N/A	295.6	301	507 (599)	18.46 (16.9)	27.82 (1.059)	65.32	Yes 0.48	A & B	mca325	968
	2.67×10^{-6}	B	L	934.5	0.2885	NA	275.3	285.5	472.4 (570)	20.77 (18.90)	31.89 (1.043)	64.78	Yes 0.51%	B & C	jda3b1	937
60	2×10^{-6}	A	L	1160.1	0.3294	NA	274.1	281.4	535 (617)	15.20 (14.20)	22.92 (0.871)	58.15	Yes 1.01%	A & E	mca360	949
	2.67×10^{-6}	B	L	-	-	-	-	-	-	-	-	-	-	-	-	-
100	2×10^{-6}	A	L	1487.2	0.3634	NA	276.4	287.9	614.3 (710)	15.53 (14.4)	21.03 (0.639)	47.25	Yes 1.19	B	mca3100	939
	2.67×10^{-6}	B	L	1709.8	0.4355	NA	254	274	605 (699)	15.60 (14.40)	22.5 (0.665)	48.58	Yes 0.21%	C & E	jda3b2	975
150	2×10^{-6}	A	L	1950.6	0.4580	N/A	262.7	293.4	658.8 (752)	14.11 (13.20)	21.77 (0.566)	43.24	Yes 1.19	A, B, E	mca3150	927
	2.67×10^{-6}	B	L	1755.6	0.4395	NA	248	272	650 (763)	17.20 (15.90)	24.77 (0.560)	42.92	Yes 0.33%	A & B & C	jda3b3	929
200	2×10^{-6}	A	L	1740.9	0.4106	N/A	269.6	291.4	666.5 (785)	17.78 (16.40)	27.76 (0.590)	45.07	Yes 1.07	A & B	mca3200	956
	2.67×10^{-6}	B	L	1903.3	0.5163	NA	266	N/A	614.6 (737)	19.9 (18.10)	32.44 (0.642)	47.39	no	A & E	jda3bz	890
250	2×10^{-6}	A	L	1486.5	0.3746	N/A	236.9	250.9	632.1 (762)	20.49 (18.6)	30.88 (0.740)	52.33	Yes 0.52	A & B	mca3250	905
	2×10^{-6}	B	L	-	-	-	-	-	-	-	-	-	-	-	-	-
300	2×10^{-6}	A	L	1444.5	0.3726	300	N/A	N/A	604.1 (700)	15.94 (14.8)	26.75 (0.794)	54.82	no	A & B	mca3300	888
	2.67×10^{-6}	B	L	1250.5	0.3627	280	N/A	N/A	541.3 (635)	17.25 (15.90)	28.39 (0.858)	57.62	no	A & C	jda3b5	836
350	2×10^{-6}	A	L	1103.8	0.3138	240	N/A	N/A	519 (609)	17.23 (15.90)	25.33 (0.884)	58.69	no	A & B	mca3350	822
	2.67×10^{-6}	B	L	1459.7	0.4590	NA	241	257	501.9 (504)	15.42 (14.30)	25.16 (0.999)	63.20	no	B	jda3b6	948

Table 12. Tensile testing results for steel heats VS3783A and VS3783B.

Steel Heat.	Temperature °C.	Strength Coefficient (K).	Work Hardening Exponent (n).	True Fracture Stress (σ_f MPa).	True strain to UTS. (ϵ_u %). & True UTS (MPa).	Engineering strain to fracture. (ϵ_f %). And true strain to fracture based on Z.	Reduction in area. (Z).
VS3764A	20	812	0.221	946	16.88 (544)	31.2 1.20	70.10
VS3764B	20	912	0.2854	809	14.5 (523)	26.6 1.084	66.18
VS3783A	20	983.1	0.2651	968	16.9 (599)	27.8 1.059	65.32
VS3783B	20	934.5	0.3294	937	18.90 (570)	31.8 1.043	64.78
VA3764A	50	886	0.2419	929	14.49 (538)	24.6 1.056	65.22
VS3783A	60	1160.1	0.3294	949	14.20 (617)	22.92 0.871	58.15
VS3764A	100	1113	0.2857	946	11.6 (594)	21.3 0.898	59.22
VS3764B	100	1049	0.2440	843	11.1 (567.7)	20.4 0.797	54.94
VS3783A	100	1487.2	0.3634	939	14.4 (710)	21.0 0.639	47.25
VS3783B	100	1709.8	0.4355	975	14.4 (699)	22.5 0.665	48.58
VS3764A	150	1310	0.3238	850	11.77 (650)	20.6 0.674	49.07
VS3764B	150	1049	0.2322	806	11.1 (632.6)	19.5 0.572	47.35
VS3783A	150	1950.6	0.4580	927	13.2 (752)	21.7 0.566	43.24
VS3783B	150	1755.6	0.4395	929	15.9 (763)	24.7 0.560	42.92
VS3764A	200	1188	0.2770	753	14.32 (672)	24.7 0.597	44.97
VS3764B	200	1268	0.2830	774	15.5 (678.4)	25.3 0.628	43.85
VS3783A	200	1740.9	0.4106	956	16.4 (785)	27.7 0.590	45.07
VS3783B	225	1903.3	0.5163	890	18.10 (737)	32.4 0.642	47.39
VS3764A	250	1205	0.3134	837	15.35 (655.4)	28.1 0.871	58.17
VS3764B	250	1177	0.3000	836	15.7 (645.6)	26.2 0.801	55.13
VS3783A	250	1486.5	0.3746	905	18.6 (762)	30.8 0.740	52.33
VS3764A	300	1121	0.3009	877	14.84 (629)	27.7 0.978	62.42
VS3764B	300	1126	0.2957	853	12.9 (613)	26.5 0.917	60.22
VS3783A	300	1444.5	0.3726	888	14.8 (700)	26.7 0.794	54.82
VS3783B	300	1250.5	0.3627	836	15.90 (635)	28.3 0.858	57.68
VS3764A	350	1091	0.3325	815	12.9 (540)	26.5 1.122	67.44
VS3764B	350	1013	0.2830	756	12.3 (545.7)	26.3 1.047	64.91
VS3783A	350	1103.8	0.3138	822	15.90 (609)	25.3 0.884	58.69
VS3783B	350	1459.7	0.4590	948	14.30 (504)	25.1 0.999	63.20

Table 13. Comparison of the main mechanical parameters for VS series of steel heats.

Table 13 shows a comparison of the main mechanical parameters for the VS series of steel heats. VS3783B is included for completeness, unfortunately due to an oversight in the machining of the specimens, by the company who made them the average gauge length of the VS3783B specimens was only

14 mm, whereas the average gauge length of the other VS specimens was 17.27 mm. Time constraints and material shortage, meant further specimens could not be made to complete the testing programme.

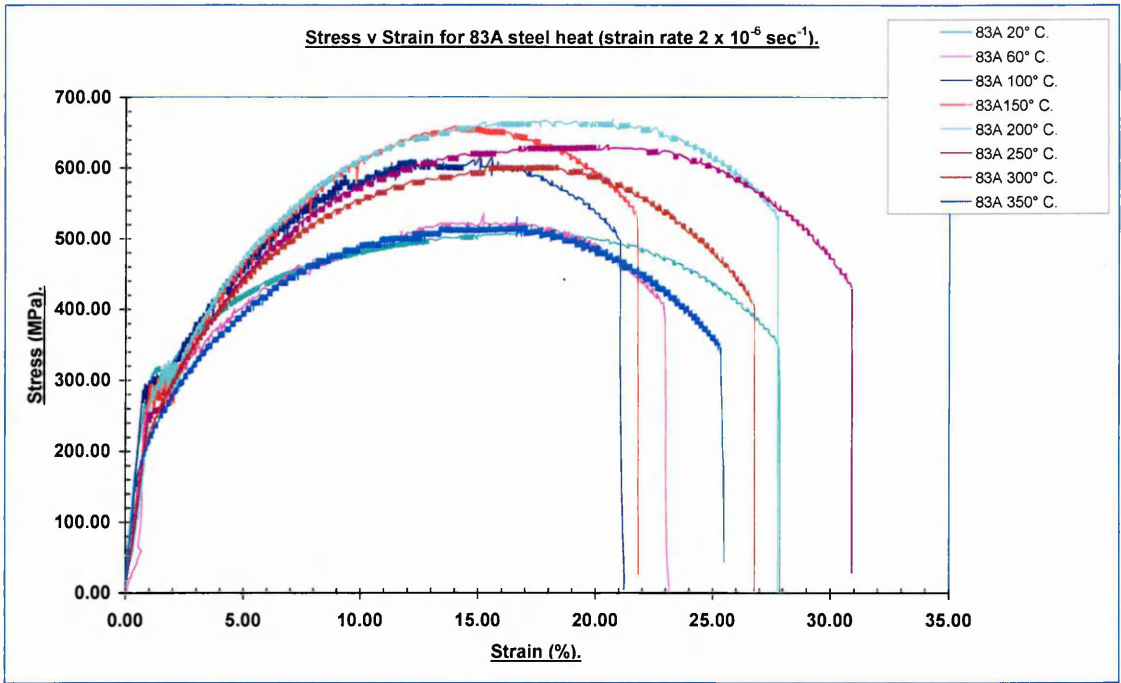


Figure 114. Graph of Stress vs Strain for VS3783A.

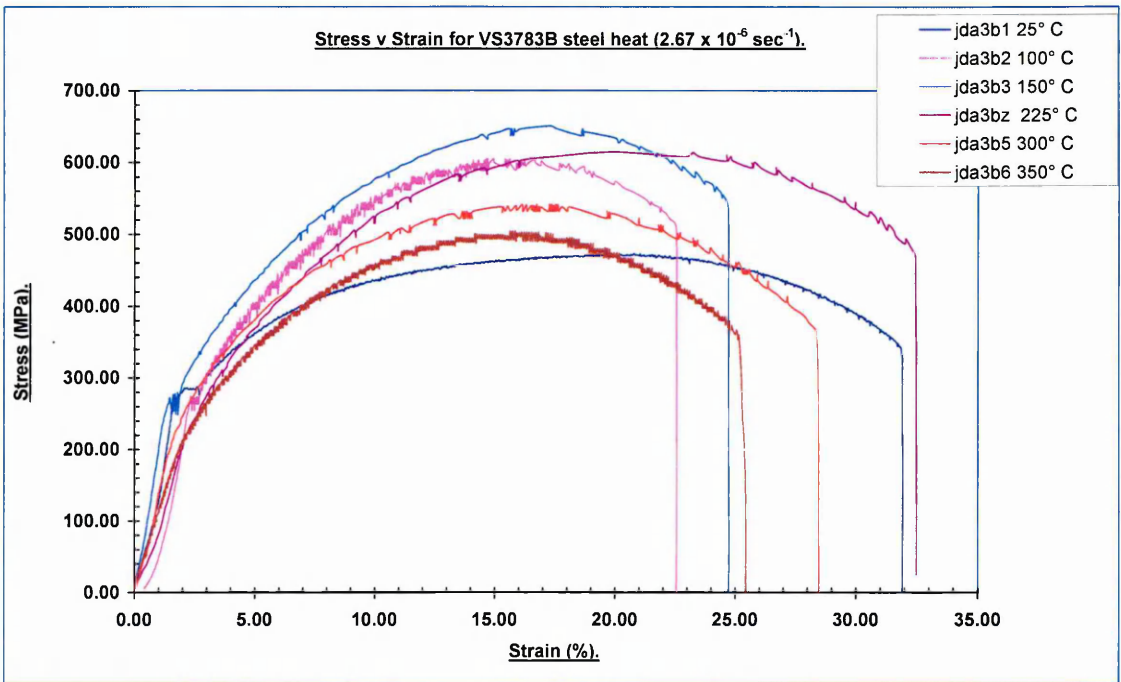


Figure 114A Graph of Stress vs Strain curve for VS3783B.

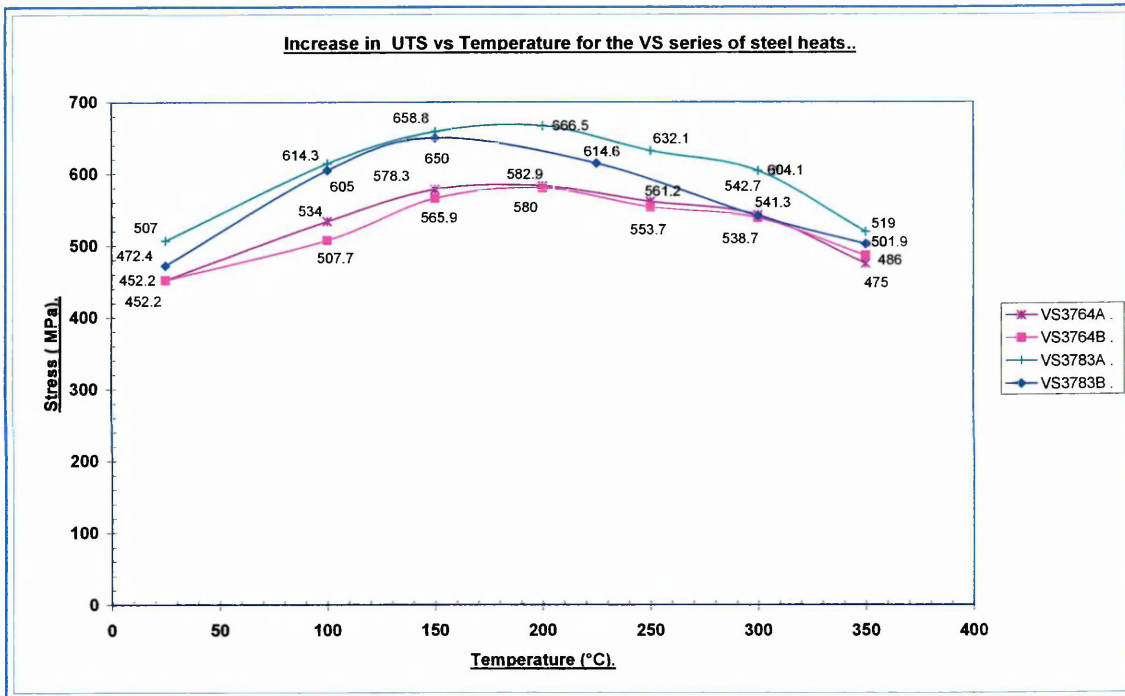


Figure 115. Graph of Increase in UTS vs Temperature for the VS series of steel heats.

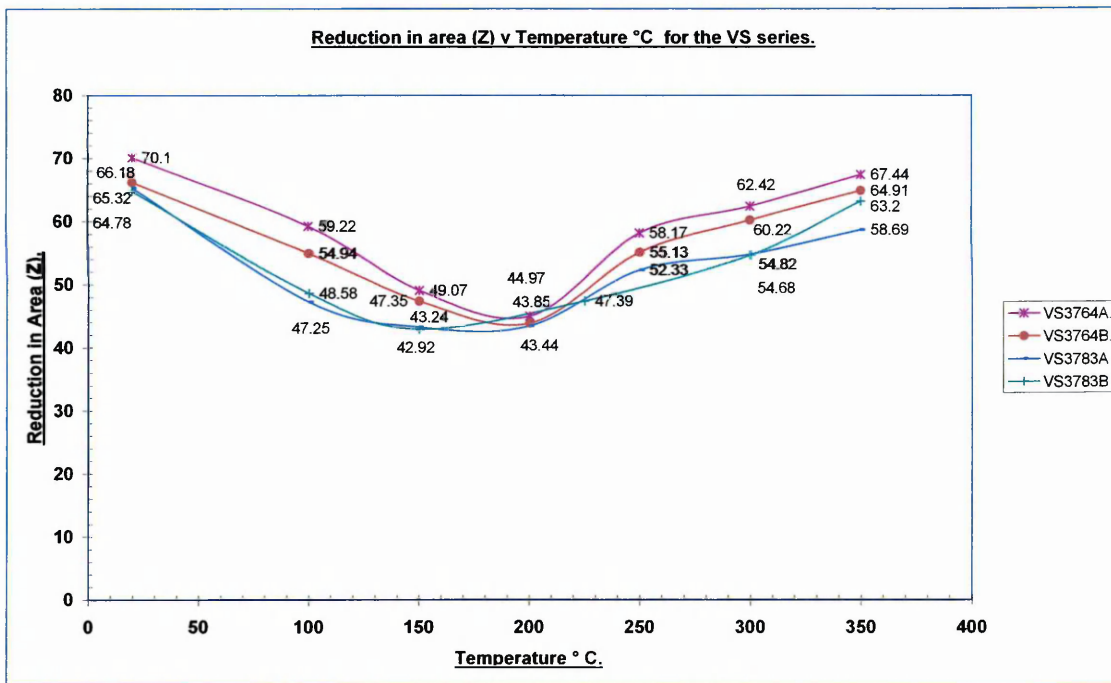


Figure 116. Graph of Reduction in Area (Z) vs Temperature for the VS series of steel heats.

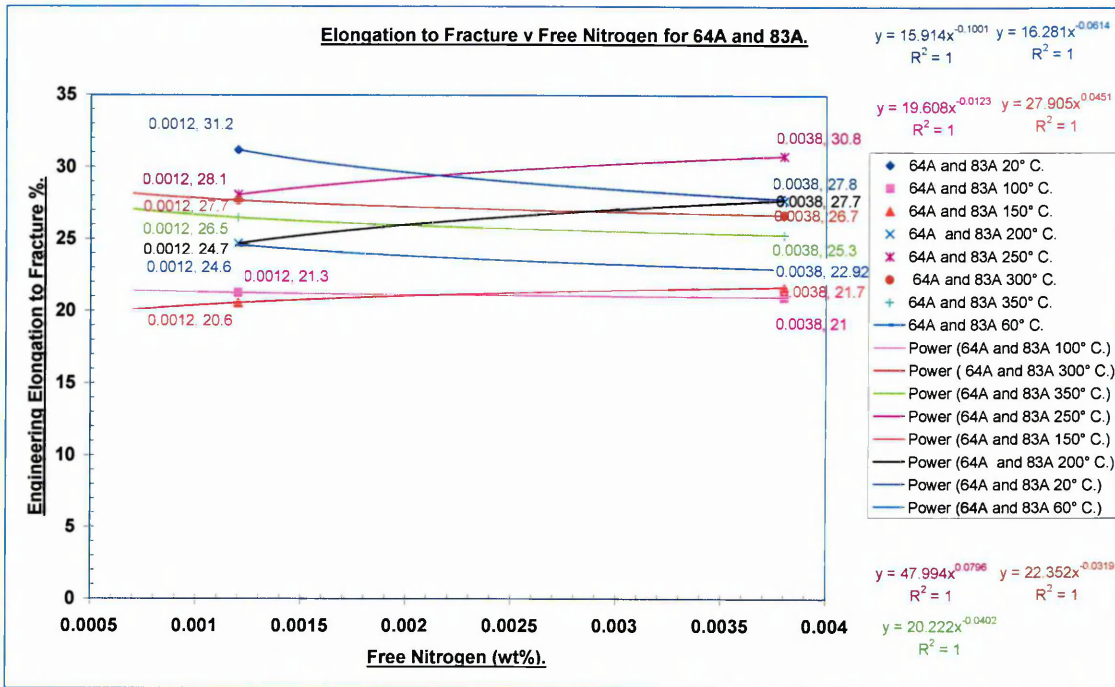


Figure 117. Elongation to Fracture vs Free Nitrogen for VS3764A and VS3783A.

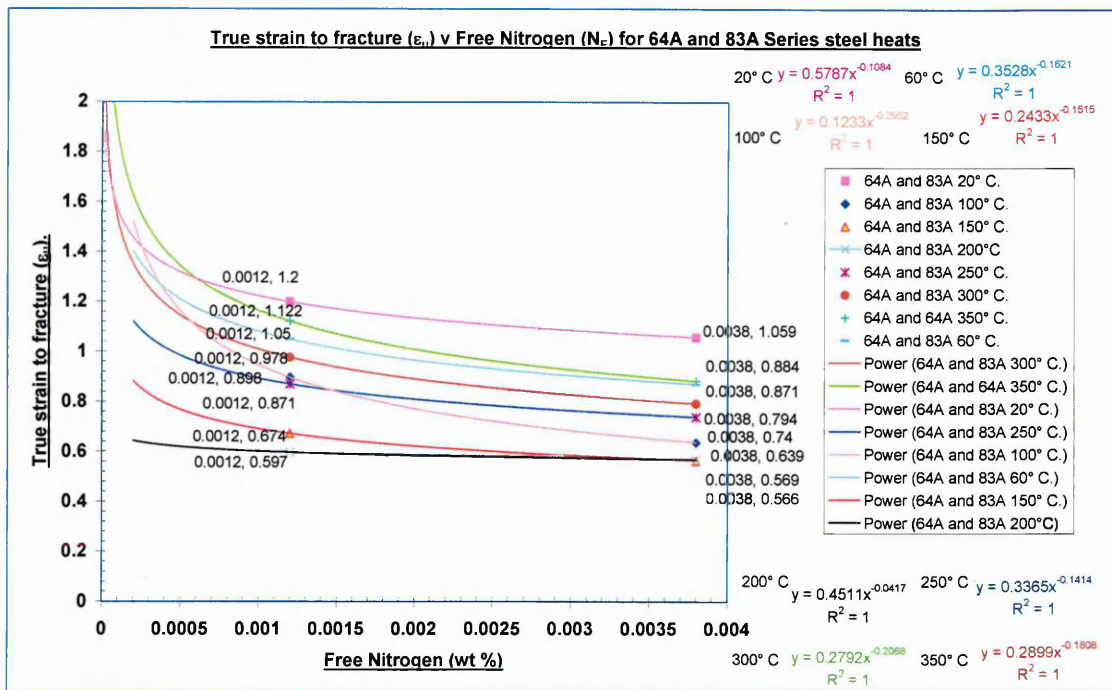


Figure 118. True Strain to Fracture vs Free Nitrogen for VS3764A and VS3783A.

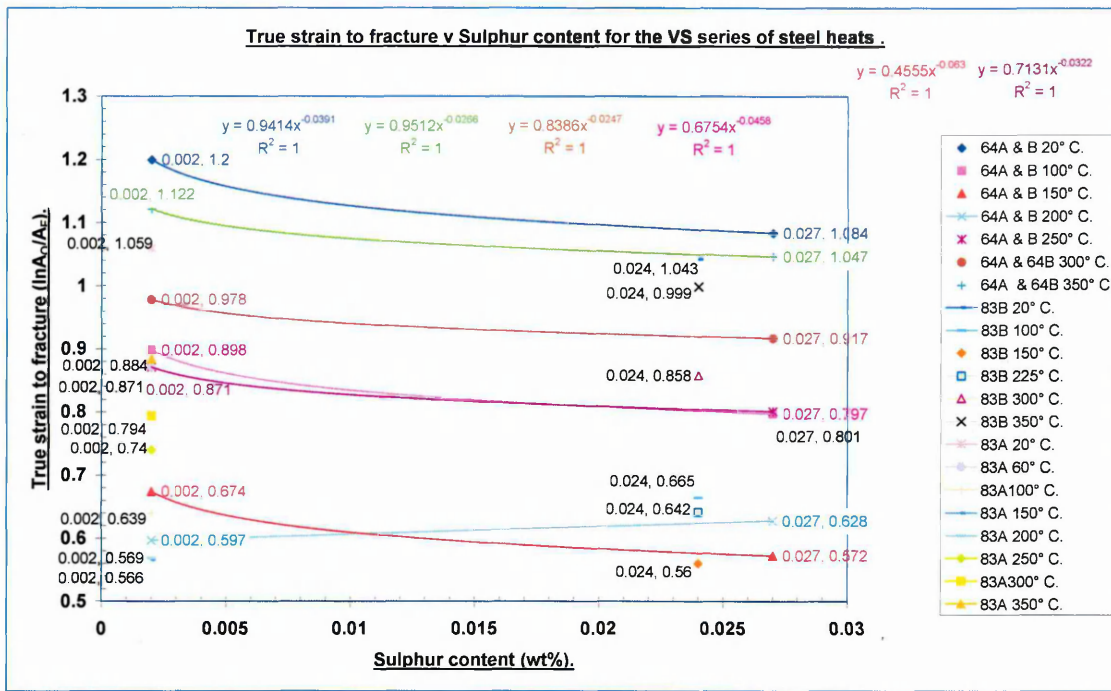


Figure 119. True strain to Fracture vs Sulphur content for the VS series of steel heats.

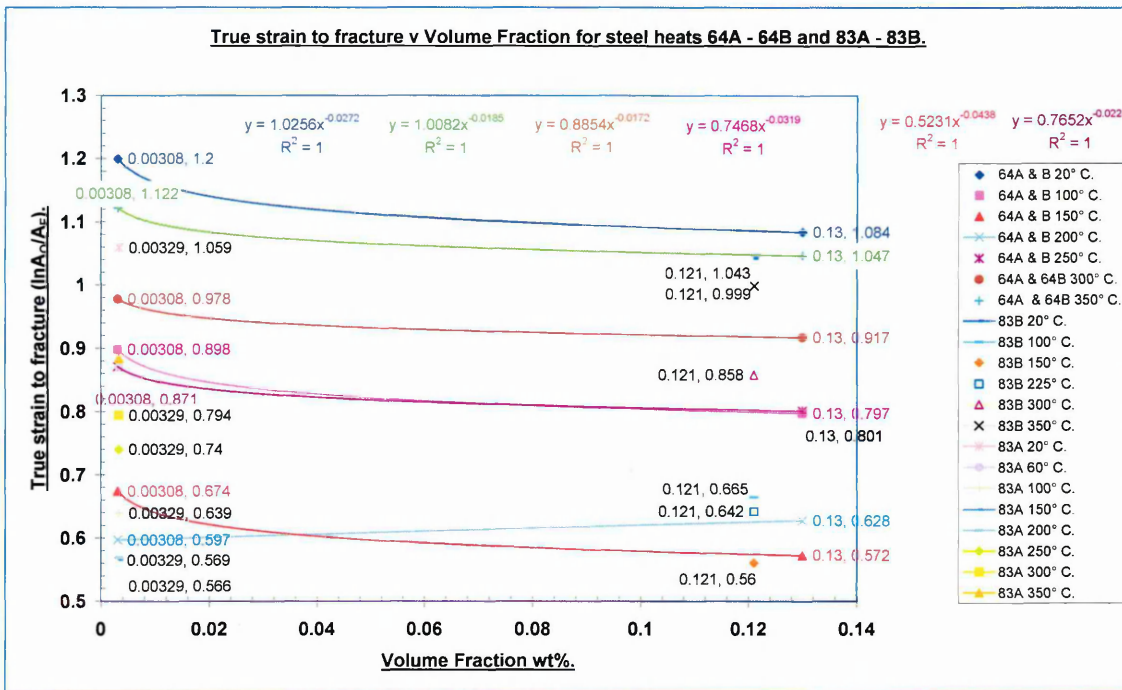


Figure 120. True strain to Fracture vs Volume Fraction for the VS series of steel heats.

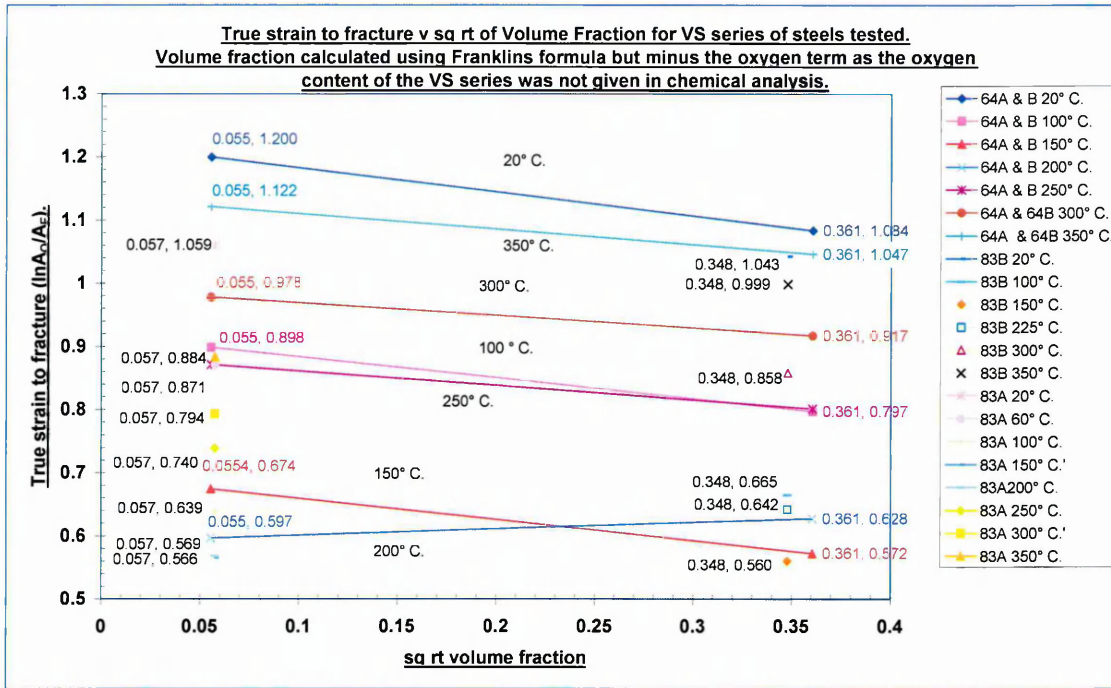


Figure 121. True Strain to Fracture vs $\sqrt{\text{sq rt of the Volume Fraction}}$ for the VS series of steel heats.

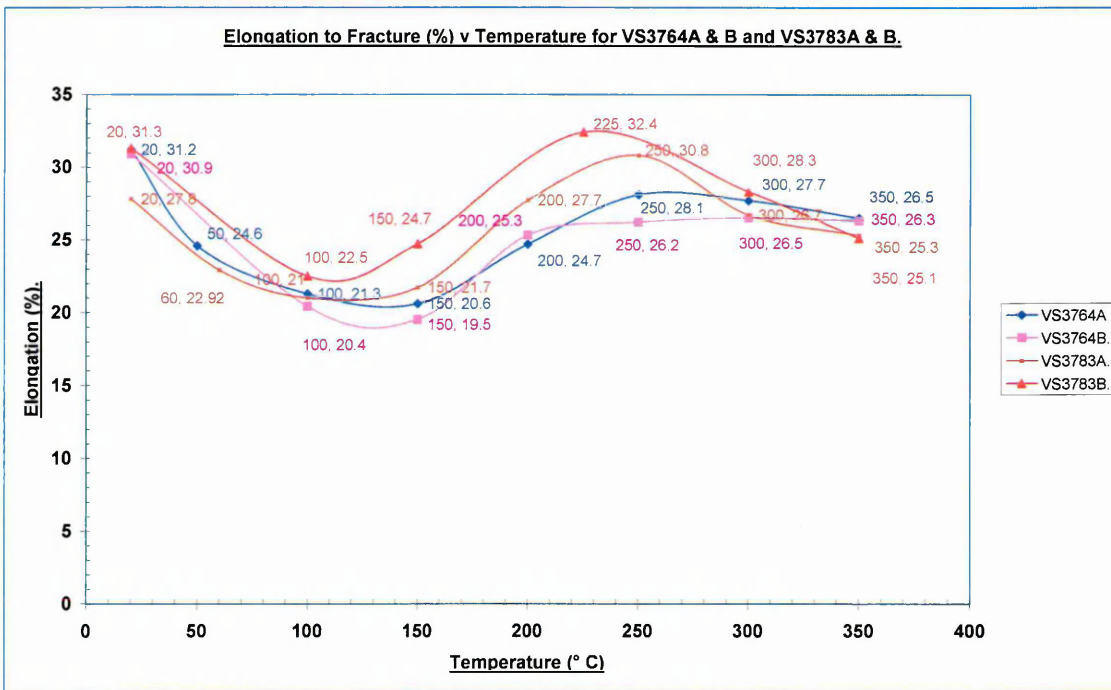


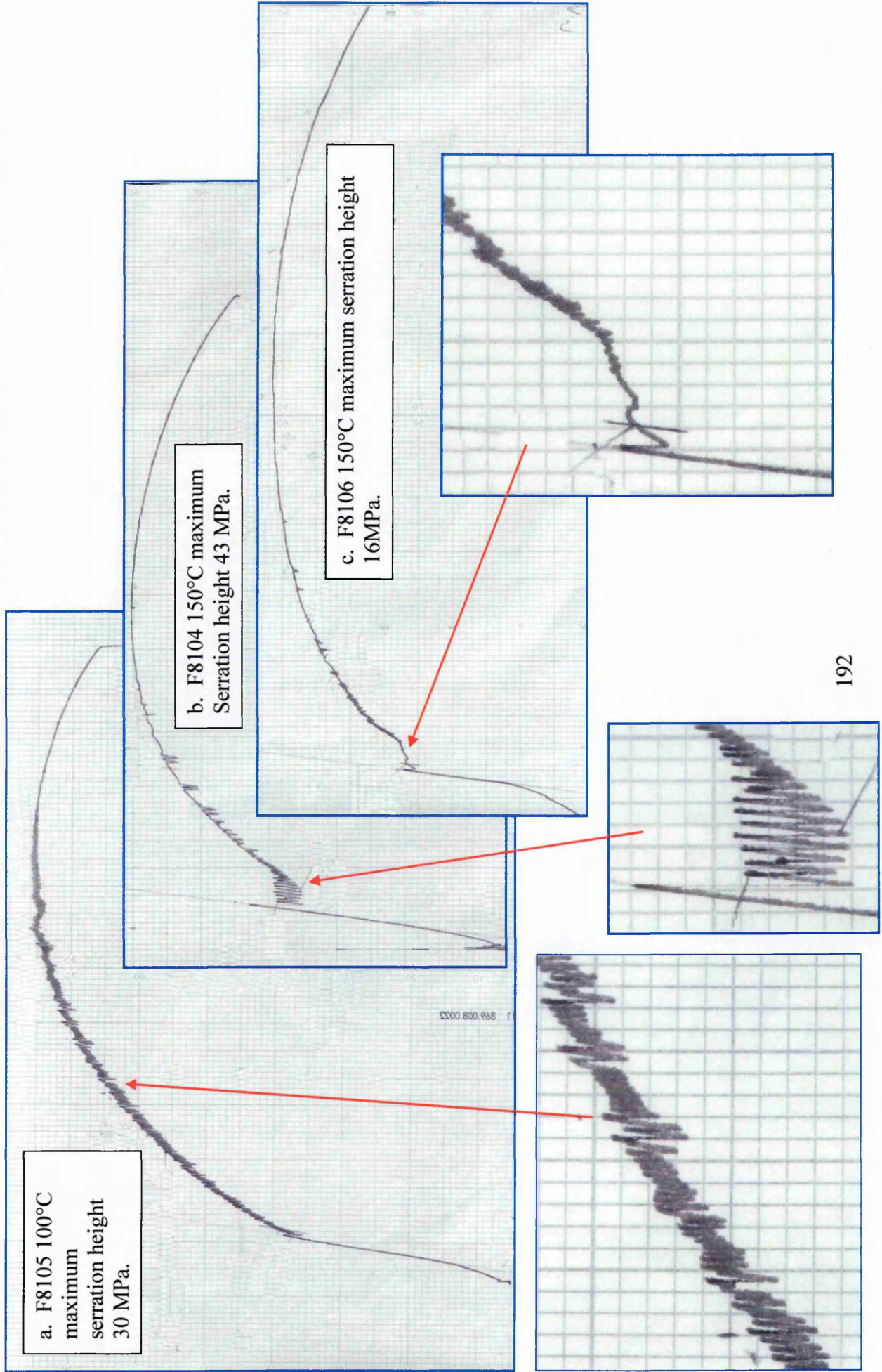
Figure 122. Elongation to Fracture vs Temperature for the VS series of steel heats.

Specimen Batch & Number.	Environment A: Air W: Water.	Temperature (° C).	Strain Rate.	Yield Stress. MPa.	Eng Ultimate Tensile Strength. MPa. & True Stress.	True Failure Stress MPa.	Uniform Strain to UTS ϵ_u (%).	Strain To Fracture ϵ_f (%).	True Strain to fracture Based on $\ln(A_0/A_f)$	Reduction In Area. Z (%).	Serrated Flow (Y or N).	Luders Deformation. Primary Deformation. (Y or N).	Strength Coefficient and work hardening exponent.
F8104/7	A	23	2.7e-6	403	550*	1888*	-	-	1.38	75	N	Y/?	Fast strain rate
F8104/3	A	150	2.7e-6	405	590 650	1133	10.31 (9.8)	21.3	0.973	62.2	Y	Y/N	1267.3x 0.262
F8104/6	A	200	2.7e-6	294	623 704	1131	13.1 (12.6)	24.6	0.917	60	N	Y/N	1455.1x 0.352
F8104/1	A	250	2.7e-6	246	648 759	1167	17.2 (16.4)	29.8	0.9861	62.7	N	Y/N	1564.9x 0.404
F8104/5	A	300	2.7e-6	196	603 645	1132	15.3 (14.8)	31.0	1.094	66.5	N	N/N	1445.2x 0.385
F8104/2	180ppb DOW	250	2.7e-6	231	607 713	1100	17.6 (16.9)	31.1	1.385	57	N	Y/N	2025.2x 0.590
F8105/6	A	21	2.7e-6	269	530 606	1179	14.5 (14)	28.1	1.162	68.7	N	Y/N	1038.9x 0.275
F8105/7	A	100	2.7e-6	318	701 768	558	9.7 (9.4)	19.8	0.629	46.7	Y	Y/N	2025.2x 0.440
F8105/3	A	150	2.7e-6	317	732 822	628	12.4 (11.9)	19.9	0.603	45.3	N	N/N	3109.5x 0.573
F8105/4	A	200	2.7e-6	278	723 835	1077	15.7 (15.1)	23.9	0.559	42.9	N	N/N	1884.7x 0.432
F8105/2	A	250	2.7e-6	296	691 784	1095	13.67 (13.1)	25.2	0.817	55.8	N	N/N	1817.6x 0.451
F8105/5	A	100	2.7e-6	576*	695* 749	928	7.9 (7.6)	13.9	0.670	48.8	Y	?/N	1436.5x 0.245
F8105/1	180ppb DOW	250	2.7e-6	205	607 688	930	13.5 (12.1)	31.3	0.528	40.8	N	N/N	1116.4x 0.238
F8106/7	A	20	2.7e-6	271	473 555	503	17.5 (16.8)	32.3	1.35	74.1	N	Y/N	868.5x 0.253
F8106/3	A	150	2.7e-6	289	497 564	969	13.5 (12.8)	27.3	1.172	69	Y	Y/N	938.4x 0.250
F8106/4	A	200	2.7e-6	299	519 595	1175	14.7 (14.1)	28.3	1.241	71.1	N	Y/N	1022.4x 0.327
F8106/1	A	250	2.7e-6	214	543 609	847	12.3 (11.7)	27.3	1.26	71.6	N	N/N	1022.5x 0.278
F8106/5	A	300	2.7e-6	188	569* 674	886	18.5 (17.8)	35.8	1.397	75.3	N	N/N	1248.9x 0.360
F8106/6	A	350	2.7e-6	149	462 519	186	12.5 (12)	36.5	1.299	81.7	N	N/N	1060.1x 0.338
F8106/2	180ppb DOW	250	2.7e-6	156	537 633	1084	18.0 (17.3)	32.4	1.387	68.7	N	N/N	1648.1x 0.548

Text in red is the true strain values, text in blue SCC work. Asterisked text influenced by Mayes testing machine.

Table 14. Tensile testing results for steel heats F8104, F8105, and F8106.

Figure 123. Graph showing the specimens which had maximum Luders deformation and serrations for steel heats F8104, F8105 and F8106.



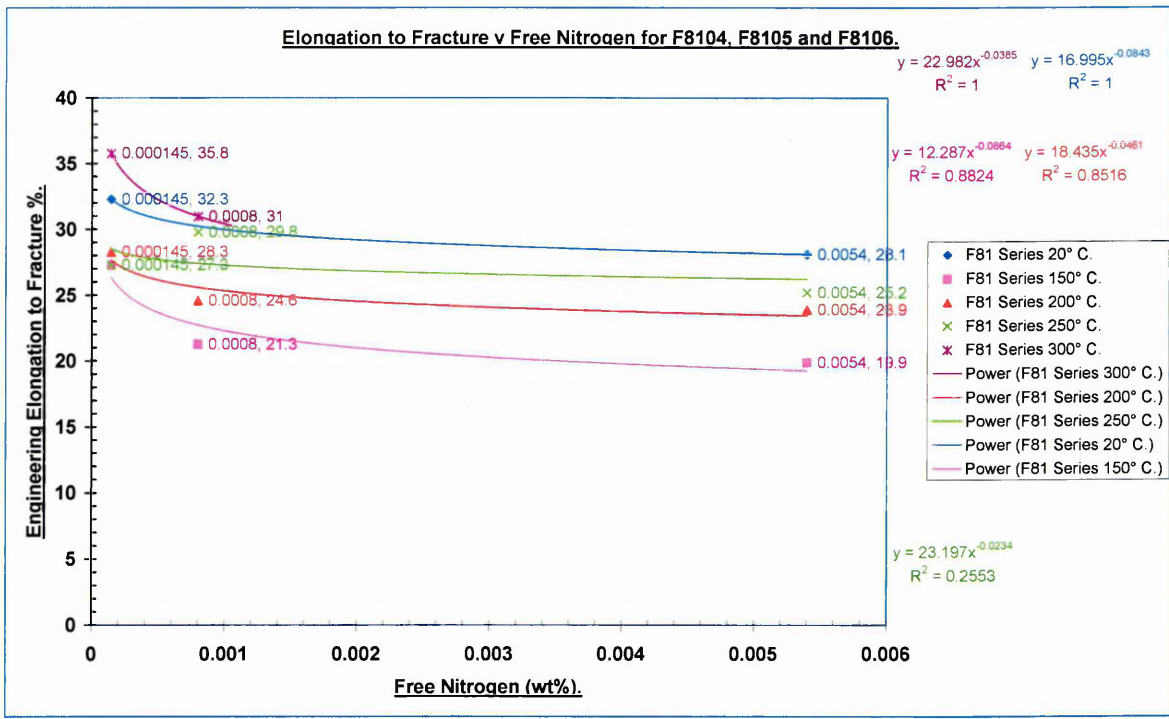


Figure 124. Elongation to Fracture vs Free Nitrogen for steel heats F8104, F8105 and F8106.

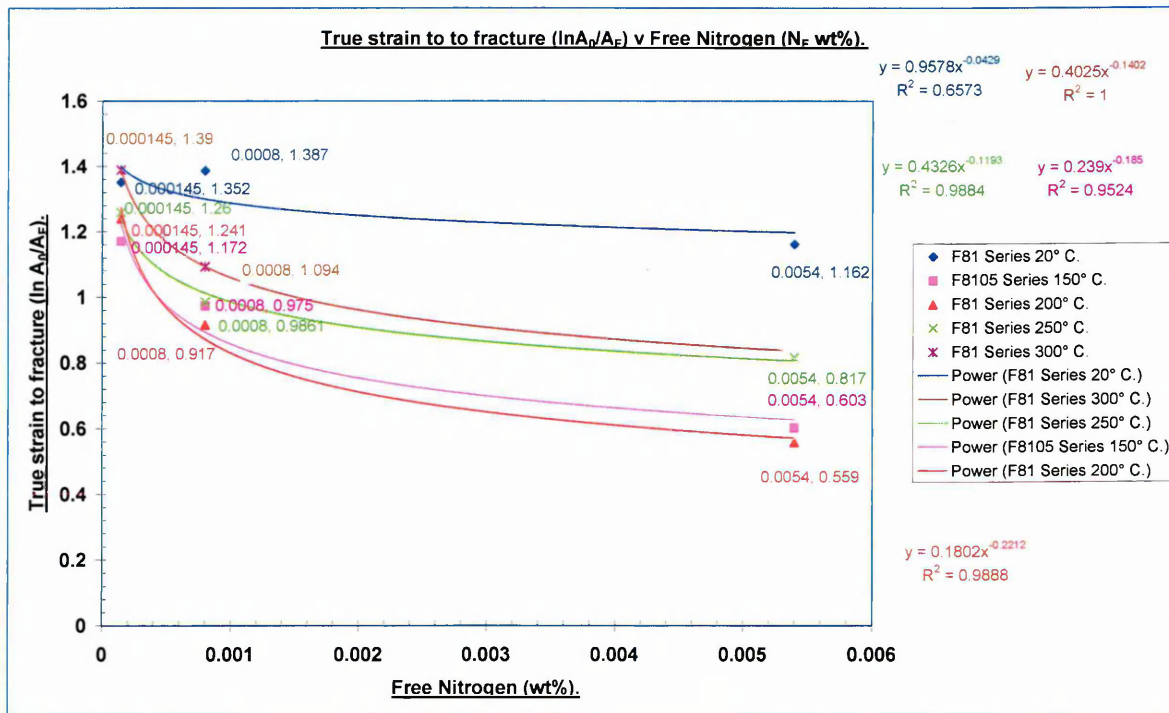


Figure 125. True strain to Fracture vs Free Nitrogen for F8104, F8105, and F8106.

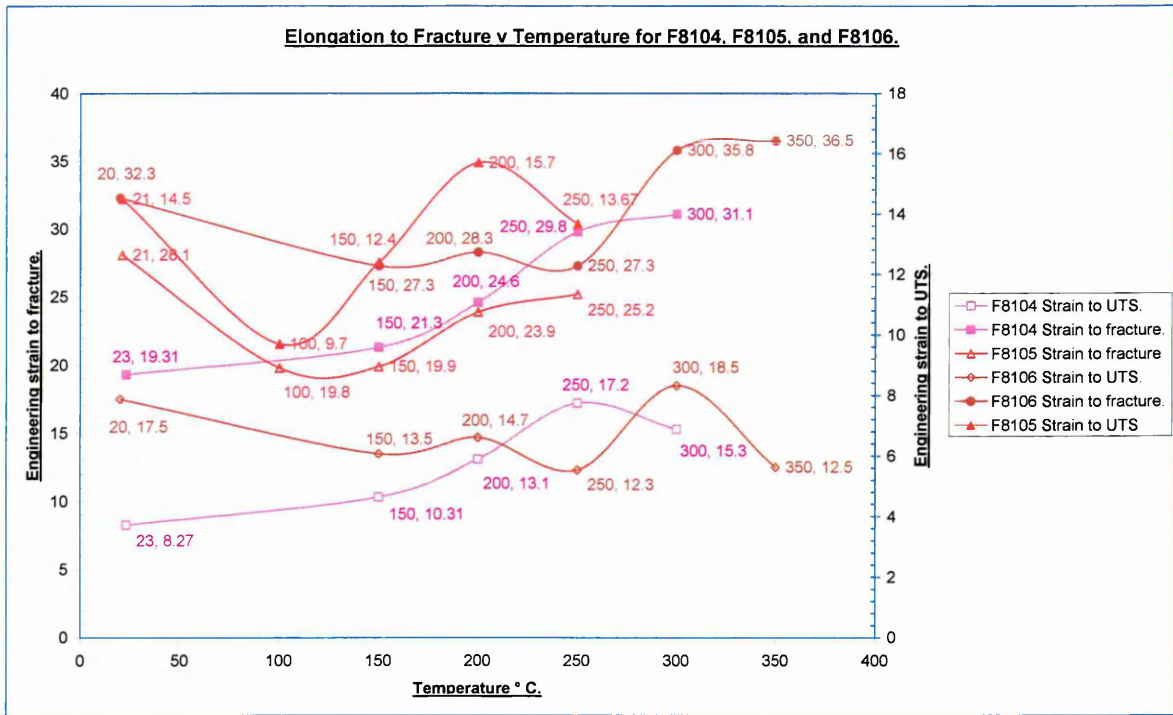


Figure 126. Elongation to UTS and to Fracture vs Temperature for steel heats F8104, F8105 and F8106.

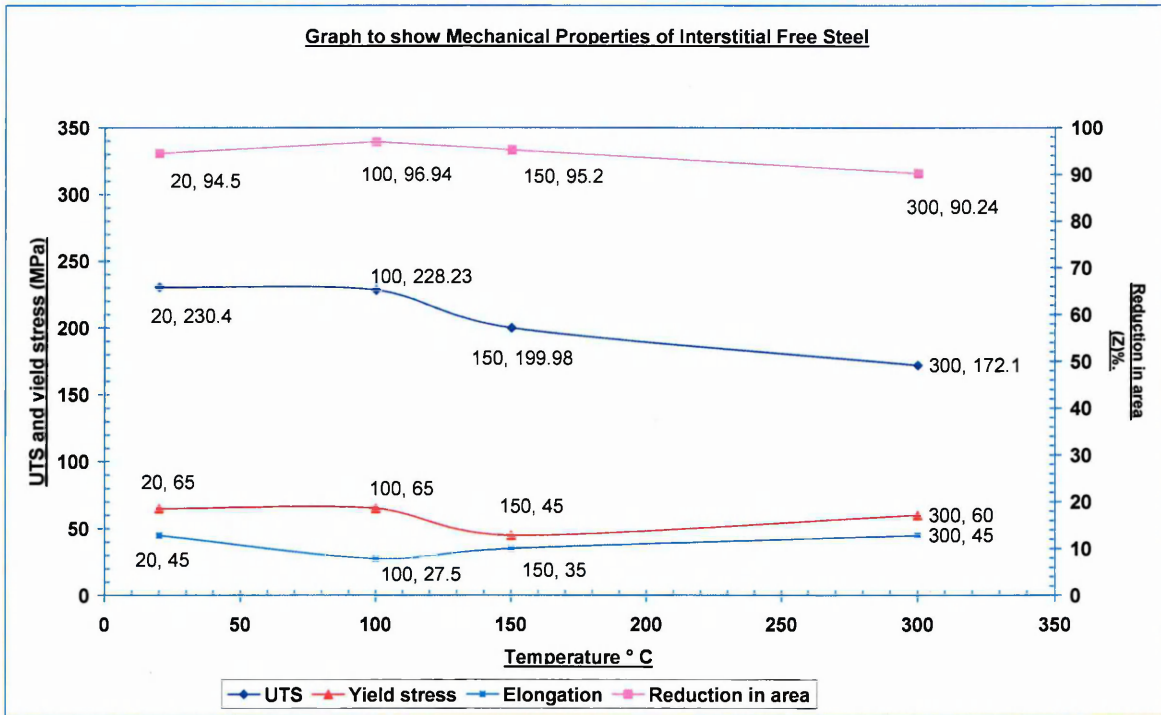


Figure 127. Graph showing Mechanical Properties of Interstitial Free Steel from tensile testing done in air.

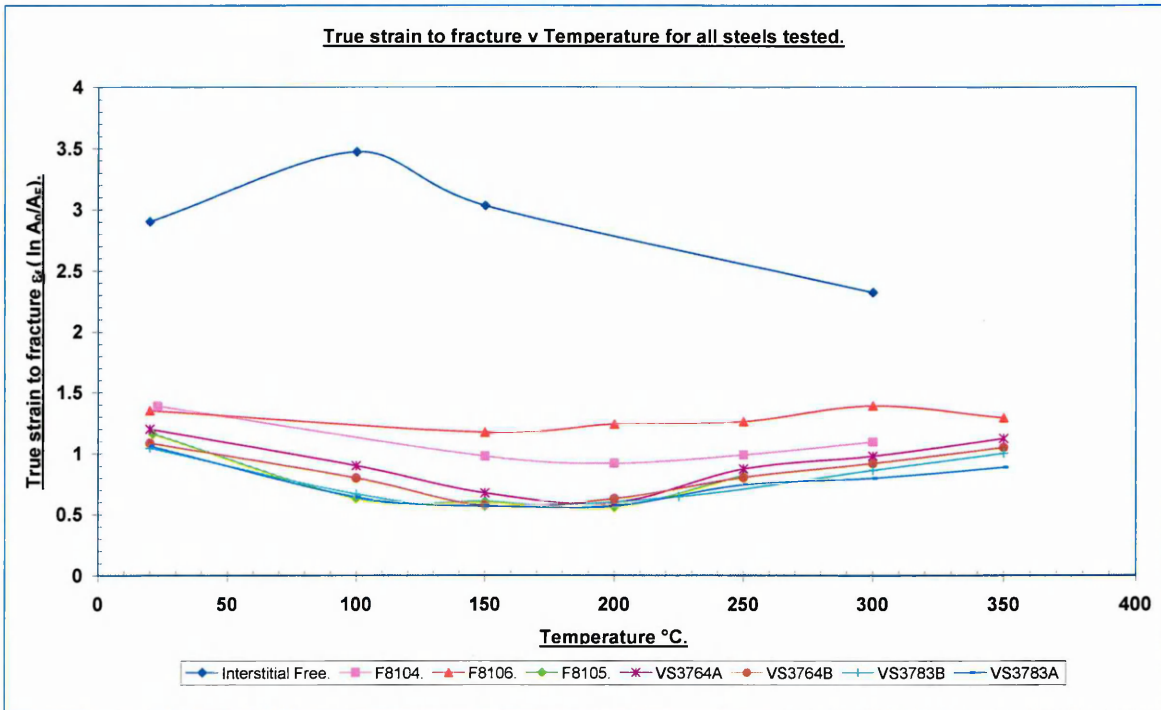


Figure 128. Graph showing True strain to fracture vs Temperature for VS3764A, VS3764B VS3783A, VS3783B, F8104, F8105 F8106 and Interstitial Free steel done in air.

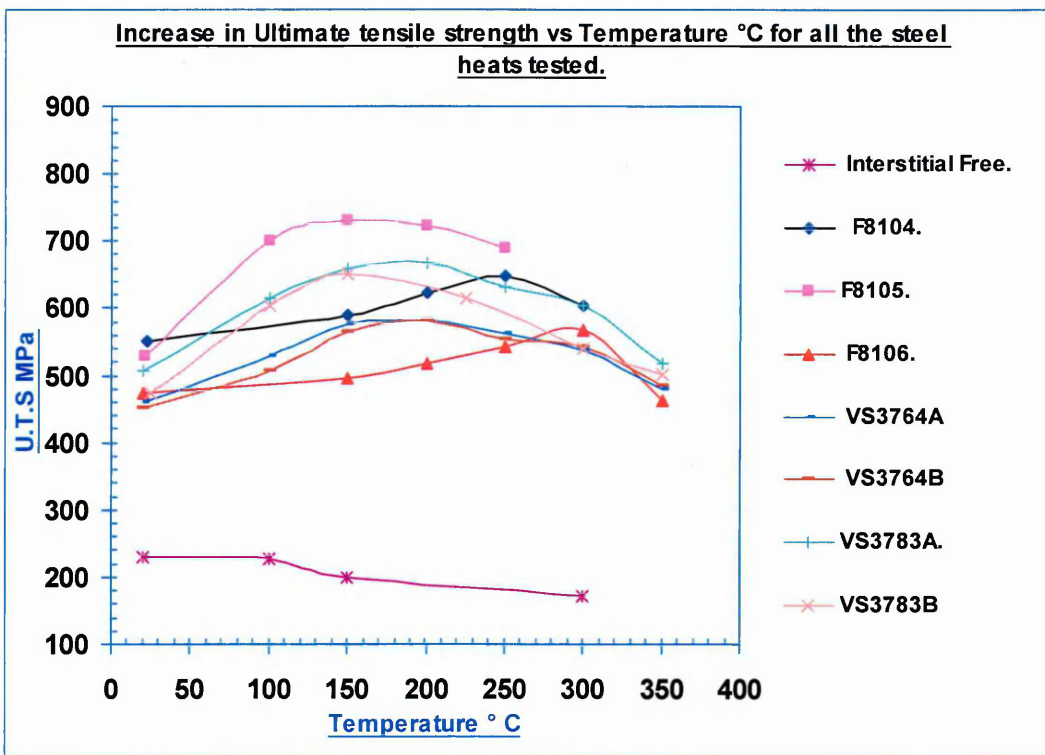


Figure 129. Increase in UTS vs Temperature for VS3764A, VS3764B, VS3783A, VS3783B, F8104, F8105 F8106 and Interstitial Free steel. (results courtesy of Professor J.D.Atkinson).

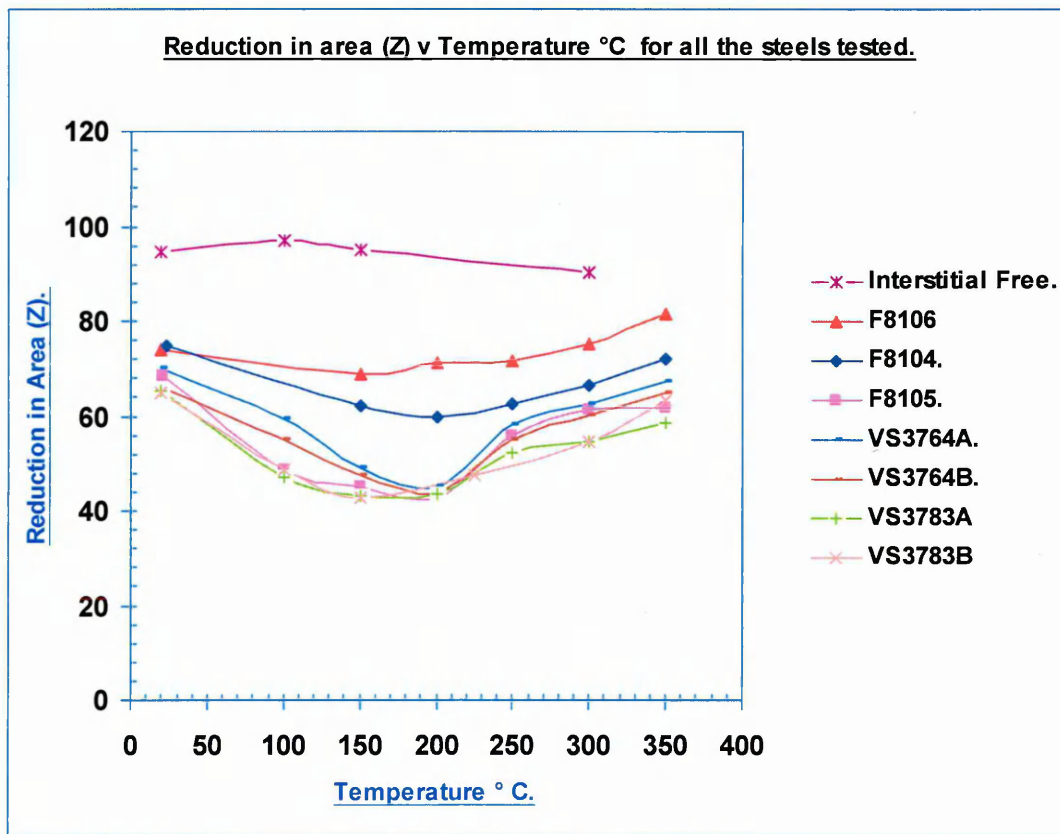


Figure 130. Reduction in area vs temperature for VS3764A, VS3764B, VS3783A, VS3783B, F8104, F8105 F8106 and Interstitial Free steel.

4.6. Fracture Toughness Testing Results (J_{1C} test results).

The results of the fracture toughness tests are given in Table 15, Figure 131 and Figure 132. Figure 131 shows the load versus load line displacement for all the specimens tested (the compliance curve). That is for steel heats VS3764A and VS3764B. Specimens J1A and JB7, were tested at 23°C in air, specimens J2A and J7B were tested at 200°C in air. Specimen J3A was tested at 200°C in 8 ppm DOW, and a conductivity of $0.2 \mu\text{Scm}^{-1}$. All the specimens were tested at the loading rates specified in the experimental section.

The J vs Δa curves are given in Figure 132. These were obtained from the Rubicon J_{1C} Analysis software programme. To determine the difference in the tearing modulus between the specimens at selected crack lengths, a trend line was fitted to the curves, and a quadratic equation obtained using Excel. The equations and correlations of the fit are given in Figure 132. The tearing modulus was obtained by determining the gradient changes of the J vs Δa graph at selected points on the curve. The results are given in Table 15. It can be seen that several specimens were taken to different load line displacements this was part of the learning curve, in doing the tests. The J3A test finished prematurely at a load line displacement of 3.196 mm this was due to a trip operating, which was unforeseen.

Figure 133 shows two J vs Δa curves for two specimens tested at 200°C (VS3764A) one tested in air and the other in 8 ppm DOW. This was used to determine the degradation in the tearing modulus, as the J vs Δa plot could not be seen very clearly in Figure 132.

Figures 134 to 138 are photographs of half sections of the specimens, taken in plan view after being broken open. Figures 139, 141, 143, and 145 are photographs of the specimens taken in oblique view, prior to breaking open. Figures 140, 142, 144, and 146, are photographs of the specimen taken in side elevation, prior to breaking open. The plastic zones are clearly visible in Figures 142, 144, and 146. The largest plastic zone is Figure 144 (J7B) then Figure 142 (J2A), then Figure 146 (J1A). This is not surprising as they were

taken to crack lengths of 8.55, 5.01, and 2.12 mm respectively.

In Table 15 the text in green indicates the J_{1C} value, the text in blue indicates the crack length on the J vs Δa curve where the tearing modulus dJ/da was taken on. The black text in red brackets is the final crack length.

Figures 147 to 151 are side elevations of the crack profiles for the steel heats tested prior to being broke open.

Steel Heat and specimen number. and Δa	Temp °C and J_{1C} value kJm^{-2}	V_{LL} to yield mm	V_{LL} to UTS mm	Total V_{LL} mm	Load at yield kN	Max load At UTS kN	dJ/da (kJm^{-2}).														
							Figures in bold blue indicate the points at which dJ/da was determined for all the specimens (mm). From the J v Δa curve. mm														
VS 3764A J1A. (2.12)	23° 290	0.329	5.67	6.6	45.68	45.69	0.47	0.79	0.95	1.26	1.58	1.74	2.06	2.22	2.53						
The black text in the red brackets indicates Δa the amount of crack extension for each specimen.																					
VS 3764A J2A. (5.01)	200° 192	0.296	2.99	5	42.24	42.24	256	316	345	401	453	478	524	546	588						
VS 3764A J3A. (2.10)	200° 165	0.28	2.82	3.196	40.77	40.77	229	297	329	389	443	468	514	534	571						
VS 3764B J7B. (8.55)	20° 153	0.281	2.10	6.6	35.28	35.28	195	241	264	306	356	370	416	425	466						
VS 3764B J11B.(14.8)	200° 42	0.203	1.19	4.95	33.21	35.21	58	76	86	103	120	129	145	154	170						

Table 15. Tabulated Fracture Toughness Results.

Figure 131. Unloading Compliance Curve for all the VS specimens.

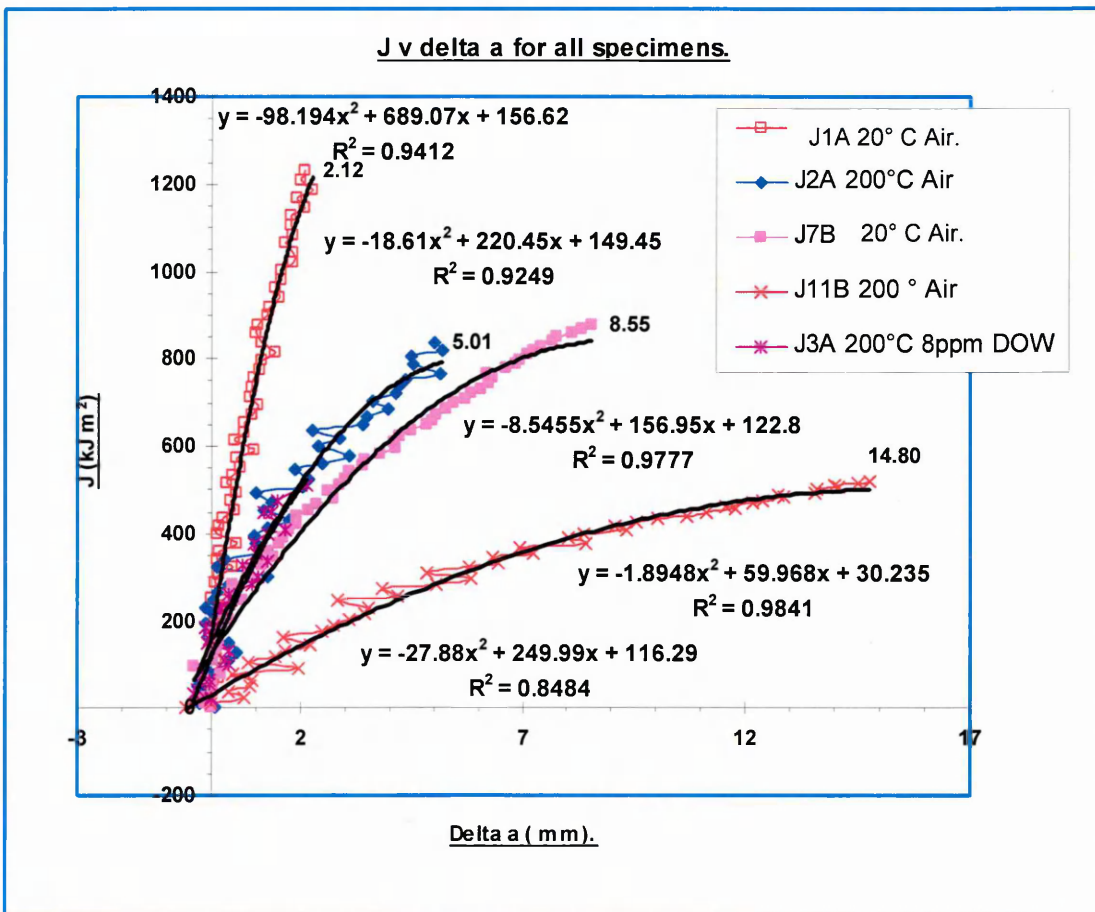
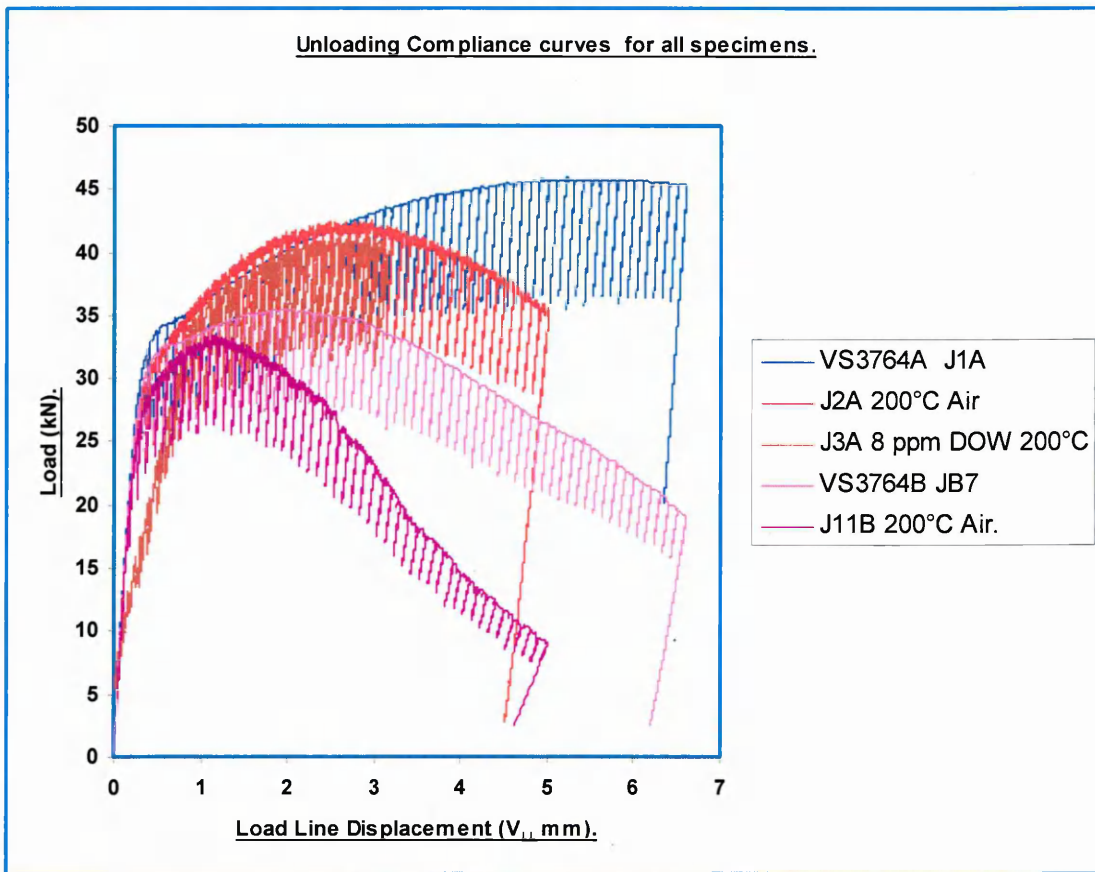


Figure 132. J vs Δa curves for steel heats VS3764A and VS3764B.

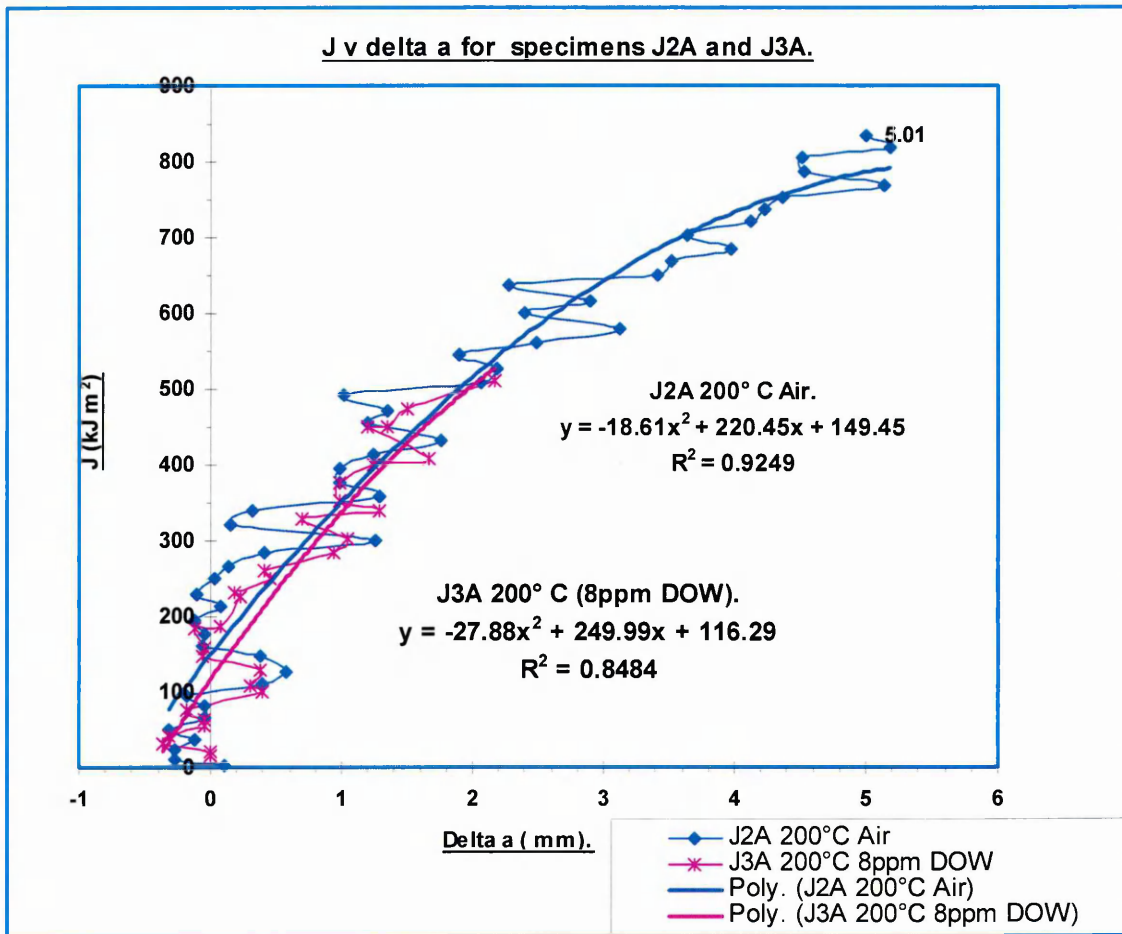


Figure 133. J vs Δa curves for VS3764A in Air and Water at 200°C.

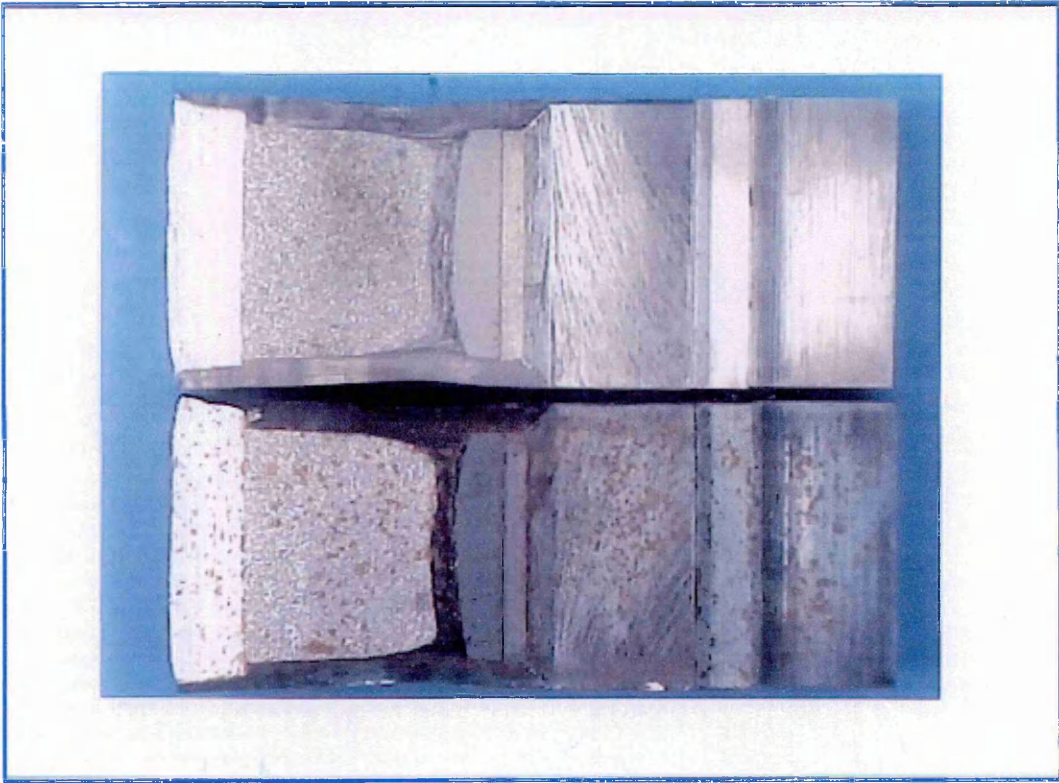


Figure 134. Half sections of specimen J1A (VS3764A 20°C Air).

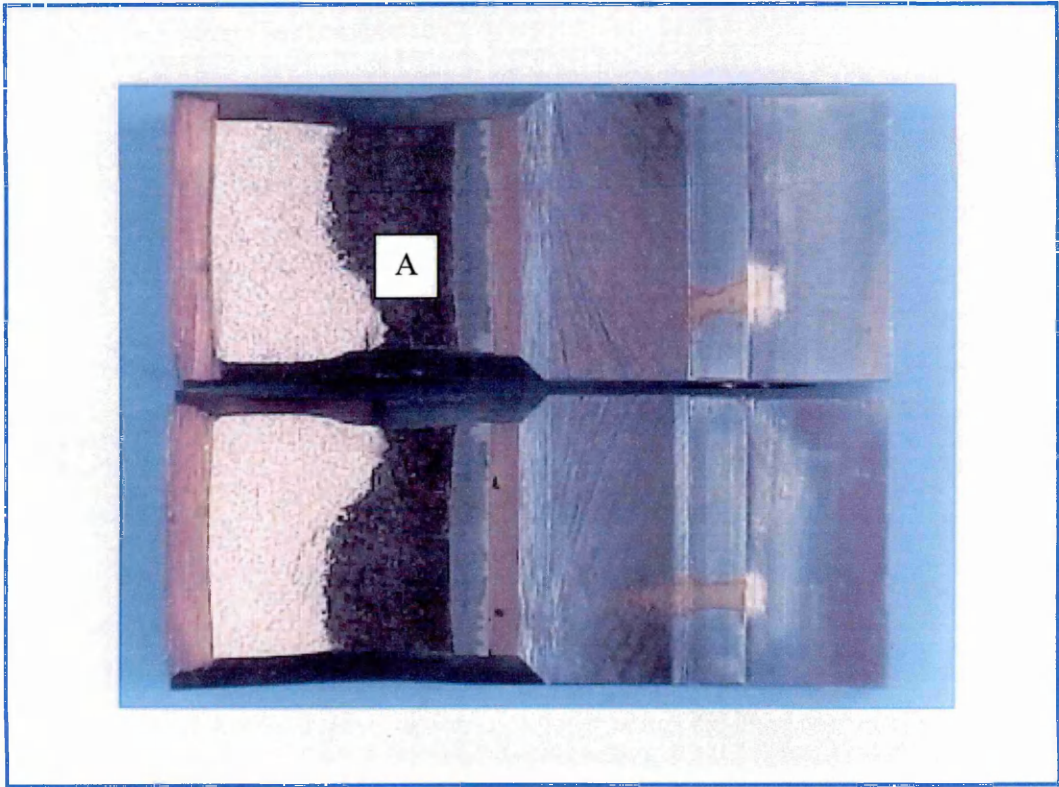


Figure 135. Half sections of specimen J7B (VS3764B 20°C Air).

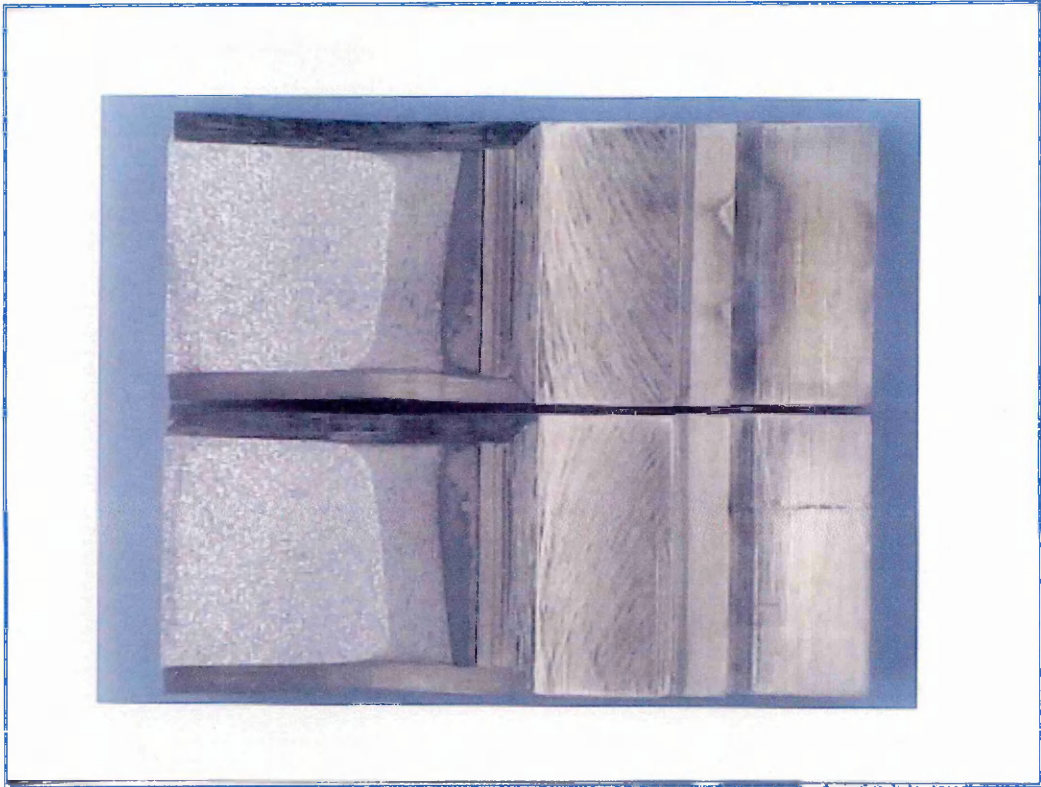


Figure 136. Half sections of specimen J2A (VS3764A 200°C Air).



Figure 137. Half sections of specimen J11B (VS3764B 200°C Air).

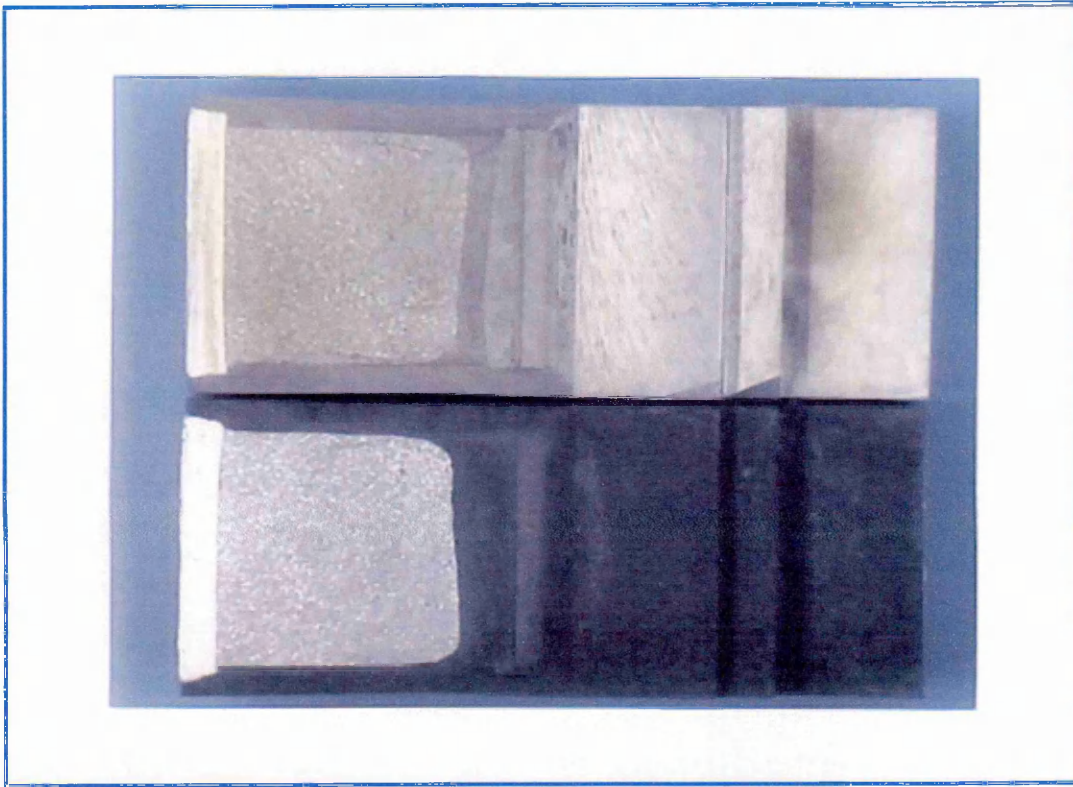


Figure 138. Half sections of specimen J3A (VS3764A 200°C Water).

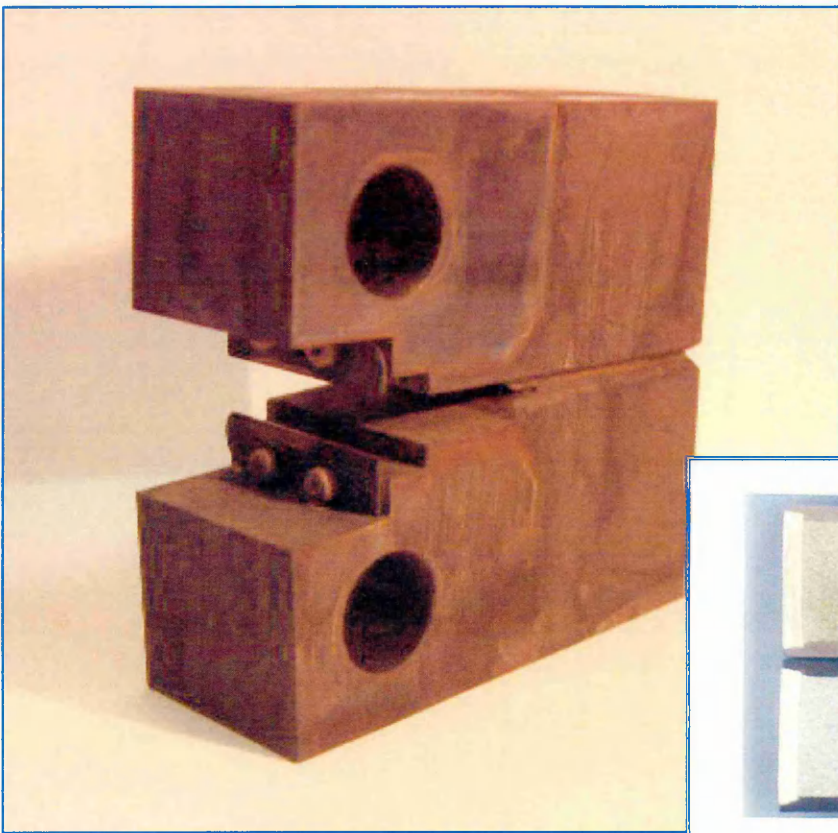


Figure 139 A.

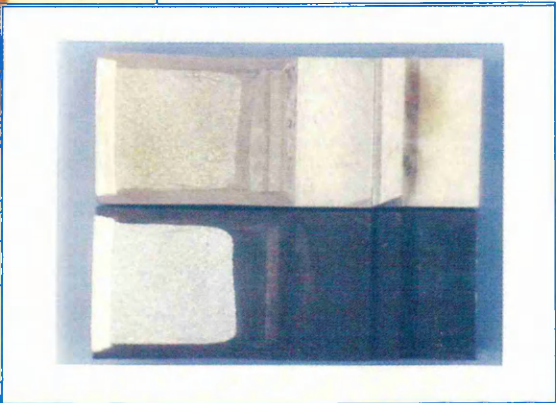


Figure 139. Photograph of J3A prior to breaking open (oblique view).

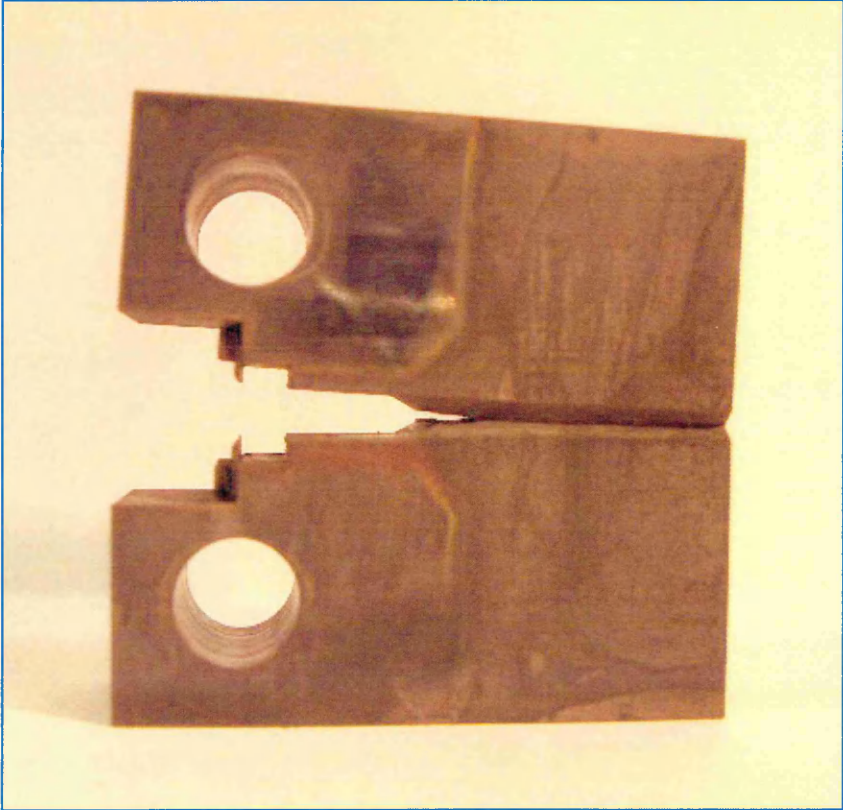


Figure 140. Photograph of J3A prior to breaking open (side view).

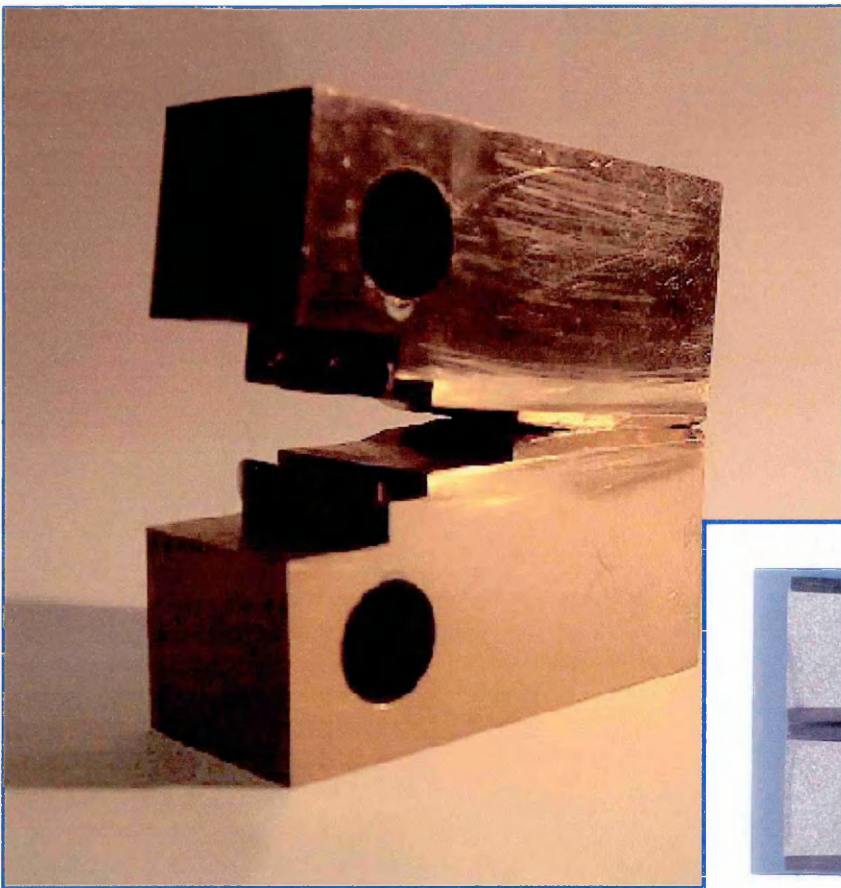


Figure 141 A.

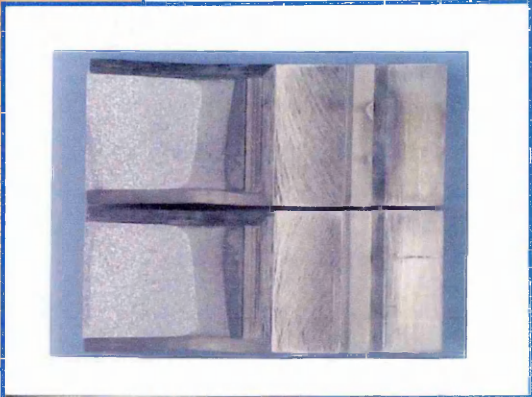


Figure 141. Photograph of J2A prior to breaking open (oblique view).

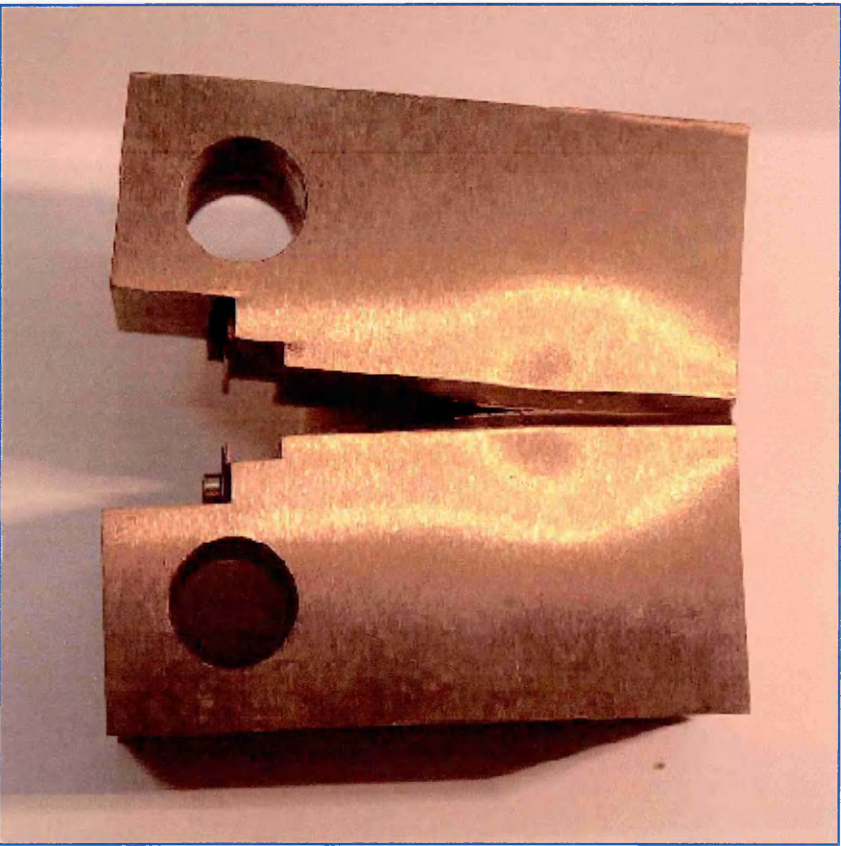


Figure 142. Photograph of J2A prior to breaking open (side view).

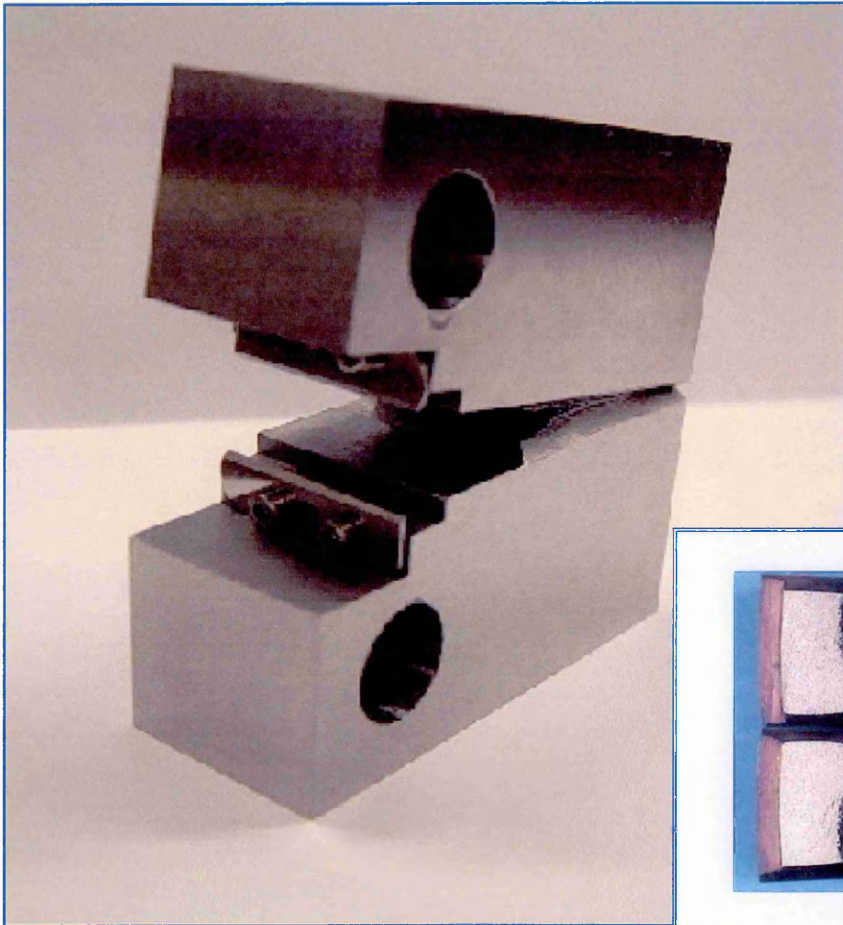


Figure 143 A.

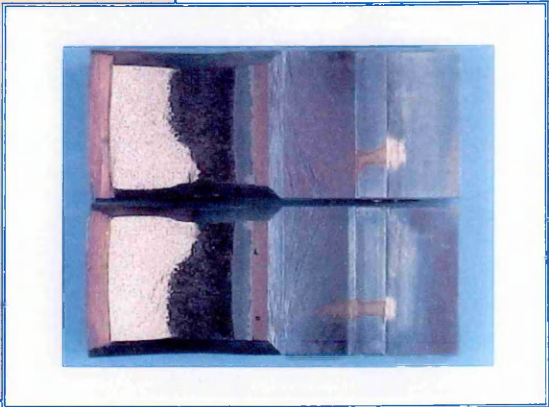


Figure 143. Photograph of J7B prior to breaking open (oblique view).

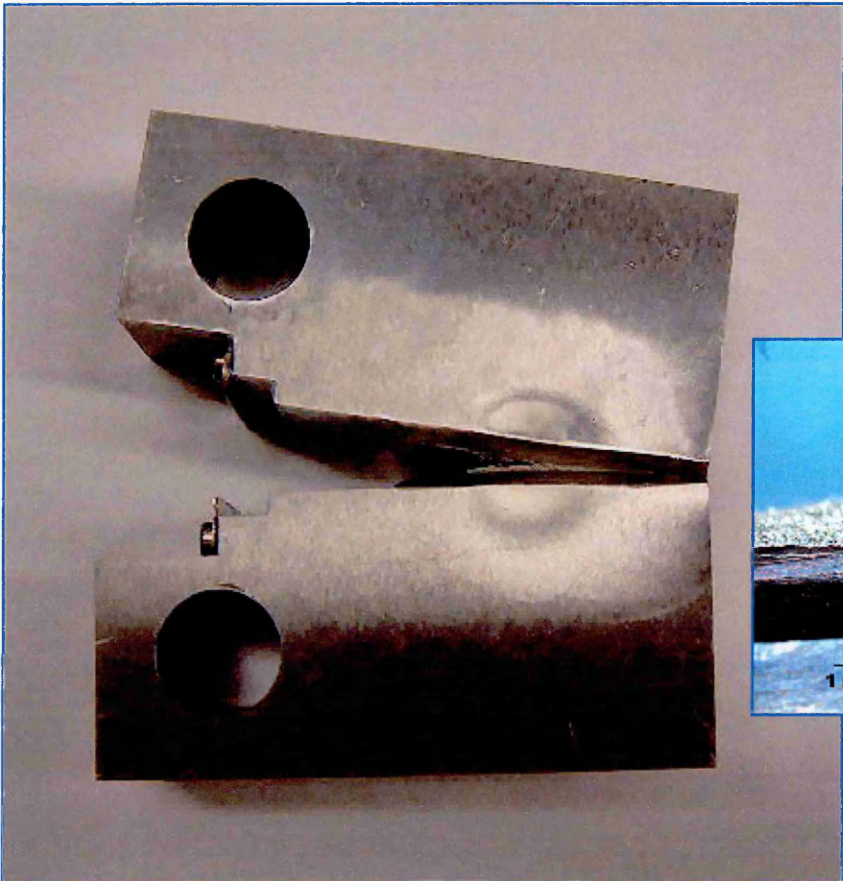


Figure 144 A.



Figure 144. Photograph of J7B prior to breaking open (side view).

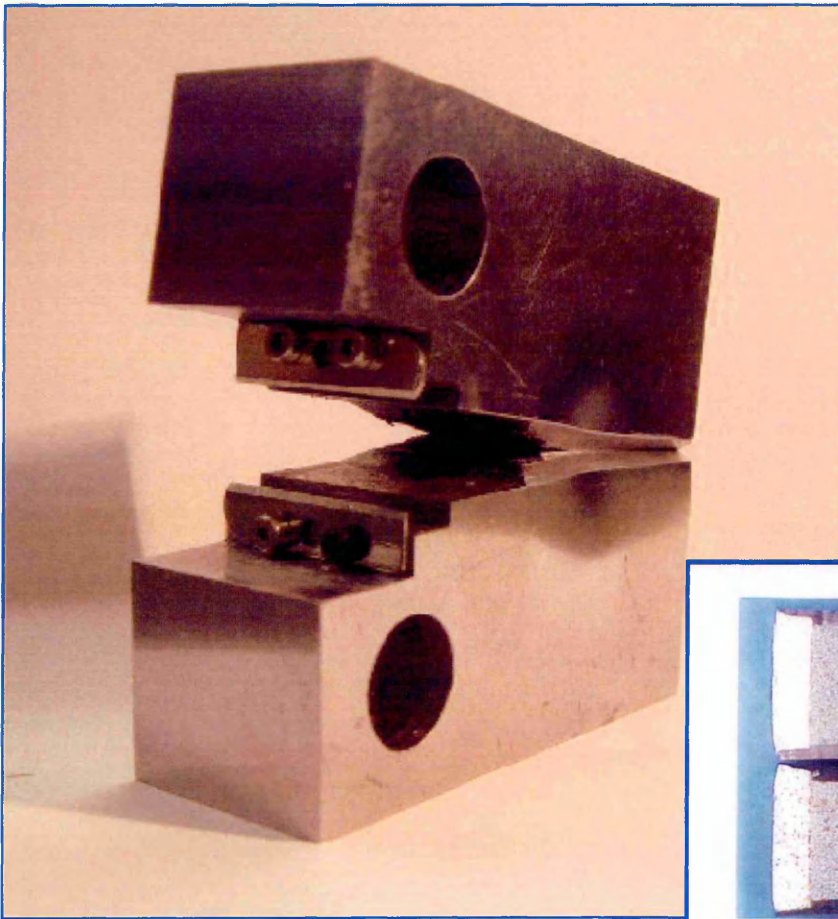


Figure 145 A.



Figure 145. Photograph of J1A prior to breaking open (oblique view).

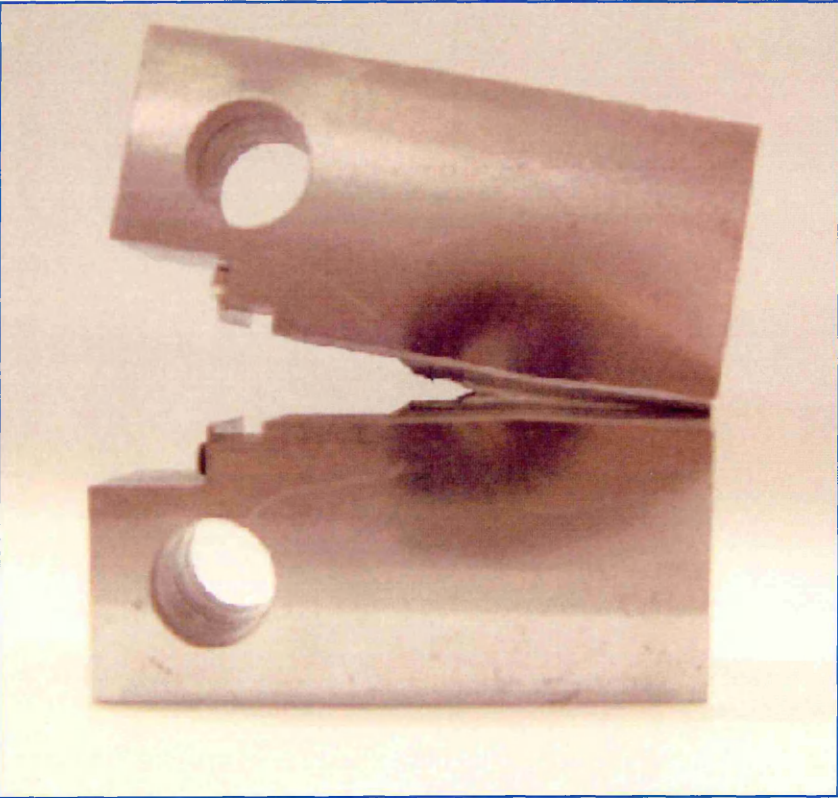


Figure 146. Photograph of J1A prior to breaking open (side view).

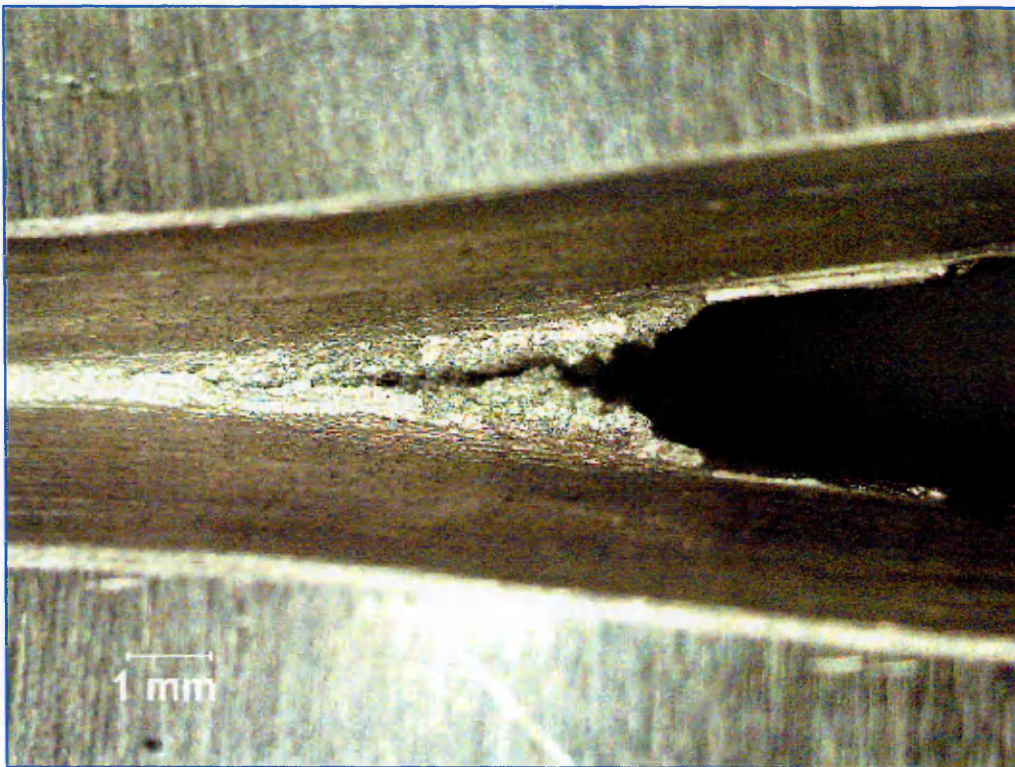


Figure 147. J1A 20°C, Mag x 17, total $V_{LL} = 6.6$ mm, $\Delta a = 2.12$ mm.

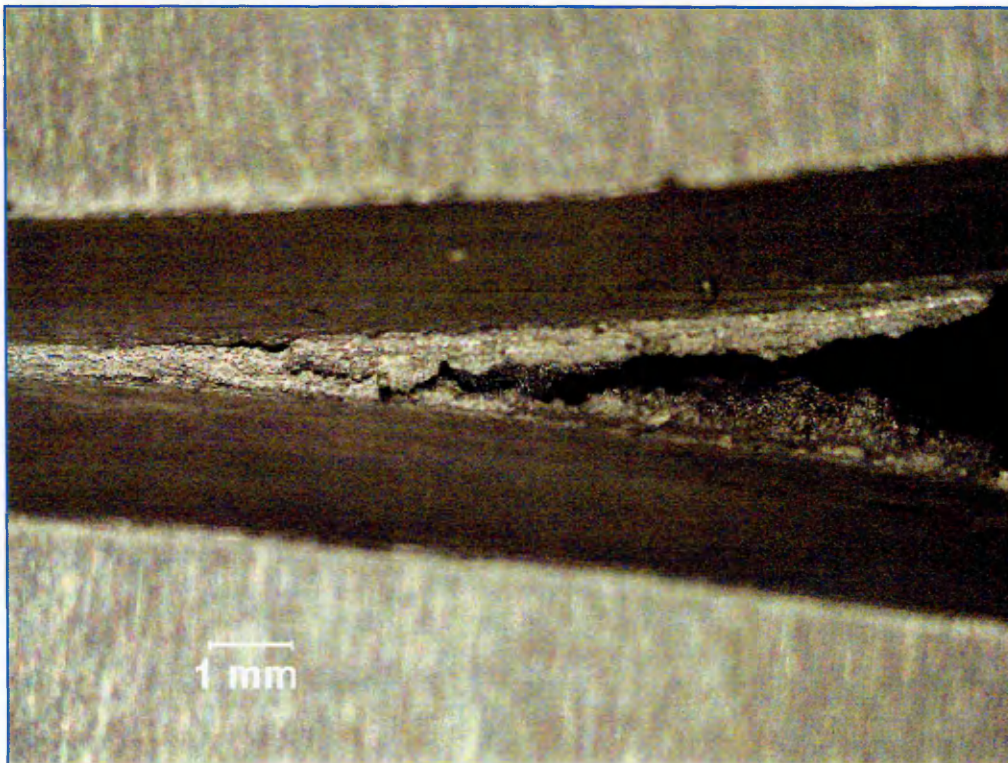


Figure 148. J7B 20°C, Mag x 17, total $V_{LL} = 6.6$ mm, $\Delta a = 8.55$ mm.

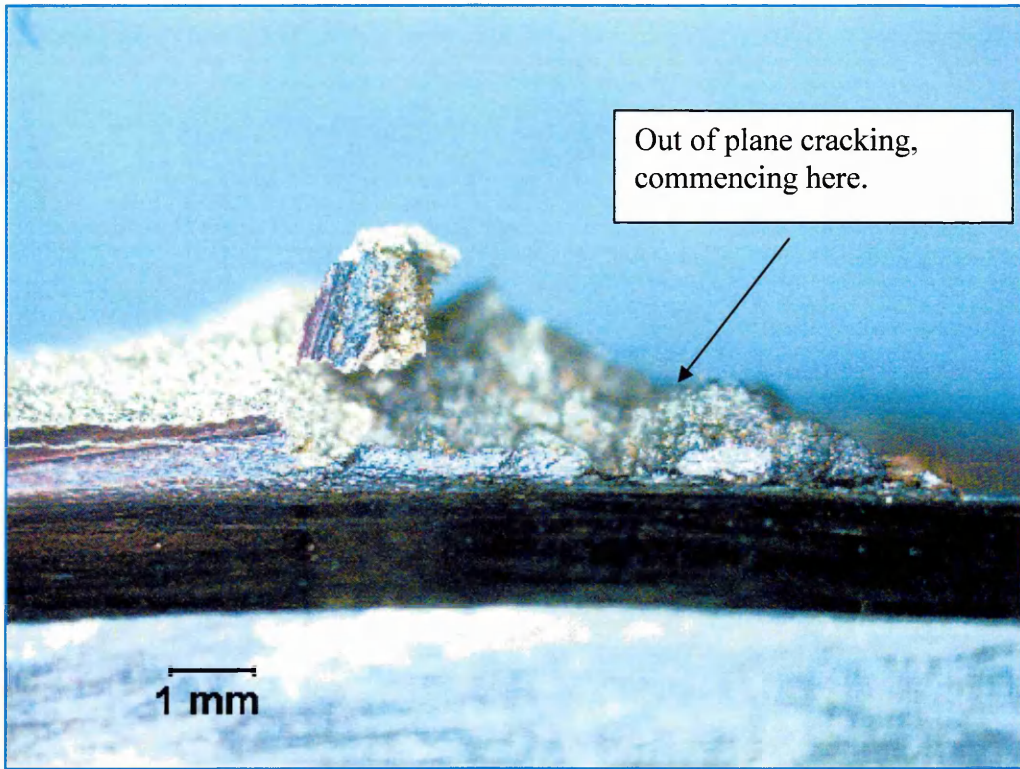


Figure 149. J7B. 20°C. Mag x 17, total V_{LL} 6.6 mm $\Delta a = 8.55$ mm.

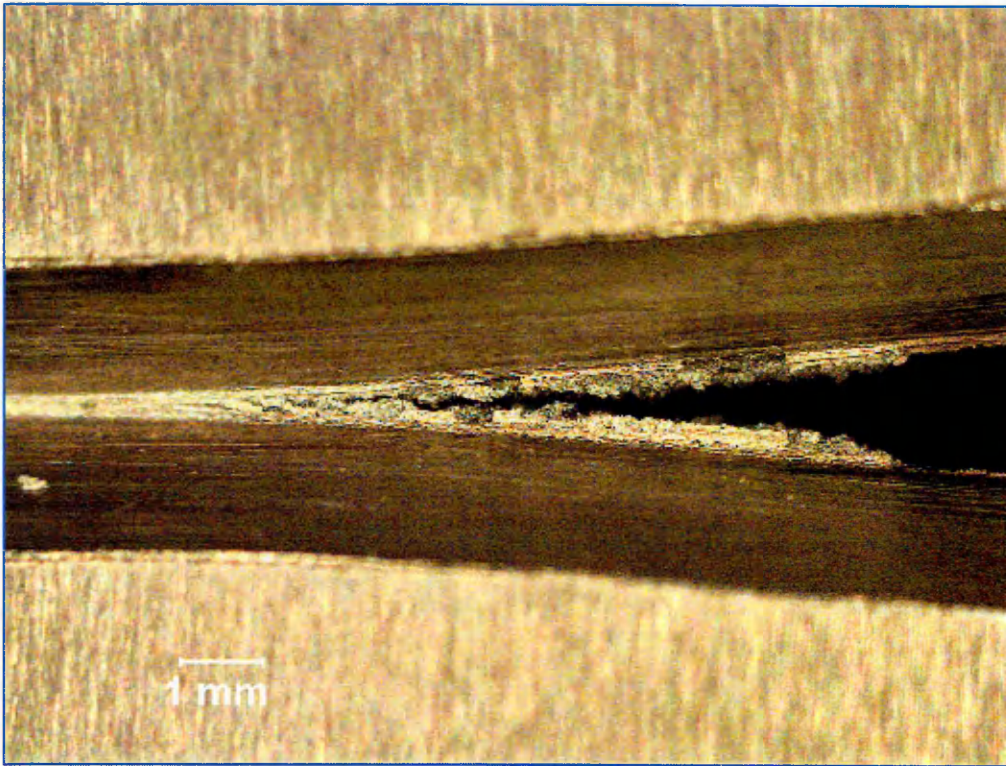


Figure 150. J2A 200°C, Mag x 17, total $V_{LL} = 5$ mm, $\Delta a = 5.01$ mm.

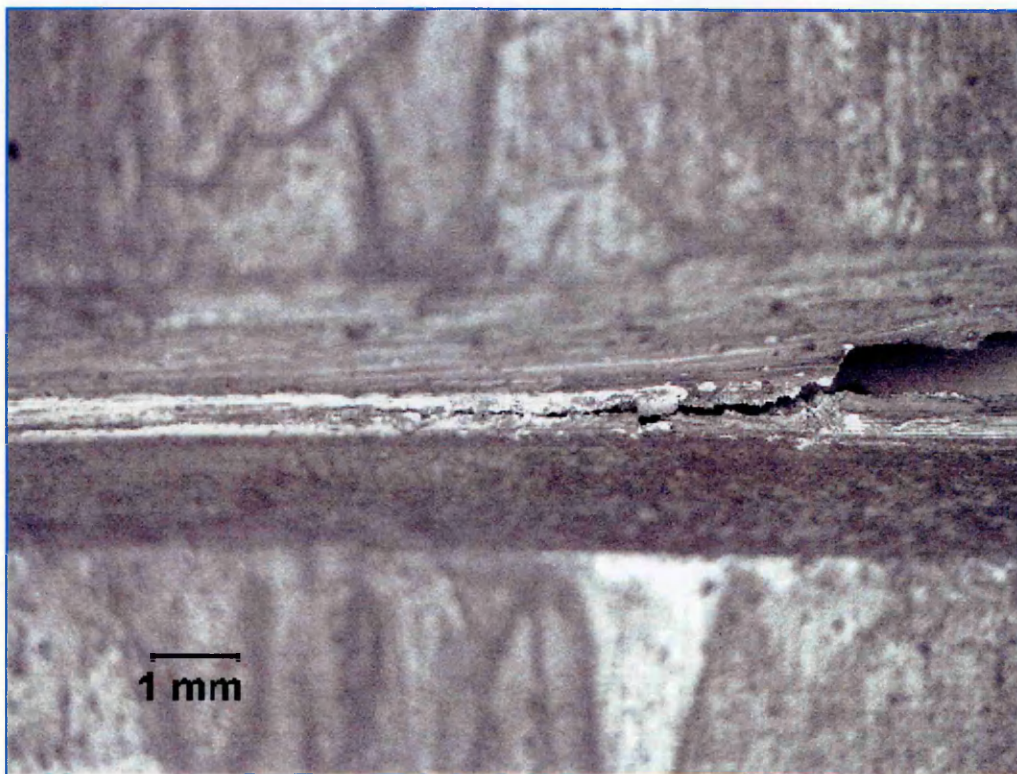


Figure 151. J3A. 200°C, 8ppm DOW, x17, total $V_{LL} = 3.19$ mm, $\Delta a = 2.10$ mm.

5. Discussion of results.

It has been appreciated for some time that the stress vs strain curve of a specimen of low carbon steel displays serrations in the work hardening region when tensile tested at slightly elevated temperatures [55,56,57,93,139,141]. This serrated behaviour also known as the Portevin LeChatelier effect, is accompanied by increased rates of work hardening, negative strain rate dependences of the flow stress, and reductions in ductility. In commercial steels, these phenomena are due to interactions during deformation between dislocations and primarily, solute nitrogen. Such regular pinning and unpinning is termed dynamic strain aging [132-142 & 156 - 160] and the most important variables are the temperature, deformation rate, and interstitial concentration [55,56,57,92,102].

5.1. Parameters used to characterise the effect of dynamic strain ageing in the tensile specimens.

According to Pickering [8] free nitrogen, either as precipitates or interstitially dissolved, markedly decreases the uniform strain and the substitutional solutes have a similar but much less marked effect. These effects can be described with respect to the flow stress and work hardening rate. Any element which increases the flow stress relative to the work hardening rate will decrease the value of uniform strain. An element which increases the fracture stress relative to the flow stress, as in the case of manganese will automatically increase the strain to fracture. Free nitrogen increases the fracture stress, but has little effect on the strain at fracture at room temperature [8,78], presumably because the increase in flow and fracture stresses due to nitrogen are virtually self canceling. The effect of sulphur is more detrimental on the total ductility.

Plastic instability depends directly on the work-hardening characteristics of a material. In steels which exhibit low-strain rate dependence of flow stress, uniaxial tension instability occurs when the work-hardening rate is insufficient to maintain the rate of decrease of the cross-sectional area. The strain to instability is controlled by the intersection between work-hardening and flow

curves (implied in the Considere construction). Therefore, higher strength steels (i.e., steels with elevated yield and flow stresses) show reduced elongation values .

A direct consequence of this generalisation is that the highest level of uniform strain is obtained with low strength steels. Further, although the pearlite content of the steel does not directly affect the yield strength, it reduces the Luder's extension and consequently increases the flow stress, again to a greater extent than it increases the work hardening rate, thereby reducing the maximum uniform strain. Consequently, low carbon low strength steels have been developed extensively for applications requiring the highest levels of formability [78].

The effects of various solutes on the flow stress, σ , at a true strain of $\epsilon = 0.2$, and on the work hardening rate ($d\sigma/d\epsilon$) at the same true strain are shown in Table 16 [78]. Although all of the solutes shown have greater effects on the flow stress than on the work hardening rate, the differential between the two effects is less in the case of silicon and phosphorus than for the other solutes (manganese and nitrogen). Thus, for a given increase in flow stress, the loss of uniform strain (or stretch formability) is least for those elements which produce the larger increase in work hardening rate, i.e. silicon and phosphorus.

Solute	Increase in flow stress at $\epsilon = 0.2$ MPa/wt%	Increase in W.H.R. at $\epsilon = 0.2$ MPa/wt%
Mn	68	23
Si	148	115
P	862	554
N	4004	1509

Table 16. Effect of solutes on flow stress and work hardening rate at a true strain $\epsilon = 0.2$ [78].

To verify the work of Pickering and Gladman and to characterise one of the effects of dynamic strain ageing the work hardening exponent n (generally an increase in n , is observed in the blue brittleness region) was calculated for seven of the eight of steel heats VS3764A, VS3764B, VS3783A, VS3783B, F8104, F8105, and F8106. Ideally the instantaneous load against the

instantaneous cross sectional area would have been used to give the true Cauchy stress, which would have given the true stress vs true strain curve. But since a diametral extensometer was not used for the tensile tests, the engineering stress vs engineering strain was converted to true stress (σ_T) and true strain (ϵ_T), through the relationships listed below.

$$\text{True stress } \sigma_T = \sigma(1+\epsilon) \quad (37)$$

$$\text{True strain } \epsilon_T = \ln(1+\epsilon) \quad (38)$$

Where σ is the engineering stress and ϵ is the engineering strain.

The flow curve of many metals in the region of uniform plastic deformation can be expressed by the simple power curve relation.

$$\sigma = K \cdot \epsilon^n \quad (39)$$

where n is the strain-hardening exponent and K is the strength coefficient. A log-log plot of true stress and true strain up to maximum load will result in a straight-line if eq. 39 is satisfied by the data (Figure 152). The linear slope of this line is n and K is the true stress at $\sigma = 1.0$. The strain-hardening exponent may have values from $n = 0$ (perfectly plastic solid) to $n = 1$ (elastic solid). For most metals n has values between 0.10 and 0.50.

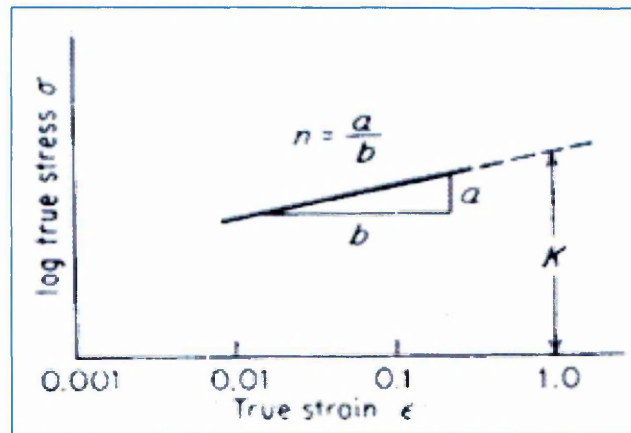


Figure 152. Log/log plot of true stress-strain curve.

The strains chosen for all the steel heats to determine n were from 5% true strain to 10% or to the UTS for those steel heats with smaller strains to the UTS. It is important to note that the true fracture stress is the load at fracture divided by the cross-sectional area at fracture. This stress should be corrected

for the triaxial state of stress existing in the tensile specimen at fracture. The triaxial stress state was taken into account for the true fracture stress. The true stress to the UTS in all cases was obtained as described. They are included in Tables 11 to 14 to illustrate the dynamic strain ageing effect, as it is an important parameter. Although the engineering stress could have been used to show the effect.

5.2. Discussion of the tensile testing results for VS3764A, VS3764B, VS3783A and VS3783B.

The stress vs strain curves displayed significant changes in appearance as the temperature was increased; this occurred at all the temperatures and strain rates investigated, in agreement with previous work [52,53,54,55,102,139,141]. A series of such curves for all specimens tested between room temperature and 350°C is illustrated in Figure 103 for VS3764A and VS3764B for the tests which showed serrations (charted load vs extension curves, for a strain rate of $2 \times 10^{-6} \text{ s}^{-1}$), and in Figures 114 for VS3783A and Figure 114A for VS3783B (for a strain rate of $2.67 \times 10^{-6} \text{ s}^{-1}$). At the lower strain rate, (64A and 64B) serrations began to appear in the work hardening region at about 100°C, with their magnitude and frequency decreasing as the temperature is increased to 200°C. At higher temperatures up to 350°C no serrations were observed. Only type A, B, and D serrations were observed in the tests which did show serrations (see Table 11).

In contrast in the tests done on steel heats VS3783A and VS3783B, serrations were observed in every test, at every temperature from room temperature up to 350°C, and throughout the entire stress vs strain curve, from the onset of the work hardening region to fracture. This was also observed by Keh [102] and Taheri [84]. Their magnitude and frequency increasing as the temperature is increased as observed by Keh et al [102] see Figure 153 and Taheri et al [84] see Figures 154 and 154a. Taheri's work also shows the strain rate dependency in the DSA regime (Figures 154 and 154a). All types of serration were observed A, B, C, D, and E as described by Robinson [93] and Rodriguez [139] (see Figure 28). They were of greater magnitude than the serrations observed in 64A and 64B.

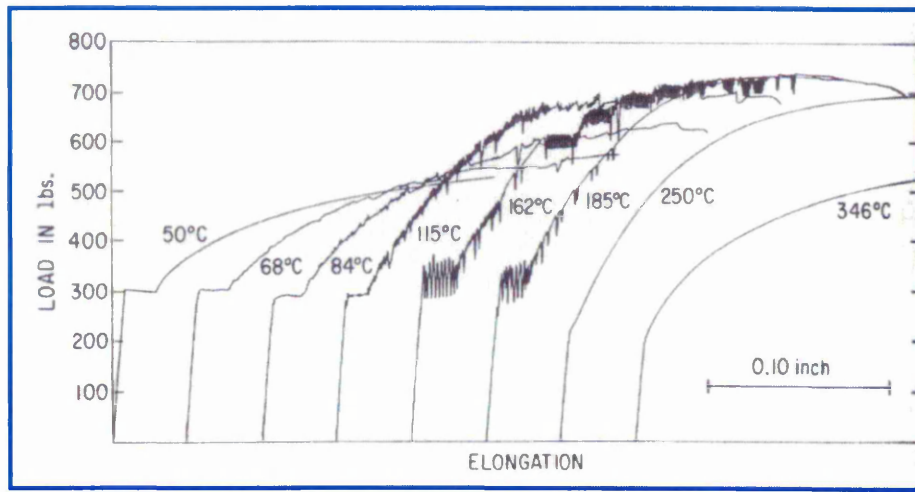


Figure 153. Load vs Elongation curves of a 0.035 C steel strained in tension at a crosshead speed of 0.0025inmin^{-1} (cross sectional area 0.014in^2 , gauge length 1") [102].

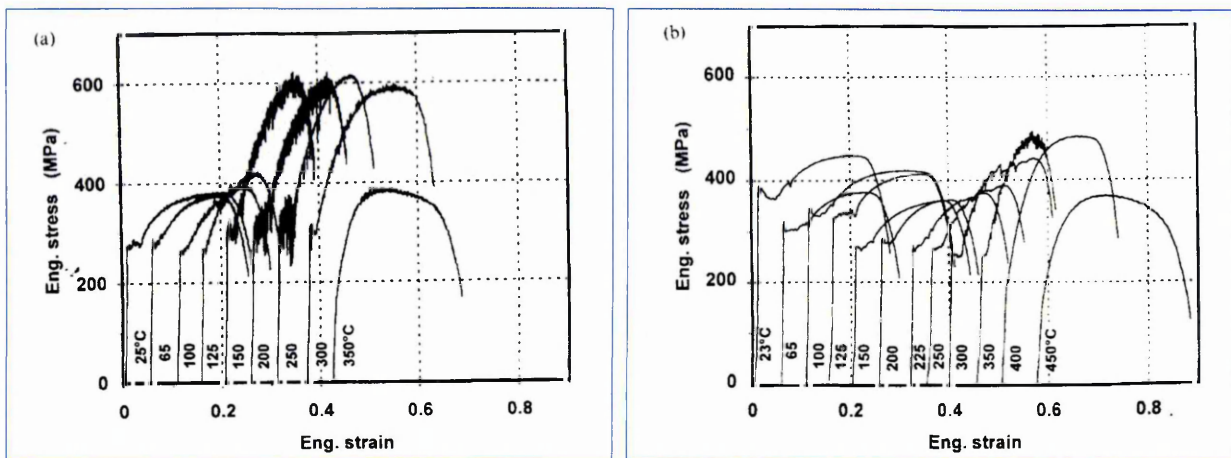


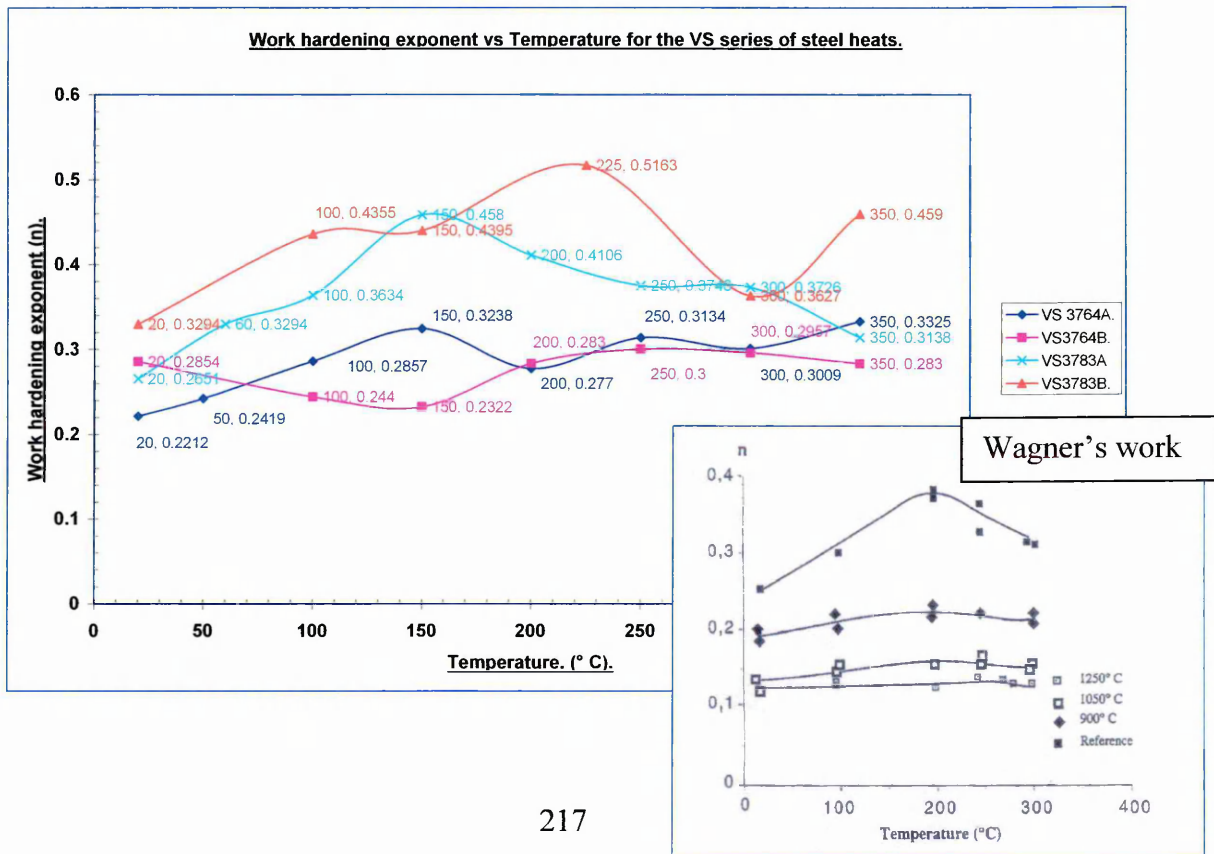
Figure 154. Stress vs strain curves (for specimens tensile tested at various temperatures and a strain rate of: (a) $\dot{\epsilon} = 10^{-5} \text{s}^{-1}$ (b) $\dot{\epsilon} = 10^{-4} \text{s}^{-1}$ [84].

Taheri's [84] work Figures 154a and 154b also reveals that the amount of the Luders strain depends on the testing temperature and strain rate. As was the case with this work see Tables 11, 12, and 13.

This dependence of the work hardening behaviour on temperature for the VS series of steel heats is shown in Figure 155 where the work hardening exponents are plotted as a function of temperature. In those cases where the curves were serrated, the stress levels at the mid-height of the serrations were selected to represent the flow stresses, fracture stresses, and UTS's. To show the variation in n as shown schematically in Figure 152 an example is taken from Wagner et al's work [48,85,86]. Inset in the graph (Figure 155).

Wagner et al [85] did tests on an AFNOR (French Standard) NFA 36205 grade A 48 steel. The purpose of the studies was to assess the decrease in fracture toughness of the weld metal relative to the base metal, using J fracture parameters and a local approach. In the temperature range of interest both materials displayed a maximum UTS at 200°C a ductility minimum located at 150°C for elongation and strain rate sensitivity, and 200°C for reduction of area. It was found both materials were sensitive to dynamic strain ageing. In view of the fact that the A 48 steel had a sulphur content of 0.012 wt% compared to the 0.007 wt% of the MMAW weld metal, both materials gave the above results see Figure 155 (inset in graph).

Figure 155. Work hardening exponents vs Temperature for VS3764A, VS3764B, VS3783A and VS3783B compared to Wagner's work [85].



It shows that the data obtained in this work follows the expected trend, that is an increase in n with temperature in the dynamic strain ageing regime.

To verify the work of Pickering and Gladman a comparison was made between VS3764A and VS3783A steel heats to illustrate the effect of n on the strain to UTS and to fracture. Bearing in mind that VS3764A and VS3783A are alike in chemical composition (see Table 5) and only differ in their free nitrogen and free carbon content. It can be seen from Tables 11, 12, and 13 for the two steel heats that:

1. VS3783A has lower true strains to fracture in every case at every temperature over VS3764A and VS3764B (see Figure 128).
2. The effect of free nitrogen is to raise the flow strength (see Figure 115). Though the effect on the yield strength is minimal (see Tables 11, 12, and 13).
3. VS3783A has higher work hardening exponents (n) and strength coefficients (K) than VS3764A and VS3764B for all of the tests done (see Figure 155).
4. VS3783A also has higher uniform strains (ϵ_U) to the ultimate tensile strength and elongations to fracture over VS3764A and VS3764B in every test done.
5. VS3783A has lower ductility in reductions in area (Z) in all of the tests over VS3764A and VS3764B in every test done. The minimum in ductility for reduction in area for steel heat VS3783A was 150°C, 200°C for VS3764A and VS3764B, and 150°C for VS3783B.
6. Serrated flow is present in every test for VS3783A, but it is only seen in one of the seven tests done on VS3764A. The serrations observed on VS3783A are also larger. More serration types are also seen in VS3783A.

7. The Luder's strain is present in five of the tests done on VS3783A, at 20°, 60°, 100°, 150°, and 200°C whereas it is not present in any test on VS3764A. It is only present in one test for VS3764B at 100°C. It is also present in three of the tests done on VS3783B at 20°, 100°, and 150°C.

8. The maximum in the ultimate tensile strength was obtained by steel heat VS3783A (666.5 MPa) at a temperature of 200°C, then VS3783B (650 MPa) at 150°C, then VS3764A (582.9 MPa) and finally VS3764B (580.9 MPa) both at 200°C.

9. The true fracture stress for VS3783A is higher than VS3764A in five of the six tests done, and higher than VS3764B for all the tests done.

10. For VS3783A and VS3783B the minimum elongation to fracture occurs at a temperature of 100°C, for VS3764A and for VS3764B the temperature is 150°C.

Points 3 and 8 verifies the work of Gladman and Pickering in that VS3783A has higher work hardening exponents and this is reflected in larger strains to UTS. VS3783A has higher true fracture stresses, and this can only be attributable to the higher free nitrogen content.

Green and Knott [253] in their work found that if more work hardening can occur, that the strain distribution ahead of the crack tip, yet local to it, is more widespread, because each successive increment of strain cause hardening which cause the next increment of strain to occur in different positions. As a result far more "*uniform strain*" occurs before the condition for final necking.

What is interesting to note is that in Figures 114 and 114A the stress vs strain curves for VS3783A and VS3783B, (more so in VS3783A) is that plateau's of serrations can be seen prior to reaching the UTS this was observed by Leslie et al [102,109] suggesting that the localised exhaustion of free nitrogen prior to the UTS, was more difficult in the higher free nitrogen steel.

For VS3764A and VS3764B the specimens oriented in the longitudinal direction (rolling direction), exhibited greater strains to the UTS point and to failure, for all the specimens. Although one specimen 64BT3 (steel heat VS3764B) did exhibit higher ϵ_u and ϵ_f strains, but this was attributable to a larger initial diameter than the VS3764A (64A5) specimen. For calculation purposes this was normalised in calculating the engineering stress. The trend observed from the results was that all the specimens from the steel heat VS3764A, exhibited larger ϵ_u and ϵ_f strains, than the VS3764B specimens.

The transverse results show a similar trend, although only four specimens were tested (see Table 11), two from each steel heat at temperatures of 20°C and 200°C. An unexpected result was obtained at 200°C, the VS3764A specimen (64AT1A) failed before the VS3764B specimen (64BT1A) in both the strains to UTS (ϵ_u) and fracture (ϵ_f), but on closer examination of the fracture surface, it was revealed that the VS3764A heat specimen had more inclusions see Figure 107. This is possible as all of the four specimens were taken from the cut off point of the ingot where the specimen was forged.

Figure 106 shows five photographs of VS3764A tensile specimens, after testing in air from 20°C to 250°C at a strain rate of $2 \times 10^{-6} \text{ sec}^{-1}$. Here the change in fracture mode is evident i.e. from cup and cone fracture at 20°C to the characteristic shear fracture in the blue brittle range. Maximum UTS was attained at 200°C also the maximum shear fracture indicative of strain localisation.

It can be seen from the SEM photographs (Figures 108 to 113) that microvoid coalescence is more pronounced in steel heat VS3764A at 20°C and even at 200°C. In VS3764B there are more featureless zones.

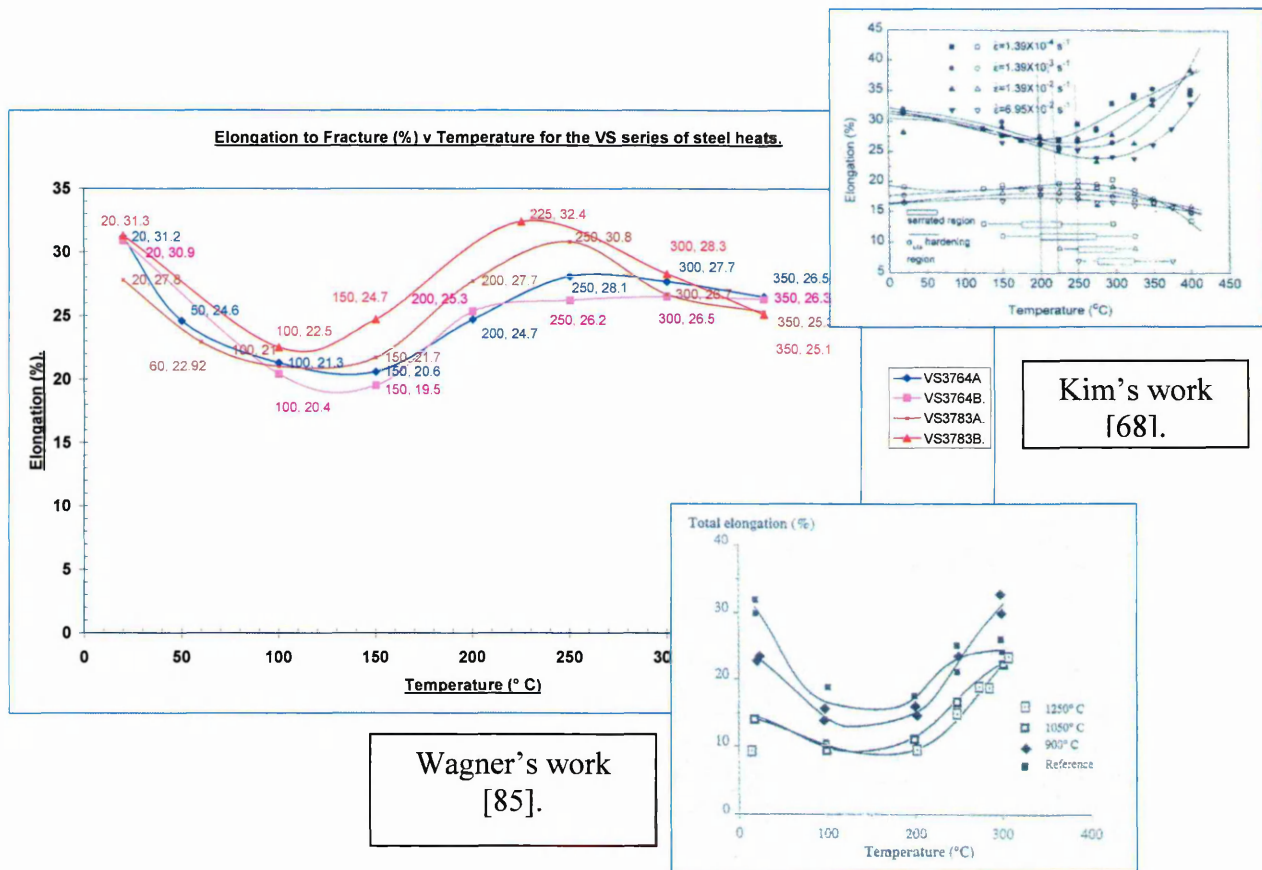
5.2.1. Discussion of the Ductilities and Flow Stresses for VS3764A, VS3764B, VS3783A and VS3783B.

The dependence of the fracture strain (elongation to fracture) on test temperature is illustrated in Figure 122 for the VS series of steel heats, and the

true strain to fracture for all the steel heats in Figure 128. It is evident that there is a considerable reduction in ductility at intermediate temperatures.

The minima in the fracture strains, shown in Figures 122 and 128 are in accordance with the findings of other investigators [68,85,86,92,142]. Kim et al [68] and Wagner et al [85] attributed these minima to the optimal locking of stationary dislocations under conditions where the mobile dislocations remain unpinned. Dynamic strain aging has also been considered to reduce the fracture strain in mild steel by promoting the lining of up of voids [97]. Thereby creating an excess of edge dislocations [167,184]. Figure 156 shows the results of their work (inset in the graph) compared to this work.

Figure 156. Elongation to Fracture vs Temperature for the VS series of steel heats compared to Kim et al [68] and Wagner et al's [85] work.



The flow stress peaks produced by varying the temperature, (Figures 115, and 129) are considered to be major features of dynamic strain aging [55,75,142]. The increased stress seems to result from the pinning and regeneration of dislocations. From dislocation density measurements it is clear

that these peaks are associated with an enhanced rate of dislocation multiplication [102,112].

Another important effect associated with dynamic strain aging is the negative rate dependence of the flow stress, which is displayed on the low temperature side of the ductility minimum [55,75,92,142]. The flow stress decreases when the strain rate is increased. It has been shown that, if as a result of the negative rate dependence, flow can take place at a lower stress, then straining will lead to unstable deformation and to eventual flow localisation [75,134]. Measurements of the mobile dislocation density carried out by various workers indicate that ρ_m increases continuously and almost linearly with strain [134].

It can be seen in this work, that the elongation to fracture depends on, the temperature and free nitrogen as the strain rates are comparable. These minima are located at temperatures below those associated with the UTS peaks for all the steel heats.

5.2.2. Discussion of the Effect of Free Nitrogen Content for VS3764A, VS3764B, VS3783A and VS3783B.

The general features of dynamic strain aging in steels with different chemical compositions, prior heat treatment, and production procedures have been described by several workers. [54,55,102,109]. It is generally accepted that these effects are due to the interaction between mobile dislocations and active interstitial solutes, mainly nitrogen in commercial steels [108,132-136]. Solute concentrations as low as 10 ppm are considered sufficient to produce dynamic strain aging in these materials [55,75,109].

Previous workers have demonstrated that nitrogen is primarily responsible for dynamic strain aging effects in commercial steels, and that the minimum temperature for serrated flow decreases as the nitrogen content is increased [55,75,142]. This is illustrated in Figure 115 in that VS3764B has a free nitrogen content of 12ppm and the UTS peak is at 200°C, VS3783B has a free

nitrogen content of 36ppm, and has a UTS peak at 150°C. The UTS peak for VS3783B is shifted to the left by 50°C for an increase in free nitrogen of 24 ppm. Both the steels were tested at comparable strain rates. The decrease in strain rate (from $2.67 \times 10^{-6} \text{ sec}^{-1}$ for VS3783B to $2 \times 10^{-6} \text{ sec}^{-1}$ for VS3783A) was considered to be too small to cause a temperature shift of 50°C to 200°C [248].

Many investigations have been performed on the effects of nitrogen in steel. The first cited in this work to illustrate the effect of increasing nitrogen content on the elongation to fracture is taken from 1953. The authors Darken and Curry [246] citing the work of Tschischewski (1915) on the effect of nitrogen in decreasing the elongation of a wire 0.63mm in diameter. This is shown in Figure 157 (the nitrogen content specified is total nitrogen). Tschischewski found like many other authors the embrittling effect of nitrogen, which is accompanied by an increase in strength. Tschischewski noted that a total nitrogen content of 0.3%, the wire broke and at 0.4% nitrogen, it broke like glass.

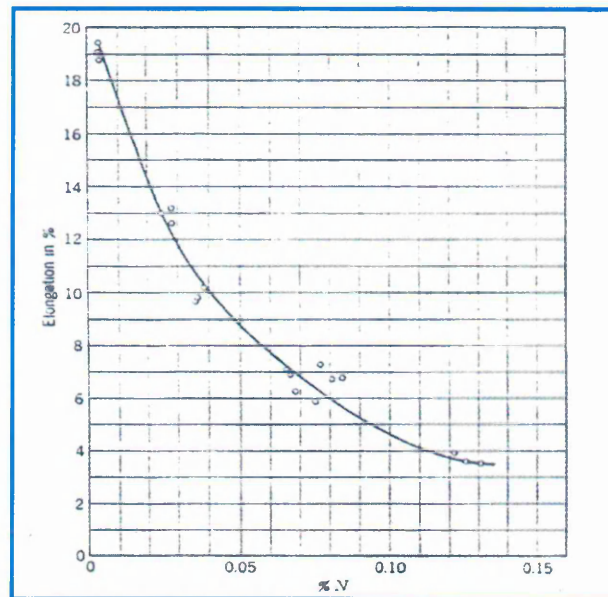


Figure 157. The effect of Nitrogen content on the elongation of iron wire strained in tension [246].

Baird and Jamieson [142] carried out a study of the effects of separate and combined additions of up to 1.6% Mn and up to 0.04% N on the tensile

properties of iron in the range 20° - 600°C. The compositions of the steels studied and their manganese, nitrogen and carbon content are given in Tables 17 and 18. They found that at all temperatures, nitrogen addition gives greater increase in yield stress in the presence of manganese than in its absence and at high temperatures the rate of strain hardening is also greater. These effects were ascribed partly to a solid solution hardening mechanism due to pairs or small clusters of manganese and nitrogen atoms. They also found that this hardening persists up to much higher temperatures than solid solution hardening due to nitrogen alone. A second effect is that dynamic strain age hardening due to nitrogen persists to higher temperature in the presence of manganese due to the reduction in mobility of nitrogen atmospheres around moving dislocations.

Alloy designation*	C	Si	S	P	Mn	Ni	Cr	Cu	Sn	O ₂	Ce
a Fe	0.036	0.004	0.0025	...	0.002	0.004	0.008
b Fe-0.55Mn	0.08	0.01	0.012	0.004	0.55	0.02	0.01	0.001	0.001
c Fe-1.0Mn	0.06	Nil	0.011	0.007	1.02	0.03	0.01	0.001	0.001
d Fe-1.6Mn	0.04	0.02	0.015	0.005	1.61	0.02	0.01	0.001

* Casts a, b, c vacuum-melted; cast c air-melted; ... denotes not analysed

Table 17. Composition of the base alloys used in Baird and Jamieson's work [142].

Alloy designation	Manganese, %	Carbon, %	Nitrogen, %
Fe	0.002	0.0010	0.00035
Fe-0.55Mn	0.55	0.0009	0.00035
Fe-1.0Mn	1.02	0.0013	0.00010
Fe-1.6Mn	1.61	0.0011	0.00055
Fe-0.01N	0.002	0.0010	0.009
Fe-0.55Mn-0.01N	0.55	0.0009	0.009
Fe-1.0Mn-0.01N	1.02	0.0013	0.0082
Fe-1.6Mn-0.01N	1.61	0.0011	0.011

Table 18. Manganese, carbon, and nitrogen contents used in Baird and Jamieson's work [142].

The effects of nitrogen additions of 0 - 0.04% on the tensile properties of the iron and of the Fe - 1% Mn alloy were studied at three temperatures, 20°, 225°, and 600°C.

and 450°C. The tensile results for the elongations to fracture of the Fe and Fe – Mn base alloys, with varying nitrogen contents are shown in Figure 158.

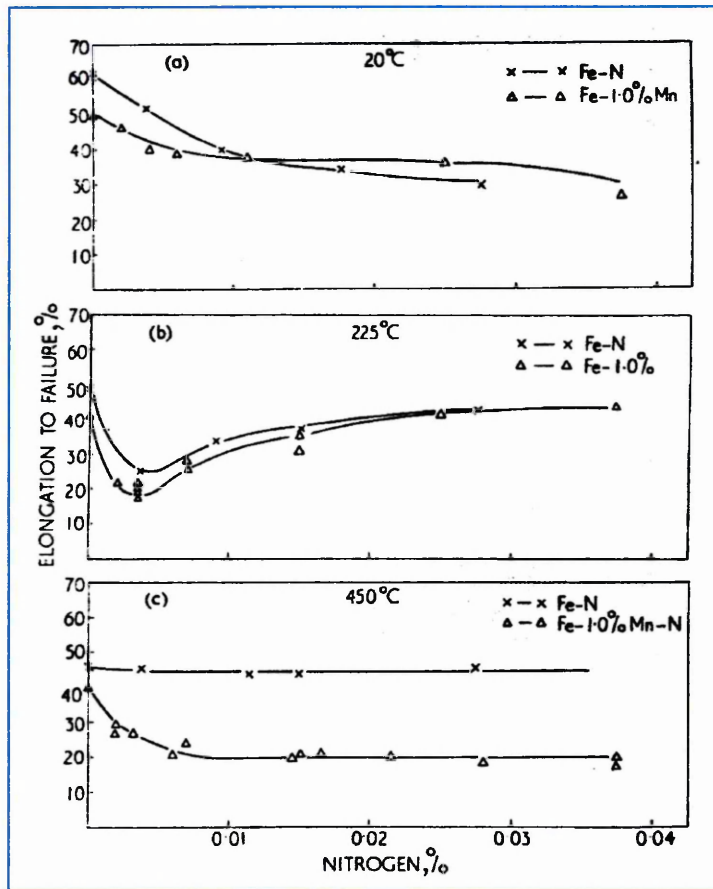


Figure 158. Elongation to Fracture of Fe and Fe – 1% Mn base alloys with varying nitrogen contents at (a) 20°C (b) 225°C and (c) 450°C [142].

Another interesting feature Baird and Jamieson found in their work was the the elongations to fracture of some of the tensile tests done. At 200°C and 450°C the effect of nitrogen on ductility is in general the converse of its effect on strength properties, but at 225°C, although the strength properties show a continuous increase with increasing nitrogen content, the elongations to fracture show a pronounced minimum at 0.003%N, while large additions of nitrogen completely restore the ductilities of the base alloys this can be seen in Figure 158. Thus a loss in tensile ductility does not necessarily accompany dynamic strain ageing. This was also observed by Wagner [48,85,86], Taheri [84], and Abe [247].

Baird thought that this behaviour at 225°C could be linked to the form of the stress vs strain curves and to the appearance of the fractured specimens. With low nitrogen additions the specimens strain hardened rapidly in the initial stages and showed low amplitude serrations on the stress vs strain curve. However, at a critical strain, some serrations of very large amplitude began to occur, after several of which the specimens broke. The test piece showed the same number of deep narrow Luder's bands as there had been coarse serrations in the curve, and it was clear that fracture had occurred at one of these bands of intense highly localised deformation. As the nitrogen level was increased, the critical strain at which these coarse serrations began also increased, and the onset of fracture was thereby delayed. Baird postulated that the zones where highly localised deformation occurred were regions in which the nitrogen available for strain aging had become exhausted. Once initiated, these regions continued to deform until they either work hardened up to the strength of the surrounding regions or fractured.

Figures 117 and 118 show the engineering and true strains to fracture vs free nitrogen content (in weight %) for 64A and 83A. The steel heats have comparable sulphur contents and only differ in their free nitrogen content (see Table 5). From the work of Tschischewski (Figure 157) and Baird (Figure 158c), it can be seen that the elongations to failure vs nitrogen content, follow a power law equation of the form $y = ax^{-n}$. Based on this trend lines were fitted to the data points. Even though only two data points were plotted for each temperature, one for each steel at the same temperature. It can be seen that a family of curves are produced that move down the y axis, as the temperature is increased, the equations of which are given in the right hand side of the Figures 117 and 118. That is the strain to failure decreases with increasing temperature. The higher free nitrogen steel exhibiting lower true strains to fracture in every case, with the exception of steel (83A), when the elongations to fracture followed the same trend for temperatures of 20°, 60°, 100°, 300° and 350° C, but the trend was reversed at temperatures of 150°, 200°, and 250°C.

Figure 117 illustrates the increased free nitrogen content on the elongations to fracture, in the DSA regime for 64A and 83A. The increase in

the work hardening exponent, results in larger uniform elongations to UTS, and hence elongations to fracture [78,253].

5.2.3. Discussion of the Effect of Sulphur Content for VS3764A, VS3764B, VS3783A and VS3783B.

Figure 119 shows the true strain to fracture vs sulphur content, and Figure 120 shows the true strain to fracture vs volume fraction for the VS series of steel heats. The volume fraction was calculated according to Franklin [237] minus the oxygen term as the oxygen content was not specified by Corus from whom the steel was purchased. The volume fraction and corresponding strain to fracture is at the side of the relevant data point in Figures 119 and 120.

It has been found that a reciprocal type of relationship between toughness and inclusion volume fraction has been found for many inclusion systems [9,10] (see Figure 3). Likewise a similar behaviour has been observed for the effect of volume fraction on tensile ductility [11-17] (see Figure 4) and plane strain fracture toughness [18].

From the point of view of void initiation Ashby's model [14,15] predicts an inverse relationship between inclusion size and the stress required for void initiation, and this tends to be confirmed by Palmer's [16] observations of voids associated with very small SiO₂ particles in copper.

From the work of Edelson and Baldwin [12] (Figure 4) and Ashby et al [14] (Figure 5), it can be seen that the true strains to failure vs sulphur content, follow a power law equation of the form $y = ax^{-n}$. Based on this a comparison was made between 64A and 64B. Trend lines were fitted to the data points for 64A and 64B, although data points are included for all the VS series. Even though only two points were plotted for each temperature, one for each steel at the same temperature, it can be seen that a family of curves are produced that move down the y axis, as the temperature is increased, the equations of which are given at the top hand side of the Figures 119 and 120. That is the strain to failure decreases with increasing temperature. The higher volume fraction steel

exhibiting lower strains and elongations to fracture in every case.

From Figures 119 and 120 and Tables 11,12, and 13, it can be seen that within the range of sulphur contents examined for the VS series of steel heats, higher fracture strains were obtained, with a lower volume fraction of inclusions in the steel heat. Even though the trend followed the literature reviewed, the strains to fracture were higher than expected. With ten times more sulphur in one steel heat than in the other for example 64B vs 64A the reciprocal relationship of Ashby et al [14] and Edelson and Baldwin [12] predicts lower fracture strains for VS3764B. However, these models neglect stress triaxiality and according to Thomason [2,3] this is one of the main shortcomings of the model and this work reflects that. It is also thought that another possible reason is the distribution and orientation of the inclusions, brought about by the forging process. Gladman's [220], work is used to illustrate this.

According to Gladman [220], the stress concentration (and hence the strain concentration) is dependant upon the frontal radius of curvature. The concept of the frontal radius of curvature is illustrated in Figure 159. For particles suffering complete decohesion, as is the case for non metallic inclusions, the void size starts with a size equal to the inclusion. Void growth occurs in the direction of the tensile stress. The presence of the hard non-deformable inclusions maintains the void at its original dimension normal to the stress axis. As the void grows in the tensile direction, the radius of curvature decreases, and the strain concentration at the edge of the void decreases throughout void growth.

Thus the volume fraction of voids present at any given strain is dependent upon the initial volume fraction of voids and also upon the aspect ratio of the inclusions. The rate of increase in void fraction with strain also increases as the aspect ratio of the inclusion decreases. That is inclusions present as prolate spheroids with their long axis parallel with the tensile force result in lower volume fractions of void than do oblate spheroids with their short axis parallel with the tensile force, at any given strain [78].

The steel heats used in this study were received from Corus as ingots

(vacuum induction melted) each 45 cm x 150 cm x 150 cm. They were forged at Corus Stocksbridge, to a section of 20 cm x 4cm x 7.5cm. The forging temperature was done between 1250°C to 900°C followed by air cooling as discussed in the experimental section. Two of the above section sizes were obtained for each of the steel heats from the original ingots.

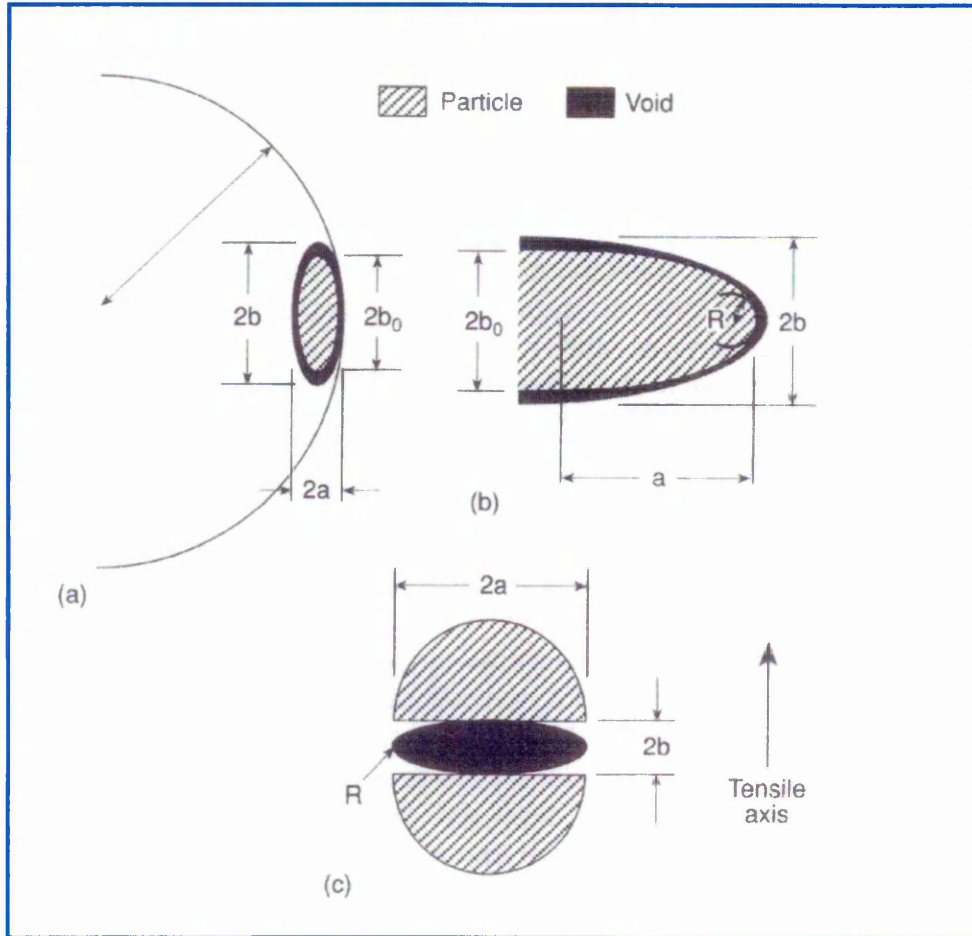


Figure 159. Illustration of the concept of the frontal radius of curvature for voids formed at second phase particles during plastic straining. The void growth during straining is proportional to the frontal radius of curvature (a) Prolate spheroid – large frontal radius of curvature (b) oblate spheroid – small frontal radius of curvature (c) particle cracking [78].

It is thought that with the material being upset forged, without rolling that the majority of inclusions present would have been in the prolate spheroid form in VS3764B due to the nature of the forging process [1], and this accounted for the difference.

If this was the case then the strain to fracture decreases as the shape of the inclusion changes from being elongated in the direction of tensile straining to being elongated in a direction normal to the tensile straining axis. That is the distance between neighbouring voids (the ligament is increased for VS3764B) in Thomason's model [2,3] in Figures 1 and 2, hence larger strains to fracture.

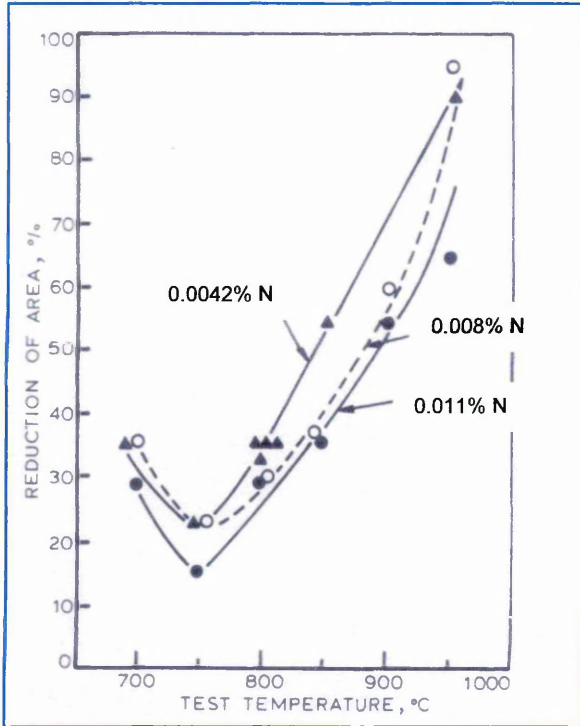
5.3. Discussion of the tensile testing results for F8104, F8105, and F8106.

It can be seen from Table 6, that the sulphur contents of F8104, F8105, and F8106 are comparable, so no data was plotted against the sulphur content or volume fraction of the steel heats.

5.3.1. Discussion of the effect of free Nitrogen on the Ductilities and Flow Stresses for F8104, F8105, and F8106.

The results of the slow strain rate tests done in air are given in Table 14 for the steel heats F8104, F8105, and F8106. Figure 126 shows the engineering elongation to UTS and to fracture for the heats from which it can be seen and that the steel with the lowest free nitrogen content F8106 has the largest elongation to fracture for all the testing temperatures. Then F8104 and finally F8105, this corresponds to free nitrogen contents of 1.45ppm, 8ppm, and 54ppm respectively. This trend is followed for the reduction of areas [68,85,86,251] for all the the steel heats see Figure 130. Although not associated directly with conventional mechanical properties there is a detrimental effect of nitrogen which is directly relevant to the production of structural steel. It has been found that nitrogen promotes the hot cracking of continuously cast slabs through its adverse effect on hot ductility see Figure 160 [251]. In this example Mintz and Arrowsmith [251] studied a C – Mn – Al – Nb steel in which the niobium and aluminium contents were kept constant as shown in Figure 160.

Figure 160. The influence of nitrogen on the hot ductility of a C- Mn-Al- Nb HSLA steel [251].



Although the influence of nitrogen, as shown in the figure, is not large. It is greatly magnified by an increase in aluminium level. As the aluminium content increases from 0.03 to 0.05%, the minimum ductility, as measured by the reduction of area in the tensile test, is spread over a wide range of temperatures up to 950°C. The reason for this adverse effect of aluminium and nitrogen is that AlN particles can precipitate and pin grain boundaries. Thus reducing the tensile stresses induced during

casting. It has been found [251] that by making a small addition of titanium the free nitrogen content is reduced with improved hot ductility.

Figure 129 shows the increase in UTS vs temperature for all the steels tested. The maximum in ultimate tensile strength for the F81 series of steel heats was F8105 (732 MPa), then F8104 (648MPa), then F8106 (569MPa). Figure 161 compares the results obtained in this work with the published work of Wagner [85,86] and Kim [68] inset in the graph .

Kim's work shows the effect of strain rate in the DSA regime in that increasing the strain rate shifts the UTS peak to higher temperatures.

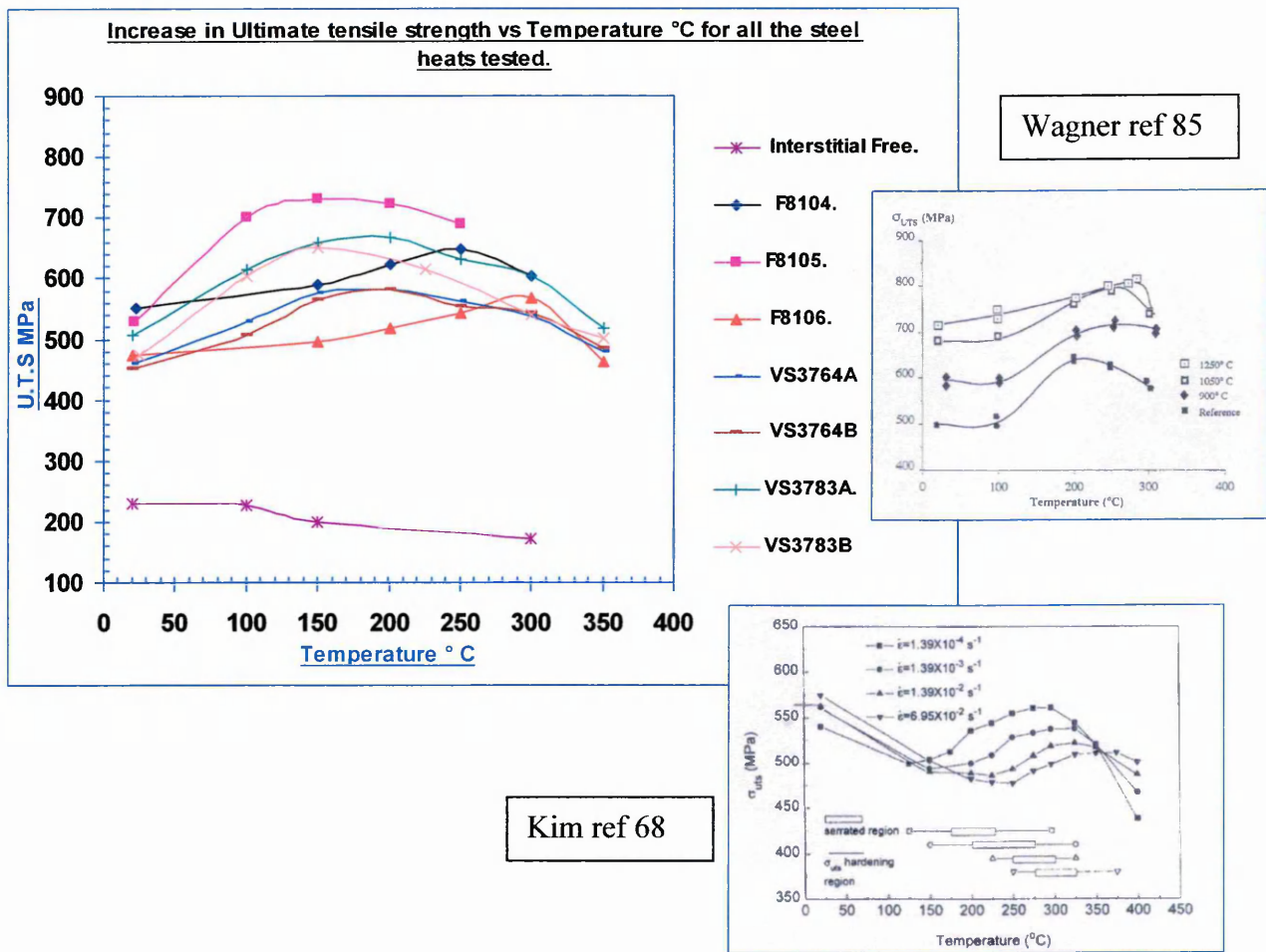


Figure 161. Comparison of increase in UTS for VS3764A, VS3764B, VS3783A, VS3783B, F8104, F8105, F8106 and Interstitial Free steel with refs [67,68,85].

The variation in work hardening exponent with temperature is shown in Figure 162, inset in the graph is the data obtained by Wagner et al [85,86] the same data was inset in Figure 154 for the VS series of steel heats. This time the data is more systematic, in that the work hardening exponent increased with temperature to a maximum, for each of the three steel heats, and this was coincident with the maximum in UTS in each case in agreement with Wagner [85,86]. It can be seen from Table 14 that F8105 has the highest strength coefficients, then F8104, and finally F8104, in the DSA regime in every case.

Wagners data.

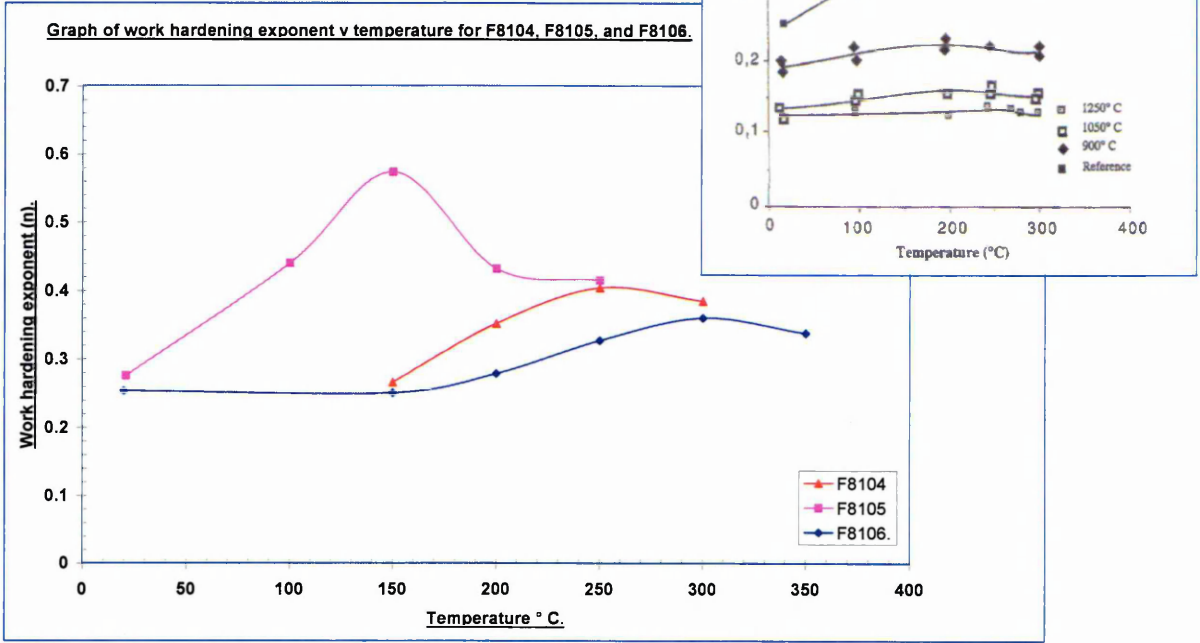


Figure 162. Work hardening exponents vs Temperature for F8104, F8105, and F8106.

5.3.2. Discussion of the Effect of Free Nitrogen on the Stress vs Strain curve for F8104, F8105, and F8106.

Figure 123 is a collage of the charted load vs extension cuves for the heats showing the specimens which had maximum serration height and maximum Luders deformation. Figure 124 shows the engineering elongation to fracture vs free nitrogen for the heats. Figure 125 shows the true strain to fracture vs free nitrogen for the heats.

Increasing the free nitrogen content one would expect the fracture stress to rise [8,78] so it should follow that steel heat F8105 should have the highest fracture stresses. This is not the case. From the Table 14 it can be seen that the medium nitrogen steel (F8104) has the highest fracture stress, then F8105, and finally F8106. This is in agreement with Baird and Jamieson [142] in that there must be a limit to the strengthening effect of free nitrogen. In that they found

increasing the nitrogen content in their work restored the ductility in tests at elevated temperature.

The highest amplitude serration is seen in F8104 tested at 150°C this was 43MPa but this was seen in the Luders plateau, and was a B type serration. The average height of the remaining serrations up to ultimate tensile strength was 21MPa to 25MPa and were mainly type A (see Figure 123b). F8105 tested at 150°C has the biggest amplitude serrations over the entire stress strain curve averaging 30MPa in height, (see Figure 123a) and this is maintained up to the ultimate tensile strength. They are mainly B type serrations. The last stress strain curve (c) in Figure 123 is for F8106 this specimen tested at 150°C, this was the only other specimen which exhibited a Luders plateau and serrations, the average amplitude of the serration up to ultimate tensile strength was 15 MPa to 16 MPa. The serration type was mainly type A and E.

Figures 124 and 125 show the engineering and true strains to fracture vs free nitrogen content (in weight %) for the F81 series of steel heats. The steel heats have comparable sulphur contents and only differ in their free nitrogen content (see Table 6). From the work of Tschischewski (Figure 157) and Baird (Figure 158 c), it can be seen that the elongations to failure vs nitrogen content, follow a power law equation of the form $y = ax^{-n}$ (where y is the elongation to failure). Based on this trend lines were fitted to the data points. This time the power law could be verified in that four data sets had three points, again one data point was taken for each steel heat at the same temperature. It can be seen that a family of curves are produced that move down the y axis, as the temperature is increased. The equations of which are given in the right hand side of the Figures 124 and 125. That is the strain to failure decreases with increasing temperature. The higher free nitrogen steel exhibiting lower strains and elongations to fracture in every case.

5.3.3. Discussion of the Interstitial - Free Tensile Results.

The results for the slow strain rate tests done on the interstitial-free steel in air are given in Figure 127. Figure 128 shows the true strain to fracture vs

temperature for all the steels tested. Figure 129 shows the increase in UTS vs temperature for all the steels tested. Figure 130 shows the reduction in area vs temperature for all the steels tested.

It can be seen from the above figures that the interstitial-free steel has far superior strains to fracture, and reductions in area of all the steels tested. In the DSA regime the effect on the UTS is virtually zero.

Sachdev [94] in his work studying the dynamic strain aging characteristics of two dual phase steels, a high strength low alloy (HSLA) steel, a 1008 steel and an interstitial free (IF) from tensile properties at temperatures in the range 295 to 460 K (22° to 187°C) and strain rates between 6×10^{-6} to 10^{-2} s^{-1} . All except the IF steel were found to be susceptible to dynamic strain aging, as evidenced by increases in tensile strength. The largest positive change was observed in the 1008 steel while the dual phase and HSLA steels showed much smaller increases. Also, large decreases (up to 75 pct) in uniform elongation were noted for the 1008 steel while the decreases were minimal for the dual phase and HSLA steels. The IF steel did not strain age and showed a slight increase in uniform elongation with increasing temperature. The compositions and mechanical properties are given in Tables 19 and 20.

Category	Steel I. D.	C	N	Mn	Si	V	Other
Dual phase	DP-Lo*	0.12	0.007	1.52	0.52	0.061	Cr 0.028 Nb 0.010
	DP-Hi*	0.12	0.020	1.44	0.52	0.130	Cr 0.022
HSLA	VAN-80	0.13	0.015	1.31	0.39	0.11	
Interstitial free	IF	0.012	0.006	0.22	0.003	0.001	Nb 0.047 Ti 0.039
Plain carbon	1008	0.048	0.003	0.32	<0.001	0.001	

Table 19. Chemical Composition of the Steels studied by Sachdev [94].

Category	Steel I. D.	Microstructure	<i>t</i> (mm)	YS (MPa)	UTS (MPa)	ϵ_u (Pct)	ϵ_f (Pct)
Dual phase	DP-Lo	Alloyed ferrite + martensite	2.2	367	639	23.1	32.5
	DP-Hi	Alloyed ferrite + martensite	3.0	406	654	20.0	29.0
HSLA	VAN-80	Alloyed ferrite + pearlite	3.1	504	640	13.5	23.4
Interstitial free	IF	Ferrite	1.7	152	310	28.5	45.6
Plain carbon	1008	Ferrite + pearlite	2.0	253	316	26.2	42.6

Table 20. Mechanical Properties of the steel tested at a strain rate of $2 \times 10^{-4} \text{ sec}^{-1}$ at room temperature [94].

The purpose of the study was to provide an insight into the forming

characteristics of these steels as affected by dynamic strain aging which can occur as a result of the elevated temperatures resulting from forming operations.

The specimens used were standard 12 mm wide ASTM E8 tensile bars with the gauge length parallel to the rolling direction. The test strain rate was introduced after the yield point, an increase or positive change in ultimate tensile strength (pct Δ UTS), rather than the yield strength was used as the criterion for evaluating the extent of dynamic strain ageing. A percent change normalised to the room temperature value (determined at the strain rate of interest) was used to offset the widely different tensile properties of the steels used. Figure 163(a) shows pct Δ UTS as a function of testing temperature at a strain rate of $6 \times 10^{-6} \text{ s}^{-1}$ for all steels studied. The 1008 steel strain aged the most, registering the largest pct Δ UTS, while the IF steel did not strain age at any temperature. Rather, a continuous decrease in pct Δ UTS was observed with increasing testing temperature for the IF steel. Similar to the results obtained in this work. The results of tests done at faster strain rates are also shown in Figure 163. Figure 164 shows the variation in uniform elongation with increase in strain rate.

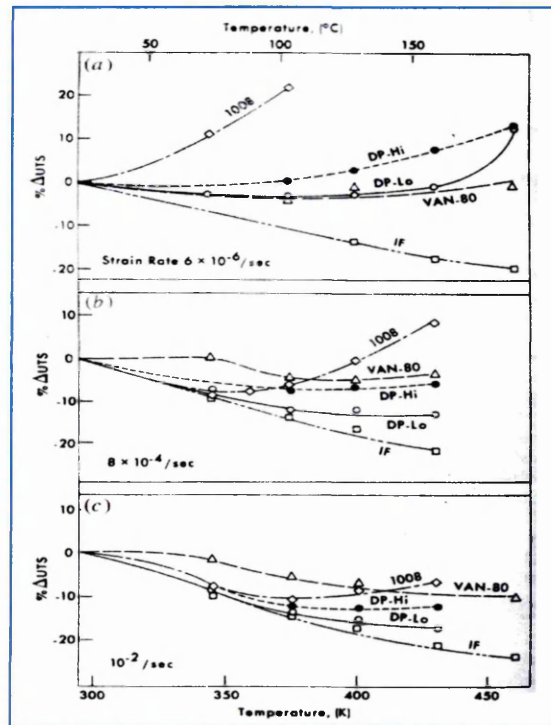


Figure 163. Plots of pct change in ultimate tensile strength vs temperature at strain rates of (a) $6 \times 10^{-6} \text{ s}^{-1}$ (b) $8 \times 10^{-4} \text{ s}^{-1}$ (c) 10^{-2} s^{-1} [94].

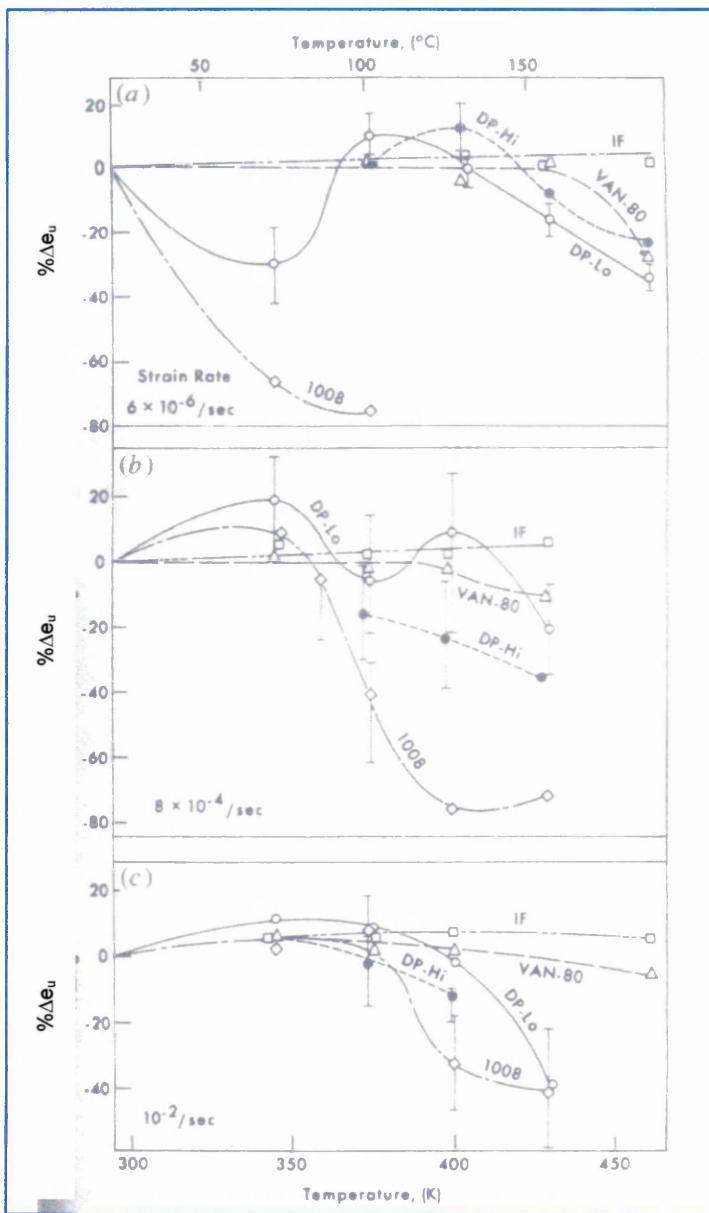


Figure 164. Plots of pct change in uniform elongation vs testing temperature at strain rates of (a) $6 \times 10^{-6} \text{ s}^{-1}$ (b) $8 \times 10^{-4} \text{ s}^{-1}$ (c) 10^{-2} s^{-1} [94].

An increase in uniform elongation was noted for the dual phase steels at certain temperatures. The uniform elongation for the IF steels appeared to increase slightly at higher testing temperatures for all strain rates studied whereas the HSLA steel showed a slight decrease in the uniform elongation up to a test temperature of about 400K beyond which a larger decrease was observed. The percent change in total elongation (pct $\Delta\epsilon_t$) data for the steels is shown inset in Figure 165. These changes closely parallel changes observed in uniform elongation; however, it must be noted that the total elongation data are not strictly correlative to a particular strain rate because the strain rate in the neck progressively becomes larger than the initially imposed strain rate.

A direct comparison between the present work and Sachdev's results is more easily seen, in Figure 165 by comparing the test done at $8 \times 10^{-4} \text{ s}^{-1}$ by Sachdev (Inset in the graph) and the tests done in this work at $2 \times 10^{-6} \text{ s}^{-1}$ and $2.67 \times 10^{-6} \text{ s}^{-1}$. All except the IF steel (the top curve on the inset graph) were found to be susceptible to dynamic strain ageing, as evidenced by the reduction in the elongation to fracture in the DSA regime of temperature for the other steels.

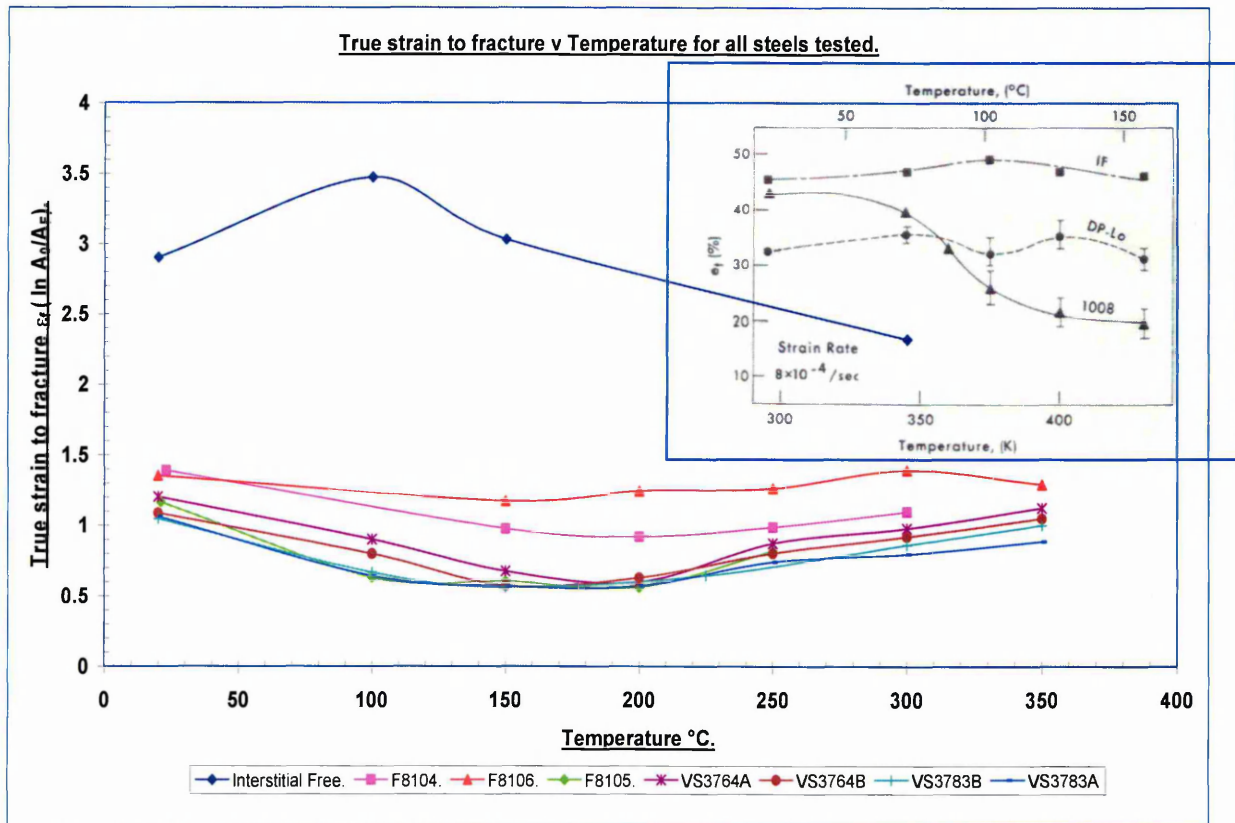


Figure 165. Comparison of strain to fracture vs temperature with Sachdev's work [94].

According to Gladman [256] ductility and toughness are general terms which are not specifically related to each other and are not definitive. The ductility of a steel can be defined in terms of its resistance to either plastic instability or fracture. Resistance to plastic instability is integrally tied to the strength and work hardening characteristics of the material. While fracture resistance depends on the volume fraction, shape, and characteristics of second phase particles. An example of an instability controlled ductility is the elongation to fracture in the uniaxial tensile test. An example of a fracture controlled ductility is the reduction of area in the same test [256].

It can be seen from Tables 11 to 14 that the elongation to fracture decreases as the nitrogen content increases so can be considered an instability controlled ductility in the dynamic strain ageing regime. It can also be seen from Tables 10 to 14 that the reduction of area decreases as the initial volume fraction of inclusion increases. This effect is reflected in the reduction of area in the tensile test, so can be considered a fracture controlled ductility.

To show the effect of free nitrogen and inclusion content of the steels tested, the reduction of area was plotted against the elongation to fracture. This was done for all the tensile tests, and through the full temperature range for each steel heat. Trend lines were then fitted through the data for each steel heat. The results are given in Figure 166.

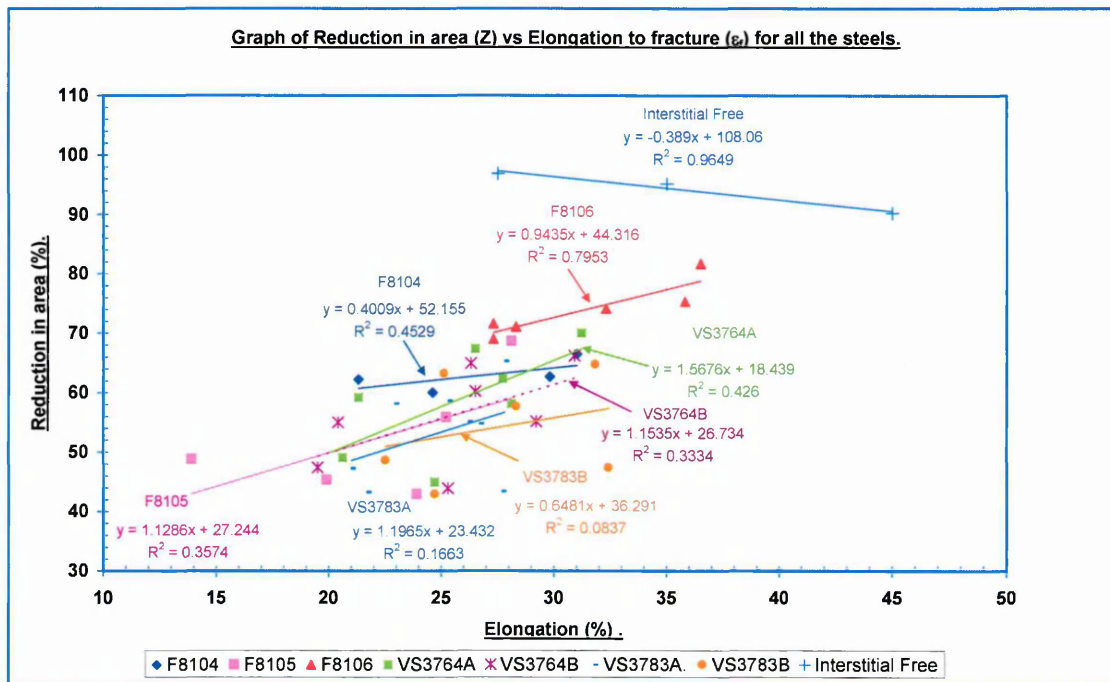


Figure 166. Graph of Reduction in Area vs Elongation to Fracture for all the steels tested.

It can be seen from figure that the interstitial-free steel has the largest elongations to fracture, and reductions in area. The steel heat with the lowest elongations to fracture and reductions in area is F8105. The trend lines were ranked in order for each steel heat, starting with interstitial-free as no1, and F8105 as no 8. The results are given in Table 21.

Steel Heat	Rank	Free Nitrogen (ppm).	Volume Fraction (%) calculated using Franklins formula minus the oxygen term.	sq rt Volume Fraction (%).	Sulphur Content wt %.
Interstitial Free	1	1 to 2	0.0342	0.184	0.013
F8106	2	1.45	0.0157	0.125	0.004
F8104	3	8	0.0204	0.142	0.005
VS3764A	4	12	0.00308	0.0554	0.002
VS3764B	5	12	0.13	0.36	0.027
VS3783A	6	38	0.00308	0.0573	0.002
VS3783B	7	36	0.121	0.347	0.024
F8105	8	54	0.0205	0.143	0.005

Table 21. Ranked data for elongation to fracture vs reduction in area graph for all the steels tested.

It is interesting to note that the VS3764B sits exactly on the top half of the F8105 data trendline in Figure 166. From the tabulated results it seems that the main fracture controlling parameter is the free nitrogen content. From the ranking table it can be seen that as the free nitrogen content is increased the degradation in the material properties reduction in area and elongation to fracture both lower. The R squared correlation of the trend lines of the equations may be low in some cases, but the relationship between the two fracture parameters (elongation to fracture vs reduction in area and free nitrogen) is more than a coincidence.

The presence of interstitial elements in steel has pronounced effects on the properties of steel. It is the mere presence of the interstitial atoms carbon and nitrogen which results in the discontinuous behaviour of steel. The kinetics

of strain ageing are highly dependant upon the interstitial content, and the return of the yield point is accelerated as the interstitial content increases [55,92,92,112].

It is clear from the above that an alloying addition which forms very stable carbides and nitrides and which would virtually eliminate interstitial carbon and nitrogen in the ferrite, would also eliminate the discontinuous yield phenomenon. Whilst low ageing steels have been produced for many decades by using aluminium, titanium, or boron, to form a stable nitride, the extension of this to form a stable carbide is relatively recent. One of the features of these modern interstitial free steels is their extremely low carbon and nitrogen contents. The carbon and nitrogen contents of modern interstitial free steel are each limited to about 0.003 wt %. The composition of the modern interstitial free steels is tailored to give an essentially pure iron with a minimum solute content which gives a high level of plastic anisotropy [78].

The sequence of events involved in the ductile fracture process, that is void nucleation, void growth, and void coalescence the main features of any inclusion distribution that control ductility are the inclusion shape (particularly the frontal radius of curvature) and volume fraction of inclusions [78,228,229]. Void initiation is virtually spontaneous in the case of non metallic inclusions, the voids being initiated by interface decohesion in the earliest stages of plastic deformation. The initial shape of the void is essentially that of the inclusion on which the void is formed. The void growth rate, although dependant on the inclusion shape, is also dependent upon the stress and strain state involved in the deformation process [2,3].

It can be seen from Tables 11 to 14 that the strain to fracture decreases as the volume fraction of inclusions increases, this is reflected in the reduction of area for the steel heats, more so in the VS series of steel heats as these were made specifically to show this effect. The effect was not as pronounced as it thought it should be, for the reasons discussed earlier [78].

5.3.4. Determination of the Law of the Peak Strengthening Stress ($\Delta\sigma_p$) vs Free Nitrogen and Free Carbon.

Measurements of the increase in $\Delta\sigma_p$ with temperature has been carried out by various workers [248,272]. Atkinson et al [271] has postulated that an Ln relationship exists between the increase in $\Delta\sigma_p$ and the free nitrogen content of low carbon and carbon manganese steels and work is currently ongoing to determine the significance of free carbon in the ductile fracture process. To verify the Ln relationship between $\Delta\sigma_p$ vs free nitrogen, the data for all the steels tested was plotted and a trend line fitted to the data as shown in Figure 167.

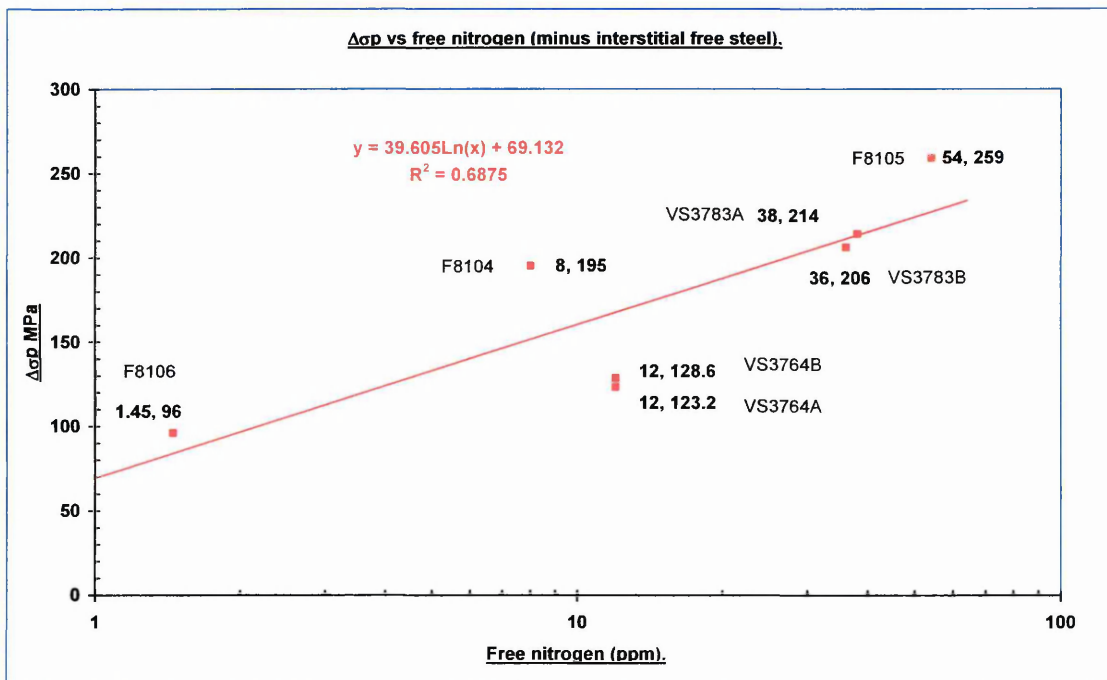


Figure 167. $\Delta\sigma_p$ vs Free Nitrogen Content for all the steels tested.

The positive Y axis intercept at zero (69.132 MPa) indicates that carbon may be equally important.

Recently Atkinson et al [271] have discussed the additive effect of free carbon and free nitrogen ($C_f + N_f$) and the possibility that it is related to the logarithm of the solute concentration from Cottrell atmosphere theory [108]. The residual $\Delta\sigma_p$ effects (49.74 MPa) seen in Figure 168 may be the result of low concentrations of other interstitial atoms such as oxygen, and boron.

Further verification would be worthwhile.

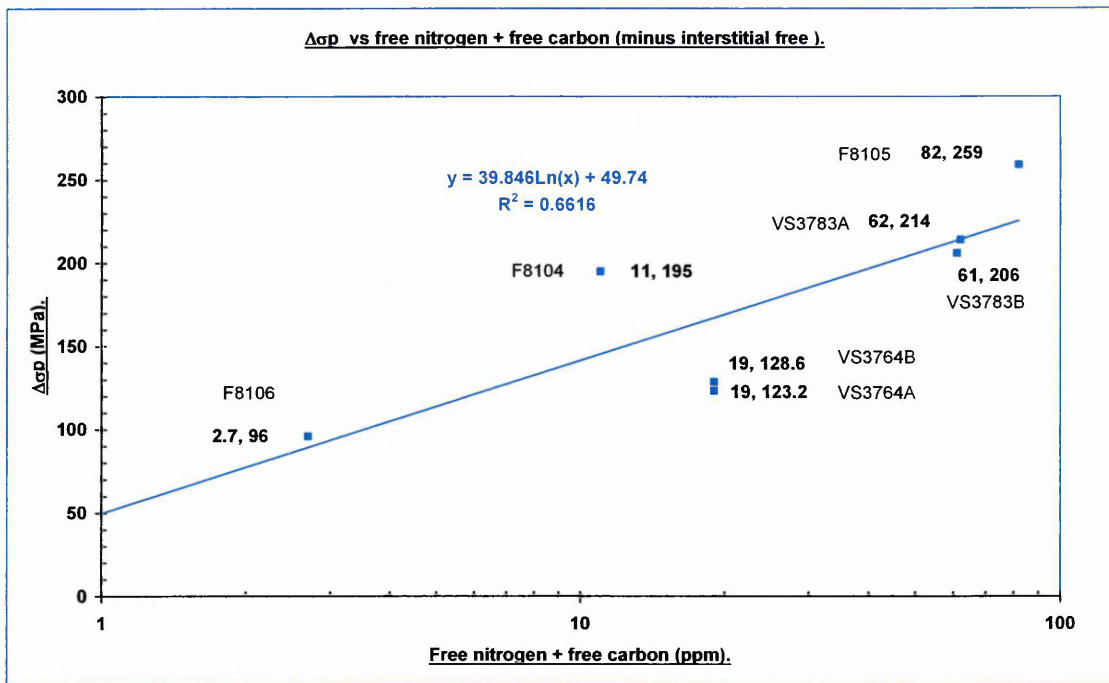


Figure 168. Δσp vs Free Nitrogen plus Free Carbon Content for all the steels tested.

Using the same data input values for each steel it can be seen that the better correlation is obtained with the total of free nitrogen vs Δσp ($R^2 = 0.6875$ as opposed to 0.6616 for Δσp vs free nitrogen plus free carbon). The Ln equations are shown in the Figures 167 and 168.

5.4. Charpy testing discussion of results.

Dimpled rupture occurs in three stages: nucleation of cavities during plastic flow, the growth of these cavities with continued deformation, and finally their coalescence with complete rupture. The details of these three stages may vary widely in different materials and with the state of stress existing during deformation. Similarly, the fractographic appearance of the final fracture surface is influenced by these same factors.

Nucleation may occur in systems containing second-phase particles, by particle/matrix interface separation or by particle cracking. Void nucleation can also occur at blocked slip bands in the absence of second-phase particles [1]. Both the nucleation and the growth stages appear to require greater deformations if hydrostatic compression is superimposed during deformation [2,3] and a greater strain to fracture is observed [3]. The VS high sulphur series of steel heats falls into the category particle/matrix separation.

5.4.1. Discussion of results for VS3764A, VS3764B, VS3783A and VS3783B the effect of sulphur content.

Figure 84 shows the Impact Energy absorbed vs Temperature for this work. It can be seen from the figure that as the sulphur content of a steel is increased then the upper shelf energy is lowered [8,11,184,249]. It can be seen for the VS series of steel heats, that the steel with the highest absorbed impact energy is VS3783A, then VS3764A, then VS3764A, and finally VS3783B. Though there is some concern over the last data point for VS3783B, it could be attributable to the degree of data scatter as shown by other data in Figure 84.

Franklin [249] examined the impact properties of five steels En 5, 14, 16, 19 and 40b over a range of tensile strengths and structures for two sulphur contents of 0.025% and 0.005%. The composition of the steels used are given in Table 22.

He found that brittle impact values and brittle ductile transition

temperature did not vary with sulphur content, but the desulphurized steel had markedly higher ductile impact values. Studies of the fractured specimens

Chemical analyses of five low-alloy steels, %									
Type of steel	En no.	C	Si	Mn	Ni	Cr	Mo	S	P
'30' carbon	5	0.29	0.22	1.01	0.017	0.011
		0.28	0.21	0.96	0.005	0.011
C-Mn	14	0.22	0.20	1.50	0.46	0.011	0.011
		0.20	0.19	1.43	0.46	0.007	0.011
Mn-Mo	16	0.32	0.23	1.54	0.19	0.022	0.011
		0.31	0.22	1.49	0.18	0.007	0.011
1%Cr-Mo	19	0.36	0.28	0.68	...	1.06	0.31	0.024	0.011
		0.32	0.17	0.70	...	1.06	0.30	0.006	0.011
3%Cr-Mo	40b	0.20	0.34	0.45	0.43	2.94	0.52	0.027	0.011
		0.22	0.33	0.49	0.47	3.07	0.49	0.010	0.011
		0.22	0.32	0.50	0.48	3.13	0.56	0.0045	0.011

Table 22. Chemical analysis of the five low alloy steels used [249].

revealed that such increases are associated with a change in the fracture mode of cavity initiation. The fracture paths in the high sulphur steels were very irregular and the most prominent feature was the recurrence of deep V shaped inlets in the fracture coinciding with bands of sulphide inclusions. In the low sulphur steels, the fracture path was more regular with fine cusp like inlets in the fracture surface. Also in the low sulphur steels no large sulphide particles were observed and the dimples were smaller.

Under conditions of brittle fracture in the impact test, the sulphur content had little effect on the impact values since the fracture behaviour was governed by the cleavage of the matrix. Thus, the presence or absence of sulphides had little or no effect on the temperature of transition from brittle to ductile fracture.

Franklin also observed that under conditions of ductile fracture in the impact test, there was a marked increase in ductile impact values for a reduction in sulphur content for a wide range of UTS values and a variety of structures. He thus concluded that, inclusions have a much greater effect on ductile fracture in a notch impact than in a tensile test, due to the presence of triaxial tension in the former as soon as yielding occurs at the base of the notch.

This point has been emphasized by Green and Knott [253] who point out that, although the first cavities form near the surface of the root, the ones that subsequently grow are located further inside the metal, where the triaxial tension can develop. They suggest a cavity growth mechanism based on relaxation of a transverse stress at the surface of a cavity formed under triaxial tension.

Other workers have discussed the role of inclusions as cavity formers in ductile rupture, Green and Knott [253] studying the effects of work hardening behaviour and inclusion content on the initiation and propagation of ductile fracture in low strength steels and correlated this with the crack opening displacement. They concluded that in the high sulphur mild steel the crack grows by a mechanism of void coalescence and that the amount of crack opening per inclusion spacing is of the same order as the inclusion spacing. The mechanism of crack growth in the low sulphur mild steel however, is one involving void growth until a critical displacement is reached between the expanded void and the crack tip. This ligament shears once it has hardened sufficiently, in a manner analogous to that of the initiation of fibrous fracture.

The present observations in this work give further information on the influence of inclusion size and properties. In the case of the high - sulphur steels, it is postulated that the cavities open up fairly readily around the large sulphide inclusions, while, in the low - sulphur steels, cavity formation around the smaller carbide particles is more difficult, due to the smaller particle size as reported by Ashby [14,15]. The higher the sulphur content, the more numerous and larger are the sulphide particles and hence cavities formation can be formed more readily particularly around large fractured particles. The reduction in sulphur content appears to have a greater effect on the ductile impact values for the VS steels of higher strengths, presumably because of the difficulty in forming cavities around the finer, more coherent particles in the desulphurized steels. The impact energy absorbed in fracturing the specimen is proportional to the amount of deformation. If long fissures are formed then less energy is absorbed, because the triaxial stresses can more easily neck down the regions between such long fissures, though the force needed to break the specimen

may be much greater.

The role of strain rate in determining the type of fracture and the influence of inclusions has been discussed by Crussard [254] who suggests that the smooth, featureless areas in the dimples are the result of shear due to the high local rate of strain at the particle/matrix interface. Crussard suggests that ductile fracture is propagated by jumping from one local sheared region to another. Crussard's observations of the featureless areas in the dimples could explain the observations made in this work on the tensile tests done on the 64B steel heat at 200°C. The featureless zones are observed on the SEM fractograph at a magnification of 2000, (see Figure 113).

However, the present observations in this work support the suggestions of Franklin, in that, as the metal stretches beneath the root of the notch, it tends to flow away from or past the particles to form cavities with smooth shear faces. The metal between these cavities then necks down and the cavities open up laterally at right angles to the axis of the sample. These cavities then become linked to produce the final fracture, having the very wide and deep V-inlets observed on the fracture surfaces.

Hertzberg citing the work of Hodge et al [250], who like Franklin observed the degradation in the upper shelf energy with increased sulphur content. The work of Franklin and Hodge et al is compared with this work in Figure 169 (inset in the graph 169a and 169b). Hodge et al [250] also reported that variations in the sulphur content of 0.005% to 0.179% had no significant effect on the impact-transition temperature of isothermally transformed ferrite-pearlite steels. Whereas Gladman et al [255] observed that an increase in the sulphur content of carbon-manganese steels between 0.01% and 0.05% increased the transition temperature. The present observations in this work support the findings of Hodge et al [250].

Figure 3 shows work of Pickering [8] in this work controlled experiments were carried out on low carbon manganese steels of varying sulphur contents. The properties were examined in the longitudinal and transverse directions. There was a clearly defined effect of increasing the sulphur content i.e sulphide

volume fraction to lower the ductile impact shelf energy. From the work of Pickering [8] (Figure 3), it can be seen that Impact Energy absorbed vs sulphur content, follows a power law equation of the form $y = ax^{-n}$.

Where y = Impact energy absorbed (Joules).

Figure 169. Results of this work compared with Franklin [249] and Hertzberg [250].

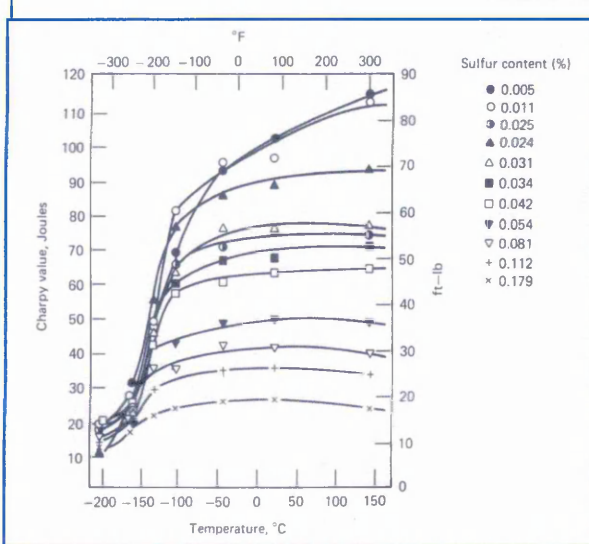
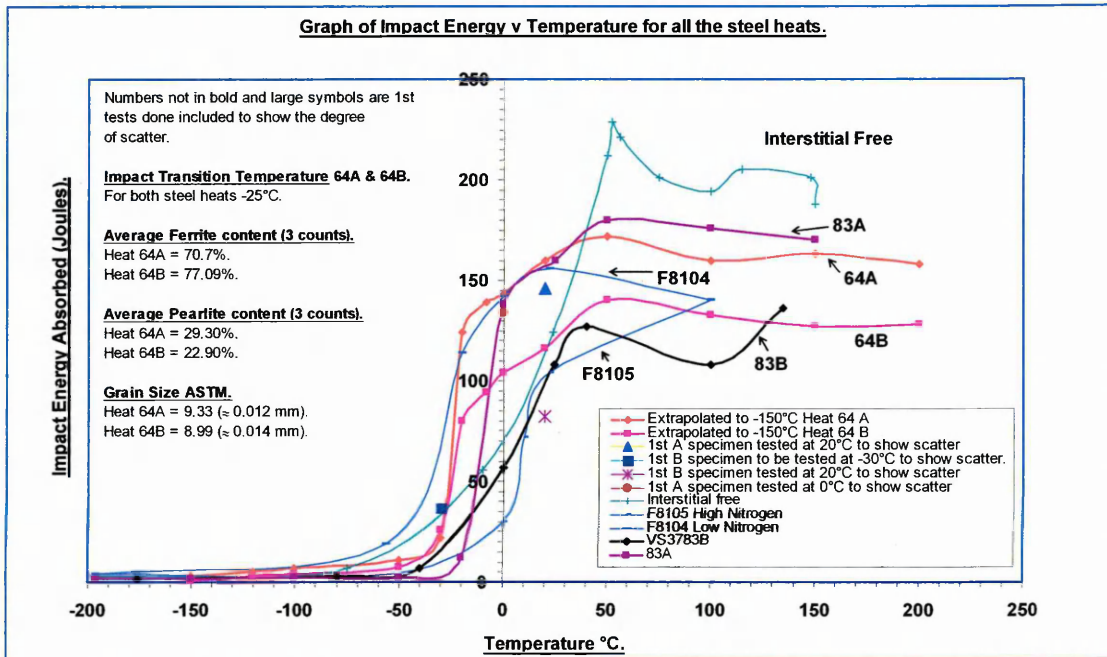


Figure 169a.
The Effect of Sulphur content on the Charpy Impact Energy in steel plate. [250].

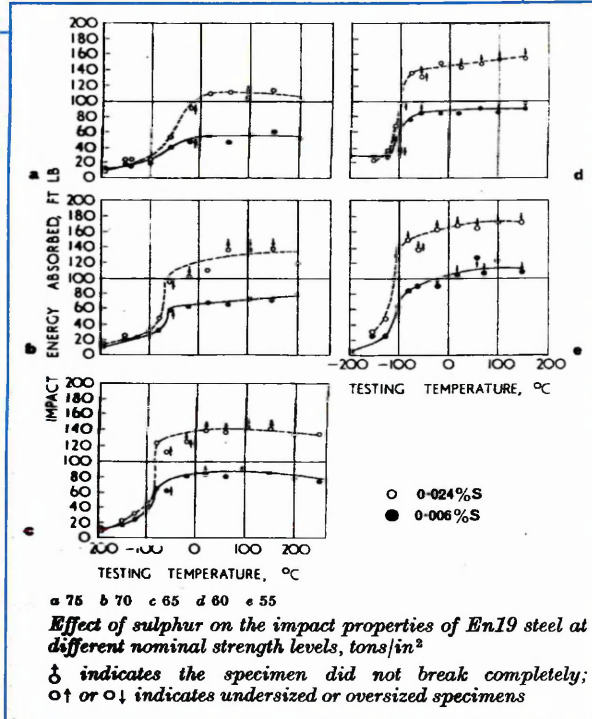


Figure 169b.
The Effect of Sulphur on the Impact Properties of En 19 steel at different nominal strength levels, tons/in² [249].

Based on this trend lines were fitted to the data points for all the VS series of steel heats. The corresponding pairs were 64A and 64B, and 83A and 83B for temperatures of 50°, 100°, 150°, 200°C. That is all the data point pairs were on the upper shelf. It can be seen that a family of curves are produced that move down the y axis, as the sulphur content is increased. The equations of which are given in the right hand side of Figure 85. The equation colour corresponds to the matching trend line colour. That is the upper shelf energy increases with decreasing sulphur content.

5.4.2. Discussion of results for VS3764A, VS3764B, VS3783A and VS3783B the effect of free nitrogen content on the Impact Transition Temperature.

From Figure 84 it can be seen that as the free nitrogen content is increased the impact transition temperature is increased for all the steel heats tested. The effect of sulphur content is also evident in that it lowers the upper shelf toughness and raises the impact transition temperature.

Mintz et al [219,222] determined the effect on the impact transition temperature by changing the free-nitrogen content (N_f) in steels of different silicon and manganese levels. For low silicon or balanced steels he obtained a square root relationship, while for higher silicon steels corresponding to silicon-killed steels he obtained a linear relationship with nitrogen content. The results are shown in Figure 60 [219]. Mintz found that when the results are corrected for differences in grain size and pearlite volume fraction and correction is made for the effect of silicon in solid solution on toughness, that at zero nitrogen the curves for silicon killed and balanced steels come together. He found that the effect of adding nitrogen is considerably greater in the case of the low-silicon steel than in the silicon - killed steel.

Morrison [252] citing the work of Thewlis who did work on the effect of nitrogen on the welding of line pipe by the submerged arc process. He found that as the nitrogen content is increased the weld metal toughness deteriorates, and that the 80 J Charpy V notch transition temperature increased with increasing nitrogen content see Figure 170.

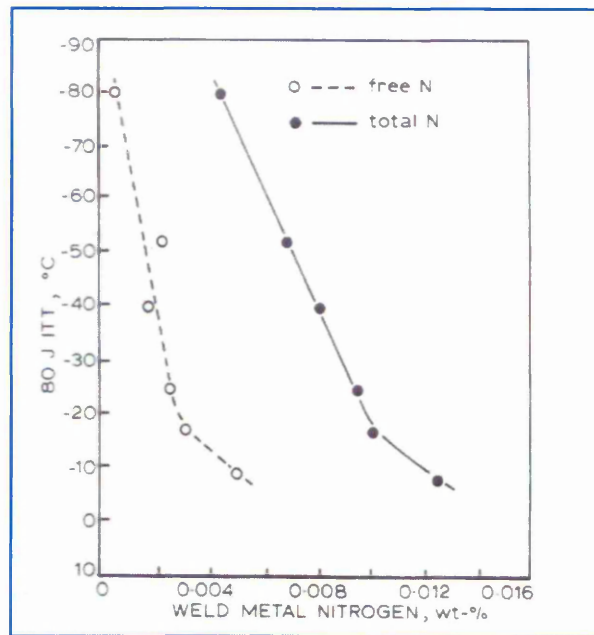


Figure 170. Variation in 80 J Charpy transition temperature with weld metal nitrogen content [252].

Darken et al citing Enzian et al [246] also found that the toughness of rimmed steels lowered with increasing nitrogen content when conducting Izod tests on rimmed steels in 1945 (see Figure 171).

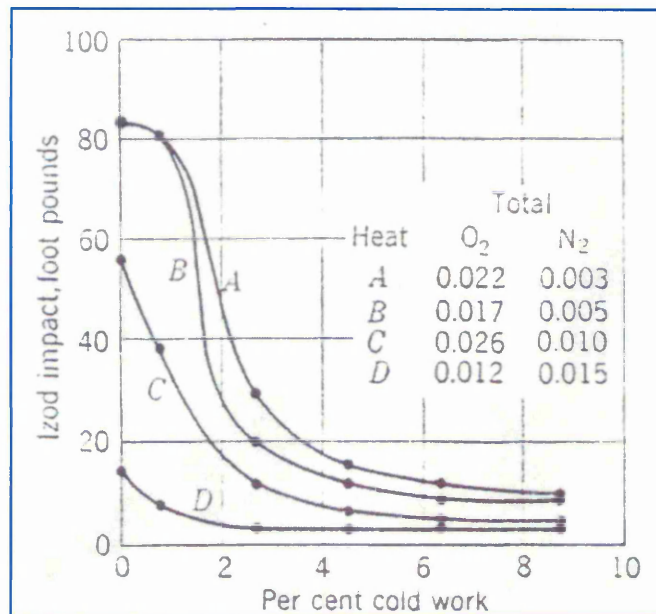


Figure 171. Effect of Nitrogen on the Brittleness of rimmed steels [246].

Gladman [220], observed that the change in impact transition temperature is proportional to the square root of free nitrogen content, while Bucher et al. [221], found that it varied linearly with nitrogen content.

To check the data in Figure 84 Pickering's equation was used (Table 23).

Steel Heat	Grain Size μm	V_f Pearlite	N_F ppm	Si	Al
VS 3764 A	12 (ASTM 9.33)	29.30	12	0.2	0.034
VS 3764 B	14 (ASTM 9)	22.90	12	0.2	0.032
VS 3783A	-	-	36	0.19	0.005
VS 3783 B	17.89	28.25	38	0.19	0.005
F 8104	7.5 [257]	26.32 [258]	8	0.33	0.03
F8105	13 [257]	41.13 [258]	54	0.33	0.004
IFS	-	0	0	0.004	0.04

Table 23. Input values used in the Pickering equation.

Pickering's equation [229].

For normalized as rolled steels.

$$\text{ITT } (^\circ\text{C}) \pm 20^\circ = -19 + 44(\% \text{Si}) + 700(N_F)^{1/2} + 2.2(\% \text{Pearlite}) - 11.5d^{1/2} \quad (33)$$

Where N_F is the free nitrogen content (wt%) and d is the mean linear intercept ferrite grain size. Table 24 shows the results for all the steel heats tested. The text in blue is based on the 27Joules standard, red text based on 50% fracture appearance transition temperature (FATT).

Steel Heat	Calculated Temperature $^\circ\text{C}$	Observed Temperature $^\circ\text{C}$
VS 3764 A	-26.47	-23 (-25)
VS 3764 B	-32.76	-25 (-25)
VS 3783 A	-	-18 (-10)
VS 3783 B	7.5	-21 (5)
F 8104	-45.68	-46 (-30 to -37.5)
F8105	36.58	-2.5 (5 - 7.5)
IFS	-	-38 (15)

Table 24. Observed temperatures vs calculated temperatures using the Pickering equation.

It can be seen from Table 24 that the difference between the observed and calculated values are reasonable and well within the tolerance of $\pm 30^{\circ}\text{C}$ [256].

The effects of silicon and free nitrogen are to increase the impact transition temperature [78], free nitrogen being the most detrimental on a weight percentage basis. For example a 1% addition of silicon would increase the transition temperature by some 44°C , whereas only 0.01wt% of free nitrogen raises the impact transition temperature by 70°C .

Increasing the pearlite content in the microstructure increases the impact transition temperature significantly despite the minimal strengthening by the presence of pearlite in these structures [78] .

Steel heats VS3763B and VS3783B are identical steel heats their only difference being the free nitrogen content. A temperature shift of 30°C has occurred for an increase in free nitrogen of 26 ppm.

From the data obtained and compared with the literature it can be seen that the effect of an increase in the free nitrogen content of a steel is to shift the impact transition temperatures to higher temperatures.

The effect of sulphur is to lower the upper shelf fracture energy i.e. to reduce the toughness.

5.4.3. Discussion of results for F8104, F8105 , and F8106.

It can be seen from Figures 84 and 169 that the low nitrogen steel (F8104) has a higher upper shelf energy than the higher nitrogen steel (F8105). Allowing for differences in grain size, and pearlite volume fraction, and chemical composition and keeping things the same, it can be seen from Table 24 (experimental data) that for the F8104, F8105 steel heats a temperature shift of 30°C has occurred for an increase in free nitrogen content of 46 ppm (F8105 = 54 ppm = 0.0054% wt N_F and F8104 = 8 ppm). Based on using the 50% FATT as the datum. This can be seen in Figure 172 (the other data has been removed for clarity).

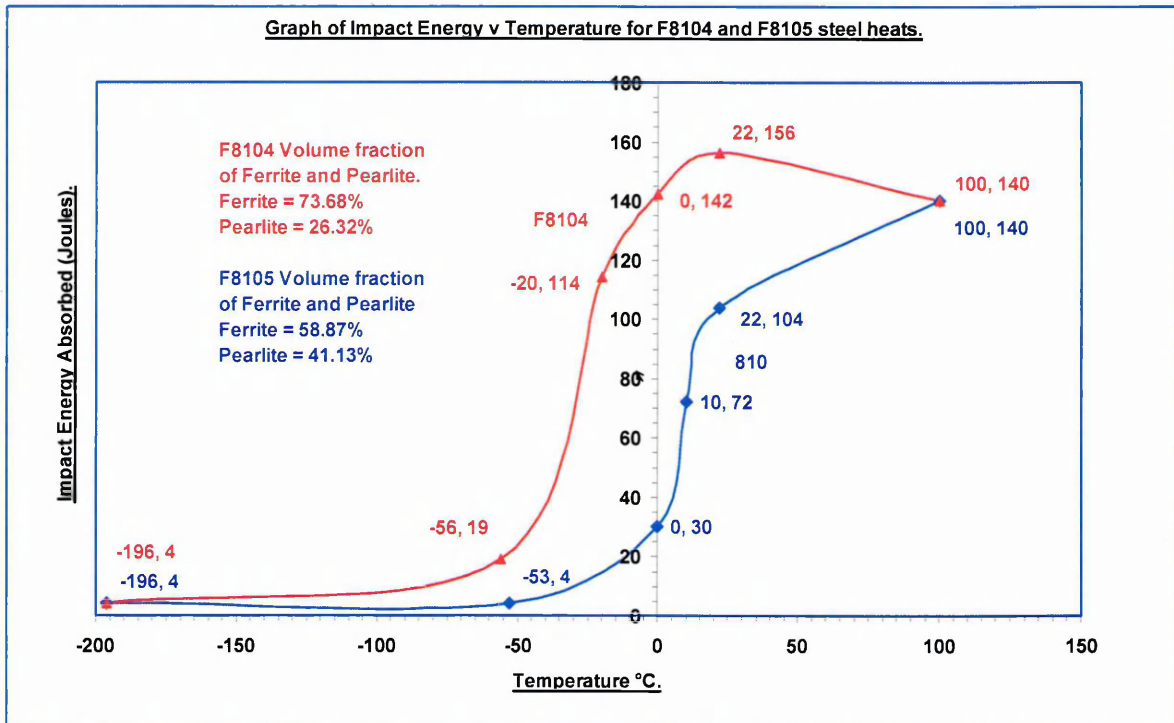


Figure 172. Graph of Impact Energy absorbed vs Temperature for F8104 and F8105 steel heats.

According to Gladman [78] the effects of silicon and free nitrogen are to increase the impact transition temperature, free nitrogen being the most detrimental on a weight percentage basis. For example a 1% addition of silicon would increase the transition temperature by some 44°C, whereas only 0.01wt% of free nitrogen raises the impact transition temperature by 70°C [78].

The shift in ITT of 30°C is in excellent agreement with Gladman [78], which could be even better dependent upon where the 50% FATT is taken. This is the average as the 50% FATT for F8104 can be between -30°C and -35°C, and the 50% FATT for F8105 can be between 5°C and 7.5°C. Using -30°C for F8104 and 5°C for F8105, would satisfy Gladmans predicted values.

The experimental results of Impact transition temperature vs $\sqrt{\text{free nitrogen}}$ are shown in Figures 173 and 174. These figures do not include the interstitial free steel as the free nitrogen content was tested and found to be zero. This could be due to the testing capability of the Vibran testing machine. The testing capability is typically within a tolerance of ± 1 ppm [248]. An analysis by British Steel at their Port Talbot Laboratories put the total nitrogen at 0.0024 and 0.0032 weight per cent. So the true free nitrogen content could lie between zero and these values. If the free nitrogen content was zero, the impact transition temperature would have been -55°C as it would have simply been the value on the y axis based on the trendlines in Figures 173 and 174.

Bucher [221] found that a linear relationship existed between the impact transition temperature and the free nitrogen content. While Gladman and Pickering [229] and Mintz et al [219] observed that the change in the impact transition temperature is proportional to the square root of free nitrogen. The results obtained in this work are in agreement with Gladman, and Mintz (for low silicon steels). To show this the results were superimposed on Mintz's work. This is illustrated in Figure 175 it can be seen that the data from this work runs parallel with Mintz's work.

Gladman's linear relationship is also illustrated in the figure inset in the top right, taken from the work of Gladman [256]. This is for normalized carbon manganese and carbon manganese aluminium steels. In steels with a free nitrogen content of 0.010 wt %, the embrittling component is 75°C . The impact transition temperature in Gladman's work has been corrected for differences in silicon content, pearlite percentage and ferrite grain size.

The text in red in Table 24 is based on 50% FATT, (as per the Gladman equation). Text in blue is the ITT based on the 27J standard. Table 24 illustrates the point highlighted by Hertzberg, in that "*which transition temperature to use is a puzzlement*" [184]. The difference in values is shown in Table 24. It can be seen from equations inset in Figures 173 and 174 that the impact transition temperature based on the 50% FATT, gives the better correlation and is used in this work ($R^2 = 0.7517$ for 27J standard and 0.8989

based on 50% FATT).

Figure 173 shows the expected trend for all the steel heats (that is increased ITT with increased free nitrogen content). Figure 174 shows the same expected trend for four of the results, but for VS3783A and VS3783B, the expected trend is reversed. The results are somewhat contradictory in that Hodge et al [250] also reported that variations in the sulphur content of 0.005% to 0.179% had no significant effect on the impact-transition temperature of isothermally transformed ferrite-pearlite steels. Where as Gladman et al [255] observed that an increase in the sulphur content of carbon-manganese steels between 0.01% and 0.05% increased the transition temperature. The present observations in this work would support the findings of Gladman et al [255] in that the higher sulphur content steel (VS3783B) has a higher impact transition temperature for comparable free nitrogen contents.

All effects of static and dynamic strain aging are explained in terms of either segregation of solute atoms to dislocations to form condensed Cottrell atmospheres or precipitates, or Snoek (stress-induced) ordering of solute atoms in the dislocation core structure. In ferrite C and N are producing a nearly identical lattice misfit strain, which they can reduce by moving to the dislocation core regions, resulting in an overall reduction in the total strain energy. In ferrite N and C have similar diffusion coefficients and thus these two elements are expected to produce nearly similar DSA effects in LAS. Therefore, in general, the effects produced by C and N can be considered as additive. For example, with a typical dislocation density of $10^8/\text{cm}^2$ in Fe a C concentration of 10^{-6} wt% is sufficient to provide one interstitial C atom per atomic plane along all the dislocation lines present [78]. Thus, very small C and N contents are sufficient to form condensed atmospheres on dislocations in ferrite and cause yield point phenomena. At room temperature, the residual solubility of N in ferrite is about 100 times greater than that of C - N solubility in steel is higher at all temperatures than that of C. It is generally assumed that N, rather than C, is mainly responsible for DSA. However, at higher temperatures in the DSA range the increasing solubility of carbon may cause DSA even in the absence of N [75,85,86].

Based on this it was decided to plot the impact transition temperature vs the square root of free nitrogen plus free carbon. This is illustrated in Figure 176. The ITT vs square root of free nitrogen is also included for reference. It can be seen that the correlation (the R squared value is increased marginally from 0.8989 for $\sqrt{N_f}$ to 0.9066 for $\sqrt{N_f + C_f}$ equations inset in Figure 176). This suggests that the Pickering equation needs further modification to include a free carbon term and the appropriate adjustment factor.

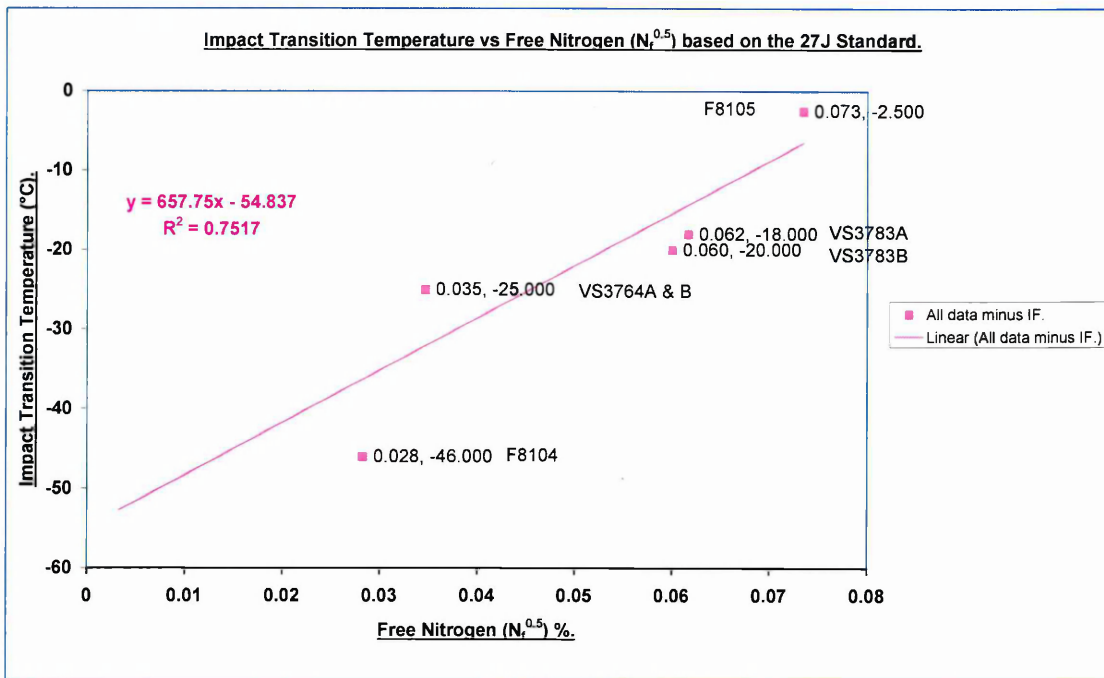


Figure 173. Graph of Impact Transition Temperature vs $\sqrt{\text{Free nitrogen}}$ based on 27J standard.

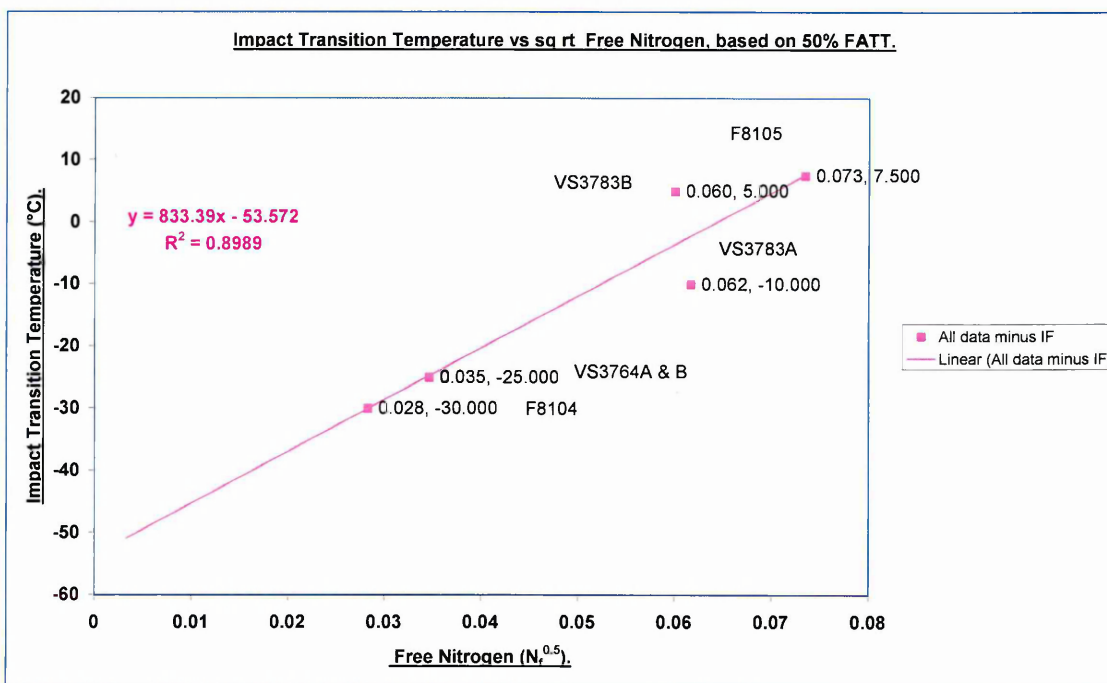
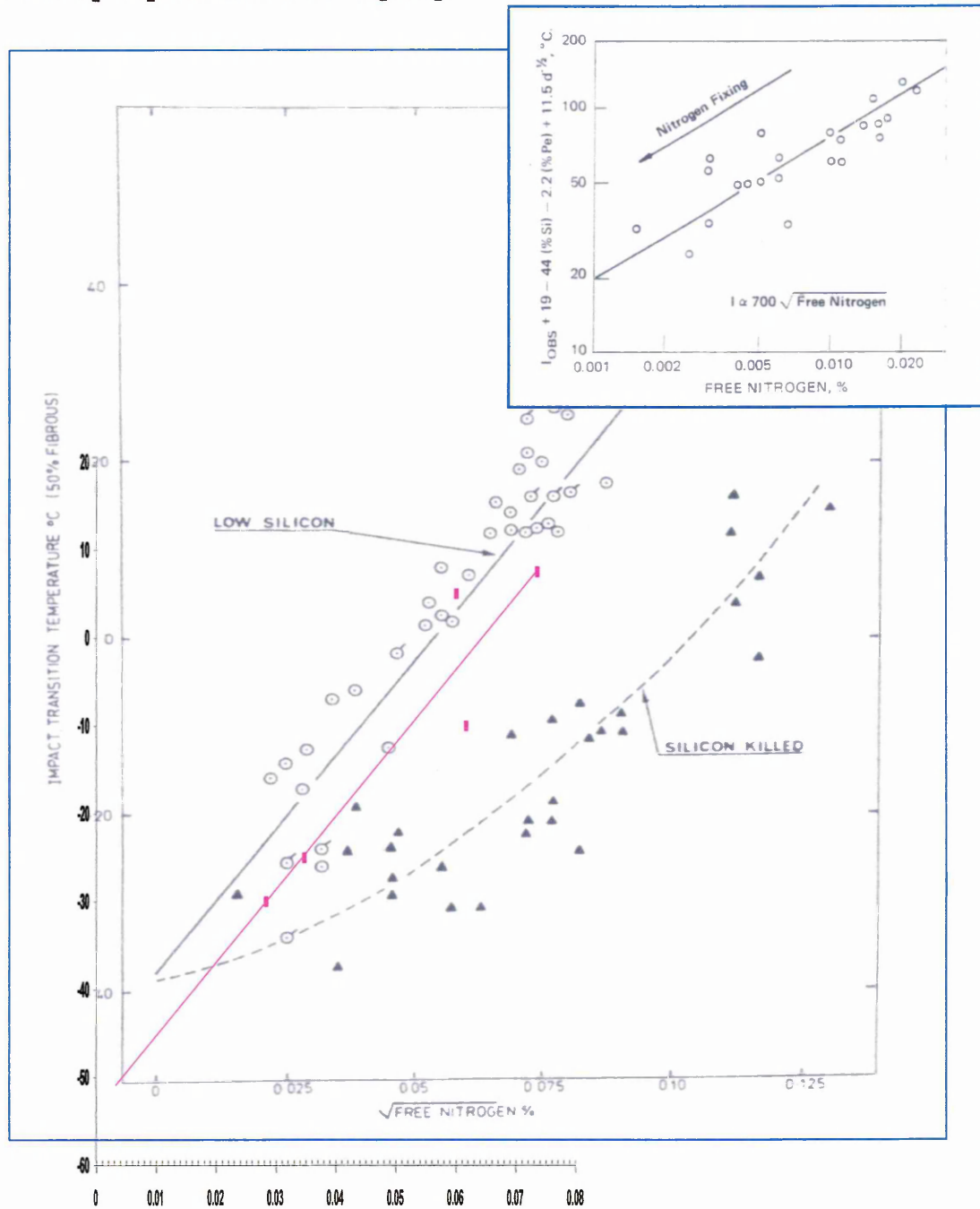


Figure 174. Graph of Impact Transition Temperature vs $\sqrt{\text{Free nitrogen}}$ based on 50% FATT.

Figure 175. Comparison of Impact Temperature vs $\sqrt{\text{free nitrogen}}$ with Mintz's work [219] and Gladman's [256].



It is evident from Figures 84, 169, and 172, that a different fracture mechanism is operating in the F8104 and F8105 steel heats than the VS series of steel heats. The difference in the fracture mechanism between F8104 and F8105 is illustrated by the change in slopes from the top of the 50% FATT slope to the upper shelf. This is shown by Hertzberg [184] in Figure 177. The higher strength steels in Figure 177, reflect the behaviour of F8104 and F8105 in Figure 172. The variance in the slope can be seen quite clearly.

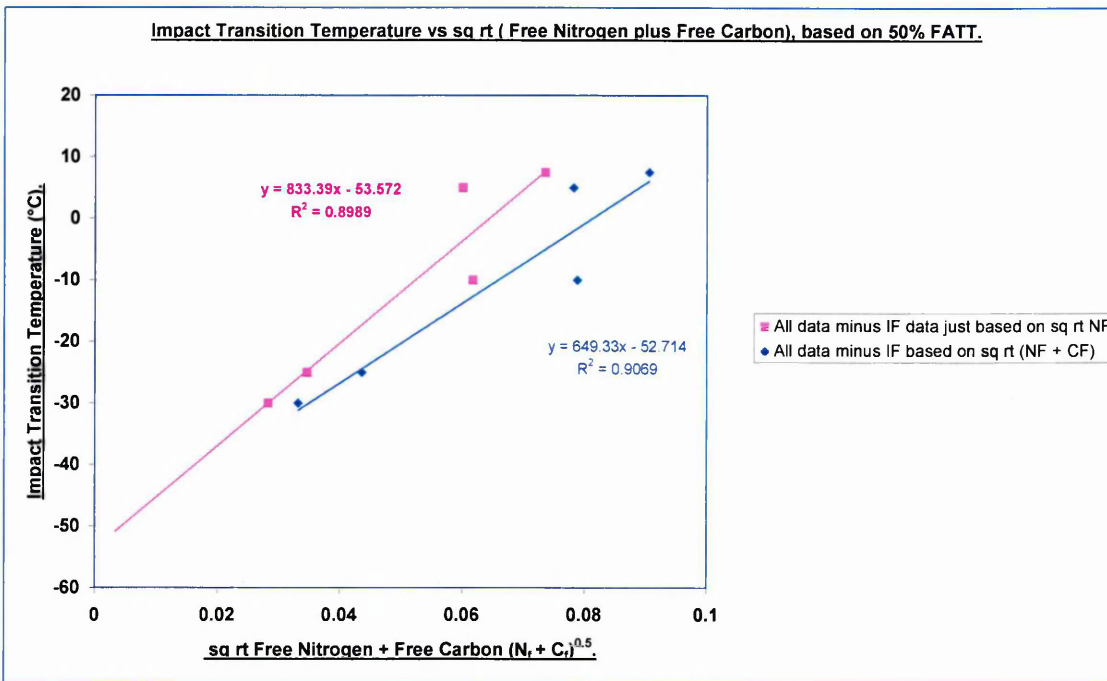


Figure 176. Graph of Impact transition temperature vs $\sqrt{\text{free nitrogen plus free carbon}}$.

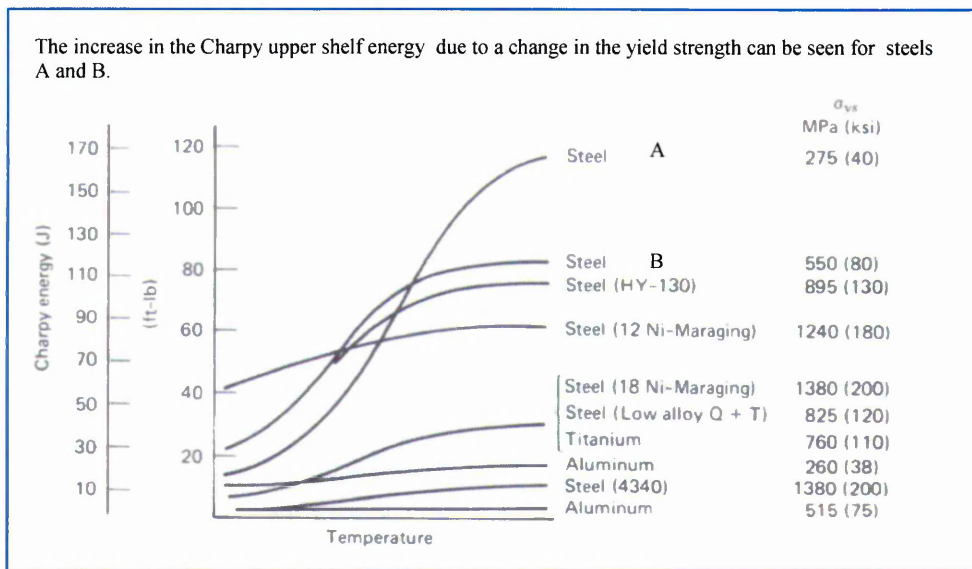


Figure 177. Charpy impact energy vs temperature behaviour for several engineering alloys [184].

The transition from ductile to brittle fracture occurs when the yield stress equals or exceeds the brittle fracture stress. The brittle fracture stress, however, in the absence of any substantial discontinuous yielding, is also sensitive to grain size. The shift in the impact transition temperature (ITT) due

to increased strength is also evident. This is illustrated in Figure 178 [256].

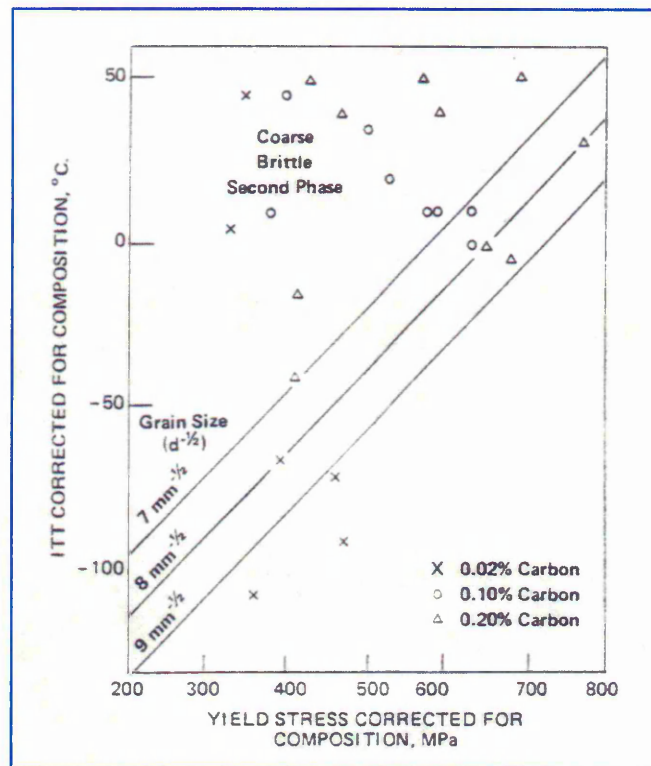


Figure 178. Strength toughness relationships for bainitic steels [256].

To a first approximation, the relative notch sensitivity of a given material may be estimated from the yield to tensile strength ratio. When the ratio is low, the plastic constraint associated with a biaxial or triaxial stress state at the crack tip will elevate the entire stress vs strain curve and allow for a net section stress greater than the smooth bar tensile strength value. On the other hand, in materials that have less ability for plastic deformation, the stress concentration at a notch root is not offset by the necessary degree of crack-tip plasticity needed to blunt the crack tip. Consequently, the notch with its multiaxial stress state raises the local stress to a high level and suppresses what little plastic deformation capacity the material possesses, and brittle failure occurs [184].

It is thought that the change in slopes is also attributable to the following. Increasing the pearlite content in the microstructure increases the impact transition temperature significantly [78]. It can be seen from Table 23, that F8105 contains 36% more pearlite than F8104.

Dimpled rupture occurs in three stages: nucleation of cavities during plastic flow, the growth of these cavities with continued deformation and finally their coalescence with complete rupture. The details of these three stages may vary widely in different materials and with the state of stress existing during deformation. Similarly, the fractographic appearance of the final fracture surface is influenced by these same factors.

Nucleation may occur in systems containing second-phase particles, by particle/matrix interface separation or by particle cracking. It proves convenient to divide types of fracture into two categories: cracking processes and rupture processes. The former is ideally modelled by cleavage fracture in mild steel, the latter by ductile void coalescence.

Cleavage fracture in mild steel depends on two components: the initiation and the propagation of microcracks. usually formed in grain boundary carbides. At moderately low temperatures, microcracks are initiated by slip of dislocations and the fracture criterion for a yielded region then becomes simply the attainment of sufficient local tensile stress, σ_F to propagate the microcracks through the ferrite grains. The stress can be measured conveniently in notched bars and is found to be substantially independent of temperature.

When the fracture is produced by fibrous mechanisms, the difference between the first crack extension and instability is increased. In a moderately ductile material, possessing high work-hardening capacity, the crack tip blunts to a rounded shape and coalesces with a void formed around nearest inclusions to the tip by internal necking, as illustrated in Figure 179 by Knott et al. [61,224,253].

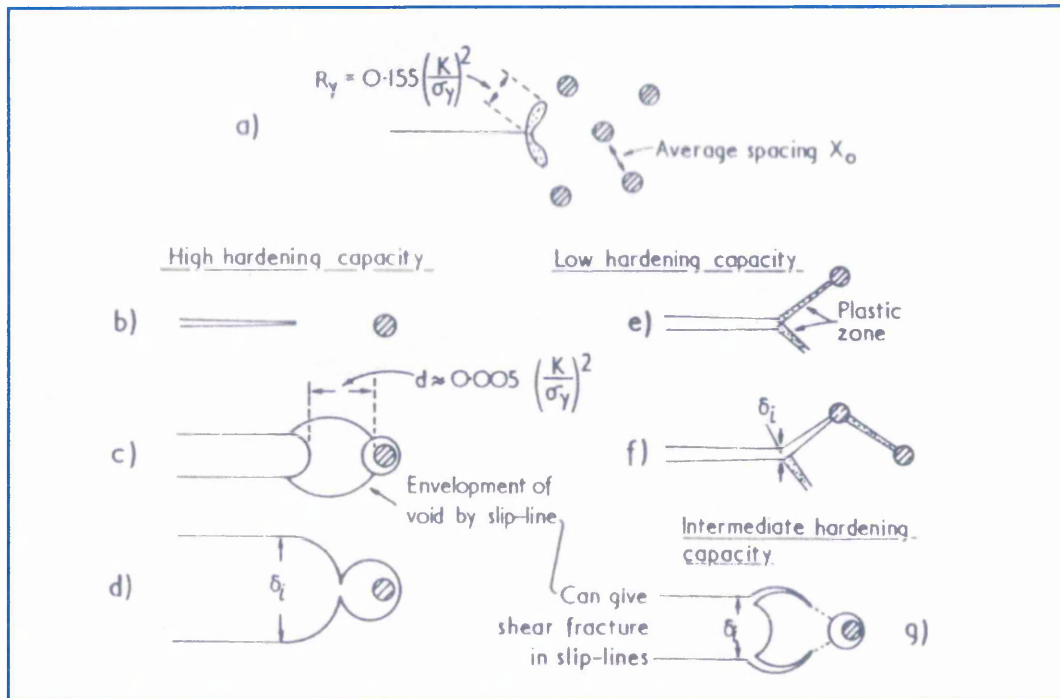


Figure 179. Modes of ductile fracture separation [224].

Figure 179 a shows a general picture of crack tip separation, Figures 179 b, c, and d, show internal necking, Figures 179 e and f show shear decohesion, and Figure 179 g shows termination of internal necking by shear decohesion.

Several theories have been proposed to account for cracking; for example cleavage or interfacial failure. The case of slip initiated transgranular cleavage, under K_{1C} conditions is believed to conform to the attainment of a critical fracture stress over a characteristic distance l_0 . For the case of low carbon steels that possess ferrite pearlite microstructures, l_0 is found to be equal to several grain diameters and conforms to the spacing between grain boundary carbide particles [61,253,259].

For conditions involving ductile fracture a stress modified critical strain criterion has been formulated [1]. With fracture defined when a critical strain ϵ_f exists over a critical distance [260] (see Figure 180).

In the ductile to brittle transition region at the initiation point of fracture

there is a competition between if cracking of an inclusion will lead to growth of a governing void or if the crack will continue as a cleavage crack in the matrix. If

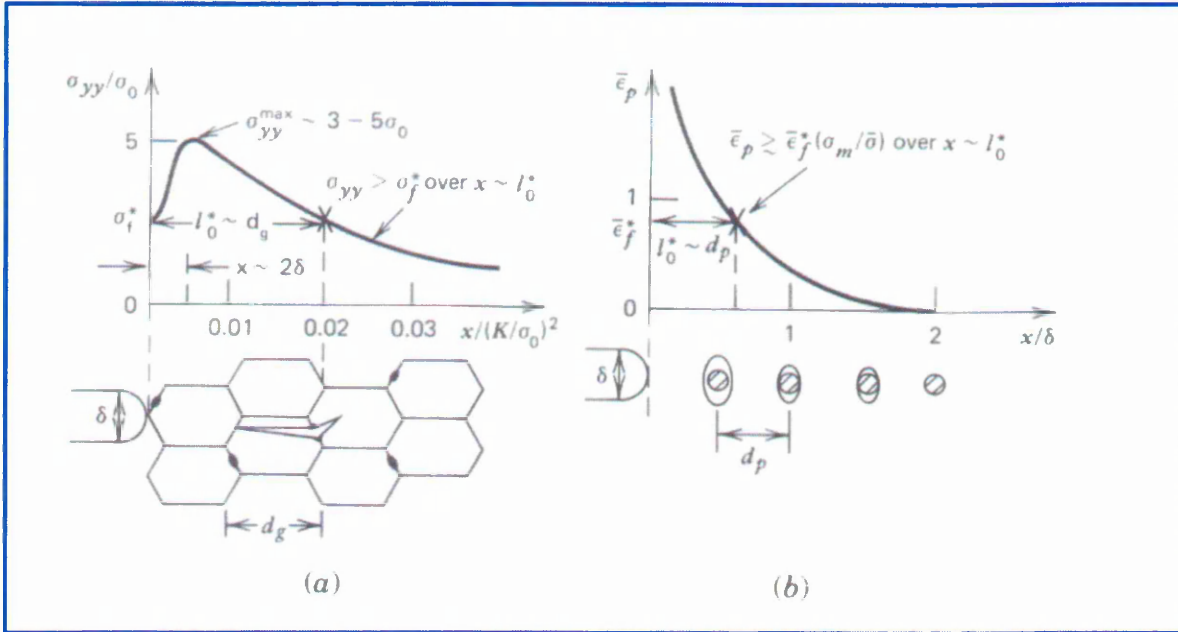


Figure 180. Schematic representation of theoretical models for (a) critical stress controlled model for cleavage fracture and (b) stress modified critical strain controlled model for microvoid coalescence [260].

the void is getting larger the crack grows in a ductile manner, but if a micro crack forms this may result in a global brittle fracture.

The presence of interstitial nitrogen is known to cause embrittlement of the ferrite [228]. It is thought that the change in slopes is also attributable to increasing the pearlite content in the microstructure which increases the impact transition temperature significantly [78]. It can be seen from Table 23, that F8105 contains 36% more pearlite than F8104 [258].

When austenite transforms isothermally just below 723°C the reaction product is pearlite. Pearlite is not a phase but a mixture of two phases, ferrite and cementite. Ferrite forms a continuous phase, with the plates of the cementite surrounded by the ferrite matrix. Ferrite is tough and ductile this makes the pearlite tougher and stronger if it is present in greater quantities

[261]. The mechanism by which this is achieved is discussed by Honeycombe [262] and Gladman et al [228,255].

The ductility of steel is also influenced by the carbide distribution which can vary from spheroidal particles to lamellar pearlitic cementite. Comparing spheroidal cementite with sulphides of similar morphology, the carbide particles are stronger and do not crack or exhibit decohesion at small strains, with the result that a spheroidized steel can withstand substantial deformation before voids are nucleated and so exhibits good ductility. The strain needed for void nucleation decreases with increasing volume fraction of carbide and so can be linked to the carbon content of the steel [262].

Pearlitic cementite also does not crack at small strains, but the critical strain for void nucleation is lower than for spheroidized carbides. Another factor which reduces the overall ductility of pearlitic steels is the fact that once a single lamella cracks, the crack is transmitted over much of a pearlite colony leading to well-defined cracks in the pearlite regions. The result is that the normal ductile dimpled fractures are obtained with fractured pearlite at the base of the dimples.

The effects of second phases on the ductility of steel are summarised in Figure 181, where the sulphides are shown to have a more pronounced effect than either carbide type. This arises because, in the case of the sulphide inclusions, voids nucleate at a very early stage of the deformation process. The secondary effect of the particle shape both for carbides and sulphides is also indicated [78,255].

Cementite has significant effects on the fracture strain of medium and high carbon steel. The cementite particles, however, are reasonably strongly bonded to the ferrite matrix, and failure is commonly initiated by carbide shear cracking. In low carbon steels, however, the stresses required to cause carbide shear cracking require considerable plastic deformation of the ferrite matrix, and fracture can often precede carbide cracking due to the presence of non-metallic inclusions in the steel. These inclusions include both sulphides and oxides, commonly initiate failure by interface decohesion [2,3,253].

Void initiation is virtually spontaneous in the case of non-metallic inclusions, the voids being initiated by interface decohesion in the earliest stages of plastic deformation. The initial shape of the void is essentially that of the inclusion on which the void is formed. The void growth rate, although dependent on the inclusion shape, is also dependent upon the stress and strain state involved in the deformation process itself [78].

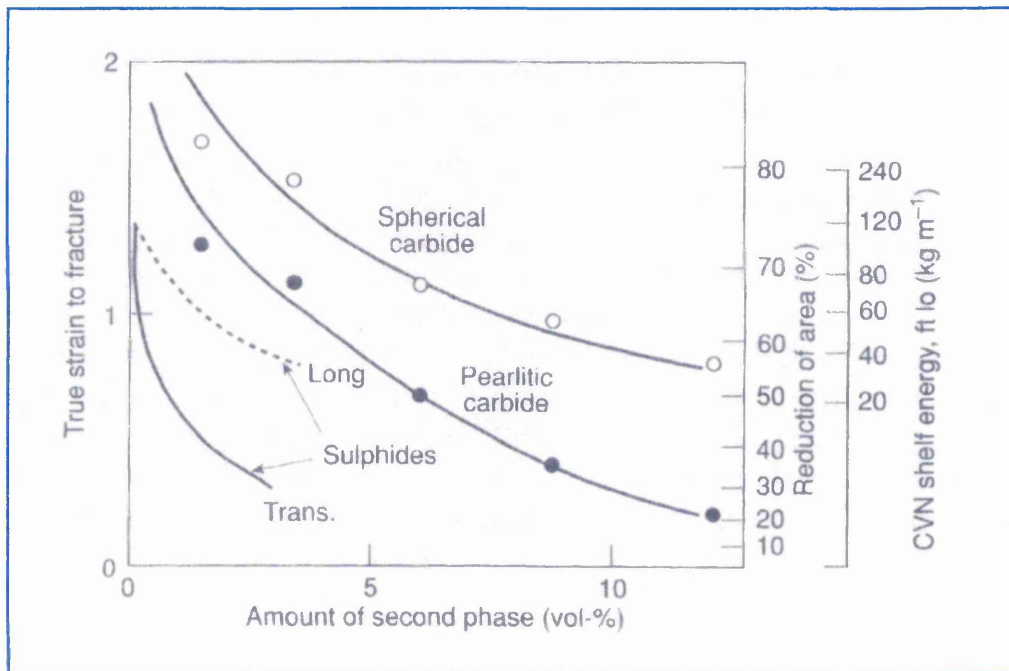


Figure 181. The effect of second phase particles on the ductility of steel [78].

It has been shown that pearlite has an adverse effect on ductility and toughness temperature. Quantitative studies have shown that as the carbon content is increased, the impact transition is raised substantially [239]. Figure 182 shows the effect of pearlite on the ITT.

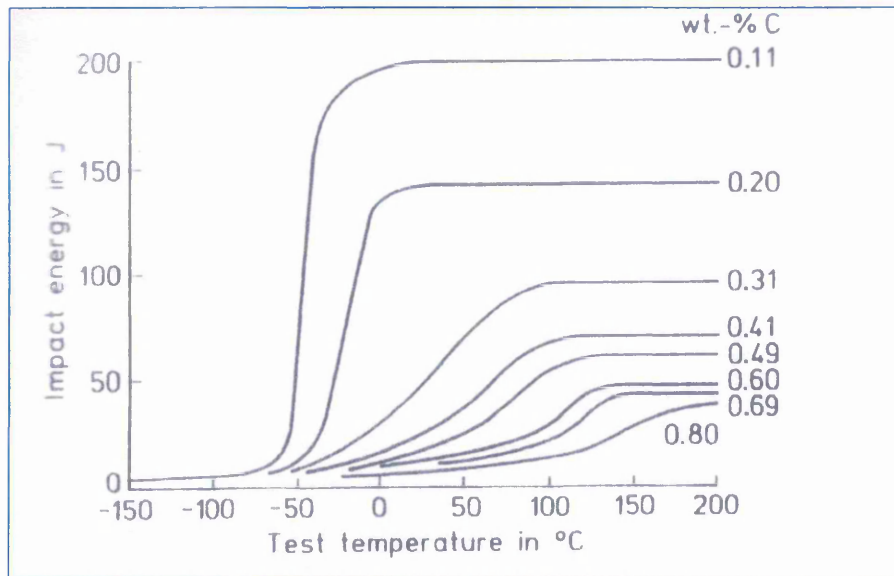


Figure 182. The effect of pearlite on toughness measured by Charpy impact transition temperature [239].

It has been shown that 1% by volume of pearlite raises the transition temperature by about 2°C [78]. The presence of pearlite in the microstructure provides sites for easy nucleation of cracks, particularly at the ferrite cementite interfaces. However as the crack can only propagate in ferrite a short distance before encountering another cementite lamella, energy is absorbed during propagation. The result is that there is a wide transition temperature range. In contrast the low energy absorbed overall in impact tests on pearlitic structures arises from the fact that many crack nuclei can occur at the pearlitic interfaces which together with the high work hardening rate, restricts plastic deformation in the vicinity of the crack.

It was stated earlier that the transition from ductile to brittle fracture occurs when the yield stress equals or exceeds the brittle fracture stress. It has been shown in the discussion on the tensile testing results that free nitrogen increases the strength of a steel significantly as the temperature is increased. The decrease in the upper shelf energy as the strength of a steel is increased as shown in this work and by Hertzberg who citing Hodge et al [250] (see Figures 172 and 177) is explained quantitatively in Figure 183 by Callister [263]. Which shows the temperature dependence of the Charpy V notch energy curve for an A283 steel.

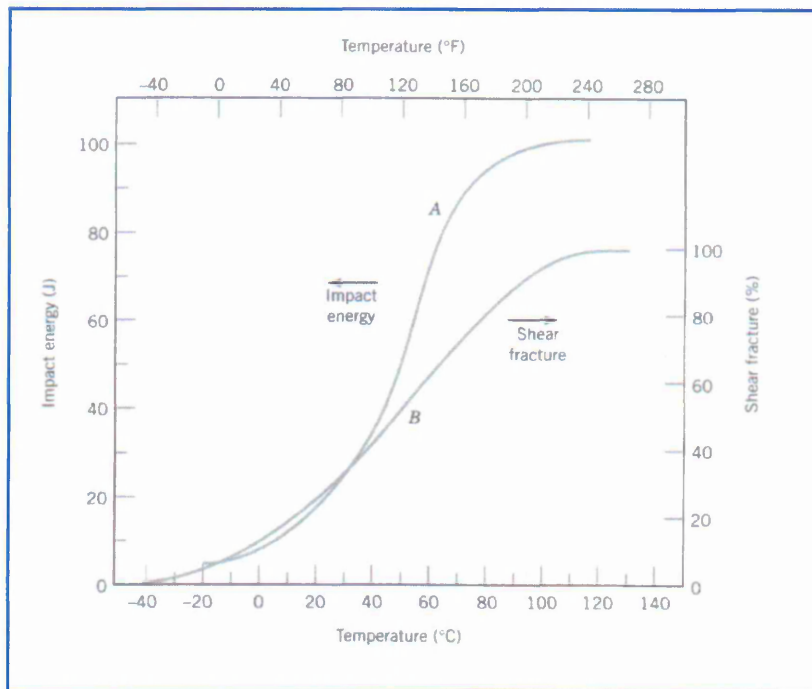


Figure 183. Temperature dependence of the Charpy impact energy for an A283 steel [263].

The ductile to brittle transition is represented by curve A, in Figure 183. At higher temperatures the Charpy upper shelf energy is relatively large, in correlation with a ductile mode of fracture. As the temperature is lowered, the impact energy drops suddenly over a relatively narrow temperature range, below which the energy has a constant but small value, that is the mode of fracture is brittle.

The appearance of the fracture surface is indicative of the mode of fracture, for ductile fracture the surface appears fibrous or dull (see Figure 88) or of shear fracture. Conversely totally brittle fracture surfaces have a granular or shiny texture (see Figure 86). The per cent shear fracture is plotted as a function of temperature in curve B. This steel has an ITT of 110°C. From Figure 172 it can be seen that nitrogen in conjunction with the methods discussed, must be lowering the materials ability to deform plastically, (by a decrease in the upper shelf energy) and this would be reflected in an increase in the shear fracture surface area. The interaction between the yield strength and brittle fracture strength which gives rise to the transition behaviour has been observed and is dependent upon many factors both microstructural and compositional.

5.4.4. Discussion of the results for Interstitial free steel.

It can be seen from Figure 84 and Figure 129 that the Interstitial free steel has the highest elongations, true strains to fracture, reductions in area, and the highest upper shelf energy of all the steels tested.

Pickering [8] observed that there was a unique relationship between the impact shelf energy and the total strain at fracture. A linear relation was observed between the true strain at fracture and the logarithm of the shelf energy. The results of this work are shown in Figure 184. Pickering's work is shown inset in the graph for comparison (Figure 184a).

Figure 184. True strain to fracture vs the logarithm of the shelf energy for all the steels tested.

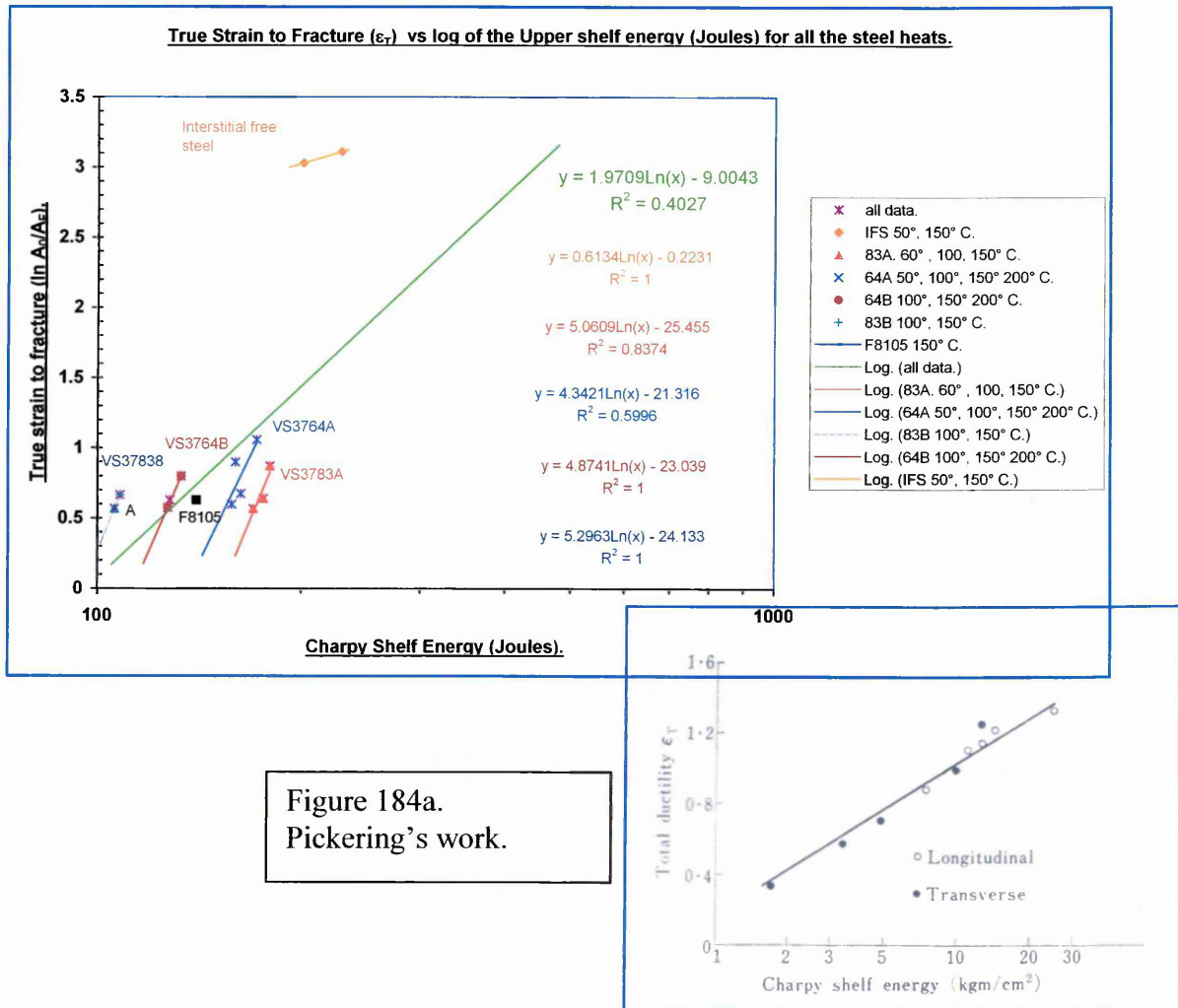


Figure 184a.
Pickering's work.

Gladman [78] noted that the effect of inclusion shape and content on the true strain to fracture in the tensile test (or reduction in area) is qualitatively the same as their effects on the Charpy ductile shelf energy, or the strain to fracture in transverse bends (as measured by the ratio of the bend radius to plate or strip thickness).

It can be seen from Figure 184 that the interstitial free steel has far superior upper shelf energies and strains to fracture. The data was first plotted for each steel heat using the true strain values in Table 13, and the upper shelf energy values from Figure 84. The temperatures used for each steel heat are given in the legend. A trend line was then fitted to the data for each steel heat. It can be seen that a family of lines are generated for each steel heat, roughly parallel to each other for the VS series of steel heats. The equations of which are given in the figure. The equation colour corresponds to the relevant steel heat. It can be seen that the highest upper shelf energy values correspond to the lowest sulphur values. Only one upper shelf data point was used for the F81 series and this was for F8015 at 100°C, as no tensile data was available for the corresponding upper shelf temperature value (see Table 14).

All the data for all the steel heats was then graphed as a block and a trend line put through it all. This is what was used for comparison with Pickering's work. It is pointed out that the bottom data point for VS3783B is based on the trend of all the steel heats (point A on the graph). As stated in the results section it was thought that the last data point for VS3783B could be due to scatter, as indicated by other data points in Figure 84. The value used was 106 Joules, instead of 136 Joules. It should also be noted that Pickering's x axis (log of the shelf energy is in kgm/cm^2).

It was stated in the introduction in this work that the ductile fracture of metals generally occurs by the formation and subsequent growth and coalescence of voids or cavities. If cavity nucleation could be delayed or suppressed altogether, large increases in ductility could be achieved.

In body centred cubic (BCC) and face centred cubic (FCC) polycrystalline

metals of very high purity, the absence of inclusions and second phase particles leads virtually to a complete absence of microvoids in any sustained process of plastic flow. Under these conditions a uniaxial tension specimen will usually fail by virtually 100% reduction in area of the external neck that develops when the specimen becomes plastically unstable [1]. This is illustrated in Figure 127 where the interstitial free steel had the maximum reduction in area 96.5% at 100°C.

The composition of the modern interstitial free steels is tailored to give an essentially pure iron, with a minimum solute content, and very low carbon and nitrogen contents. This minimisation of solutes in commercially annealed interstitial free steels is also augmented by a minimisation of the fraction of second phase particles by control of the overall impurity levels as can be seen from Table 5.

Essentially interstitial free steel can be considered a single phase system and void nucleation occurs by slip band intersection with MnS inclusions. Void nucleation can occur at blocked slip bands in the absence of second phase particles [1]. In this situation a relatively higher strain is required to nucleate the voids, which implies a greater energy input (as reflected in the highest upper shelf energy). The other steels possess ferritic – pearlitic microstructures. In such particle bearing systems void nucleation should occur at second phase particles either by decohesion of the particle matrix interface or by the breaking of the particles.

5.5. Fracture Toughness Testing (J_{1C}) discussion of results.

Figure 131 shows the set of compliance curves for the steel heats tested (VS3764A and VS3764B). It can be seen that the load vs load line displacement curves for the tests done at 200°C for both the steel heats, show serrated flow on them.

This was also observed by Miglin et al [65], this is due to the unloading procedure used, in that a static strain aging phenomenon occurs. Figure 185 taken from their paper illustrates this effect.

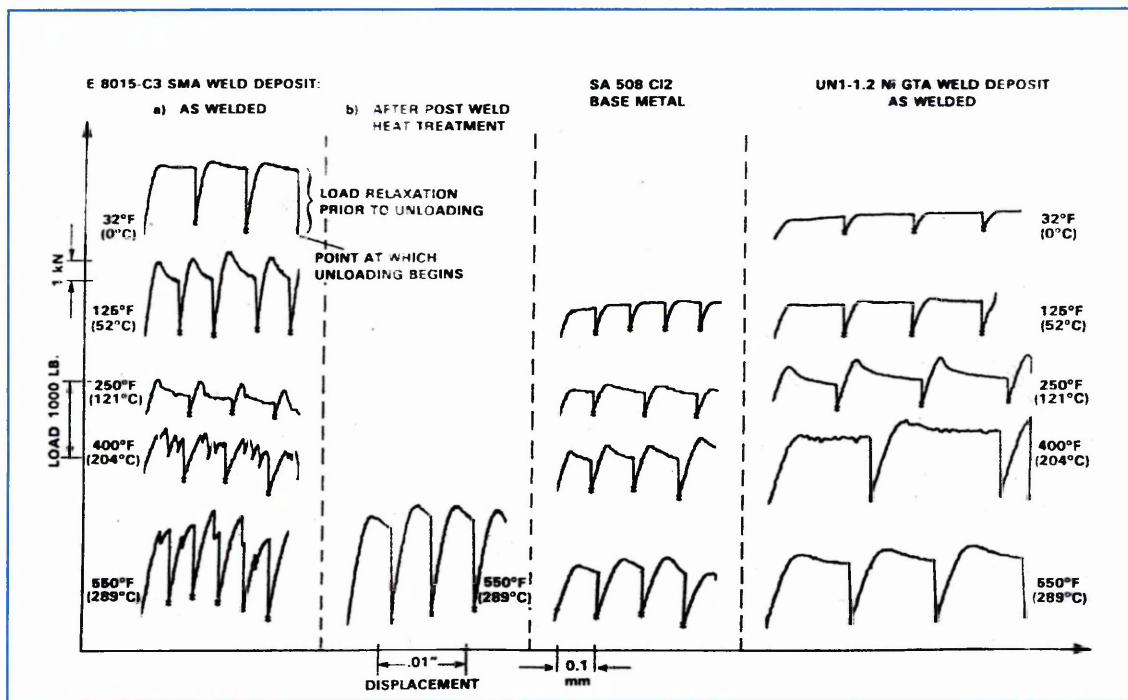


Figure 185. Portions of unloading compliance traces [65].

This effect is clearly revealed by the appearance of transient overload peaks on the reloading curves.

Wagner et al [48,85,86] also observed this effect in their work, [48] done on C – Mn steels at 100°C and 200°C. The effect being more pronounced at 100°C (see Figures 186 and 187).

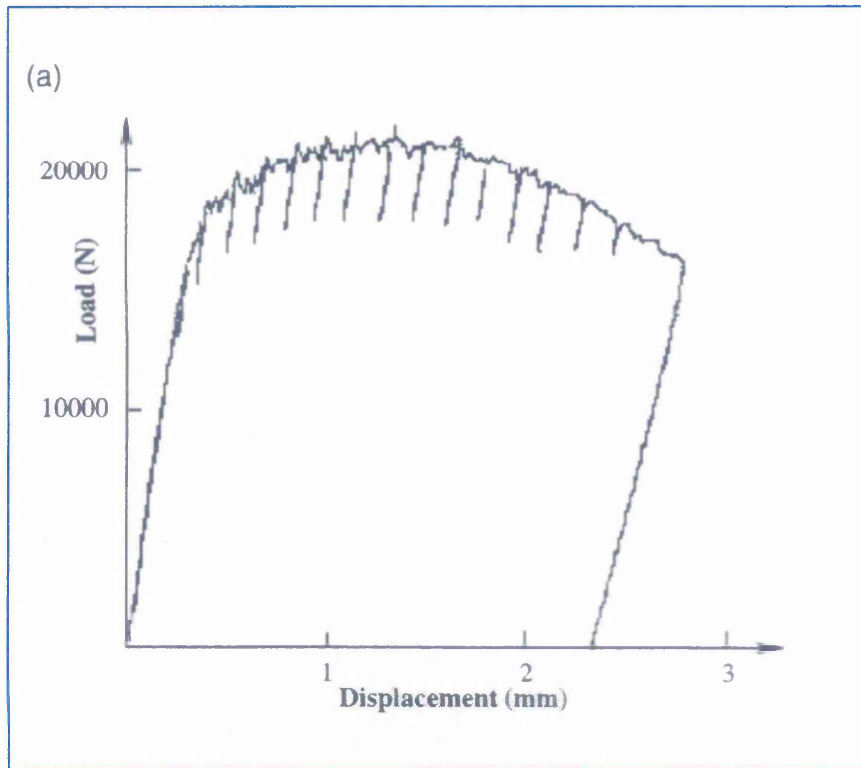


Figure 186. Load Displacement Curve (temperature 100°C) [48].

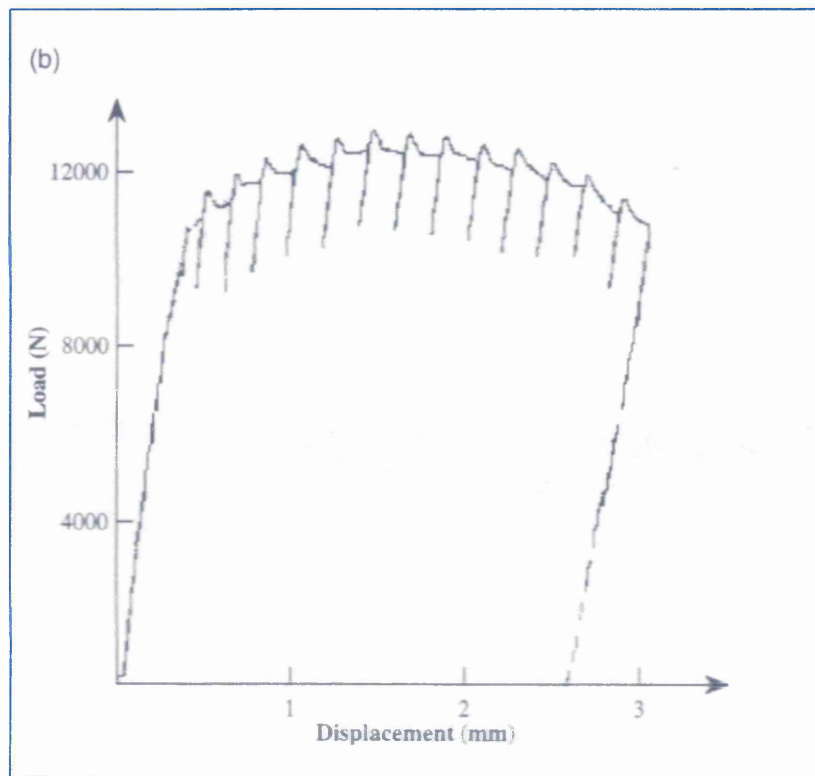


Figure 187. Load Displacement Curve (temperature 200°C) [48].

Figure 188 shows the compliance curve for steel heat VS3764A (specimen J2A) tested at 200°C in air, inset is an exploded view of the compliance curve between a load line displacement of 2 to 3 mm. Serrations are clearly visible though the transient peak overloads are not as pronounced as those of Miglen [65]. But the free nitrogen content of their steel heat was for heat 645, 0.004 weight % N_f and heat 649 0.003 weight % N_f . A factor of approximately three times and twice as much as N_f as VS3764A and VS3764B.

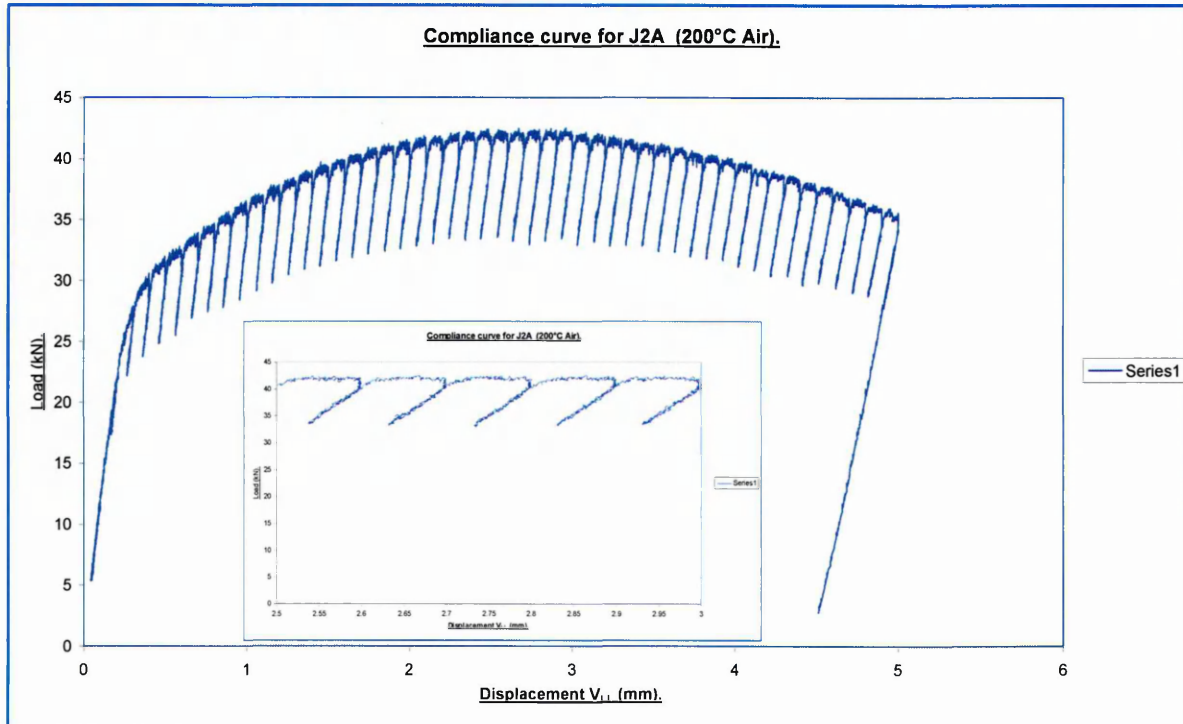


Figure 188. Compliance curve for specimen J2A.

In line with the literature reviewed [62 - 68] the sequence of degradation in the J vs Δa curves (see Figures 131 to 133) was as follows starting with the lowest J_{1C} value first (see Table 25).

Specimen.	Steel heat.	Temperature. °C	Environment	J _{1C} kJm ⁻²
J11B.	VS3764B.	200°	Air.	42
J7B.	VS3764B.	20°	Air.	153
J3A.	VS3764A.	200°	8ppm DOW	165
J2A.	VS3764A.	200°	Air.	192
J1A.	VS3764A.	20°	Air.	290

Table 25. Degradation in J_{1C} of the steel heats tested.

The detrimental effects of sulphur content and elevated temperature on J_{1C} are clearly evident as seen in Table 25. Schellenberger and Diemel [51] saw this reduction in their work. They did a study on 20 MnMoNi 5 5 to determine the J - R curves of the steels with two different sulphur contents (0.003 and 0.011 wt%). The tests were done at 240°C in 8ppm DOW high temperature water and air. The single specimen unloading compliance technique was used at load line displacement rates from $1 \times 10^{-4} \text{ mm sec}^{-1}$ down to $1 \times 10^{-6} \text{ mm s}^{-1}$ on 20% side-grooved 2T CT specimens in an autoclave testing facility. A pressure of 7MPa was used under quasi-stagnant flow conditions. They saw a reduction in the J_{1C} value in the high sulphur material decrease from 45 N mm^{-1} when tested in air, to 3 N mm^{-1} when tested in 8ppm DOW. As opposed to the optimized material which went from a J_{1C} value of 50 Nmm^{-1} when tested in air to 20 Nmm^{-1} when tested in the 8ppm DOW. The testing temperature was 240°C.

James and Porr [41] conducted tests on ASTM A508 Class 2 steel in both air and water environments at 243°C using the monotonic rising load tests, and specimen loading rates of 0.0254mm/min and 0.1524mm/min respectively. The multi-specimen method was used to eliminate corrosion fatigue

interactions that could occur in the unloading compliance method. They verified that subsequent tearing appears to require less energy in the water environment, than it does in air, and also observed that post J_{1C} tearing in the water environment was characterised by *pop in* events and that these were more numerous in the water environment and were of greater magnitude than those in air. James [41] postulated that the main cause of these could be attributed to MnS inclusions. They postulated that this phenomenon was due to strain aging in the steel. The degradation in J_{1C} and the tearing modulus in air and water environments is shown in Figure 189.

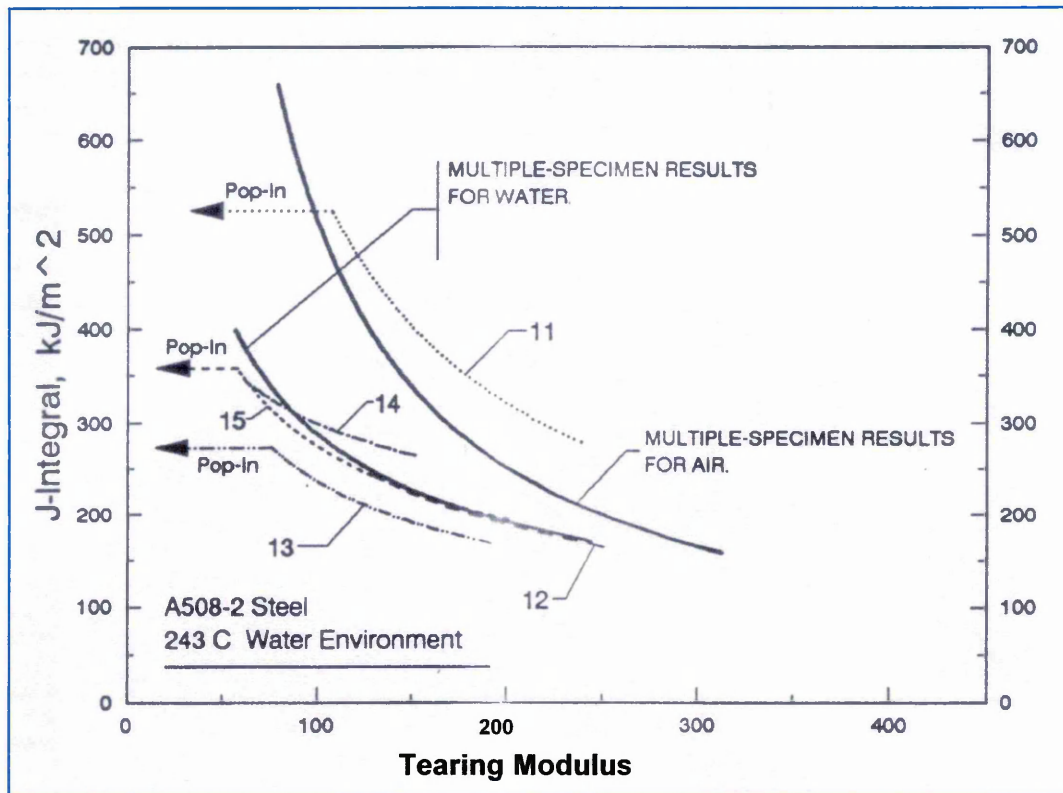
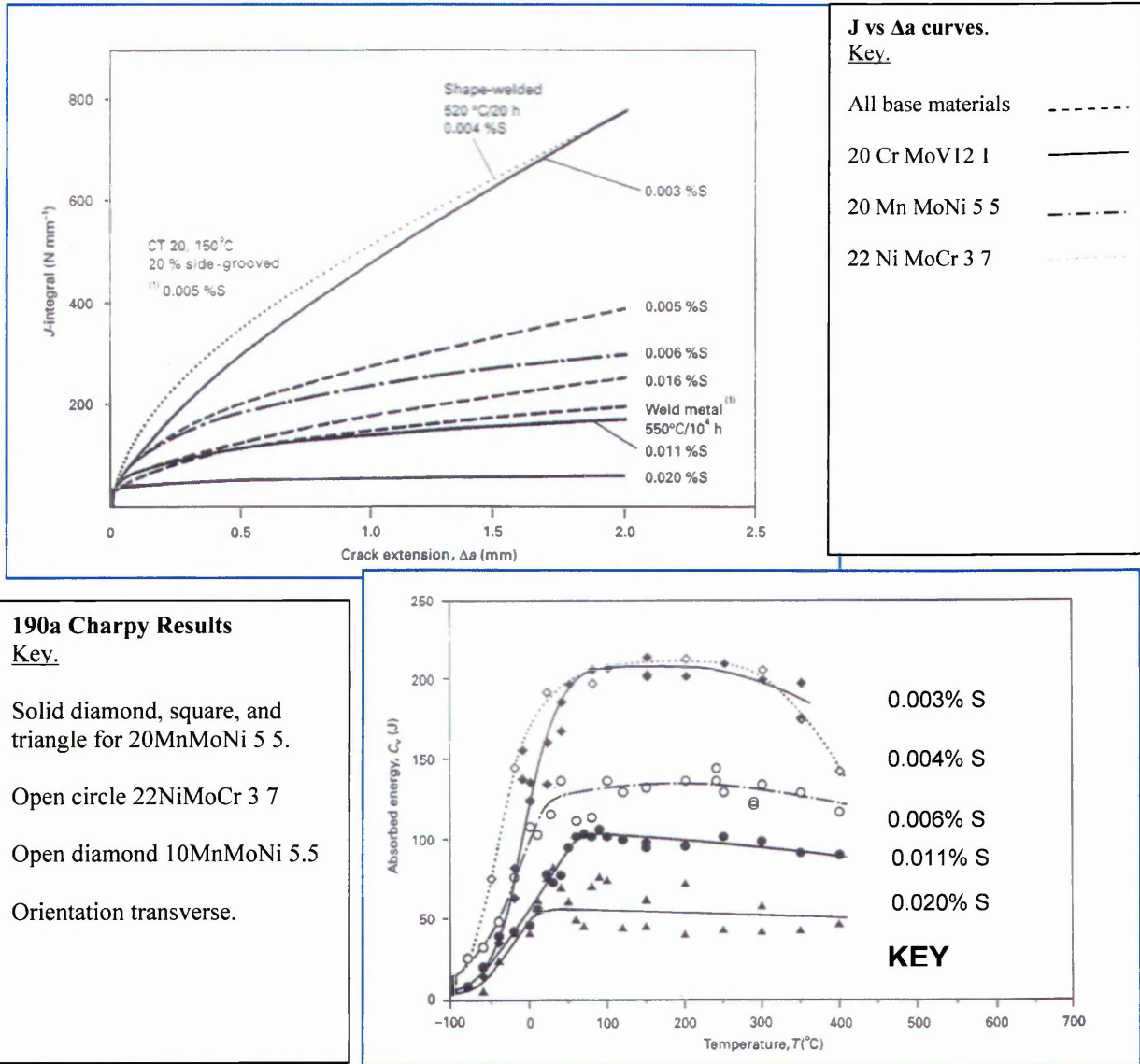


Figure 189. Degradation in J_{1C} and tearing modulus [41].

Diemel and Sattler [264] in work conducted in an air environment on 12% Cr steel X 20 CrMoV12 1, A 508 Class 3, and A 508 Class 2, steels using tensile, fracture mechanics, and Charpy impact tests to assess the relationship between non metallic inclusions and the J Integral. They also noted a degradation in the fracture toughness values, and Charpy upper shelf energy values as the sulphur content of the steel was increased (see Figures 190 and 190a). Fracture toughness tests were done at 150°C. The irregular crack shaped front seen in Figure 135 (region A for the VS high sulphur steel heat

64B) is thought to be attributable to MnS inclusion inhomogeneity due to the forging process. Resulting in an increase in the MnS inclusion cluster density [1,43,238]. Figure 149 is a side elevation of the crack front at region A in Figure 135, it shows that immediately after the stretch zone (see Appendix 1) the crack front goes out of plane, assisted by the increased MnS inclusion cluster density.

Figure 190. J vs Δa curves and Charpy upper shelf energy for ref [264].



It can be seen from Figures 190 and 190a that the highest sulphur content steels have the lowest fracture toughness, and shelf energy values. The trend followed in this work.

Gibson and Druce [43] in work done on a A 508 Class 3 forging also found this degradation in J_{1C} due to sulphur content, (see Figure 14) but they also had

another two variables in their test programme, in that they changed the sulphate content of the environment. The loading rates were also varied, and the test temperature was 288°C.

From the fracture toughness testing results it can be deduced that the deterioration of the J – R fracture resistance is due to dynamic strain ageing in the steel heat VS3764A and VS3764B. The degradation in the fracture toughness (J_{1C}) and the tearing modulus seen in Table 25 has been observed by numerous authors [48,62 – 68,85,86]. The collated work of references [41,62 – 68] are shown in Figure 14. It is pointed out that the dJ/da values obtained in Table 25 are the derivatives of the graphed equations in Figure 132.

The degradation in the tearing modulus for VS3764A and VS3764B obtained in this work is shown in Figure 191 for temperatures of 20°C and 200°C. It is thought that the VS3764B results give a more realistic result.

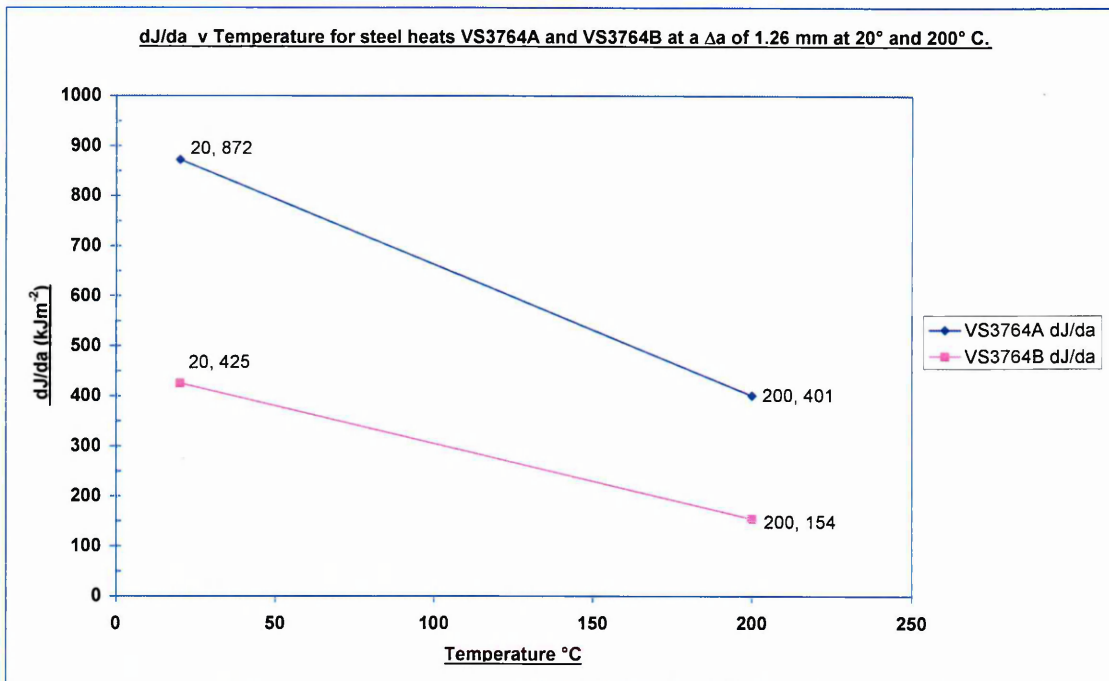


Figure 191. dJ/da vs Temperature for VS3764A and VS3764B.

The values for Figure 191 were taken from Table 25 at 1.26mm of crack growth. It is pointed out that the values for VS3764A at 20°C may be a bit high (see Figure 131 the curve nearest to the y axis), and could be attributable to friction in the cleavages (see Appendix 5). Although Miglen et al [65] had a similar result in their work and attributed this to unstable crack growth (see

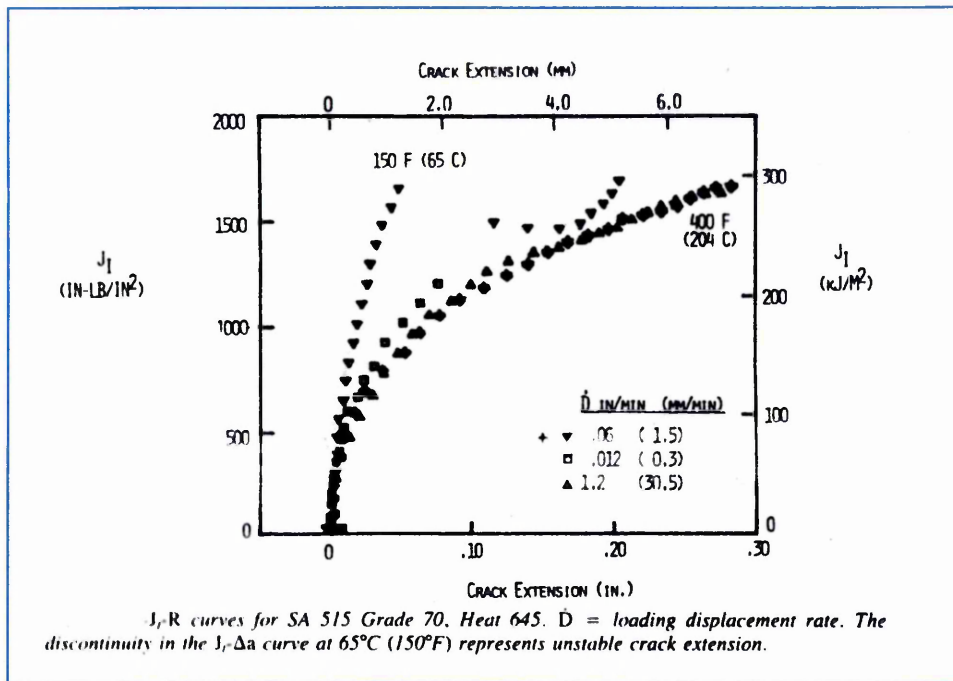


Figure 192. J – R curves from Miglen et al [65].

Many investigations have been devoted to the study of ductile tearing, which takes place in the upper shelf region in low and medium strength steels in air [62,63,64,65,66] and aqueous environments [42]. It is generally found that there is a decrease in J_{IC} (the crack extension resistance under conditions of crack tip plain strain) and the tearing modulus (the crack growth resistance dJ/da [40]). Kim and Kang [62,67,68] found that the tearing modulus was 30 - 40% smaller than that at room temperature in the dynamic strain aging region at elevated temperature see Figures 193A, 193B, 193C. Druce [42] and James [41] conducted similar tests in aqueous environments and found the same observations.

The collated work of Kim et al [68] is shown in Figure 193A shows the degradation in the tearing modulus, Figure 193B the degradation in J_{IC} , and Figure 193C the effect of strain rate on the J vs Δa curve.

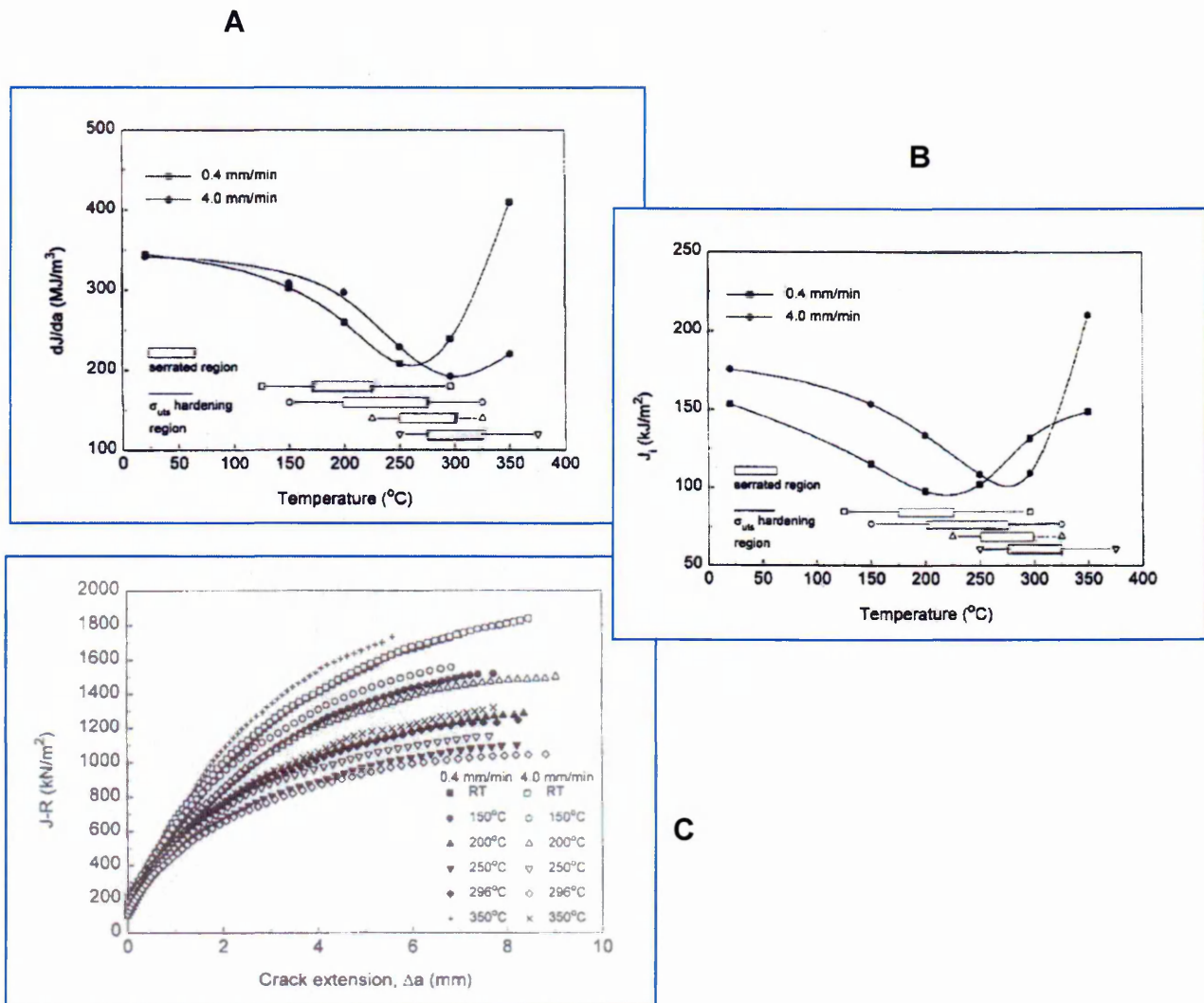


Figure 193. Variation in the Tearing modulus and J_{1C} with temperature [68].

What is also interesting is that Kim et al [68] observed the same effect in their tensile testing programme in work conducted on SA 106 Gr.C piping steel as was seen in this work. The composition of which is given in Table 26. The fact that uniform elongation does not decrease and the fraction of uniform elongation in the total elongation increases in the DSA region contrary to the usual expectation that both uniform and total elongation are reduced by DSA. They attributed this to the continuous work-hardening effect caused by the high manganese content (1.22%). Usually, the reduction of uniform elongation in the DSA region has been explained by a localised exhaustion of sufficient interstitial solute to lock dislocations [55,142] or a decrease in rate of work-hardening rapidly after high dislocation multiplication in the range of initial deformation

[97]. They concluded that, the dislocation locking resulting from interstitial exhaustion may not be as high in the lower strain region, since the diffusion of the solute atom was not sufficient to lock the mobile dislocation completely. The high dislocation multiplication in the initial strain region may be limited, while with increasing deformation continuous work-hardening may also occur with dynamic strain ageing (DSA) until the elongation to the ultimate tensile strength (UTS).

Chemical composition in wt %.											
C	Mn	P	S	Si	Ni	Cr	Mn	V	Al	Cu	Hppm
0.19	1.22	0.009	0.007	0.27	0.11	0.05	0.03	0.004	0.029	0.13	1.6

Table 26. Chemical composition of SA 106 Gr C steel used by Kim [68].

Ingham et al [265] in work conducted on SA533B – 1 plates, SA508 – 3 forgings and a weld metal also observed this degradation in J_{1C} . Figure 194 shows the results for one of the steel heats studied steel F2. The composition of all the materials studied are given in Table 27. The results of the whole testing programme are given in Tables 28 and 29.

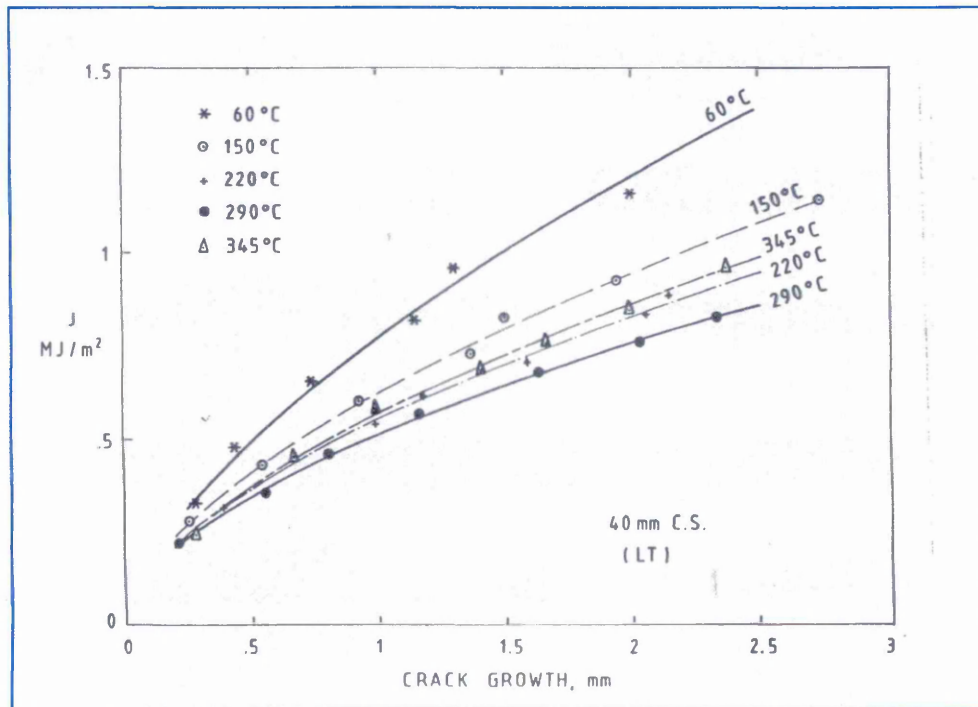


Figure 194. J vs Δa for F2 forging [265].

The degradation in material properties in the dynamic strain ageing regime is quite evident in Tables 28 and 29.

Table 27. Chemical Analysis of Materials studied by Ingham [265].

TABLE 1. ANALYSIS (wt.%) OF MATERIALS

Material	C	Si	Mn	Ni	Cr	Mo	S	P	Cu
P1	0.19	0.20	1.40	0.66	0.13	0.49	0.006	0.010	0.10
F1	0.21	0.26	1.45	0.75	0.12	0.52	0.002	0.005	0.01
F2	0.20	0.24	1.36	0.73	0.13	0.48	0.007	0.006	0.06
F3	0.175	0.28	1.36	0.77	0.13	0.49	0.004	0.007	0.046
F4	0.15	0.26	1.36	0.73	0.245	0.52	0.0065	0.007	0.059
W1	0.12	0.36	1.41	0.10	0.05	0.56	0.016	0.004	0.03
Forging*	0.20 max	0.15-0.30	1.2-1.5	0.4-0.85	0.15 max	0.45-0.6	< 0.008	< 0.008	< 0.09
Weld*	0.15 max	0.15-0.40	1.2-1.5	0.85 max	0.15 max	0.45-0.6	< 0.01	< 0.01	< 0.07

* Sizewell B specification

Table 28. Results of testing Programme studied by Ingham [265].

Material	Temp °C	Orientn.	Thickness mm	K _i MPa√m	K _{0.2} MPa√m	K _{JC} MPa√m	K _{0.5} MPa√m	K _{2.0} MPa√m	K _{2.0} (Ref) MPa√m
F1	20	LS	40	246	238	-	340	570	421
F1	20	TS	40	286	242	425	327	522	421
F1	290	LS	40	211	202	289	282	456	304
F1	20	LS	15 (SG)	263	229	-	321	502	421
F1	150	LS	15 (SG)	251	216	-	288	432	~364
F1	290	LS	15 (SG)	216	192	-	253	440	304
F1	350	LS	15 (SG)	231	204	-	282	367	~304
F2	60	LT	40 (SG)	262	234	349	318	500	~404
F2	150	LT	40 (SG)	243	216	302	288	439	~364
F2	220	LT	40 (SG)	231	205	269	269	395	~334
F2	290	LT	40 (SG)	216	197	253	261	376	304
F2	345	LT	40 (SG)	222	200	272	265	397	~304
F3	290	TL	25 (SG)	217	210	262	245	369	304
F3*	290	TL	25 (SG)	217	216	257	245	350	304
F4	290	TL	25 (SG)	211	208	243	241	315	304
F4*	290	TL	25 (SG)	199	194	196	233	311	304
F4	250	TL	25 (SG)	198	206	-	245	326	~321
F4*	250	TL	25 (SG)	-	178	-	233	329	~321

* Irradiated

Table 29. Toughness values for W1 forging [265].

TABLE 5. TOUGHNESS VALUES FOR W1 MATERIAL

Temp °C	Thickness mm	Condition	K _i MPa√m	K _{0.2} MPa√m	K _{0.5} MPa√m	K _{2.0} MPa√m	K _{2.0} (Ref) MPa√m
~ 5	40	-	200	215	267	383	335
"		St. aged	259	205	259	378	335
290	25 (SG)	-	153	143	173	233	251

This detrimental effect of DSA on ductile tearing resistance does not occur in all iron base materials as stated in the introduction. Srinivas et al [22] show the opposite behaviour in pure armco iron, i.e. the fracture toughness (crack initiation resistance and tearing modulus) increases from room temperature to 200°C and then decreases see Figures 7 and 8. However, this material shows the same DSA effect as other materials on tensile properties (i.e. a maximum in UTS and work hardening rate, a minimum in elongation and reduction of area). This different behavior is attributed to the absence of inclusions in pure iron which modifies the ductile damage mechanism as discussed earlier.

However, all engineering metals and alloys contain inclusions and second-phase particles, to a greater or lesser extent, and this leads to microvoid nucleation and growth, which is terminated at a very much earlier stage in a tension test by a localised internal necking of the intervoid matrix across a sheet of microvoids [2,3]. Under these conditions ductile fracture occurs in tension specimens at approximately 70% reduction in area of the external neck, by the classical 'cup and cone' fracture mechanism. The general effect of an increasing volume fraction V_f of inclusions or second phase particles is to reduce both the true fracture strain $\epsilon_F = \ln(A_o / A_f)$ and the % reduction in area $RA = 100(A_o - A_f)/A_o$ where A_o and A_f , are the original and final cross-sectional areas of the specimen-neck region.

To explain the fact that common ductile metals normally show less than 100% reduction in area at fracture and begin to crack internally, much attention has been focused on the importance of second-phase particles, particularly hard non-metallic inclusions [5,6]. Such particles can act as barriers against which dislocations can pile up, and this leads to a concentrated local stress which is difficult to relieve owing to the hard nature of the obstacle. The stress can build up until the theoretical strength of the interface between inclusion and matrix is exceeded, so that a crack forms and then grows by plastic deformation. Many such cracks link together to produce macroscopic failure by internal necking.

5.5.1. Comparison of Charpy and J Integral Tests.

In order to simplify the determination of the ductile fracture resistance, several correlations between ductile fracture parameters and simplified tests have been developed. The most common correlator is the Charpy V notch (CVN) impact test. The CVN test is a logical choice, since in the test a specimen is broken in half and the required energy is measured. As ductile fracture is also related to the energy of fracture, the CVN test measures the materials fracture resistance. J_{1C} is related to the energy of fracture, for the reasons discussed in section 2. The J integral can be thought of as the generalisation of the strain energy release rate, G, to cases of non linear elastic stress - strain curves as shown in Figure 10.

At room temperature, the fracture toughness of C – Mn steels is essentially governed by the volume fraction of MnS inclusions. In this case fracture toughness tests can be estimated from Charpy V notch tests through various correlations. In the DSA temperature regime, the upper shelf Charpy V notch data are not affected by the DSA phenomena [248]. This is due to the high strain rate of Charpy V notch tests [48].

Several authors have proposed equations to relate the Charpy fracture energy with fracture mechanics parameters, usually referring to crack initiation [223] for example K_{1C} or J_{1C} . For low-strength high-toughness materials, it is known that crack initiation in the Charpy test accounts for only a small fraction of the total fracture energy [43]. Any correlation between the Charpy fracture energy and fracture mechanics testing, should therefore, consider both initiation and crack growth parameters. Belcher et al [43] proposed such a correlation in that the Charpy fracture energy is the energy required to initiate a crack from a blunt notch and propagate that crack across a ligament of 8 mm. Similarly the area under the J - R curve is a measure of the energy required for fracture.

Therefore evaluation of the $\int J da$ provides a basis for comparing the two types of test [43]. It should be noted that, although energetically the integral $\int J da$ embodies the essence of the Charpy test, direct comparison is without

rigorous theoretical foundation, since J-domination will not be maintained throughout the Charpy test. Table 30 gives the results of their evaluation for specific comparisons of different materials and specimen orientations using both the linear and exponential J versus Δa regression analyses extrapolated to $\Delta a = 8$ mm.

	J Integral comparison		
	Charpy USE Comparison	Linear Regression	Exponential Regression
A533R RW:A533R WI	1.25:1	0.97:1	0.96:1
A533B RW:A533B TW	2.43:1	1.78:1	1.86:1
A533B WI: A533B 1W	1.94:1	1.84:1	1.94:1
A508 1/2W:A508 1W	0.96:1	1.02:1	1.03:1
A508 1/2W:A533R RW	1.54:1	1.59:1	1.73:1

Table 30. Comparison of Charpy fracture energy and J - integral data [43].

These results suggest that this correlation can provide an approximate method for relating Charpy energy and JR - curve toughness parameters. However, an exact correlation would not be anticipated due to the differing strain rates and geometric constraints of these two types of test [43].

Based on the linear and exponential regressions obtained by Belcher et al, [43] the results from this work was plotted to see which regression gave the best correlation. First plotted was the charpy upper shelf energy vs the integral $\int_0^c J da$ (see Figure 195). The J_{1C} values at 20°C and 200°C, (see Table 15) and the corresponding Charpy shelf values at these temperatures are used for VS3764A and VS3764B (see Figure 84). The equations used to evaluate $\int_0^c J da$ are taken from Figure 132. The data was graphed in pairs initially for both the steel heats and then as a block. Exponential and linear trend lines were then fitted to the block data. It should be noted that the 20°C Charpy upper shelf value is on the ductile to brittle transition temperature (DBTT) slope for both the steel heats.

Figure 196 is the above procedure repeated but this time the 50°C Charpy upper shelf value is used for both the steel heats. It can be seen from Figure 196 that using Charpy shelf energies at 20°C (this value was used to correspond with the J tests done at 20°C) for both the steel heats the correlation for both the linear and exponential regressions is low 0.3503 and 0.3240 respectively.

The correlations in Figure 196 are considerably improved to 0.8346 for the linear regression, and to 0.8548 for the exponential regression. But the J_{IC} data points are based on values at 20°C. It is thought that the correlation could be improved further if J tests were done at 50°C to match the shelf energies. For ease of comparison the blocked data (for both the steel heats) based on the trends in Figures 195 and 196 is plotted in Figure 197. It can be seen from Figure 197 that both the linear and exponential regression correlations have roughly doubled in each case. The exponential regression being marginally better at 0.9463 as opposed to the linear correlation of 0.9428. In agreement with Belcher et al [43]. The correlation though is too close to ascertain the particular law of the trend for the upper shelf correlation with J_{IC} . Based on the original data it would favour a linear relationship, with a correlation of 0.4937.

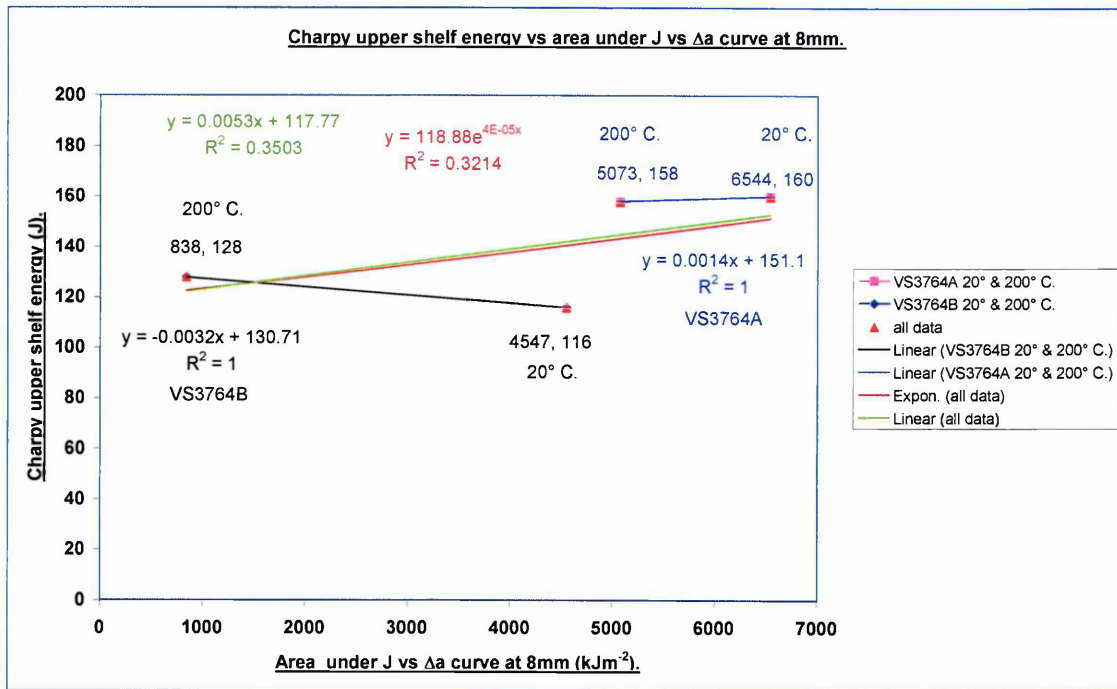


Figure 195. Charpy upper shelf energy vs area under J vs Δa curve at 8mm (20° and 200°C).

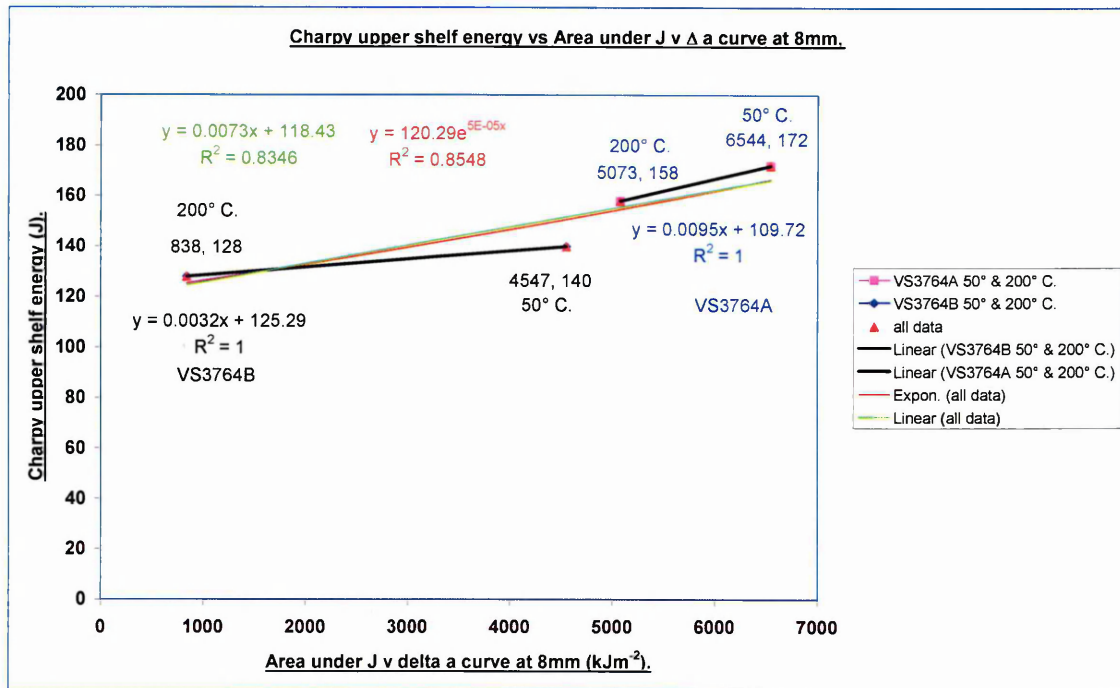


Figure 196. Charpy upper shelf energy vs area under J vs Δa curve at 8mm (50° and 200°C).

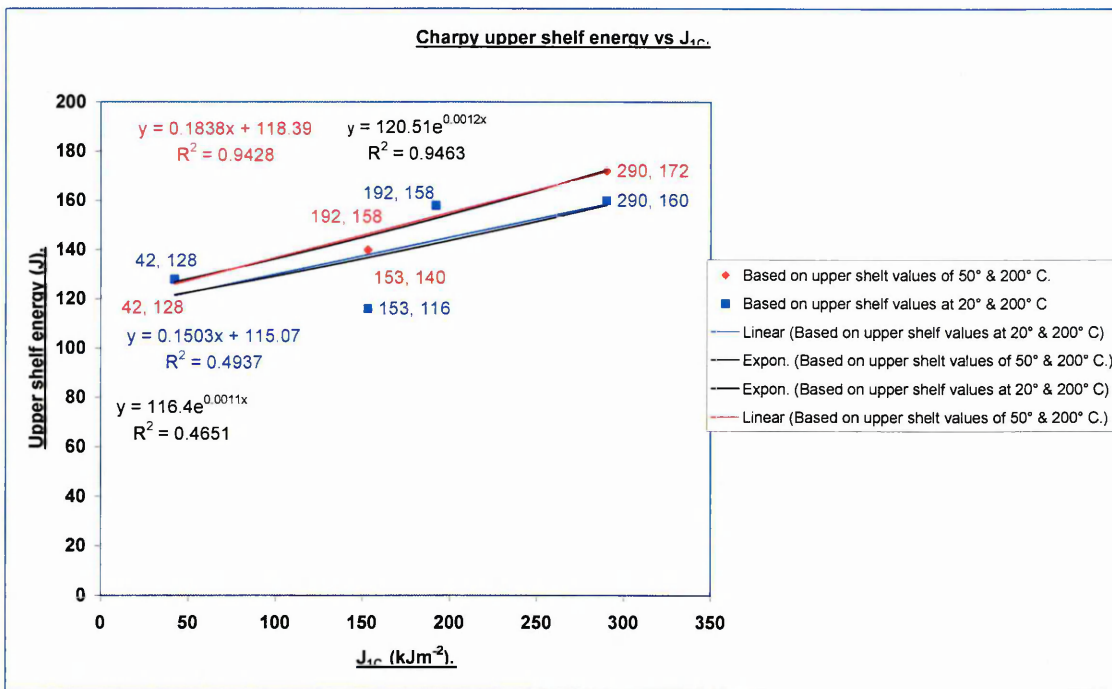


Figure 197. Charpy upper shelf energy vs J_{1C} (based on temperatures of 20° and 200°C. 50° and 200°C).

Void initiation at inclusions is known to occur at low strains the exact value being dependent on stress triaxiality [1,2,3,78,253]. Near the crack tip, the stress triaxiality is high and the contribution of void initiation to the overall ductile crack growth process may be considered negligible [1,2,3,78,253]. The results are therefore discussed in terms of models based on void growth and coalescence.

It is well established that elongated inclusion morphologies cause marked anisotropy of tensile ductility and toughness behavior. In section 5.4 Gladman's [78] model on the effect of inclusion orientation was discussed. From which it can be ascertained that where fracture occurs by the coalescence of voids formed at elongated inclusions, the projected inclusion length in the local direction of fracture governs toughness by determining the strain intensification at the crack tip. Specifically, the model predicts that initiation toughness depends inversely on the projected inclusion length in the direction of crack advance, while resistance to crack propagation is minimised when the major inclusion axis lies in the crack plane (see section 5.2.3). That is, for ductile initiation, the inclusion dimension in the direction of propagation dominates, while for

propagation, inclusion dimensions both parallel and perpendicular to this direction must be considered.

Therefore, on the basis of this model, making the assumption that fracture results principally by void growth at the elongated MnS inclusions and subsequent coalescence with the crack tip. Figure 62 shows the inclusion orientation in relation to specimen orientation from which it can be seen that the orientation exposing the minimum surface area of inclusion to the crack tip is the L – T orientation. The fracture toughness specimens in this work had this orientation. From Figure 81 it can also be seen that VS3764B had 3.92 times more inclusions in the transverse plane, 7.346 times more inclusions in the longitudinal plane and 4.149 times in the short transverse direction than VS3764A. That is there was 3.92 more times inclusions in the L – T plane in VS3764B. In the transverse plane VS3764A has more inclusion sites 115 as opposed to 87, but the inclusion cluster density is far greater in VS3764B. These clusters of inclusions can act as supervoids, as their formation provides an increased void width with attendant adverse effects on the strain concentration [78]. Inclusions influence the strain to initiate fracture and the gauge lengths over which the fracture strain is attained. It has been found that a reciprocal type of relationship between toughness and inclusion volume fraction has been found for many inclusion systems [9,10] (see Figure 3). Likewise a similar behaviour has been observed for the effect of volume fraction on tensile ductility [11-17] (see Figure 4). It is generally observed that as the volume fraction of inclusions increases, the plane strain fracture toughness decreases [18, 253].

In the L – T plane VS3764B has 3.92 more times more inclusions in the L – T plane than VS3764A. If this was the case then. the distance between neighbouring voids is decreased (the interparticle spacing is decreased, the distance $2d$ in Figure 1) in Thomason's model [2,3]. Thus the void shearing mechanism is made easier in VS3764B by the linking of inclusions at lower applied strains. Resulting in the corresponding loss in fracture toughness as shown in Tables 15 and 25.

An alternative mechanism has been proposed whereby void growth cannot occur at inclusions until they are enveloped by the logarithmic shear lines that are generated ahead of the blunted crack [253] see Figure 198, 198a, and 198b. For inclusions aligned normal to the fracture plane this mechanism requires a higher crack opening displacement or (equivalently a larger value of J) than when the inclusion axis lies in the crack plane. It is thought that this could be one of the reasons to account for the higher load line displacements in VS3764A when tested in the air environments as the area fraction of inclusions and cluster density for VS3764B in the L, S, and T directions was significantly higher on all three planes. Therefore the chance of more inclusions being in the crack plane, for VS3764B is greater. With the increased inclusion cluster density and greater number of inclusions in the cluster, the possibility of other specimen orientations other than L – T was present. Thereby lowering the fracture toughness as seen in VS3764B was possible. This was observed by Druce et al [43] they found a marked orientation dependence on fracture toughness. In that the slope of the initial $J - R$ curve in A533B, and SA508, for the short transverse direction short transverse direction was approximately half that for the longitudinal or long transverse orientations.

Green and Knott [253] have discussed the role of inclusions as cavity formers in ductile rupture, studying the effects of work hardening behaviour and inclusion content on the initiation and propagation of ductile fracture in low strength steels and correlated this with the crack opening displacement. They concluded that in the high sulphur mild steel the crack grows by a mechanism of void coalescence and that the amount of crack opening per inclusion spacing is of the same order as the inclusion spacing. The mechanism of crack growth in the low sulphur mild steel however, is one involving void growth until a critical displacement is reached between the expanded void and the crack tip. This ligament shears once it has hardened sufficiently, in a manner analogous to that of the initiation of fibrous fracture It is proposed that a similar fracture mechanism is operating in VS3764A and VS3764B.

Green and Knott [253] also proposed that materials with a high work hardening capacity had a larger plastic zone. As illustrated in Figure 198b.

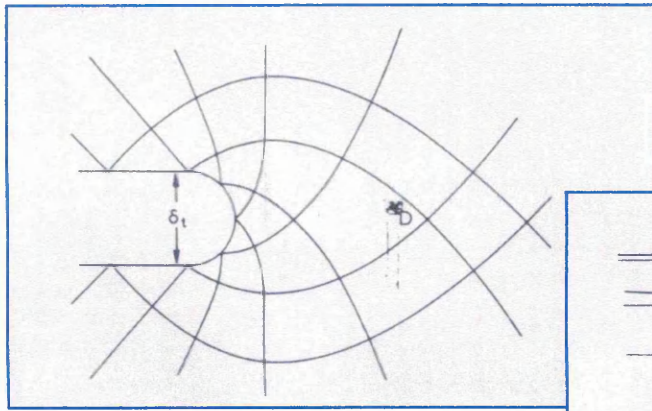


Figure 198b. Influence of plastic zone size on work hardening rate.

198a Void growth model.

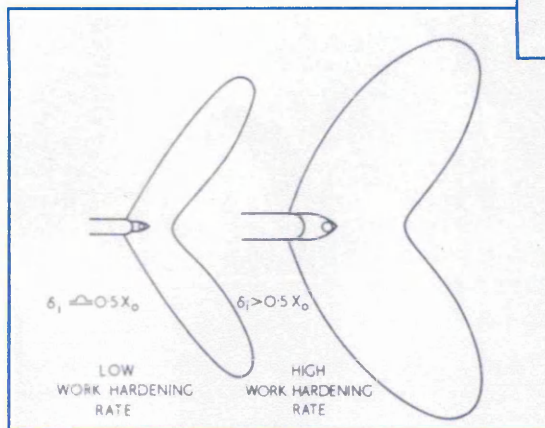
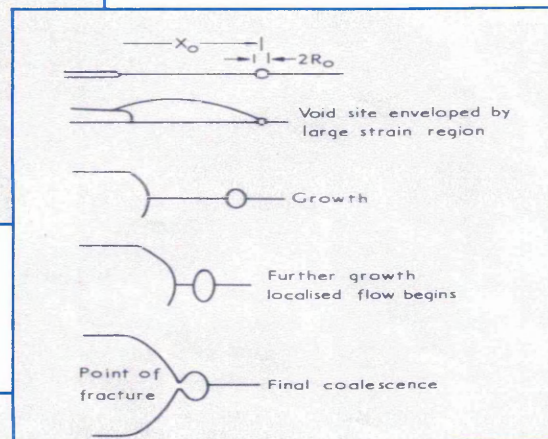


Figure 198. Slip line fields for a blunted crack tip in plain strain [253].

The greatest effect of inclusions on the energy for ductile crack initiation is on the characteristic distance over which the fracture strain is reached [2,3]. This dictates the process zone size, which in itself determines the plastic zone size for given work hardening properties. In the model proposed by Knott he found that elongated inclusions aligned normal to the crack tip, will need a larger process zone to 'envelop' them and the rate of void growth from such inclusions will be lower compared with that from inclusions in transverse specimens thus producing enhanced ductility. The larger plastic zone due to increased work hardening facilitates this. Green and Knott [253] also noted the effect of inclusion orientation has a much smaller effect in uniaxial tension than in fracture toughness testing.

It is thought that another mechanism assisting in the degradation of the

fracture toughness seen in VS3764B is due to the increase in the work hardening exponents. Table 31 shows the strength coefficients and work hardening exponents for VS3764A and VS3764B at 20°C and 200°C. The values are taken from Table 11 for ease of comparison.

Steel Heat	Temperature °C.	Strength Coefficient (K).	Work Hardening Exponent.
VS3764A	20	812	0.2212
VS3764B	20	912	0.2854
VS3764A	200	1188	0.2777
VS3764B	200	1140	0.2838

Table 31. Increase in work hardening exponents for 64A and 64B at 20° and 200°C.

It is thought that the increased pearlite content in VS3764A, and material inhomogeneity in the steel heats, as discussed in the experimental section, may have contributed to the differences in Table 31. This may also account for the difference in the closeness of the strains to fracture for both the steel heats.

According to Gladman [85] the presence of pearlite in the microstructure provides sites for easy nucleation of cracks, particularly at the ferrite cementite interfaces. However as the crack can only propagate in ferrite a short distance before encountering another cementite lamella, energy is absorbed during propagation. If an analogy is made between the low energy absorbed overall in impact tests on pearlitic structures which arises from the fact that many crack nuclei can occur at the pearlitic interfaces which together with the high work hardening rate [78], restricts plastic deformation in the vicinity of the crack.

It is thought that the larger work hardening exponents seen in VS3764B does not contribute to a larger plastic zone size, but that it assists in the formation of the many crack nuclei that can occur at the pearlitic interfaces which further restricts plastic deformation in the vicinity of the crack. Knott citing Chipperfield [266] found that in materials with a high work hardening capacity

where the small inclusions are closely spaced together it is possible for internal necking to proceed directly and a reduction in ductility is observed. Further tests are required to verify this result, since material inhomogeneity could have influenced the result. As stated in the experimental section the tensile specimens were not taken from one plane within the forging i.e $\frac{1}{4}T$ (one quarter the thickness of the forging) due to material being at a premium.

The effect of increased work hardening exponents (n) and strength coefficients (K) is illustrated in Figure 199 Taken from the work of Pickering [8] it shows the factors required for low extrusion pressures in wire drawing viz:

1. A low yield stress.
2. A low work hardening exponent.

It is included to show what the effect of altering K and n , and shows what is happening to the stress vs strain curves for all the steel heats in the DSA regime.

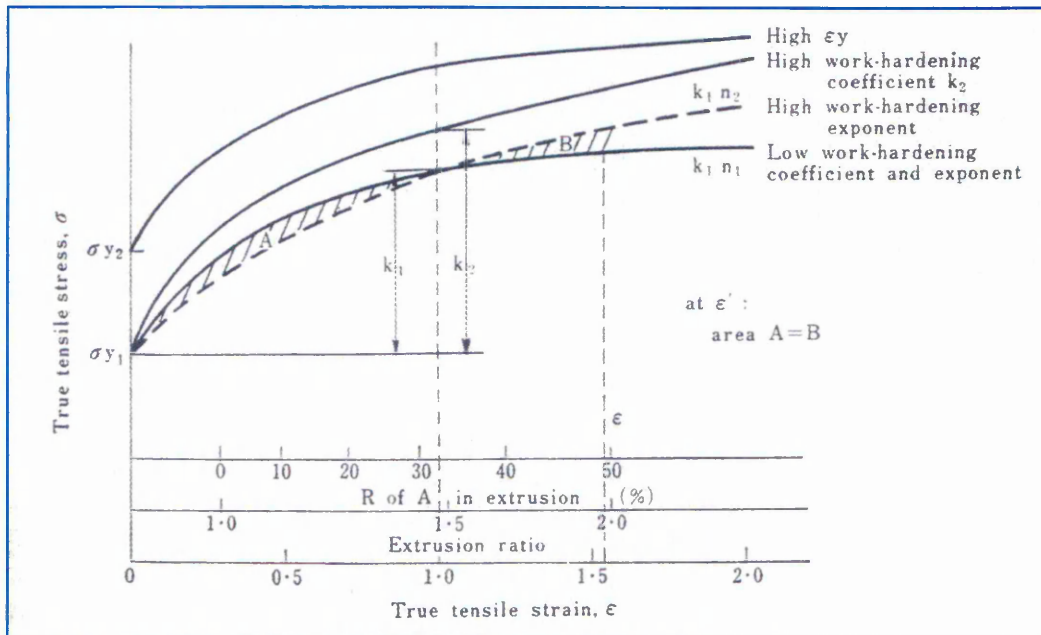


Figure 199. The effect of strength coefficient and work hardening exponent in wire drawing [8].

Another interesting feature observed from Figure 131 is that the slope of the compliance curve for the specimen tested in 8 ppm DOW water (J3A) is not

as steep as the other curves in the elastic region. Initially the compliance curve gave a V_{LL} (load line displacement) to yield of 0.82 mm (text in red in Table 15). This was seen to be too high a figure. This was attributed to load train misalignment in the vertical plane, when on test termination the system was reassembled, dial test indicators put into position and the load train was found to be 0.540 mm out of true. So this was taken off the compliance curve, before being input into the Rubicon J1C Analysis software. This gave a V_{LL} to yield of 0.28 mm.

The V_{LL} to yield and V_{LL} to UTS of the specimens are given in Table 15. For steel heat VS3764A it can be seen that the specimen tested at room temperature has the largest V_{LL} to yield and V_{LL} to UTS of the specimens tested. These are 0.329 mm and 5.67 mm respectively. Second is the specimen tested at 200°C with a V_{LL} to yield and V_{LL} to UTS of 0.296 mm and 2.99 mm. And last the specimen tested at 200°C in 8ppm DOW with a V_{LL} to yield and V_{LL} to UTS of 0.28 mm and 2.82 mm respectively.

For steel heat VS3764B a similar trend is followed. The specimen tested at room temperature with the largest V_{LL} to yield and V_{LL} to UTS. The specimen tested at 200°C had the lowest V_{LL} to yield and V_{LL} to UTS of all the specimens tested 0.203 mm and 1.19 mm respectively.

It can be seen from the above trend that strain to V_{LL} and strain to V_{LL} UTS, for both the steel heats are lowered due to temperature, sulphur and the aqueous environment. Strain localisation is occurring in the air and water environment, due to dynamic strain ageing as shown in the serrated compliance curves. A further reduction in J_{1C} is seen in the aqueous environment. This is due to the additional energy input supplied to the system for the reasons mentioned in section 2.5.

Sulphur is also seen to lower the J_{1C} value in aqueous environments for both the steel heats, in line with the literature, as seen in Figure 14, a reduction in the tearing modulus is also seen and the trend followed is the same for the V_{LL} at yield and V_{LL} at UTS for both the steel heats.

The problem of negative crack growth can be seen in Figure 131 for some of the steels tested, this was experienced by Kim [50] (in that Δa goes negative). The problems of which are discussed by Voss et al [243] in Appendix 4. It is also postulated that friction at the knife edges may also have been a possible cause or insufficient use of the flat bottom holes. The latter would not allow the specimen to rotate thereby creating friction at the contact surface.

From the fracture toughness testing results it can be deduced that the deterioration of the J – R fracture resistance is due to dynamic strain ageing in the steel heats VS3764A and VS3764B. Furthermore the test carried out in 8 ppm DOW at 200°C on steel heat VS3764A had a marginally lower CTOD to yield 0.28mm, as opposed to 0.296 mm for the test done in air at 200°C (see Table 15). The test done at room temperature on the same steel heat had a CTOD to yield of 0.329). Therefore it can be said that the effect of the environment is to sharpen the crack tip. Further tests are required on the high sulphur steel to quantify the effect of sulphur.

5.6. Strain rate sensitivity (m) discussion of results.

The test results from the strain rate sensitivity are given in Table 10 and Figure 99. It can be seen that the maximum values for F8105 were obtained at 100°C with a strain rate differential of 100. This was also used for the F8105 specimen tested at 145°C where all m values were negative. This was not so for all the steels, the transient nature of m can be seen in Figure 99. The strain rates used for F8105 were $2.7 \times 10^{-4} \text{ sec}^{-1}$ and $2.7 \times 10^{-6} \text{ sec}^{-1}$. This strain rate differential used was the same for all the steels tested for the reasons stated in experimental section. The maximum in UTS for F8105 was obtained in air at 150°C using a strain rate of $2.7 \times 10^{-6} \text{ sec}^{-1}$. It can be seen from the results section and the literature reviewed that the maximum dynamic strain ageing effect on material properties can occur at different temperatures and strain rates.

One or two of the results were not expected particularly the result for steel heat F8106. In that all the m results were positive at 250°C. At 200°C m was

initially positive at 2.33% strain but at 3.9% strain m went negative, then positive again at 4.63% strain. Similar observations were seen at 100°C m was positive at 2.24% strain then negative at 5.35% strain and positive again at 6.24% strain. The maximum in UTS for steel heat F8106 was obtained in air at 300°C using a strain rate of $2.7 \times 10^{-6} \text{ sec}^{-1}$. This steel had a maximum m value at 200°C (i.e. most negative value). Picu et al [153,154] and Lee [155] observed this temperature and strain dependence on m . A possible explanation for the above could be due to the low free nitrogen content (1.45 ppm), and to machine transients in the strain rate change.

The maximum in UTS for steel heat F8104 was obtained in air at 250°C using a strain rate of $2.7 \times 10^{-6} \text{ sec}^{-1}$. This test also followed the same trend as the F8106 for the specimen tested at 200°C in that m was positive at 2.38% strain, negative at 5.4% strain and then positive at 7.5% strain. Unfortunately the trend for the specimen tested at 250°C could not be determined after 3.61% strain as the machine lost power. The value of m was positive at 2.18% strain, and negative at 3.61% strain, before premature test termination.

The maximum value of m (i.e. the most negative value) was achieved in steel heat F8105 at 100°C. It is thought that the strain rate differential and strain rates were more suited to this steel heat, for optimum DSA conditions. As mentioned the strain rates used were $2.7 \times 10^{-4} \text{ sec}^{-1}$ and $2.7 \times 10^{-6} \text{ sec}^{-1}$. The maximum in UTS for F8105 was obtained in air at 150°C using a strain rate of $2.7 \times 10^{-6} \text{ sec}^{-1}$. As dynamic strain ageing is only operative in certain temperature and strain rate regimes, this could explain some of the results. That is for the other steel heats there could have been a mismatch between the strain rate and temperature ranges.

It can be seen from the Table 14 (the tabulated results of the tensile tests done in air for steel heats F8104, F8105, and F8106). That the same trend is observed in these three steel heats, as is seen in VS3764A, VS3764B (Table 11) and VS3783A and VS3783B (Table 12). In that although the maximum in UTS was obtained at temperatures at 250°C for F8104 ($\sigma_{\text{UTS}} = 640 \text{ MPa}$) 150°C for F8105 ($\sigma_{\text{UTS}} = 723 \text{ MPa}$), and 300°C for F8106 ($\sigma_{\text{UTS}} = 569 \text{ MPa}$). The minimum in ductility (strain to fracture) was observed at 200°C for F8104

(21.3%), for F8105 was 100°C (13.9%), and for F8106 was 150°C (27.3%).

What is interesting to note is that in all of the tests exhibiting minimum ductility (strain to fracture) in all the cases mentioned, is that serrated flow only occurred in these tests and at 150°C for F8105 (strain to fracture 19.9% the second lowest strain to fracture) and at no other temperature for all the other tests done on F8105.

Serrated flow was also observed in F8104 at 150°C and only at this temperature for all the specimens tested. As stated earlier this was the temperature at which the minimum in ductility occurred. Similarly for F8106 serrated flow was only observed at 150°C for all the specimens tested, and this also corresponded to a minimum in ductility (strain to fracture).

Referring to Table 10 and Figure 99 it can be seen that the maximum m values (i.e. most negative) for steel heat F8105 were observed at 100°C and all were negative going more positive with increasing strain. It can be seen that this maximum value correlates with the minimum in ductility (strain to fracture). The m values for 150°C for F8105 follow a similar trend, and this corresponds to the second minimum in ductility (see Table 14).

The plots to determine the m values are shown in Figures 101 and 102. It can be seen that as the strain rate differential is increased from $2.7 \times 10^{-4} \text{ sec}^{-1}$ to $2.7 \times 10^{-6} \text{ sec}^{-1}$ (corresponding to the strain rate used for the tensile testing) that serrations can be seen at this strain rate. Being more pronounced and larger at the test done at 100°C. This was also seen in the slow strain rate tests done on F8105 at 100° and 150°C, at a strain rate of $2.7 \times 10^{-6} \text{ sec}^{-1}$. Figure 123 is a collage of the slow strain rate tests done on the F81 series of steel heats. It shows the only tests of the twenty done which showed serrations (F8105 at 100° and 150°C) and maximum Luders band deformation with serrations (F8104 at 150°C). From Figure 123 it can be seen that the maximum serration height for F8105 at 100°C is 30 MPa, whereas at 150°C it is 16 MPa. The maximum serration height was seen in F8104 and this was 44 MPa in the Luders plateau in the test done at 150°C. Serrations seen in the remainder of the load vs extension curve were in general lower than F8105.

Referring to Table 10 and Figure 99 again it can be seen that the most negative value for F8106 occurred at 150°C (-2.5×10^{-3}) and again this temperature corresponded to a minimum in ductility (strain to failure).

The strain rate sensitivity parameter was calculated using the equations of Picu et al (section 2.3.5.1 eq. 16 [153,154]) and Haasen [268] (eq. 40 shown below). Both equations give similar results.

$$m' = \frac{1}{\sigma} \left. \frac{\partial \sigma}{\partial \ln \dot{\epsilon}} \right|_{\epsilon} \quad (40)$$

Experimental observations indicate that m depends upon a number of factors, strain, strain rate, temperature, microstructure evolution, deformation mode, and kind of loading [143,144,145]. Some investigations have shown that m is independent of strain [143,146]. However it is also reported that m may vary with strain [147]. The findings of this work support the work of Ling and McCormick [147] in that it can be seen from Figure 99 that the value of m varies with strain.

5.7. Fatigue testing- discussion of the results.

The relationship between fatigue crack growth rate and the cyclic stress intensity range for steel heats F8104 and F8105 are shown in Figure 88. From the figure it can be seen that for steel heat F8105 at a frequency of 0.0167Hz there is the lowest crack growth rate (da/dN m/cycle see Appendix 5 for tabulated growth rates for both the steel heats). For F8105 at a frequency of 5 Hz the crack growth rate is comparable to F8104. Steel heat F8104 exhibits comparable da/dN at both 5 Hz and 0.0167 Hz.

Trend lines were fitted through the data points to determine m and the equations and correlation coefficients obtained see Table 32.

Steel Heat	Frequency (Hz)	Equation of Trend line	Value of power m	Correlation
F8104	0.0167	$2 \times 10^{-11}x^{2.66}$	2.66	0.9940
F8104	5	$2 \times 10^{-11}x^{2.585}$	2.585	0.9963
F8105	0.0167	$2 \times 10^{-11}x^{2.365}$	2.365	0.9977
F8105	5	$2 \times 10^{-11}x^{2.623}$	2.623	0.9912

Table 32. Tabulated values of the Paris exponent for steel heats F8104 and F8105 in air at R = 0.2.

Strictly speaking the value m is only valid in the second stage of fatigue crack growth (stage 2 see Figure 50). But this was a step fatigue test with alternating frequencies of 5Hz and 0.0167 Hz. It was done to show the change in the slope "*Paris exponent*" m .

Models of striation formation and stage 2 fatigue crack growth have been proposed by Laird [173], Neumann [174], and Pelloux [175], they indicate that

small scale plasticity at the crack tip at K_{\max} is converted to small increments of crack growth at K_{\min} . This is the plastic blunting model of fatigue crack growth [175]. In its simplest form this model predicts a relationship between da/dN [183].

$$\frac{dc}{dN} = \frac{0.041}{EY} (\Delta K_I - \Delta K_{th})^2 \frac{1}{1 - \left(\frac{K_{I\max}}{K_{IC}} \right)^2} \quad (1)$$

Hence crack growth rates should be inversely proportional to alloy strength. Barsom [273,274] has confirmed the relationship for structural steel.

Hertzberg [184] citing several authors, Tomkins, Hickerson et al, Majumber et al, and Antolovich et al (see page 691 of reference 184). These authors conducted studies to establish correlations between cyclic strain and fatigue crack propagation data. They found that the slope m of the da/dN vs ΔK plot is seen to decrease with increasing cyclic yield strength σ'_{ys} and cyclic strain hardening exponent n' . As Hertzberg quotes, "*Although it is encouraging to find such correlations, more work is needed before it will be possible to predict FCP rates from cyclic strain data*". He further suggests that fatigue crack propagation does not depend on typical tensile properties because monotonic properties are not the controlling parameter. Cyclically stabilized properties may hold the key. Starting or monotonic stabilized properties between two given alloys may differ widely, but their final or cyclically stabilized properties would not. Soft alloys would strain harden and hard ones would strain soften. As a result the materials would be more similar in their final state than at the outset of testing [184].

5.8. Calculation of the crack tip strain rate for fatigue testing.

In an attempt to calculate the crack tip strain rate and to correlate it with the strain rate used for the maximum UTS obtained by the tensile testing of steel heat F8105, Lidbury's equation was used [206]. Where T is the loading period (in seconds).

$$\dot{\varepsilon}_{av} = \frac{1}{T} \int_0^T \varepsilon(t) dt = -\frac{1}{T} \ln \left(1 - \frac{1}{2} (1 - R)^2 \right) \quad (32)$$

Using input values of $R = 0.2$ and a frequency of 0.0167 Hz the strain rate at the crack tip was estimated to be 0.0128 sec^{-1} . It should be remembered that the crack tip strain rate given by Lidbury's equation is an approximation and only applicable to small scale yielding. If the plastic zone ahead of the crack tip is relatively large, the true crack tip strain rate could be much lower [52].

It has been shown that $\log A$ varies inversely with m in the Paris equation.

$$da/dN = A\Delta K^m \quad [184].$$

It can be seen that the intercept value in the Paris equation is also important in the determination of fatigue crack propagation rates. In Figure 200 [184] for example alloy A would be better than alloy C but alloy D which has the same slope as A would be worse than C. Furthermore the choice between alloy B and C would depend on the anticipated growth rate regime for the engineering component. If many fatigue cycles were anticipated, the designer should opt for alloy B, since fatigue cracks would propagate more slowly over most of the component life and allow for much greater fatigue life. In a low cycle situation, representative of conditions to the right of the crossover point alloy C would be preferred.

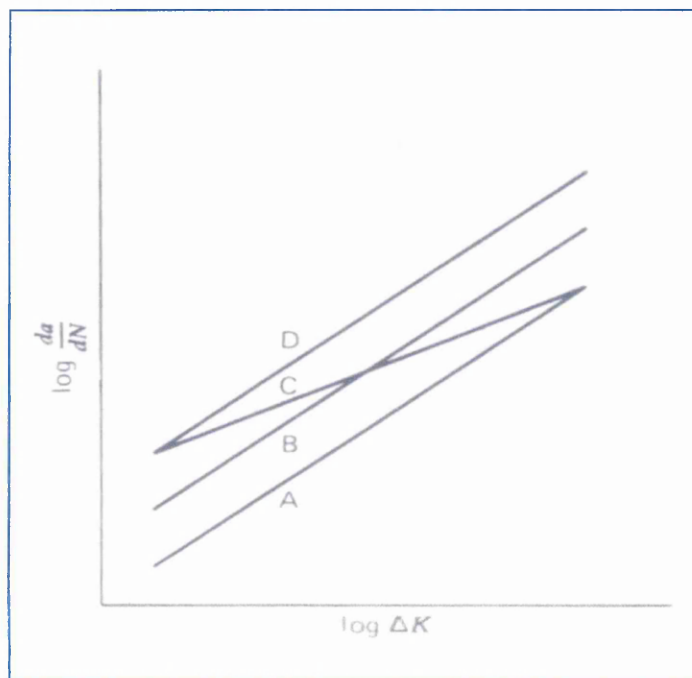


Figure 200. Diagram showing relative fatigue crack propagation behaviour of several materials [184].

A materials resistance to fatigue fracture is determined by the increasing plastic zone development and strain hardening [184]. A higher yield strength signifies a smaller plastic zone so that there is more material in plane strain [23].

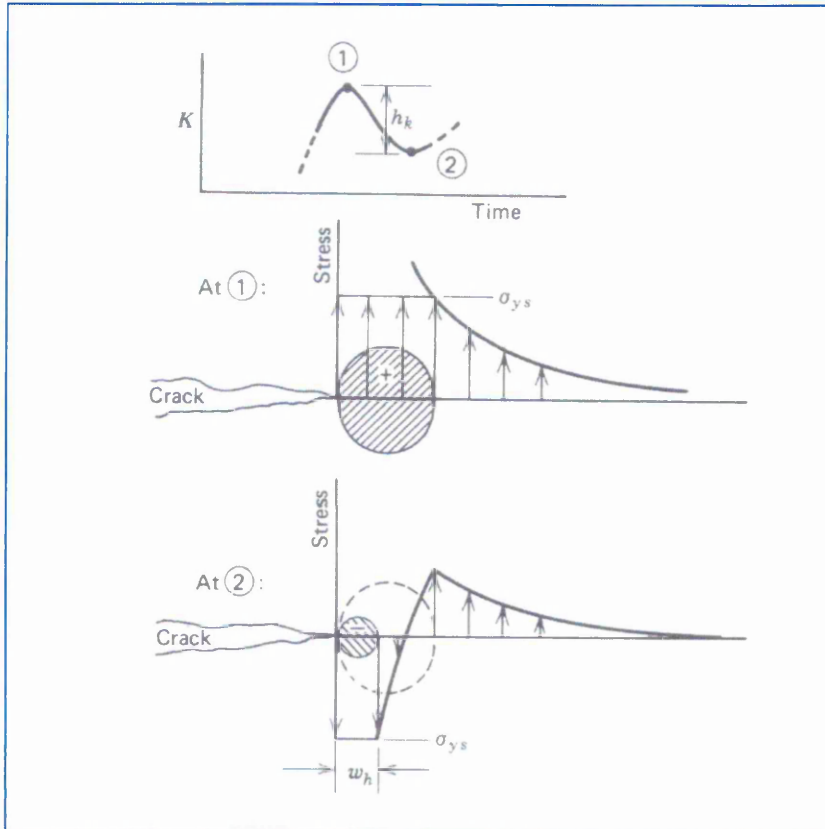


Figure 201. Monotonic and reversed plastic zone development at tip of advancing fatigue crack [184] .

The plastic zone is developed by the application of a stress intensity factor of magnitude K_1 (see Figure 201). If this is reduced by h_k , the direction of loading is reversed, the local stress level is reduced to that corresponding stress intensity K_2 . Since the elastic stress distribution associated with K_1 was truncated at σ_{ys} by local yielding, subtraction of an elastic stress distribution in going from K_1 to K_2 will cause the final stress field to drop sharply near the crack tip and go into compression. At K_2 a smaller plastic zone is formed in which the material undergoes compressive yielding.

Since the material within this smaller plastic zone experiences reversed cyclic straining, it might be expected that cyclic strain hardening or softening

would result depending on the starting condition of the material.

Unfortunately on reading the literature it seems there has been no reported studies that have quantified the local strain rate at the crack tip in the case of large plastic deformation. The figure of $12.8 \times 10^{-3} \text{ sec}^{-1}$ calculated using Lidbury's equation could be much lower. If the plastic zone ahead of the crack tip is relatively large, the true crack tip strain rate could be much lower. So it is feasible to assume that the crack tip strain rate conditions were favourable for the maximum effect for dynamic strain ageing in F8105 at 0.0167 Hz. With the resulting increase in cyclic work hardening exponent, and increase in the flow stress. As a consequence the plastic zone size would be reduced, resulting in a reduced reversed cyclic straining, thereby lowering the crack growth rate since crack growth rate is inversely proportional to the materials strength.

Perhaps knowing the free nitrogen content of a steel and strain rate sensitivity at various temperatures for a steel could form two of these "*Cyclically stabilized properties*" that Hertzberg thinks hold the key to fatigue crack propagation.

5.8.1. Comparison of F8104 and F8105 fatigue crack growth rates with the literature.

To compare the fatigue crack growth rates with published data Figure 88 was superimposed on the work of Tseng et al [245] and Ramsamooj et al [183] see Figures 202 and 203. Tseng et al studied the effect of nitrogen on the corrosion fatigue crack growth of 22% duplex stainless steel in chloride solutions. Their results showed that the tensile strength and elongation of 22% Cr DSS increased with increasing amounts of nitrogen. The results also revealed that nitrogen (range 0.103% – 0.195 wt %) did not significantly affect the fatigue crack growth rate of 22% Cr DSS in air, and in 3.5% NaCl solution. The tests were only done at 20°C, so it is likely the full effect would not be seen. Temperatures of 100°C or 150°C would probably give the full effect at the frequencies used (0.1Hz and 5 Hz). Figure 202 shows F8104 & F8105 da/dN vs ΔK compared with Tseng et al data [245].

Figure 203 shows the work Ramsamooj et al [183] (citing Paris) compared to F8104 and F8105. The work cited by Ramsamooj done by Paris was conducted on A533B which has a K_{IC} of 220 MPam^{0.5} and a K_{max} of 90 MPam^{0.5}. It can be seen that for F8104 at frequencies of 5 Hz and 0.0167 Hz the fit between Ramsamooj's data, and Tseng's data is reasonable. The same can be said for F8105 at a frequency of 5Hz. But it can be seen that F8015 at a frequency of 0.0167 Hz the fatigue crack growth rate is lower in both cases.

Similar observations to those seen in this work were made by Huang et al [267] (see Figure 204) who conducted fatigue tests under constant amplitude load on compact tension specimens of SA533B3 steels with four different levels of sulphur content at temperatures of 25°, 150°, 300°, and 400°C, at a frequency of 20Hz. They observed that the Young's moduli measured at a strain rate of $4 \times 10^{-3} \text{ s}^{-1}$ for the SA533B3 steels at 150°C and 300°C do not decrease with increasing temperature. They attributed this to the presence of dynamic strain ageing. The fatigue crack growth rates at 150° and 300°C were about two and half times slower than those tested at 400°C because dynamic strain ageing was only prevalent at 150° and 300°C.

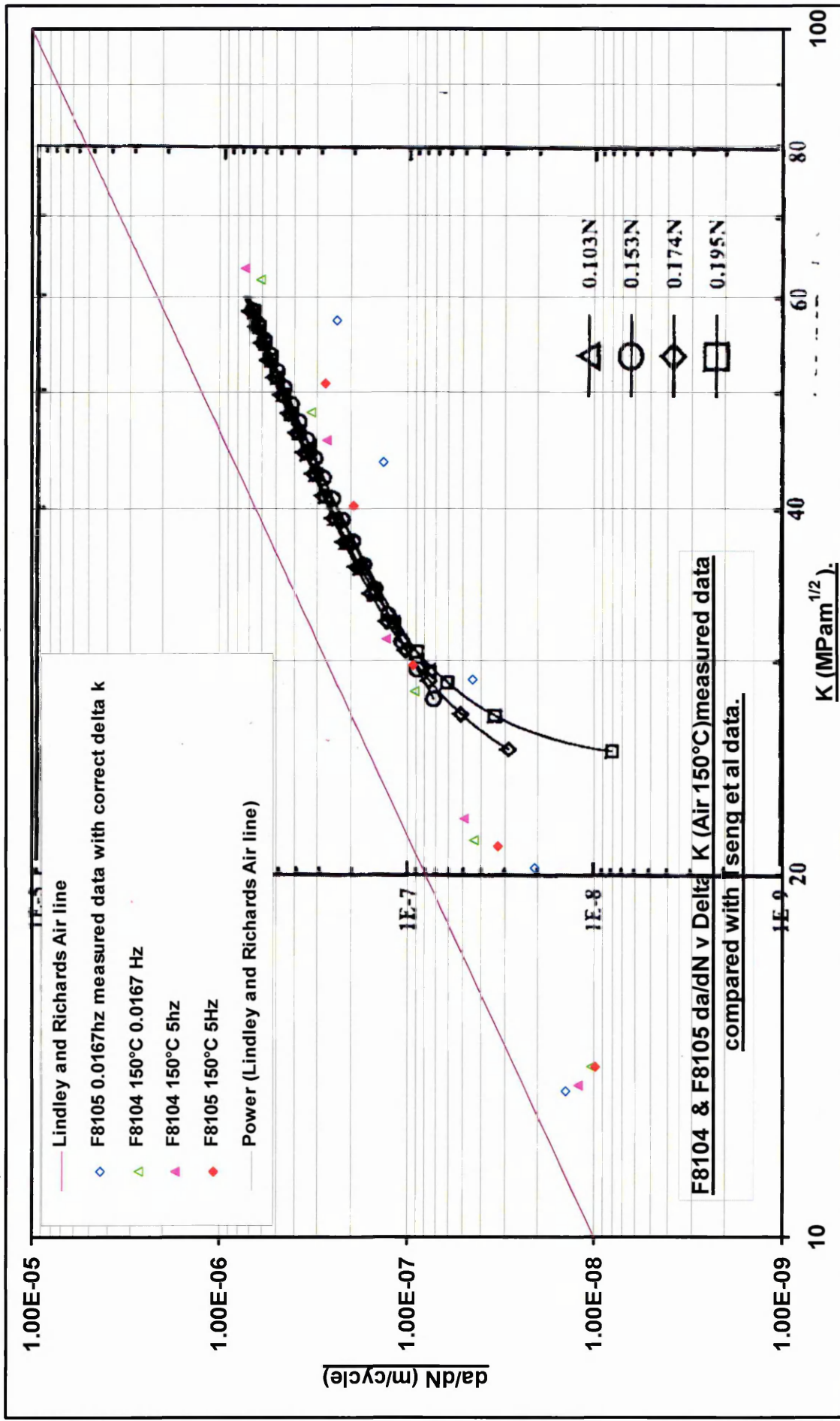
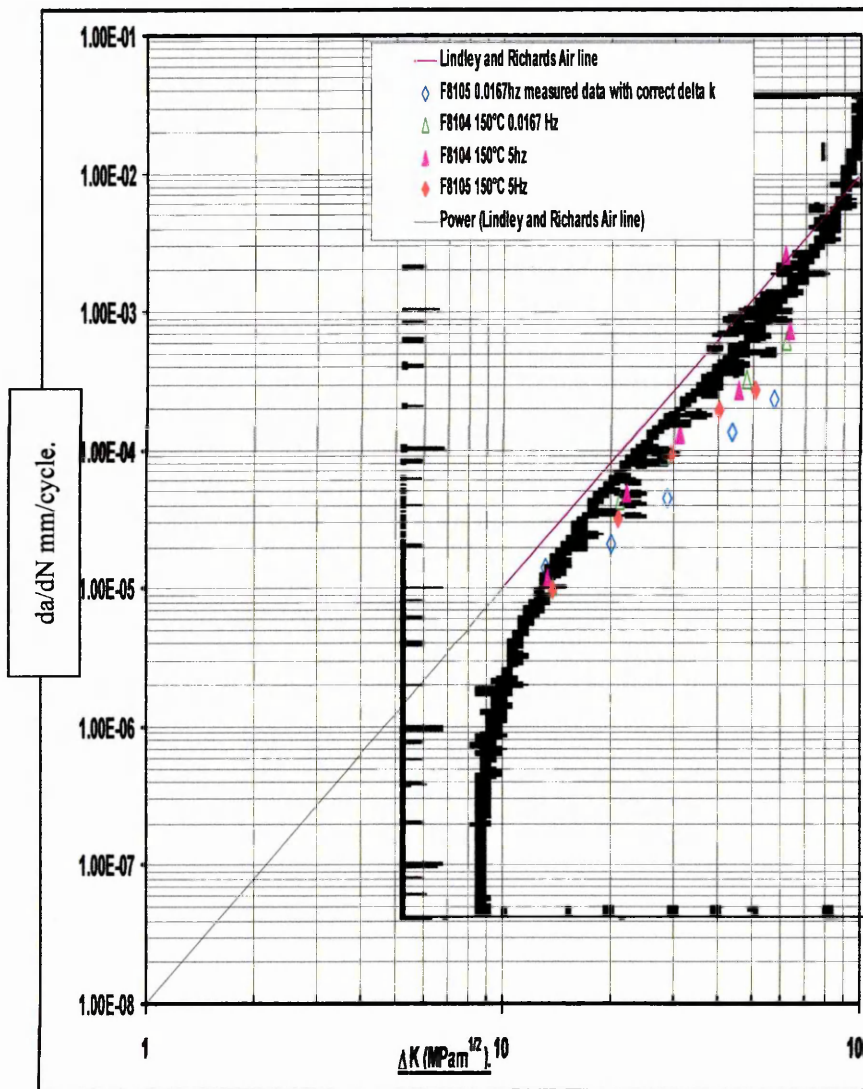


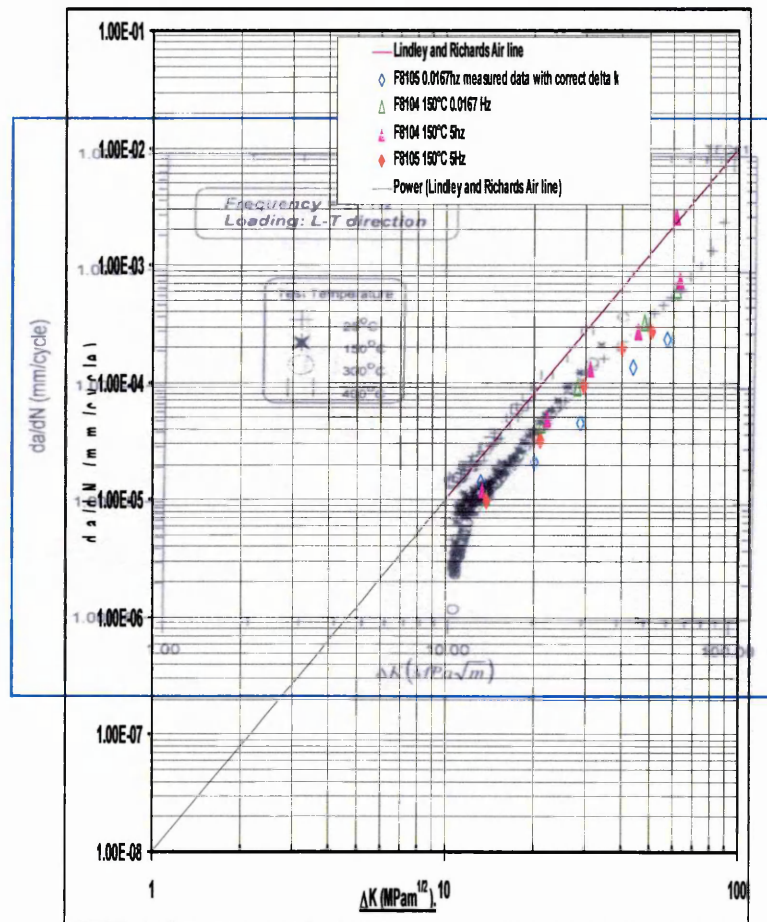
Figure 202. Graph of F8104 & F8105 da/dN vs ΔK compared with Tseng et al data [245].

Figure 203. Graph of F8104 & F8105 da/dN vs ΔK compared with Ramsamooj [183] citing Paris et al.



Huang's fractographic examination results suggested that inclusions embedded in secondary cracks enhanced the fatigue crack initiation rather than the fatigue crack growth. The results of this work are superimposed on Huang's work and this is shown in Figure 204. It can be seen from Figure 204 that Huang's 25°C data sits exactly on the Lindley and Richards dry line and that the data for F8105 at 5Hz, and F8104 at 1Hz and 5Hz, are comparable. The crack growth rates for F8105 at 0.0167 Hz are slightly lower. The strength effect predicted by the authors is evident.

Figure 204. Comparison of Huang's work [267] with this work.



In this study it has been shown for C – Mn steels that at low stresses (below the cavitation strain) for example as in the plastic zone near a crack tip in the threshold or Paris region of the fatigue crack growth curve, MnS inclusions do not significantly influence the growth rate and the ductile striation growth process. However free nitrogen has a large influence on the peak flow stress (see Figure 129). Consequently free nitrogen is beneficial to reduce the fatigue crack growth rate in air due to reductions in the plastic zone size, and crack tip opening displacement, in accord with the recent observations of Huang et al [267] on A533B pressure vessel steel. In contrast at high stresses when cavitation takes place at MnS inclusions the volume fraction and spacing of non metallic inclusions has a large effect on the tensile ductility of a steel.

5.8.2. Relationship between da/dN and striation spacing.

Zappfe and Worden [170] first observed a pattern of ripples or striations on a fatigue fracture surface, and subsequently this has been characterised by many authors as the accepted mechanism of fatigue failure. Programmed loading has shown that each striation is produced by one cycle of stress although every cycle does not necessarily produce a striation [171]. The morphology of the striations differs widely and depends on strength level, symmetry and number of available slip systems.

In the mid ΔK or Paris region it has been observed that in some cases there is a one to one correlation between da/dN and the regular spaced markings on the fracture surface perpendicular to the growth direction [172]. In the threshold region striations may not be visible, and at high ΔK values non striation modes of crack advance such as void coalescence and cleavage are often present.

Figure 88 shows the da/dN vs ΔK for steel heats F8104 and F8105, determined from the length of the step divided by the number of cycles for that step (before the frequency was changed). Figure 89 shows da/dN vs ΔK using the striation spacing measured from SEM fractographs using Figures 92 – 98. The white arrows indicate the direction of crack growth and from where the measurements were taken. It can be seen from Figure 89 that at the lowest ΔK 's ($\Delta K = 20 \text{ MPa}\sqrt{\text{m}}$) there is a considerable difference between the macroscopic da/dN (measured by p.d.) and the microscopic measurements (striation spacing) for both the steel heats. In the mid ΔK range (see Figures 92 to 97) it can be seen that relatively large multiple striations can be seen consisting of several finer striations, and the distinction between the finer striations cannot easily be made. The striation spacing in Figure 89 is based on the smallest visible striations.

McMinn [171] also observed this phenomenon in fatigue tests carried out on three steels A533B 3, Ducoil W 30 (a carbon manganese steel) and type 304 stainless steel. Testing was done at room temperature. Fractographic analysis was used for the three steels to explain the anomalous behaviour between the microscopic and macroscopic crack growth rates and the crack tip opening displacement (CTOD). McMinn [171] found that each striation is produced by one cycle of stress although every cycle does not necessarily produce a striation [171].

The carbon manganese steel used in McMinn's work [171] was tested in air and in an oxygenated (8 ppm) neutral water of low conductivity (0.08 μmho). The steel had a ferritic pearlitic microstructure with an average grain size of 24 μm and a volume fraction between 20% and 25%. When tested in air, crack growth rates were independent of frequency and stress ratio (R) and fracture surfaces showed ductile, transgranular striations over a wide range of cyclic stress intensity (ΔK). Two types of striations were observed, relatively large "multiple" striations which consisted of several finer regular markings. The larger striation spacings corresponded well with an estimate of half the maximum crack tip opening displacement (CTOD) defined as:

$$\delta = \frac{0.22 K_{\max}^2}{E\sigma_y} \quad (41)$$

where for C - Mn steel σ_y = yield stress = 340 MNm^{-2} and $E = 1.86 \times 10^5 \text{ MN}^{-2}$.

The smaller striations showed a good correlation with the macroscopic crack growth rate see Figure 205. Although not shown on Figure 205, McMinn [171] observed that for the C – Mn and the other ferritic steels, that at high crack growth rates the distinction between fine and large striations could not easily be made. As the crack growth rates approached the CTOD, the striation spacings reflect both da/dN and $\delta/2$, and in some cases the measured spacings were slightly lower than the da/dN and CTOD. At low growth rates the striations were not very well pronounced $\Delta K < 18 \text{ MNm}^{-3/2}$ (as was found in this work see Figures 92 - 93).

Fatigue crack growth in air or inert environments is characterised by ductile striation formation, which is often termed Stage II of a three stage process. Stage II denotes an intermediate growth rate region (10^{-8} to 10^{-5} m/cycle) where crack tip deformation spreads over several grains in a polycrystal, giving plastic continuum behaviour. Stage I denotes the threshold region or low growth rate region ($< 10^{-8}$ m/cycle), where deformation in the

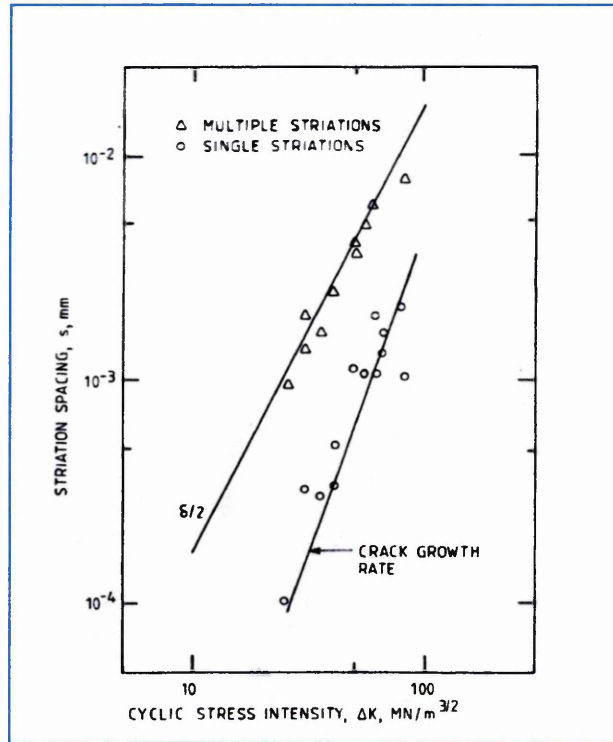


Figure 205. Correlation between striation spacing, crack growth rate and crack tip opening displacement for C – Mn steel tested in air $R = 0$ [171].

crack tip plastic zone is often on a scale less than the grain size and therefore crack advance is crystallographically controlled. Cracks propagate along one of the maximum shear planes or along grain boundaries favourably oriented to the principal stress. Stage III is the region of high growth rate ($> 10^{-5}$ m/cycle) where material inhomogeneities, such as inclusions and precipitates, nucleate voids ahead of the crack tip, leading to crack advance by tearing and finally instability [173,174,175].

In Stage II, crack advance occurs by the simultaneous localised shear deformation of the two 45° maximum shear bands, leading to the creation of new crack surfaces by decohesion at the crack tip. This localised flow is by dislocation movement and accommodates the plastic CTOD δ . Hence it follows

that there should be a correlation between the amount of new crack surface (Δa) and therefore da/dN , with the CTOD. Results show [171] that in Stage II, $da/dN < \delta/2$ (not δ since resharpener on stress reversal produces two equal crack faces).

McMinn [171] attributed the lack of correlation between da/dN and $\delta/2$ to crack flank material being incorporated into the crack tip deformation. In the low growth rate region of Stage II, δ is small and the crack flank contribution dominates and $da/dN < \delta/2$ (say two orders of magnitude), whereas at the higher Stage II growth rates, δ consists mainly of new crack surface and therefore da/dN approaches $\delta/2$. An upper bound to Stage II growth is given by $\delta/2$, as this represents the largest amount of crack tip blunting that can be accommodated by this process of crack advance. In Stage III, da/dN can exceed $\delta/2$ since fracture processes ahead of the crack tip contribute to crack advance.

Striations are caused during tensile loading as a result of this localized shear process (as in stretch zones), and are accentuated by unloading and reversal of the shear flow. Striations do not necessarily represent the amount of new crack surface created each cycle, as they reflect the shear process that accommodates the crack tip opening [173,174,175]. McMinn's [171] observations of large striations correlating with $\delta/2$ and finer striations agreeing with da/dN , but with a lower limit of approximately $0.05 \mu\text{m}$, indicate a complex process of striation formation. This is shown in work done by McMinn [171] on type 304 stainless steel at $R = 0$. He found that at low growth rates ($0.01 \mu\text{m}/\text{cycle}$) one fine striation ($0.05 \mu\text{m}$) is created over a number of cycles, crack growth only being continuous if the crack tip shear planes accommodate a fraction of new crack surface each cycle. Over several cycles, the accumulated surface is enough to create a fine striation on unloading and the process is repeated. During each cycle the maximum CTOD ($> 10^{-7} \text{ m}$) is achieved due to crack flank involvement, but shearing on several planes at the crack tip (several fine striations) is required before the CTOD is achieved at the tip, producing a large striation which may not always be distinct. At high growth rates ($10^{-6} \text{ m}/\text{cycle}$) and larger CTOD, several flow bands operate and contribute to CTOD

which is achieved in one load increment. Thus crack growth can produce several fine striations, but the crack increment per cycle now approaches the maximum CTOD. It is thought that at the low growth rates ($\Delta K = 20 \text{ MPa}\sqrt{\text{m}}$) for both the steel heats (F8104 and F8105) the mechanism operating in McMinn's work at the low growth rates ($0.01 \mu\text{m}/\text{cycle}$) is operating in both the steel heats and explains the growth rates for F8104 and F8105 being above the Lindley and Richard air line. McMinn's observations in the mid ΔK range were also seen in this work in that the larger multiple striations in most cases consisted of finer regular markings. From Figures 88 and 89 it can be seen that the macroscopic differs from the microscopic da/dN (striation spacing) for the reasons discussed.

The observations of McMinn of striation spacing correlating the macroscopic da/dN at the higher ΔK 's is verified for steel heat F8104. Using Figure 98 as an example $\Delta K = 57.39 \text{ MPa}\sqrt{\text{m}}$ (the blue diamond in Figure 89), the areas indicated by the white arrows was chosen to select the striations. The average width of the large striations was $4.39 \times 10^{-7} \text{ m}$. The macroscopic da/dN at the end of the step for F8104 step (step 10 see Appendix 5) was $6.08 \times 10^{-7} \text{ m}/\text{cycle}$ which agrees favourably with McMinn's observations, in that at high ΔK values the striation spacing reflects the macroscopic da/dN , and in some cases the measured spacings were slightly lower. The use of the McMinn equation to predict the CTOD (eq 41) for F8104 at this value, gives a value of $7.292 \times 10^{-6} \text{ m}$ using the data obtained from this work. The required value for this work would be $8.79 \times 10^{-7} \text{ m}/\text{cycle}$ based on the assumed CTOD marks in Figure 98. It is thought that this may be attributable to different material compositions, especially the grain size in McMinn's work. This determines the reverse plastic zone size, which affects the mode of fracture and stress intensity for a given da/dN [171].

In the present study Mc Minns study has been confirmed, it has also been shown that free nitrogen does not induce brittle fracture modes. High free nitrogen appears to be beneficial due to the effect of yield stress on da/dN . As determined by numerous authors [178,183,245,267,273,274].

5.9. Residual Life Model.

5.9.1. Fatigue life calculations.

In the nuclear power industry, they use what is called a “*fail safe*” design philosophy. This recognises that cracks can develop in components but ensures that the structure will not fail prior to the time that the defect is discovered and repaired. It pertains to the “*leak before break*” design of pressure vessels and pipes. This approach to design requires periodic inspection of load bearing components with sufficient flaw detection resolution so as to enable defective parts to be either repaired or replaced in a timely manner.

A specific application of the fail safe design philosophy involves removal of a particular component only when there is clear evidence for the existence of a defect of critical dimensions. That is based on fracture mechanics analysis, the part would be replaced if failure were expected. As such the component is subject to retirement for cause. If no defect is found the part is returned to service with the next inspection interval being determined from a fracture mechanics calculation, based on the existence of a crack whose length is just below the inspection resolution limit [184].

For example say an inspection of a steel component reveals the presence of an 18.5mm long edge crack and is subjected to repeated stresses of 125MPa what would be the number of cycles to failure. Several pieces of information are needed before one can work out the fatigue life of a component. These include the crack growth rate vs ΔK relationship and the size of the final crack.

When conducting a failure analysis it is often desirable to compute component life for comparison with the actually recorded service life. Alternatively, if one were designing a new part and wished to establish for it a safe operating service life, fatigue life calculations would be required.

The simplicity of the Paris power law relationship provides a means of

estimating the useful life of a fatigued component for design or failure analysis. The fatigue life or the number of cycles to failure is calculated by integrating the Paris equation.

$$\frac{da}{dN} = C(\Delta K)^m \quad (42)$$

It is assumed that the crack is treated as an edge crack in a semi infinite plate. Where the stress intensity factor is defined as .

$$\Delta K = \Delta\sigma(\pi a)^m \quad (43)$$

So that equation 42 may be written as,

$$\frac{da}{dN} = A\Delta\sigma^m \pi^{m/2} a^{m/2} \quad (44)$$

Variables (a and N for constant $\Delta\sigma$) may be separated to give.

$$a^{-m/2} da = A\Delta\sigma^m \pi^{m/2} dN \quad (45)$$

It is then possible to integrate the two sides of the equation. The left hand side is integrated between limits a_0 (the initial defect size) and a_f (the final defect size, determined by fast fracture or plastic collapse). The right hand side is integrated between limits zero and the number of cycles to failure N_f .

$$\int_{a_0}^{a_f} \frac{da}{a^{m/2}} = (\Delta\sigma)^m \pi^{m/2} \int_0^{N_f} dN \quad (46)$$

The resulting fatigue life is for $m \neq 2$ and.

$$\frac{2m}{(2m-1)} a_f^{1-m/2} - a_0^{1-m/2} = A\Delta\sigma^m \pi^m N_f \quad (47)$$

And for $m = 2$

$$\ln \frac{a_0}{a_f} = A \Delta \sigma^2 \pi N_f \quad (48)$$

In general Y (the compliance factor in $K = \sigma \sqrt{\pi a} Y$) varies with a , consequently cycle life may be estimated by numerical integration procedures by using different values of Y held constant over small crack length increments (see Table 33).

Where.

N_f = number of cycles to failure.

a_0 = initial crack size.

a_f = final crack size.

$\Delta \sigma$ = stress range.

C and m are material constants.

a/W	0.000	0.001	0.002	0.003	0.004	0.005	0.006	0.007	0.008	0.009	0.010
	Y-Compliance Function										
0.300	5.85	5.86	5.87	5.88	5.89	5.91	5.92	5.93	5.94	5.95	5.96
0.310	5.96	5.98	5.99	6.00	6.01	6.02	6.04	6.05	6.06	6.07	6.09
0.320	6.09	6.10	6.11	6.12	6.14	6.15	6.16	6.18	6.19	6.20	6.22
0.330	6.22	6.23	6.24	6.26	6.27	6.28	6.30	6.31	6.32	6.34	6.35
0.340	6.35	6.37	6.38	6.40	6.41	6.42	6.44	6.45	6.47	6.48	6.50
0.350	6.50	6.51	6.53	6.54	6.56	6.57	6.59	6.60	6.62	6.63	6.65
0.360	6.65	6.66	6.68	6.70	6.71	6.73	6.74	6.76	6.77	6.79	6.81
0.370	6.81	6.82	6.84	6.86	6.87	6.89	6.91	6.92	6.94	6.96	6.97
0.380	6.97	6.99	7.01	7.02	7.04	7.06	7.07	7.09	7.11	7.13	7.14
0.390	7.14	7.16	7.18	7.20	7.22	7.23	7.25	7.27	7.29	7.31	7.32
0.400	7.32	7.34	7.36	7.38	7.40	7.42	7.43	7.45	7.47	7.49	7.51
0.410	7.51	7.53	7.55	7.57	7.59	7.61	7.63	7.65	7.67	7.68	7.70
0.420	7.70	7.72	7.74	7.76	7.78	7.80	7.83	7.85	7.87	7.89	7.91
0.430	7.91	7.93	7.95	7.97	7.99	8.01	8.03	8.05	8.07	8.10	8.12
0.440	8.12	8.14	8.16	8.18	8.20	8.23	8.25	8.27	8.29	8.32	8.34
0.450	8.34	8.36	8.38	8.41	8.43	8.45	8.47	8.50	8.52	8.54	8.57
0.460	8.57	8.59	8.61	8.64	8.66	8.69	8.71	8.73	8.76	8.78	8.81
0.470	8.81	8.83	8.86	8.88	8.91	8.93	8.96	8.98	9.01	9.03	9.06
0.480	9.06	9.09	9.11	9.14	9.16	9.19	9.22	9.24	9.27	9.30	9.32
0.490	9.32	9.35	9.38	9.41	9.43	9.46	9.49	9.52	9.55	9.57	9.60
0.500	9.60	9.63	9.66	9.69	9.72	9.75	9.78	9.81	9.84	9.87	9.90
0.510	9.90	9.93	9.96	9.99	10.0	10.1	10.1	10.1	10.2	10.2	10.2
0.520	10.2	10.2	10.3	10.3	10.3	10.4	10.4	10.4	10.5	10.5	10.5
0.530	10.5	10.6	10.6	10.6	10.7	10.7	10.8	10.8	10.8	10.9	10.9
0.540	10.9	10.9	11.0	11.0	11.0	11.1	11.1	11.2	11.2	11.2	11.3
0.550	11.3	11.3	11.3	11.4	11.4	11.5	11.5	11.5	11.6	11.6	11.7
0.560	11.7	11.7	11.7	11.8	11.8	11.9	11.9	12.0	12.0	12.0	12.1
0.570	12.1	12.1	12.2	12.2	12.3	12.3	12.4	12.4	12.4	12.5	12.5
0.580	12.5	12.6	12.6	12.7	12.7	12.8	12.8	12.9	12.9	13.0	13.0
0.590	13.0	13.1	13.1	13.2	13.2	13.3	13.3	13.4	13.4	13.5	13.5

Table 33. Y the compliance function [26].

The data obtained in this work will be used to illustrate the importance of

the Paris exponents C and m. Tables 32 and 35 gives these values and the table in Appendix 5 the K values. The data for F8104 and F8105 at 0.0167 Hz and 5 Hz will be used.

Assuming that the crack is treated as an edge crack in a semi infinite plate where the stress intensity factor is defined as; (See Table 34 and Figure 206), for $a/w > 0$, $y = 1.12$.

$$K_{1C} = 1.12\sigma\sqrt{\pi a} \quad (49)$$

Type of Crack	Stress Intensity
Centre-crack, length $2a$, in an infinite plate.	$K_I = \sigma_{app}(\pi a)^{1/2}$
Centre-crack, length $2a$, in plate of width W .	$K_I = \sigma_{app} \left[W \tan\left(\frac{\pi a}{W}\right) \right]^{1/2}$ or $K_I = \sigma_{app} \left[\pi a \sec\left(\frac{\pi a}{W}\right) \right]^{1/2}$
Central, penny shaped crack, radius a , in infinite body.	$K_I = 2\sigma_{app} \left(\frac{a}{\pi}\right)^{1/2}$
Edge crack, length a , in semi-infinite plate.	$K_I = 1.12\sigma_{app}(\pi a)^{1/2}$
2 symmetrical edge-cracks each length a , in plate of total width W .	$K_I = \sigma_{app} W^{1/2} \left[\tan\left(\frac{\pi a}{W}\right) + 0.1 \sin\left(\frac{2\pi a}{W}\right) \right]^{1/2}$

Table 34. Stress Intensity K factors for various loading geometries [26].

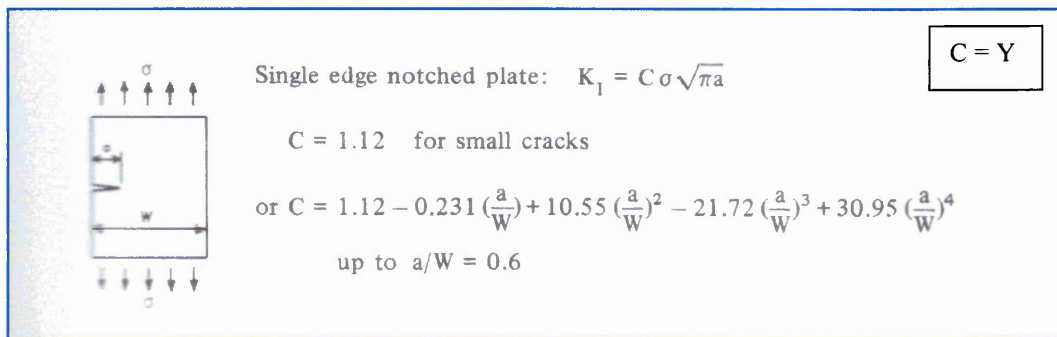


Figure 206. Stress Intensity K factor for single edge notched plate [23].

The final crack length is calculated from the instability condition $K_{max} = K_{1C}$. Using this the approximate value of the stress at fracture can be determined and a value of the stress at a_0 be approximated as around 50MPa as ΔK was

15MPa $m^{0.5}$. That is assuming the initial stress at a_0 is about a quarter of the final fracture stress.

$$K_{\max} = 71.67\text{MPa}m^{0.5} = K_{1C} = 1.12\sigma\sqrt{\pi a}$$

$$a_f = 33.68\text{mm}$$

Transposing and solving for σ the stress at fracture = 220.3 MPa

Substituting the values below into equation 47 and using MPa and m.

Using the trend line of the equation gives $2 \times 10^{-11} \Delta K^{2.365}$

(for K in MPa \sqrt{m}) and

N_f = number of cycles to failure = see Table 35.

a_0 = initial crack size = 18.5mm

a_f = final crack size = 33.68mm

$\Delta\sigma$ = stress range = 50MPa and 125 MPa

$C = 2 \times 10^{-11}$ (for K in MPa \sqrt{m})

$m = 2.365$

$$\frac{2m}{(2m-1)} a_f^{1-m/2} - a_0^{1-m/2} = A \Delta \sigma^m \pi^m N_f \quad (47)$$

$$\frac{2 \times 2.365}{(2 - 2.365)} \left| (33.68 \times 10^{-3})^{1-2.365/2} - (18.5 \times 10^{-3})^{1-2.365/2} \right| = 2 \times 10^{-11} \times 50^{2.365} \pi^{2.365/2} \cdot N_f$$

Using the same test input parameters for F8104 at 0.0167 and 5 Hz shows the difference in the number of cycles to failure.

N_f = number of cycles to failure = see Table 35

a_0 = initial crack size = 18.5mm

a_f = final crack size = 34.227mm

$\Delta\sigma$ = stress range = 50MPa and 125 MPa

$C = 2 \times 10^{-11}$

$m = 2.585$

For F8105 and using a stress range of 50 MPa the number of cycles to failure $N_f = 3443725$ cycles but this is assuming the compliance factor Y remains constant. The actual cycles to failure was 321647. To allow for the increase in

compliance as shown in Table 33 the initial starting stress at a_0 was increased to 125 MPa. The actual value under test conditions would have been closer to the first stress value used. The stress has been increased to show the effect of an increase in the compliance. To give 394366 cycles to failure. The results for stress ranges of 50 MPa and 125 MPa for both the steel heats are shown in Table 35.

Steel Heat.	Frequency (Hz).	Paris exponent (m). Determined at 0.0167 & 5 Hz	Stress Range $\Delta\sigma$. (50 MPa).	Cycles to Failure. (N_f).	Stress Range $\Delta\sigma$. MPa	Cycles to failure. (N_f).
F8104	0.0167	2.66	50	1.82×10^6 1822703	125	1.59×10^3 159292 Actual N_f 243628
F8105	0.0167	2.365	50	3.44×10^6 3443725	125	3.94×10^3 394366 Actual N_f 321647
F8104	5	2.585	50	2.13×10^6 2139529	125	1.99×10^3 199549 151510
F8105	5	2.623	50	1.93×10^6 1935029	125	1.74×10^3 174940 198122

Table 35. Results from integrated Paris equation for F8104 and F8105.

The Paris exponents m in Table 35 were obtained by putting trend lines through the data points of 5 Hz and 0.0167 Hz for both the steel heats as can

be seen in Figure 89. It can be seen from Table 35 for steel heat F8105, that there is a considerable difference in the m values for steel heat F8105 (2.365 at 0.0167Hz as to 2.623 at 5 Hz). Compared to F8104 whose m values are comparable at both frequencies (2.66 at 0.0167Hz and 2.585 at 5 Hz).

It is clear that for steel heat F8105 at 150°C in the DSA region, that at the lower frequency where the m value is lower dynamic strain ageing effects must be occurring. It is possible that the frequency of 0.0167 is creating a crack tip strain rate in which the dynamic strain ageing effects are most pronounced. This was the temperature (150°C) at which the maximum in UTS was achieved for F8105 at a strain rate $2.7 \times 10^{-6} \text{ sec}^{-1}$. It is feasible to assume that the crack tip strain rate of the fatigue specimen at 0.0167 Hz must be of a similar order, since no quantifiable estimate has been made of the crack tip strain rate. As stated in section 5.8 the calculated crack tip strain rate value of 0.0128 sec^{-1} obtained using Lidbury's equation [206] could be much lower. It is also possible that the strain at the crack tip is suitable for conditions for the most negative strain rate sensitivity (m) at the lower frequency. Since the tensile specimens tested at 100°C and 150°C exhibited a strain rate dependence for m .

To summarise the section it appears that the higher free nitrogen steel (F8105) has not had any deleterious effect on fatigue crack growth in the dynamic strain ageing regime. The striations appear fully ductile and there are no static modes of fracture present in the micrographs. The size of the striations is reduced by an increase in the free nitrogen content. This is determined by the strength of the steel, which affects the size of the plastic zone. The yield strength at 150°C for F8104 is 497.5MPa and for F8105 is 524.5MPa (see Table 14 based on $\sigma_f = (\sigma_y + \sigma_{uts})/2$). The inverse relationship between da/dN and the yield strength of a material has been shown to be beneficial in the DSA regime.

5.9.2. Residual Life Model part 2.

The ductile fracture process was discussed in the introduction and the literature review. The assumed physics underlying the localisation of flow is described by Thomason [2,3] and Brown and Embury [17]. They both use a critical distance of approach of the growing voids as a criterion. Although their models differ in detail, both require that a local slip line field can be developed between adjacent voids. A condition that is met when the void height $2h$ is equal to its separation from its neighbours $2l$ [15] (see Figures 1 and 2), α is constant of the order unity.

$$2h = \alpha(2l - 2r_v). \quad (50)$$

where $2r_v$ is the void width.

According to Ashby et al [14,15] fracture occurs when the void length becomes about equal to the planar spacing of the voids. Ashby's results suggested that an amplification factor of 1.4 (C) should be incorporated into the Brown and Embury [17] equation to give.

$$\varepsilon_g = \frac{1}{C} \ln \left[\alpha \left(\frac{2l - 2r_v}{2r_v} \right) \right] \approx \frac{1}{C} \ln \left[\alpha \left(\frac{1}{f_v^{1/2}} \right) - 1 \right] \quad (51)$$

Where ε_g is the true strain required for coalescence [15].

It should be recognised that the Ashby et al equation (equation 51) does not include the effect of macroscopic instabilities, such as necking or the zones of concentrated shear (that is stress triaxiality or dynamic strain ageing effects are not taken into account). This is a serious omission according to Thomason [2,3] since the onset of necking is known to influence both the nucleation and growth of holes, and localised shear can cause holes to coalesce by void sheeting [2,3]. The process of void growth is strongly influenced by the state of stress during plastic deformation. The higher the dominating tensile stresses (the higher the triaxiality) the higher is the void growth rate (see Appendix 6). Zero triaxialities predominantly cause a change of void shape rather than a

change in the volume. Hydrostatic stresses or mean stress σ_H causes only a change in volume and not in shape in an isotropic medium, deviatoric stress components bring about a change of shape in the body and influence the plastic deformation [2,3]. The Ashby equation is only valid for room temperature [15].

Despite the shortcomings of the Ashby et al equation, it was decided to see what effect temperature had on the C value. So the C value was worked out for all the VS series of steel heats using the input parameters given in Table 36 from 20°C to 350°C. From now on denoted by C_M . The text in blue are the calculated true strains to fracture values determined using the Ashby values for C (1.4). Text in red are the calculated results of C_M for this work. The graphed results are given in Figures 207 and 208. The best fit trend lines were then fitted to the data and the equations and their correlation to the data obtained. Also included in Figures 207 and 208 are the UTS vs Temperature curves for the VS series of steel heats.

It was found that a 2nd order polynomial trendline best described C_M vs Temperature data for 83A, a 2nd order polynomial trendline best described the data for 64A in Figure 207. Two second order polynomials best described the data for 64B and 83B in Figure 208. Second order polynomials were also used to describe the UTS vs Temperature data sets for the four heats in Figures 207 and 208, (C_M is plotted on the primary y axis, UTS on the secondary y axis).

Other trend lines were fitted to the C_M vs Temperature data in Figure 207 to see the correlation. That is power law trend lines were fitted to the data (to and from the maximum UTS) to see if the trend line fits could be improved and simplify calculation.

To correlate the F81 series of data with the VS series of steel heats to determine such things as the strain rate sensitivity and other material parameters and mechanical properties Figure 209 was plotted. The data plotted in Figure 209 for the F81 series and the VS series showed any correlation between the series.

Steel Heat	Temp ° C.	Sq rt volume fraction.	True strain to fracture (ϵ_T).	Ultimate Tensile Strength. (MPa).	Free Nitrogen (ppm).	Volume Fraction. V_f	Predicted values of ϵ_T using Ashby eq	Calculated C_M values for this work.
64B	20	0.3605	1.084	452.2	12	0.13	0.409	0.527
64A	20	0.0554	1.2	459.7	12	0.00308	2.025	2.35
83B	20	0.3478	1.043	472	36	0.121	0.449	0.6
83A	20	0.0573	1.059	507	38	0.00329	2.000	2.65
64B	100	0.3605	0.797	507	12	0.13	0.409	0.72
64A	100	0.0554	0.898	534	12	0.00308	2.025	3.15
83B	100	0.3478	0.665	605	36	0.121	0.449	0.95
83A	100	0.0573	0.639	614.3	38	0.00329	2.000	4.425
64B	150	0.3605	0.572	565.9	12	0.13	0.409	1
64A	150	0.0554	0.674	576.3	12	0.00308	2.025	4.2
83B	150	0.3478	0.56	650	36	0.121	0.449	1.115
83A	150	0.0573	0.566	658	38	0.00329	2.000	4.99
64B	200	0.3605	0.628	580.9	12	0.13	0.409	0.92
64A	200	0.0554	0.597	582.9	12	0.00308	2.025	4.75
83B	225	0.3478	0.642	614.6	36	0.121	0.449	0.975
83A	200	0.0573	0.569	667	38	0.00329	2.000	5
64B	250	0.3605	0.801	553.7	12	0.13	0.409	0.715
64A	250	0.0554	0.871	561.2	12	0.00308	2.025	3.25
83A	250	0.0573	0.74	632.1	38	0.00329	2.000	3.75
64B	300	0.3605	0.917	538.7	12	0.13	0.409	0.629
64A	300	0.0554	0.978	542.7	12	0.00308	2.025	2.9
83B	300	0.3478	0.858	541.3	36	0.121	0.449	0.735
83A	300	0.0573	0.794	604.1	38	0.00329	2.000	3.5
64B	350	0.3605	1.047	486	12	0.13	0.409	0.55
64A	350	0.0554	1.112	475	12	0.00308	2.025	2.55
83B	350	0.3478	0.999	501.9	36	0.121	0.449	0.625
83A	350	0.0573	0.884	519	38	0.00329	2.000	3.15

Table 36. Values used to calculate the C_M value in the modified Ashby equation.

It is pointed out in Figure 209 that the strain rate sensitivity (m) values used for F8106 were outside the DSA temperature regime for the maximum in UTS (see Tables 14 and 37, maximum in UTS obtained at 300°C). So the m values used for F8106 were not coincident with the maximum in UTS temperature. Whereas the m values used for F8104 and F8105 were in the temperature range for the maximum DSA effects in UTS, more so in F8105 (see Tables 14 and 37).

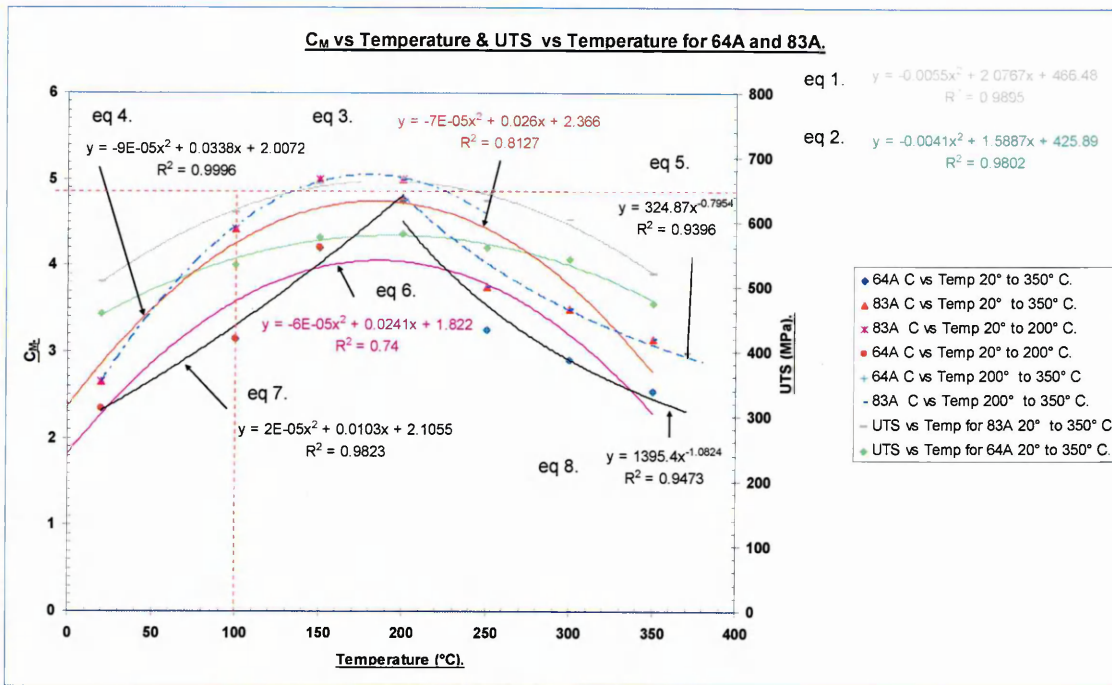


Figure 207. C_M vs Temperature and UTS vs Temperature for VS3764A and VS3783A.

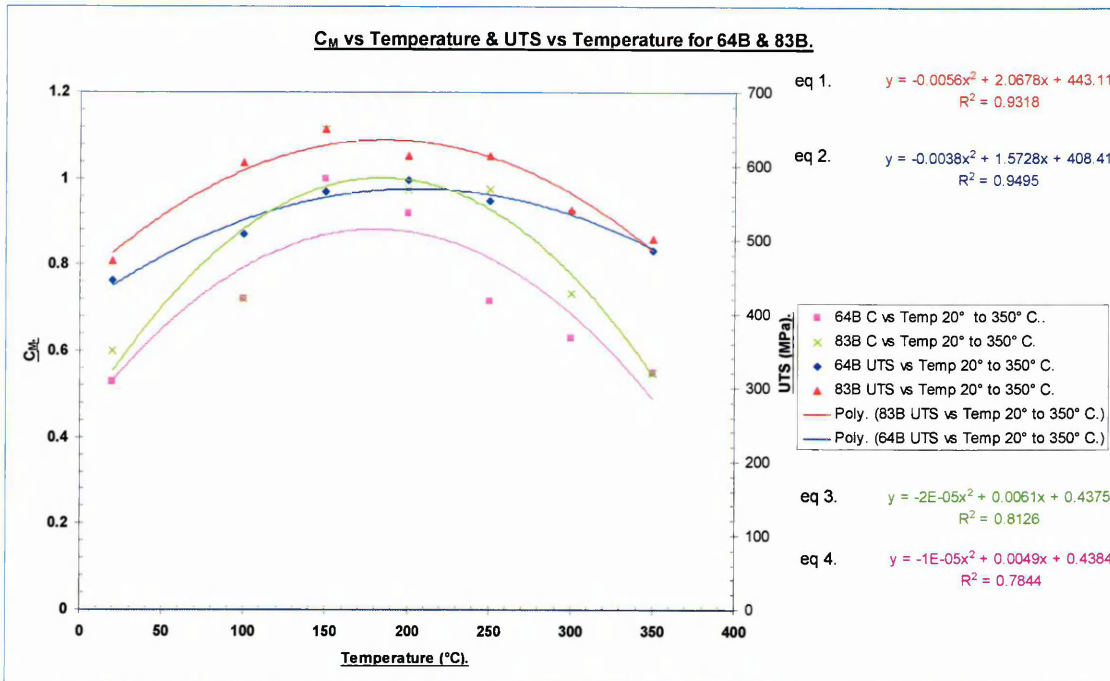


Figure 208. C_M vs Temperature and UTS vs Temperature for VS3764B and VS3783B.

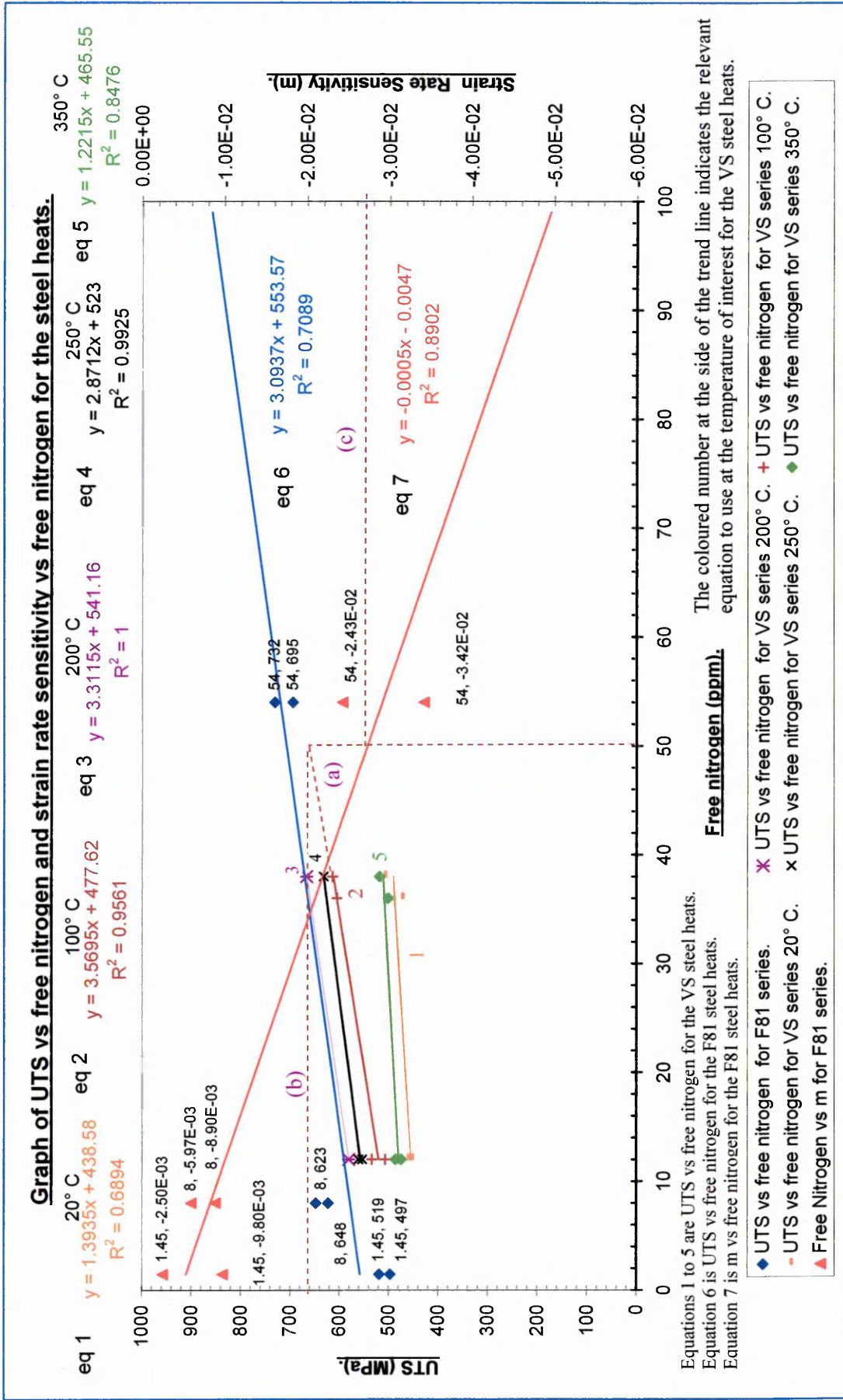


Figure 209. Graph of UTS vs free nitrogen and m vs free nitrogen for the steel heats.

The F8105 data used for plotting in Figure 209 is listed in Table 37. The red filled triangles and trend line is the data plotted for free nitrogen content (in ppm, the x axis) vs strain rate sensitivity (the secondary y axis). It can be seen by referring to Figure 99 and Table 37 that the most negative values of m were used for the steel heats. The strain dependence of m was neglected. The maximum UTS (the primary y axis) at this m value was plotted vs free nitrogen (ppm) for the F81 series. Trend lines were then fitted to all the F81 series data and the equations obtained (equation colour matches corresponding trend line).

Steel heat	Temp (° C).	free nitrogen	UTS (MPa).	Elongation (%).	Strain Rate Sensitivity (m).	Volume Fraction	sqrt Volume Fraction.	True strain to fracture.
F8106	150	1.45	497	27.3	-2.50E-03	0.0156	0.125	1.172
F8106	200	1.45	519	28.3	-9.80E-03	0.0156	0.125	1.241
F8104	200	8	623	24.6	-8.90E-03	0.0202	0.142	0.917
F8104	250	8	648	29.8	-5.97E-03	0.0202	0.142	0.9861
F8105	100	54	695	13.9	-3.42E-02	0.0204	0.143	0.629
F8105	150	54	732	19.9	-2.43E-02	0.0204	0.143	0.693

Table 37. F8105 data values used to plot data in Figure 209.

The data for the VS series of UTS vs free nitrogen (in ppm) plotted in Figure 209 is taken from Table 36. The data is plotted as block data as per Table 36 at the temperature of interest, for all the VS steel heats from 20°C to 350°C. What is interesting is that a family of lines are generated corresponding to each temperature, and all of them are virtually parallel, to the F81 series of UTS vs free nitrogen. The trend line of the data plotted from Table 37 in Figure 209 for the F81 series, of the maximum UTS's vs free nitrogen at a particular m value gave a correlation of 0.7089. Which is considered reasonable considering that F8106 had a maximum UTS at 300°C (see Table 14). As stated earlier the UTS chosen was determined by the most negative m value (see Table 37). Referring to Figure 167 the plot of $\Delta\sigma_p$ vs free nitrogen it can be seen that a correlation of 0.6875 was obtained using the maximum UTS at the temperature concerned.

Using Figures 207, 208 and 209 and the equations inset in the graphs, it is possible to predict the strain to failure for varying free nitrogen contents for the particular temperature of interest.

An illustration of the use of Figure 209 is given in the following example. A steel of similar composition to VS3783A is to be tested at 100°C at a strain rate of $2 \times 10^{-6} \text{ sec}^{-1}$. The free nitrogen content is increased from 38 ppm to 50 ppm. What would be the strain to failure and the strain rate sensitivity (m) at this temperature. The dotted lines in Figure 209 illustrate the process graphically the values obtained using the equations, line (a) represents the increase in free nitrogen, line (b) the increase in UTS, and line (c) the value of the strain rate sensitivity.

The first thing to do is to calculate the likely increase in the UTS due to the increased free nitrogen using the equation for VS series at 100°C (equation 2 in Figure 209). If other temperatures are required, the relevant equation is selected. For example if the temperature was 200°C, equation 3 in Figure 209 would be chosen. The corresponding temperature is next to the equation.

$$Y = 3.5695x + 477.62 \quad (52)$$

$$Y = \text{UTS} = (3.5695 \times 50) + 477.62$$

$$\text{UTS} = \underline{656 \text{ MPa.}}$$

This value is then put into Figure 207 into the secondary y axis (UTS) and the and the corresponding C_M value read off at the temperature of 100°C (as indicated by the red dotted line). This gives a C_M value of 4.85. This value is then substituted into the modified Ashby equation, (equation 53) using the volume fraction for 83A i.e. 0.00329 (see Table 36) assuming $\alpha = 1$.

$$\varepsilon_f = \frac{1}{C_M} \ln \left[\alpha \left(\frac{1}{f_v^{1/2}} \right) - 1 \right] \quad (53)$$

$$\varepsilon_f = \frac{1}{4.85} \ln \left[1 \left(\frac{1}{0.00329^{1/2}} \right) - 1 \right]$$

$$\varepsilon_f = \underline{0.577}$$

This gives an approximate true strain to fracture at 100°C of 0.577. The increase in free nitrogen content of 12 ppm for 83A resulted in a decrease in the strain to fracture of 10% as can be seen from Table 36. Similar calculations can be done for 64A using Figure 207, and for 64B and 83B but using Figure 208 to

determine the C_M value and using the volume fractions listed in Table 36. The likely strain rate sensitivity of the flow stress (m) is calculated using the trend line equation calculated for the F81 series (equation 7 in Figure 209).

$$Y = -0.0005x - 0.0047 \quad (54)$$

$$Y = -0.0005 \times 50 - 0.0047$$

$$Y = m = \underline{-2.97 \times 10^{-2}}$$

It is stressed that this is only an approximate value and is based on the VS series of steel heats behaving as the F81 series would in the DSA regime. It also neglects the strain dependency of m .

To illustrate the effect on C_M for increasing free nitrogen for a constant sulphur level Figure 210 was plotted. From the figure it can be seen that as the free nitrogen is increased for a constant sulphur level that the value of C_M is higher for the higher free nitrogen steel at every temperature. Strictly speaking C is an amplification factor of the void growth rate of 1.4 as suggested by Ashby [15] that should be incorporated into the Brown and Embury model [17]. If Ashby's values were used throughout the full temperature range in this work the same set of values for the strain to fracture would be obtained at every temperature as in Table 36. In the dynamic strain ageing regime, specimens usually fail by a localised shear mechanism, which is generally the result of a change in the stress triaxiality brought about by the localisation of stress as reflected by larger work hardening exponents (see Tables 11 – 14), more negative m values etc. C_M can be considered as a measure of the stress triaxiality, and it can be seen from Figures 207 and 208 that C_M increases with temperature. Having the highest value of C_M at the DSA peak, for all the VS series.

Figure 210 shows a plot of C_M vs free nitrogen content for VS3764A and VS3783A, and VS3764B and VS3783B at 20°C and 100°C. The calculated values of C_M and free nitrogen contents for this work are shown. Trend lines were fitted to the data and extrapolated to 0 ppm and 100 ppm free nitrogen content and the equations obtained (a linear law). To illustrate an increase or decrease in free nitrogen content of the steel heats. The corresponding equation colour goes with the trend line.

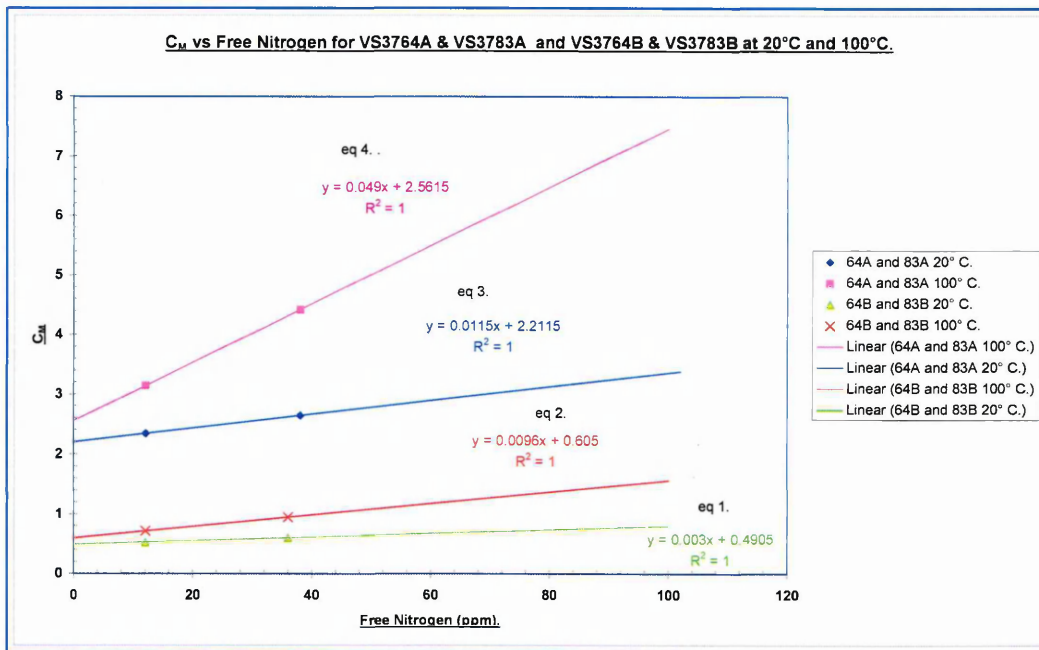


Figure 210. C_M vs Free Nitrogen for VS3764A & VS3783A and VS3764B & VS3783B at 20°C and 100°C.

For example what would be the likely strains to failure for the 64A – 83A data set if the free nitrogen content was increased from 38 ppm to 45 ppm at 20°C and 100°C. The equation applicable to the temperature is substituted into the modified Ashby equation for the C_M value and the strain to failure calculated. For 20°C. $V_f = 0.003$, $\alpha = 1$ the required equation is number 3 from Figure 210 $y = 0.0115x + 2.2115$.

$$\varepsilon_f = \frac{1}{C_M} \ln \left[\alpha \left(\frac{1}{f_v^{1/2}} \right) - 1 \right] \quad (53)$$

$$\varepsilon_f = \frac{1}{0.0115x + 2.2115} \ln \left[1 \left(\frac{1}{0.003^{1/2}} \right) - 1 \right] \quad (55)$$

substituting 45 ppm for x gives; $\varepsilon_f = \underline{1.04}$

For 100°C; required equation is number 4 from Figure 210, $y = 0.049x + 2.5615$ substituting for C_M and $x = 45$ ppm the free nitrogen value gives.

$$\varepsilon_f = \frac{1}{0.049x + 2.5615} \ln \left[1 \left(\frac{1}{0.003^{1/2}} \right) - 1 \right] = \varepsilon_f = \underline{0.59} \quad (56)$$

Similarly if done for VS3764B and VS3783B with $V_f = 0.125$ average of 0.12 and 0.13 see Table 36, would give strains to failure of 0.96 and 0.58 at 20°C

and 100°C respectively. The model predicts lower true strains to fracture due to the increased free nitrogen content, as can be seen if compared with Table 36. This can be done for any temperature by repeating the above procedure.

Variations in the sulphur and free nitrogen content can also be accommodated by the model for any temperature. Taking the above temperatures to illustrate this.

For example what would be the strain to failure at 100°C if the sulphur content was decreased for the 64B – 83B data set to 0.01 wt % and the free nitrogen content was increased to 55ppm (keeping other material composition the same i.e same manganese, silicon content etc). The first thing to do is to calculate, the increase in C_M due to the increase in sulphur content from 20°C to 100°C. This is done by subtracting the equations of the trendlines at the temperatures of interest. This gives the equation of the difference in the C_M value for the two sulphur levels, as the trendlines for the heats are for constant sulphur level. The equation used to determine the C_M value to substitute into the modified Ashby equation, at 100°C for the 64A – 83A data set is given by equation number 4 in Figure 210.

$$Y = C = 0.049x + 2.5615 \quad (57)$$

This is for 0.002 wt % sulphur. The equation used to determine the C_M value to substitute into the modified Ashby equation, at 100°C for the 64B – 83B data set is given by eq. 2 in Figure 210: (This is for a 0.025 wt % sulphur content actual values 64B = 0.027 wt %, 83B = 0.024 wt %):

$$Y = C = 0.0096x + 0.605 \quad (58)$$

By subtracting eq. 58 from eq. 57 the variance in C_M due to the increase in sulphur of approximately 12.5 times is given viz:

$$Y = C = 0.0394x + 1.9565 \quad (59)$$

By using the law of mixtures the C_M value can be calculated for a given sulphur content. For the sulphur content of 0.01 wt %.

What fraction is 0.01 wt % of 0.025 wt % (difference in sulphur content) = 0.40

Multiplying eq. 59 by 0.4 gives:

$$Y = C = 0.01576x + 0.7826 \quad (60)$$

This gives the C_M value for a sulphur content of 0.01 wt %. The required free nitrogen value is substituted for x as shown in equations 61 and 62.

The volume fraction of MnS inclusions is calculated using Franklin's [237] formula minus the oxygen term for the calculations done in this work (but if known can be used).

Franklin's formula [237].

$$f_v = 0.054 \left[\%S - \frac{0.001}{\%Mn} \right] + 0.05\%O \quad (36)$$

$$f_v = 0.054 \left[0.01 - \frac{0.001}{0.7} \right]$$

$$f_v = 0.0463\%$$

or can be calculated from Figure 211 using the equations of the trend lines. This converts a known sulphur content to a volume fraction for the VS series of steel heats using Franklin's formula minus the oxygen term.

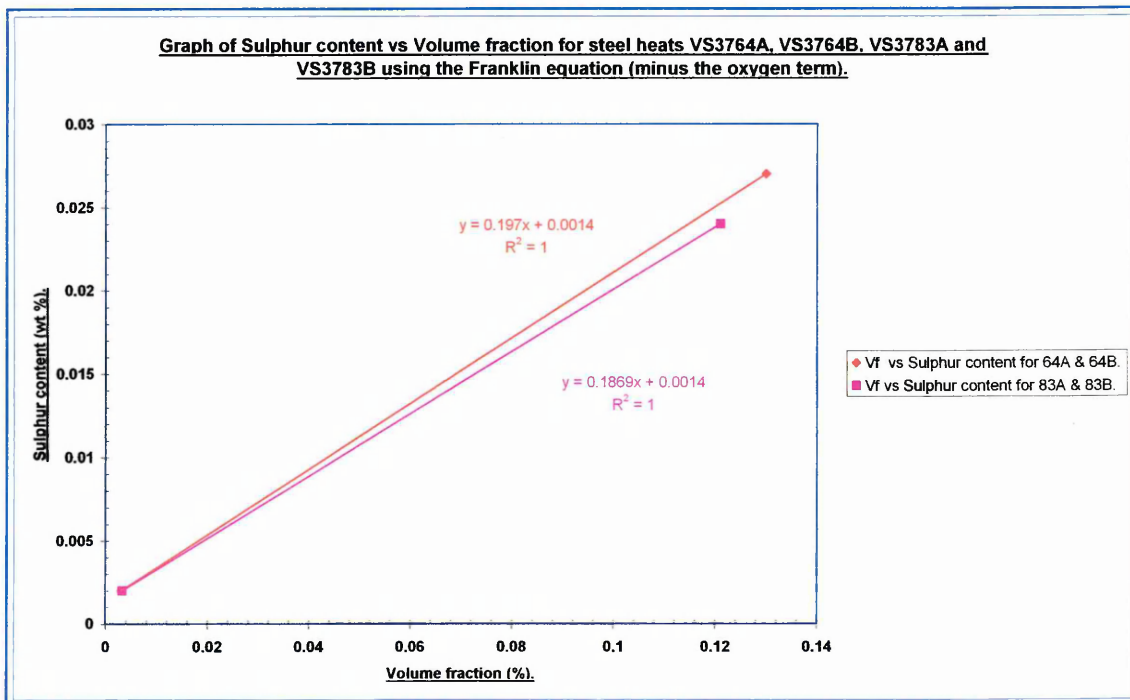


Figure 211. Sulphur vs Volume fraction for VS3764A and VS3764B and VS3783A and VS3783B.

Equation 60 and the volume fraction of 0.0463 are then substituted into the modified Ashby equation to give (assuming $\alpha = 1$):

$$\varepsilon_f = \frac{1}{C_M} \ln \left[\alpha \left(\frac{1}{f_v^{1/2}} \right) - 1 \right] \quad (53)$$

$$\varepsilon_f = \frac{1}{0.01576x + 0.7826} \ln \left[\alpha \left(\frac{1}{0.0463^{1/2}} \right) - 1 \right] \quad (61)$$

Substituting for $x = 55$ the free nitrogen content.

$$\varepsilon_f = \frac{1}{0.01576 \times 55 + 0.7826} \ln \left[1 \left(\frac{1}{0.0463_v^{1/2}} \right) - 1 \right] \quad (62)$$

$$\varepsilon_f = \underline{0.78}$$

5.9.3. The relationship between C_M and m for the F81 series of steel heats.

Figure 212 is a plot of strain rate sensitivity (m) versus C_M for the F81 series of steel heats. The data used to calculate C_M is given in Table 38. The strain rate sensitivity values were taken from Table 10. The temperatures chosen to illustrate the relationship were 100°C and 150°C, as these were the only temperatures that exhibited serrated flow for the F81 series.

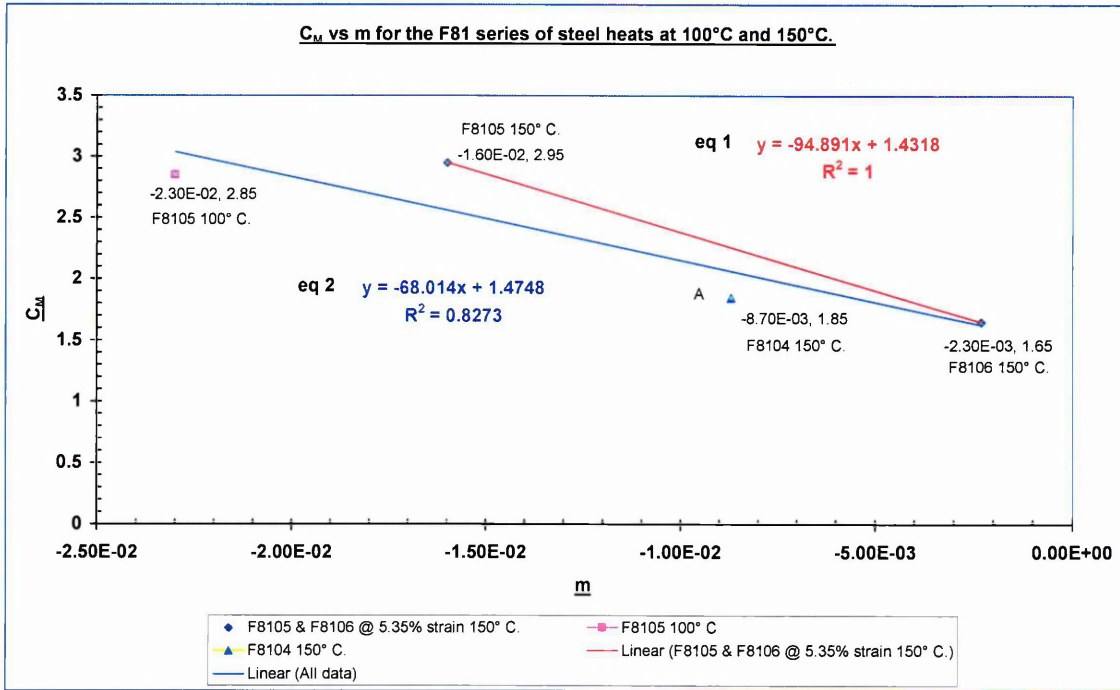


Figure 212. C_M vs m for F8105 and F8106 at 100°C and 145°C.

as can be seen from Table 14. This is illustrated in Figure 123. This was also found in the strain rate jump tests in Figures 100 and 101. From which it can be seen that serrations are present on the upper plateau of the stress vs strain curves when the strain rate was lowered to $2.7 \times 10^{-6} \text{ sec}^{-1}$ from $2.7 \times 10^{-4} \text{ sec}^{-1}$.

It was found that a linear relationship existed between C_M and m . The red trendline and equation 1 in Figure 212, is for F8105 and F8106 at 145°C at 5.35% strain and 150°C and 5.38% strain respectively. Bearing in mind that m for F8105 is negative at all strains tested, F8106 goes negative at 5.38% strain (see Table 10 and Figure 99). These values were used to illustrate the effect of

Steel Heat	Temp ° C.	Sq rt volume fraction.	True strain to fracture (ϵ_T).	Ultimate Tensile Strength. (MPa).	Free Nitrogen (ppm).	Volume Fraction. V_f	Predicted values of ϵ_T using Ashby eq	Calculated C_M values for this work.
F8104	20	0.142	1.38	560	8	0.0202	1.28	1.3
F8105	20	0.143	1.162	530	54	0.0204	1.27	1.535
F8106	20	0.125	1.35	503	1.45	0.0156	1.39	1.435
F8104	100	0.142	NA	NA	NA	0.0202	1.28	NA
F8105	100	0.143	0.629	701	54	0.0204	1.27	2.85
F8106	100	0.125	NA	NA	1.45	0.0156	1.39	NA
F8104	150	0.142	0.973	590	8	0.0202	1.28	1.85
F8105	150	0.143	0.603	732	54	0.0204	1.27	2.95
F8106	150	0.125	1.172	497	1.45	0.0156	1.39	1.65
F8104	200	0.142	0.917	623	8	0.0202	1.28	1.96
F8105	200	0.143	0.559	723	54	0.0204	1.27	3.25
F8106	200	0.125	1.241	519	1.45	0.0156	1.39	1.565
F8104	250	0.142	0.9861	648	8	0.0202	1.28	1.83
F8105	250	0.143	0.817	691	54	0.0204	1.27	2.2
F8106	250	0.125	1.26	543	1.45	0.0156	1.39	1.545
F8104	300	0.142	1.094	603	8	0.0202	1.28	1.635
F8105	300	0.143	NA	NA	54	0.0204	1.27	NA
F8106	300	0.125	1.397	569	1.45	0.0156	1.39	1.4
F8104	350	0.142	NA	NA	8	0.0202	1.28	NA
F8105	350	0.143	NA	NA	54	0.0204	1.27	NA
F8106	350	0.125	1.299	462	1.45	0.0156	1.39	1.49

Table 38. Values used to determine C_M for the F81 series of steel heats.

constant temperature as the strains were comparable. Ideally three experimental data points would have been used to give a better correlation, by using the F8104 specimen tested at 150°C but the specimen broke (see Table 10). An approximation of what the likely m value for the F8104 specimen was tested at 150°C was made from Figure 209. Equation 7 and trend line in Figure 209 is a plot of strain rate sensitivity vs free nitrogen for the F81 series using the maximum m values (i.e. most negative) at all the testing temperatures. The equation of the trend line is.

$$y = m = -0.0005x - 0.0047 \quad (54)$$

substituting the free nitrogen content of 8ppm for F8104 gives an m value of -8.7×10^{-3} . Which is not far removed from the values obtained for the F8104 series tested at higher temperatures (see Table 37). This was then plotted vs the corresponding C_M value given in Table 38 for 150°C (blue triangle in Figure 212, point A). Also included in Figure 212 is a data point for F8105 at 100°C at 5.19% strain. A trend line was then fitted through all the data points. Although at different temperatures the linear relationship is verified. It should be noted that the maximum m values were not used for F8105 (as can be seen from Table 10). That is the m values used, were used so that comparable strains could be identified. Though it is not suggested that m goes negative at similar strains the strain dependency of m is shown in Figure 100.

Figure 213 is a plot of C_M versus m for all the F81 series of steel heats, for all of the testing temperatures 100°C to 250°C. Here the strain dependency of m is not taken into account and only the most negative values of m are used (see Table 37). The C_M values are taken from Table 38.

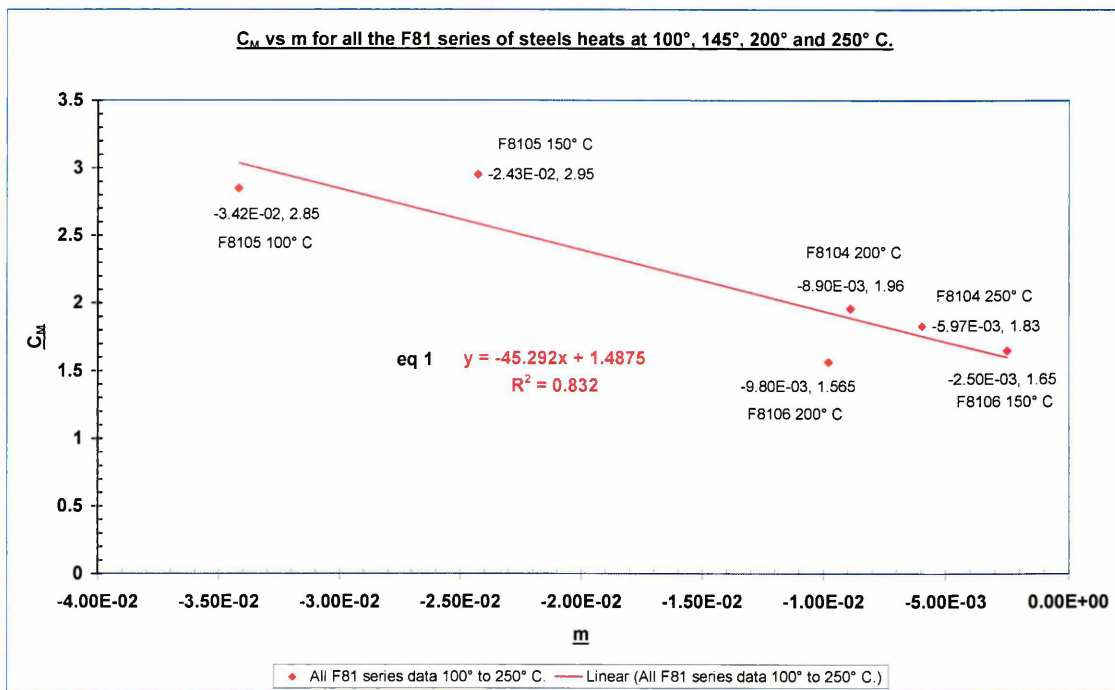


Figure 213. C_M v m for F8104, F8105, & F8106 at 100°, 145° 200°, & 250°C.

A trend line was then fitted through all the data. The equation of the trend line is (equation 1 in Figure 213)

$$Y = C = - 45.292x + 1.4875 \quad (63)$$

Next to the data point is also shown the temperature at which the m value was obtained. The use of Figure 213 is illustrated in the following example.

For example if a steel had a similar composition to the F81 series of steel heats, but the free nitrogen content was increased to 70 ppm what would be the likely strain to failure if tested at 50°C. Assuming the strain rate remains the same that is $2.7 \times 10^{-6} \text{ sec}^{-1}$.

The procedure is as follows:

eq. 54 is substituted into eq. 63 for x (where x is the free nitrogen content in ppm in eq. 54, and $x = m$ in eq. 63). This is then substituted for C_M in the modified Ashby equation, and using the relevant volume fraction in Table 37 eg for F8105 see equations 64 and 65.

$$\varepsilon_f = \frac{1}{C_M} \ln \left[\alpha \left(\frac{1}{f_v^{1/2}} \right) - 1 \right] \quad (53)$$

$$\varepsilon_f = \frac{1}{-45.292x + 1.4875} \ln \left[1 \left(\frac{1}{0.0204^{1/2}} \right) - 1 \right] \quad (64)$$

$$\varepsilon_f = \frac{1}{-45.292(-0.0005x - 0.0047) + 1.4875} \ln \left[1 \left(\frac{1}{0.0204^{1/2}} \right) - 1 \right] \quad (65)$$

$$\varepsilon_f = \frac{1}{-45.292(-0.0005 \times 70 - 0.0047) + 1.4875} \ln \left[1 \left(\frac{1}{0.0204^{1/2}} \right) - 1 \right]$$

$$\varepsilon_f = 0.54$$

It can be seen that the increase in free nitrogen content of 16 ppm considerably lowers the strain to fracture (see Table 14) and shifts the UTS peak to lower temperatures. The temperatures in Figure 213 are included to give an approximation of the expected results for the strain rate sensitivity due to the increased free nitrogen content at the temperature of interest. It can also be seen that the value of C_M increases as the free nitrogen content increases. As stated earlier C_M is a numeric value representing the increase in stress triaxiality.

Similar calculations can be done for the VS series of steel heats using Table 36 (to obtain the relevant C_M value and volume fraction) and Figure 209 to obtain the relevant m value at the temperature of interest in the DSA regime.

It was stated earlier the process of void growth is strongly influenced by the state of tensile stress during plastic deformation. The higher the dominating tensile stresses (the higher the triaxiality) the higher is the void growth rate. This is reflected in higher C_M values.

5.9.4. Model predictions compared to published work.

5.9.4.1. Model predictions compared to Miglen's work [65].

To validate the model with published work it was compared to the work of Miglen et al's data [65], work done on SA 515 Grade 70 steel and Wagner et al [48] (discussed in section 5.9.4.2). The compositions of the SA 515 Grade 70 steels used by Miglen et al [65] are given in Table 39 in wt%.

Heat	C	Mn	P	S	Si	Al	Free Nitrogen N _f (wt %).
645	0.29	0.72	0.009	0.015	0.23	<0.005	0.004
649	0.29	0.76	0.008	0.023	0.18	<0.005	0.003

Table 39. Chemical composition of SA 515 Grade 70 steel Heats 645 and 649 [65].

Figure 214 shows Miglen et al's data [65] on which the comparison is to be made, the top curve with open circles (Heat 649).

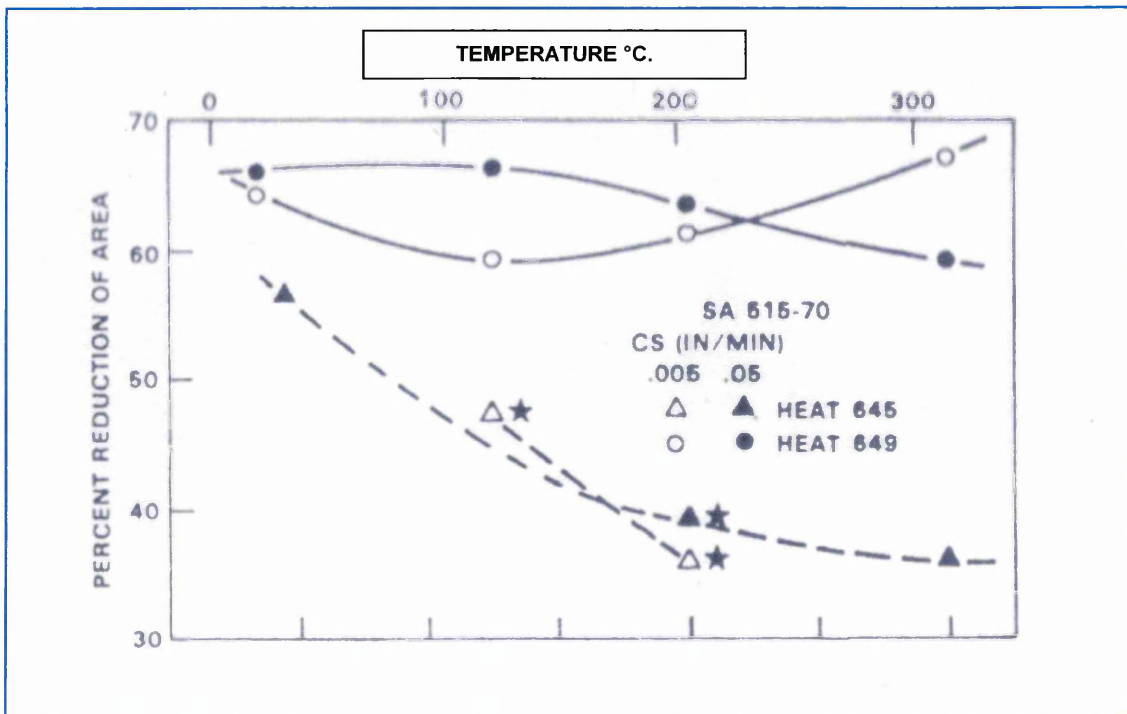


Figure 214. Percent reduction of area vs Temperature, for the two heats of SA 515 Grade 70 steel Heat 645 and Heat 649. The stars denote serrated flow [65].

It can be seen from Figure 214 that the y axis is percent reduction of area, the modified Ashby model requires that the strain to fracture, needs to be the true strain to fracture. The percent reduction of area taken from Figure 214 was therefore converted to the true strain at fracture through the relationship.

$$\epsilon_f = \ln \frac{1}{1-q} \quad (66)$$

Where q is the reduction in area expressed as a fraction.

This was done for steel Heat 649. The results are given in Table 40. Also given in Table 40 is the temperature for the particular true fracture strain. The values chosen were based on the strain rate of 0.005in min⁻¹ which is 0.013 mm min⁻¹. This machine rate was chosen as it was the closest to the machine rate used for the tensile testing programme done in this work which was 8.259 x 10⁻⁵ in min⁻¹ (which equates to a strain rate of 2 x 10⁻⁶ sec⁻¹).

Heat.	Temperature ° C.	Percent reduction in area.	Free Nitrogen N _f (wt %).	Actual True strain to fracture. ϵ_f	Calculated True strain to fracture by model. ϵ_f	Calculated C _M values using eq. 67.
649	23	64	0.003	1.02	1.15	0.5672
649	121	58	0.003	0.86	0.74	0.8827
649	204	62	0.003	0.96	0.77	0.8495
649	300	67	0.003	1.10	1.30	0.4675

Table 40. Reduction of area converted to True strain to fracture and compared with model predictions.

It can be seen from Table 39 that of the two steel heats Heat 645 and Heat 649, that Heat 649 has a similar chemical composition and free nitrogen content, to VS3783B and so will be used to illustrate the use of the model. The graphed data for the VS series of steel heats with the high sulphur content is shown in Figure 208, the use of it is shown below. The first thing to do is to select the required equation to determine the C_M value, for substitution into the modified Ashby equation. This is equation 3 in Figure 208 which is.

$$y = -2E - 05x^2 + 0.0061x + 0.4375 \quad (67)$$

where $y = C_M$ and $x = \text{Temperature } ^\circ\text{C}$. It is pointed out that E is the Microsoft Excel way of giving numbers to a base 10 e.g. 7E1 = 70.

Equation 67 describes the relationship between C_M vs Temperature for the high sulphur, high nitrogen VS steel heat (VS3783B). The temperatures used by Miglen [65] (taken from Figure 214) are shown in Table 40. These temperatures are then substituted into equation 67 to give the C_M values listed in Table 40. The volume fraction is calculated using Franklin's formula [237]. The oxygen term was omitted as Miglen et al did not specify it.

$$f_v = 0.054 \left[\%S - \frac{0.001}{\%Mn} \right] + 0.05\%O \quad (36)$$

$$f_v = 0.054 \left[0.023 - \frac{0.001}{0.76} \right]$$

$$f_v = 0.117\%$$

The listed C_M values in Table 40, and the calculated volume fraction of 0.117% are then substituted into the modified Ashby equation (eq. 53) to give the predicted true strains to fracture in Table 40.

$$\varepsilon_f = \frac{1}{C_M} \ln \left[\alpha \left(\frac{1}{f_v^{1/2}} \right) - 1 \right] \quad (53)$$

Figure 215 shows the graphed results of the actual true strains to fracture vs

temperature [65], and the predicted true strains to fracture vs temperature predicted from the model.

It can be seen from Figure 215 that the model provides a reasonable fit, compared to the actual data. From Figure 215 it can be seen that three of the four data points lie within the 20% error bars. The maximum percentage error bar was 24% with a standard deviation of one for the data point outside the error bars. Seventy five per cent of the data points fitting within 20% error bars is considered reasonable as a model prediction for the true strain to fracture.

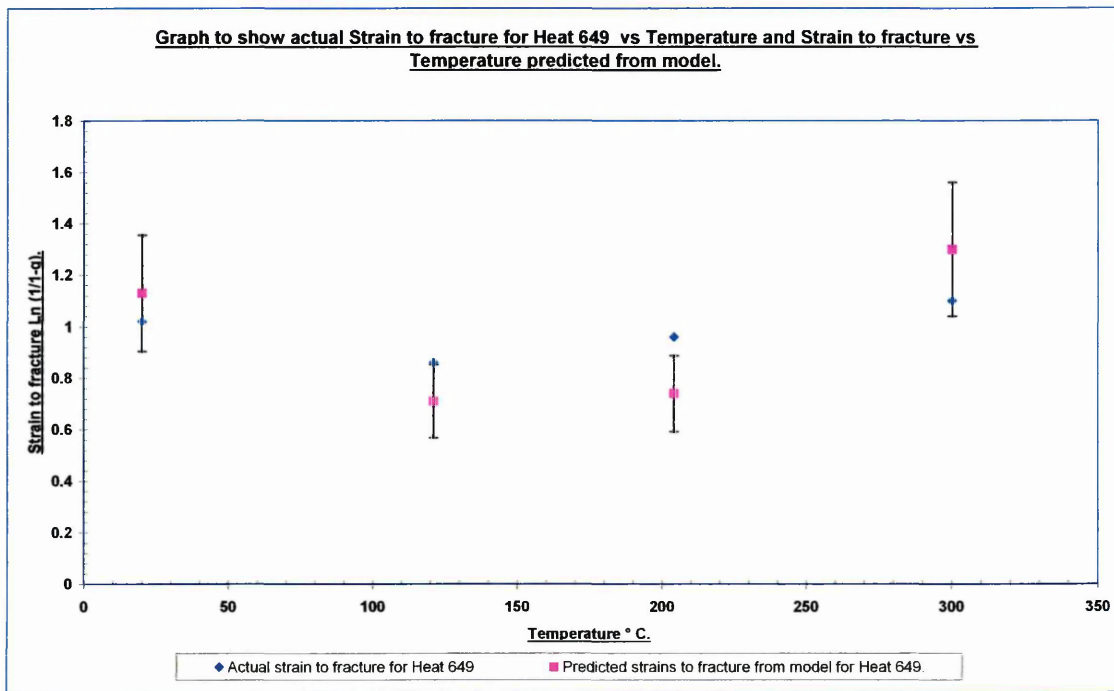


Figure 215. Actual True strain to fracture vs Temperature from Miglen et al data [65] compared to True strains to fracture predicted from model.

5.9.4.2. Model predictions compared to Wagner's work [48].

To validate the model it was compared to a second published work, that of Wagner et al [48]. In this work conducted on C – Mn steels, the purpose of which was to assess the degradation in fracture toughness in the dynamic strain ageing regime, (20°C - 300°C) using a local approach. The degradation in the J – R tearing resistance ($J_{0.2}$), and tearing modulus (dJ/da) was assessed relative to a base metal (AFNOR NFA 36205 grade A 48 French standard steel) and manual metal arc deposited metals (SAFER MF 48). The compositions of which are given in Table 41 in wt%.

Heat	C	S	P	Si	Mn	Ni	Cr	Mo	V	Cu	Sn	Al	N	O	Ti	Nb
A48	0.198	0.012	0.010	0.207	0.769	0.135	0.095	0.025	0.003	0.273	0.023	0.004	0.0083	0.0049	0.003	0.004
MF48	0.049	0.007	0.018	0.4	0.86	0.043	0.021	0.008	0.023	0.016	0.005	0.005	0.0120	0.038	0.009	0.005

Table 41. Chemical composition of A48 and MMAW MF48 [48].

Two sets of tensile specimens were used, smooth cylindrical tensile specimens (4 mm diameter), and axisymmetric notched tensile specimens, with varying notch root radius. The notch root radii were two, four, and ten millimetres respectively. The strain rate for the smooth tensile specimens (made from material A48) was $2 \times 10^{-4} \text{ sec}^{-1}$. The strain rate used for the axisymmetric tensile specimens was nominally 10^{-4} sec^{-1} .

The smooth tensile specimens were chosen from Wagner's work [48] against which to make a comparison. The A48 plate received a prior normalisation thermal treatment consisting of austenitizing at 870°C, then air cooling. Similar to the forging process for the VS series of steel heats, discussed in the experimental section. It can also be seen from Table 41 that the A48 steel heat has comparable total nitrogen content if compared with Table 5 for the VS3783 series of steel heats. It is assumed that the A48 and VS3783 series of steel heats have comparable free nitrogen (see Appendix 9). They have similar aluminium to total nitrogen ratios. As can be seen from Tables 5 and 41. The A48 steel heat also has similar yield and UTS strengths (see Figures 216a and 216b the comparison is being made against the reference tests). The results were obtained by Wagner et al [85,278] in earlier works,

done on the same steel under the same testing conditions. The smooth tensile specimens used in Wagner's work [48,85,278], also have comparable diameters to the tensile specimens used in this work (3.68 mm see Figure 73). Wagner's results are given in Figure 216.

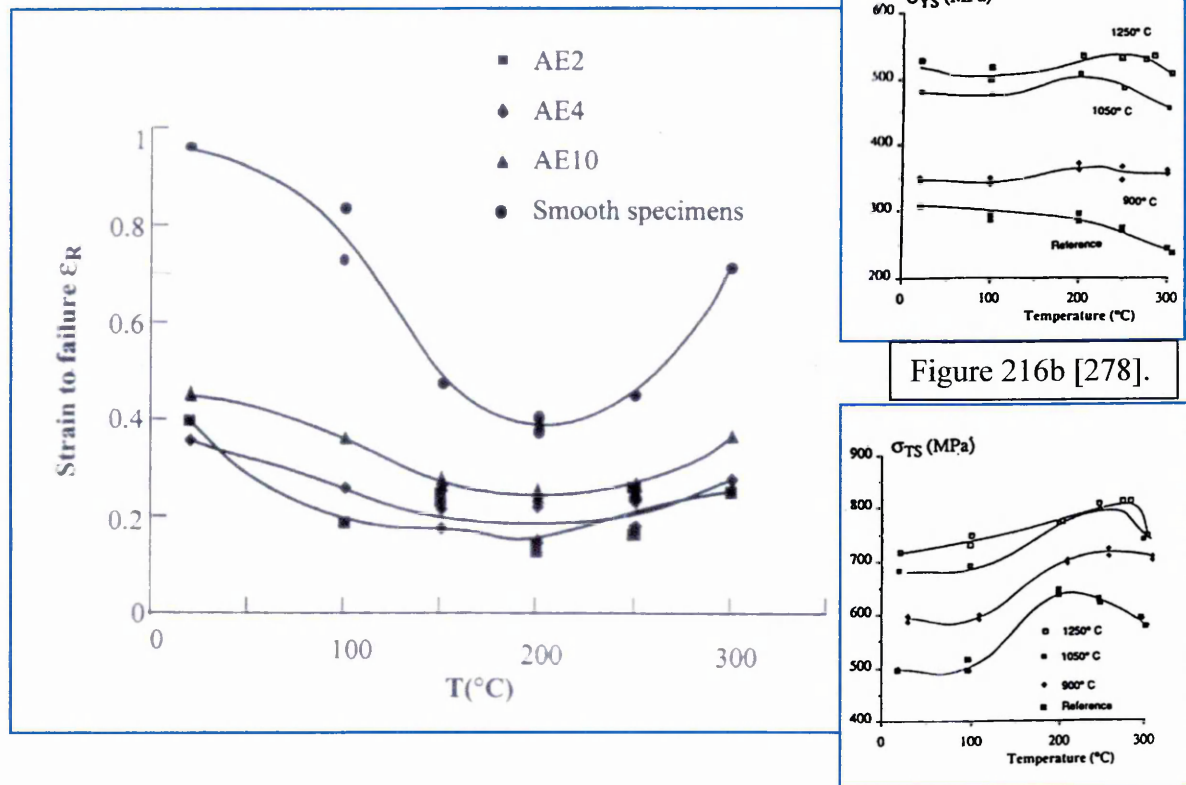


Figure 216. Variation of Strain to failure vs Temperature for different specimen geometries [48].

The volume fraction of inclusions for the A48 steel heat used in Wagner's work was 0.079%. It can be seen from Table 41, that the sulphur content for the A48 steel is 0.012 wt %. The strain to fracture in Figure 216 was calculated by Wagner using the relationship.

$$\epsilon_f = Ln \frac{1}{1-q} \quad (66)$$

which was used in this work to compare data from this work with Miglen et al's data [65].

Using Figures 207 and 208 the graphs of C_M vs Temperature for VS3783A, and VS3783B. The C_M value is calculated for 0.012 wt % sulphur as follows. Equation 3 in Figure 207 is the equation of the trend line for the data set

(C_M vs Temperature) for VS3783A (0.002 wt% sulphur) over the temperature range 20° - 350°C. Similarly equation 3 in Figure 208 is the trend line for the data set (C_M vs Temperature) for VS3783B (0.024 wt% sulphur) over the temperature range 20°C - 300°C. By subtracting one equation from the other the variance in C_M for a difference in sulphur content of 0.024 wt% sulphur can be calculated see Table 5.

Equation of the trend line for VS3783A data series eq. 3 Fig. 207 (20° - 300°C).

$$y = -7E-05x^2 + 0.026x + 2.366 \quad (67)$$

Equation of the trend line for VS3783B data series eq. 3 Fig. 208 (20° - 300°C).

$$y = -2E-05x^2 + 0.0061x + 0.4375 \quad (68)$$

1. Subtracting equation 67 from equation 68 gives.

$$y = -5E-05x^2 + 0.0199x + 1.928 \quad (69)$$

2. The sulphur content for A48 is 0.012 wt%, this needs to be expressed as a fraction of 0.024 wt% sulphur, i.e. 0.5.

3. Equation 69 is then multiplied by 0.5, this gives the C_M values for a 0.012 wt% sulphur over the temperature range 20° - 300° C to give.

$$y = -2.5E-05x^2 + 0.00995x + 0.964 \quad (70)$$

4. The temperature of interest in then substituted for x in equation 70.

From Figure 216 it can be seen that the testing temperatures used by Wagner were 20°, 100°, 150°, 200°, 250°, and 300°C. These values are substituted into equation 70 to give the values listed in Table 42.

5. The listed C_M values in Table 42 are then put into the modified Ashby equation, using Wagner's calculated volume fraction of 0.079%. To give the true strains to fracture listed in Table 42.

Figure 217 shows the actual true strains to fracture from Wagner et al data [48] compared to true strains to fracture predicted from model. It can be seen from Figure 217 that the predicted strains to fracture from the model, provide a reasonable fit to the Wagner et al data [48]. Four out of the six data points lie within the 19% error percentage bars, with a standard deviation of one. The two data points outside the 19% error percentage bars, lie within 33% error bars with the same standard deviation. Sixty six per cent of the data points fitting within 19% error bars is considered reasonable for model predictions of the true strain to fracture.

Heat.	Temperature ° C.	Total Nitrogen N _f (wt %).	Actual True strain to fracture. ϵ_f	Calculated True strain to fracture by model ϵ_f	Calculated C _M values using eq. 70.
A48	20	0.0083	0.95	0.814	1.153
A48	100	0.0083	0.72	0.549	1.709
A48	150	0.0083	0.46	0.495	1.894
A48	200	0.0083	0.40	0.480	1.954
A48	250	0.0083	0.43	0.497	1.889
A48	300	0.0083	0.72	0.552	1.699

Table 42. Tabulated results of strains to fracture predicted from model compared to Wagner et al data [48].

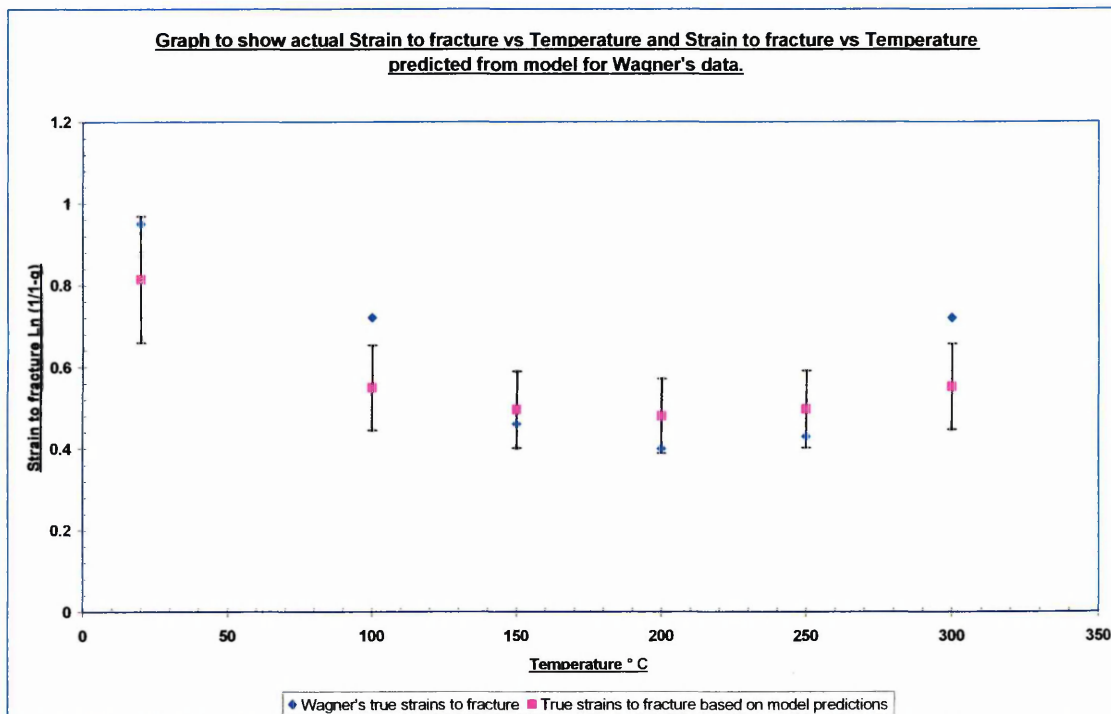


Figure 217. Actual True strains to fracture vs Temperature from Wagner et al data [48] compared to True strains to fracture predicted from model.

It can be seen that the model provides a reasonable fit when the data is compared to the published work of Miglen [65] and Wagner [48]. The strain rate used by Miglen was 60.54 times faster, and that used by Wagner was 100 times faster than was used in this work. It is thought that the data fit could have been improved if comparable strain rates were used by Miglen and Wagner.

6. *Conclusions.*

It is well known that the stress vs strain curve of a specimen of low carbon steel displays serrations in the work hardening region when tensile tested at slightly elevated temperatures. This serrated behaviour, also known as the Portevin LeChatelier effect, is accompanied by increased rates of work hardening, negative strain rate dependences of the flow stress, and reductions in ductility. In commercial steels, these phenomena are due to interactions during deformation between dislocations and primarily solute nitrogen. Such regular pinning and unpinning is termed dynamic strain aging and the most important variables are the temperature, deformation rate, and interstitial concentration.

The dynamic strain ageing behaviour of seven C-Mn steels and an interstitial free steel has been examined at room temperature to 350° C using tensile testing at strain rates of $2 \times 10^{-6} \text{ s}^{-1}$ and $2.67 \times 10^{-6} \text{ s}^{-1}$. The effects of temperature on the yield stress, flow stress, UTS, fracture stress, and fracture strain were investigated in detail. In agreement with previous studies, work hardening peaks, minima in ductility, and negative strain rate dependences of the flow stress were observed between 100° and 350°C, the positions of which depended on the free nitrogen content and strain rate. In addition fatigue crack propagation tests were carried out on two of the steels of different nitrogen content, at 150°C in air and at two different frequencies. Also from the Fracture toughness tests and Charpy tests done. The following conclusions were drawn.

1. The negative strain rate dependence of the flow stress attributable to dynamic strain ageing is considered to promote flow localisation and, therefore, smaller strains to fracture as seen in all the steel heats.
2. The higher free nitrogen content VS series of steel heats (VS3783A and VS3783B) exhibited larger uniform strains relative to the total strains to fracture in the dynamic strain ageing regime. This was considered to be attributable to the higher free nitrogen. The total strains to fracture for the

higher sulphur VS series of steel heats were larger than expected from Ashby predictions [15]. It is thought that this was attributable to the orientation of the inclusions due to the forging process. In that the majority of inclusions were present as prolate spheroids rather than oblate spheroids (see Figure 159). This acts to increase the planar distance between inclusions, hence larger strains to fracture. This can be seen in Figures 1 and 2, the model proposed by Thomason [2,3].

3. The magnitude and frequency of the serrations on the stress vs strain curves, increased with free nitrogen content. The higher the free nitrogen content the larger the increase in UTS (and $\Delta\sigma_p$), since $\Delta\sigma_p$ is directly dependent on the number of interstitial atoms concentrated at the mobile dislocation. The DSA strengthening due to interstitials was found to be proportional to the log of the free carbon plus free nitrogen.

(where $x = C_f + N_f$);

$$\Delta\sigma_p = 39.846\ln(x) + 49.74$$

(see Figure 168, R^2 value 0.6616).

The equation for determining $\Delta\sigma_p$ based on free nitrogen was found to be proportional to the log of the free nitrogen (where $x = N_f$); (see Figure 167, R^2 value 0.6875).

$$\Delta\sigma_p = 39.605\ln(x) + 69.132$$

where x is in ppm. Free nitrogen giving the marginally improved correlation.

4. A generic model has been developed in terms of the modified Ashby et al equation, for prediction of the true strain to fracture. The tensile properties of a series of C – Mn steels can be modelled in terms of the interstitial carbon and nitrogen content and the volume fraction of MnS inclusions. This modified Ashby model is able to explain most ductile fracture observations made in the blue brittle region.

$$\varepsilon_f = \frac{1}{C_M} \ln \left[\alpha \left(\frac{1}{f_v^{1/2}} \right) - 1 \right]$$

Where $C_M = f(m, T, N_f)$, m = strain rate sensitivity, T = Temperature °C.

The C term in the Ashby et al equation has been replaced by C_M . Which

considers C_M in the equation as a numeric increase in the stress triaxiality. It is found that the value of C_M increases in the dynamic strain ageing temperature regime.

5. The balance between inclusion cavitation and localised shear at voids, and nitrogen strengthening is shown to vary greatly with strain rate and temperature. However the framework has been established to make engineering evaluations of the effect volume fraction of inclusions and free interstitial content from room temperature to 300°C.

6. It has been shown that the reduction of sulphur content from about 0.025 to 0.002% in the VS series of steel heats results in marked increases in ductile impact upper shelf energy values for a number of low - alloy steels, over a range of tensile strengths and metallographic structures.

7. Increasing the free nitrogen content of a steel was found as expected from the work of Pickering and Gladman [229] to have a pronounced effect on the Impact Transition Temperature (ITT). This is interpreted as a flow stress effect of the free nitrogen. This is supported by the findings of Mintz [219,222]. The equation used to determine the ITT based on free nitrogen for this work was (based on 50% FATT, R^2 value 0.8989, see Figure 174).

$$y = 833.39x - 53.572$$

where x is the square root of the free nitrogen content in wt%.

The equation used to determine the ITT based on free nitrogen plus free carbon for this work was (based on 50% FATT, R^2 value 0.9069 see Figure 176).

$$y = 649.33x - 52.714$$

where x is the square root of the free nitrogen content in wt%. Free nitrogen plus free carbon giving a marginally improved correlation.

8. A linear law best approximates the relationship between the integral of the J vs Δa resistance curve and the Charpy upper shelf fracture energy.

9. It has been shown that dynamic strain ageing lowers the tearing modulus dJ/da , and J_{1c} in air at elevated temperature. With further reductions in an 8 ppm DOW environment at 200°C. The results of the J – R tests showed that J_{1c} and dJ/da decrease and exhibit negative loading rate dependence as the temperature is increased. The J_{1c} reduction for VS3764A in the DSA region (200°C) was 34% lower and dJ/da was about 45% lower than at room temperature. The J_{1c} reduction for VS3764B in the DSA region (200°C) was 27% lower and dJ/da was about 35% lower than at room temperature.

10. From fatigue crack propagation tests carried out on F8104 and F8105 at frequencies of 0.0167 and 5 Hz it was found that the fatigue crack growth rates obtained on F8105 at a frequency of 0.0167 Hz, were between 2.09 and 2.57 times lower than F8104. It is thought that this was attributable to the higher free nitrogen in F8105 being beneficial, due to the flow stress effect on the yield stress (reduced plastic zone size). It appears that the higher free nitrogen steel (F8105) has not had any deleterious effect on fatigue crack growth in the dynamic strain ageing regime. The striations appear fully ductile and there are no static modes of fracture present in the micrographs. The size of the striations is reduced by an increase in the free nitrogen content. This is determined by the strength of the steel, which affects the size of the plastic zone. The yield strength at 150°C for F8104 is 497.5MPa and for F8105 is 524.5MPa (see Table 14 based on $\sigma_f = (\sigma_y + \sigma_{uts})/2$). The inverse relationship between da/dN and the yield strength of a material as shown by Ramsamooj et al [183] and numerous authors has been shown to be beneficial in the DSA regime.

Chapter 7.

7. *Suggestions and further work.*

1. In the tensile testing and Charpy testing programme correlations have been made between certain test parameters and free nitrogen, and in some cases the additive effect of free nitrogen and free carbon. Where this has been done the correlation between the testing parameters has been marginally improved as shown by the better R^2 value of the trend line to data fit. Future work could involve developing a generic model based on the data obtained in this work.

2. It would be interesting to see if there was any relationship between this work done on fatigue and the reported work done by Huang et al [267]. It seems more than fortuitous that the data obtained in this work sits directly on his data when superimposed on his work, and the lower crack growth rates obtained in his work, are of the same order as this work.

3. Do step fatigue tests at 20°C on F8104, and F8105 under the same test conditions used in this work, and see if there is a relationship with the strain rate sensitivity parameter, m . For example does a more negative m signify lower crack growth rates, or is the effect controlled by the flow stress.

4. It has been shown that dynamic strain ageing lowers the tearing modulus dJ/da , and J_{1C} in air at elevated temperature, with further reductions in a 8 ppm DOW environment at 200°C. It would be interesting to see what part sulphur played in the degradation of J_{1C} in the same aqueous environment, and to see what an increase in free nitrogen content would have. To this end specimens have been made with increased sulphur, and free nitrogen content.

5. It has been shown that increasing the free nitrogen content of a steel, lowers the strain rate sensitivity i.e makes it more negative, if the test is conducted at optimum dynamic strain ageing conditions (i.e. temperature and strain rate). It would be interesting to quantify the increase in strain localisation brought about by DSA by being able to correlate the increase in strain in a Luders band due to the free nitrogen. To this end the free nitrogen specimens would be used i.e flat

specimens. This would promote the generation of Luders bands more readily than round tensile specimens. The necessary machine adaptations have been made.

6. In this work the crack tip strain rate was calculated using Lidbury's equation, this gives an approximation. The crack tip strain rate could be lower depending on the size of the plastic zone. To be able to quantify the crack tip strain rate would be of assistance in correlating the data obtained from tensile testing results. Instead of assuming a correlation and fitting constants to suit equations.

7. To be able to quantify the strain and strain rate at the crack tip of a J specimen under test, and correlate this with the crack tip opening displacement (CTOD), for varying sulphur and free nitrogen contents using Finite Element Analysis (FEA) see Appendix 8. Then see if there is any relationship between the above parameters.

8. References.

1. Van Stone, R.H., Cox, T.B., Low, J.R. Jr., and Prioda J.A., *Int. Metals Reviews*, Vol. 30, no. 4, pp. 157 - 179, 1985.
2. Thomason, P.F., "A View on Ductile Fracture Modelling", *Fat. and Fract. of Eng. Mat. and Struct*, Vol. 21, no 9, pp. 1105 -1122, 1998.
3. Thomason, P.F., "Ductile Fracture of Metals", 1990, ISBN 0-08-040178-3.
4. Cottrell, A.H., *Trans. A.I.M.E*, Vol. 212, pp. 192, 1958.
5. Tipper, C.F., "The Fracture of Metals", *Metallurgia*, 39, pp. 33 -137, 1949.
6. Puttick, K.E., "Ductile Fracture in Metals", *Phil Mag*, 4, pp. 964 - 969, 1959.
7. Baker, T.J., and Charles, J.A., "Deformation of MnS inclusions in Steel", *JISI*, pp. 680 - 690, Sept. 1972.
8. Pickering, F.B., "The Effect of Composition and Microstructure on Ductility and Toughness", *Towards Improved Ductility and Toughness*, Iron and Steel Institute of Japan, Kyoto International Conference Hall, October 25th to 26th, pp. 9 - 30, 1971.
9. Franklin, A.G., and Tegart, W.J. McG., *JISI*, pp. 588 - 592, July, 1964.
10. Gurland, J., and Plateau, J., *Trans. ASM*, Vol. 56, pp. 442 - 454, 1963.
11. Gladman, T., Holmes, B., McIvor, I.D., "Effect of Second Phase Particles on the Mechanical Properties of Steels", p. 68, ISI, London, 1971.
12. Edelson, B.I., and Baldwin, W.M. Jnr., "The Effect of Second Phases on the Mechanical Properties of Alloys", *Trans. ASM*, Vol. 55, p. 230, 1962.
13. Goods, S.H., and Brown, L.M., "The Nucleation of Cavities by Plastic Deformation", *Acta - Metallurgica*, Vol. 27, no. 1, pp. 1 – 15, 1979.
14. Ashby, M.F., Roy, G.Le., Embury, J.D. and Edwards, G., "A Model of Ductile Fracture based on the Nucleation and Growth of Voids", *Acta Metallurgica*, Vol. 29, no. 8, pp. 1509 - 1522, 1981.
15. Ashby, M.F., Ghandi, C., and Taplin, D.M.R., "Fracture Mechanism Maps and Their Construction for F.C.C Metals and Alloys", *Acta Metallurgica*. Volume 27, pp. 699 - 729, 1979.
16. Palmer, I.G., and Smith G.C., "Fracture of Internally Oxidised Copper Alloys", *Bolton Landing Conference*, New York, June 27th - 29th, 1966, Oxide Dispersion Strengthening, Gordon and Breach, Metallurgical Society Conferences, Metallurgical Society of AIME, pp. 253 - 290, Vol. 20248214.

17. Brown, L.M., and Embury, J.D., "*The Initiation and Growth of Voids at Second Phase Particles*", Proceedings of the 3rd International Conference on Strength of Metals and Alloys, Institute of Metals, London, 1973, pp. 164 - 169, (data used for paper taken from ref 269).
18. Birkle, A.J., Trans. ASM, Vol. 59, pp. 981, 1966.
19. Hodge, J.M., and Mogford, I.L., Proceedings of the Institute of Mechanical Engineers, Vol. 193, p. 93, 1979.
20. Fred, F.L. Jnr., Corrosion, Vol. 39, p. 120, 1983.
21. Bocquet, P., Cheviot, A., and Dumont, R., "*Some examples of the Evolution of Materials for Nuclear Applications. Metallurgical improvements of 16MND5 steel grade and new technologies for manufacturing heavy components*", Paper presented at 18 MPA Seminar, Stuttgart 8th and 9th October 1992, pp. 39.1 - 39. 20, Safety and Reliability of Plant Technology with special emphasis on Nuclear Technology.
22. Srinivas, M., Malkondaiah, G., Linga Murty, K., Rama Rao, P., "*Fracture Toughness in the Dynamic Strain Ageing Regime*", Scripta Metallurgica et Materialia, Vol. 25, pp. 2585 - 2588, 1991.
23. Ewalds, H.L., and Wanhill, R.J.H., Fracture Mechanics, 1984, Edward Arnold Publishers, ISBN 90 6562 024 9.
24. ASTM E 1737 - 96, Standard Test Method for J - Integral Characterisation of Fracture Toughness.
25. McMeeking, R.M., "*Advances in Fracture Mechanics*", In Fracture Mechanics, Microstructure and Micromechanisms, ASM International, Metals Park, Ohio, pp. 1 - 30, 1989.
26. Fracture Mechanics Worked Examples, Knott, John., and Whitney, Paul., Institute of Materials, 1993, ISBN 0 - 901716 - 28 - 6.
27. British Standards Institution, British Standard 7448, Part 1, 1991, Fracture Mechanics Toughness Tests, Method for determination of K_{IC} , critical CTOD, and critical J values for metallic materials.
28. Abramson, G., Evans, J.T., and Parkins, R.N., "*Investigation of Stress Corrosion Crack Growth Using J - integral Estimations*", Metallurgical Transactions A, Volume 16A, no. 1, pp. 101 - 108, Jan. 1985.

29. Clark W.G., Landes J.D., "An evaluation of Rising Load K_{ISCC} Testing, Stress Corrosion - New Approaches", ASTM STP 610, American Society for Testing and Materials, Philadelphia, 1976, pp. 108 - 127.
30. Krafft, J.M., Sullivan, A.M., Boyle, R.W., Symposium on Crack Propagation, Cranfield, Paper 1, 1961.
31. BS5762, Crack Opening Displacement (COD) Testing, 1979.
32. Barr, R.N., Elliot, D., Terry, P., and Walker, E.F., Metal Construction, p. 604, 1975.
33. Smith, N.F., and Knott, J.F., Practical Application of Fracture Mechanics to Pressure Vessel Technology, Inst. Mech. Engrs, 1971, p. 65.
34. Paris, P.C., Tada, H., Ernst, H., and Zahoor, A., "Treatment Instability", US Nuclear Regularity Commission Report, Nureg 0311, 1977.
35. Rice, J.R., "Mechanics and Mechanisms of Crack Growth", ed., May, M.J., British Steel Corporation, London, 1974, pp 14 – 39.
36. Rice, J.R., and Sorenson, E. P., J. Mech. and Phys. of Solids, Vol. 26, p. 163, 1978.
37. Herman, L., and Rice, J.R., Metal Science, Vol. 14, p. 285, 1980.
38. Parkins, R.N., "Stress Corrosion Spectrum", British Corrosion Journal, Volume 7, pp. 15 - 28, January 1972.
39. Stress Corrosion Cracking - The Slow Strain Rate Technique. ASTM STP 665, eds. Ugiansky, G, M., and Payer, J.H., 1979.
40. Paris, P.C., Tada., H., Zahoor, Z., and Ernst. H., "The Instability of the Tearing Mode of Elastic Plastic Crack Growth", ASTM 668, Elastic Plastic Fracture, pp. 5 - 36, 1979, Eds, Landes, J.D., Begley, J.A., Clarke, G.A.
41. James, L.A., and Porr, W.C., "The Effect of an Elevated Temperature on the J controlled Tearing of a Low Alloy Steel", Int. Journal of Pressure Vessels and Piping", Vol. 76, pp. 769 – 779, 1999.
42. Gibson, G.P., Druce, S.G., "Effect of Water Environments and Loading Rate on Ductile Crack Growth Resistance of an A 508 Class 3 Forging at 288°C", CEGB report, PWR/RCC/MWG/P(85)P569.
43. Druce, S.G., and Belcher, W. P. A., ASTM STP, 803, 1981, Elastic Plastic Fracture Second Symposium, Vol. 2, pp. 739 - 763, ISBN 04 - 803002 - 30.

44. Gabetta, G., Rinaldi, C., and Radaelli, M.M., "*Stress Corrosion Tests in Water Using the Unloading Compliance Technique*", ECF 8, Fracture Behaviour and Design of Materials and Structures, 1990, pp. 1083 - 1089.
45. Alvarez, J.A., "*A Methodology to Determine the SCC Behaviour of Steels in the EPFM regime application and validation*", ECF 11, Mechanisms and Mechanics of Damage and Failure, Vol. 11, p. 1513, Sept. 1996, France.
46. Kawakubo, T., and Hishida, M., "*Elastic Plastic Fracture Mechanics Analysis on Environmentally Accelerated Cracking of Stainless Steel In High Temperature Water*", Journ. Eng. Mater. Technol. (Trans ASME), Vol. 107, no. 3, pp. 240 - 245, July 1985, ISSN 0094 - 4289.
47. Dietzel, W., Daum, K.H., Straider, K., and Kocak. M., "*Fracture Mechanics SCC Testing of Weldments*", Proceedings of the 13th International Conference on Offshore Mechanics and Arctic Engineering, The American Society of Mechanical Engineers, Eds. Salama, M. M., Toyoda, M., Lui, S., Santos, J. F., Kocak, M., Patterson, E.A., and Berge, S., Book No. H00898, 1994.
48. Wagner, D., Moreno, J.C., Prioul, C., Freund, J.M., and Houssin, B., "*Influence of dynamic strain aging on the ductile tearing of C – Mn steels: modelling by a local approach method*", Journal of Nuclear Materials, Vol. 300, 2002, pp. 178 - 191.
49. Hackett, E.M., Moran, P.J., Gudas, J.P., "*Evaluation of Environmentally Assisted Cracking of a High Strength Steel Using Elastic Plastic Fracture Mechanics Techniques*", ASTM 905, Fracture Mechanics, Vol. 17, 1986, pp. 512 - 541.
50. Kim, K.C., Kim, J.T., Sung, U.H., and Kwon, H.K., "*Influences of the Dynamic Strain Aging on the J – R Fracture Characteristics of the Ferritic Steels for Reactor Coolant Piping System*", Internet Dowson Heavy Industries and Construction Co., Ltd., Korea, online, Yahoo, 29/04/03.
51. Schellenberger, R., and Diemel, P., "*J_R curves of the low alloy steel 20 MnMoNi 5 5 with two different sulphur contents in oxygen containing high temperature water at 240°C*", Nuclear Engineering and Design, Vol. 151, (1994), pp. 449 - 461.

52. Atkinson, J.D., and Yu, J., "*The Role of Dynamic Strain Ageing in the Environment Assisted Cracking Observed in Pressure Vessel Steels*", Fatigue and Fract. of Eng. Materials, Volume, 20, no. 1, pp.1 - 12,1997.
53. Atkinson, J.D., Zhao, Z.J., and Yu, J., "*Interactive Effect of Dynamic Strain Ageing with High Temperature Water on the Crack Initiation Behaviour of Reactor Pressure Vessel Steels. Effects of the Environment on the Initiation of Crack Growth*", ASTM STP 1298, pp. 199 - 215, 1997.
54. Hall, E.O., "*The Deformation of Low Carbon Steel in the Blue Brittle Range*", Journal of the Iron and Steel Institute, April 1952, pp. 331 - 336.
55. Baird, J.D., "*The Effect of Strain Ageing due to Interstitial Solutes on the Mechanical Properties of Metals*", Metallurgical Revues, 16, Review 149, Feb. 1971, pp. 1 - 18.
56. Brindley, B.J., and Barnby, T.J., "*The Effect of Nitrogen Content on the Dynamic Strain Ageing in Mild Steel*", Acta Metallurgica, Volume 16, January, 1968, pp. 41 - 44.
57. Blakemore, J.S., and Hall, E.O., "*Blue Brittle Behaviour of Mild Steel*", Journal of the Iron and Steel Institute, August 1966, pp. 817 - 820.
58. Leslie, W.C., The Physical Metallurgy of Steels. McGraw - Hill series, in Materials Science and Engineering, 1982, ISBN. 0070377804.
59. Dingley, D.J., and Mclean, D., "*Components of the Flow Stress of Iron*", Acta Metallurgica, Volume 15, pp. 885, May. 1967.
60. Knott, J.F., "*The Crack Tip Ductility of Structural Steels*", Strength of Metals and Alloys Conf, Melbourne, Australia, 16th - 20th August, p. 799, 1982.
61. Knott, J.F., Jour. of the Iron and Steel Institute, pp. 104 - 111, Feb, 1966.
62. Kim, I.S., and Kang, S.S., "*Dynamic Strain Aging in A 508 Class 3 Pressure Vessel Steel*", International Journal of Pressure Vessel and Piping, Vol. 62, pp. 123 - 129,1995.
63. Yung, Y.H., and Murty, K.Linga., "*The Effect of Interstitial Impurities on the Fracture Characteristics of A533B Class 1 Pressure Vessel Steel. Influence of Radiation on Material Properties*", 13th International Symposium, ASTM 956, Garner, F, A., Henager, C, H, Jnr., and Igata, N., Eds, ASTM, Philadelphia. 1987, pp. 395 - 407.

64. Ostensson, B., "*The Fracture Toughness of Pressure Vessel Steel at Elevated Temperatures*", Proceedings IAEA Conf. on Reliability Problems of Reactor Pressure Vessel Components, Vol. 1, pp. 303 - 315, 1978.
65. Miglin, M.J., Van Der Sluys, W.A., Futato, R.J., Domanian, Henry A., "*Effects of Strain Ageing in the Unloading Compliance J Test*", Elastic Plastic Fracture Test Methods, The Users Experience, ASTM 856, Wessel, E, T., and Loss, F, J., Eds. ASTM. 1985, pp. 150 - 165.
66. James, L.A., and Carlsen, K.W., "*The fatigue crack growth and ductile fracture toughness behaviour of ASTM A387 grade 91 steel*", Journal of Pressure Vessel Technology, 1985, Volume 107, no. 3, pp. 271-278.
67. Kang, S.S., and Kim, I.S., "*Dynamic Strain Aging Effect on the Fracture Toughness of Pressure Vessel Steels*", Nuclear Technology (USA), Volume 97, no. 3, (1992), pp. 139 - 144.
68. Kim, J.W., and Kim, I.S., "*Investigation of Dynamic Strain Aging in SA 106 Group C Piping Steel*", Nuclear Engineering and Design, Vol. 172, (1997), pp. 49 - 59.
69. Chu, W.Y., Wang, Y.B., and Quao, L.J., "*Interaction Between Blue Brittleness and Stress Corrosion Cracking*", Journal of Nuclear Materials, Volume 280, no, 2, pp. 250 - 254, 1st July 2000.
70. Scully, J.C., "*The Mechanical Parameters of Stress Corrosion*", Corrosion Science, 1968, Volume 8, pp. 759 - 769.
71. Long, G.D., The Determination of Mobile Nitrogen and Nitrides in Steel, PhD theses, Sheffield University, 1974.
72. Swinburn, D.G., "*The Separation and Determination of Nitride Phases in Steel*", British Steel Corporation, CDL/CAC/48174.
73. Jenkins, N., and Stevens, S. M. Miss., "*Nitrogen in Ferrous Welding*", The Welding Institute Research Bulletin, January, 1977, pp. 3 - 6.
74. Dijkstra, I.J., Philips, I. J., "*Elastic Relaxations and some other Properties of the Solid Solutions of Carbon and Nitrogen in Iron*", Research Report 2, (5), October 1947, 357, 81.
75. Baird, J.D., "*Strain Ageing of Steel a Critical Review*, reprinted from Iron and Steel ", May/September 1963, parts i, ii, and iii, pp. 1 - 36.

76. Waber, T., and McDonald, H.J., "*Relation of Strain Ageing to the Stress Corrosion Cracking of Mild Steel*", *Welding Journal*, 25, (4), 1946, pp. 223s - 234s.
77. Chu, W.Y., Wang, Y.B., and Quao, L.J., "*Interaction Between Blue Brittleness and Stress Corrosion Cracking*", *The Journal of Nuclear Materials*, Vol. 280, no, 2, pp. 250 - 254, July 2000.
78. Gladman, T., *The Physical Metallurgy of Microalloyed Steels*, Institute of Materials, Book 0792, 2002, (p. 319).
79. Hill, R.E.R., and Abbaschian, R., *Physical Metallurgy Principles*. ISBN. 0-534 - 98236 - 0, 1994.
80. Hoile, S., "*Processing and Properties of Mild Interstitial Free Steels*", *Materials Science and Technology*, Vol. 16, no. 10, pp. 1079 - 1093, 2000.
81. Brindley, B.J., and Barnby, T.J., "*The Effect of Nitrogen Content on Dynamic Strain Ageing in Mild Steel*", *Acta Metallurgica*, Volume 16, January 1968, pp. 41- 44.
82. Brindley, B.J., and Barnby, T.J., "*Dynamic Strain Ageing in Mild Steels*", *Acta Metallurgica*, Volume 14, December, 1966, pp. 1765 - 1780.
83. Crowther, D.N., "*The Effect of Nitrogen on Steel Properties*", Corus Research Design and Technology, Swindon Technology Centre, UK, Conference Nitrogen in Steel, Processing and Product Requirements 27th - 28th September, London, 2000.
84. Taheri, Karimi., Maccango, T.M., and Jonas, J.J., "*Dynamic Strain Ageing and the Wire Drawing of Low Carbon Steel Rods*", *ISIJ, International*, Vol. 35, 1995, no. 12, pp. 1532 - 1540.
85. Wagner, D., Moreno, J.C., and Prioul. C., "*Dynamic Strain Ageing Sensitivity in Heat Affected Zones in C – Mn Steels*", *Journal of Nuclear Materials*, Vol. 252, (1998), pp. 257 - 265.
86. Wagner, D., Prioul, C., and Francois, D., "*Sensitivity to Dynamic Strain Ageing in Carbon Manganese Steels*". *Journal of Alloys and Compounds*, 211/212, (1994), pp. 132 – 135.
87. Headridge, J.D., and Long G.D., "*The Determination of Mobile Nitrogen in Steel using an Ammonium Ion-selective Electrode*", *Analyst*, Vol. 101, 1976, pp. 103 - 110.

88. Jenkins N., and Stevens S.M. Miss., "*The Determination of Nitrogen and Nitrides in Steel*", The Welding Institute Research Bulletin, April 1977.
89. Takizawa, Y., Hata, T., and Endo, Y., *Ageing of Powdered Sample and its Influence on Free Nitrogen Analysis by Constant Temperature Hydrogen Hot Extraction Method*, ISIJ, Vol 70, No. 16, pp. 2301 - 2304
90. Fast, J. D., *Interaction of Metals and Gases volume 2, Kinematics and Mechanisms*, SBN 333075641.
91. Pan, Zhanliang., and Hosbons. R., "*Determination of Interstitial Carbon and Nitrogen In Low Carbon Steels*", Iron and Steel Society, The 39th Mechanical Working and Steel Processing Conference, Indianapolis USA, 19th - 22nd October 1998, Volume XXXV.
92. Baird, J.D., *The Inhomogeneity of Plastic Deformation*, (1973), ASM Metals Park, OH, p. 191.
93. Robinson, J.M., and Shaw, M.P., *Microstructural and Mechanical Influences on Dynamic Strain Ageing Phenomena*. International Materials Reviews, Vol. 39, no. 13, pp. 113 - 122, (1994).
94. Sachdev, Anil. K., "*Dynamic Strain Ageing of Various Steels*", Metallurgical Transactions A, Vol. 13A, 1982, pp. 1793 - 1797.
95. Hong, Sun. Ig., "*Influence of Dynamic Strain Ageing on the Dislocation Substructure in a Uniaxial Tension Test*", Material Science and Engineering, Vol. 79, 1986, pp. 1-7.
96. Aran, A., and Demirkol, M., "*Effect of Heat Treatment on the Bauschinger Effect for a Medium Carbon Steel*", Material Science and Engineering, Vol. 47, 1981, pp. 89 - 92.
97. Brindley, B. J., "*The Effect of Dynamic Strain Ageing on the Ductile Fracture Process In Mild Steel*", Acta Metallurgica, Volume, 8, no. 3, 1970, pp. 325 - 325.
98. McCormick, P.G., "*Theory of Flow Localization Due to Dynamic Strain Ageing*", Acta Metallurgica, Vol. 36, no. 12, 1988, pp. 3061 - 3067.
99. Penrose, J.D., and Brown, A.F., "*Role of Impurity Reaction in Serrated-Yielding Process in Iron*", Journal of the Iron and Steel Institute, 1971, pp. 862 - 868.
100. Pickering, F.B., *Constitution and Properties of Steel*, Material Science and Technology, Vol. 7, 1992.

101. Pickering, F.B., *Physical Metallurgy and the Design of Steel*, Materials Science Series, 1978.
102. Keh, A.S., Nakada, Y., and Leslie, W.C., "*Dynamic Strain Ageing in Iron and Steel*", From Dislocation Dynamics, (McGraw-Hill series in Material Science and Engineering), 1968, Library of Congress Catalogue, no. 68 - 11937, pp. 381 - 408, Eds. Rosenfield, A.R., Hahn G.T.,
103. Meyers, Mark. A., and Chawla, Krishan. K., *Mechanical Behavior of Materials*, 1999.
104. Hulka, K., "*Ultra Low Carbon (Interstitial Free) Sheet Steel for the Automotive Industry*", *Metallurgy and New Materials*, Vol. IV, no. 3, 1996, pp. 101 - 118.
105. Jones, A., and Evans, P.J., *Hardenability – "The Role of Aluminum and Nitrogen in Sheet Steel"*. *Treatment of Metals*, 1993, 4, pp. 99 - 100.
106. Takizawa, Yoshiro., Toshihiko, Hata., and Yoshihide Endo., "*Ageing of Powdered Sample and Its Influence on Free Nitrogen Analysis by Constant Temperature - Hydrogen Hot Extraction Method*", *ISIJ*, 1984, Vol. 70, no.16, pp. 2301 - 2304.
107. Wen, Yiting., Su, Quanmin., and Wutting, Manfred., "*Interstitial Analysis of Ultra Low Carbon and Interstitial Free Steels*", 39th Conference of Mechanical Working and Steel Processing in Indianapolis, ISS, Vol. XXXV, 1998, pp. 271-280.
108. Cottrell, A.H., and Bilby, B.A., "*Dislocation Theory of Yielding and Strain Ageing of Iron*", *Proceedings of the Physical Society, London*, 62A, 1949, pp. 49 - 62.
109. Leslie, W.C., *The Physical Metallurgy of Steels*, (McGraw-Hill series in Material Science and Engineering), 1982, ISBN. 0070377804.
110. Wilson, D.V., and Russell, B., "*The contribution of precipitation to strain ageing in low Carbon steels*", *Acta Metall*, Vol. 8, pp. 468 - 479, 1960.
111. Orowan, E., Discussions in: "*Symposium on Internal Stresses in Metals and Alloys*", Institute of Metals, London, 451, 1947.
112. Keh. A. S., and Leslie, W. C., "*Recent observations on quench-ageing and strain-ageing of Iron and Steel*", *Mater. Sci. Res*, 1, pp. 208 - 250, 1963.

113. Wilson, D.V., and Ogram, G.R., "*Directionality of yield point in strain aged steel*", J. Iron Steel Inst, London, 206, pp. 911 - 920, 1968.
114. Philips, V.A., "*An electron microscopic study of quench ageing and strain ageing in a dilute Fe-C-N alloy*", Trans. Am. Soc. Met, 56, pp. 600 - 617, 1963.
115. Rudee, M.L., and Huggins, R.A., "*Grain boundary segregation and the cold - work peak in Iron containing C or N*", Trans. Metall. Society, AIME, 236, pp. 1662 - 1666, 1966.
116. Leslie, W. C., Bain, Edgar. C., "*Nitrogen in ferritic steels, a critical survey of the literature*", Laboratory, Monroeville Pa, 1959.
117. Harper, S., "*Precipitation of Carbon and Nitrogen in cold-worked alpha-Iron*", Phys Rev, 83, pp. 709 - 712, 1951.
118. Ham, F.S., "*Stress-assisted precipitation on dislocations*", J. Appl. Phys, 30, pp. 915 - 926, 1959.
119. Kamber, K., Keefer, D., and Wert, C., "*Interactions of interstitials with dislocations in Iron*", Acta Metall, Vol. 9, pp. 403 - 414, 1961.
120. Hosson, J. Th. De., and Sleswyk, A. W., "*Atomic configuration of $\frac{1}{2}$ $\langle 111 \rangle$ $\{110\}$ edge dislocations in pure V, W, Mo and Fe, and Fe containing C interstitials*", Phys. Status Solidi, B71, pp. 595 - 607, 1975.
121. Stephenson, E.T., and Conard, G.P., "*Damping near the Snoek peak in Fe*", Acta Metall, Vol. 16, pp. 1253 -1266, 1968.
122. Thomas, W.R., and Leak, G.M., "*The strain ageing of alpha Iron*", J. Iron Steel Inst. London, 180, pp. 155 -161, 1955.
123. Schwier, F., Stahl Eisen, "*Influence of drawing temperature on the mechanical properties of drawn steel*", 79, pp. 1338 -1391, 1959.
124. Rose, K.S.B., and Glover, S.G., "*A study of strain-ageing in austenite*", Acta Metall, Vol. 14, pp. 1505 -1516, 1966.
125. Rosinger, H.E., Craig, G.B., Bratina, W.J., "*The recovery of internal friction in an Iron-Carbon alloy*", Philos. Mag, 6, pp. 1331 -1343, 1972.
126. Rosinger, H.E., "*Snoek rearrangement and long term diffusion during strain ageing in Iron*", Met. Sci. J, 9, pp. 1 - 7, 1975.
127. Humphreys, J.H., Plumtree, A., Bratina, W.J., "*Dislocation-interstitial interactions in an Iron-0.05% C alloy*", Acta Metall, 17, pp. 775 - 781, 1969.

128. Wilson D.V., and Russell, B., "*The Contribution of Atmosphere Locking to the Strain Ageing of Low Alloy Steels*", Acta Metallurgica, Volume 8, January 1960, pp. 36 - 45.
129. Wepner, W., *Measurements of internal friction on slightly strained Iron Carbon alloys*, Acta Metall, 5, pp. 703 - 710, 1957.
130. Butler, R.D., "*The effect of heat-treatment and microstructure on Carbon strain ageing in low Carbon steels*", Trans. Metall. Soc. AIME, 224, 89-96, 1962.
131. Askew, B.A., Wells, T.C., "*Quench-ageing at 240°C in a low Carbon steel after rapid annealing*", J. Iron Steel Inst. London, 205, pp. 869 - 873, 1967.
132. Cottrell, A.H., "*A Note on the Portevin Le Chatelier Effect*", Philosophical Magazine, Volume 44, pp. 829 - 832, (1953).
133. Cottrell, A.H., "*Effect of Solute Atoms on the Behaviour of Dislocations*", Proceedings of the Conference on the Strength of Solids, Bristol, pp. 30 - 38, (1947).
134. McCormick, P.G., "*A Model for the Portevin Le Chatelier Effect in Substitutional Alloys*", Acta Metallurgica, Volume 20, pp. 351 - 354, (1972).
135. Beukel, A, van den., "*Theory of the Effect of Dynamic Strain Ageing on Mechanical Properties*". Physics Status Solidi (A), Volume 30, (1975), pp. 197 - 206.
136. Sleswyk, A.W., "*Slow Strain Hardening of Ingot Iron*", Acta Metallurgica, Volume 6, pp. 598 - 603, (1958).
137. Snoek, J.L., "*On the Decarburisation of Steel and Related Problems*", Physica, Volume 8, pp. 734 - 744, (1941).
138. Mulford R.A., and Kocks, U. H., "*New Observations on the Mechanisms of Dynamic Strain Ageing and of Jerky Flow*", Acta Metallurgica, Volume 27, pp. 1125 - 1134, (1970).
139. Rodriguez, P., "*Serrated Plastic Flow*", Bulletin of Materials Science, Volume 6, no. 4, September 1984, pp. 653 - 663.
140. Morris, J.G., "*Dynamic Strain Ageing in Aluminium Alloys*", Materials Science and Engineering, Volume 13, pp. 101 - 108, 1974.
141. Brindley, B.J., and Worthington, P.J., "*Yield Point Phenomenon in Substitutional Alloys*", Metallurgical Revues, August 1970, Volume 15, no. 145, pp. 101 - 114.

142. Baird, J.D., and Jamieson, A., "*Effects of Manganese and Nitrogen on the Tensile Properties of Iron in the range 20 - 600°C*", Journal of the Iron and Steel Institute, August 1968, pp. 793 - 803
143. Mahmoudi, R., "*Strain Rate Sensitivity of a Wrought Al - 2% Alloy*", Scripta Met et Materialia, Vol. 32, no. 12, pp. 2061 - 2065, (1995).
144. Melander, A., Husby, K.O., "*Influence of the Strain Rate Sensitivity on Diffuse Necking in Tensile Tests*", Materials Science and Engineering, Vol. 46, no.1, pp. 103 - 112. (Nov 1980).
145. Melander, A., "*The Influence of Strain Rate Sensitivity on Ductile Fracture*", Scripta Metall, Vol 14, no 12, pp. 1271 - 1278. (Dec 1980).
146. Wagoner, R.H., Scripta Metall, 15, pp. 1135 - 1137 (1981).
147. Ling, C.P., McCormick, P.G., Acta. Met. Mater, 41, pp. 3127 - 3131 (1993).
148. Klepaczko, J.R., Chein, C.Y., J. Mech. Phys. Solids, 34, 29, (1986).
149. Christodoulou, N., Jonas, J.J., Acta Met, Vol. 32, p. 1655, (1984).
150. Van Den Brink, S.H., Van Den Beukel, A., McCormick, P.G., Phys. Status Solidi (a), 27, p. 469, (1975).
151. Parker, B.A., Pro. 5th ICSMA, Aachen, Germany, p. 899, 1979.
152. Ling, C.P., McCormick, P. G., Acta Metall Mater, 38, p. 2631 (1990).
153. Picu, R.C., Vince, G., Ozturk, F., Gracio, J.J., Barlat, F., Maniatty, A.M., "*Strain Rate Sensitivity of the Commercial Aluminium Alloy AA5182 – 0*", Mat. Sci.Eng. A, 390, pp. 334 - 343, (2005).
154. Soare, M.A., Picu, R.C., "*Multiscale Modeling of the Negative Rate Sensitivity in Solid Solutions A Constitutive Formulation*", Inter. Journal, for Multiscale Computer Eng, Vol. 3, pp. 413 - 435, 2005.
155. Lee, D., "*The Strain Rate Dependent Plastic Flow Behavior of Zirconium and its Alloys*", Met. Trans, Vol. 1, no. 6, pp. 1067 - 1616, June, 1970
156. McCormick, P.G., Acta Metall 36, pp. 3061 - 3067, (1988).
157. Van Den Beukel, A., Physica status solidi (a), 30, p. 197, (1975).
158. Sleeswijk, A.W., Acta Metall, 26, p. 1605, (1978).
159. Van Den Brink, S. H., McCormick, P. G., Scripta Met, 8, p 1251, (1974).
160. Mulford, R.A., Kocks, Acta Metall, 27, p. 1125, (1979).
161. Jackson, P.J., "*Comments on Dislocation Dynamics during Rate Changes*", Scripta Metall, 12, pp. 653 - 654, (1978).

162. Wielke, B., Schoek, G., "Reply to comments on Dislocation Dynamics during Rate Changes", Scripta Metall, 12, pp. 653 - 654, (1978).
163. Frost, N.E., Journal. Mech. Eng, Sci. 2(2), 109, (1960).
164. Liu, H.W., Journal. Basic Eng, (Trans. ASME Series D) 85, 116, (1963).
165. Paris, P.C., and Erdogan, F., Journal. Basic Eng, (Trans. ASME Series D) 85, p. 528, (1963).
166. Clark, W.G., and Wessel, E.T., ASTM STP 463, p. 106, (1970).
167. Reed Hill, Robert, E., and Abbaschian, Reza., Physical Metallurgy Principles (third edition), p. 820, ISBN 0 - 534 - 98236 - 0, 1994.
168. Lindley, T.C., Richards, C.E., and Ritchie, R.O., "The Mechanics and Mechanisms of Fatigue Crack Growth in Metals", CEGB (Central Electricity Generating Board), 1975, Job No. VH267, Paper presented at The Mechanics and Physics of Fracture, Churchill College Cambridge, 6th - 8th January, 1975.
169. Janssen, M., Zuidema, J., Wanhill, R., Fracture Mechanics, second edition, ISBN 0 - 415 - 34622 - 3 - 2002.
170. Zappfe, C.A., and Worden, C.D., Trans Am Soc Metals, 41, 396, 1949.
171. McMinn, A., "Fractographic Analysis in the Understanding of Corrosion Fatigue Mechanisms", Fatigue of Engineering Materials and Structures, Vol 4, no. 3, pp. 235 - 251, 1981.
172. Forsyth, P.J.E., and Ryder, D. A., Metallurgia 63, p. 117, (1963).
173. Laird, C., ASTM STP 415, p. 139, 1967.
174. Neumann, P., Acta Metallurgica et Materialia, Vol. 17, p. 1219, 1969.
175. Pelloux, R.M., Trans. Quart, ASM 62, (1), p. 281, (1969).
176. Laird, C. and Smith, G.C., Phil. Mag, 7, 847, (1962).
177. Ritchie, R.O., and Knott, J.F., Acta Met. 21, p. 639, (1973).
178. Lindley, T.C., and Richards, C.E., Proc. Conf. of Effects of Second Phase Particles on Mech. Props. of Steel, Scarborough, p. 119, (1971).
179. Ritchie, R.O., and Knott, J.F., Mater. Sci. Eng, 14, 7, 1974.
180. Ritchie, R.O., Pickard, A.C., Knott, J.F., Met. Tech, 2, 6, pp. 258, 1975.
181. Forman, R. G., Kierney V. E., Engle, R. M., J. Basic Eng, Trans ASME, 89, p. 459, (1967).
182. Heald, P.T., Lindley, T.C., and Richards, C.E., Mater. Science. Eng, 10, p. 235, (1972).

183. Ramsamooj, D.V., Shugar, T.A., International Journal of Fatigue, 23, (2001), pp. S287 - S300. (on pp. S291 cites Paris et al ref 18 from ASTM, STP 513, 1971, pp. 141 - 176).
184. Hertzberg, R.W., Deformation and Fracture of Engineering Materials, Fourth Edition, ISBN 0-471-01214-9, cited Suresh, S., Zamiski, G.F., Ritchie, R. O., Met. Trans. 12A, pp. 1435, (1981), ref. 62, p. 624.
References cited by Hertzberg pp. 691 refs 179 - 183 in Chapter 13 (Fatigue Crack Propagation).
Tomkins, B., Philos. Mag, 18, p. 1041, (1968).
Hickerson, J.P. Jnr., and Hertzberg, R. W., Met Trans. 3, p. 179, 1972.
Majumdar, S., and Morrow, J. D., ASTM STP 559, 1974, p. 159.
Antolovich, S.D., Saxena, A., Chanani, G.R., Eng. Fract. Mech 7, p 649, 1975.
Saxena, A.and Antolovich, Met. Trans. 6A, p. 1809, (1975).
185. Elber, W., ASTM STP, 486, pp. 230 - 247, 1971.
186. Heald, P.T., Mats. Sci. Eng, 35, (1978), pp. 165 - 169.
187. Roselmeir, F.O., Pippon., R., Fatigue and Fracture of Engineering Structures and Materials, Vol. 21, pp. 1425 - 1433, 1998.
188. Roselmeir, F.O., Pippon., Fatigue and Fracture of Engineering Structures and Materials, Vol. 20, no. 11, pp. 1529 - 1540, 1997.
189. Bachman, V., Munz, D., Eng. Fract. Mech, 11, pp. 61 - 71, (1979).
190. Ritchie, R.O., Proc. Int. Conf, Analytical and Experimental Fracture Mechanics, Rome, 1980, p. 81.
191. Romaniv, O.N., Tkach, A.N., and Lenets, Y.N., Fract. Eng. Mater. Struct, 10, (1987), p. 203.
192. Ritchie, R.O., Proc. Conf. Fatigue, Charlottesville VA, 1987, EMAS.
193. Austen, I. M., Jutla, T., Shutter, D.M., and Tubby, P.J., "A Review of Fatigue crack Growth Characterisation by Linear Elastic Fracture Mechanics", Part 3, Corrosion Fatigue, November, 1988.
194. Griffiths, J.R., and Richards, C.E., Mater. Sci. Eng, 11, p. 305, 1973
195. Ritchie, R.O. and Knott, J.F., Proc. B.S.C. Conf. on the *Mechanics and Mechanisms of Crack Growth*, Cambridge, April. 1973.
196. Reed Hill, R., Abbaschian, R., Physical Metallurgy Principles, Third Edition, ISBN 0 - 534 - 98236 - 0, PWS, Publishing Company.

197. Duquette, D.J., Corrosion Fatigue, Chemistry, Mechanisms and Microstructure, Houston 1982, NACE, 32.
198. Metals Handbook 8th Edition Volume 10, Fatigue Analysis and Prevention, ASM, Ohio, 1975, p. 2.
199. Atkinson, J.D., Yu, J., and Chen, Z.Y., "*An Analysis of the Effects of Sulphur Content and Potential on Corrosion Fatigue Crack Growth in Reactor Pressure Vessel Steels*", Corrosion Science, Volume 38, no. 5, pp. 755 - 765, 1996.
200. Atkinson, J.D., Yu, J., Chen, Z.Y., Zhao, Z.J., "*Modelling of Corrosion Fatigue Crack Growth Plateaux for Reactor Pressure Vessel Steels in High Temperature Water*", Nuclear Eng and Design, 184, pp. 13 - 25, 1998.
201. James, L.A., Moshier, W.C., "*The Effect of Potential upon the High Temperature Fatigue Crack Growth Response of Low Alloy Steels, Part 1: Crack Growth Results*", Corrosion Science, 41, pp. 373 - 399, 1999.
202. Atkinson, J.D., and Forrest, J.E., Corrosion Science, 25, p. 607, 1985.
203. Atkinson, J.D., and Lindley, T.C., "*Effect of Stress Waveform and Hold Time on Environmentally Assisted Crack Propagation in C-Mn Structural Steel*", Metal Science, pp. 444 - 448, July 1979.
204. Katada, Yasayuki., Nagata, Norio., and Sato, Shunji., "*The Effect of Temperature on Fatigue Crack Growth Behaviour of a Low Alloy Pressure Vessel Steel in a Simulated BWR environment*", Corrosion Science, Vol. 25, nos. 8 - 9 , pp. 693 - 704, 1985.
205. Hanninen, H., Torronen, K., Kempainen, M., and Salonen, S., "*On the Mechanisms of Environment Sensitive Cyclic Crack Growth of Nuclear Reactor Pressure Vessel Steels*", Corrosion Science, Vol. 23, no. 6, pp. 663 - 679, 1983.
206. Lidbury, D.P.G., "*The Estimation of Crack Tip Strain Rate Parameters Charactering Environment Assisted Crack Growth*", pp. 149, Embrittlement by the Localised Crack Environment, ISBN 0 - 89520 - 480 - 0, 1985 .
207. Congleton, J., "*Corrosion Fatigue*", in Corrosion Processes, edited by Parkins, R. N., ISBN 0-85334-147-8, , pp. 209 - 271, 1982.

208. Marini, B., Mudry, F., and Pineau, A., "*Ductile Rupture of A 508 Steel under Non - Radial Loading*", Engineering Fracture Mechanics, Volume 22, No 3, pp. 375 - 386, 1985.
209. James, L.A., Moshier, W.C., *The Effect of Potential upon the High Temperature Fatigue Crack Growth Response of Low Alloy Steels. Part 2: Sulphide Potential Interaction*", Corrosion Science, 41, pp. 401 - 415, 1999.
210. Arai, Taku., Mayuzumi, Masami., Ohta, Joji., "*SCC Maps for Low Alloy Steels by SSRT Method*", Corrosion 98, Paper 140, NACE International.
211. Beremin, F.M., *Cavity "Formation from Inclusions in Ductile Fracture of A 508 Steel"*, Met. Trans. A, Vol. 12A, May 1981, pp. 723 - 731.
212. Shih, C.F., "*Relationships between the J Integral and the Crack Opening Displacement for Stationary and Extending Cracks*", Journal of the Mechanics and Physics of Solids, Vol 29, no. 4, pp. 305 - 326, August 1981.
213. Rice, J.R., "*The Elastic Plastic Mechanics of Crack Extension*". Inter. Journal of Fracture, March 1968, Vol. 4, no. 1, pp. 41 - 49.
214. Elastic Plastic Fracture, ASTM STP 668, STM Philadelphia, PA 1979. Edited by Landes, J.D., Begley, J.A., and Clarke, G.A., Article by I.Milne, Curry D.A., and Chell, G.G., p. 586.
215. Srinivas, M., and Kamat, S.V., "*Effect of Strain Rate on the Fracture Toughness of Mild Steel*", Materials Science and Technology, (UK), Volume 17, no. 5, pp. 529 - 535, May. 2001.
216. Ritchie, R.O., and Thompson, A.W., "*On Macroscopic and Microscopic Analysis for Crack Initiation and Crack Growth Toughness in Ductile Alloys*", Metallurgical Transactions A, 16 A, p. 233, (1985).
217. Knott, J.F., Bowen, P., Druce, S.G., "*Micro - mechanical Modelling of Fracture Toughness*", Acta Metallurgica, Volume 35, no 7, pp. 1735 - 1746, 1987.
218. "*The Micro - mechanisms of Fracture in Steels Used for High Integrity Structural Components*", Fracture Plastic Flow and Structural Integrity, The Proceedings of the 7th Symposium organised by the Technical Advisory Group on Structural Integrity in Nuclear Plant (TAGSI), held at TWI, Abingdon UK, 29th April 1999, Eds Hirsch, P., and Lidbury, D., pp. 21 - 45.

219. Mintz, B., Cochrane, R.C., and Baird., J.D., *Some Effects of Nitrogen on the Impact Properties of Ferrite/Pearlite Steels*, Scandinavian Journal of Metallurgy, 1, (1972), pp. 279 - 283.
220. Gladman T. *The Physical Metallurgy of Microalloyed Steels*, Book 0792, Published by the Institute of Materials, 2002, (p.70).
221. Bucher, J. H., Grozier, J.D., & Enrietto, J.F., "*Strength and toughness of hot-rolled ferrite-pearlite steels*", Fracture 6, (1968), pp. 244 - 297.
222. Mintz, B., "*The Influence of Si and N on the Impact Properties of As-Rolled Mild and C- Mn Steels*", JISI, Vol. 211, pp.151 - 154, Feb. 1973.
223. Wallin, K., "*Low - Cost J - R curve estimation based on CVN upper shelf energy*", Fatigue and Fract Eng. Mater and Struct, pp. 537 - 549, 2001.
224. Knott, J.F., "*The Science and Engineering of Fracture*", 8th International Conference on Fracture, ICF8, Resistance and Structural Integrity. Kyiv, Ukraine, 8th - 14th , 1993.
225. Griffith, A.A., "*The Phenomenon of Rupture and Flow in Solids*", Philosophical Transactions of the Royal Society of London, A221, 163, (1920).
226. Ljokl, M., Vitek, V., McMahon C.J. Jnr., "*A Microscopic Theory of Brittle Fracture on Deformable Solids. A Relation between ideal work to Fracture and Plastic Work*", Acta Metallurgica, Volume 28, no.11, pp. 1479 - 1488, Nov. 1980.
227. Siegmund, T., Brocks, W., "*A Numerical Study on the Correlation between the work of Separation and the Dissipation Rate in Ductile Fracture*", Engineering Fracture Mechanics, 67, (2000), pp. 139 -154.
228. Gladman, T., and Mclvor, I.D., "*The Distribution of Interstitials in Carbon Manganese and Grain Refined Steels*", Scandinavian Journal of Metallurgy, 1, (1972), pp. 247 - 253.
229. Pickering. F.B., Gladman. T., "*Metallurgical Developments in Carbon Steels*", Iron and Steel Institute, Special Report, No. 81,1963, p. 10.
230. Brashaw, C., C. Brashaw Technical Services, Sheffield.
231. Johnson, H.H., "*Calibrating the Electric Potential Method for Studying Slow Crack Growth*", Materials Research & Standards, pp. 442 - 445, September. 1965.

- 232.** Standard Test Method for Measurement of Fracture Toughness, ASTM Standard F 1820, Annual Book of ASTM Standards, 3.01, (1999).
- 233.** Dautovich, D.P., and Floreen, S., "*The Stress Corrosion and Hydrogen Embrittlement Behaviour of Maraging Steels*", Conference - Stress Corrosion Cracking and Hydrogen Embrittlement of Iron Base Alloys, Unieux-Firminy, France, 12th - 16th, June. 1973, pp. 3:78 - 3:91.
- 234.** Hackett, E.M., Moran, P.J., and Gudas, J.P., "*Evaluation of Environmentally Assisted Cracking of a High Strength Steel Using Elastic Plastic Fracture Mechanics Techniques*", Fracture Mechanics, 17th Volume, ASTM STP 905, National Symposium on Fracture Mechanics, pp. 512 - 541, ISBN -0-8031-0412-3.
- 235.** Hackett, E.M., Joyce, J.A., "*Dynamic J - R Curve Testing of a High Strength Steel Using the Key Curve and Multispecimen Techniques*". Fracture Mechanics 17th Volume, ASTM STP 905, National Symposium on Fracture Mechanics, pp. 741 - 774, ISBN -0-8031-0412-3.
- 236.** Sutton, G.E., Vassilaros, M.G., "*Influence on Partial Unloadings Range on the J_i Curves of ASTM A106 and 3 - Ni Steels*", Fracture Mechanics 17th Volume, ASTM STP 905, National Symposium on Fracture Mechanics, pp. 368 - 378, ISBN -0-8031-0412-3.
- 237.** Franklin, A.G., "*Comparison between a Quantitative Microscope and Chemical Methods for Assessment of non - Metallic Inclusions*", JISI, Feb 1969, pp. 181 - 186.
- 238.** Bulloch, J.H., and Atkinson, J.D., "*An Assessment of the Influence Of Sulphide Distribution in the Promotion of Environmentally Assisted Crack Growth in Ferritic Pressure Vessel Steels*", Paper presented at the 18th MPA Seminar, Stuttgart, October 8th and 9th 1992, pp. 29.1 - 29.17.
- 239.** Burns, K.W., and Pickering, F.B., "*Deformation and Fracture of Ferrite-Pearlite Structures*", J. Iron and Steel Inst, Nov, (1964), pp. 899 - 906.
- 240.** Test Methods for Determining Average Grain Size, ASTM Standard E1 12, Annual Book of ASTM Standards, 3.01, (1999).
- 241.** Grange, R.A., "*Effects of Microstructural Banding in Steel*", Metallurgical Trans. 2, Feb. (1971), pp. 417 - 426.

242. Shanmugam, P., Pathak, S.D., "Some Studies on the Impact Behavior of Banded Microalloyed Steel", Engineering Fracture Mechanics, 53, 6, (1996), pp. 991 - 1005.
243. Voss, B., and Mayville, R.A., "The Use of the Partial Unloading Compliance Method for the Determination of J_I - R Curves and J_{1C} ", Elastic - Plastic Fracture Test Methods, ASTM 856, ISBN 0803104197.
244. Rippstein, K., and Kaesche, H., "The Stress Corrosion Cracking of Reactor Pressure Vessel Steel in High Temperature Water at High Flow Rates", Corrosion Science, Vol. 29, no. 5, pp. 517 - 534, 1989.
245. Tseng, C.M., Liou, H.Y., and Tsai, W.T. "The influence of nitrogen content on corrosion fatigue crack growth behaviour of duplex stainless steel", Materials Science and Engineering, A 344, (2003), pp. 190 - 200.
246. Darken, L.S., and Curry, R.W., Physical Chemistry of Metals. Mc Graw Hill 1953. cites the work of (1). Tschischewski, N., Journal of the Iron and Steel Institute, 92, 47, (1915), (2). Work and Enzian, Trans. AIME, 162, 723, 1945.
247. Abe, M., and Ushioda, K., "Effect of Carbon on Mechanical Properties in Mild Steel Sheets", Scand. Journal of Metallurgy, 13, pp. 276 - 282, 1972.
248. Atkinson., J.D., Professor, private communication.
249. Franklin, A.G., "Effect of desulphurisation on the impact properties of some low - alloy steels", Journal of the Iron and Steel Institute, pp. 588 - 592 July 1964.
250. Hertzberg, R.W., Deformation and Fracture of Engineering Materials, Fourth Edition ISBN 0-471-01214-9 cites Hodge, J.M., Frazier, R, H., and Boulger, F.W., Trans. AIME 215, 745, 1959, (ref 20 p.475).
251. Mintz, B., and Arrowsmith, M., Hot working and forming processes, pp. 99 - 103, 1980, London, The Metals Society.
252. Morrison, W. B., Ironmaking and Steelmaking, 1989, Vol. 16, no. 2, pp. 123 - 128, cites Thewlis, G., in Proceedings of the Conference, Pipeline Technology, Rome, Nov 1987, Associazione Italiana di Metallurgia.
253. Knott, J.F., and Green, G., "The Initiation and Propagation of Ductile Fracture in Low Strength Steels", Journal of Engineering Materials and Technology, January 1976, pp. 37 - 46.

254. Crussard, C., JISI, 1956,183, pp. 146 - 177.
255. Gladman, T., Holmes, B., McIvor, I.D., "*Effect of Second Phase Particles on the Mechanical Properties of Steels*", The Iron and Steel Institute, London, 1971, pp. 68.
256. Gladman, T., Dulieu, D., and Mc Ivor, I., "*Structure Property Relationships in High Strength Microalloyed Steels*", Microalloying 75, pp. 32 - 55, 1975.
257. Atkinson, J.D., Corrigan, M.R., and Higgins, A.D., I.C.G.E.A.C. Meeting, Antwerp, April 2005.
258. Yadav, R.R., MSc project, Sheffield Hallam University, 2002.
259. Knott, J.F., "The Fracture Toughness of Metals", A General Introduction to Fracture Mechanics, ISBN 0852983832, I.Mech.E, 1978.
260. Hertzberg, R.W., Deformation and Fracture of Engineering Materials, Fourth Edition ISBN 0 - 471 - 01214 - 9. cited. Ritchie, R, O., and Thompson, A, W., Met. Trans, 16A, 233, 1985, (ref 153, p.479).
261. Higgins, R.A., Properties of Engineering Materials, ISBN 0 340 60033 0, 1994.
262. Honeycombe, R.W.K., and Bhadeshia, K.D.H., Steels Microstructure and Properties, Second Edition, 2000, ISBN 0 340 58946 9.
263. Callister, W.D., Materials Science and Engineering an Introduction (Fourth Edition), ISBN 0 – 471 -13459 -7, 1997.
264. Diemel, P., and Sattler, E., "*Non metallic inclusions and their relation to the $J - \text{integral}$, $J_{i \text{ phys}}$ at physical crack initiation for different steels and weld metals*", Journal of Materials Science, 33, (1998), pp. 1723 - 1736.
265. Pickles, B. W., Ingham, T., Lidbury, D. P. G., "*Fracture Toughness Studies on PWR Pressure Vessel Materials*", PWR Research Co - ordination Committee Materials Working Group, PWR/RCC/MWG/P(83) 287 ND - R -1009
266. Chipperfield, C.G., Phd thesis, Cambridge University 1973, cited ref 253.
267. Huang, J.Y., Yeh, J.J., Kuo., R.C., and Hwang. J.R., "*Effect of dynamic strain aging on fatigue crack growth behaviour of reactor pressure vessel steels*", Materials Science and Technology, vol 22, pp. 944 - 954, 2006.
268. Haasen, P., Physical Metallurgy, Third Enlarged and revised edition, 1996, pp. 30, Cambridge University Press, ISBN 0 521 55092 0.
269. Atkinson, J.D., Phd thesis, Cambridge University 1973.

270. Fischer, J., *Acta Metallurgica*, 3, 1955, p. 109.
271. Atkinson, J.D., Corrigan, M.R., Higgins, A.D., "*The Interaction of Environmentally Assisted Cracking and Dynamic Strain Ageing in C – Mn piping steels*", *13th International Conference on Environmental Degradation of Materials in Nuclear Power systems*, Canadian Nuclear Society, 19th to 23rd August 2007, Whistler, British Columbia, Canada.
272. Wagner, D., Roubier, N., and Prioul, C., "*Measurement of sensitivity to dynamic strain aging in C – Mn steels by internal friction experiments*", *Materials Science and Technology*, Volume 22, number 3, pp. 301 - 307, 2006.
273. Barsom, J.M., Imhof, E. J., and Rolfe, S.T., "*Fatigue Crack Propagation in High Strength Steels*", *Engineering Fracture Mechanics*, Vol. 2, pp. 301 - 317 (1971).
274. Barsom, J. M., "*Fatigue Crack Growth Under Variable Amplitude Loading in Various Bridge Steels*", *Fatigue Crack Growth Under Spectrum Loads*, ASTM , pp. 217 - 235, (1976), Philadelphia.
275. West, J.M., "*Chemical Potential and Surface Energy in Stress Corrosion Cracking*", *Metal Science*, Vol. 14, no. 11, pp. 534 - 540, Nov. 1980.
276. Keeler, S., "*The Science of Forming*", *Metal Forming*, January, 2006
277. Soare, M.A., Picu, R.C., "*A New Mechanism for Dynamic Strain Ageing*", [online] last accessed 9/11/2005.
<http://www.scorec.rpi.edu/nanomechanics/projects/project1/results1.htm>.
278. Wagner, D., Prioul, and Francois, D., "*Influence of the Microstructure on Strain Aging of C – Mn Steels*", *Reliability and Structural Integrity of Advanced Materials*, *Proceedings of the 9th Biennial European Conference on Fracture*, Varna, Bulgaria, 21st - 25th September, 1992, Vol. 2.

Appendix 1.

The J Integral as a Fracture Parameter.

The plot of the J vs Δa curve can be assessed in two separate stages.

- (i). The region prior to crack initiation, normally termed blunting.
- (ii). The region where cracking commences normally termed growth.

With the application of load in a precracked elastic – plastic material, a discrete crack opening is produced. The initiation of crack growth is then dependent on some critical crack displacement. This is the basis of δ_{tip} measurement in the COD approach to fracture.

A schematic drawing of the process is shown in Figure 1. The crack extension in the blunting region is a minor lengthening of the crack due to plastic flow at the crack tip.

J_{IC} is defined at the intersection of the crack blunting line and the line which defines the J - Δa curve.

Crack tip blunting is described by:

$$J = 2\sigma_o \Delta a$$

This construction is necessary because it is quite difficult to define this parameter with physical detection to a high degree of consistency.

This is the basis on which such standards as ASTM 1737 are based on (first proposed by Begley and Landes [1] based on the J Integral conceptualised by Rice [2]). The accuracy of determining J_{IC} is dependent upon the slope of the blunting line chosen. The problem of accurate choice of the blunting line is accentuated in the case of ductile and tough materials for which the crack growth due to physical tearing may be virtually indistinguishable from the extensive crack tip blunting.

An alternative procedure for the determination of J_{IC} was is in terms of the **Stretch Zone Width** (SZW), of Kobayashi et al [3], (recommended by the JSME, Japan Society of Mechanical Engineers, Standard S001-1981). This

is suited for highly ductile materials.

In this method, the length of the featureless zone that appears during blunting, between the end of the fatigue pre - crack and stable crack growth is observed microscopically. This value initially increases with the load line displacement but saturates once the SZW reaches a critical value (SZW_C).

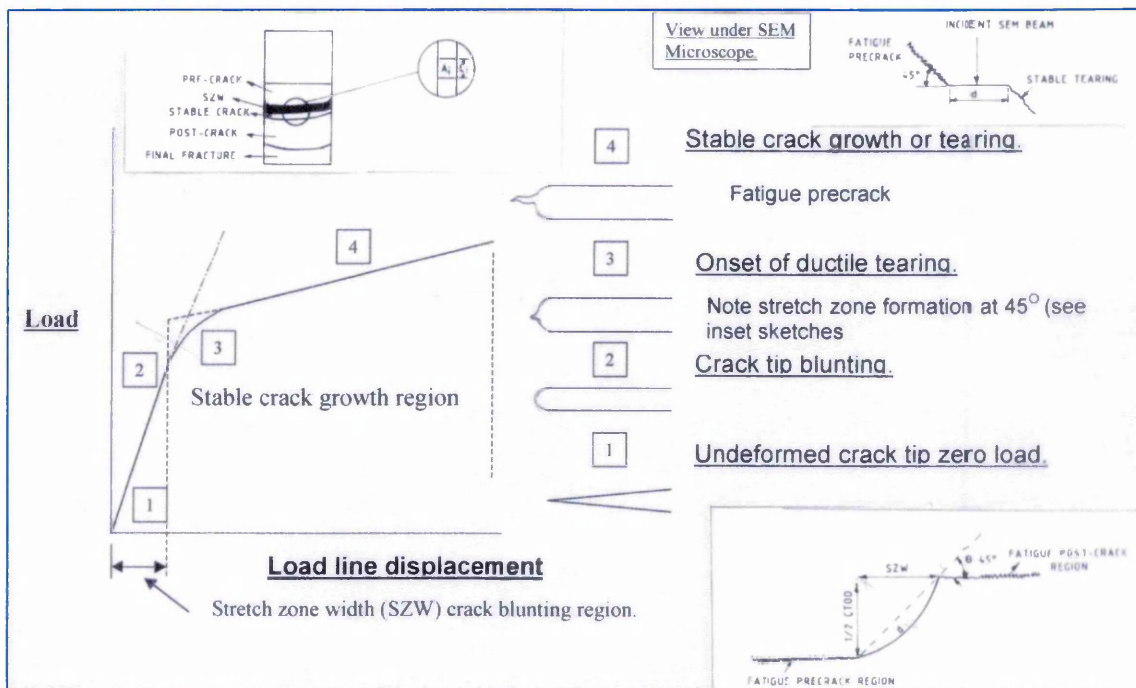
The J_{IC} is the determined using the following equation:

$$J_{IC} = m \cdot \sigma \cdot (2 SZW_C)$$

where CTOD is the crack tip opening displacement, m = the slope of the blunting line generally taken as 2 for ductile materials, σ = the average of the yield and UTS strength, and $SZW = 1/2 CTOD$.

Figure 1 is a schematic drawing showing the crack tip blunting due to stable crack extension process.

Figure 1.



References.

1. Begley, J.A., Clark, G.A., and Landes, J.D., JTEVA, Vol 8, No. 5, Sept, 1980.
2. Rice, J.R., Journal of Applied Mechanics, Vol. 35, pp. 379 – 386, 1968.
3. Kobayashi, H., Hirano, K., Nakamura, H., and Nakazarwa, H., “Advances in Fracture Research on the Strength and Fracture of Materials,” Proceedings of the 4th International Conference on Fracture (ICF4), Vol. 3, 1977, pp. 583 – 592.

APPENDIX 2.

Monitoring of Crack Growth during Mechanical Tests:

The Unloading Compliance (UC) Technique.

The Unloading Compliance (UC), or Partial Unloading Compliance (PLC) technique, is one of the single-specimen methods used in mechanical testing (mainly elastic - plastic fracture mechanics testing) for monitoring the propagation of a crack under a load monotonically applied.

In this technique, the specimen is partially unloaded and then reloaded at specified intervals during the test. The unloading slopes, which tend to be linear and independent of prior plastic deformation, are used to estimate the crack length at each unloading based on analytical elastic compliance relationships which depend on the specimen configuration and on the position where load-line displacement is measured.

As in the case of the Potential Drop (PD) technique, UC is ideally suited to computer control and subsequent analysis of test data; tests should be controlled using the transducer (clip on gauge) monitoring either mouth opening or load point displacement.

Single-specimen methods, in fracture mechanics testing, are normally considered as an alternative to the Multiple Specimen technique, which gives an average of the crack resistance behavior and of the crack initiation parameters. The single - specimen methods, on the other hand, provide individual results that can offer additional information on material inhomogeneity.

Several test procedures have been written for the UC technique none of which has really become universally accepted although the ASTM procedure is certainly the most widely used. What follows is indeed based on this version of the methodology.

In an UC test, the elastic compliance C_k is determined at each unloading reloading sequence performed during the test from.

$$C_k = \left(\frac{\Delta Q}{\Delta F} \right)_k$$

where Q is the appropriate displacement or strain, ΔF is the applied force kN.

The crack length a_k at each unloading is determined from the measured compliance C^* using theoretical or experimental correlations in the form:

$$\left(\frac{a}{W} \right)_k = f(C_k)$$

Relationships to be used for common toughness specimen geometries (Compact Tension, Single Edge Notch Bend etc) are given in the applicable standards.

Data recording and evaluation of the partial unloading may be accomplished autographically with an x-y recorder or, preferably, automatically with a computer.

Compliance is measured from either specimen mouth opening or load-point displacement; if the displacement is measured at an alternative point, then the appropriate compliance function must be evaluated.

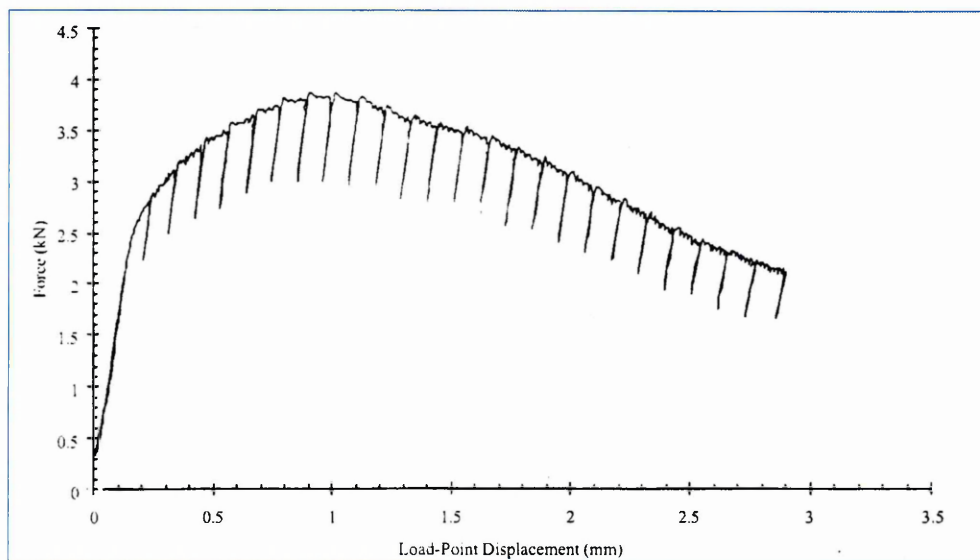
Errors may occur in the compliance measurements as a result of transducer non-linearity. Significant improvement in accuracy is possible by curve fitting the lowest-order polynomial function through the calibration data .

Before commencing the test, it is recommended that the specimen be cycled several times in the elastic regime at test temperature to allow the specimen to "bed-in".

The loading rate during unload - reload cycles should fast enough to minimise time-dependent effects, but also slow enough to ensure that sufficient data is recorded to enable the compliance to be estimated accurately. During the test. unloadings should be performed at displacement intervals selected to ensure evenly spaced data points are obtained: typically 25 to 30 unloadings are sufficient to define the crack growth fracture behaviour.

An example of a typical test diagram for an elastic-plastic fracture mechanics test performed with the UC technique is given in Figure 1.

Figure 1. Load point displacement versus applied force.



Resolution:

The resolution of the UC in predicting crack lengths is typically of the order of 0.1 mm, depending on the accuracy of the transducer used for load-point displacement measurements.

Limitations:

The use of the UC is limited from the two following points of view:

Temperature:

The maximum operating temperature for commercially available clip-on-gages is around 300° C; above such temperature, therefore, the use of this technique is not recommended (remote displacement measurements, in fact, do not provide sufficient accuracy to enable reliable compliance, and therefore crack length, evaluations);

Specimen dimensions:

If the sample size is too small to physically allow the application of a clip-on-gage for load-point displacement measurements (as in some miniaturised specimen techniques), the UC cannot be applied for the reasons already stated in the above paragraph.

Special features:

The UC method is mostly used in the field of elastic-plastic (ductile) fracture mechanics testing for the determination of crack initiation parameters and crack resistance (J - R) curves: however, if appropriate provisions are made for the integrity of the displacement transducer under high-frequency (≈ 20 Hz) cyclic loading, the UC technique can also be used for monitoring crack propagation in high cycle fatigue crack growth rate tests da/dN vs ΔK .

Alternate techniques:

For crack length measurements during a mechanical test, different techniques have been applied and can be found in the literature (acoustic emission, X - rays, ultrasonics etc); however only the Potential Drop (PD) technique, elsewhere described in this thesis is a well-established and feasible alternative to the UC method.

Appendix 3. Loading rates, and specimen type, and authors for Fig 14.

Loading rates, and strain rates, material composition, etc for various papers																					
Steel Heat	Author	Specimen Type	Parameter used	Element										Loading Rates Used T, P, B & Tensiles mm/min	Loading Rates Used CTS J tests mm/min	Strain Rates sec ⁻¹ used Tensiles	Temp for max Anp for tensiles & strain rate or loading rate	Temp Range °C T = Tensiles J = fracture specimen	Loading rate or strain rate req for temp around 200C for Jmin	Environment	load line placement where applicable mm
				C	Si	Mn	P	S	Cr	Mo	Ni	Al	Cu								
VS3763A VS3763B VS3764A VS3764A VS3763A VS3763B	Wagner et al 1	T	UTS RA Z	0.21 0.2 0.22 0.21 0.21 0.21	0.2 0.2 0.2 0.2 0.19 0.19	0.7 0.69 0.7 0.7 0.72 0.71	-0.005 -0.005 -0.005 -0.005 0.002 0.002	0.002 0.024 0.002 0.027 0.002 0.002	0.2 0.2 0.2 0.2 0.2 0.2	0.005 0.005 0.005 0.005 0.005 0.005	<0.20 <0.20 <0.20 <0.20 <0.20 <0.20	<0.005 <0.005 <0.005 <0.005 <0.005 <0.005	0.009 0.007 0.005 0.005 0.008 0.007	0.0083	0.0049	2.00E-04	200 1-275 2-250 3-250	20-300	n/a	air	n/a
Wagner et al 1	T	UTS RA Z	0.046 0.14 0.168	0.356 0.235 0.207	0.725 0.986 0.789	0.016 0.016 0.0104	0.011 0.007 0.012	0.011 0.027 0.093	0.011 0.027 0.093	0.004 0.002 0.023	0.01 0.024 0.136	0.003 0.002 0.004	0.0093 0.0082 0.0093	0.0083	0.0036	2.00E-04	20-300	20-300	na	air	na
Jung & Murty	T, P, B Tensiles Charpy	J TPB	J TPB	0.25 0.19	0.24 0.22	1.38 1.45	0.01 0.007	0.017 0.007	na 0.12	0.49 0.5	0.61 0.64	0.025 0.16	0.13 0.11	0.093	2.5 x 10 ⁻⁴ to 5x10 ⁻³ mm/sec	0.006-5.0 mm/min (8.3 x 10 ⁻³) (8.3 x 10 ⁻³) (8.3 x 10 ⁻³)	2.5 x 10 ⁻⁴ to 1.9 x 10 ⁻³ Tensiles	20-427 (283-700K)	2.5 x 10 ⁻⁴ mm/s attained min J at 200C	air	All TPB 2
Druce s/h pd	CT Multi Specimen	J	J	0.22	0.24	1.37	0.005	0.003	0.11	0.49	0.72	0.03	0.06	na	0.006-5.0 mm/min (8.3 x 10 ⁻³) (8.3 x 10 ⁻³) (8.3 x 10 ⁻³)	5x10 ⁻⁴ to 5x10 ⁻³	20-350	KJc min at 6x10 ⁻⁴ mm/min 200 (8.3x10 ⁻³) PWV 6K10 ⁻⁴ PWV 100 ppb DO 5x10 ⁻²	air & water varying SO ₂ S & DOW	na	
James & Poir s/h	T&CT Multi Specimen	J	J	0.2	0.22	0.66	0.018	0.01	0.34	0.61	0.75	na	na	na	2.5 x 10 ⁻⁴ to 1.5 x 10 ⁻⁴ mm/sec	3.3 x 10 ⁻⁴ to 2 x 10 ⁻⁴	243	not specified suggested 204 quoted other references around 200	air & water	na	
Miglen et al s/h	Heat 645 CT & T Heat 649 Unloading compliance	J	J	0.29 0.29	0.23 0.18	0.72 0.76	0.009 0.008	0.015 0.023	na na	na na	<0.005 <0.005	na na	na na	0.004 0.003	0.13 (846) 0.13 (849) (2.18x10 ⁻³) (2.18x10 ⁻³)	0.13 (846) 0.13 (849) (2.18x10 ⁻³) (2.18x10 ⁻³)	T 20-316 J 20-204	not specified suggested 204 quoted other references around 200	air	na	
Arora & Pripolu s/h	T&CT Unloading compliance	J	J	0.161 0.187	0.225 0.215	1.33 1.39	0.01 0.01	0.036 0.053	0.23 0.07	0.465 0.56	0.72 0.635	na na	na na	<5ppm <5ppm	8x10 ⁻³ to 1.3x10 ⁻² mm/min (1.3x10 ⁻²)	5x10 ⁻⁴	250	100-450	air	na	
Yoon et al s/h	T&CT	J	J	0.222	0.31	1.14	0.005	0.002	0.149	0.043	0.207	0.02	0.102	0.009	0.3-1000 mm/min (5x10 ⁻³) (16.67mm/s)	2.5 x 10 ⁻⁵ to 1 x 10 ⁻⁶	n/a	T 100-316 J 20-500	Jmin for 0.3mm/min (5x10 ⁻³) Jmin 260 0.6 mm/min (8.3x10 ⁻³) Jmin 225 0.4 mm/min (6.8x10 ⁻³) Jmin 225 0.4 mm/min (6.8x10 ⁻³)	air	na
Kim & Kang pd	T&CT	J	J	0.16	0.03	1.48	0.04	0.003	0.21	0.054	0.91	0.003	0.045	na	0.6-3 mm/min (8.3x10 ⁻³) (5x10 ⁻³)	8.25x10 ⁻⁵ to 1.25x10 ⁻³ mm/min (5x10 ⁻³)	2.08x10 ⁻⁴ at 280 810 Mpa	T20-280 J20-380	Jmin 260 0.6 mm/min (8.3x10 ⁻³) Jmin 225 0.4 mm/min (6.8x10 ⁻³) Jmin 225 0.4 mm/min (6.8x10 ⁻³)	air	na
Kim & Kim pd	T&CT	J	J	0.19	0.27	1.22	0.009	0.007	0.05	0.03	0.11	0.029	0.13	1.6ppm	0.4-4 mm/min (6.8x10 ⁻³) (5x10 ⁻³)	1.39x10 ⁻⁴ to 1.39x10 ⁻⁴ at 300 6.95x10 ⁻² 562 Mpa	1.39x10 ⁻⁴ at 300 6.95x10 ⁻² 562 Mpa	T20-400 J20-350	Jmin 225 0.4 mm/min (6.8x10 ⁻³) Jmin 225 0.4 mm/min (6.8x10 ⁻³)	air	na
Rinaldi et al uc	CT	J	J	0.18	0.23	1.41	0.008	0.009	0.11	0.48	0.48	0.045	0.13	na	1.5 to 7.5 x 10 ⁻⁶ & 2.5 x 10 ⁻⁴ mm/s	na	562 Mpa	288	Jmin 10 ⁻⁴ mm/s Got 50% SCC 10 ⁻⁴ mm/s	air and 200 ppb DOW demineralized water	na
Chu et al	T	UTS RA Z	0.19 0.25	0.15 0.42	0.22	12.2	0.009	0.009	0.11	0.48	0.48	0.045	0.13	na	1.5 to 7.5 x 10 ⁻⁶ & 2.5 x 10 ⁻⁴ mm/s	8 x 10 ⁻⁶	200 for 20 Cr 250 for 25Cr	T 20-280	SCC max 200 for 20 Cr 250 for 25Cr	air & 3.5% NaCl	na

Appendix 4.

1. Apparent Negative crack growth [243].

One of the major problems arising when testing during the unloading compliance is that of apparent negative crack growth. Many researchers have experienced this problem but Voss et al [243] gives a concise overview of the mechanisms responsible for its occurrence. Voss did tests on various steels and the implications of this apparent negative crack growth are outlined below. Voss did tests on compact tension specimens according to ASTM E 813 (the standard relating to J testing at the time until it was superseded in 1997, and then again in 2000). The specimens had relative crack lengths of $a/W = 0.6$ and 20% side grooves. But with pinhole diameters of $0.25W$ instead of the reduced pin diameter recommended in the standard. The thickness B equaled $W/2$ i.e 25mm, though some of the specimens had a reduced thickness of $W/4$. He proposed an alternative design of the clevises to minimise frictional effects based on his findings from the tests done. The following extracts are taken from his papers.

Apparent negative crack growth as a possible source of error in determining J_{1C} , from partial unloading compliance experiments may be caused by insufficient operation of flat bottom holes. This may result in non conservative J_{1C} values as demonstrated by a quantitative estimation of the effect for a special model. An alternative clevis design is presented that decreases the risk of plastic deformation of the devices and essentially eliminates this problem, even for high-temperature applications.

Particularly during tests at elevated temperature load, relaxation effects may cause errors in compliance measurements. Waiting for a nearly constant load for a few minutes will increase the quality of crack length determination. The difference between compliances calculated for unloading and reloading is a useful measure for the technical quality of the data.

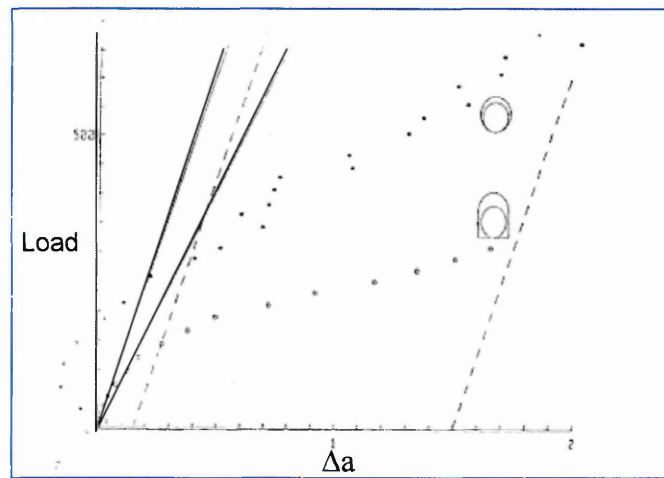
Depending on the scatter of results from the experiment, the point $\Delta a = 0$ is defined with some uncertainty thus influencing the accuracy of J_{1C} . For other evaluations, for example, full J - R curve development, this error is less important.

The conditions of ASTM E 813 to validate $J_Q \approx J_{1C}$ for clustered data points

are not sufficient. A wider spread and perhaps more than four valid data points should be required.

Figure 1 shows two J (Δa) resistance curves of different steel specimens. The upper one shows apparent negative crack growth, well known to arise sometimes in partial unloading compliance tests, the lower one does not. One possible reason for negative crack growth indicated by a round clevis hole in Figure 1 will be discussed, and an alternative clevis design to avoid this error indicated by a flat bottom hole will be proposed. The ASTM standard proposes flat bottom holes or roller bearings in the clevises for bolt loading of compact specimens to avoid friction effects. Roller bearings are difficult to handle and have some problems at elevated test temperatures. Use of flat bottom holes instead may result in negative crack growth [243].

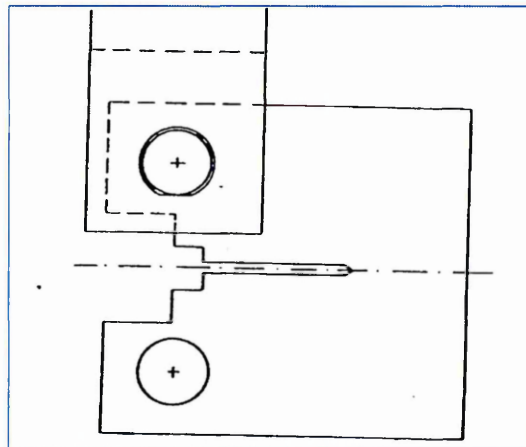
Figure 1.



Qualitatively different J – R curves (for different steels) measured with; round clevis holes, showing negative crack growth and flat bottom holes showing no negative crack growth.

Figure 2 shows a compact specimen with a clevis with flat bottom holes (schematically).

Figure 2.



By loading the specimen (Fig. 3) the loading bolts bend and may cause plastic deformation of the flat surfaces of the clevis in the regions marked by arrows.

Figure 3.

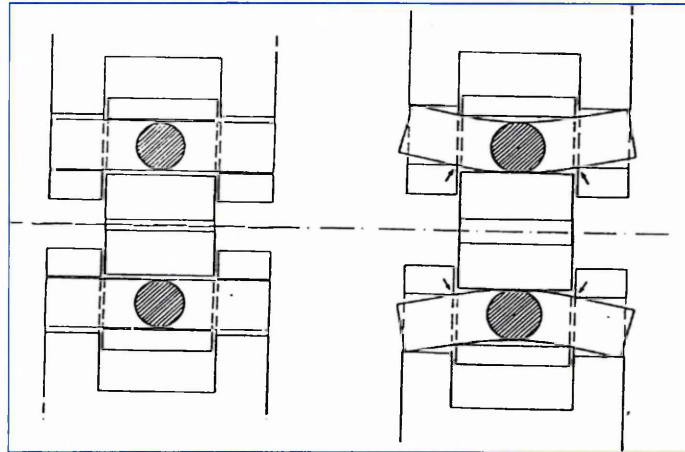


Figure 4 shows side views of the contact area of bolt and clevises.

(a). Without load.

(b). With plastic indentation by vertical loading.

(c). The effect of additional rotation of the loading bolt, necessary to maintain mechanical equilibrium while the crack is opened by loading.

Figure 4.

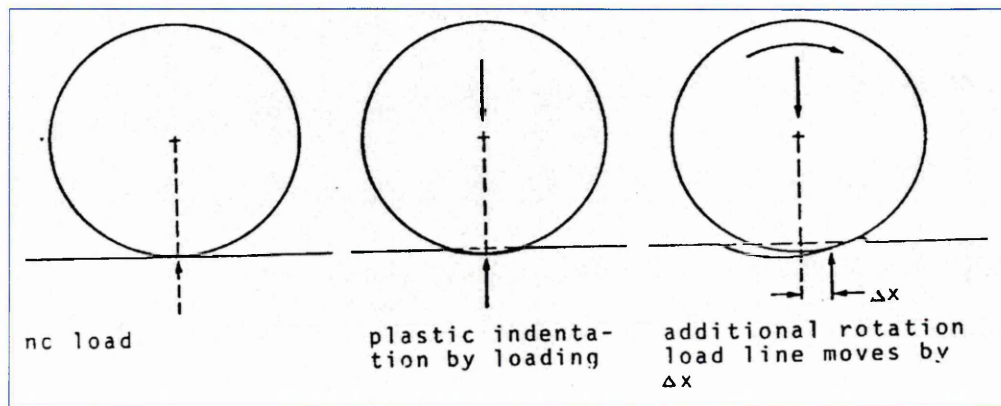
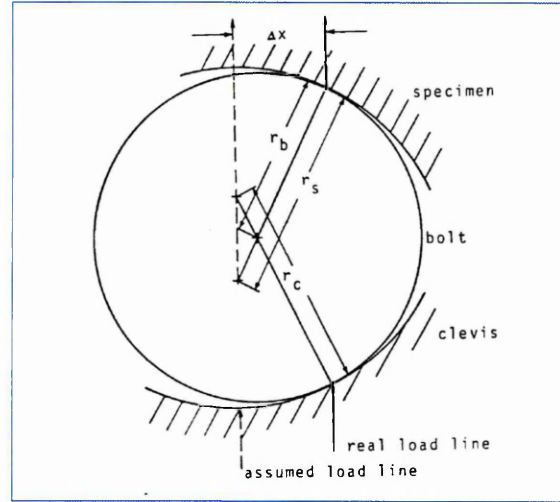


Figure 5 models this situation by loading the specimen (radius of the holes r_s) by a bolt (radius r_b) rolling on a circular surface of the clevis hole (radius r_c)

Figure 5.



At a displacement V_{LL} measured in the load line position each half of the specimen near the load line is tilted relative to the crack plane by an angle α_s . Assuming a rotation centre in front of the crack tip (crack length a) on the ligament (size b) at a distance $\varepsilon \cdot b$ ($\varepsilon \approx 0.3$) α_s is approximately given by.

$$\alpha_s = \tan \alpha_s = V_{LL} / (2(a + \varepsilon + b)) \quad (1)$$

Because of this rotation of the bolt hole region of the specimen the lines of contact of the specimen, the bolt and the clevis respectively must move towards the crack tip by a distance Δx quantified below. The assumed load line for compliance evaluation and crack length calculation passes through the centre of the bolt hole in the specimen (dashed arrows in Fig. 5). But the real load line is at a distance Δx towards the crack tip and the measured force F_m or a difference ΔF_m during a partial unloading will be greater compared to the assumed load line position. This causes an under-estimation of the compliance and the crack length and consequently results in negative Δa values before real crack growth. Assuming free rolling of the contacting surfaces without any slip Δx is by:

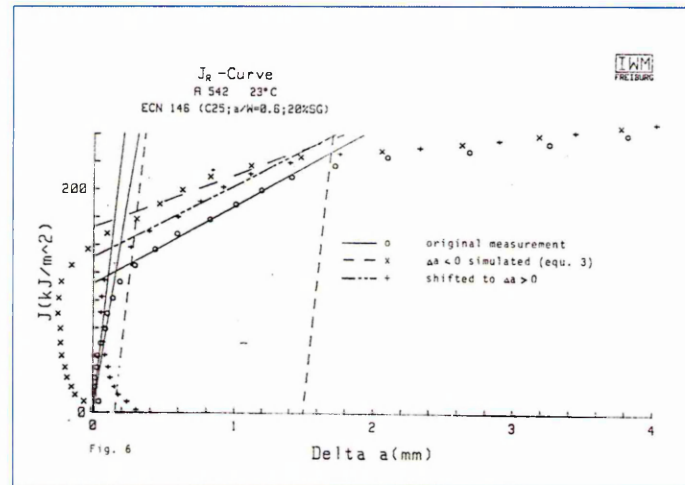
$$\Delta x = r_s + \sin(\alpha_s - r_s / (r_s + r_c - 2r_b)) \quad (2)$$

and the measured compliance y may be corrected for this error by.

$$C_{corr} = C_m \cdot \frac{a + \varepsilon \cdot b}{a + \varepsilon \cdot b - \Delta x} \quad (3)$$

In practice the correction by equation 3 normally will not be applicable because r_c ($\approx r_b$) will be an unknown and not constant number if caused by plastic indentation. For flat bottom holes ($r_c =$ tends to infinity) follows from equation 2 $\Delta x = 0$. For reasonable assumptions (CT 25; $r_s = 6.25$ mm, $r_b = 6$ mm $r_c = 6$ mm) the consequences of this model are demonstrated in Fig. 6 for a real experiment without negative crack growth by introducing the error by the inverse of equation 3 resulting in a shape of the new $J(\Delta a)$ - curve and $\Delta a_{min} = -0.25$ mm similar to Fig. 1. Obviously the value of $J_{1C} = 173 = \text{kJ/m}^2$ is greater than the correct one $J_{1C} = 122 \text{ kJ/m}^2$, but even correcting for the effect of negative Δa by shifting all points to positive Δa values with the most negative point on the blunting line results in $J_{1C} = 147 \text{ kJ/m}^2$ greater than the correct one. So apparent negative crack growth may result in non conservative J_{1C} estimations.

Figure 6.



To avoid this effect of possible plastic deformations sometimes disturbing results measured with flat bottom hole clevises an alternative design was developed and tested successfully. Figures 7 and 8 (comparable to Figs. 2 and 3) show that hardened inserts allow for tilting of the flat bottom planes if the loading bolts are bending. So line loads are applied instead of point loads (Fig. 3, arrows) thereby decreasing pressure and consequently minimizing risk of plastic deformation.

Clevises of this type were used at temperatures up to 600°C without negative crack growth and with low scatter of crack length measurements.

Figure 7.

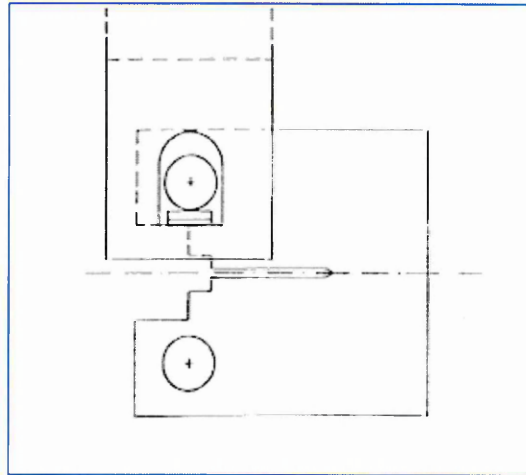
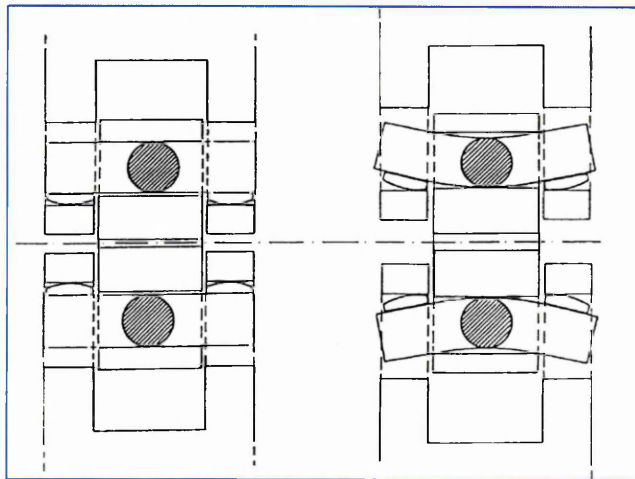


Figure 8.



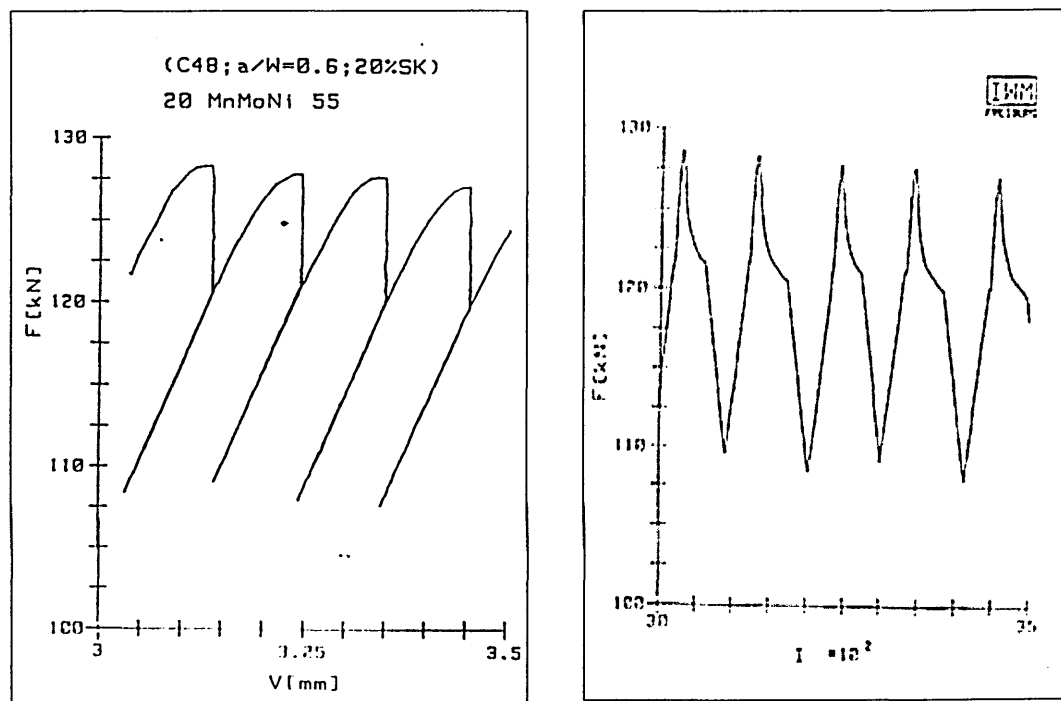
2. Relaxation.

Especially in tests at elevated temperatures (e.g. range of service temperature of light water reactors 300°C) time dependent effects in the specimen may cause problems for the crack length determination from the compliance measured in partial unloading. Two examples of CT 48 specimens (B=48 mm, W = 96 mm) will be discussed .

Figure 9 shows part of a load (F) vs. displacement (V) diagram measured at 300°C, (steel 20 Mn Mo Ni 55 Unified Classified System UNI k12539) with load drops of about 5% during constant displacement control up to 3 min. Though the nearly exponential load drop did not reach a (nearly) constant level during this time the crack length could be estimated from the compliance. The

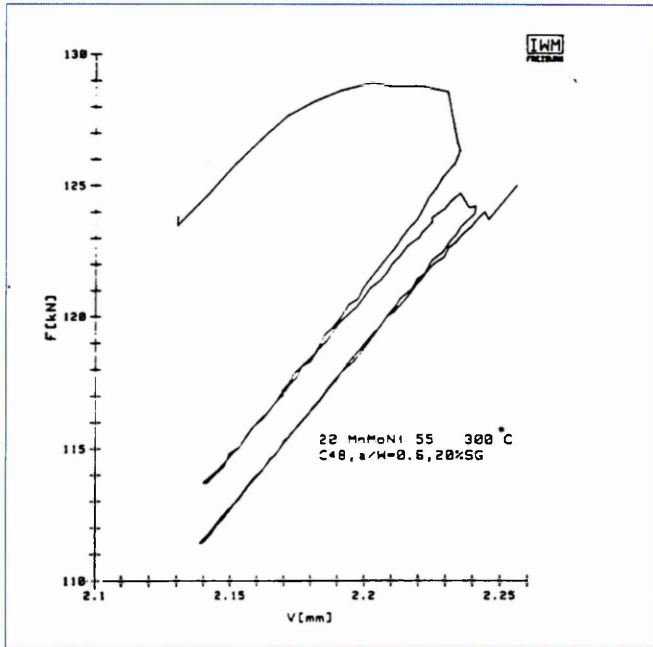
differences in crack lengths calculated from unloading and reloading compliance respectively showed an (apparent) crack growth of (0.2 + 0.2mm) during the unloading cycles. In spite of these differences the final crack length agreed with the crack surface measurement within 0.2 mm. Even without the 3 min relaxation time reasonable J_R curves can be measured. Figure 10 shows one of several unloadings without relaxation followed immediately by a second unloading in a test with a displacement velocity of about 1 mm/mm. Caused by the visible curvature of the unloading and reloading paths the differences of estimated crack lengths were 1.6 mm for the first cycle and 0.45 mm for the second one. The mean values differed by only 0.24 mm (0.02 mm to 0.29 mm for several pairs of unloadings) comparable to the "absolute accuracy" measured by the difference of 0.2 mm between the final crack lengths from the last single cycle unloading and the crack surface measurement for this test.

Figure 9.



From these results typical for several more tests it may be deduced that reliable $J(\Delta a)$ - curves may be measured. But as discussed by Voss [243] relatively small errors in the initial crack length determination (definition of the point $\Delta a = 0$) may cause relatively great changes in the extrapolated J_{1C} according to the ASTM standard.

Figure 10.



Appendix 5. Data used for Figure 97 da/dN v ΔK for F8104 and F8105.

Crack Length		1000 F8105 18.5			da/dn	measured	growth from
START	FINISH	Frequency (Hz).	no of cycles	ΔK	m/cycle	growth	p.d
18.5	19.63	5(1)	115832	13.84	9.76E-09	1.13	1.55
20.26	21.8	5(3)	47416	21.044	3.25E-08	1.54	1.4
22.34	23.97	5(5)	17702	29.78	9.21E-08	1.63	1.64
25.15	26.87	5(7)	8971	40.254	1.92E-07	1.72	2.25
29.16	31.41	5(9)	8201	50.87	2.74E-07	2.25	2
19.63	20.26	0.0167(2)	44342	13.22	1.42E-08	0.63	0.48
21.8	22.34	0.0167(4)	25897	20.182	2.09E-08	0.54	0.535
23.97	25.15	0.0167(6)	26508	28.95	4.45E-08	1.18	1.18
26.87	29.16	0.0167(8)	17149	43.84	1.34E-07	2.29	1.9
31.41	33.68	0.0167(10)	9629	57.338	2.36E-07	2.27	before apparent
33.68	35.93	0.0167(10)	9629	72.67	2.34E-07	2.25	change in fracture mode

Blue denotes steps at 5Hz, red steps done at 0.0167Hz.

Bracketed numbers in green denote step number

K_{MAX}	71.67	MPam ^{0.5}
Growth to end of step 9 by p.d	12.935	mm
Measured growth to end of step 9	12.91	mm
Growth to change in fracture mode in step 10	15.18	mm
Total cycles	321647	

No p.d measurements after step 9

Crack Length		F8104 18.5			da/dN	measured	growth from
START	FINISH	Frequency (Hz).	no of cycles	ΔK	m/cycle	growth	p.d
18.5	19.67	5(1)	97672	13.35	1.2E-08	1.17	1.3
20.14	21.649	5(3)	30331	22.241	4.98E-08	1.509	1.5
22.467	24.267	5(5)	13909	31.25	1.29E-07	1.8	1.8
25.807	27.607	5(7)	6701	45.6	2.69E-07	1.8	1.8
29.857	31.827	4(9)	2687	63.43	7.33E-07	1.97	2
34.227	34.766	3.5(11)	210	61.49	2.57E-06	0.539	before change in fracture mode
19.67	20.14	0.0167(2)	45520	13.84	1.03E-08	0.47	0.813
21.649	22.467	0.0167(4)	18728	21.32	4.37E-08	0.818	0.98
24.267	25.807	0.0167(6)	16965	28.28	9.08E-08	1.54	1.88
27.607	29.857	0.0167(8)	6957	48.06	3.23E-07	2.25	2.4
31.827	34.227	0.0167(10)	3948	62.06	6.08E-07	2.4	2.4

Blue denotes steps at 5, 4, and 3.5Hz, red steps done at 0.0167Hz.

Bracketed numbers in green denote step

K_{MAX}	76.86	MPam ^{0.5}
Growth to end of step 10 by p.d.	16.873	
Measured growth to end of step 10	16.266	
Growth to change in fracture mode in step 10	15.727	
Total cycles	243628	
Difference	78019	

Appendix 6.

Literature Review on the Micro-mechanisms and Models of Ductile Fracture.

Introduction.

The ductile fracture process described in the introduction consists of three principal stages, in which voids nucleate, grow, and finally coalesce and then failure of the specimen. The microvoid nucleation problem is greatly complicated by a range of particle types that can exist in a commercially produced alloy system and this can result in a variety of microvoid nucleation mechanisms operating simultaneously [1,2].

Most commercial steels contain more than one population of inclusions. They have several void nucleating properties which leads to the assumption that there is more than one critical value for void nucleation, one for each population. In fact microsections of steels often show the bigger MnS inclusions already loosed from the matrix, but smaller TiC or carbides still being fixed and unbroken [3]. Only higher strains can cause void nucleation at these smaller inclusions, calculations of Ashby et al [8] showed this assumption is reasonable.

It follows that an adequate model of the microvoid nucleation process needs to be developed on the basis of at least two populations in a given material [2].

1. Nucleation of Voids.

In the nucleation of voids at first high strength inclusions are released from the matrix or break in a brittle manner, their behaviour depends on the mechanical properties of the matrix and inclusions as well on inclusion shape. This can cause different stress distributions in the inclusion and at their surfaces. Because of the higher dislocation density near larger inclusions, the induced stress in larger inclusions is higher as well. If the void nucleation is stress controlled a smaller strain is needed for larger inclusions than for smaller ones. These observations as well as density measurements reveal that only a very small plastic strain is required to cause first void nucleation [3].

There are several criteria explaining void nucleation they can be divided into:

- (i). Stress controlled.
- (ii). Strain controlled.
- (iii). Energy controlled.

(i). Stress controlled models.

Models of microvoid nucleation at the sites of inclusions and second phase particles can be divided into two groups. The first group is concerned with particles of the order $2\mu\text{m}$ diameter or less, where dislocation models are required to estimate the local stress concentration effects at the particle matrix interface (i.e. the nucleation process) [1,2]. This is the criteria used in the Goods and Brown model [4].

The second group of nucleation models [6] is concerned with particles greater than $2\mu\text{m}$ where plastic continuum models are required to estimate the local stress concentration effects at the particle matrix interface (classical continuum mechanics is based on the fundamental idea that all material bodies possess continuous mass densities, and that the laws of motion and the axioms of constitution are valid for every part of the body, no matter how small they may be).

Important points to note regarding these two alternative models of microvoid nucleation is that in general that for particles less than $1\mu\text{m}$, is that the nucleation strain is strongly influenced by the particle radius, the smaller the radius the smaller the nucleation strain [1]. This effect is a direct result of the microvoid dislocation storage and elevation of the local flow stress as the particle radius increases [4,6].

In contrast the continuum model of plasticity model for relatively large particles (greater than $1\mu\text{m}$) shows no influence of absolute particle size on the magnitude on the interface stress and the corresponding nucleation strain [7].

Argon and Safoglu [5] gave a stress controlled criterion for the nucleation of voids, whereby the sum of the average stress and the Von Mises stress reaches a critical value, inclusions will be released from the surrounding matrix and cause the nucleation of voids, they used the continuum plasticity approach, and based their model on a non deformable spheroidal inclusion in a perfectly elastic or plastic matrix. They proposed that the inclusion matrix interface

breaks at a critical stress: $\sigma_c = \sigma_{eq} + \sigma_m$ where σ_m is the hydrostatic stress and σ_{eq} is the Von Mises equivalent stress which is an implicit function of the far field plastic deformation, Argon also gave an equation to calculate critical strain $\sigma_c = \sigma_m + k\sigma_{eq}$ where k is a function of the particle shape and:

$$\sigma_{eq} = (\sigma_1 - \sigma_2)^2 + (\sigma_2 - \sigma_3)^2 + (\sigma_3 - \sigma_1)^2$$

In a model proposed by Beremin [6] using finite element analysis, he carried out experiments on cavity formation from manganese sulphide inclusions on A508 steel and in his model considered the shape and orientation of the inclusions by introducing a shape factor depending on these values.

$$\sigma_c = \sum_1 + \sigma_{inh} \quad \text{where } \sigma_{inh} = \lambda E_p \cdot \epsilon_{eq}$$

λ is a function of the ellipsoidal shape ($\lambda = 1$ for a spherical particle).

\sum_1 is the maximum principal stress.

σ_c is the maximum principal stress to which the material is subjected.

σ_q is the Von Mises equivalent stress.

ϵ_{eq} is the equivalent plastic strain.

E_p is Young's Modulus.

σ_{inh} is the macroscopic principal stress required to initiate cavities.

These criteria take into account the effect of strain on nucleation in a direct way by calculating the Von Mises stress. Beremins model is based on; if the sum of certain stresses exceed a critical value then nucleation starts.

(ii). Strain controlled models.

This group contains the different strain based models, proposing that voids will be nucleated if a certain strain is exceeded. Tanaka [7] in this model proposed that there is a size below which the fracture strain is inversely proportional to the square root of the particle, and there is a size above which the applied stress causes cavitation without plastic strain.

Ashby et al [8] model consists of a dual population model of microvoid nucleation in spheroidised low alloy steels, to account for the disproportionate increase in the area fraction of microvoids. Ashby's model also contains the

mechanical properties of the matrix as well as the diameter of the inclusions and the different Young's Moduli.

(iii). Energy controlled models.

The base criteria for the majority of these models is that a necessary condition for the nucleation of a microvoid by decohesion of the particle matrix interface is that the elastic strain energy released by the particle is at least equal to the newly created surface.

The Tanaka, Mori and Nakamura [7] model shows that in a purely elastic situation, the energy criterion is always satisfied for particles of about 250Å diameter, almost upon yielding. The model also showed that for cavity formation that for particles larger than 10 – 20 nm the decohesion of the inclusion matrix is energetically favourable, and for larger particles the decohesion criterion is a critical stress σ_c .

Argon [5] in his model states that *"The energy requirement is only a necessary one and that the actual separation requires reaching the interfacial strength of the matrix."*

2. Void growth models.

Numerous models have been presented in attempts to describe the plastic growth of microvoids in plastic growth fields, but the most successful model for obtaining the continuous volumetric growth and shape change of individual models is the Rice Tracy [9] model. If the Rice –Tracy equations are integrated it can be shown that except at very high mean normal stress levels, that the growth of a microvoid should be predominantly an extensional growth in the direction of the maximum principal stress accompanied by only a relatively small dilational or volumetric growth [1,2].

The process of void growth is strongly influenced by the state of stress during plastic deformation. The higher the dominating tensile stresses (the higher the triaxiality) the higher is the void growth rate. Zero triaxialities predominantly cause a change of void shape rather than a change in the volume. (Hydrostatic stresses or mean stress σ_H causes only a change in volume and not in shape in an isotropic medium, deviatoric stress components bring about a change of shape in the body and influence the plastic deformation) [1,2,3].

The criteria chosen on which to base the model is also important for example Rice and Tracy [9] and McClintock [10] in their analysis for the growth of a single void in an infinite block of plastic material show that void growth is strongly dependant on the level of hydrostatic tension, so that fracture of by the coalescence of voids is promoted by a high level of triaxial tension. They found the void growth rate of the ideal cylindrical or spherical void in an infinite matrix, increased exponentially with the triaxiality of the stress. Other models such as Gurson [11] pay particular attention to the volume fraction in the flow behaviour of the material. This model is based on the assumption that the complete ductile fracture process of void growth and coalescence can be described in terms of the weak dilational response of an elastic plastic continuum, which displays the macroscopic effects that would result from the distribution of spherical microvoids but does not actually contain microvoids. In this approach ductile fracture is regarded as the result of an instability in the weak dilational plastic flow field allowing the formation of an intense localised shear band. It is further assumed that void coalescence by internal necking of the intervoid matrix is a secondary effect which can only develop after the formation of an intense shear band. Hence the strong dilational response associated with Gurson's model has been inadvertently eliminated from the model. This is one of the major shortcomings of the model according to Thomason [2].

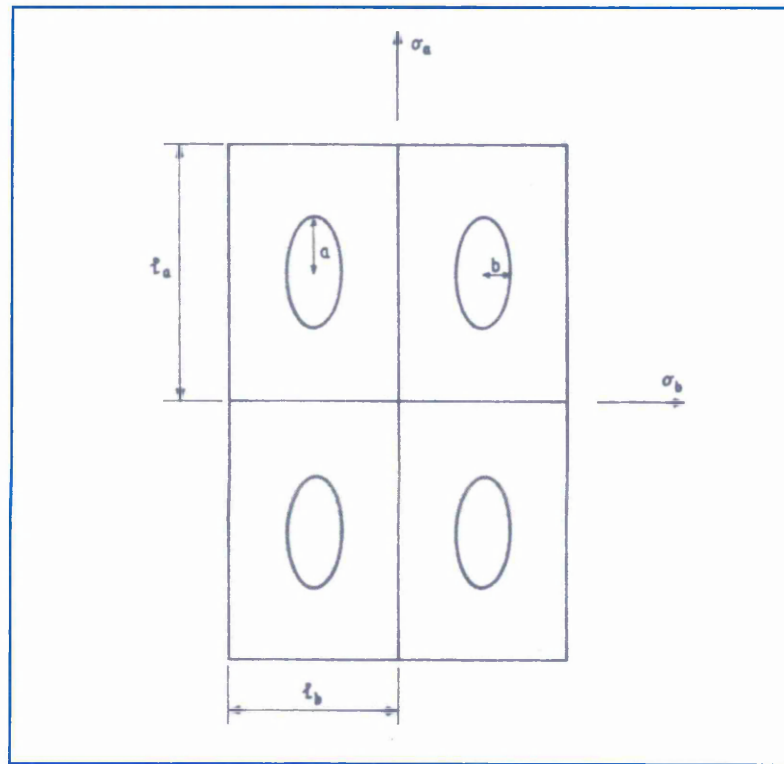
The Needleman and Tvergaard model [12] takes into account the influence of the voids and their interaction, their experiments were carried out on round tensile bars, notched and unnotched specimens were used. They were the first modellers who analysed the fracture of a round tensile bar using the Gurson model. Using finite element analysis, they modified Gurson's model by introducing three additional factors q_1 , q_2 , q_3 , to take account of the final stage of void growth by coalescence of voids, which occurs after a critical void fraction is reached f_c . They considered both a blunt and sharp notch geometry to determine what effect high triaxiality and high strain had on the specimens. They found that the axisymmetric specimens failed at the centre of the notched sections, whereas failure initiation at the surface is found in plane strain specimens with sharp notches. This modified Gurson model is one of the most used models to describe the phenomena of ductile tearing.

A brief overview of the McClintock model is included to give an insight

into some of the mechanisms responsible for hole growth.

McClintock's model [10] consists of a plastically deforming matrix containing a regular array of pre-existing pre – existing cylindrical holes of elliptical cross section, each of which may be envisaged sitting inside an identical cell as shown in Figure 1.

Figure 1. McClintocks Fracture Model [14].



The matrix is generated in plane strain such that the strain parallel to the cylinder axis is uniform but not zero. The dimensions of the cell l_a and l_b correspond to the hole spacings in these directions, and a and b are the corresponding semi – axis of the holes (a is larger semi – axis and l_a the corresponding hole spacing). Following McClintock's notation, introduce the two hole growth factors F_a and F_b .

$$F_a = (a/l_a)/(a_0/l_a^0).$$

$$F_b = (b/l_b)/(a_0/l_b^0).$$

where the subscript '0' indicates an initial value. In McClintock's model failure occurs when there is a complete loss of cross section i.e. when $a = \frac{1}{2} l_a$ or $b = \frac{1}{2} l_b$

$$F_a - F_a^f = \frac{1}{2} (l_a^0/a_0).$$

$$F_b - F_b^f = \frac{1}{2} (l_b^0/b_0).$$

The equivalent plastic strain at failure by coalescence in the a direction is given by

$$\bar{e}^f = \frac{(1-n)\ln(l_0/b_0)}{\sinh\left[\frac{1}{2}\sqrt{3}(1-n)\left(\frac{\sigma_a + \sigma_b}{\sigma}\right)\right] + \frac{3}{4}\left(\frac{\sigma_b + \sigma_a}{\sigma}\right)}$$

where σ_a and σ_b are the principal stresses in the remote matrix in the directions of the axes of the holes, and n is the hardening exponent in the Ludwik power law relation.

$$\bar{e} = \sigma_0 \left(\bar{e}^p\right)^n$$

McClintock neglected hole nucleation and identified the original hole size with the inclusion term $l_0 \sqrt{2b_0}$.

nb. In metals flow is induced by shear stresses, which cause dislocation movement, and which may be measured by an effective stress σ which is proportional to the root mean square of the principle shear stresses.

$$\bar{\sigma} = \left[\frac{1}{2}\left\{(\sigma_1 - \sigma_2)^2 + (\sigma_2 - \sigma_3)^2 + (\sigma_3 - \sigma_1)^2\right\}\right]^{\frac{1}{2}}$$

The extent of plastic flow is usually expressed by an analogous quantity, the effective plastic strain increment $d\bar{e}^p$ which is proportional to the square root of the principal shear increments.

$$d\bar{e}^p = \left[\frac{2}{9}\left\{\left(d\bar{e}_1^p - d\bar{e}_2^p\right)^2 + \left(d\bar{e}_2^p - d\bar{e}_3^p\right)^2 + \left(d\bar{e}_3^p - d\bar{e}_1^p\right)^2\right\}\right]^{\frac{1}{2}}$$

The effective stress and plastic strain being connected by a stress strain relation such as the Ludwik relation described above. Both e^p and σ are unaffected by a third important parameter the mean stress.

$$\sigma_m = \frac{1}{3}(\sigma_1 + \sigma_2 + \sigma_3)$$

which may, however be combined with σ into a single non dimensionless parameter $\sigma_m = \sqrt{\bar{\sigma}}$ which characterises a stress state and is a measure of its **triaxiality**.

The theory of perfectly (or ideally plastic) solids assumes that the yield function is unaffected by plastic deformation. If the material exhibits increasing resistance to plastic deformation with plastic straining, the simplest approach to

handle such strain hardening is to invoke the so called isotropic hardening model. During isotropic hardening the yield surface expands uniformly, but it has a fixed shape and its centre remains fixed in stress space [2].

The use of isotropic hardening for tension compression cyclic deformation in many metallic materials does not rationalise the differences in elastic limit commonly found between forward and reverse loading. In an attempt to account for this so called Bauschinger effect an alternative hardening rule, known as kinematic hardening has been proposed. In the classical model of kinematic hardening the yield surface does not change its size or shape, but merely translates in the direction of its normal.

The extensional and dilational plastic void growth, following microvoid nucleation, can be closely estimated by the Rice and Tracy [9] growth model it also allows an estimate of the plastic void growth strain ε_{1G} needed to bring the intervoid matrix to the point where the limit load stress σ_{1C} has been reduced to the level of σ_1 , thus giving the condition for incipient ductile fracture by microvoid coalescence and the corresponding ductile fracture strain [1].

$$\sigma_{1F} = \sigma_{1n} + \sigma_{1G}$$

where σ_{1F} is the ductile fracture strain, σ_{1n} , is the void nucleation strain.

3. Void Coalescence.

Coalescence of voids is equal to the initiation of a microcrack. If voids are nucleated in the centre of the material, further strain will cause their coalescence by shearing, by growing together or by nucleating further microvoids between them. If the voids are nucleated near a crack tip initiation will be caused by the connection of the crack tip and the nearest void, this process is equal to stable crack growth [1].

Several models have been proposed using only a single parameter, for example a value of stress or strain, but several models have included more than one parameter. Hancock and McKenzie [13] showed that a critical strain must be exceeded over a certain distance to initiate a microcrack. They carried out series of tests on notched tensile specimens, to study the influence of the stress

state on the ductile failure mechanism in high strength steels. Various circumferential notches on round specimens were used to obtain different degrees of stress triaxiality, as measured by the ratio of the mean tensile stress to the effective Von Mises stress, and it was found that a higher stress triaxiality results in initiation at a smaller effective plastic strain.

Other models are based on a critical stress to cause crack initiation, while others use a critical void fraction. Marini et al [14] based their model on the critical cavity void growth rate from the Rice – Tracey model [9]. Other factors affecting the nucleation, growth, and coalescence process, are the geometry of the specimen, the mode of loading, the load history, the orientation of the specimen, its toughness and strength and the temperature at which the tests are carried out.

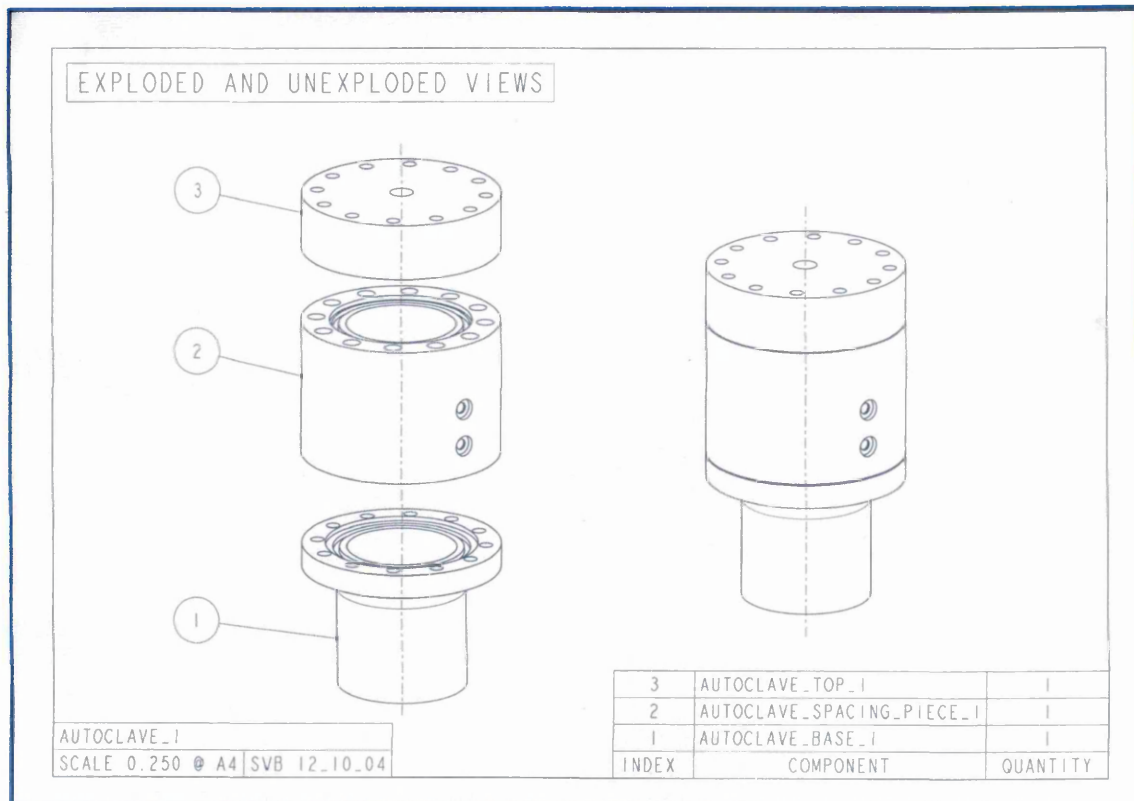
To conclude the advent of ductile fracture depends on both the current stress and strain rates as well as the strain history. No criterion based on either stress state or strain rate alone is satisfactory. Although a complete theory of ductile fracture is very complex, certain features are clear. Fracture is promoted by high levels of hydrostatic tension, large strains and concentrations of strain in narrow bands.

References.

1. Thomason, P.F., "A View on Ductile Fracture Modelling", *Fatigue and Fracture of Engineering Materials and Structures*, 1998, 21, pp. 1105 - 1122
2. Thomason, P.F., "Ductile Fracture of Metals", 1990, ISBN 0-08-040178-3.
3. Arndt, J., and Dahl, W., "Micromechanisms of Fracture and Determination of Failure Curves", *Micromechanisms of Ductile Fracture and their Structural Significance*, Institute of Materials Second Griffith Conference, 13th - 15th September, 1995, Sheffield UK, pp. 120 - 130.
4. Goods S.H., and Brown, L.M., "The Nucleation of Cavities by Plastic Deformation", *Acta - Metallurgica* 1979, 27, pp. 1 - 15.
5. Argon, A.S., and Im, J., Safoglu, R., "Cavity Formation from Inclusions in Ductile Fracture", *Metallurgical Transactions* 1975, 6A, pp. 825 - 837.
6. Beremin, F.M., "Cavity Formation from Inclusions in Ductile Fracture of A508 Steel", *Metallurgical Transactions A*, 12 A, 1981, pp. 723 - 731.
7. Tanaka, K., Mori, T., and Nakamura, T., "Cavity Formation at the Interface of a Spherical Inclusion in a Plastically Deformed Matrix". *Philosophical Magazine*, 1970, pp. 267 - 269.
8. Ashby, M.F., Roy, G.Le., Embury, J.D., and Edwards, G., "A Model of Ductile Fracture based on the Nucleation and Growth of Voids", *Acta Metallurgica*, Volume 29, pp. 1509 - 1522, 1981.
9. Rice, J.R., and Tracey, D.M., "On the Enlargement of Voids in Triaxial Stress", *Journal of the Mechanics and Physics of Solids*, 1969, pp. 201 - 217.
10. F.A. McClintock, "A Criteria of Fracture by the Growth of Holes", *Journal of Applied Mechanics*, Transactions of the ASME, 35, 1968, pp. 363 - 371.
11. Gurson, A.L., "Continuum Theory of Ductile Rupture by Void Nucleation and Growth: Part 1 – Yield Criteria and Flow Rules for Porous Ductile Media", *Jour. of Engineering Materials Technology*, Trans. of the ASME, 1977, pp. 2 - 15.
12. Needleman, A., and Tvergaard, V., "An Analysis of Ductile Rupture in Round Bars", *Journal of the Mechanics and Physics of Solids*, 1984, Vol. 32, No. 6. pp. 461 - 490.
13. Hancock, J.W., and McKenzie, A.C., McClintock's model taken from "On the Mechanisms of Ductile Failure in High Strength Steels subjected to Multi-axial Stress-States". *Jour. Mech. Phys. Solids*, Vol. 24, pp, 147 - 169.
14. Marini, B., Mudry, F., and Pineau, A., "Ductile Rupture of A508 Steel under Non Radial Loading", *Eng. Fract. Mech.* Vol. 22, No. 3, pp. 375 - 386, 1985.

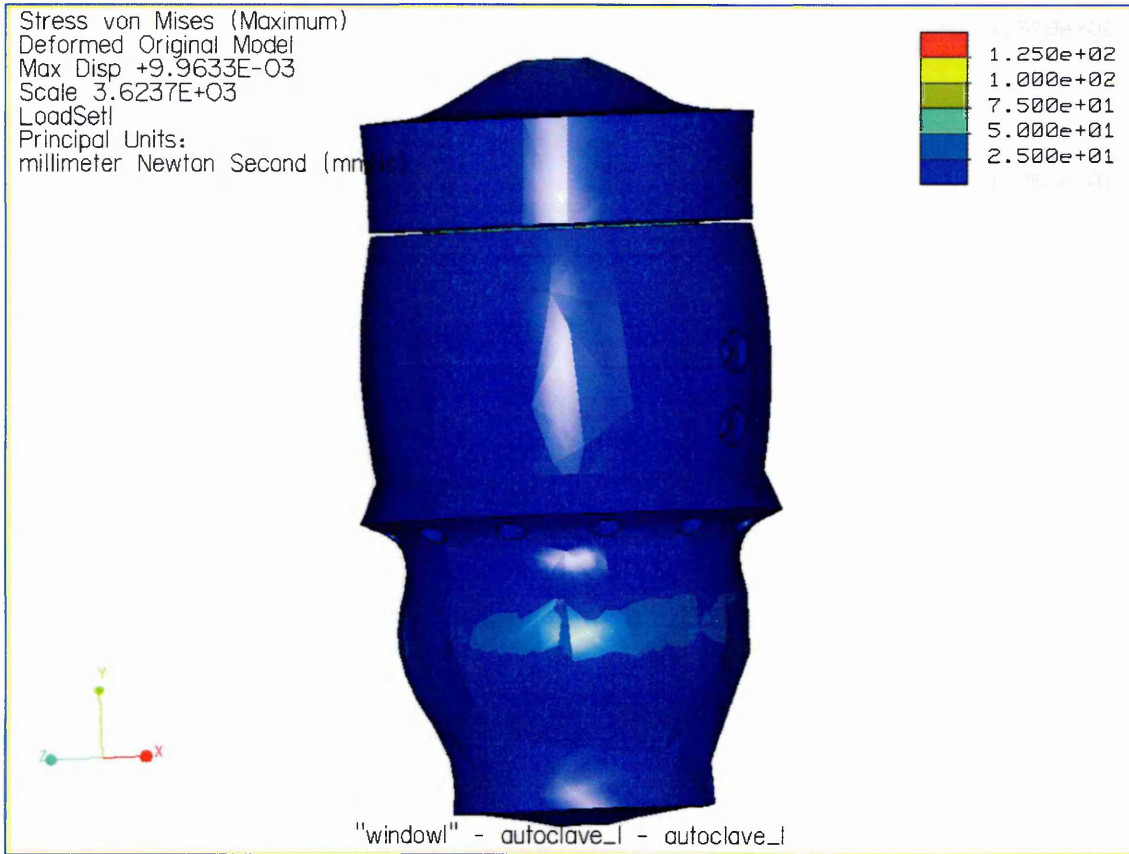
Appendix 7.

The three sections of the autoclave.

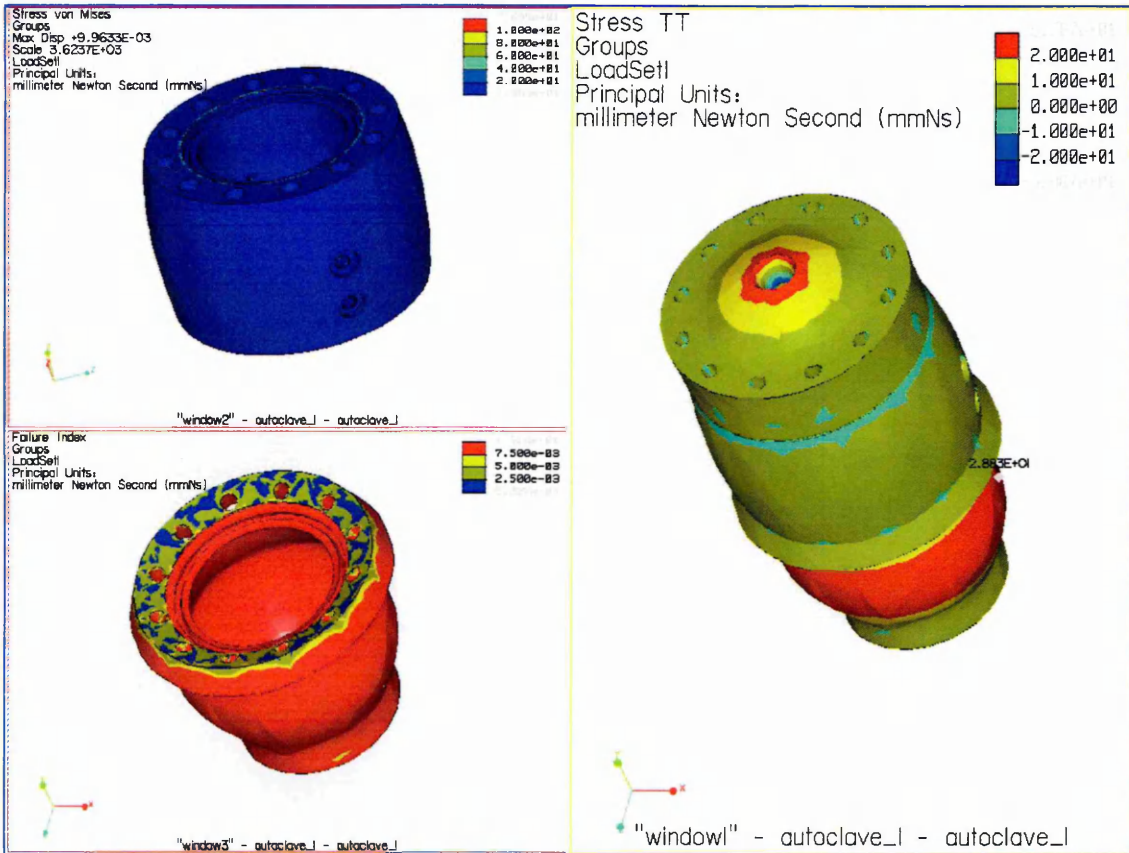


The autoclave used for aqueous J_{1C} fracture toughness testing was specifically designed for the purpose and finite element analysis was used to determine the maximum stresses that it could withstand. The holes in the mid section were to enable location of the clevises.

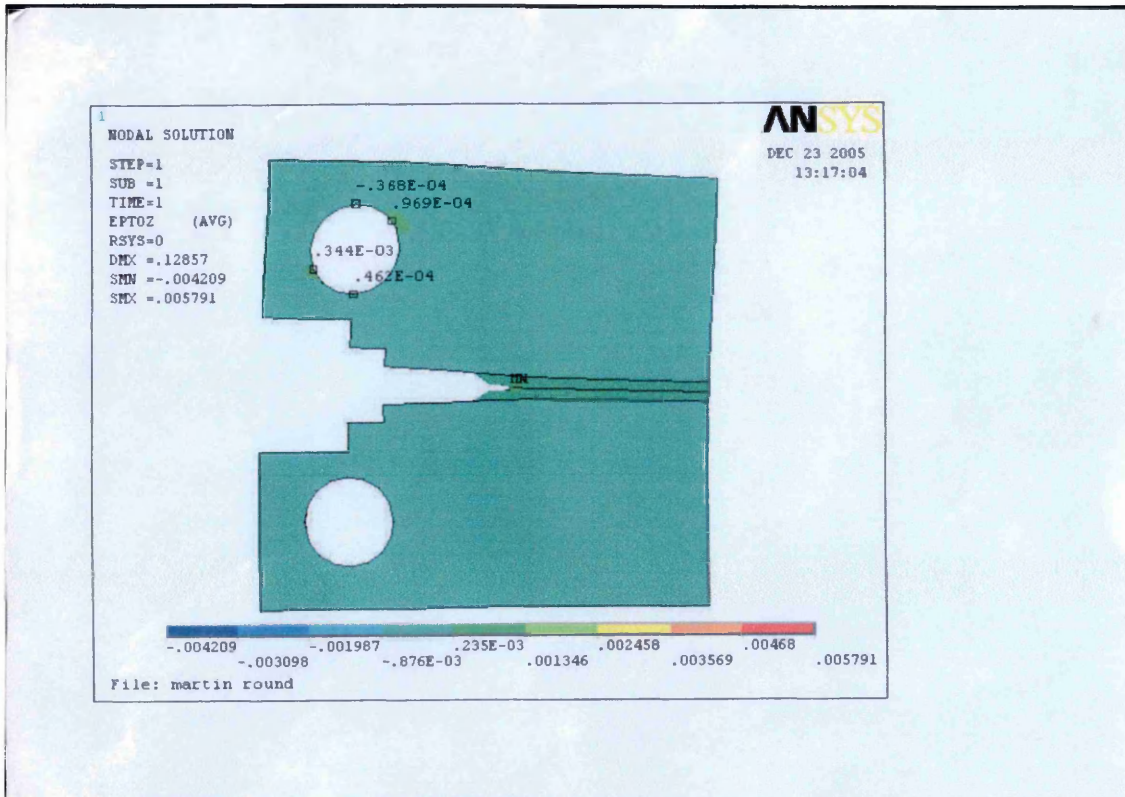
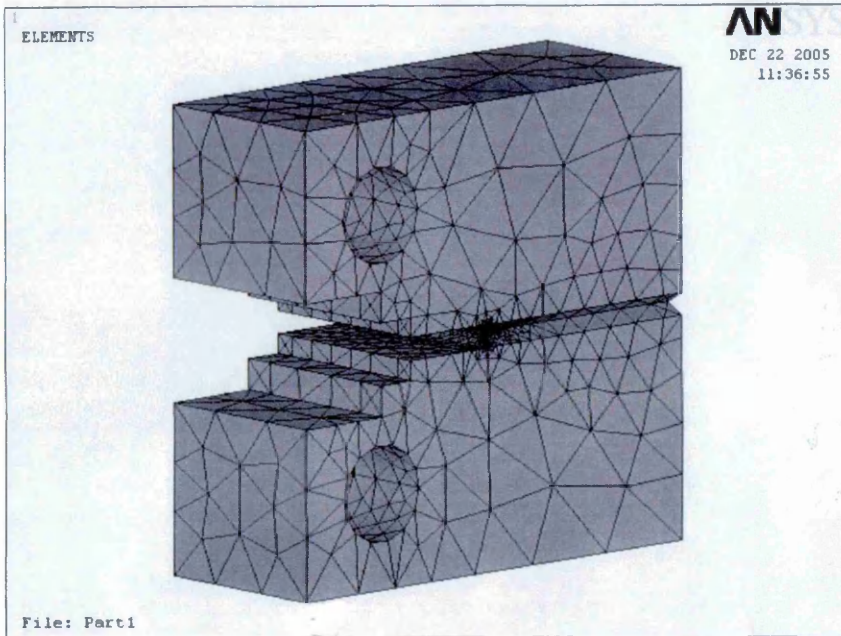
View of autoclave under an internal pressure (more than design pressure).



Exploded view of autoclave.



Appendix 8.



Appendix 9.

Figure 1 is taken from reference [272] work done by Wagner et al on the A48 steel heat. It shows the Internal friction (Q^{-1}) vs Temperature plot for the A48 and A42 steel heats. The Snoek peak marked 1 in Figure 1 is the condition (normalised) against which the comparison is being made for the A48 steel heat. It is assumed that the Snoek peak height is the total of the free nitrogen and free carbon ($N_F + C_F$). As Wagner quotes “the peak height can give a measure of the nitrogen (and carbon) content in the lattice”, and it can be inferred throughout the text that it is the total of $N_F + C_F$, as no values are specified.

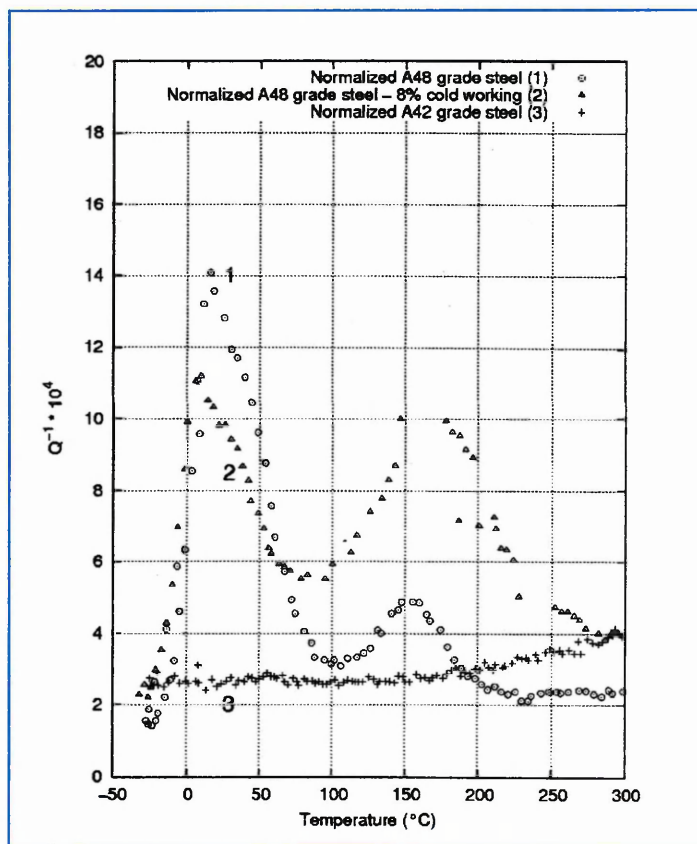


Figure 1. Internal friction Q^{-1} vs Temperature for A48 (normalised and cold worked conditions) and A42 steels [272].

The Snoek peak height (Q^{-1}) for the VS3783A steel heat was 11.667×10^{-4} for the total $N_F + C_F$ as shown in Figure 2.

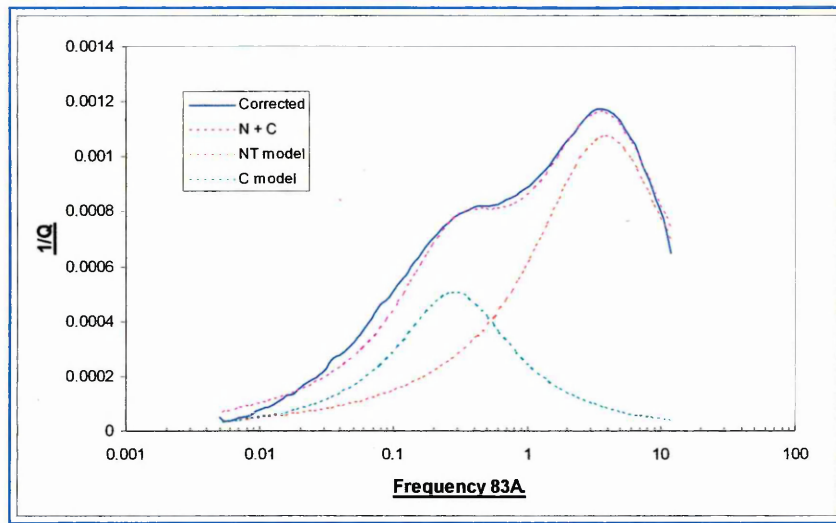


Figure 2. Internal friction analysis for VS3783A.

For VS3783B the Snoek peak height was 11.251×10^{-4} , as shown in Figure 3 (Figure 83 in the main body of text) both values obtained at 22.5°C at frequencies of 3.334 and 4.06 Hz respectively [257]. Wagner et al's [272] value for the Snoek peak height (Q^{-1}) for the A48 steel in the normalised condition is about 14×10^{-4} at 20°C . From Figure 1 it can be seen that Wagner's baseline starts at about 2×10^{-4} , whereas for this work it was zero corrected. So it is assumed that the A48 and VS3783 steel heats have comparable N_F and C_F interstitial content.

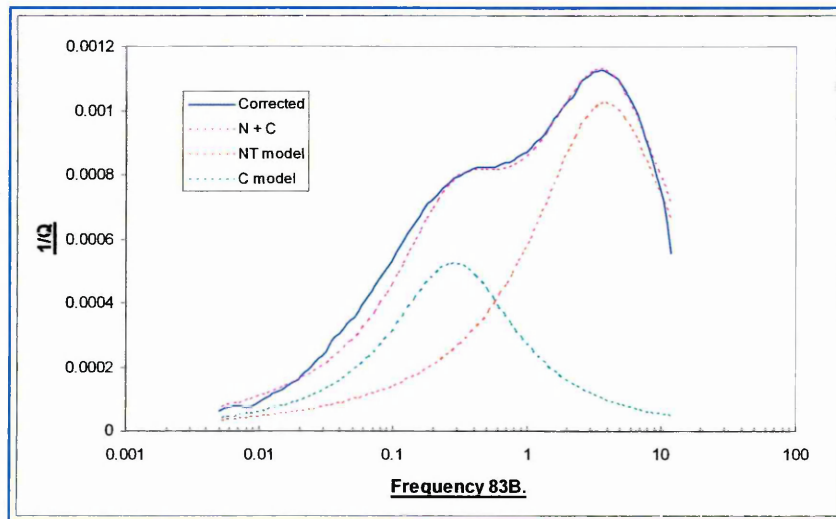


Figure 3. Internal friction analysis for VS3783B.